

**Development of techniques and
technology for full polarimetric radar
applied to concealed weapons
detection**

E J Blackhurst

PhD 2020

Development of techniques and technology for full polarimetric radar applied to concealed weapons detection

Edward Jason Blackhurst

A thesis submitted in partial fulfilment of the requirements of
the Manchester Metropolitan University for the degree of
Doctor of Philosophy

Department of Engineering
Faculty of Science and Engineering
Manchester Metropolitan University

July 2020

Abstract

One of the biggest threats to modern society is the increasing use by criminals and terrorists of concealed weapons and person born improvised explosive devices (PBIED).

Current highly mature security screening technologies using x-ray and metal detectors have limited deployment scenarios based on health and safety issues and operational range, respectively. Given that most clothing is greater than 90% transmissive in the microwave region, this spectral band is ideal for screening people for concealed threats. However, due to diffraction, imagery to screen subjects is limited due to the small number of pixels. In this regime, the exploitation of microwave polarimetry from the field of remote sensing has particular benefits, as it extracts maximum information content from a single pixel.

The work presented in this thesis has assembled a full polarimetric frequency stepped radar from a vector network analyser (VNA), a linear orthogonal mode transducer (OMT) of the turnstile type and a conical corrugated horn antenna. The system's characterisation by antenna pattern measurements, the measuring of canonical targets of the plane, dihedral, dipole and helical reflectors showed the system to be capable of making localised Sinclair matrix measurements of targets at ranges of two to three metres.

The work presents a calibration procedure comprising the VNA's internal calibration and an external calibration to compensate for dispersion and cross-polar leakage of system components. Static target measurements (canonical and various surrogate items) were analysed, using range gating for clutter rejection. Calibrated Sinclair parameter measurements compared with those from simple simulations, all software being programmed in Matlab.

Measurements of moving targets revealed the phenomenon of speckle, this introducing rapid changes in the Sinclair Parameters. Data analysis performed using the coherency matrix and the Cloude/Pottier decomposition minimised the effects of speckle in the processed data. Measurements show movement from particularly rough surfaces increased the parameter of the Cloude/Pottier entropy, the level of this being directly linked to the degree of speckle.

Application of the Huynen polarisation fork technique (a type of decomposition) has proved to aid the identification of static and moving targets. A detailed analysis of

the Huynen fork responses is made of the human torso on its own, weapons on their own and then weapons positioned against the human torso. Responses of non-dangerous objects such as keys and a smartphone are additionally presented.

Contents

Abstract	ii
Table of Figures.....	xii
List of tables	xxix
Acknowledgements.....	xxx
Introduction.....	xxxi
Aims and Objectives	xxxiv
Aim.....	xxxiv
Objectives	xxxiv
Contribution to Knowledge.....	xxxvi
List of Publications.....	xxxviii
Chapter 1 Introduction and Background.....	1
1.1 Background	1
1.2 Glossary of Radar Definitions	3
Polarisation	3
Radar Resolution	4
Coherence/Incoherence	4
Speckle	4
Glinting.....	4
1.3 Passive threat detection using radiometry	5
1.4 Active Threat detection using radar	6
1.5 Imaging Radar.....	7
1.6 Non-Imaging Radar	7
1.7 Full Polarimetric Radar	8
1.8 Synthetic Aperture Radar (SAR).....	9
1.8.1 Inverse Synthetic Aperture Radar (ISAR)	10
1.8.2 Interferometric Synthetic Aperture Radar (InSAR)	11
1.8.3 Polarimetric Synthetic Aperture Radar (POL-SAR).....	12

1.8.4 Polarimetric Interferometric Synthetic Aperture Radar (POL-IN-SAR) ..	12
1.9 Pulsed Radar.....	12
1.10 Monostatic Radar	13
1.11 Bistatic and Multistatic Radar.....	13
1.12 Late Time Response Radar	15
1.13 Frequency Modulated Continuous Wave Radar (FMCW)	16
1.14 Through the Wall Radar.....	17
1.15 Clutter.....	17
1.16 Application of Receiver Operating Characteristics	18
1.17 Literature Survey Summary	18
Chapter 2 Polarisation	20
2.1 The Stokes Vector	21
2.2 The Sinclair Matrix	22
2.3 Polarisation Basis	23
2.4 The Kennaugh Matrix	24
2.5 Polarisation on the Poincaré Sphere.....	25
Chapter 3 Millimetre-wave radar technology and Techniques.....	27
3.1 Introduction.....	27
3.2 Horn Antennas.....	27
3.3 Polarisers	29
3.3.1 Planar ortho-mode transducer (OMT).....	29
3.3.2 Turnstile OMT.....	30
3.3.3 Septum Polariser	30
3.4 Duplexer	31
3.5 Low Noise Amplifier	32
3.6 Up Converter	34
3.7 Down Converter.....	35
Chapter 4 Target Decomposition	36
4.1 Coherent Decomposition	36

4.1.1 Pauli Matrix Decomposition	36
4.1.2 Krogager (Sphere-Diplane-Helix) Decomposition	37
4.1.3 Huynen Polarisation Fork	38
4.1.4 Euler decomposition	42
4.2 Depolarisation	44
4.3 Incoherent Decomposition	45
4.3.1 H-alpha Decomposition	45
4.4 Summary	48
Chapter 5 Radar System Design	49
5.1 Introduction.....	49
5.2 Radar Calculations	50
5.2.1 Radar Cross-section of a 6.5 cm diameter sphere.....	52
5.2.2 Predicted receiver noise factor	52
5.2.3 VNA Receiver Signal to Noise Ratio	53
5.2.4 Predicted minimum detectable signal	54
5.2.5 Predicted Maximum usable range	55
5.2.6 Range Resolution	56
5.2.7 Sampling	56
5.2.8 Unambiguous Range calculation	57
Chapter 6 Microwave Measurements using vector network analysers (VNA's)	59
6.1 Scattering Parameters	59
6.2 VSWR, Reflection Coefficient and Return Loss	61
6.3 VNA calibration via the through reflect line (TRL) method.....	63
Chapter 7 Horn antenna design	66
7.1 Introduction.....	66
7.2 Calculated Horn Gain	68
7.3 Calculated Horn Beamwidth	69
7.4 Measured Horn Input Return loss (S_{11})	69
7.5 Measured Horn Beamwidth	71

7.6 Conclusion.....	74
Chapter 8 Turnstile Orthomode Transducer.....	75
8.1 Introduction.....	75
8.2 Design overview	76
8.3 Measurement procedure.....	79
8.4 Experimental Results.....	82
8.5 Conclusion.....	91
Chapter 9 Radar Calibration via Measurement of canonical targets.....	92
9.1 Introduction.....	92
9.2 Radar cross polarisation errors	93
9.3 Clutter.....	94
9.4 Range Gating	95
9.5 Radar Calibration.....	96
9.5.1 System Distortion Matrices	97
9.5.2 Deconvolution Calibration Technique	98
9.5.3 Papathanassiou and Kimura Calibration.....	99
9.5.4 Nesti and Hohmann Calibration.....	100
9.5.5 Comparison of Calibration Techniques	103
9.6 Modelling of Target Sinclair Matrices	105
9.7 Measurement results	107
9.8 Conclusion.....	114
Chapter 10 Measurement of the Huynen Polarisation fork.....	116
10.1 Introduction.....	116
10.2 Measurement results	116
10.2.1 Flat metal plate and dihedral (corner) reflector at 45°	118
10.2.2 Vertical and horizontal dihedral (corner) reflectors.....	120
10.2.3 Vertical and horizontal dipoles.....	123
10.2.4 Metal sphere.....	126
10.2.5 Waveplate with integral reflector.....	127

10.2.6 Wax block.....	129
10.3 Conclusion.....	133
Chapter 11 Characterisation of the effects of depolarisation	134
11.1 Introduction.....	134
11.2 Bistatic case	135
11.2.1 Lexicographic feature vector (f_{4L}).....	135
11.2.2 Polarimetric correlation phase preserving Pauli feature vector (f_{4P}) .	135
11.2.3 The lexicographic covariance (C_{4L}) matrix	135
11.2.4 The Pauli covariance (C_{4P}) matrix.....	136
11.3 Monostatic reciprocal case	136
11.3.1 Lexicographic feature vector (f_{3L}).....	136
11.3.2 The Pauli feature vector (f_{3P})	136
11.3.3 The Lexicographic coherency (C_{3L}) matrix.....	136
11.3.4 The Pauli coherency (C_{3P}) matrix	137
11.4 Measurement results	137
11.5 Conclusion.....	138
Chapter 12 Characterisation of threat and non-dangerous items	139
12.1 Introduction.....	139
12.2 Measurement results	139
12.2.1 Symmetric target a metal triangle	141
12.2.2 Knife measurements.....	142
12.2.3 Small vertical and horizontal knives.....	143
12.2.4 Long vertical and horizontal knives.....	145
12.2.5 Long horizontal and 45° oriented knives	147
12.2.6 Small knife at 45°, blade spine leading-edge compared with the blade edge	148
12.2.7 Long vertical and horizontal knives edge-on.....	150
12.2.8 Brass gun	152
12.2.9 Brass gun horizontal and at 45° orientations	154

12.2.10 Shrapnel target	156
12.2.11 The human torso	158
12.2.12 Human torso perpendicular to radar beam with hands above head	159
12.2.13 Human torso perpendicular to the beam of the radar with hands at the side	161
12.2.14 Human torso presented side on to the beam of the radar with hands above the head compared to hands at the side	163
12.2.15 Knife placed against the human torso.....	165
12.2.16 Small knife vertical and horizontal on the human torso	165
12.2.17 Long vertical and horizontal knives on the human torso	168
12.2.18 Vertical and horizontal guns on the human torso	170
12.2.19 Shrapnel placed against the human torso.....	174
12.2.20 Smartphone.....	177
12.2.21 Keys	180
12.3 Conclusion.....	182
Chapter 13 H/ α decomposition	183
13.1 Introduction.....	183
13.2 The Pauli feature vector (f_{3P})	183
13.3 The Pauli coherency (C_{3P}) (T) matrix	183
13.4 Measurement results	185
13.4.1 Plate and Sphere.....	186
13.4.2 Dihedral at 45°.....	186
13.4.3 Horizontal Dipole	187
13.4.4 Wax block.....	187
13.4.5 Knife perpendicular to the radar beam.....	188
13.4.6 Small knife at 45° blade spine leading compared to blade edge leading	189
13.4.7 Long knife edge-on.....	190
13.4.8 Horizontal and vertical Brass Gun	190
13.4.9 Brass Gun at 45°	191

13.4.10 Human torso with hands above head	192
13.4.11 Human torso with hands at the side.....	192
13.4.12 Human torso presented side on to the beam of the radar with hands above head	193
13.4.13 Small knife located on the human torso (hands above head).....	194
13.4.14 Long knife located on the human torso	194
13.4.15 Gun on the human torso	196
13.4.16 Shrapnel target (located on and off the torso).....	196
13.4.17 Smartphone.....	198
13.4.18 Keys	199
13.5 Conclusion.....	199
Chapter 14 Conclusion and Future Work	202
14.1 Conclusion.....	202
14.2 Future work	205
Chapter 15 Bibliography	208
Chapter 16 Appendix A.....	217
RF Safety exposure limits.....	217
Chapter 17 Appendix B.....	219
Huynen Target Parameters for selected targets	219
17.1 Flat plate and a dihedral reflector orientated at 45°	219
17.2 Vertical and horizontal dihedral	221
17.3 Vertical and horizontal dipole.....	224
17.4 Metal sphere	227
17.5 Wave plate with integral reflector.....	229
17.6 Wax block.....	231
17.7 Metal triangle.....	235
17.8 Small vertical and horizontal knives.....	236
17.9 Long Knife in vertical and horizontal orientations.....	239
17.10 Long knife horizontal and 45° orientations	242

17.11 Short knife at 45° blade spine leading compared to the blade edge ..	244
17.12 Long vertically and horizontally orientated knives edge on	247
17.13 Brass gun horizontal and vertical orientations	250
17.14 Brass gun horizontal orientation left, 45° right	253
17.15 Shrapnel target.....	255
17.16 Human torso perpendicular to radar beam with hands above head ...	257
17.17 Human torso perpendicular to the beam of the radar with hands at the side	259
17.18 Human torso presented side on to the beam of the radar with hands above the head compared to hands at the side	262
17.19 Human torso presented side on to the beam of the radar with hands above the head compared to hands at the side	264
17.20 Small knife vertical and horizontal on the human torso	267
17.21 Long vertical and horizontal knives on the human torso	270
17.22 Vertical and horizontal guns on the human torso	274
17.23 Shrapnel target on the human torso	278
17.24 Smartphone.....	282
17.25 Set of Keys.....	284

Table of Figures

Figure 0-1 Rising trend in crimes committed using knives or sharp implements in the UK. [4].....	xxxi
Figure 0-2 Crimes involving firearms in the U.K [4].	xxxii
Figure 1-1 The electromagnetic spectrum [5].....	1
Figure 1-2 SAR Radar synthetic aperture generation	10
Figure 1-3 Bistatic radar configuration.....	14
Figure 2-1 Horizontal Linear Polarisation.....	20
Figure 2-2 Vertical Linear Polarisation	20
Figure 2-3 Circularly polarised emission (right-hand circular (RHC)) [48].	21
Figure 2-4 Polarisation state plotted on the Poincaré sphere [54].....	26
Figure 3-1 Ridged pyramidal horn antenna	27
Figure 3-2 Conical corrugated horn antenna cross-section [56].....	28
Figure 3-3 Septum Polariser (assembled left) (disassembled right)	31
Figure 3-4 Septum Polariser circular (LHCP, RHCP) port (left), Linear waveguide	31
Figure 3-5 Coaxial Branch Duplexer	32
Figure 3-6 K-Band Low noise amplifier external view (left), internal view (right)	33
Figure 3-7 Friis Cascaded Noise figure and temperature.....	33
Figure 3-8 Up Converter.....	35
Figure 3-9 Down Converter.....	35
Figure 4-1 Polarisation fork plotted on the Poincaré sphere [69].....	39
Figure 4-2 Graph showing Wishart classification [75] [76].	47
Figure 5-1 A schematic of the full polarimetric monostatic FMCW radar system	50
Figure 5-2 Polariser with Corrugated Horn fitted for radar measurements.	50
Figure 5-3 Atmospheric Absorption. [79].....	51
Figure 5-4 FMCW Range extraction	57
Figure 6-1 Vector Network Analyser.....	60
Figure 6-2 Simplified S-parameter model for a two port network [88] [89] [90] [91].....	61
Figure 6-3 Forward and Reflected waves between source and load.	62
Figure 6-4 Port 1 Error terms [94].	64
Figure 6-5 TRL calibration kit.....	65
Figure 6-6 50Ω Waveguide load	65
Figure 7-1 HFSS model of a conical horn antenna.	66
Figure 7-2 Modelled antenna Return loss.....	67
Figure 7-3 Modelled antenna radiation pattern	67
Figure 7-4 Conical corrugated horn antenna.....	68

Figure 7-5 Measurement of Horn antenna return loss (S_{11}).	70
Figure 7-6 Horn Antenna Return Loss (S_{11}).	71
Figure 7-7 Horn Beamwidth measurement setup	72
Figure 7-8 Measured corrugated horn polar diagram at 18GHz.	72
Figure 7-9 Measured corrugated horn polar diagram at 22GHz.	72
Figure 7-10 Measured corrugated horn polar diagram at 26GHz.	73
Figure 8-1 Assembled Turnstile polariser.	76
Figure 8-2 Polariser circular waveguide aperture.	76
Figure 8-3 Exploded view of the polariser [60].	77
Figure 8-4 Polariser block 1 close up [60].	78
Figure 8-5 The turnstile junction [60].	78
Figure 8-6 Turnstile junction and combiner arrangement [60].	79
Figure 8-7 Anritsu 37397A VNA used to measure the OMT (port 1 left, port 2 right)	80
Figure 8-8 Circular to rectangular waveguide transition	80
Figure 8-9 Measurement set up for pol1 transmission and return loss.	81
Figure 8-10 Measurement set up for pol 2 transmission and return loss.	81
Figure 8-11 Measurement set up for cross-polarisation (Isolation).	82
Figure 8-12 Simulated Circular Waveguide return loss [60].	83
Figure 8-13 Polarisation 1 Measured and simulated input return loss for the prototype polariser designed and produced by A. Navarrini and R. L Plambeck [60].	83
Figure 8-14 Polarisation 2 measured and simulated for the prototype polariser designed and produced by A. Navarrini and R. L Plambeck [60].	84
Figure 8-15 Measured and simulated polarisation 1 transmission loss for the prototype polariser designed and produced by A. Navarrini and R. L Plambeck [60].	84
Figure 8-16 Measured and simulated polarisation 2 transmission loss for the prototype polariser designed and produced by A. Navarrini and R. L Plambeck [60].	85
Figure 8-17 Measured polarisation 1 circular waveguide return loss.	86
Figure 8-18 Measured polarisation 2 circular waveguide return loss.	86
Figure 8-19 Measured polarisation 1 rectangular (WR42) port return loss.	87
Figure 8-20 Measured polarisation 2 rectangular (WR42) port return loss.	87
Figure 8-21 Measured polarisation 1 transmission loss.	88
Figure 8-22 Measured Polarisation 2 Transmission loss.	88
Figure 8-23 Measured OMT cross-polarisation (isolation) [60].	89
Figure 8-24 Measured OMT polarisation 1 cross-polarisation (isolation).	89
Figure 8-25 Measured polarisation 2 cross-polarisation (isolation).	90
Figure 9-1 Measurement of clutter in the target range	94
Figure 9-2 Measured response of a dihedral reflector orientated at 45°	95

Figure 9-3 Huynen polarisation fork plot from the measurement of a flat metal plate, basic calibration (left), Papathanassiou and Kimura calibration (right)	104
Figure 9-4 Huynen polarisation fork plot from the measurement of a Dihedral reflector at 45°, basic calibration routine (left), Papathanassiou and Kimura calibration (right)	104
Figure 9-5 Huynen polarisation fork plot from the measurement of a horizontal Dipole array, basic calibration routine (left), Papathanassiou and Kimura calibration (right)	105
Figure 9-6 Huynen polarisation fork plot from the measurement of a vertical Dipole array, basic calibration routine (left), Papathanassiou and Kimura calibration (right)	105
Figure 9-7 Flat metal plate (top), measured linear polarisation (bottom left), circular polarisation (bottom right).	109
Figure 9-8 Dihedral reflector at 45° (top), measured linear polarisation (bottom left), circular (bottom right).	109
Figure 9-9 Horizontal dihedral reflector (top), measured linear polarisation (bottom left), circular (bottom right)	110
Figure 9-10 Vertical dihedral reflector (top), measured linear polarisation (bottom left), circular (bottom right)	110
Figure 9-11 Addition of specular and creeping waves [107].	111
Figure 9-12 8.6 cm diameter sphere (top), measured linear polarisation (bottom left), circular (bottom right)	112
Figure 9-13 Horizontal dipole array (top), measured linear polarisation (bottom left), circular (bottom right)	113
Figure 9-14 Vertical dipole array (top), measured linear polarisation (bottom left), circular (bottom right)	113
Figure 9-15 Array of helical antennas (top), measured linear polarisation (bottom left), circular (bottom right)	114
Figure 10-1 (a) Flat plate, (b) Dihedral at 45°, (c) Vertical dipole, (d) Horizontal dipole [69].	117
Figure 10-2 Flat plate reflector (top left), Dihedral reflector angled at 45° (top right), measured responses, Flat plate (bottom left), Dihedral 45° (bottom right)	118
Figure 10-3 Simulated responses for Flat plate (left), Dihedral at 45° (right)	119
Figure 10-4 Measured orientation angle. Plate (left), Dihedral at 45° (right)	119
Figure 10-5 Measured skip angle. Plate (left), Dihedral at 45° (right)	120
Figure 10-6 Measured fork angle. Plate (left), Dihedral at 45° (right)	120
Figure 10-7 Vertical dihedral reflector (top left), Horizontal dihedral reflector (top right). Measured responses, vertical dihedral (bottom left), horizontal dihedral (bottom right)	121
Figure 10-8 Measured orientation angle, Vertical dihedral (left), Horizontal dihedral (right)	121
Figure 10-9 Measured helicity angle, Vertical dihedral (left), Horizontal dihedral (right) ..	122

Figure 10-10 Measured skip angle, Vertical dihedral (left), Horizontal dihedral (right)	122
Figure 10-11 Measured fork angle, Vertical dihedral (left), Horizontal dihedral (right)	122
Figure 10-12 Vertical dipole (top left), Horizontal dipole (top right), Measured responses, Vertical dipole (bottom left), Horizontal dipole (bottom right).	123
Figure 10-13 simulated responses for Vertical dipole (left), Horizontal dipole (right).	124
Figure 10-14 simulated Dipole responses at 45° (left), Dipole at -45° (right).....	124
Figure 10-15 Measured orientation angle vertical left, horizontal right	125
Figure 10-16 Measured helicity vertical left, horizontal right	125
Figure 10-17 Measured skip angle vertical left, horizontal right.....	125
Figure 10-18 Measured fork angle vertical left, horizontal right	126
Figure 10-19 10.5 cm diameter sphere (left), Measured Huynen fork plot (right).....	126
Figure 10-20 Measured orientation angle (left), Helicity angle (right)	127
Figure 10-21 Measured skip angle (left), Fork angle (right)	127
Figure 10-22 Wave plate with integral reflector, wires horizontal (top), Measured responses, wires horizontal (bottom left), vertical (bottom right).	128
Figure 10-23 Measured helicity angle horizontal left, vertical right.....	128
Figure 10-24 Measured skip angle horizontal left, vertical right.....	129
Figure 10-25 Measured fork angle horizontal left, vertical right	129
Figure 10-26 2 cm thick wax block pictured left, 3.8 cm right.	129
Figure 10-27 Huynen fork plots from the measurement of a 2cm thick wax block left, 3.8 cm right.	130
Figure 10-28 Measured Huynen target size (m) (cavity fringes) 2cm thick wax block, $n=1.47$	131
Figure 10-29 Measured Huynen target size (m) (cavity fringes) Wax block 3.8cm thick, $n=1.47$	131
Figure 10-30 Measured orientation angle 2cm wax block left, 3.8cm right	132
Figure 10-31 Measured helicity angle 2cm wax block left, 3.8cm right.....	132
Figure 10-32 Measured skip angle 2cm wax block left, 3.8cm right.....	132
Figure 10-33 Measured fork angle 2cm wax block left, 3.8cm right	133
Figure 11-1 Huynen fork plot from the measurement of a moving dihedral reflector via averaged Sinclair.....	137
Figure 11-2 Huynen fork plot from the measurement of a moving dihedral reflector via the Coherency matrix	138
Figure 12-1 Metal triangle left, measured fork plot right	141
Figure 12-2 Metal triangle fork plots via measurement viewed from the vertical polarisation position left, and from the -45° polarisation position (right)	142
Figure 12-3 Small vertical knife (left), horizontal knife (right).	143
Figure 12-4 Small knife fork plot via measurement, vertical left, horizontal right	144

Figure 12-5 Small knife fork plot via measurement side view vertical left, horizontal right	144
Figure 12-6 Small knife measured orientation angle vertical left, horizontal right	145
Figure 12-7 Small knife measured helicity angle vertical left, horizontal right	145
Figure 12-8 Vertical Long Knife left, horizontal right.	145
Figure 12-9 Long knife fork plot via measurement vertical left, horizontal right.....	146
Figure 12-10 Long knife fork plot via measurement vertical left, horizontal right (Viewed from the vertical polarisation position)	146
Figure 12-11 Long knife measured orientation angle vertical left, horizontal right	147
Figure 12-12 Long knife measured helicity angle vertical left, horizontal right	147
Figure 12-13 Long horizontal knife left, at 45° right.....	147
Figure 12-14 Long knife fork plot via measurement horizontal left, 45° right	148
Figure 12-15 Long knife measured orientation angle horizontal left, 45° right	148
Figure 12-16 small knife at 45° spine leading left, blade edge leading right	149
Figure 12-17 Small knife at 45° fork plot via measurement blade spine leading left, sharp edge right.....	149
Figure 12-18 Small knife at 45° measured orientation angle blade spine leading left, sharp edge right.....	149
Figure 12-19 Huynen fork plot via measurement for a long knife edge-on vertical left, horizontal right	150
Figure 12-20 Huynen fork plot via measurement for a long knife edge-on vertical left, horizontal right	151
Figure 12-21 Measured orientation angle for a long knife edge-on vertical left, horizontal right	151
Figure 12-22 Measured helicity angle for a long knife edge-on vertical left, horizontal right	151
Figure 12-23 Measured skip angle for a long knife edge-on vertical left, horizontal right	152
Figure 12-24 Brass Gun, horizontal barrel (left), vertical (right).....	153
Figure 12-25 Brass gun fork plot via measurement horizontal left, vertical right.....	153
Figure 12-26 Brass gun measured orientation angle horizontal left, vertical right	153
Figure 12-27 Brass gun measured helicity angle horizontal left, vertical right.....	154
Figure 12-28 Brass gun measured skip angle horizontal left, vertical right.....	154
Figure 12-29 Brass gun horizontal orientation left, 45° right	155
Figure 12-30 Brass gun fork plot via measurement horizontal left, 45° right	155
Figure 12-31 Brass gun measured orientation angle horizontal left, 45° right	155
Figure 12-32 Brass gun measured helicity angle horizontal left, 45° right	156
Figure 12-33 Brass gun measured skip angle horizontal left, 45° right	156
Figure 12-34 Shrapnel Target left, fork plot via measurement right	157

Figure 12-35 Measured shrapnel target size left, orientation angle right.....	157
Figure 12-36 Measured shrapnel helicity angle left, skip angle right	157
Figure 12-37 Consecutive delta function plots via measurement of the human torso with hands above head left, dihedral target at 45°right	159
Figure 12-38 Fork plot from a measurement of the human torso with hands above head via coherency left, via average Sinclair right	159
Figure 12-39 Hands above head fork plot via measurement of subject 1 left, subject 2 right	160
Figure 12-40 Hands above head measured orientation angle subject 1 left, subject 2 right	160
Figure 12-41 Hands above head measured helicity angle subject 1 left, subject 2 right..	161
Figure 12-42 Hands above head measured skip angle subject 1 left, subject 2 right.....	161
Figure 12-43 Hands at side fork plot via measurement subject 1 left, subject 2 right.....	162
Figure 12-44 Hands at side measured orientation angle subject 1 left, subject 2 right	162
Figure 12-45 Hands at side measured helicity angle subject 1 left, subject 2 right	163
Figure 12-46 Hands at side measured skip angle subject 1 left, subject 2 right.....	163
Figure 12-47 Subject 1 side on fork plot via measurement hands above head left, hands at the side right.....	164
Figure 12-48 Subject 1 side on measured target size hands above head left, hands at the side right	164
Figure 12-49 Subject 1 side on measured helicity angle hands above head left, hands at the side right.....	165
Figure 12-50 Subject 1 side on measured skip angle hands above head left, hands at the side right	165
Figure 12-51 Short knife on the human torso vertical left, horizontal right	166
Figure 12-52 Fork plot via measurement of a short knife placed against the human torso vertical left, horizontal right	166
Figure 12-53 Fork plot (side view) via measurement of a short knife placed against the human torso vertical left, horizontal right	167
Figure 12-54 Measured helicity angle of a short knife placed against the human torso vertical left, horizontal right	167
Figure 12-55 Measured skip angle of a short knife placed against the human torso vertical left, horizontal right.....	167
Figure 12-56 Human torso with a long vertical knife left, horizontal right.	168
Figure 12-57 Fork plot via measurement of the human torso with a long vertical knife left, horizontal right	169
Figure 12-58 Side view of the fork plot via measurement of the human torso with a long vertical knife left, horizontal right.....	169

Figure 12-59 Measured helicity angle of the human torso with a long vertical knife left, horizontal right	169
Figure 12-60 Measured skip angle of the human torso with a long vertical knife left, horizontal right	170
Figure 12-61 Human torso with a vertical brass gun left, horizontal right.....	170
Figure 12-62 Fork plot via measurement of the human torso with a vertical gun left, horizontal right	171
Figure 12-63 Fork plot via measurement of the human torso with a vertical gun left, horizontal right (viewed from the vertical position).....	172
Figure 12-64 Fork plot via measurement of the human torso with a vertical gun left, horizontal right (viewed from the -45° position).....	172
Figure 12-65 Fork plot via measurement of the human torso with a vertical gun left, horizontal right (viewed from the zenith)	173
Figure 12-66 Measured orientation angle of the human torso with a vertical gun left, horizontal right	173
Figure 12-67 Measured helicity angle of the human torso with a vertical gun left, horizontal right	173
Figure 12-68 Measured skip angle of the human torso with a vertical gun left, horizontal right	174
Figure 12-69 Fork plot via measurement of shrapnel on its own left, located on subject 2 torso right.....	175
Figure 12-70 Fork plot via measurement of shrapnel on its own left, located on subject 2 torso right (viewed from the vertical polarisation position)	175
Figure 12-71 Fork plot via measurement of shrapnel on its own left, located on subject 2 torso right (viewed from the -45° polarisation position)	176
Figure 12-72 Fork plot via measurement of subject 2's torso with hands at side left, shrapnel on subject 2 right (viewed from the vertical polarisation position)	176
Figure 12-73 Measured orientation angle of shrapnel on its own left, located on subject 2 torso right.....	176
Figure 12-74 Measured helicity angel of shrapnel on its own left, located on subject 2 torso right.....	177
Figure 12-75 Measured skip angle of shrapnel on its own left, located on subject 2 torso right	177
Figure 12-76 Smartphone.	178
Figure 12-77 Huynen fork plot via measurement of a smartphone on its own (left). Viewed from the vertical polarisation position (right)	178
Figure 12-78 Huynen fork plot via measurement of a smartphone on its own from the -45° polarisation position (left), the zenith (right)	179

Figure 12-79 Smartphone measured orientation angle left, helicity angle right.....	179
Figure 12-80 Smartphone measured skip angle left.	179
Figure 12-81 Set of keys measured on own.....	180
Figure 12-82 Keys fork plot via measurement, viewed from the vertical polarisation position (right)	180
Figure 12-83 Keys fork plot via measurement viewed from the -45° polarisation position (left), from the zenith right	181
Figure 12-84 Measured orientation angle	181
Figure 12-85 Helicity angle left, skip angle right both via measurement	181
Figure 13-1 Graph showing Wishart classification [75] [76]	185
Figure 13-2 Flat Plate (left top), Sphere (top right), Flat Plate H/α response (bottom left), Sphere H/α response (bottom right) both via measurement	186
Figure 13-3 Dihedral (double bounce) at 45° (left), Measured H/α response (right).....	187
Figure 13-4 Horizontal Dipole (left), Measured H/α response (right)	187
Figure 13-5 A 3.8cm thick wax block (smooth burnt side to beam) (left), measured H/α response (right).....	188
Figure 13-6 3.8cm thick wax block (textured side to beam) (left), measured H/α response (right).....	188
Figure 13-7 Small metallised plastic knife (left) horizontal no dominant leading-edge, measured H/α response (right).....	189
Figure 13-8 small knife at 45° spine leading left, blade edge leading right	189
Figure 13-9 Small metallised plastic knife at 45°, blade spine presenting leading edge (left), blade edge presenting the leading edge (right), measured H/α responses	190
Figure 13-10 long knife edge-on, vertical left, horizontal right. Measured H/α responses	190
Figure 13-11 Horizontal brass gun (left), Vertical brass gun (right), Horizontal bass gun measured H/α response (bottom left), Vertical brass gun measured H/α response (right)	191
Figure 13-12 Brass gun on its own at 45° (left), measured H/α response (right)	191
Figure 13-13 Subject 1 (Left), Subject 2 (right) torso on its own perpendicular to beam hands above head measured H/α responses.....	192
Figure 13-14 Subject 1 (Left), Subject 2 (right) torso on its own perpendicular to beam hands at side measured H/α responses.....	193
Figure 13-15 Subject 1 side on hands above head left, hands at side right measured H/α responses.....	193
Figure 13-16 Short knife on the human torso vertical left, horizontal right	194
Figure 13-17 Measured H/α response for a small metallised plastic knife against the human torso (subject 1). Vertical orientation left, horizontal right.....	194

Figure 13-18 Subject 1 with a long horizontal knife on torso hands above head (left), hands at the side (right) measured H/α responses.....	195
Figure 13-19 Subject 1 with a long vertical knife on torso hands above head (left), hands at the side (right) measured H/α responses	195
Figure 13-20 Human torso with a vertical brass gun left, horizontal right.....	196
Figure 13-21 Human torso with vertical gun left, horizontal right measured H/α responses.	196
Figure 13-22 Horizontal Shrapnel target (left), measured H/α response (right).....	197
Figure 13-23 Horizontal shrapnel on subject 2 (left), Horizontal shrapnel 40cm in front of subject 2, measured H/α responses	197
Figure 13-24 Horizontal shrapnel on subject 2 torso whilst torso rotating from left to right, measured H/α response	198
Figure 13-25 Smartphone on own (left), measured H/α response (right)	198
Figure 13-26 Keys on own (left), measured H/α response (right).....	199
Figure 16-1 Power intensity at a range.....	218
Figure 17-1 Flat plate reflector (top left), Dihedral reflector angled at 45° (top right). Measured fork plot responses, Flat plate (bottom left), Dihedral 45° (bottom right).	219
Figure 17-2 Measured target size. Plate (left), measured dihedral at 45° (right).....	219
Figure 17-3 Measured orientation angle. Plate (left), Dihedral at 45° (right).....	219
Figure 17-4 Measured helicity angle, Plate (left), Dihedral (right)	220
Figure 17-5 Measured skip angle. Plate (left), Dihedral at 45° (right)	220
Figure 17-6 Measured fork angle. Plate (left), Dihedral at 45° (right)	220
Figure 17-7 Phase of the polarisation ratio. Plate (left), Dihedral at 45° (right)	220
Figure 17-8 Measured spinor angle Plate. (left), Dihedral at 45° (right)	221
Figure 17-9 Vertical dihedral reflector (top left), Horizontal dihedral reflector (top right). Measured fork plot responses, vertical dihedral (bottom left), horizontal dihedral (bottom right).....	221
Figure 17-10 Measured target size, Vertical dihedral (left), Horizontal dihedral (right)	222
Figure 17-11 Measured orientation angle, Vertical dihedral (left), Horizontal dihedral (right)	222
Figure 17-12 Measured helicity angle, Vertical dihedral (left), Horizontal dihedral (right)	222
Figure 17-13 Measured skip angle, Vertical dihedral (left), Horizontal dihedral (right)	223
Figure 17-14 Measured fork angle, Vertical dihedral (left), Horizontal dihedral (right)	223
Figure 17-15 Measured phase of polarisation ratio, Vertical dihedral (left), Horizontal dihedral (right).....	223
Figure 17-16 Measured spinor angle, Vertical dihedral (left), Horizontal dihedral (right)	224

Figure 17-17 Vertical dipole (top left), Horizontal dipole (top right), Measured fork plot responses, Vertical dipole (bottom left), Horizontal dipole (bottom right)	224
Figure 17-18 Measured target size vertical left, horizontal right	225
Figure 17-19 Measured orientation angle vertical left, horizontal right	225
Figure 17-20 Measured helicity vertical left, horizontal right	225
Figure 17-21 Measured skip angle vertical left, horizontal right.....	225
Figure 17-22 Measured fork angle vertical left, horizontal right	226
Figure 17-23 Measured polarisation phase ratio vertical left, horizontal right.....	226
Figure 17-24 Measured spinor angle vertical left, horizontal right	226
Figure 17-25 10.5cm in diameter sphere.	227
Figure 17-26 Huynen fork plot via measurement (left), measured target size (right)	227
Figure 17-27 Measured orientation angle (left), Helicity angle (right)	227
Figure 17-28 Measured skip angle (left), Fork angle (right)	228
Figure 17-29 Measured polarisation phase ratio (left), Spinor angle (right)	228
Figure 17-30 Wave plate with integral reflector, wires horizontal (top), Measured fork plot responses, wires horizontal (bottom left), vertical (bottom right).	229
Figure 17-31 Measured target size horizontal left, vertical right	229
Figure 17-32 Measured orientation angle horizontal left, vertical right	230
Figure 17-33 Measured helicity angle horizontal left, vertical right.....	230
Figure 17-34 Measured skip angle horizontal left, vertical right.....	230
Figure 17-35 Measured fork angle horizontal left, vertical right	230
Figure 17-36 Measured polarisation phase ratio horizontal left, vertical right.....	231
Figure 17-37 Measured spinor angle horizontal left, vertical right	231
Figure 17-38 2 cm thick wax block pictured left, 3.8 cm right.	231
Figure 17-39 Measured fork plots, 2cm thick wax block left, 3.8 cm right	232
Figure 17-40 Measured Huynen target size (m) (cavity fringes) 2cm thick wax block, $n=1.47$	232
Figure 17-41 Measured Huynen target size (m) (cavity fringes) Wax block 3.8cm thick, $n=1.47$	232
Figure 17-42 Measured orientation angle 2cm wax block left, 3.8cm right	233
Figure 17-43 Measured helicity angle 2cm wax block left, 3.8cm right.....	233
Figure 17-44 Measured skip angle 2cm wax block left, 3.8cm right.....	233
Figure 17-45 Measured fork angle 2cm wax block left, 3.8cm right	234
Figure 17-46 Measured polarisation phase ratio 2cm wax block left, 3.8cm right.....	234
Figure 17-47 Measured spinor angle 2cm wax block left, 3.8cm right	234
Figure 17-48 Metal triangle left, measured fork plot right	235

Figure 17-49 Metal triangle measured fork plots viewed from the vertical polarisation position left, and from the -45° polarisation position (right)	235
Figure 17-50 Metal triangle measured target size left, orientation angle right	235
Figure 17-51 Metal triangle measured helicity angle left, skip angle right.....	236
Figure 17-52 Metal triangle measured fork angle left, polarisation phase ratio right	236
Figure 17-53 Small vertical knife (left), horizontal knife (right).	236
Figure 17-54 Small knife measured fork plots vertical left, horizontal right	237
Figure 17-55 Small plastic knife measured fork plots side view vertical left, horizontal right	237
Figure 17-56 Small knife measured target size vertical left, horizontal right	237
Figure 17-57 Small knife measured orientation angle vertical left, horizontal right	238
Figure 17-58 Small knife measured helicity angle vertical left, horizontal right	238
Figure 17-59 Small knife measured skip angle vertical left, horizontal right	238
Figure 17-60 Small knife measured fork angle vertical left, horizontal right.....	238
Figure 17-61 Small knife measured polarisation phase ratio vertical left, horizontal	239
Figure 17-62 Small knife measured spinor angle vertical left, horizontal right.....	239
Figure 17-63 Long knife measured fork plots vertical left, horizontal right	239
Figure 17-64 Long knife measured fork plots vertical left, horizontal right	240
Figure 17-65 Long knife measured target size vertical left, horizontal right	240
Figure 17-66 Long knife measured orientation angle vertical left, horizontal right	240
Figure 17-67 Long knife measured helicity angle vertical left, horizontal right	241
Figure 17-68 Long knife measured skip angle vertical left, horizontal right	241
Figure 17-69 Long knife measured fork angle vertical left, horizontal right.....	241
Figure 17-70 Long knife polarisation phase ratio vertical left, horizontal right	241
Figure 17-71 Long knife measured spinor angle vertical left, horizontal right.....	242
Figure 17-72 Long horizontal knife left, at 45° right.....	242
Figure 17-73 Long knife measured fork plots horizontal left, 45° right.....	242
Figure 17-74 Long knife measured target size horizontal left, 45° right	243
Figure 17-75 Long knife measured orientation angle horizontal left, 45° right	243
Figure 17-76 Long knife measured helicity angle horizontal left, 45° right.....	243
Figure 17-77 Long knife measured skip angle horizontal left, 45° right.....	243
Figure 17-78 Long knife measured fork angle horizontal left, 45° right	244
Figure 17-79 Long knife measured polarisation phase ratio horizontal left, 45° right	244
Figure 17-80 Small knife at 45° spine leading left, blade edge leading right	244
Figure 17-81 Small knife at 45° measured fork plots blade spine leading left, sharp edge right	245

Figure 17-82 Small knife at 45° measured target size blade spine leading left, sharp edge right	245
Figure 17-83 Small knife at 45° measured orientation angle blade spine leading left, sharp edge right.....	245
Figure 17-84 Small knife at 45° measured helicity angle blade spine leading left, sharp edge right.....	246
Figure 17-85 Small knife at 45° measured skip angle blade spine leading left, sharp edge right	246
Figure 17-86 Small knife at 45° measured fork angle blade spine leading left, sharp edge right	246
Figure 17-87 Small knife at 45° measured polarisation phase ratio blade spine leading left, sharp edge right.....	247
Figure 17-88 Small knife at 45° measured spinor angle blade spine leading left, sharp edge right.....	247
Figure 17-89 Measured Huynen fork plots for a long knife edge on vertical left, horizontal right	247
Figure 17-90 Measured Huynen fork plots for a long knife edge on vertical left, horizontal right	248
Figure 17-91 Measured target size for a long knife edge on vertical left, horizontal right	248
Figure 17-92 Measured orientation angle for a long knife edge on vertical left, horizontal right	248
Figure 17-93 Measured helicity angle for a long knife edge on vertical left, horizontal right	249
Figure 17-94 Measured skip angle for a long knife edge on vertical left, horizontal right	249
Figure 17-95 Measured fork angle for a long knife edge on vertical left, horizontal right.	249
Figure 17-96 Measured polarisation phase ratio for a long knife edge on vertical left, horizontal right	250
Figure 17-97 Measured spinor angle for a long knife edge on vertical left, horizontal right	250
Figure 17-98 Brass Gun, horizontal barrel (left), vertical (right).	250
Figure 17-99 Brass gun measured fork plots horizontal left, vertical right.....	251
Figure 17-100 Brass gun measured target size horizontal left, vertical right	251
Figure 17-101 Brass gun measured orientation angle horizontal left, vertical right	251
Figure 17-102 Brass gun measured helicity angle horizontal left, vertical right.....	252
Figure 17-103 Brass gun measured skip angle horizontal left, vertical right.....	252
Figure 17-104 Brass gun measured fork angle horizontal left, vertical right	252
Figure 17-105 Brass gun polarisation ratio phase horizontal left, vertical right	252
Figure 17-106 Brass gun measured spinor angle horizontal left, vertical right	253

Figure 17-107 Brass gun measured forks plot horizontal left, 45° right.....	253
Figure 17-108 Brass gun measured orientation angle horizontal left, 45° right.....	253
Figure 17-109 Brass gun measured helicity angle horizontal left, 45° right	254
Figure 17-110 Brass gun measured skip angle horizontal left, 45° right	254
Figure 17-111 Brass gun measured fork angle horizontal left, 45° right.....	254
Figure 17-112 Brass gun polarisation ratio phase horizontal left, 45° right.....	254
Figure 17-113 Brass gun measured spinor angle horizontal left, 45° right	255
Figure 17-114 Shrapnel Target left, measured fork plot right.....	255
Figure 17-115 Shrapnel measured target size left, orientation angle right.....	255
Figure 17-116 Shrapnel measured helicity angle left, skip angle right	256
Figure 17-117 Shrapnel measured fork angle left, polarization phase ratio right	256
Figure 17-118 Shrapnel measured spinor angle.....	256
Figure 17-119 Hands above head measured fork plot subject 1 left, subject 2 right	257
Figure 17-120 Hands above head measured target size subject 1 left, subject 2 right	257
Figure 17-121 Hands above head measured orientation angle subject 1 left, subject 2 right	257
Figure 17-122 Hands above head measured helicity angle subject 1 left, subject 2 right	258
Figure 17-123 Hands above head measured skip angle subject 1 left, subject 2 right	258
Figure 17-124 Hands above head measured fork angle subject 1 left, subject 2 right.....	258
Figure 17-125 Hands above head measured polarisation phase ratio subject 1 left, subject 2 right	259
Figure 17-126 Hands above head measured spinor angle subject 1 left, subject 2 right.	259
Figure 17-127 Hands at side measured fork plot subject 1 left, subject 2 right	259
Figure 17-128 Hands at side measured target size subject 1 left, subject 2 right.....	260
Figure 17-129 Hands at side measured orientation angle subject 1 left, subject 2 right..	260
Figure 17-130 Hands at side measured helicity angle subject 1 left, subject 2 right	260
Figure 17-131 Hands at side measured skip angle subject 1 left, subject 2 right	261
Figure 17-132 Hands at side measured fork angle subject 1 left, subject 2 right.....	261
Figure 17-133 Hands at side polarisation phase ratio subject 1 left, subject 2 right	261
Figure 17-134 Hands at side measured spinor angle subject 1 left, subject 2 right.....	261
Figure 17-135 Subject 1 side on measured forks plot hands above head left, hands at the side right.....	262
Figure 17-136 Subject 1 side on measured target size hands above head left, hands at the side right.....	262
Figure 17-137 Subject 1 side on measured orientation angle hands above head left, hands at the side right	262

Figure 17-138 Subject 1 side on measured helicity angle hands above head left, hands at the side right.....	263
Figure 17-139 Subject 1 side on measured skip angle hands above head left, hands at the side right	263
Figure 17-140 Subject 1 side on measured fork angle hands above head left, hands at the side right	263
Figure 17-141 Subject 1 side on polarisation phase ratio hands above head left, hands at the side right.....	264
Figure 17-142 Subject 1 side on measured spinor angle hands above head left, hands at the side right.....	264
Figure 17-143 Subject 1 side on measured fork plots hands above head left, hands at the side right	264
Figure 17-144 Subject 1 side on measured target size hands above head left, hands at the side right.....	265
Figure 17-145 Subject 1 side on measured orientation angle hands above head left, hands at the side right	265
Figure 17-146 Subject 1 side on measured helicity angle hands above head left, hands at the side right.....	265
Figure 17-147 Subject 1 side on measured skip angle hands above head left, hands at the side right	266
Figure 17-148 Subject 1 side on measured fork angle hands above head left, hands at the side right	266
Figure 17-149 Subject 1 side on measured polarisation phase ratio hands above head left, hands at the side right	266
Figure 17-150 Subject 1 side on measured spinor angle hands above head left, hands at the side right.....	267
Figure 17-151 Fork plots measurement of a short knife placed against the human torso vertical left, horizontal right	267
Figure 17-152 Fork plots (side view) measurement of a short knife placed against the human torso vertical left, horizontal right	267
Figure 17-153 Measured target size of a short knife placed against the human torso vertical left, horizontal right	268
Figure 17-154 Measured orientation angle of a short knife placed against the human torso vertical left, horizontal right	268
Figure 17-155 Measured helicity angle of a short knife placed against the human torso vertical left, horizontal right	268
Figure 17-156 Measured skip angle of a short knife placed against the human torso vertical left, horizontal right	269

Figure 17-157 Measured fork angle of a short knife placed against the human torso vertical left, horizontal right	269
Figure 17-158 Measured polarisation phase ratio of a short knife placed against the human torso vertical left, horizontal right	269
Figure 17-159 Measured spinor angle of a short knife placed against the human torso vertical left, horizontal right	270
Figure 17-160 Human torso with a vertical long knife left, horizontal right.	270
Figure 17-161 Fork plots via measurement of the human torso with a vertical long knife left, horizontal right.....	270
Figure 17-162 Fork plots of the human torso via measurement with a vertical long knife left, horizontal right.....	271
Figure 17-163 Measured target size of the human torso with a long vertical knife left, horizontal right	271
Figure 17-164 Measured orientation angle of the human torso with a vertical long knife left, horizontal right.....	271
Figure 17-165 Measured helicity of the human torso with a vertical long knife left, horizontal right	272
Figure 17-166 Measured skip angle of the human torso with a vertical long knife left, horizontal right	272
Figure 17-167 Measured fork angle of the human torso with a vertical long knife left, horizontal right	272
Figure 17-168 Measured polarisation phase ratio for the human torso with a vertical long knife left, horizontal right	273
Figure 17-169 Measured spinor angle for the human torso with a vertical long knife left, horizontal right	273
Figure 17-170 Human torso with a vertical brass gun left, horizontal right.	274
Figure 17-171 Fork plots via measurement of the human torso with a vertical gun left, horizontal right	274
Figure 17-172 Fork plots of the human torso via measurement with a vertical gun left, horizontal right (viewed from the vertical position).....	274
Figure 17-173 Fork plots of the human torso via measurement with a vertical gun left, horizontal right (viewed from the -45° position).....	275
Figure 17-174 Fork plots of the human torso via measurement with a vertical gun left, horizontal right (viewed from the zenith)	275
Figure 17-175 Measured target size of the human torso with a vertical gun left, horizontal right	275
Figure 17-176 Measured orientation angle of the human torso with a vertical gun left, horizontal right	276

Figure 17-177 Measured helicity angle of the human torso with a vertical gun left, horizontal right	276
Figure 17-178 Measured skip angle of the human torso with a vertical gun left, horizontal right	276
Figure 17-179 Measured fork angle of the human torso with a vertical gun left, horizontal right	277
Figure 17-180 Measured polarisation phase ratio of the human torso with a vertical gun left, horizontal right.....	277
Figure 17-181 Measured spinor angle of the human torso with a vertical gun left, horizontal right	277
Figure 17-182 Fork plots of shrapnel via measurement on its own left, located on subject 2 torso right.....	278
Figure 17-183 Fork plots of shrapnel via measurement on its own left, located on subject 2 torso right (viewed from the vertical polarisation position)	278
Figure 17-184 Fork plots of shrapnel via measurement on its own left, located on subject 2 torso right (viewed from the -45° polarisation position)	279
Figure 17-185 Fork plots of shrapnel via measurement on its own left, located on subject 2 torso right (viewed from the zenith).....	279
Figure 17-186 Fork plots via measurement of Subject 2 torso with hands at side left, shrapnel on subject 2 right	279
Figure 17-187 Measured target size of shrapnel on its own left, located on subject 2 torso right	280
Figure 17-188 Measured orientation angle of shrapnel on its own left, located on subject 2 torso right.....	280
Figure 17-189 Measured helicity angel of shrapnel on its own left, located on subject 2 torso right.....	280
Figure 17-190 Measured skip angle of shrapnel on its own left, located on subject 2 torso right	281
Figure 17-191 Measured fork angle of shrapnel on its own left, located on subject 2 torso right	281
Figure 17-192 Measured polarisation phase ratio of shrapnel on its own left, located on subject 2 torso right.....	281
Figure 17-193 Measured spinor angle of shrapnel on its own left, located on subject 2 torso right.....	282
Figure 17-194 Smartphone.....	282
Figure 17-195 Measured Huynen fork plots of a smartphone on its own (left). Viewed from the vertical polarisation position (right)	282

Figure 17-196 Measured Huynen fork plots of a smartphone on its own from the -45° polarisation position (left), the zenith (right).....	283
Figure 17-197 Smartphone measured target size left, orientation angle right	283
Figure 17-198 Smartphone measured helicity angle left, skip angle right.....	283
Figure 17-199 Smartphone measured fork angle left, polarisation phase ratio right	284
Figure 17-200 Smartphone measured spinor angle	284
Figure 17-201 Set of keys measured on own.....	284
Figure 17-202 Fork plots via measurement for a set of keys	285
Figure 17-203 Keys fork plots via measurement viewed from the -45° polarisation position (left), from the zenith right	285
Figure 17-204 Set of keys measured target size left, orientation angle right	285
Figure 17-205 Set of keys measured helicity angle left, skip angle right.....	286
Figure 17-206 Set of keys measured fork angle left, polarisation phase ratio right.	286
Figure 17-207 Set of keys measured spinor angle	286

List of tables

Table 1-1 Radio Frequency Spectrum.....	2
Table 2-1 Stokes Parameters for common types of polarised radiation	22
Table 4-1 H- α class descriptions [75] [76].	47
Table 5-1 Radar Specification	58
Table 7-1 Horn measurement results	74
Table 8-1 Measured turnstile polariser return loss, transmission loss and isolation.	90
Table 9-1 Radar cross-polarisation Errors	93
Table 10-1 Target physical dimensions.	117
Table 12-1 Target details	140
Table 13-1 H/ α class descriptions [75] [76].	185

Acknowledgements

I would like to express my sincere gratitude to my director of studies Dr Neil Salmon for all of his patience, and dedication during my research. It has been an absolute honour and pleasure to work with you.

Many thanks to Dr Alessandro Navarrini for allowing me to use his ortho-mode transducer design that was instrumental to the measurements presented in this thesis.

Many thanks to the mechanical engineers at MMU who expertly manufactured the ortho-mode transducer used for the measurements. Also, many thanks to Anthony Gregory and his team for their support and guidance in the labs.

I want to thank Dr Christopher Johnson and Dr Kirstie Andrews for their kind support throughout my studies, and I would also like to thank all of my friends and family for their kind help.

Introduction

Since 2011 there has been a significant increase in the number of fatalities caused by terrorist activities. A study carried out by the Institute for Economics and Peace [1] indicates nine times as many people killed in terrorist activities in 2017 than in the year 2000. Figures presented in 2015 in a report prepared for the U.S. State Department [2], indicate that in 2014, 13,500 terrorist attacks took place with 32,700 deaths and 34,700 injuries, and compared to 2013, global attacks were up by 35%, and deaths by 81%. From a report compiled by Anderson Q.C. [3], the threat level from terrorism rose from substantial too severe in 2014.

A bulletin produced by the U.K's Office for National Statistics indicates a steady increase in fatal, serious and non-fatal incidents due to knife crime. This increase is associated with the rise in robberies (Figure 0-1) [4].

There were 20,196 offences in the year ending December 2019 related to the crime of "assault with injury and assault with intent to cause serious harm". There were 19,943 offences where knives or sharp objects were used in robberies [4].

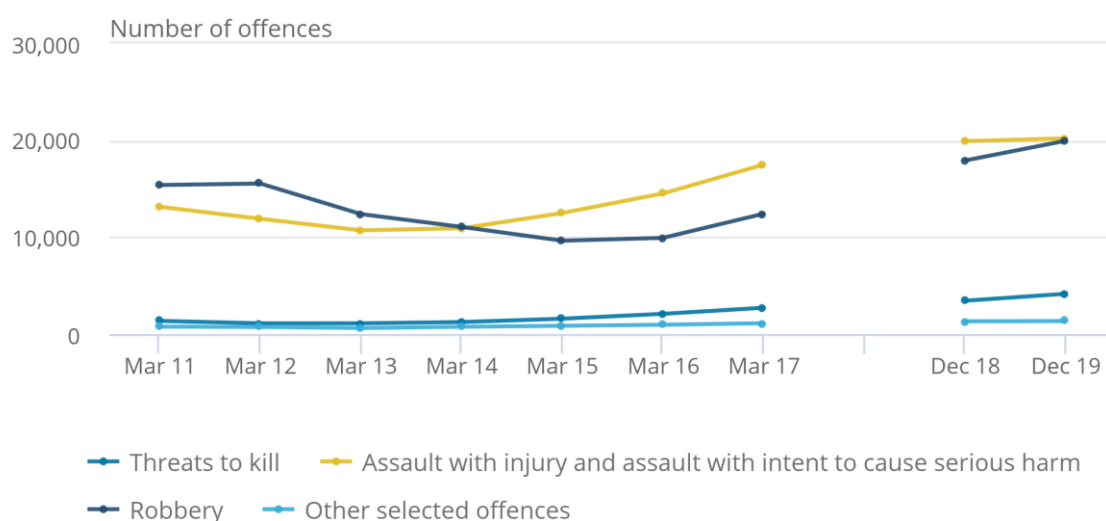


Figure 0-1 Rising trend in crimes committed using knives or sharp implements in the UK. [4]

Recorded offences involving firearms were at 6,060 in the year ending December 2019, a 3% decrease from the previous year in England and Wales but excluding Greater Manchester [4].

Offences using firearms had declined over the past few years; however, an increasing trend has been noted with imitation firearms. Figure 0-2 [4].

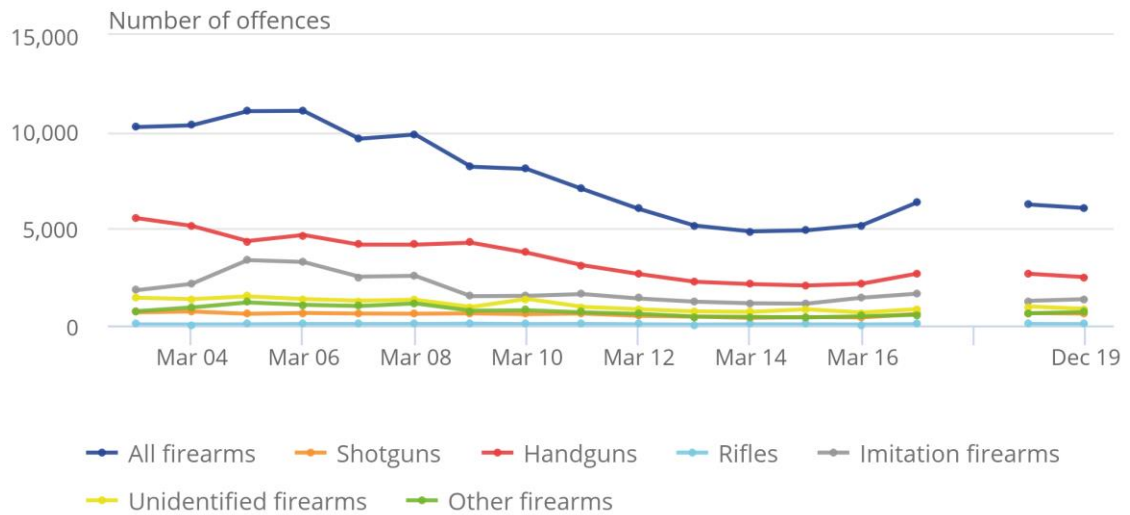


Figure 0-2 Crimes involving firearms in the U.K [4].

Security screening in public places (transport networks, shopping centres, and public arenas) centres on the application of video cameras, police surveillance, stop and search, and pat down checks. Entrances to airports and airport departure lounges are places where security screening of individuals and their baggage is particularly severe.

Currently, the detection of threat objects predominantly occurs in airports with mainly large fixed screening systems such as metal detectors and X-ray systems. Metal detectors detect metal knives and guns on individuals but are of no use to detect plastic guns or ceramic knives.

Typically, transmission x-ray detectors help to detect objects on individuals and in bags. X-ray backscatter detectors illuminate the target with ionising X-ray radiation with the production of a reflection that is dependent upon the atomic structure of the target or objects located on the target. The application of X-ray backscatter imaging has associated health risks this has led to its general withdrawal of use for this application. However, the X-ray transmission system for people screening gives superior images revealing concealed threat targets on the body.

An alternative is to use microwave radar systems; these have the potential of being able to detect non-metallic threats such as ceramic knives, ceramic or plastic guns and the person born improvised explosive devices (PBIED's). Additionally, a portable microwave radar system could help screen people at standoff range and in crowd situations. Using wideband microwave-based radar can provide sufficient

depth resolution to give information about the thicknesses for dielectric targets and other materials used in PBIED's.

Aims and Objectives

Aim

This research aims to develop a fully polarimetric radar as a proof of concept demonstrator to enable measurements of the polarimetric scattering caused by weapons and person born improvised explosive devices (PBIED's) concealed on a person at a standoff range of 10 metres

Currently, very little research is published into weapons detection using full polarimetric radar. The radar developed operates in the K band part of the electromagnetic spectrum (18 to 26 GHz) where attenuation from clothing and the atmosphere is low. The radar operates in a stepped frequency mode using a single antenna and analyses the amplitudes and phases of the orthogonal co and cross-polar linear polarisation returns from the target.

Objectives

The research objectives for this thesis are as follows:

- Develop a frequency modulated continuous wave fully polarimetric stepped frequency monostatic radar based on a vector network analyser, an orthomode transducer and a broadband conical horn antenna.
- Select and characterise an orthomode transducer and conical horn antenna.
- Make theoretical performance evaluation of the full polarimetric radar and compare this with the measured performance from simple targets.
- Investigate deconvolution techniques to remove system-induced dispersion.
- Investigate range gating as a means of rejecting clutter from the scene. (clutter unwanted by definition)
- Measure and scrutinise the polarimetric responses via analysis of the Sinclair backscatter matrices for a range of canonical targets and ascertain suitable decomposition techniques to enable identification, focussing on the Huynen polarisation fork method.
- Generate the Huynen polarisation fork coordinates and target parameters for the canonical targets and compare with current theoretical models.
- Compare the measured target responses with simulations.
- Generate the Huynen polarisation fork coordinates and target parameters for surrogate knives and guns and investigate how they vary with frequency.

- Investigate the effects of depolarisation and speckle on the Sinclair matrices, the Huynen polarisation fork and target parameters.
- Investigate if a statistical approach to analysis using the coherency and or covariance matrices can recover the Huynen target parameters when depolarisation prevents these being extracted directly from the Sinclair matrices.

Contribution to Knowledge

The work presented in this thesis details the development of a novel fully polarimetric stepped frequency monostatic radar, based around a VNA, an orthomode transducer and a corrugated horn antenna. The system makes use of the complex (phase and amplitude) nature of microwaves scattered from concealed weapons and PBIED's hidden on individuals at a standoff range.

No research in the public domain has detailed the development of a fully polarimetric monostatic stepped frequency (FMCW) radar for security screening.

An in-depth assessment of the Huynen polarisation fork decomposition technique assesses its suitability for the detection of concealed weapons.

No research into the application of this technique is published for this application.

A review of other techniques such as the Krogager SDH and H- α decompositions are compared.

The significant contribution of this work has been to:

- Take hardware designed for radio astronomy applications and commercial instrumentation to form a radar concept demonstrator.
- Demonstrate a suitable calibration strategy to keep systematic errors to an absolute minimum.
- Demonstrated classical radar targets measured responses such as a flat metal plate, dihedral, and dipole structures match with published theory.
- An in-depth look at applying the Huynen polarisation fork technique and its seven associated parameters is presented. This coherent technique is similar to other decomposition methods, but seldom used is evaluated as a means to identify targets.
- Present the measured Huynen polarisation fork responses of classical radar targets such as a flat metal plate, dihedral and dipole structures match published theory and simulations.
- We have demonstrated that the Huynen polarisation fork technique is a viable technique to detect dielectric targets such as PBIED's.
- Measurements are presented of the human torso for two individuals via the generation of the Huynen polarisation fork technique and plotted on the Poincaré sphere, to ascertain characteristics that could lead to the removal of the effects of the torso with concealed weapons placed against it.

- Measurements of concealed objects placed on the human torso for two individuals are presented via the generation of the Huynen polarisation fork technique and plotted on the Poincaré sphere to ascertain the change in response with concealed weapons placed on the torso compared to the torso on its own.
- The presence of depolarisation is investigated with mathematics presented to enable a coherent decomposition method to be used in the presence of depolarisation via application of the coherency matrix method.
- A review of different target decompositions such as the coherent Pauli, Krogager (SDH), the Huynen polarisation fork techniques and the incoherent H- α technique are assessed for their suitability for concealed weapons detection.

List of Publications

1. E.J Blackhurst, N. Salmon, M. J. Southgate, “Full Polarimetric Millimetre Wave Radar for Stand-off Security Screening”, Proc. SPIE 10439, Millimetre Wave and Terahertz Sensors and Technology X, 1043906 (6th October 2017).
2. E.J Blackhurst, N. Salmon, M. J. Southgate, “Experimental determination and simulations of the Huynen target parameters for full polarimetric millimetre wave concealed weapon recognition”, Proc. SPIE 10800, Millimetre Wave and Terahertz Sensors and Technology XI, 1080007, SPIE Security + Defence, 2018, Berlin, Germany (5th October 2018).
3. Eddie Blackhurst, N. Salmon, “Experimental determination of Huynen target parameters for the human torso for full polarimetric millimetre wave concealed weapon recognition”, Proc. SPIE 11164, Millimetre Wave and Terahertz Sensors and Technology XII, 111640D, SPIE Security + Defence, 2019, Strasbourg, France (18th October 2019).
4. Eddie Blackhurst, N. Salmon, “Detection of concealed explosives and shrapnel weapons using decompositions of microwave polarimetric radar data”, Proc. SPIE 11541, Millimetre Wave and Terahertz Sensors and Technology XIII, 1154107, SPIE Security + Defence, 2020, Edinburgh, U.K (September 2020)

Chapter 1 Introduction and Background

This chapter provides a review of current radar techniques and looks at each type's relative merits and their suitability to detect concealed weapons.

1.1 Background

Radar (radio assisted detection and ranging) in the H.F, VHF and microwave bands (Figure 1-1 and Table 1-1) developed rapidly in the 1930s and 40s as a necessity by both the British and German nations to detect enemy aircraft and ships.

The range to the target calculated from the time it takes the radio waves to travel to and from the target using equation 1-1;

$$r = \frac{c.t}{2} \quad (1-1)$$

Where;

r is the range to the target.

c is the velocity of light.

t is the round trip time taken for the radar pulse to propagate to and from the target.

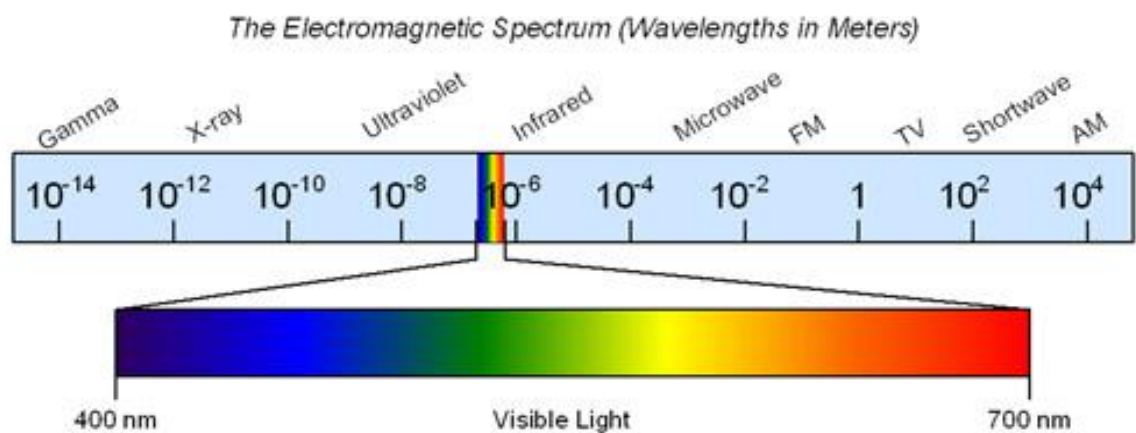


Figure 1-1 The electromagnetic spectrum [5].

Band	Frequency range	Wavelength
HF	3 - 30 MHz	10 - 100 m
VHF	30 - 300 MHz	1 - 10 m
UHF	300 - 1000 MHz	30 - 100 cm
L	1 - 2 GHz	15 - 30 cm
S	2 - 4 GHz	7.5 - 15 cm
C	4 - 8 GHz	3.75 - 7.5 cm
X	8 - 12 GHz	25 - 37.5 cm
Ku	12 - 18 GHz	16.7 - 25 mm
K	18 - 26.5 GHz	11.3 - 16.7 mm
Ka	26.5 - 40 GHz	5.0 - 11.3 mm
Q	30 -50 GHz	6.0 - 9.0 mm
U	40 - 60 GHz	5.0 - 7.5 mm
V	50 - 75 GHz	4.0 - 6.0 mm
W	75 - 110 GHz	2.7 - 4.0 mm
F	90 - 110 GHz	2.1 - 3.3 mm
D	110 - 170 GHz	1.8 - 2.7 mm

Table 1-1 Radio Frequency Spectrum

In the mid-1930s, the air ministry looked into the possibility of developing a 'death ray' to destroy aircraft and their pilots. It soon became clear that the 'death ray' using radio energy was not a practical weapon of war. Progress would soon see aircraft detection for the RAF fighter command take place using this radio energy.

Robert Watson-Watt at this time superintendent of the Radio Department of the National Physical Laboratories at Teddington looked into the feasibility of developing some kind of radio direction finding (RDF) equipment by using a chain of transmitters and presented his ideas in a memorandum to the air ministry on the 12th of February 1935. On the 26th of February in the same year, Watson-Watt demonstrated that he could detect one of the RAF's Handley Page Heyford bombers at a range of 8 miles (13 km).

This crude experiment used the backscattered signal from the Heyford bomber from the BBC's shortwave transmitter at Daventry with a wavelength of around 50 meters. Detection was carried out in a field using a simple receiver. Watson-Watt's work led to installing a series of radar stations located all along the south and east coasts of

England, known as Chain Home and Chain Home Low arriving just in time for the 2nd world war.

Chain Home provided coverage for higher altitudes with a range of around 100 miles (160 km), while Chain Home Low detected aircraft as low as 500 ft (150 meters) but with somewhat shorter range.

At around the same time, the Germans were developing there Freya radar with 50 miles (80 km) range and the Würzburg gun-laying radar with 25 miles (40 km) range. The Freya radar provided long-range aircraft detection and ranging whilst the Würzburg radar-guided fighter aircraft on to the target at a shorter range. The Würzburg radar was a pulsed radar using a parabolic reflector producing a peak power of 8 kW at an operating frequency of 560 MHz. The combination of Freya and Würzburg formed a potent radar combination.

Other notable early radar systems from this time are the airborne interception (AI) radars developed by E. G (Taffy) Bowen and the H₂S radar developed by Sir Bernard Lovell was one of the first airborne imaging radars enabling an operator to distinguish targets on the ground regardless of weather conditions and proved particularly useful for submarine detection.

All radars in use today have origins dating back to these pioneering times. A significant advancement took place in the 1950s in the USA when Wiley et al. developed and tested the first synthetic aperture (SAR) radar that is now commonly used in remote sensing and security screening [6].

1.2 Glossary of Radar Definitions

Polarisation

Polarisation defined by the orientation of the electric field at the point of transmission. The electromagnetic wave's polarisation orientation remains unchanged until the wave interacts with a target (or clutter).

Radar sensors are sensitive to one or more polarisations depending upon the application. Air traffic control radars typically produce a narrow vertically polarised beam whereas conventional weather radars use horizontal polarisation, although recent developments have led to dual polarised systems.

Radar Resolution

Radar resolution is a measure of the radar's ability to resolve two objects located in close proximity, applying to the range, azimuth cross-range, elevation cross-range and Doppler. If the two targets separated by an amount smaller than the range resolution, then the radar will only be able to identify the two as a single object. If the objects separated by a value larger than the range resolution the radar will then see two targets. Improvement in resolution is improved by increasing the radiation bandwidth and reducing the 3dB beamwidth of the antenna.

Coherence/Incoherence

Electromagnetic waves are said to be coherent if they possess the same frequency and a fixed relative phase.

Electromagnetic waves are incoherent when their phases are randomly distributed relative to one another.

Speckle

Speckle is an interference phenomenon associated with the coherence of the illuminating radiation. The signal amplitude measured is a vector sum over multiple path lengths between the transceiver and the target. When there is relative movement between transceiver and target, or the target is viewed from a different direction, these path lengths change, giving a new vector sum and a different amplitude and phase. Multipath interactions with the environment surrounding a target will also contribute to these changes. When forming radar images of a target, it can manifest itself as a bright and dark grainy structure [7] [8].

Glinting

It is glinting produced by a target's shape and or aspect change relative to the radar resulting in a shift in the radar reflection's apparent centre, caused by specular reflections from smooth surfaces relative to the radiation wavelength. (Note: glinting is an intensity effect, this being at a maximum when the angle of incidence equals the angle of reflection from the surface).

1.3 Passive threat detection using radiometry

Radiometry is not a radar technique; however, it can generate an image at mm-wave frequencies at 35 or 94 GHz where atmospheric transmission is relatively low.

Radiometric (or passive) sensors measure the thermal or Planck radiation from objects. When the photon energy (hf) is less than the thermal energy (kT), where k is Boltzmann's constant and T is the temperature in Kelvin, the thermal radiation at a frequency f from an object ranges from 0 to 1 and is equal to $1-R$ where R is the object's reflectance. When the emissivity is unity it radiates as a blackbody and its intensity is just given by the Planck blackbody function. When the emissivity is zero it radiates nothing and reflects 100% of the incident radiation, and this is characteristic of metals in the microwave and millimetre wave band. Generally, objects have intermediate emissivity values, radiating some emission and reflecting radiation that falls upon them from other objects and the atmosphere. Radiation from a target may originate partly from the target itself and partly from other objects around it and the atmosphere. The contrast generally defined as the difference between the maximum and minimum levels of emission in a field of regard. In outdoor measurement scenarios, metallic objects tend to reflect emission from the sky which is radiometrically cold compared to objects in the measurement scene producing sufficient contrast in the image [6] to enable identification of some types of weapons concealed on individuals.

A paper presented by Essen et al. [9] demonstrates two approaches working at around 94 GHz with both systems providing imaging, the first being based on a Dicke type radiometer with a PIN diode single pole dual throw (SPDT) switch on the input to the receiver.

The SPDT switch limited the bandwidth. Additionally, the transmission loss produced by the switch degrades the noise performance of the receiver. A total power radiometer gave an improved performance with the development of superior low noise amplifiers. A passive system measures the thermal radiation emitted by a target, and contrast in the background emission enables detection.

Environmental issues tend to limit passive systems, to overcome such limitations, incoherent target illumination helps improve sensitivity. Polarised reflections or emissions generally are not produced using this approach.

Passive systems have been with some success when applied to counterterrorism applications, typically producing images. Images formed by thermal emission at mm

wavelengths from objects do not tend to suffer from significant absorption levels caused by smoke, fog or clothing [6] as they do with the visible or infrared band systems.

One limitation is that relatively large apertures are required to attain good image resolution compared to optical imagery [6]. Furthermore, to obtain images at high frame rates, it is necessary to use multiple receiver channels because image acquisition time is inversely proportional to the number of receiver channels [6]. The use of numerous receiver channels enables a longer dwell time per pixel to reduce the noise.

One limitation of passive imagery has been down to the high cost of low noise amplification. However, technology in this area partly for radio astronomy applications has developed rapidly, bringing higher performances and lower costs over the past few years.

1.4 Active Threat detection using radar

Active radar can function at night or day and radar operating at a longer wavelength; for example, air traffic control radars can work regardless of weather conditions and provide accurate range to target information [6]. It is not as susceptible to ambient conditions, unlike passive infrared systems.

One limitation that can cause issue though is 'glinting' off objects carried by the target individual [10]. Active radar radiation is coherent, like laser radiation and generates speckle, like a laser, constituting clutter in the imagery.

Targets can have resonances at some frequencies producing enhanced features, and glinting can make image interpretation more difficult [6]. Andrews et al. [11] indicate that concealed threat objects can be detected under clothing so long as the object has a sufficiently different reflectance to that of human skin.

Radiation in the millimetre wave (30 to 300 GHz) band is not significantly attenuated by clothing [10] [12]. Improvement in range resolution benefits from operating the radar at higher frequencies as this can lead to increased bandwidth compared to operation at lower frequencies. [6] [10] [13].

Active radar has the advantage of being able to detect both metallic and non-metallic objects, making it potentially a viable method to detect dielectric objects with low

permittivity such as explosives [14]. The detection of concealed weapons, along with associated limitations, are presented below:

1.5 Imaging Radar

An imaging radar generates an image of a scene, but unlike a visible camera, it needs to illuminate the scene with radio waves, microwaves or millimetre wave radiation.

Essen et al. [9] demonstrated a frequency modulated continuous wave (FMCW) active imaging system working at 94 GHz. The paper suggests that further work is required, indicating specular reflections were encountered even from clothing and thought to be due to the monostatic radar configuration's geometry. Solutions proposed were to implement a multistatic approach and that a full polarimetric system needs developing.

Limitations listed by Harmer et al. [10] are spatial resolution which is the ability to resolve the smallest feature in an image, and radiometric sensitivity, which is the smallest change in brightness, or radiance that can be detected by the radar [15]. Cross-range spatial resolution can become an issue at the increased range; however, the radial spatial resolution improves with increased bandwidth attained by working at higher frequencies [10].

High-quality artefact free images are required to maximise the information extractable [6]. Radar like a laser is coherent and just like a laser, images can exhibit speckle further complicating target identification [6].

1.6 Non-Imaging Radar

A paper produced by Harmer et al. [10] presents a technique to detect concealed weapons using an active non-imaging technique. Active non-imaging radar has the following advantages when compared with imaging types [10] [11];

- Mechanically simpler as scanning is not required.
- Data is obtained more rapidly from a target.
- It can have reduced size and weight.
- It can benefit from lower fabrication costs.
- Identification is not reliant on the operator's ability (current imaging radar security systems analyse their data in a machine – the human operator never sees the image).

But with the disadvantage of;

- It is reliant on the quality of the identification algorithm used for target detection.
- Speckle can be a problem for both imaging and non-imaging coherent radar types.

A non-imaging radar developed at Manchester Metropolitan University called 'Mirtle' [16] [17] [18] used an intensity-based approach. The radar using orthogonal linear polarisation performs identification autonomously. It applies neural network analysis to the scattered polarimetric radar reflection.

Object size and orientation relative to the human body can reduce the system's ability to positively identify a threat object, larger objects being easier to detect. Threat detection improves when the person under surveillance moves and presents a changing aspect to the radar.

1.7 Full Polarimetric Radar

Full Polarimetric radar uses dual orthogonal polarisation usually in the linear (HV) basis but could also use the circular polarisation basis (LR) to illuminate a target of interest. The radar typically would be of the monostatic single antenna type but could use a bistatic approach.

Full polarimetric radar measurements are made by stimulating a target with one polarisation and measuring the phase and amplitude response in both the co and cross-polar returns. The radar then stimulates the target in the orthogonal polarisation again measuring both the co and cross-polar reflection. From this, a 2x2 (complex) polarimetric scattering matrix is measured, commonly referred to as the Sinclair (back) scatter matrix [19] in more depth in chapter 3.

Objects with smooth flat surfaces tend to retain the linear polarisation state of the incident wave upon reflection. An object with sharp edges and angular features tend to transform the incident wave's polarisation state, into the opposite polarisation state upon reflection [14].

Further target-related information may be obtainable through the use of radar polarimetry [6]. When used in a broadband configuration, to provide improved range resolution, dielectric objects with low permittivity such as explosive devices can be detected, however broad bandwidth radar is expensive [14].

1.8 Synthetic Aperture Radar (SAR)

Synthetic aperture radar is a coherent method that usually uses the beam of a single (monostatic) antenna arrangement to produce high-resolution images in the cross-range dimension. This technique exploits the vehicle's movement that the radar is fitted to and is a preferred technique used by the remote sensing community [20] [21].

A side-scan arrangement is required as the radar needs to transmit and receive perpendicular to the line of motion and usually fitted to either an airborne or a spaceborne platform [22]. The radar can either use single or dual polarisation.

It uses the movement caused by flight to create an electronically generated antenna of much larger effective aperture than that of the single antenna on its own. However, for concealed weapons detection, a more convenient arrangement could involve a static array of sequentially switched antennas [23].

The radar can implement either frequency sweeping or hopping or transmit a series of pulses at a rate known as the pulse repetition frequency (PRF), illuminating the target from a slightly different angle each time. The motion of the platform causes this angular change. The radar stores the magnitude and phase of the reflected response produced by each pulse. It needs to operate over broadband to obtain the required radar resolution, all of the SAR variants are coherent.

After several target measurements, the on-board signal processor uses the stored responses to reconstruct a signal as if a single large antenna had produced it. The process is similar to that used for phased array radars that use many evenly spaced antennas; however, the SAR approach relies on the change in a single antenna's location over some time. (Figure 1-2).

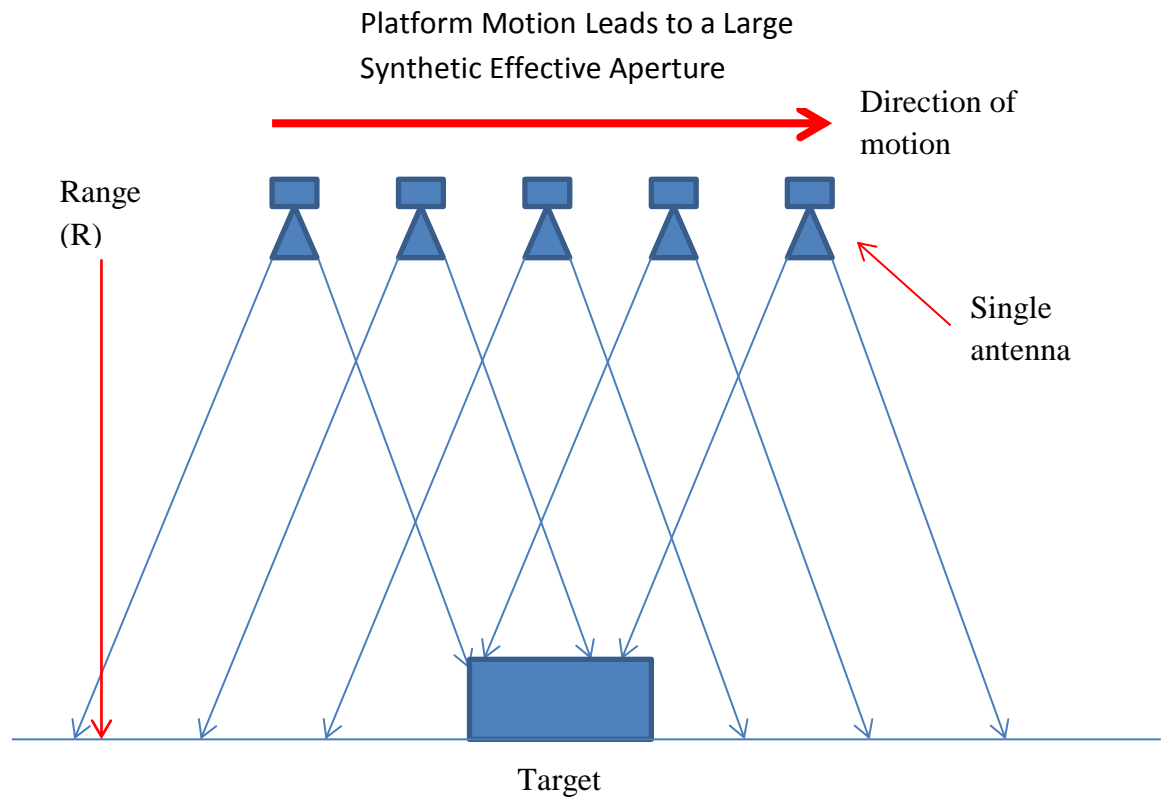


Figure 1-2 SAR Radar synthetic aperture generation

Under ideal circumstances, SAR has two limiting factors that govern the effective length of the synthetic aperture [21]:

- The beamwidth of the radar's single 'real' antenna.
- Knowledge of the precise locations of the transceivers along the transit path.

For the former, the length of the effective aperture can be no greater than the width of the region that is illuminated and is a function of range. The second limitation requires the aperture size to be limited to ensure the wavefront phase to be that of a plane wave and in this configuration to be unfocused. However, this limitation can be compensated for mathematically to correct for the wavefront having a spherical response.

Several groups have independently developed the SAR approach into potentially viable systems for the detection of concealed weapons. Ultra-wide bandwidth is desirable as this provides improved range resolution.

1.8.1 Inverse Synthetic Aperture Radar (ISAR)

The ISAR technique is very similar in operation to SAR. However, it uses the motion of the target past the microwave radar to create the synthetic aperture leading, after

data processing, to the image generation. The target's motion (in the case of an individual walking past the radar in the cross-range) provides horizontal resolution whilst vertical resolution comes from positioning the sensor array or mechanical scanning vertically. Scanning needs to occur quickly enough to maintain coherent processing and is a function of target velocity [24]. Recent developments to the ISAR technique have enabled a degree of platform motion, indicating that increased phase errors caused by target and platform motion require a different approach to the data processing technique to compensate [25].

One such system developed uses a vertical linear array of transmitters and receivers to provide the vertical resolution. The natural motion of an individual provides the horizontal resolution whilst walking through the array [26]. The arrangement could provide a low-cost approach partly due to the lack of requirement for mechanical platform movement. Concealed threat detection would occur in an environment where the radar is static and where people walk past the array.

1.8.2 Interferometric Synthetic Aperture Radar (InSAR)

Interferometric SAR has proved very useful to the remote sensing community for monitoring with centimetre and even millimetre precision changes in displacement of targets (ground features), including information about vertical structures. This radar type has a high spatial resolution. Detection takes place over time and performs a comparison of multiple SAR images. The resulting interferograms produced via comparison of the phase information between images. The difference in phase for a given wavelength is closely related to the displacement of the target between images [27] [28]. The complicated scattering from objects affects the InSAR technique's precision, leading to uncertainty about the phase centre for these targets [29].

Benefits of In-SAR;

- High precision: 1 to 2mm are possible. (Note that any SAR precision is about half the wavelength – some books show proof of this. Whether this realised depends on other things like depolarisation)
- The technique provides a large area of coverage.

Typically, the satellites can measure displacement every 2 to 12 days.

1.8.3 Polarimetric Synthetic Aperture Radar (POL-SAR)

This technique is an enhanced version of SAR that applies polarimetric techniques. It uses either the linear or circular polarisation basis for transmitting and receiving. The method provides further details of the polarimetric scattering from objects, such as fine textural structure, target orientation, system metrics and material constituents [30].

1.8.4 Polarimetric Interferometric Synthetic Aperture Radar (POL-IN-SAR)

This relatively recent SAR family development combines polarimetric techniques with interferometric SAR. This technique provides high spatial resolution and information about the orientation, textural structure, system metrics, and material constituents. [29] [30].

1.9 Pulsed Radar

The pulsed radar has several applications but primarily used for air traffic control. The radar transmits a brief, powerful pulse lasting around 0.1 μ s to 1 μ s that when incident upon a target produces a reflection that the radar receives.

The transmitter is typically off for around 1ms to allow this reflection to return to the radar set. Accurate timing is required with the leading edge of transmit pulse acting as the time reference and the end set by the leading edge of the received pulse. Removal of systematic delays present in the system is required to enable precise range calculations. The pulsed radar is ideal for the detection of range and bearing of the object [31]. Long-range applications are suited for this type of radar. The duration of the pulse determines the range resolution as can be seen in equation 1-2;

$$\Delta R = \frac{\tau \cdot c}{2} \quad (1-2)$$

Where;

ΔR is the range resolution in meters.

T is the pulse transmission duration in seconds.

c is the speed of light.

1.10 Monostatic Radar

This radar type uses a single antenna for both transmit and receive initially developed in the late 1930s [21]. A system using separate transmit and receive antennas co-located is classed as a pseudo monostatic radar. Dr D. O'Reilly used such a system for concealed weapons detection [32].

1.11 Bistatic and Multistatic Radar

The bistatic radar is one of the earliest radar types to be developed. An example is the Chain Home radar developed in the 1930s and 40s, documented in this chapter's introduction.

A bistatic radar is composed of one transmitter and receiver spaced typically by a considerable distance from one another, at least equal to that of the target [33] [21]. Figure 1-3 shows the bistatic configuration with transmitter (T_x) located at a distance (D_b) from the transmitter (R_x), distance to the target is (D_t), and distance from target to the receiver is (D_r).

An accurate time reference is required between the transmitter station and receiver station. This requirement is performed either via direct reception from the transmitter or via synchronised clocks located at both sites [21].

A radar with transmitting and receiving antennas co-located would be classed as pseudo monostatic and not bistatic. Multistatic radars are typically composed of one transmitter with several distributed receivers located at separate spatially distributed locations providing coverage of the same area again with significant separation [21].

Both types are composed of several monostatic radars [34]. Both bistatic and multistatic radars can provide Doppler frequency shift information provided the transmitter frequency is known.

Knowledge of the transmitter frequency and distance between transmit and receive antennas is required to enable extraction of the maximum possible amount of information [21].

Both the bistatic and multistatic radar types will operate in a passive configuration based around the forward scattering from targets illuminated by 'illuminators of opportunity' located in the target environment. These could be VHF FM and UHF (Table 1-1) television transmitters typically high power [6].

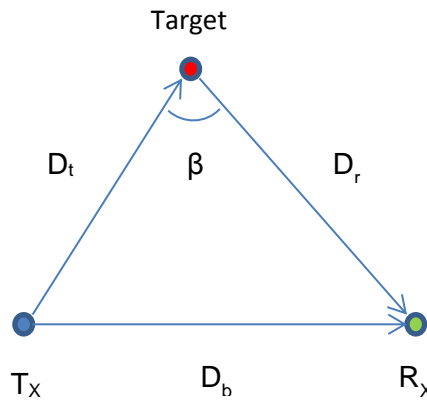


Figure 1-3 Bistatic radar configuration

Using a monostatic configuration has the benefits over a bistatic configuration of:

- Simpler geometry.
- Control over transmit power.
- Control over radar constellation positions.

But has limitations of:

- The increased cost of fabrication when compared to the bistatic.
- High possibility of detectability (not covert).

The bistatic approach configuration offers:

- Lower cost (If broadcast transmitters provide the source of illumination).
- Lower vulnerability to detection (system in this configuration is passive and hence covert).
- Improved ability to detect stealthy objects designed to prevent detection with the monostatic approach.

Having the limitation of:

- No control over the power level of broadcast transmitters.
- Clutter caused by unwanted reflections.
- Direct reception of transmitter (not via reflection).
- Complicated geometry.

A method that has shown the capability of detecting dielectric objects is a polarimetric version of the multistatic radar, utilising the Sinclair matrix [14].

1.12 Late Time Response Radar

When metallic or dielectric targets illuminated with electromagnetic radiation from a radar an early time reflection occurs, this is from the object's surface. Some of the electromagnetic radiation will also attach and propagate around the target's surface in the form of a surface wave. Features of the target structure can then reradiate some of the electromagnetic radiation at a later time and known as the late time response.

The late-time response (LTR) radar was developed and utilised to detect aircraft and missiles since the 1970s. The investigation into its potential as a method to detect concealed weapons on terrorists is relatively recent.

The method used for this radar type can be either the pulsed type or an ultra-wideband frequency swept continuous wave (FMCW) exploiting targets natural and complex resonances in response to excitation from the radar. [35]

A target produces two separate responses when illuminated with the radar, the first an early time response caused by direct reflection from the target. The second the late time response arrives at a time delayed from the early time reflection. It looks like LTR is a weighted sum of decaying sinusoids [36].

The LTR can extend beyond five ns after the early time response produced by objects concealed against the human body [35]. The LTR mode can change markedly with aspect. However, the resonant modes can provide an aspect-independent signature [37].

The excitation mechanism might not always stimulate target resonances leading to target classification problems [38] [39]. An important feature of this technique is aspect independence as the target can be orientated at any angle.

The LTR method requires relatively large bulky antennas due to the relatively low (lower region of the microwave spectrum) natural resonant frequencies produced by threat objects [40].

Such antenna beamwidths tend to be wide limiting the radar application to short ranges, such as in a portal scenario. At longer ranges, issues with clutter leading to difficulty in target identification could be an issue.

A method to provide beam steering and focusing using a phased array antenna has been presented by Harmer et al. that could provide a solution to this issue [41].

Currently, the technique tends to be suited to portal applications due to the antenna's short-range limitations.

Portal applications cause inconvenient constrictions in flow rates of individuals trying to pass through them [42].

1.13 Frequency Modulated Continuous Wave Radar (FMCW)

This radar type originates from around the same time as for pulse radars. Development took place in the 1920s for ionospheric measurements and altimetry in the 1930s [21].

The frequency modulated carrier wave radar can benefit from improved range resolution compared to other radar types. Range resolution is the radar's ability to distinguish between targets located close to one another. The FMCW radars range resolution is related to the inverse bandwidth (Δf), as shown in equation 1-3.

$$\Delta_R = \frac{c}{2\Delta_f} \quad (1-3)$$

Where;

ΔR is the range resolution in meters.

c is the speed of light meters per second.

Δf is the radar bandwidth in Hz.

Compare this to the range resolution for the pulsed radar found using equation 1-2. For the pulsed radar to obtain the best range resolution, a very short pulse is required.

This radar type has the following advantages:

- High accuracy of range measurement.
- Good range resolution.
- No high peak power caused by pulsed radar emission.

The transmitted frequency steadily increases typically in a linear manner across a spectral band over time. Once the radar reaches the upper-frequency limit, the frequency then drops back down to the start frequency, and the process starts again. If an object at a range, R causes a reflection, this will take time (t_r) of:

$$t_r = \frac{2R}{c} \quad (1-4)$$

The change in frequency, also known as the beat frequency is related to the target's range R by the following equation [21] [43]:

$$f_b = \frac{2R\Delta_f}{T_m c} (Hz) \quad (1-5)$$

Where Δ_f is the bandwidth of the radar, T_m is the modulating period, and c is the speed of light. The broadband operation gives improved range resolution.

1.14 Through the Wall Radar

This radar type has applications for military, law enforcement and search and rescue services. Most radars of this type operate in the 1 to 3 GHz range as the loss caused by buildings is lowest below 3 GHz. Due to the two-way propagation through walls and target defocusing, problems caused by signal fading due to increased path losses are known issues. Structures between the target and radar are unwanted clutter, removal from the data is possible, but with difficulty [44]. Another problem caused by reflections from the buildings structure and unwanted objects in the scene is multipath delayed reflections, which usually cause ghosting in generated images [45].

1.15 Clutter

The definition of clutter is as anything in the measured signal that is not the target and arises from reflection of the radar transmit beam from objects in the field of regard that is not the target [21]. Radars tend to be clutter limited rather than noise-limited because the radar signal to noise ratio is improvable by transmitting higher powers and as a result, increasing the received signal level, whilst the receiver noise remains constant.

However, the radar clutter is environment-dependent, so one of the critical radar signal processing strategies is clutter rejection.

Isolated targets such as a metal tower or composite (volumetric) scatterers such as raindrops, ice crystals or chaff might cause clutter. The signal to clutter ratio is dependent on the radar cross-section and the amount and reflectivity of the unwanted clutter objects [21].

Improvement of clutter discrimination is possible in several ways [6];

1. The utilisation of interferometric signal processing to aid the generation of high-resolution three-dimensional target-related information.
2. The utilisation of polarimetric radar, this is particularly effective if the target scattering properties are somewhat different from the clutter, especially if the target has dihedral or trihedral features.
3. The utilisation of higher bandwidths for finer range resolution.
4. The utilisation of larger apertures for finer angular resolution.
5. Application of Doppler processing to isolate moving targets from static clutter.

1.16 Application of Receiver Operating Characteristics

Development of receiver operating characteristics (ROC) took place during the Second World War to help detect targets (aircraft during the Battle of Britain) using radar. Not all reflections received were from aircraft many proved to be from birds.

This graphical technique plots the true positive rate (sensitivity) on the y-axis against the false positive rate (probability of false alarm, fallout) on the x-axis. The ROC curve is the true positive rate as a function of the probability of false alarm. It provides a method for visualising, organising and selecting classifiers based on their performance and shows the trade-offs between the true positives and false positives [46].

1.17 Literature Survey Summary

To summarise, passive threat detection using radiometry can be used to produce images of subjects with concealed weapons; however, ambient conditions can reduce performance and being an incoherent technique provides no phase information.

Active threat detection using radar has the advantage of being unaffected by ambient conditions and providing the capability for either imaging or non-imaging based applications. Active threat detection can operate with an intensity only (incoherent) approach, such as in the 'Mirtle' system or a coherent strategy is possible using phase and amplitude information. Coherent, active threat detection can suffer from speckle, while active threat detection generally can also suffer from glinting.

Synthetic aperture radar widely used for remote sensing where platform motion produces a larger effective aperture than would otherwise be possible. The ISAR approach uses the motion of the target instead of the platform to synthesise the aperture. With all the SAR technique variants exact knowledge of platform and or target motion and velocity are required [47]. The technique can provide high spatial resolution and information about target orientation, textural structure, system metrics and material constituents. Concealed weapons detection using the SAR approach has provided some success. Limiting factors for this radar type are relatively slow data acquisition times and the requirement of large amounts of computing power and exact knowledge of the platform and or target motion.

Range resolution for a pulsed radar requires the generation of a very short pulse with associated problems of high peak power.

Bistatic and multistatic radars use single or multiple spatially diverse transmitters and receivers and can also operate passively using 'illuminators of opportunity' located in the target environment.

Through-the-wall-radar can provide images of individuals with or without threat devices through the walls of a building. However, signal fading (path loss) and defocusing caused by structural components between the target and the radar cause limitations. Other limitations are the low operating frequency required to penetrate building structure, leading to a lower range resolution than if higher frequency operation were possible. This radar type can also suffer from image ghosting caused by the delayed reflections from objects located in the target scene.

Fully polarimetric radar has the potential to provide the maximum amount of target-related information. In the monostatic configuration, the Sinclair backscatter matrix provides six independent pieces of information. The fully polarimetric monostatic approach combined with the FMCW technique gives superior range resolution enabling improved capability to detect PBIED's. The monostatic system is compact, having a single antenna and is ideally suited to standoff applications. The monostatic radar using a single horn antenna can provide a narrow beam enabling illumination of just the target of interest and reduce the visibility of unwanted clutter in the target environment.

Of paramount importance for the detection of concealed weapons and PBIED's is range resolution.

Chapter 2 Polarisation

Linearly polarised electromagnetic radiation from an antenna remains in this state as it propagates through space. Antennas of varying types create different polarisations by using voltages in conductors to force electrons in the antenna to move in specific directions. A horizontal linear motion of electrons creates a horizontal polarisation, this wave having an electric field vector in the horizontal direction perpendicular to the direction of propagation (Figure 2-1 and Figure 2-2). The magnetic field (not shown) is perpendicular to the electric field.

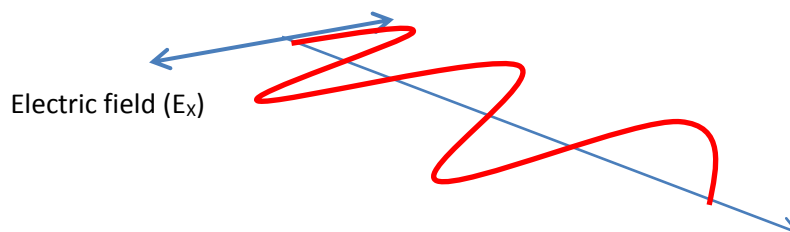


Figure 2-1 Horizontal Linear Polarisation

Linear polarisation is the most common type found in radar systems, as it is the easiest to produce. Upon reflection from a plain flat surface, the polarisation orientation remains in a linearly polarised form. A combination of orthogonal linearly polarised waves with the same frequency but differing magnitudes and phase results in elliptical polarisation, if the electric field's frequency and magnitudes are equal and the phase difference between the orthogonal polarisations is 90° , then we get circular polarisation Figure 2-3. Upon reflection from a plain flat surface, circularly polarised wave orientation is converted so left-hand circular polarisation (LHC) becomes right-hand circular (RHC).

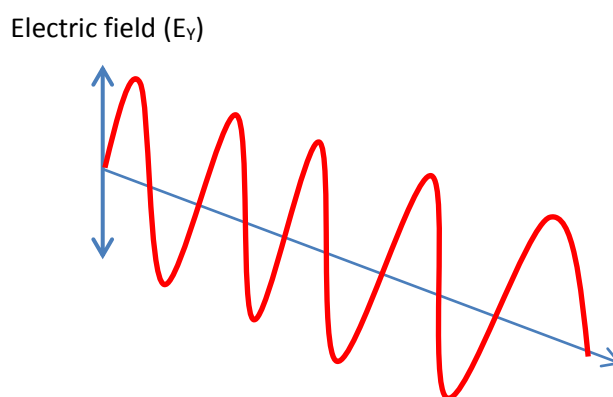


Figure 2-2 Vertical Linear Polarisation

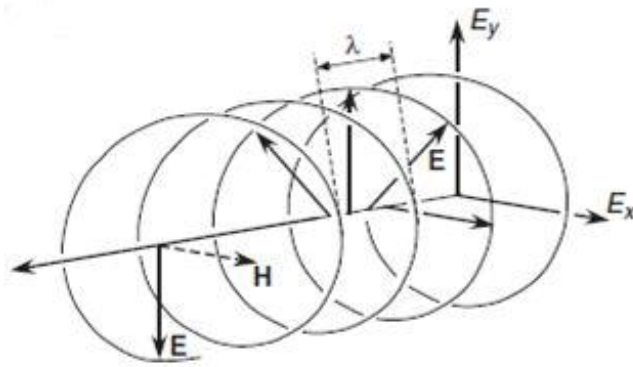


Figure 2-3 Circularly polarised emission (right-hand circular (RHC)) [48].

2.1 The Stokes Vector

The Stokes vector describes the general state of polarisation of an electromagnetic wave;

$$Stokes = \begin{bmatrix} I \\ Q \\ U \\ V \end{bmatrix} \quad (2-1)$$

Where the Stokes parameters represent;

I = the total intensity.

Q= linear polarisation (horizontal value is positive, vertical value is negative).

U= linear polarisation (+45° value is positive, -45°, value is negative).

V= Circular polarisation (RHC value is positive, LHC value is negative).

Stokes parameters for the common polarisation states presented in Table 2-1.







Stokes Parameters	Horizontal polarisation	Vertical polarisation
I	 1	 1
Q	1	-1
U	0	0
V	0	0
	+45° polarisation	-45° polarisation
I	1	1
Q	 0	 0
U	1	-1
V	0	0
	RHC polarisation	LHC polarisation
I	 1	 1
Q	0	0
U	0	0
V	1	-1

Table 2-1 Stokes Parameters for common types of polarised radiation

2.2 The Sinclair Matrix

The 4-elements of the Sinclair matrix represent the electric fields ratios to the transmitted electric fields in two orthogonal polarisations [49]. Its values are complex representing the magnitude and phase response produced by reflection from a target. The elements are independent of the incident target illumination and related to the target incident wave's frequency and the target geometry. Equation. 2.2 presents the Sinclair matrix.

$$S = \begin{bmatrix} S_{HH} & S_{HV} \\ S_{VH} & S_{VV} \end{bmatrix} \quad (2-2)$$

S_{HH} = Horizontal polarisation transmitted, horizontal polarisation received.

S_{VV} = Vertical polarisation transmitted, vertical received.

S_{VH} = Vertical polarisation transmitted, horizontal received.

S_{HV} = Horizontal transmitted, vertical received.

The Sinclair matrix is based on the backward scatter alignment (BSA) convention and is related to but not equivalent to the Jones matrix which is based on the forward scatter alignment (FSA) convention [50].

2.3 Polarisation Basis

Polarisation basis indicates the polarisations that need to be measured to characterise the polarimetric response of a target fully. Targets can be fully characterised by measuring the Sinclair matrix. This requires the target to be illuminated in two orthogonal polarisations and measured in two orthogonal polarisations. There is an infinite number of orthogonal polarisations, indicated by the anti-polar pair on the Poincaré sphere. Any one of these pairs constitutes a measurement basis. Because the Sinclair matrix captures all the polarimetric information of a target, measurement of the Sinclair matrix in one polarisation basis can be transformed into that measurement which could have been made in a different basis. That transformation is made by a unitary similarity transformation [51].

The easiest polarimetric basis to measure is the linear HV basis because two orthogonal linear polarisations are relatively easy to generate using transmission line and waveguide components. Measurement in the linear (HV) polarisation basis requires stimulating the target with horizontal polarisation and measuring the return in both the horizontal and vertical polarisations, then stimulating the target with vertical polarisation and again measuring the return in both horizontal and vertical polarisations. These measured responses are contained in the Sinclair matrix, so this matrix is referred to as the Sinclair matrix as measured in the linear (HV) basis. Conversion from the linear polarisation basis to circular requires a unitary similarity transformation equation 2-3.

$$\begin{bmatrix} S_{RR} & S_{RL} \\ S_{RL} & S_{LL} \end{bmatrix} = \frac{1}{2} \begin{bmatrix} S_{HH} - S_{VV} - 2jS_{HV} & -j(S_{HH} + S_{VV}) \\ -j(S_{HH} + S_{VV}) & S_{VV} - S_{HH} - 2jS_{HV} \end{bmatrix} \quad (2-3)$$

2.4 The Kennaugh Matrix

The Kennaugh matrix is also known as the Stokes scattering matrix is a real 4 x 4 matrix and relates to the backscattered power reflected from a target when illuminated with electromagnetic radiation. The matrix describes the target polarimetric behaviour and is unique for each target. Its alternate form used to represent forward transmission is known as the Mueller matrix [52].

Elements of the Kennaugh matrix are generated using the following Kronecker multiplication (equation 2-4) [53];

$$K = 2[A]^T^{-1}([S] \otimes [S]^*)[A]^{-1} \quad (2-4)$$

Where [S] represents the Sinclair (back) scattering matrix shown in equation 2-2 and where the 4x4 expansion matrix [A] is given by equation 2-5.

$$A = \begin{bmatrix} 1 & 0 & 0 & 0 \\ 1 & 0 & 0 & -1 \\ 0 & 1 & 1 & 0 \\ 0 & j & -j & 0 \end{bmatrix} \quad (2-5)$$

In the following equation 2-6, we see the relationship between the transmitted Stokes vector, and after multiplication by the target-related Kennaugh matrix we arrive at the Stokes reflection vector;

$$[stokes]_{rx} = [K] \times [stokes]_{tx} \quad (2-6)$$

To see a practical example of this, consider the reflection a monostatic radar would receive from a flat metal plate or a metal sphere. These objects shown in chapter 9, can be used as one of the targets for radar calibration. The flat plate/sphere in the linear (HV) basis is a co-polar reflector and in the ideal case does not generate any cross-polar radiation. Equation 2-7 shows the Sinclair matrix for this target with the S_{HH} and S_{VV} terms being unity. If the target is illuminated with horizontal or vertical polarisation then the reflection will arrive back at the radars receiver with the same polarisation state as that transmitted, the S_{VH} and S_{HV} terms indicate that there is no polarisation conversion. The Sinclair matrix produced by these targets is;

$$S_{plate} = \begin{bmatrix} S_{HH} & S_{HV} \\ S_{VH} & S_{VV} \end{bmatrix} = \begin{bmatrix} 1 & 0 \\ 0 & 1 \end{bmatrix} \quad (2-7)$$

Using this Sinclair matrix and using equation 2-4 yields the targets Kennaugh matrix;

$$K_{plate} = \begin{bmatrix} 1 & 0 & 0 & 0 \\ 0 & 1 & 0 & 0 \\ 0 & 0 & 1 & 0 \\ 0 & 0 & 0 & -1 \end{bmatrix} \quad (2-8)$$

Referring to equation 2-9, when a metal plate or sphere is illuminated with linear polarisation, (Stokes (tx) parameters Q and U) then after reflection the Stokes reflection vector Stokes (rx) shows that for the linear polarisation states there is no polarisation conversion. For circular polarisation, when target illumination takes place with left-hand circular (LHC) polarisation, the target converts this into right-hand circular (RHC) polarisation and also (RHC) to (LHC), conversion indicated by the negative sign of element K44 in the Kennaugh matrix.

$$\begin{bmatrix} 1 \\ 1 \\ 1 \\ -1 \end{bmatrix}_{rx} = \begin{bmatrix} 1 & 0 & 0 & 0 \\ 0 & 1 & 0 & 0 \\ 0 & 0 & 1 & 0 \\ 0 & 0 & 0 & -1 \end{bmatrix} \begin{bmatrix} 1 \\ 1 \\ 1 \\ 1 \end{bmatrix}_{tx} \quad (2-9)$$

2.5 Polarisation on the Poincaré Sphere

Graphical representation of any polarisation state can be defined as a point P when plotted on the Poincaré sphere (Figure 2-4) [54]. Henri Poincaré developed this unit radius sphere in 1892 to represent the polarisation state of polarised light. The zenith (top) represents left-hand circular (LHC) and the nadir (bottom) right-hand circular (RHC) polarisation. All of the linear polarisation states lie around the equator. Elliptical polarisation states lie everywhere else. Two angles are required to define the point P on the sphere, (τ, ϕ) referred to as Deschamps parameters or (α, δ) referred to as spinor parameters, and their values range accordingly;

- τ : Ellipticity angle (radians) ($-\pi/4$ to $+\pi/4$), $-\pi/4$ (LHC), 0 (linear), $+\pi/4$ (RHC).
- ϕ : Orientation (tilt) angle (radians) ($-\pi/2$ to $+\pi/2$), (τ, ϕ).
- α : Auxiliary (or spinor) angle (radians) (0 to $+\pi/2$).
- δ : Phase difference ($-\pi$ to $+\pi$) between two orthogonal linear polarisations (radians).

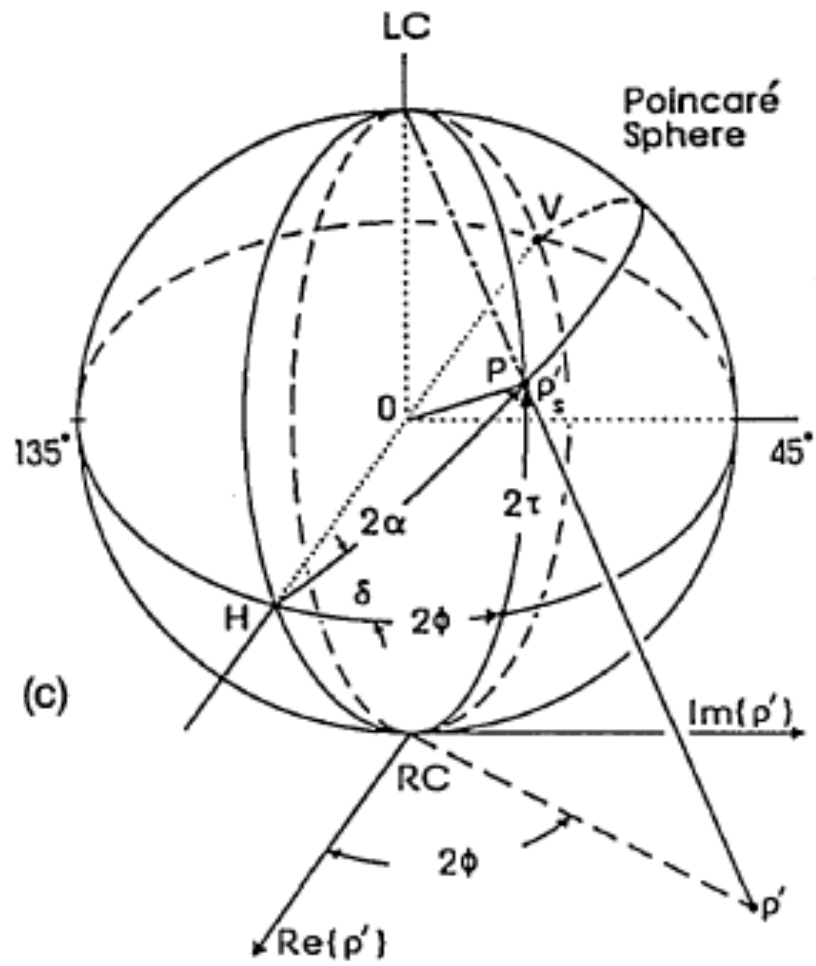


Figure 2-4 Polarisation state plotted on the Poincaré sphere [54]

Chapter 3 Millimetre-wave radar technology and Techniques

3.1 Introduction

This chapter introduces some of the key components used in millimetre wave radar systems and reviews their properties.

3.2 Horn Antennas

A horn antenna is a device used to concentrate electromagnetic radiation into a concentrated directional beam and typically used in the microwave region above 1 GHz or higher. There are just two basic types pyramidal and conical. The addition of ridges to the pyramidal horn's inside increases the horns bandwidth (Figure 3-1). The addition of corrugations to the conical horns inside improves the horns match. Corrugations also improve sidelobe suppression and help to lower polarisation conversion over the operation band. The conical corrugated horn additionally produces a constant beamwidth over a wide frequency range.

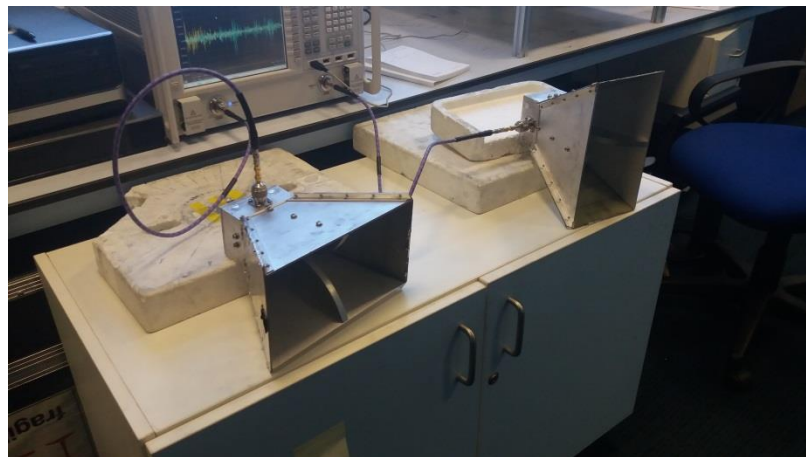


Figure 3-1 Ridged pyramidal horn antenna

Work carried out by D. O'Reilly [43] demonstrated the suitability of pyramidal horn antennas for concealed weapons detection with the development of a quasi mono-static radar. One horn antenna radiated vertical polarisation, whilst the other horizontal.

O.L Daniyan et al. [55] reviewed the concepts and considerations required to design horn antennas stating that essentially the horn is an impedance transformer matching 50-ohm waveguide to the free space impedance of 377 ohms.

The lower cut off frequency of a conical horn antenna is determined by the circular waveguide feeds cut off wavelength. The dominant mode in a circular waveguide is the transverse electric TE_{11} mode.

A smooth-walled conical horn has a major limitation of being fed with and radiating the fundamental TE_{11} mode, which does not present polarisation purity [56]. An adaption of the smooth-walled horn that overcomes this is the corrugated horn antenna, a cross-sectional view presented in Figure 3-2 [56]. From this figure, we see that the first three or four corrugations are a half-wavelength deep. This part of the horn is called the mode-matching section and is used to convert the TE_{11} mode into the hybrid electric HE_{11} mode. The remainder of the corrugations along the horn's internal walls are a quarter wavelength deep. These corrugations are helping to suppress the horns unwanted sidelobe response. This antenna style has a rotationally symmetrical beam shape.

The corrugations and symmetry of this horn antenna type produce equal boundary conditions for all polarisations, leading to the so-called hybrid electric mode HE_{11} . This mode is a combination of the TE_{11} and TM_{11} modes which gives lower cross polarisation at the antenna aperture. Low cross polarisation is essential to enable the maximum amount of information about a target to be extracted.

- Typically corrugated feed-horns present very low levels of cross-polarisation.
- They have a symmetrical radiation pattern.
- They tend to offer a good match (S_{11}) ($\leq -15\text{dB}$).
- The design of a corrugated horn tends to be simple. However, manufacture can be difficult and costly.
- Corrugated conical horns tend to have wider bandwidths than smooth walled equivalents.
- Non-corrugated conical horns tend to have low polarisation purity.

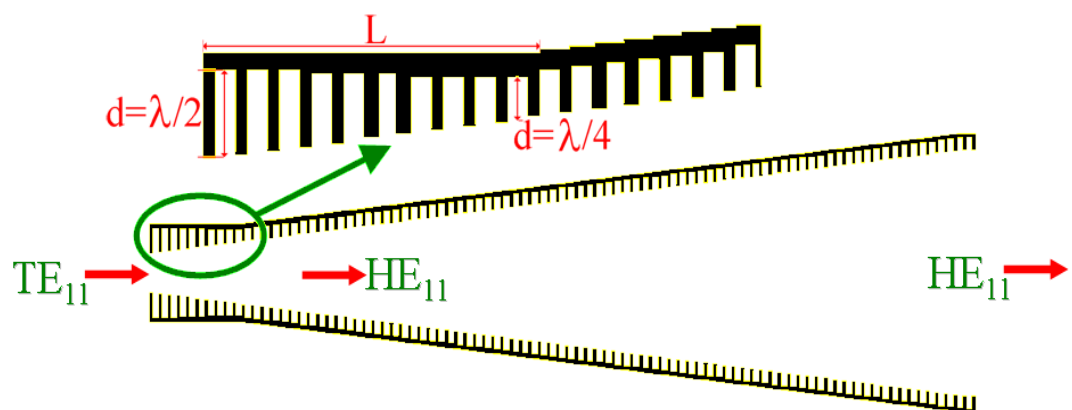


Figure 3-2 Conical corrugated horn antenna cross-section [56].

3.3 Polarisers

Polarimetric radars require some means of radiating and receiving orthogonally polarised radiation. An ortho-mode transducer (OMT) is a device that enables this using a single antenna in a monostatic configuration. The OMT enables transmission of two orthogonal polarisation modes and the measurement of both co and cross reflections from the target. This transmission allows for four separate measurements to be made of the polarimetric reflections. The following presents several different methods of linear and circular polarisation extraction.

3.3.1 Planar ortho-mode transducer (OMT)

Perhaps one of the easiest from a manufacturing point of view is the planar OMT, a linear polariser type. A high-performance planar OMT based on superconducting technology is presented in a paper by G. Valente and A. Navarrini [57]. Development of this OMT meant optimisation at cryogenic temperatures making it less suitable for room temperature application. Only simulated results were available due to fabrication issues preventing a prototype from being realised. Simulated results predicted input return loss of -12dB and a cross-polarisation of -80dB with a transmission loss of 1dB over the 84 to 116GHz band.

A planar OMT developed by P.K. Grimes et al. [58] for use at C-band (4 to 8 GHz) performed well. The stray capacitance between the probes and circular waveguide walls kept to a minimum by tapering the probes to the point where they feed through the waveguide body. A 180° phase shift between the probes is required and provided by a rat race coupler arrangement. Return loss of -20dB and cross-polarisation of less than -58dB were recorded.

G. Engargiola and R.L. Plambeck [59] developed a planar OMT to work at L band (1 to 2 GHz) intending to scale the design to work at W band (75 to 110 GHz) and above. The probes and baluns were fabricated on a low loss substrate. The baluns were of the slotline type, and this balun has improved bandwidth performance compared to the rat race coupler. Input return loss was of the order of -18dB with cross-polarisation of -35dB.

Generally, the loss tangent of the substrate dielectric and track resistance used to form the probes and balun lead to resistive losses in tracks that lead to increased transmission loss. Additionally, bandwidth performance can be a problem.

3.3.2 Turnstile OMT

Waveguide polarisers tend to offer superior performance in bandwidth and transmission loss compared to a planar design but can be complicated to manufacture mechanically. This polariser is of the linear type.

A. Navarrini and R. L. Plambeck [60] presented a design operating at K-band (18 to 26GHz). The design has been engineered and fabricated around the split block method to simplify manufacture, the polariser machined out of four separate blocks of aluminium. The assembled blocks are aligned using dowel pins to ensure accurate alignment. This method of manufacture is much simpler and cheaper than the alternatives that rely on electroforming.

Average input and output return losses measured at -19dB, cross-polarisation at -48dB and transmission loss of 0.15dB recorded over the 18 to 26 GHz band.

The turnstile concept originated in 1955 with work carried out by M.A.Mayer and H.B.Goldberg [61]. A. Navarrini, A. Bolatto and R. L. Plambeck [62] scaled the K-band turnstile polariser to work over W band. Tolerances at such a short wavelength become far more of an issue. A slight misalignment of fractions of a millimetre of the split block arrangement used and dimensional differences caused some problems. At K band the wavelength is 14 times longer than the W band hence tolerances are far less of an issue. At room temperature, five identical polarisers were tested, all with average input and output return losses of -18dB, transmission loss of around 1db and cross-polarisation of -30dB.

3.3.3 Septum Polariser

The septum polariser is a four-port waveguide device used to convert linear to circular and circular to linear polarisation. The square waveguide section shown in the left image of Figure 3-4 is effectively two ports, left-hand circular and right-hand circular polarisation (LHCP and RHCP).

The two rectangular ports (Figure 3-4 right) are the linear ports. The circular polariser converts linear polarisation to circular or circular to linear with a 90° phase shift provided by the septum plate (visible in the centre of the right picture in Figure 3-3).

Circular polarisation has the advantage of high cross-polarisation isolation. P. Lecian and M. Kasal [63] presented a paper on an X band polariser's design to feed a parabolic antenna. The paper indicates that the septum plate's thickness and the

septum teeth height are critical to obtaining good axial ratio performance and return loss. This initial design was derived from applying a mathematical equation that was then modelled using finite element analysis (FEM) techniques to optimise.

Figure 3-3 shows an assembled septum polariser on the left, the disassembled polariser on the right. The right image centre shows the septum plate that provides the 90° phase shift, required to convert circular polarisation to the linear polarisation basis.

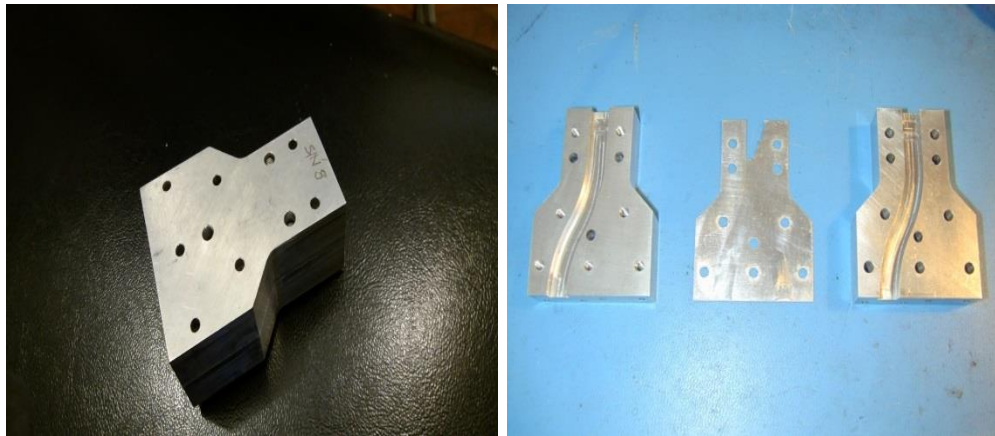


Figure 3-3 Septum Polariser (assembled left) (disassembled right)

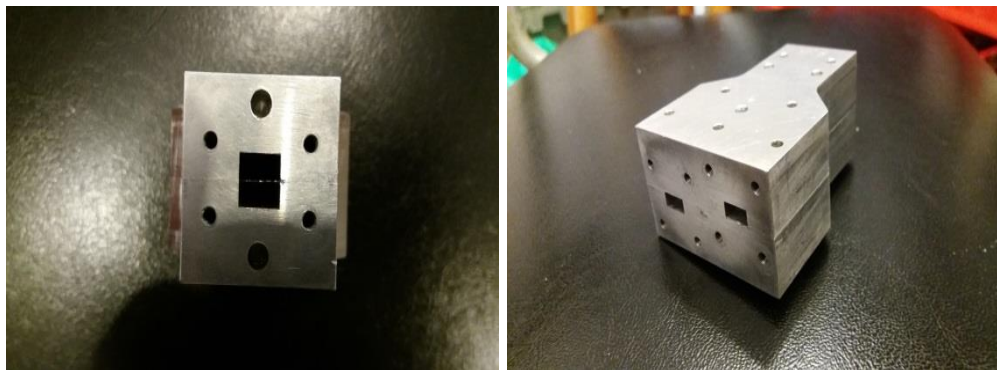


Figure 3-4 Septum Polariser circular (LHCP, RHCP) port (left), Linear waveguide

3.4 Duplexer

The duplexer was one of the critical components developed in the early days of airborne microwave radar and is still used for radar application to this day along with test equipment such as vector network analysers.

When the transmitter transmits it;

- Allows the transmitter to radiate from the antenna.
- Isolates the receiver during the transmission phase to protect the receiver.

When the transmitter is off during reception it:

- Allows the receiver to receive signals via the antenna.
- It isolates the transmitter from the antenna and receiver.

The duplexer enables both transmitter and receiver to share the same antenna, with several types available depending on the application. The example shown in Figure 3-5 is a coaxial branch line variant which uses gas discharge tubes (TR and ATR-tubes) to protect the receiver when transmitting. The tubes filled with a gas such as Argon under low pressure become ionised, producing a short circuit to protect the receiver whilst transmitting.

The main limitation of the coaxial branch line duplexer is its limited bandwidth. Other variations include waveguide duplexers again using the gas discharge principle, and circulator duplexers.

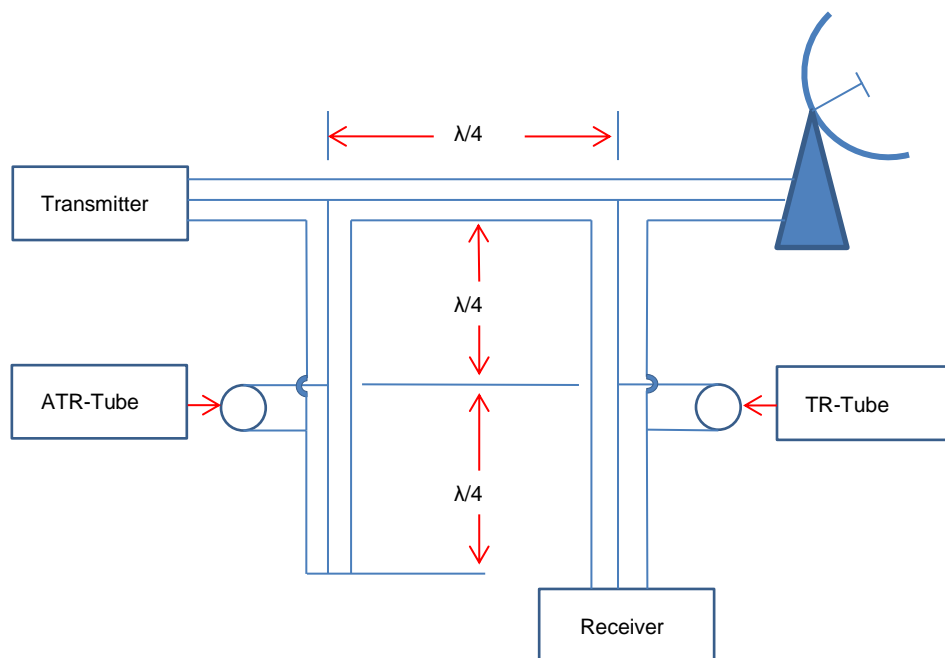


Figure 3-5 Coaxial Branch Duplexer

3.5 Low Noise Amplifier

Radar systems are predominantly cluttered limited. However, unwanted noise produced by the radar's receiver can also affect the maximum usable range. There are three types of unwanted noise produced in receiver systems listed below:

- Thermal (Johnson) noise.
- Shot noise.

- 1/F also known as pink or flicker noise.

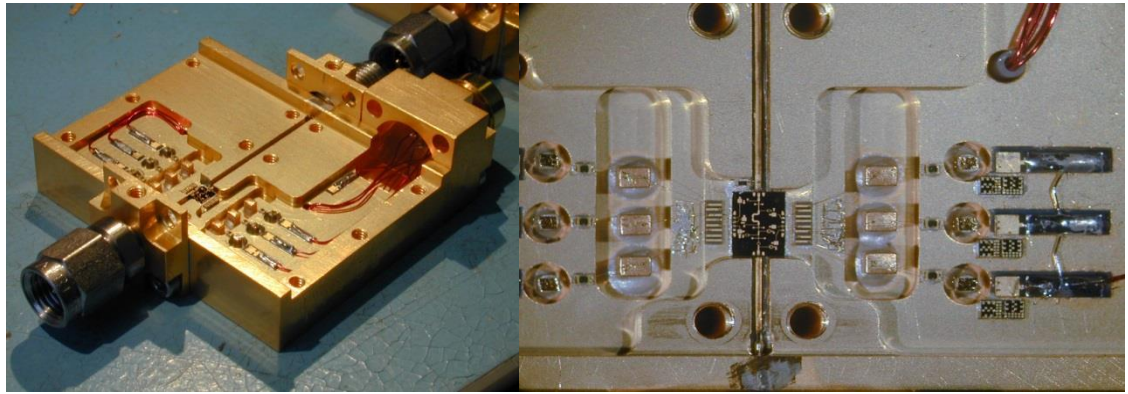


Figure 3-6 K-Band Low noise amplifier external view (left), internal view (right)

Thermal noise is produced by the agitation of charge carriers present within resistive elements inside low noise amplifiers but is also caused by any resistive loss connected to the amplifier's input. Figure 3-6 shows a high-performance K-band low noise amplifier designed for radio astronomy applications. Equation 3-1 defines the thermal noise voltage generated by resistive components.

$$V_n = \sqrt{4RKT B} \quad (3-1)$$

R = resistance in ohms.

K = Boltzmann's constant (1.38×10^{-23} J/K).

T = Temperature of the resistance in Kelvin.

B = The bandwidth of operation.

The dominant noise contribution in low noise amplifier design comes from the first transistor, assuming that all resistive losses on the input are kept to a minimum. Cascaded components after this first transistor have a smaller effect on the overall noise contribution. The Friis formula for the cascaded noise figure (Figure 3-7 and equation 3-2) enables its calculation:

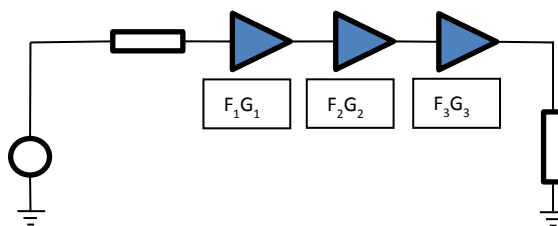


Figure 3-7 Friis Cascaded Noise figure and temperature.

$$F_{total} = F_1 + \frac{F_2-1}{G_1} + \frac{F_3-1}{G_1 G_2} + \frac{F_4-1}{G_1 G_2 G_3} + \frac{F_n-1}{G_1 G_2 G_3 \dots G_n} \quad (3-2)$$

Where:

F_{total} = the total cascaded noise factor (dB).

$F_1 \dots F_n$ = Noise factor of each stage (dB).

$G_1 \dots G_n$ = Gain of each stage (dB).

An alternative representation of the Friis equation expressed in noise temperature is given by:

$$T_{total} = T_1 + \frac{T_2}{G_1} + \frac{T_3}{G_1 G_2} + \frac{T_n}{G_1 G_2 \dots G_n} \quad (3-3)$$

Where:

T_{total} = the total cascaded noise temperature (Kelvin).

$T_1 \dots T_n$ = Noise temperature of each stage (Kelvin).

$G_1 \dots G_n$ = Gain of each stage (dB).

3.6 Up Converter

The up-converter (Figure 3-8) is a cost-effective way of generating a high-frequency waveform such as the swept frequency chirp produced by a VNA or radar, and its function is to:

- Translate a low-frequency waveform into a high-frequency output.
- Reduce system costs, it being cheaper to produce waveforms at a lower frequency.

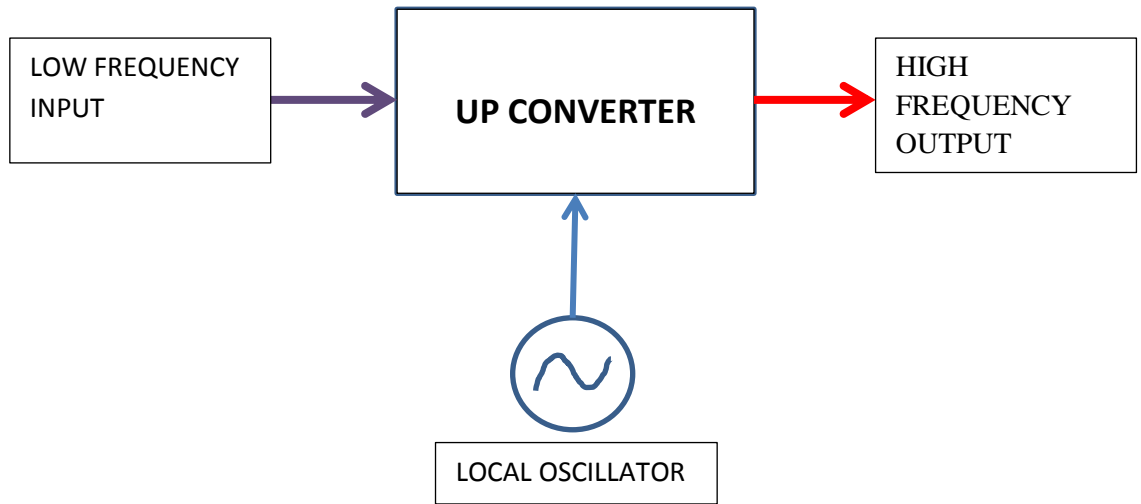


Figure 3-8 Up Converter

3.7 Down Converter

The down-converter (Figure 3-9) transforms the received high-frequency input from a radar or VNA and converts it to a lower frequency for signal processing. Its function is to:

- Convert the received signal frequencies down to more convenient lower frequencies.
- Reduce costs and takes advantage of the wider dynamic range that analogue to digital (A/D) converters possess at lower frequencies.

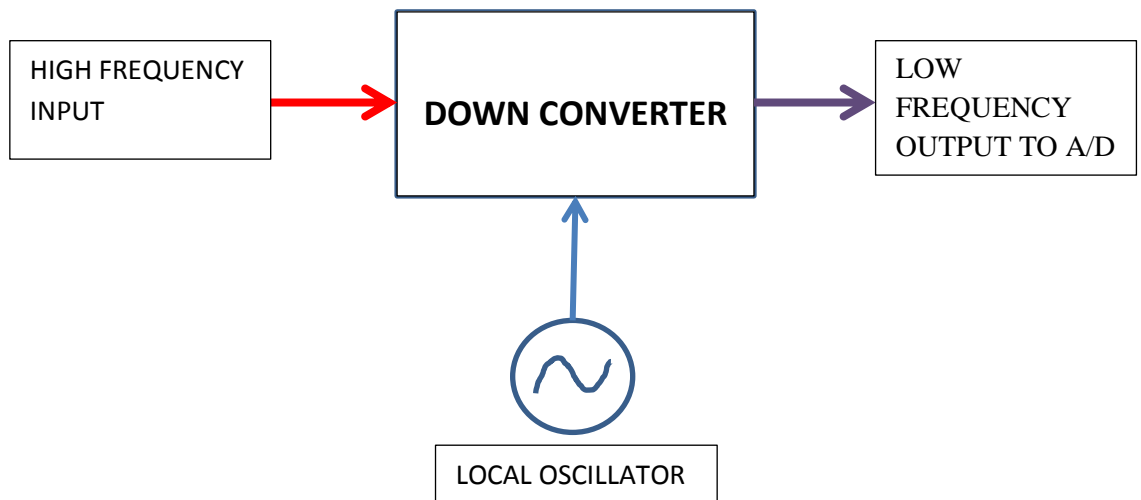


Figure 3-9 Down Converter

Chapter 4 Target Decomposition

Target decomposition is a process used in radar polarimetry and provides a technique to extract physical information from a targets scattering (Sinclair) matrix [64]. There are two main types; coherent and incoherent decomposition.

4.1 Coherent Decomposition

Coherent decomposition techniques are used for targets where coherent scattering occurs, breaking the scattering matrix down into a combination of responses from a set of simpler canonical targets. The following techniques represent coherent decompositions.

4.1.1 Pauli Matrix Decomposition

The Pauli decomposition expresses the Sinclair scattering matrix $[S]$ in the Pauli basis, equations are taken from [65] as can be seen below;

$$[S] = \begin{bmatrix} S_{HH} & S_{HV} \\ S_{VH} & S_{VV} \end{bmatrix} = \alpha[S_a] + \beta[S_b] + \gamma[S_c] \quad (4-1)$$

Where;

- $[S_a] = \frac{1}{\sqrt{2}} \begin{bmatrix} 1 & 0 \\ 0 & 1 \end{bmatrix}$ Single (odd bounce) scattering (flat metal plate, sphere)
- $[S_b] = \frac{1}{\sqrt{2}} \begin{bmatrix} 1 & 0 \\ 0 & -1 \end{bmatrix}$ Horizontal or vertical dihedral (even bounce) scattering
- $[S_c] = \frac{1}{\sqrt{2}} \begin{bmatrix} 0 & 1 \\ 1 & 0 \end{bmatrix}$ Dihedral scattering orientated at 45° (between orthogonal polarisations)
- $[S_d] = \frac{1}{\sqrt{2}} \begin{bmatrix} 0 & -i \\ i & 0 \end{bmatrix}$ Transforms all polarisation states into their orthogonal states (disappears in backscattering)

Note a flat metal plate and sphere produces a single bounce reflection, the dihedral (corner) reflector produces a double bounce reflection.

Note $[S_d]$ is redundant in the monostatic case where $S_{HV} = S_{VH}$.

Where coefficients are given by;

$$\alpha = \frac{S_{HH} + S_{VV}}{\sqrt{2}}$$
$$\beta = \frac{S_{HH} - S_{VV}}{\sqrt{2}}$$

$$\gamma = \sqrt{2S_{HV}}$$

The coefficients α , β and γ represent the contribution of each type of scattering [S_a], [S_b] and [S_c]. The intensity (power) for each of the scattering types can be found by $|\alpha|^2$, $|\beta|^2$ and $|\gamma|^2$. This decomposition is composed of six independent parameters.

4.1.2 Krogager (Sphere-Diplane-Helix) Decomposition

The Krogager decomposition expresses the Sinclair (scattering) matrix as a combination of scattering responses from standard canonical targets such as the sphere, diplane (dihedral) and helical targets. The diplane and helical targets present an orientation angle of θ to the beam of the radar. The decomposition provides five independent parameters $\{\varphi_s, \theta, k_s, k_d, \text{ and } k_h\}$ the φ term represents the absolute phase, which depends on the distance between the radar and the target. The KDH decomposition factorisation can be seen below taken from [65] [66];

$$[S] = \begin{bmatrix} S_{HH} & S_{HV} \\ S_{VH} & S_{VV} \end{bmatrix} = e^{(i\varphi)} \{ e^{(i\varphi_s)} K_S [S_S] + K_D [S_D] + K_H [S_H] \} \quad (4-2)$$

Where;

Sphere Scattering

Single (odd bounce) scattering (flat metal plate, sphere)

$$[S_S] = \begin{bmatrix} 1 & 0 \\ 0 & 1 \end{bmatrix} \quad (4-3)$$

Diplane Scattering

Diplane (dihedral) even (double bounce) scattering orientated at an angle θ .

$$[S_D] = \begin{bmatrix} \cos(2\theta) & \sin(2\theta) \\ \sin(2\theta) & -\cos(2\theta) \end{bmatrix} \quad (4-4)$$

Helix Scattering

Left hand or right-hand circular reflection

$$[S_H] = \begin{bmatrix} 1 & \pm i \\ \pm i & 1 \end{bmatrix} \quad (4-4)$$

To calculate φ_s , φ , θ , k_s , k_d , and k_h a unitary transformation is used to change the polarisation basis of equation 4-2 from the linear (HV) basis into circular (RL) equation 2-3 Chapter 2.

$$k_s = |S_{rl}| \quad (4-5)$$

When $|S_{rr}| > |S_{ll}|$ the helical component (k_h) has a left sense;

$$k_d^+ = |S_{ll}| \quad (4-6)$$

$$k_h^+ = |S_{rr}| - |S_{ll}| \quad (4-7)$$

When $|S_{ll}| > |S_{rr}|$ the helical component (k_h) has a right sense;

$$k_d^- = |S_{rr}| \quad (4-8)$$

$$k_h^- = |S_{ll}| - |S_{rr}| \quad (4-9)$$

The phase components are given by;

$$\varphi = \frac{1}{2}(\varphi_{rr} + \varphi_{ll} + \pi) \quad (4-10)$$

$$\theta = \frac{1}{4}(\varphi_{rr} - \varphi_{ll} - \pi) \quad (4-11)$$

$$\varphi_s = \varphi_{rl} - \frac{1}{2}(\varphi_{rr} + \varphi_{ll} + \pi) \quad (4-12)$$

The Krogager decomposition provides role invariant parameters $\{k_s, k_d$ and $k_h\}$ making it useful as a technique to extract information about concealed weapons [32].

4.1.3 Huynen Polarisation Fork

The Huynen polarisation fork developed on early work carried out on minimum-maximum polarisation state analysis was initially developed by Kennaugh [67] and further developed by Huynen [68]. It can be used as a representation of the full polarimetric radar signature representing a unique and natural description of a target.

The Huynen polarisation fork represents the monostatic, reciprocal (symmetric matrix) case, with all of the six characteristic polarisation states lying on a great circle on the Poincaré sphere. The Poincaré sphere is of unit radius and is used as a method to represent polarisation states graphically. When plotted on the Poincaré sphere, the fork has one handle, and three prongs (Figure 4-1) with two additional antipodal (X-pol max) points at right angles to the handle. The polarisation fork is used because it can represent physical target characteristics based on the location of the nulls. In total there are three distinct pairs of characteristic polarisation states for the symmetrical monostatic radar;

- X-pol null (X1) and the Co-pol max are co-located (the handle)

- X-pol null (X_2) – a second one is exactly opposite of X_1
- Co-pol nulls (C_1, C_2) (symmetric about X_2 -origin at an angle of 2γ from X_2)
- X-pol max's (S_1, S_2) (antipodal and at 90° from X_2)

The cross-polar nulls (X_1 and X_2) are polarisations that do not have any return in the cross polarisation (optimum polarisations) when transmitted. When transmitted, the co-polar nulls (C_1 and C_2) do not have any return in the co-polarisation. The cross-polar maximum, when transmitted, has maximum cross-polarisation return [69].

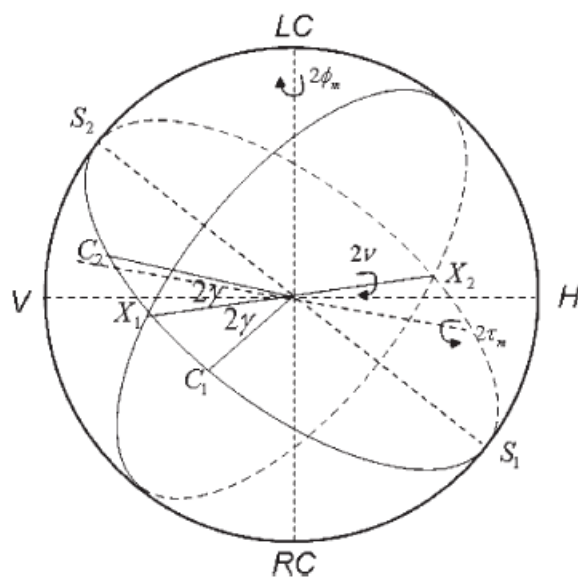


Figure 4-1 Polarisation fork plotted on the Poincaré sphere [69].

The cross-polar nulls are the same as the co-polar maximums and are always antipodal (at 180° , opposite) to one another when plotted on the Poincaré sphere. The cross-polar maxima and saddle points are distinct and also antipodal. The co-polar nulls are in the same plane on the Poincaré sphere as the cross-polar null/co-polar maximum pair [70]. Cross-polar null X_1 forms the handle connected with X_2 which forms the fork's central prong, with the co-polar nulls forming the other two prongs either side, all on the same plane in the Poincaré sphere. Figure 4-1 [69] shows an example of the fork represented on the Poincaré sphere.

The Huynen target parameters [68] are composed of seven fundamental parameters (listed below) generated from just three complex numbers of the Sinclair matrix. The Huynen polarisation parameters are derived from the cross-polar nulls (p -formulation) [54].

Figure 4-1 shows the polarisation fork plotted on the Poincaré sphere and shows its relationship with the Huynen parameters (absolute magnitude and phase are not represented on the sphere).

There are seven Huynen geometrical target parameters;

1. m = Target size (m^2).
2. ϕ_m = Target orientation (tilt) angle (radians). ϕ ($-\pi/2$ to $+\pi/2$) about the view direction in the horizontal plane of the Poincaré sphere.
3. τ_m = Target Ellipticity angle (radians): the angle of the Copol max and Xpol null (X1) on the Poincaré sphere, ranging from $-\pi/4$ to $+\pi/4$. Some refer to this as the target helicity and is zero for symmetric targets.
4. ν = Target skip angle (radians): ν ($-\pi/4$ to $+\pi/4$) 0 for flat plate, $\pi/4$ radians for dihedral, $\pi/8$ radians for quarter waveplate and is related to the number of reflections from the target.
5. Y = Target characteristic (fork) angle (radians), varying from 0 to $\pi/4$.
6. δ_m = Phase of the polarisation ratio of the co-polar maximum (radians) varying from $-\pi$ to $+\pi$.
7. α_m = Spinor angle (radians), varying from 0 to $+\pi/2$.

That is generated from just three parameters; ρ_{xn1} or ρ_{xn2} and λ_1 and λ_2

Cross-polar null's in HV basis:

$$\rho_{xn1,2} = \frac{-B \pm \sqrt{B^2 - 4AC}}{2A} \quad (4-13)$$

$$A = S_{HH}^* S_{HV} + S_{HV}^* S_{VV} \quad (4-14)$$

$$B = |S_{HH}|^2 - |S_{VV}|^2 \quad (4-15)$$

$$C = -A^* \quad (4-16)$$

Co-polar null's in HV basis are given by:

$$\rho_{cn1,2} = \frac{(-S_{HV} \pm \sqrt{(S_{HV}^2 - S_{HH} S_{VV})})}{S_{VV}} \quad (4-17)$$

The co and cross-polar nulls presented are calculated in the linear (HV) basis but could easily be defined in another basis via the application of a unitary transformation.

Deschamps parameters for the co and cross-polar nulls:

$$\alpha_{n1,2} = \tan^{-1}(|\rho_{n1,2}|) \quad (4-18)$$

$$\delta_{n1,2} = \arg(\rho_{n1,2}) \quad (4-19)$$

Phase of the unitary transformation matrix [U] ψ_1 and ψ_4 are:

$$\psi_1 = -\frac{\delta_{xn2}}{2} - \frac{\pi}{2} \quad (4-20)$$

$$\psi_4 = \frac{\delta_{xn2}}{2} - \frac{\pi}{2} \quad (4-21)$$

Orientation angle ϕ for the co and cross-polar nulls are:

$$2\phi_{n1,2} = \tan^{-1}(\tan 2\alpha_{n1,2} \sin \delta_{n1,2}) \quad (4-22)$$

Ellipticity angles of co and cross-polar nulls are:

$$2\tau_{1,2} = \sin^{-1}[\sin(\delta_{n1,2}) \sin(2\alpha_{n1,2})] \quad (4-23)$$

Unitary transformation matrix is:

$$[U(\rho_{xn1})] = \frac{1}{\sqrt{(1+\rho_{xn1}\rho_{xn1}^*)}} \begin{bmatrix} 1 & j\rho_{xn1}^* \\ \rho_{xn1} & -j \end{bmatrix} \quad (4-24)$$

Transformation of the Sinclair matrix into the new basis is:

$$[S'(AB)] = [U(\rho_{xn1})]^T [S] [U(\rho_{xn1})] \quad (4-25)$$

Basis vector based on ρ_{xn1} of the Sinclair (HV) matrix gives:

$$[S'(AB)] = \begin{bmatrix} \lambda_{11} & 0 \\ 0 & \lambda_{22} \end{bmatrix} \quad (4-26)$$

Target characteristic (fork) angle Υ is:

$$\Upsilon = \frac{1}{2} \tan^{-1} \frac{\sqrt{|\lambda_{22}|}}{\sqrt{|\lambda_{11}|}} \quad (4-27)$$

Target skip angle ν is:

$$\nu = \frac{1}{4} (\arg(\lambda_{11}) - \arg(\lambda_{22})) \quad (4-28)$$

Target size m is:

$$m = |\lambda_{11}| \quad (4-29)$$

Target spinor parameter α_m is:

$$\alpha_m = \tan^{-1} |\rho_{xn1}| \quad (4-30)$$

The Huynen Parameters generated from this technique are for a particular basis, but if the orientation (psi or phi) is taken out by applying a first rotation, the roll

dependence is taken out, so that the resulting Huynen parameters are independent of orientation, so basis independent.

Work presented in Chapter 12 of this thesis, the fork and associated parameters are generated from the coherency matrix's dominant Eigenvector values to reduce speckle effects. Using this approach fails to get the Huynen target size parameter correctly. However, this could be recovered using the Kennaugh matrix generated from the coherency matrix.

4.1.4 Euler decomposition

Closely related to the Huynen polarisation fork technique is the Euler decomposition. First developed by Huynen and Kennaugh [68] [71] with further research carried out by Baird in 2006. The Huynen fork parameters and the Euler parameters represent the fork coordinates, derived by two different methods, but the fork produced is the same in both cases.

Work started with Huynen where he discusses the Sinclair Matrix and the Kennaugh Matrix (although he calls it the Stokes Matrix). Boerner calculated using the Euler parameters derived from the Sinclair Matrix.

This decomposition produces the same set of parameters as that of the Huynen polarisation fork but derives them from diagonalisation of the targets scattering matrix. Diagonalisation of the scattering matrix is the same as a transformation to a common basis allowing extraction of phenomenological (Euler) parameters relating to information about a target's scattering properties [72].

Baird calculated them from the Kennaugh Matrix and found the analytical expressions for these, which is more convenient. This technique correctly gets the target size.

The technique is not without limitations being affected by ambiguities produced by some targets scattering properties. Baird indicating that a flat plate or sphere has no defined orientation angle ϕ , (ψ) and that, a dipole (long thin wire) when aligned vertically has an orientation angle of $\pm 90^\circ$. Another limitation is azimuth related non-persistence this is due to more than one type of scattering taking place in the image cell (pixel) [72].

Euler parameters are directly linked to the Huynen Parameters. Basis independence can be achieved in the same way as for the Huynen polarisation fork previously mentioned.

Baird's paper [72] provides a method of extracting the Euler parameters via the Kennaugh matrix generated from the Sinclair matrix as follows;

$$S = e^{ig} \begin{bmatrix} ae^{ib} & c \\ c & de^{if} \end{bmatrix} \quad (4-13)$$

Where;

$$a = |S_{hh}|$$

$$b = \text{Arg}(S_{hh}) - \text{Arg}(S_{hv})$$

$$c = |S_{hv}|$$

$$d = |S_{vv}|$$

$$f = \text{Arg}(S_{vv}) - \text{Arg}(S_{hv})$$

$$g = \text{Arg}(S_{hv})$$

The Kennaugh matrix represents the backscattered power from the target. At this point the Kennaugh matrix is still basis dependant:

$$K = \begin{bmatrix} \frac{1}{2}(a^2 + 2c^2 + d^2) & \frac{1}{2}(a^2 - d^2) & ac \cos b + d \cos f & ac \sin b - cd \sin f \\ \frac{1}{2}(a^2 - d^2) & \frac{1}{2}(a^2 - 2c^2 + d^2) & ac \cos b - cd \cos f & ac \sin b + cd \sin f \\ ac \cos b + cd \cos f & ac \cos b - cd \cos f & c^2 + ad \cos(b - f) & ad \sin(b - f) \\ ac \sin b - cd \sin f & ac \sin b + cd \sin f & ad \sin(b - f) & c^2 - ad \cos(b - f) \end{bmatrix} \quad (4-14)$$

Simplification of the Kennaugh matrix is then applied using new variables based on known parameters:

$$K = \begin{bmatrix} A_0 + B_0 & C_\varphi & H_\varphi & F \\ C_\varphi & A_0 - B_0 & E_\varphi & G_\varphi \\ H_\varphi & E_\varphi & A_0 - B_0 & D_\varphi \\ F & G_\varphi & D_\varphi & -A_0 + B_0 \end{bmatrix} \quad (4-15)$$

To remove the basis dependence of the Kennaugh matrix a series of back rotations are now performed one by one to remove the dependence of the orientation (ψ), ellipticity (τ) and the skip (ν) angles.

$$\varphi = \tan^{-1} \left(\frac{-C_\varphi + \sqrt{C_\varphi^2 + H_\varphi^2}}{H_\varphi} \right) \quad (4-16)$$

$$\tau = \frac{1}{2} \tan^{-1} \left(\frac{F_{\varphi}}{C_{\varphi} \cos(2\varphi) + H_{\varphi} \sin(2\varphi)} \right) \quad (4-17)$$

$$\nu = \frac{1}{2} \tan^{-1} \left(\frac{B - A_0 + \sqrt{(B - A_0)^2 + (D \cos(2\tau) - E \sin(2\tau))^2}}{D \cos(2\tau) - E \sin(2\tau)} \right) \quad (4-18)$$

Where;

$$B = B_{\varphi} \cos(4\varphi) + E_{\varphi} \sin(4\varphi)$$

$$E = E_{\varphi} \cos(4\varphi) - B_{\varphi} \sin(4\varphi)$$

$$D = D_{\varphi} \cos(2\varphi) - G_{\varphi} \sin(2\varphi)$$

The resulting Kennaugh matrix is now independent of the orientation, ellipticity and skip angles:

$$K''' = m^2 \begin{bmatrix} \frac{1}{2}(1 + \tan(\gamma)^4) & \frac{1}{2}(1 - \tan(\gamma)^4) & 0 & 0 \\ \frac{1}{2}(1 - \tan(\gamma)^4) & \frac{1}{2}(1 + \tan(\gamma)^4) & 0 & 0 \\ 0 & 0 & \tan(\gamma)^2 & 0 \\ 0 & 0 & 0 & -\tan(\gamma)^2 \end{bmatrix} \quad (4-19)$$

From this form of the Kennaugh matrix, the roll invariant Euler parameters can now be found using equations (4-20) and (4-21).

Where;

m is the target's size (m²).

Y is the target characteristic (fork) angle (radians).

$$m = \sqrt{A_0 + B_0 + \sqrt{C_{\varphi}^2 + F_{\varphi}^2 + H_{\varphi}^2}} \quad (4-20)$$

$$\gamma = \tan^{-1} \left[\frac{A_0 + B_0 - \sqrt{C_{\varphi}^2 + H_{\varphi}^2 + F_{\varphi}^2}}{A_0 + B_0 + \sqrt{C_{\varphi}^2 + H_{\varphi}^2 + F_{\varphi}^2}} \right]^{1/4} \quad (4-21)$$

4.2 Depolarisation

One of the key issues in polarimetry is something referred to as depolarisation. In this context depolarisation is a change in the target with respect to its illumination, which causes a change in the target scattering (Sinclair) matrix. It is an assumption by the remote sensing community that depolarisation is caused by physical movement of the target or the radar or both. These movements can be much smaller

than the wavelength of the radiation. Understanding the level of depolarisation is important. If there is no depolarisation, or the depolarisation can be reduced below a certain level, it is possible to use coherent processing techniques to analyse data. If there are considerable depolarisation levels, a wave coherency matrix approach needs to be taken, whereby multiple samples of the Sinclair matrix need to be processed.

The coherency matrix is also important for decomposition, as it contains information related to the physical properties of a target [64]. The coherency matrix contains essentially the same information as the covariance matrix and the Kennaugh matrix. The information cannot be captured from a single Sinclair matrix measurement but must be derived from multiple samples of this matrix, as discussed later.

4.3 Incoherent Decomposition

Naturally occurring (distributed) targets exhibit a degree of random speckle. Certain targets may have a degree of depolarisation, meaning that the Sinclair matrix $[S]$ cannot be used independently without applying a second-order statistical approach. The application of the second-order 3×3 Hermitian average covariance $[C_3]$ or coherency $[T_3]$ matrices are suitable for this, and both are equivalent at representing the polarimetric information [65] [73] [32].

4.3.1 H-alpha Decomposition

Cloude and Pottier developed the H- α decomposition technique based on eigenvalue decomposition of the targets coherency matrix in 1997 [43]. It is regarded by the remote sensing community as the superior incoherent polarimetric decomposition and widely used. The method has the advantage of being roll invariant (target aspect independent), making it ideal for detecting concealed weapons.

Measurements made by [74] [32] taken in the linear (HV) basis led to a set of target-related Sinclair matrices. Vectorisation then applied to these via the Pauli spin matrix set led to a set of target vectors used to generate the 3×3 coherency matrix.

The coherency matrix's eigenvalues provide the statistical weights for the three target scattering types (surface, volumetric, double bounce) [49]. Where anisotropy (α) describes the average behaviour of the target scattering, represented by an

angle ranging from 0° to 90° , where 0° indicates the target is causing a single bounce (surface) reflection such as that caused by the human body or a flat metal plate. An angle of 45° indicates the target has a volumetric scattering response such as that produced by reflection from a forest in remote sensing. An angle of 90° would indicate the target is producing a double bounce (dihedral) scattering.

The H term represents the level of polarimetric entropy. It ranges from values of 0 to 1, where 0 indicates the target is causing minimal depolarisation, and a value of 1 indicates the scattering process is stochastic (noise-like) in nature. Graphical representation of the different scattering types is presented in Figure 4-2 and tabulated in Table 4-1. The β term indicates the targets physical orientation angle.

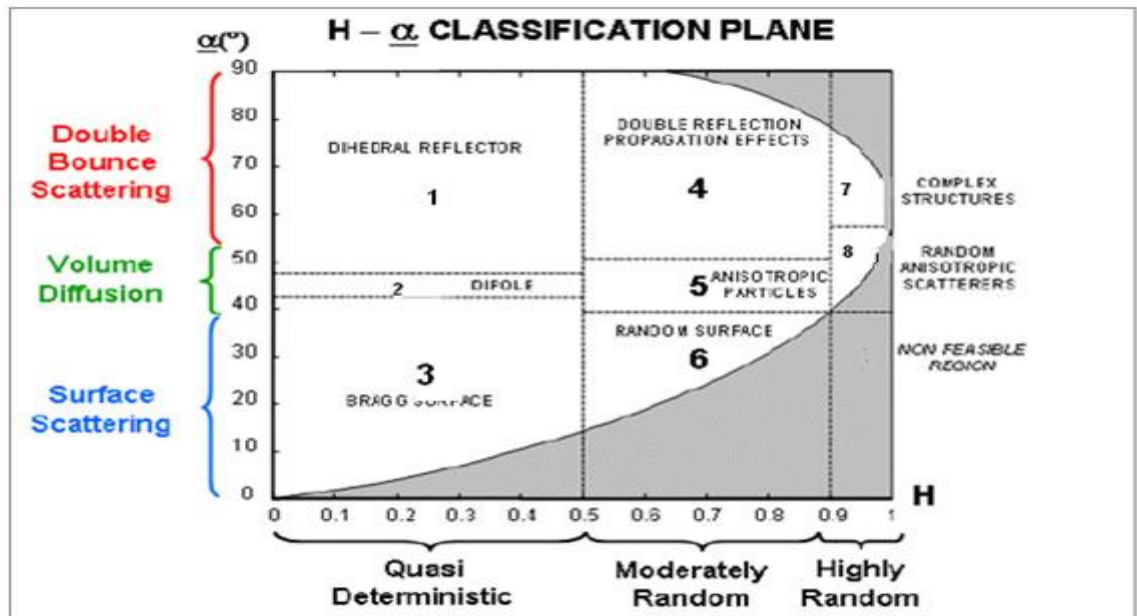


Figure 4-2 Graph showing Wishart classification [75] [76].

Class	Description	Criteria
1	Low entropy (double bounce) scattering	$\alpha > 48$, $H < 0.5$
2	Low entropy (dipole) scattering	$\alpha > 42 \leq 48$, $H \leq 0.5$
3	Low entropy (surface) scattering	$\alpha \leq 42$, $H = 0.5$
4	Medium entropy (multiple) scattering	$\alpha \geq 50$, $H = 0.5$ to 0.9
5	Medium entropy (dipole) scattering	$\alpha \geq 40 \leq 50$, $H = 0.5$ to 0.9
6	Medium entropy (surface) scattering	$\alpha \leq 40$, $H = 0.5$ to 0.9
7	High entropy (double bounce) scattering	$\alpha \geq 55$, $H > 0.9$
8	High entropy (multi target) scattering	$\alpha \geq 40 \leq 55$, $H > 0.9$

Table 4-1 H- α class descriptions [75] [76].

4.4 Summary

In summary, the coherent decompositions such as the Pauli and Krogager (SDH) and Huynen techniques express the scattering matrix as a set of simpler canonical radar targets. Using the Pauli technique, these are an odd bounce reflector such as a sphere or plate and a dihedral at 0° and 45° orientations.

The Krogager technique decomposes the target's response into that of a sphere, diplane (dihedral) and helix. Both decomposition types provide six independent variables; however, the Krogager realistically only provides five independent parameters. The real phase term (ψ) is an arbitrary value dependant on the range between the radar and the target.

The Huynen polarisation fork technique provides seven parameters derived from just three complex numbers taken from the target's scattering matrix. These parameters provide information about target size, orientation, ellipticity (helicity), skip, characteristic (fork), and spinor angles plus the polarisation phase ratio.

The Euler parameters are the same as the Huynen parameters, providing information about target size, target orientation, ellipticity (helicity), skip, characteristic (fork), and spinor angles plus the polarisation phase ratio. The first rotation produces a roll invariant Kennaugh matrix.

A limitation of using coherent decomposition techniques is that they can suffer from speckle issues, especially from distributed scatterers.

The H-alpha decomposition is an incoherent technique providing a statistically based role invariant method to extract information about a targets type; (surface, volumetric and double bounce). It includes information regarding the polarimetric entropy from minimally depolarised to fully stochastic. Concerns have been raised over this decomposition, however. Corr and Rodrigues [77] compare the decompositions response to a helix and a dihedral, and both produce the same value of alpha ($\alpha=90^\circ$), also reported by Lee et al. [78].

The advantage of using incoherent decompositions is that they reduce speckle from distributed scatterers acting as a speckle filter and perform this by applying the covariance or coherency matrices.

The Huynen fork technique provides seven target related parameters but being a coherent technique has limited susceptibility to speckle. It is possible to adapt the method to a coherent technique by application of the coherency matrix.

Chapter 5 Radar System Design

5.1 Introduction

From the literature survey (chapter 1) and an assessment made of millimetre wave radar technology and techniques (chapter 3), the radar type chosen is of the stepped frequency (FMCW) type using a vector network analyser (VNA). The VNA does not operate as an FMCW radar, but rather as a stepped-frequency carrier wave (CW) radar. That is, at each frequency, it stops to illuminate a scene and mixes the return at that frequency with the transmitted signal, then repeats the process across the bandwidth at each chosen frequency step. FMCW works on a beat principle of mixing the return signal with the frequency currently being transmitted. You end up with the same result from the two schemes after appropriate processing. FMCW allows for a much quicker bandwidth sweep time, which would be a consideration here to reduce target movement effects (especially for the Sinclair decomposition), however only a VNA was available at the time measurements were taken. Unlike an FMCW, a stepped frequency VNA radar has to illuminate all parts of the scene and collect the return before moving on to the next frequency.

The horn type used is a conical corrugated one and the OMT of the Turnstile type. The frequency range is 18 to 26 GHz (K-band).

The output power for the VNA (source) is set to 1mW to meet with health and safety exposure limits (please refer to risk assessment in appendix A).

This chapter presents the mathematical steps taken to design the radar. Figure 5-1 shows a block diagram of the proposed radar configuration. Figure 5-2 shows the assembled radar with its 'state of the art' turnstile OMT fitted with a conical corrugated horn antenna ready for radar trials.

Full radar polarimetry was chosen because it provides the maximum amount of information about the physical properties of targets including size and orientation, combined with the stepped frequency (FMCW) radar technique, the thickness of dielectric targets can also be obtained.

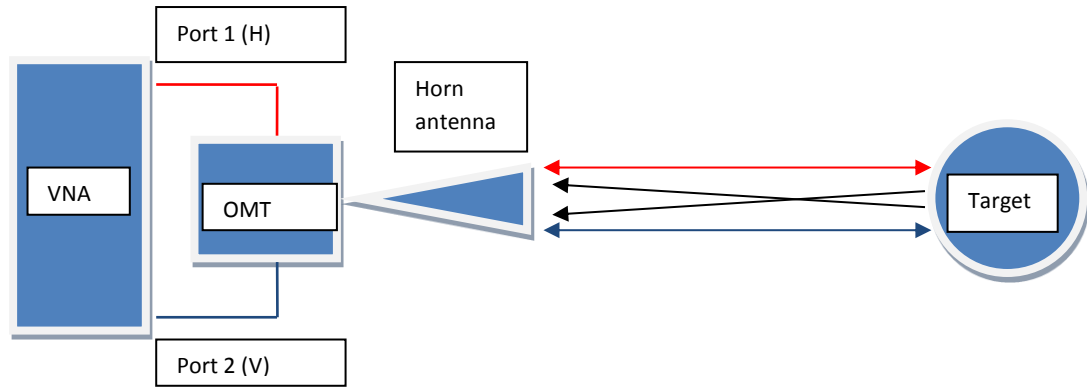


Figure 5-1 A schematic of the full polarimetric monostatic FMCW radar system

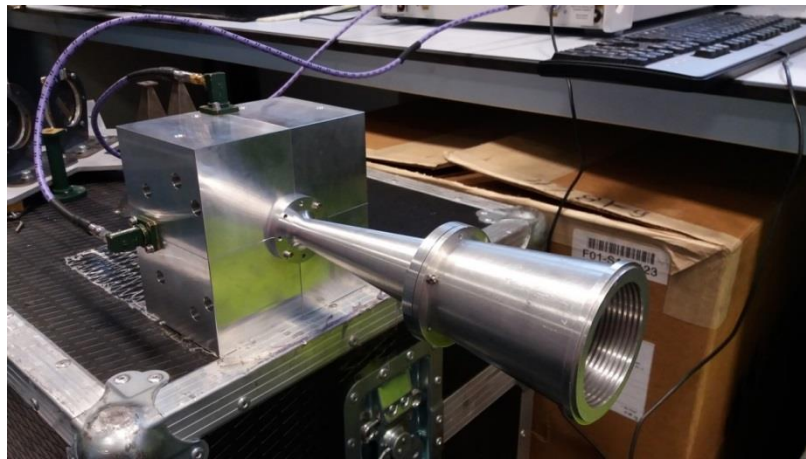


Figure 5-2 Polariser with Corrugated Horn fitted for radar measurements.

5.2 Radar Calculations

The following section utilises an analytical approach to try to determine the radar's performance. Due to space constraints in the laboratory, targets were positioned at a range of two meters and beyond this an anechoic wall of microwave absorber at five meters to reduce clutter. Path attenuation at sea level for K-band under standard conditions is of the order of 0.1dB/km rising to around 0.8dB/km when rain is present (Figure 5-3). It is not considered a limiting factor for the radar presented here as the maximum design range will only be of the order of 15 metres or less.

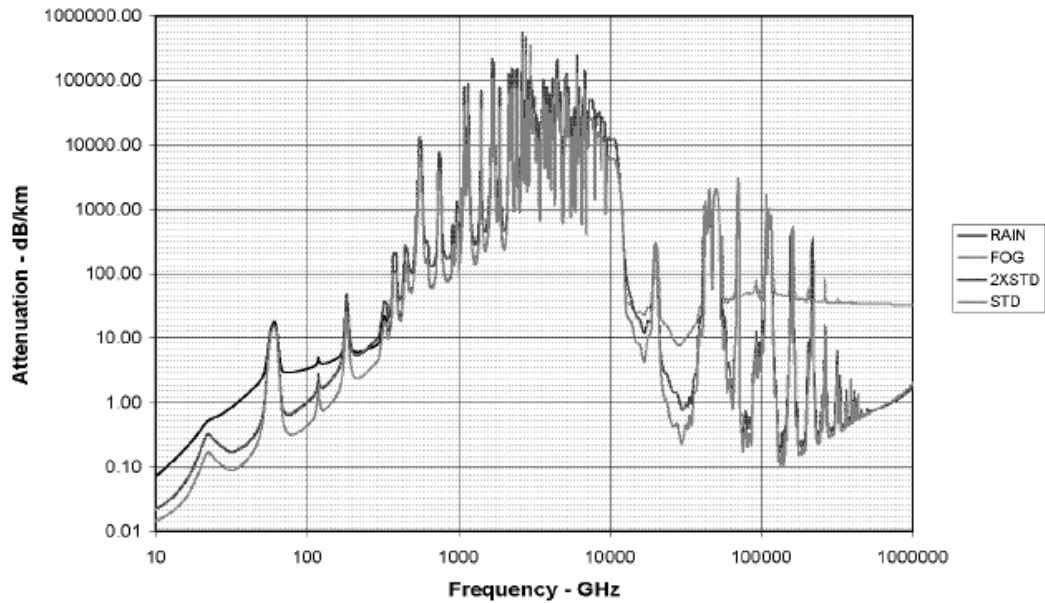


Figure 5-3 Atmospheric Absorption. [79]

List of parameters used in the calculations to predict radar performance:

- $T_{\text{amb}} = 290\text{K}$
- $k = 1.38 \times 10^{-23} \text{ J/K}$ (Boltzmann's constant)
- $P_T = 1\text{mW}$ (VNA output power)
- $\sigma = 3.32 \times 10^{-3}\text{m}^2$ (Radar cross section of a 6.5cm diameter metal sphere)
- $T_r = 500\text{K}$ (VNA receiver noise temperature)
- $B_n = 10\text{kHz}$ (VNA I.F bandwidth)
- $G_T = 100$ as a ratio. (Horn gain 20dB).
- $\Delta_f = 8\text{GHz}$ (Radar bandwidth).
- $\lambda_{22\text{GHz}} = 0.013636 \text{ m}$ (wavelength at 22 GHz).
- S_{min} = Minimum signal power detectable by the receiver.
- k = Boltzmann's constant ($1.38 \times 10^{-23} \text{ J/K}$)
- B_n = Receiver intermediate frequency (I.F) bandwidth (10kHz).
- F_n = Receiver noise factor.
- S_o = Receiver output signal.
- N_o = Total receiver noise.
- $(S_o/N_o)_{\text{min}}$ = Minimum signal to noise ratio required by the receiver to detect the signal.

Note an I.F bandwidth of 10 kHz was chosen to reduce the VNA's noise floor. Measured target-related information is proportional to bandwidth, so a larger bandwidth has the potential to extract more target-related information, but only if

that information is present in the first place. Using a wider I.F bandwidth would give a higher noise level with a VNA based stepped frequency radar. Using a narrower I.F bandwidth could lead to a decrease of target-related information.

5.2.1 Radar Cross-section of a 6.5 cm diameter sphere

To calculate the radar's maximum usable range a target with known radar cross-section is required. A 6.5 cm diameter sphere was chosen for this calculation, as this is most representative of the size of an object carried on an individual. Additionally, this is a standard size of stainless steel sphere available commercially with radar cross-section (σ) given by equation 5-1 [80]:

$$\sigma = \pi \cdot r^2 \quad (5-1)$$

$$\sigma = \pi \times 0.0325^2$$

$$\sigma = 3.3 \times 10^{-3} m^2$$

5.2.2 Predicted receiver noise factor

The VNA receiver produces a level of noise that will limit the maximum usable range of the radar. In turn, the signal reflected by an object will decrease with increased range. At some point, this signal becomes lost in the noise produced by the VNA's receiver. The noise factor is defined as the signal to noise ratio at the receiver's input to the signal to noise ratio at the output. Noise figure is the noise factor expressed in dB. Both noise figure and factor are used to represent the degradation of the signal to noise ratio as a signal passes through a device [81]. Noise figure can also be expressed in terms of noise temperature T_r (in Kelvin) as can be seen in equation 5-2

Receiver noise factor [82]:

$$F_n = \frac{T_r}{T_{amb}} + 1 \quad (5-2)$$

$$F_n = \frac{500}{290} + 1$$

$$F_n = 2.72$$

5.2.3 VNA Receiver Signal to Noise Ratio

The signal to noise ratio provides information about the desired signal (in this case backscattered from a target) to the unwanted noise produced in the VNA receiver.

The typical co-polar backscattered rms voltage by reflection from the human torso can be calculated using the radar equation. The rms voltage is related to the received power (P_r) using the equation:

$$V_{rms} = \sqrt{P_r \chi Z} \quad (5-3)$$

Where Z is the system impedance (50Ω).

The received power is related to the transmit power (P_t) by the radar equation [21] for the monostatic configuration:

$$P_r = \frac{P_t \lambda^2 \sigma G^2}{(4\pi)^3 R^4 L^2} \quad (5-4)$$

Where:

P_t is the VNA transmitter power (1mW).

λ is the radiation wavelength (m) (0.0136 metres at 22 GHz).

σ is the radar cross-section, in this case of the human torso illuminated by the antenna beam (m).

G is the antenna gain (as a numerical ratio) approximately 100 for the antenna used.

R is the range (m).

L is the loss of the VNA front-end components and path attenuation (as a numerical ratio) typically 1.3 in this case.

The radar cross-section of the human torso can be calculated assuming it is a plane surface normal to the beam of the radar beam given by [83] (page 121):

$$\sigma = \frac{4\pi A^2 \Gamma}{\lambda^2} \quad (5-5)$$

Where:

A is the area of the torso in the antenna beam assumed to be approximately 0.12 m².

Γ is the reflectance of the human body, assumed to be approximately 0.5.

Using the values from equations 5-4 and 5-5, for a range of 2 metres, give an estimated rms voltage from equation 5-3 to be:

$$V_{rms(torso)} = 0.03 \text{ (Volts)}$$

The noise power produced by the receiver at the reference point at the input to the VNA is:

$$P_{VNA} = F_n \cdot K \cdot T_{amb} \cdot B \quad (5-6)$$

Where:

F_n is the receiver noise factor from the previous calculation.

K is Boltzmann's constant given at the beginning of this chapter.

B is the receivers I.F BW given at the beginning of this chapter.

$$P_{VNA} = 2.72 \times 1.38 \times 10^{-23} \times 290 \times 10 \times 10^3$$

$$P_{VNA} = 1.089 \times 10^{-16} \text{ Watts}$$

The rms noise voltage produced by the VNA's receiver is:

$$V_{rms(VNA)} = \sqrt{P_{VNA} \times Z} \quad (5-7)$$

Where Z is the system impedance of 50Ω .

$$V_{rms(VNA)} = 73.77 \times 10^{-9} \text{ Volts(rms)}$$

The signal to noise ratio is:

$$VNA_{SNR} = \frac{V_{rms(target)}}{V_{rms(VNA)}} \quad (5-8)$$

$$VNA_{SNR} = \frac{0.03}{73.77 \times 10^{-9}}$$

$$VNA_{SNR} = 410.958 \times 10^3$$

The above-estimated signal to noise ratio is very high and make the point that this is possible in radar due to the large signal powers used in relation to the noise.

5.2.4 Predicted minimum detectable signal

The receiver noise figure can be used to estimate the minimum detectable signal, a benchmark used to evaluate system performance. It indicates the magnitude of the signal required to equal the noise. Equating the signal level to the noise indicates the minimum detectable signal is [21] [84]:

$$S_{min} = kT_{amb}B_nF_n \left(\frac{S_o}{N_o} \right)_{min} \quad (5-9)$$

If the minimum signal to noise ratio of the receiver is unity this then gives the minimum detectable signal as;

$$S_{min} = 1.38 \times 10^{-23} \cdot 290 \cdot 10 \times 10^{-3} \cdot 2.72$$

$$S_{min} = 108 \times 10^{-18} W$$

This metric does not indicate the level of power that should be detected to extract information from a target, but merely as an indication of the power of the signal that needs to enter the system to equal the effect of the noise.

Receiver operating characteristics (ROC) are frequently used to indicate system performance. Central to this analysis in the ROC curve it shows how the detection probability for a particular target (y-axis) varies with the false alarm rate (x-axis) as the threshold of a particular detection metric is changed [85]. The optimal place on the curve has the coordinates (0,1), whilst the diagonal line from the coordinate (0,0) to (1,1) is the so-called line of no discrimination, corresponding to a random decision as to whether a signal represents a target or not. The ROC curve is dependant on the target, the detection algorithm and the noise in the system. A performance metric commonly used to evaluate systems is the area under the ROC curve (AUC), where systems normally have a value between the optimum of unity and 0.5. The use of ROC curves to evaluate performance would constitute the next phase of this work on polarimetry for target identification.

5.2.5 Predicted Maximum usable range

The maximum usable range calculation is derived from the radar equation and provides the maximum range that a target of given radar cross-section is detectable. The radar cross-section (σ) of a 6.5cm diameter stainless steel sphere calculated using equation 5-1 provides the target for this calculation. Predicted maximum usable range [86];

$$R_{Max} = \sqrt[4]{\frac{P_T \cdot G^2 \cdot \lambda^2 \cdot \sigma}{(4 \cdot \pi)^3 \cdot S_{min}}} \quad (5-10)$$

$$R_{max} = \sqrt[4]{\frac{(1 \times 10^{-3}) \times 100^2 \times 0.0136363^2 \times (3.3 \times 10^{-3})}{(4 \cdot \pi)^3 \times 108 \times 10^{-18}}}$$

$$R_{Max} = 73 \text{ m}$$

5.2.6 Range Resolution

The range resolution is a measure of the radar's ability to resolve two objects that are in close proximity. If the two targets are separated by an amount smaller than the range resolution, then the radar will only resolve them as a single object. If the separation is larger than the range resolution, the radar will see two targets. Radar range resolution [87];

$$\Delta_R = \frac{c}{2\Delta_f} \quad (5-11)$$

Where;

Δ_R is the range resolution (m).

c is the speed of light (m/s).

Δ_f is the radar's bandwidth (Hz).

$$\Delta_R = \frac{3 \times 10^8}{2 \cdot (8 \times 10^9)}$$

$$\Delta_R = 1.875 \text{ cm}$$

5.2.7 Sampling

The FMCW radar produces a linear sweep of the transmitted frequency from the start frequency (18GHz) to the stop frequency (26GHz) which takes a time t_m . The reflection back from the target arrives back at the radar after time t_r and produces a beat frequency f_b . The beat frequency is highest at the maximum working range of the radar, which is 5 metres. The beat frequency determines the sampling frequency, which to satisfy the Nyquist sampling criteria must be at least twice the beat frequency to prevent aliasing. The sampling time for the stepped frequency radar presented is the time taken to perform the frequency increments from 18 to 26 GHz. Sampling takes place on the VNA at the instrument's intermediate frequency (I.F) which has several predefined settings, 10 kHz selected in this case. The IFBW must, therefore, be at least twice that of f_b where f_b is defined by [32]:

$$f_b = \frac{2R\Delta_f}{T_s c} \quad (5-12)$$

In practice, the VNA sets T_s and hence f_b automatically to avoid aliasing and depends on the IFBW and the radars maximum working range. With a maximum working range in the lab of five metres, the VNA has a sweep time of 98.859ms which gives a beat frequency $f_b = 2.697 \text{ kHz}$:

$$T_S = \frac{2R_{max}\Delta f}{f_b c} = \frac{2 \times 5 \times (8 \times 10^9)}{(2.6974 \times 10^3)(3 \times 10^8)} = 98.859 \text{ms} \quad (5-13)$$

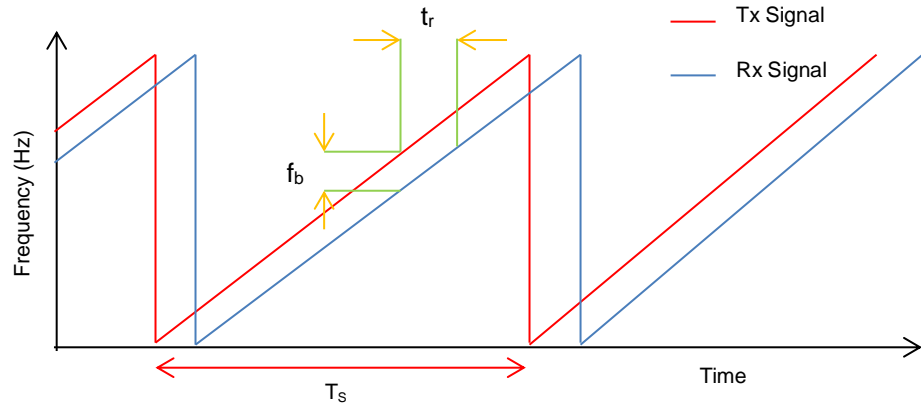


Figure 5-4 FMCW Range extraction

5.2.8 Unambiguous Range calculation

For the FMCW radar this the range at which reflections can be recovered before the next frequency sweep is performed, the unambiguous range is:

$$R_{unambiguous(FMCW)} = \frac{c}{2f_p} \quad (5-14)$$

Where f_p is the sweep rate (or 1/time for 1 sweep).

For the VNA-based stepped frequency radar this is the maximum range at which a transmitted pulse can be successfully recovered and processed before the next pulse is transmitted.

If the next pulse or frequency sweep is performed before the reflections from the previous pulse or frequency sweep are received then there will be no way of discriminating which pulse or frequency sweep produced those reflections leading to erroneous measurements.

It is important to understand the environment in which a target is to be measured. For example, if an object beyond the target's position produces reflections, then the radar's unambiguous range needs to be larger than this to stop potential erroneous measurement issues.

The VNA based radar operates in a similar way to that of an FMCW system but is one in which discrete frequency steps are made. Equation 5-15 shows unambiguous range calculation from these discrete frequency increments.

The VNA allows setting the number of predefined spectral increments (points) that the instrument uses to sweep across the desired band of operation (18 to 26GHz),

Δf of 8 GHz. A step frequency of 10 MHz (801 points across the 18 – 26 GHz band) was chosen to set the unambiguous range ($R_{unambiguous}$) to 15 metres, the intended operating range. Unambiguous range [32]:

$$R_{unambiguous} = \frac{c \cdot points}{2\Delta f} \quad (5-15)$$

$$R_{unambiguous} = \frac{(3 \times 10^8) \times 801}{2 \times (8 \times 10^9)}$$

$$R_{unambiguous} = 15m$$

Measurements at smaller step sizes indicate that no radiation from ranges greater than 15 m is measured with 0 dBm transmit power (1mW), which means that measurements out to 15 m will be unambiguous.

Table 5-1 shows the proposed radar specification from the calculations detailed in this chapter.

Radar parameter	Value
Frequency Range	18 to 26 GHz
Number of points	801
Number of samples per point	10
Maximum unambiguous usable range	15 meters
Range resolution	1.875 cm
Sweep time (T_s)	98.859 ms
I.F bandwidth	10 kHz
Antenna gain	20 dB
3dB beamwidth	12°
Transmit power	0 dBm

Table 5-1 Radar Specification

Chapter 6 Microwave Measurements using vector network analysers (VNA's)

In this chapter, we examine how microwave measurements using a VNA are acquired. The voltage standing wave ratio (VSWR), reflection and transmission coefficients and their relation to the scattering parameters are shown. Sources of errors affecting VNA measurements and a method of calibration to remove these error sources also presented.

6.1 Scattering Parameters

Scattering parameters describe the behaviour of linear electrical networks. They are used to characterise microwave components like filter loss and amplifier gain and can be measured by a vector network analyser (VNA).

The scattering parameters are dimensionless quantities representing voltage ratios at the input and output of electrical networks. They can be measured at different frequencies and contain magnitude and phase information and represented in a matrix form.

Figure 6-1 shows a VNA with ports 1 and 2 visible at the instrument's lower left and right, where devices under test (DUTs) are connected.

Figure 6-2 shows a simplified flow diagram of a device under test (DUT) connected to a 2-port network such as VNA.

An incident wave propagates from the VNA to the DUT represented by the letter 'a', the reflected wave from the DUT represented by the letter 'b' with the relationship between scattering parameters and the incident and reflected waves given in equation 6-1.

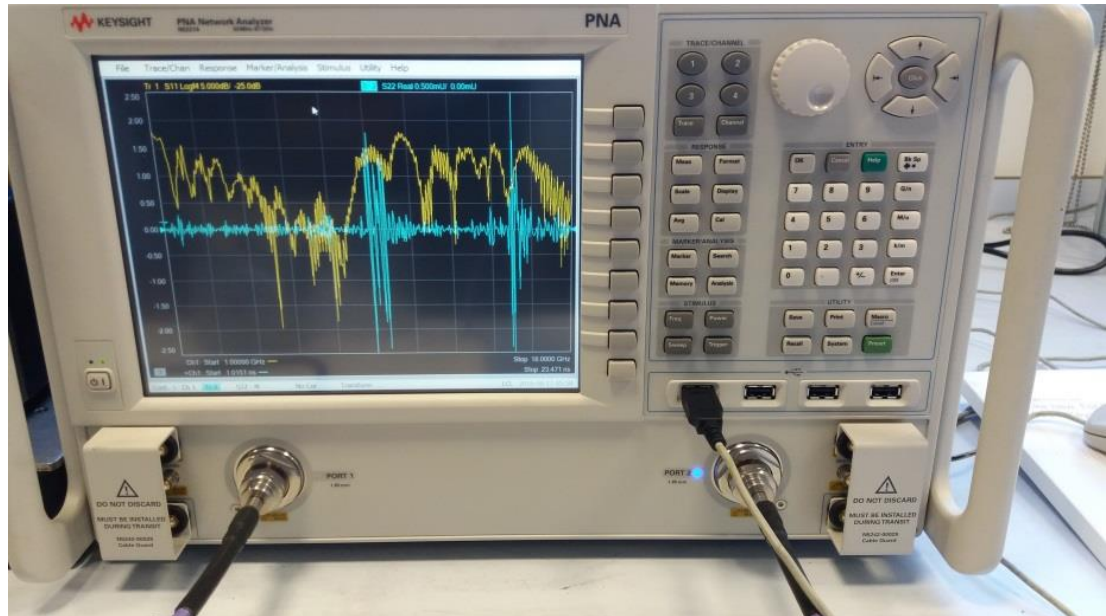


Figure 6-1 Vector Network Analyser

With reference to Figure 6-2 and equation 28, the scattering parameters are;

- $S_{11}=b_1/a_1$ this is Γ_1 at port 1 when Γ_L and $a_2=0$.
- $S_{21}=b_2/a_1$ this is the reflection coefficient from port 1 to 2 when $\Gamma_L=0$ and a matched load is placed on port 2.
- $S_{12}=b_1/a_2$ this is the reflection coefficient from port 2 to 1 when $\Gamma_g=0$ and a matched load is placed on port 1.
- $S_{22}=b_2/a_2$ this is Γ_2 at port 2 when Γ_g and $a_1=0$.

Where Γ_1 is the port 1 reflection coefficient, Γ_2 is the port 2 reflection coefficient, Γ_g is the reflection coefficient of the VNA source (signal generator), Γ_L is the matched load reflection coefficient.

Scattering parameters are dimensionless parameters although once converted to decibels (dB), are useful to calculate the gain or loss of cascaded devices such as an amplifier with an attenuator connected to its output. If the input of the device under test is connected to port 1 then;

- S_{11} is input return loss $(-20\log_{10}|S_{11}|)$ dB.
- S_{22} is output return loss $(-20\log_{10}|S_{22}|)$ dB.
- S_{21} is the forward transmission loss/gain $(20\log_{10}|S_{21}|)$ dB.
- S_{12} is the forward transmission loss/gain $(20\log_{10}|S_{21}|)$ dB

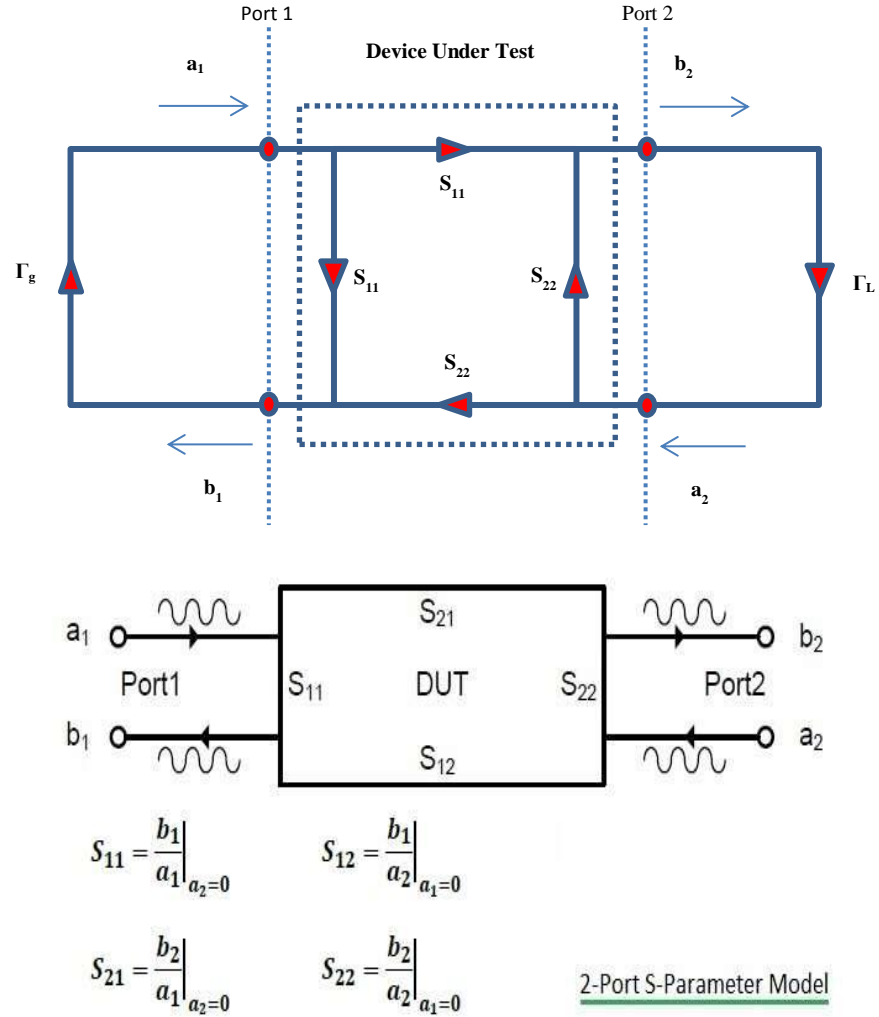


Figure 6-2 Simplified S-parameter model for a two port network [88] [89] [90] [91].

$$\begin{bmatrix} b_1 \\ b_2 \end{bmatrix} = \begin{bmatrix} S_{11} & S_{12} \\ S_{21} & S_{22} \end{bmatrix} \begin{bmatrix} a_1 \\ a_2 \end{bmatrix} \quad (6-1)$$

6.2 VSWR, Reflection Coefficient and Return Loss

For maximum signal transfer from a source to a load, the source impedance must be equal to the load impedance. If this is not the case, then some of the incident signal will be reflected back to the source due to the load impedance mismatch. Any discontinuities along the transmission line between source and load will also cause unwanted reflection.

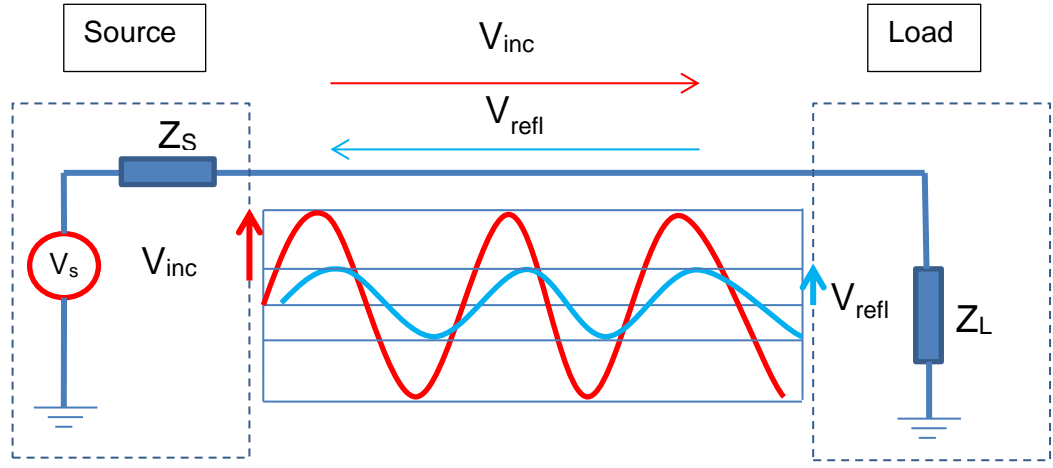


Figure 6-3 Forward and Reflected waves between source and load.

Figure 6-3 and equation 6-2, shows that the voltage standing wave ratio (VSWR) is dimensionless and is simply the maximum voltage of the incident and reflected waves divided by the minimum voltage, the difference between incident and reflected waves [92].

$$VSWR = \frac{V_{max}}{V_{min}} = \frac{V_{inc} + V_{refl}}{V_{inc} - V_{refl}} \quad (6-2)$$

The reflection coefficient found using equation 6-3 is a dimensionless number related to the incident and reflected waves and impedance of the signal source and load impedance [92].

$$\Gamma = \rho = \frac{V_-}{V_+} = \frac{Z_L - Z_S}{Z_L + Z_S} \quad (6-3)$$

The transmission coefficient found using equation 6-4 again a dimensionless number and both reflection and transmission coefficients are complex values [92].

$$\tau = \frac{V_L}{V_+} = \frac{2Z_S}{Z_L + Z_S} \quad (6-4)$$

$$\tau - \rho = 1 \quad (6-5)$$

The VSWR can also be found from the reflection coefficient as can be seen in equation 6-6 [92].

$$VSWR = \frac{1 + |\rho|}{1 - |\rho|} \quad (6-6)$$

Return loss (RL) in dB can be found from the reflection coefficient using equation 6-7 [92].

$$RL = -20 \log_{10} |\rho| \quad (6-7)$$

Return loss can be found from the S_{11} scattering parameter using equation 6-8

$$RL = -20\log_{10}|S_{11}| \quad (6-8)$$

Return loss can also be found from the VSWR using equation [92].

$$RL = -20\log_{10} \frac{VSWR-1}{VSWR+1} \quad (6-9)$$

Return loss can also be related to the incident and received power using equation 6-10.

$$Return Loss(db) = 10 \cdot \log_{10} \left(\frac{P_i}{P_r} \right) \quad (6-10)$$

6.3 VNA calibration via the through reflect line (TRL) method

Calibration of vector network analysers is required to account for unwanted errors. These errors can be broken down into three types, systematic, random and drift errors. [93]

Systematic errors caused by:

- Directivity and crosstalk.
- Mismatch of source and load impedances.
- Reflection and transmission issues leading to frequency response errors.

Random errors caused by:

- Instrument noise.
- Internal switch repeatability.
- Connector mate, de-mate repeatability.

Drift errors caused by:

- VNA internal component drift associated with temperature change.

Systematic errors can be reduced with calibration.

Random errors caused by noise can be reduced by calibration using higher source power, reducing intermediate frequency (I.F) bandwidth, and using trace averaging.

Drift errors can be reduced by allowing the VNA to warm up after being switched on so that the temperature can stabilise before calibration. Ideally, the VNA should be located in an environment with a stable temperature.

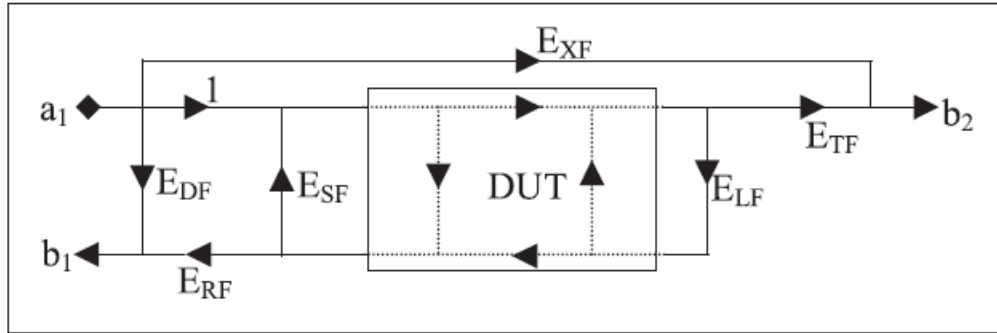


Figure 6-4 Port 1 Error terms [94].

Each port on the VNA has six error terms shown in Figure 6-4 giving 12 terms in total. Ten error terms can be found mathematically via measurement of the through, reflect and line (TRL) calibration standards (Figure 6-5). The remaining two error terms are the forward and reverse isolation found via measurement of 50Ω terminations fitted to the end of each test port lead (Figure 6-6).

The Error terms are;

- E_{DF} = The directivity term.
- E_{RF} = The reflection tracking term.
- E_{LF} = The load match term.
- E_{TF} = The transmission tracking term.
- E_{SF} = The source match term.
- E_{XF} = The isolation term.

The TRL calibration method can be performed with coaxial standards or as in this case, waveguide; the method provides a very accurate low-cost approach to calibration.

The through standard is obtained simply by connecting the waveguide to coax transitions connected to the test port leads on port 1 and 2 of the VNA together.

The reflect standard is a flat metal plate (Figure 6-5) that fits over the end of the waveguide part of the waveguide to coax transitions.

The Line (top right in Figure 6-5) is a short section of the waveguide of a quarter wavelength thick in this case at 22 GHz fitted in between the waveguide to coax transitions.

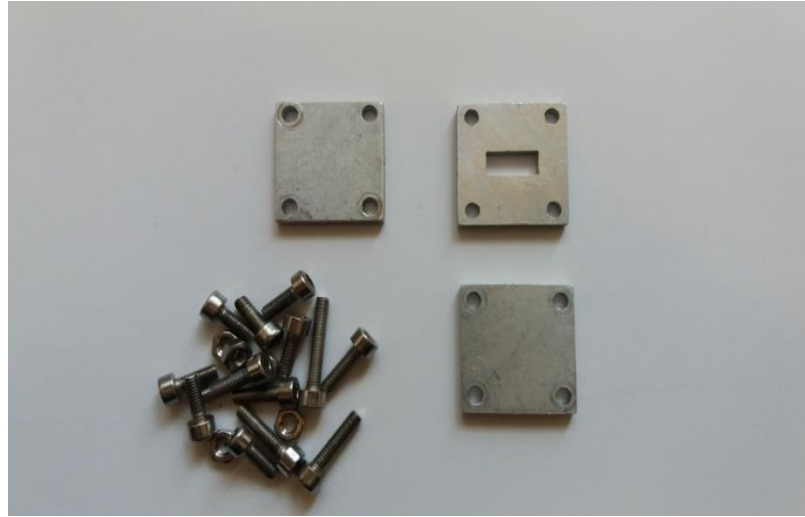


Figure 6-5 TRL calibration kit.



Figure 6-6 50Ω Waveguide load

The scattering parameters are related to the Sinclair parameters by equation 6-11.

$$|S_{ij}^2| = \frac{P_r}{P_t} = \frac{G^2 \cdot \lambda^2 \cdot \sigma_{ij} \cdot L}{(4\pi)^3 \cdot R^4} \quad (6-11)$$

Where:

P_r = is the received power.

P_t = is the transmitted power.

G = the horn antenna's gain (same antenna for transmitting and receiving, monostatic configuration).

λ = the wavelength.

L = the path loss.

R = the range.

Chapter 7 Horn antenna design

7.1 Introduction

A review of antenna types shown in chapter 3 revealed that a conical corrugated horn antenna would be ideal for the monostatic radar configuration. This chapter details the design process required to realise an antenna for the radar.

A conical horn antenna was evaluated using an HFSS model (Figure 7-1). The horns return loss Figure 7-2 suggests that the horn has a good match from 18 to 26GHz, which is essential to prevent reflection between horn and polariser and ensure that maximum signal is transmitted and received. The horns radiation pattern (Figure 7-3) indicates that the antenna has very low sidelobes and a narrow beam.

Figure 7-4 shows the conical corrugated horn antenna used to perform radar measurements in the lab.

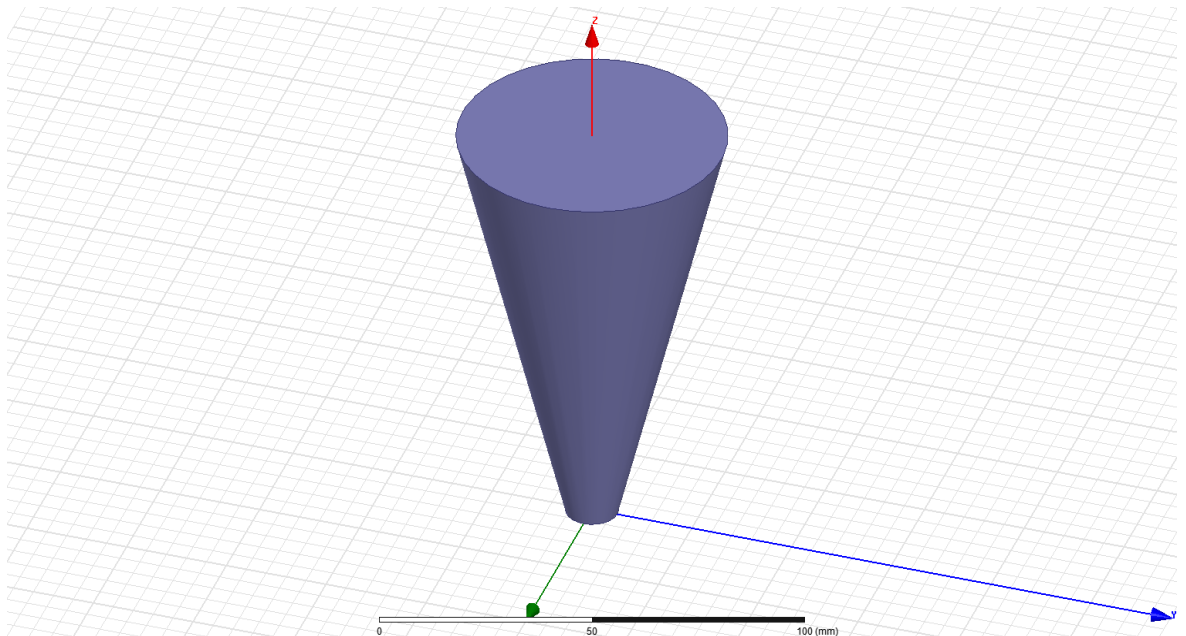


Figure 7-1 HFSS model of a conical horn antenna.

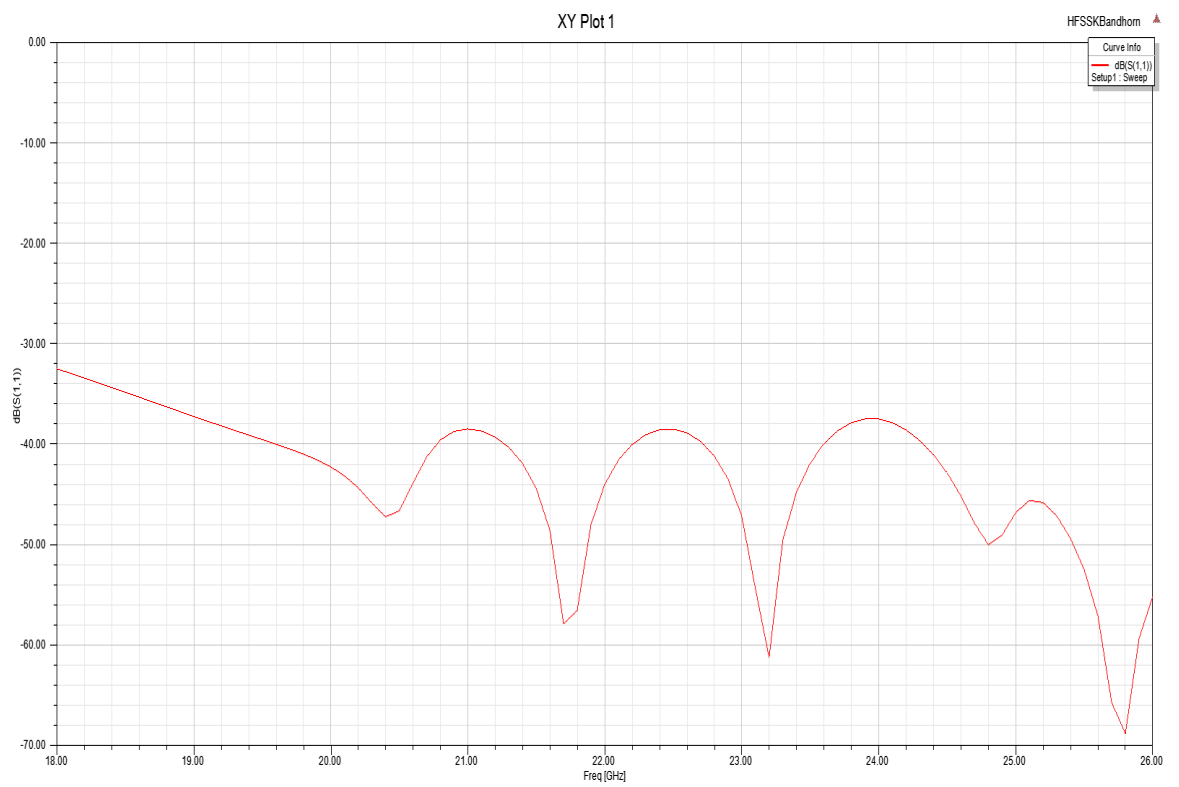


Figure 7-2 Modelled antenna Return loss

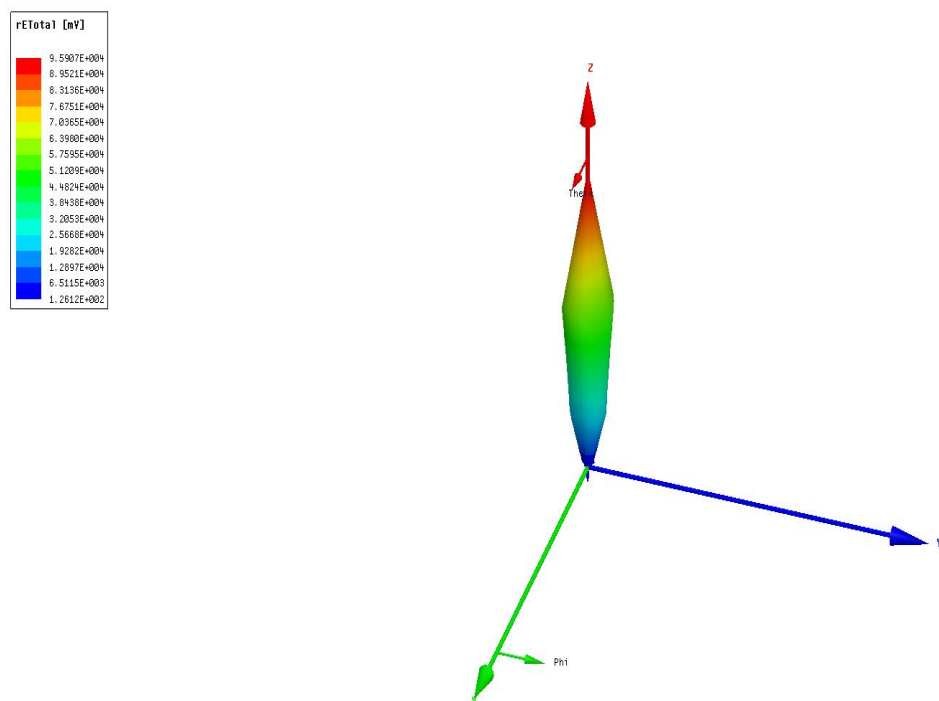


Figure 7-3 Modelled antenna radiation pattern

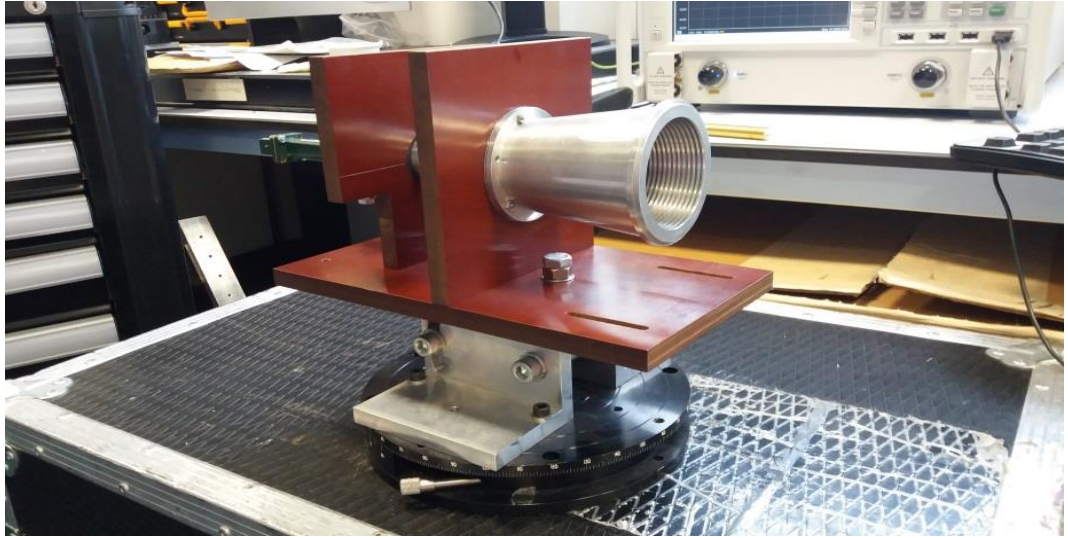


Figure 7-4 Conical corrugated horn antenna.

7.2 Calculated Horn Gain

Calculation of the horn antenna gain is found using equation (7-1) [95]:

$$Gain = \left[\frac{\pi \cdot d}{\lambda} \right]^2 \cdot e_A \quad (7-1)$$

Where;

A=Area of the horn aperture (m²).

d=The aperture of the conical horn (m).

λ =The wavelength (m).

e_A = A dimensionless parameter between 0 and 1, called the aperture efficiency.

For conical horns, the optimum value for the aperture efficiency is $e_A = 0.522$

The gain for the conical corrugated horn used in this project has an internal diameter of 6.5 cm (0.065 metres) at the large end, and the wavelength at 22 GHz (centre band) is 0.01363 metres giving a gain of:

$$Gain = \left[\frac{\pi \cdot 0.065}{0.01363} \right]^2 \cdot 0.522$$

$$Gain = 117.1$$

$$Gain \text{ (dB)} = 10\text{Log}_{10}(117.1) = 20.7\text{dBi}$$

7.3 Calculated Horn Beamwidth

The horn half-power beamwidth (3dB point) is calculated as follows;

$$Beamwidth^{\circ} = 58.4 \times \left[\frac{\lambda}{2a} \right] \quad (7-2)$$

Where;

a = the radius of the horn's large aperture (m).

The half-power beamwidth for the conical corrugated horn used in this project is;

$$Beamwidth^{\circ} = 58.4 \times \left[\frac{0.01363}{2 \times 0.0325} \right]$$

$$Beamwidth^{\circ} = 12.3^{\circ}$$

Measurement of the corrugated horn beamwidth is carried out by rotating the horns large aperture through the beam produced by a distant transmitting horn. The horn measurement is performed in the far-field also known as the Fraunhofer region and is defined by [96];

$$R > \frac{2D^2}{\lambda} \quad (7-3)$$

Where;

R is the range in metres ($R \gg D$) and D is the maximum linear dimension of the horn ($R \gg \lambda$) in this case the horn diameter is used.

In the Fraunhofer region, the electromagnetic waves arriving at the corrugated horn under test from the transmitting horn are almost parallel and behave like plane waves.

7.4 Measured Horn Input Return loss (S_{11})

The horn antenna's return loss should be less than -15dB to reduce unwanted reflections, refer to chapter 6 for a description of return loss calculation.

Figure 7-5 shows the experimental setup, with port 1 of the VNA connected via a (WR42) waveguide to coax transition followed by a Flann microwave model 20644 rectangular to circular transition (Figure 8-8) and finally to the horn antenna.

Calibration using the SOLT (short, open, load, through) method applied to port 1 of the VNA, please refer to chapter 6 for further details on calibration.

The circular to rectangular transition's transmission loss is between -0.05 to -0.1dB, return loss is -20dB or better across the band. The return loss of the waveguide to coax transition is better than -15dB across the band.

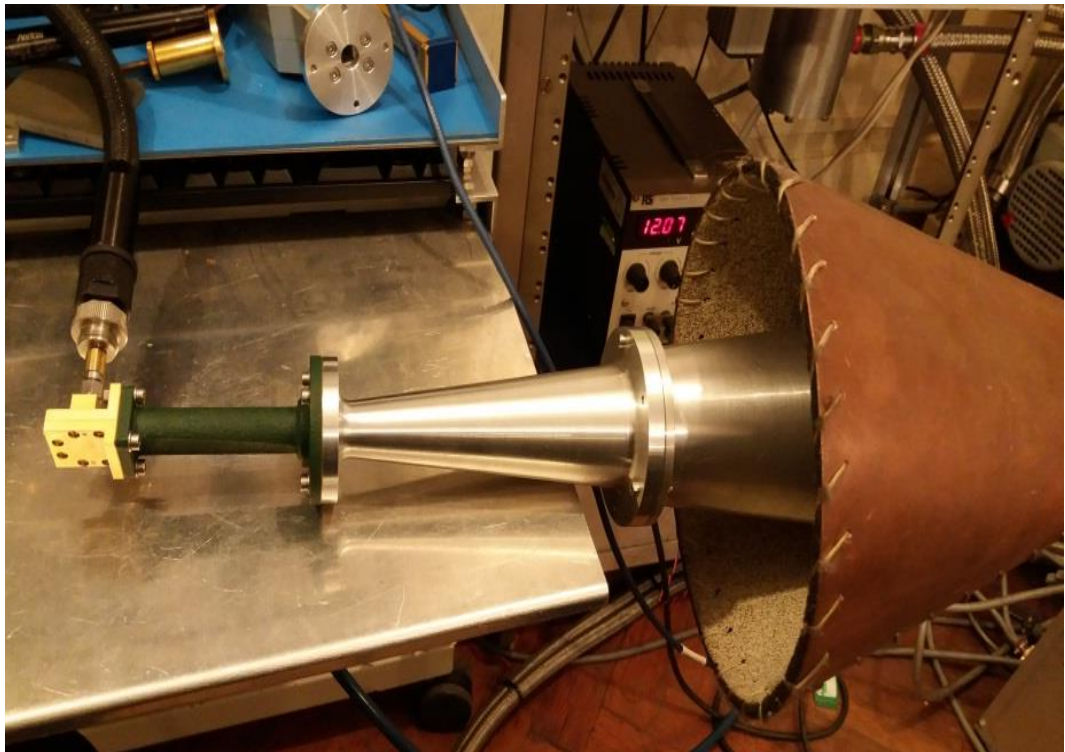


Figure 7-5 Measurement of Horn antenna return loss (S_{11}).

The measured return loss for the horn antenna can be seen in Figure 7-6. Resonance at 19 GHz is caused by internal reflection in the horn itself. It does not cause a problem as the radar calibration process presented in chapter 9 removes its effects. The return loss across the rest of the band is better than -15 dB.

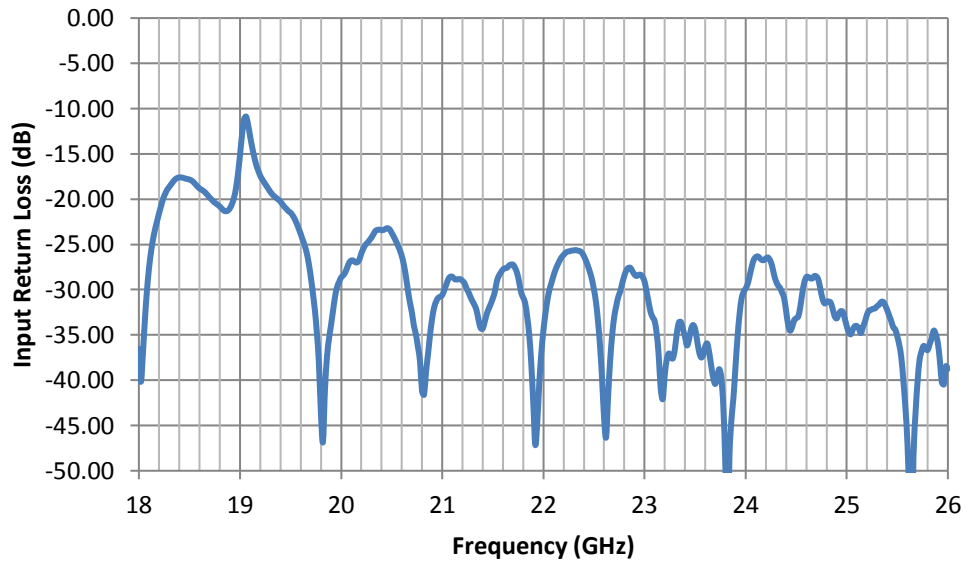


Figure 7-6 Horn Antenna Return Loss (S_{11}).

7.5 Measured Horn Beamwidth

Experimental evaluation of the corrugated horn antenna's beamwidth compares the measured responses to the theoretical. Figure 7-7 shows the experimental set up used to find the measured beam width via the horns polar diagram generation. The polar diagram provides a sectional view of the antenna's beam shape, which is three-dimensional.

A Hewlett Packard 8350B sweep oscillator with an 83595A R.F plugin covering 0.01 to 26.5 GHz provided the source and the spectrum analyser used as a detector is an Agilent E4408B covering 9KHz to 26.5GHz.

The pyramidal and conical horn antennas are set to vertical polarisation with a separation placing the measurement antenna in the far-field. The sweep oscillator produces a carrier wave (C.W) at the desired frequency with a power level of -10dBm. The pyramidal (standard gain) horn has a gain of 20dB. The corrugated horn antenna rotated in azimuth in 2° increments with a precision of 0.25° gave 180 measured values for 360° of rotation.

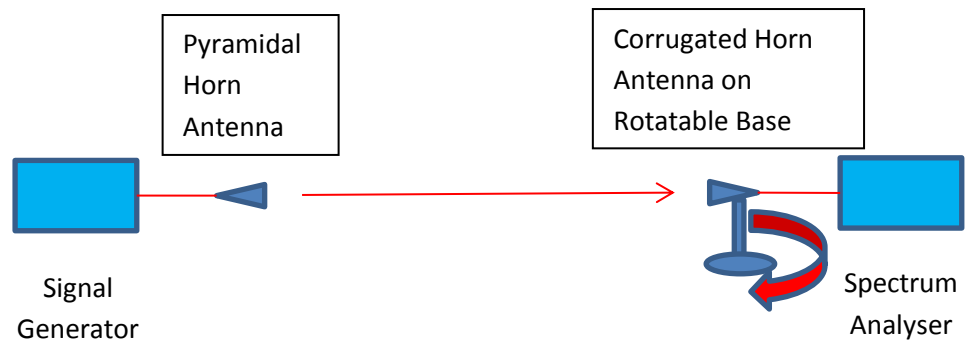


Figure 7-7 Horn Beamwidth measurement setup

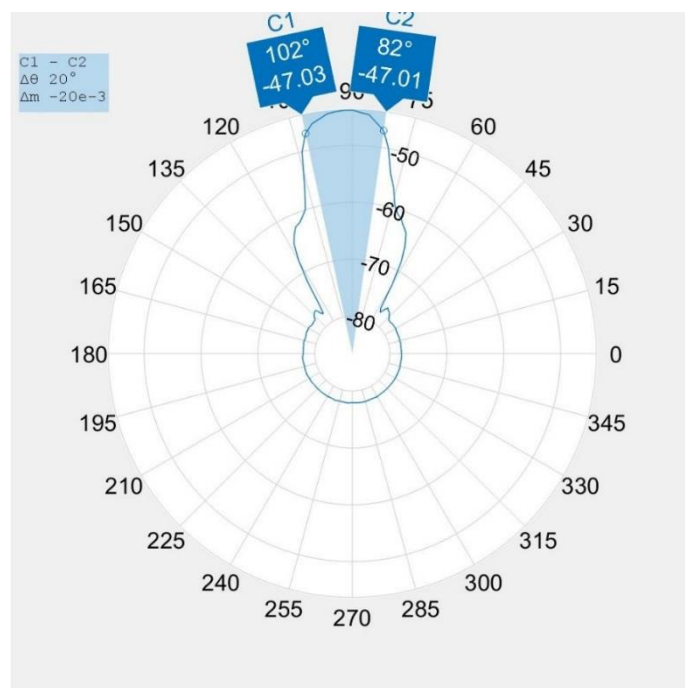


Figure 7-8 Measured corrugated horn polar diagram at 18GHz.

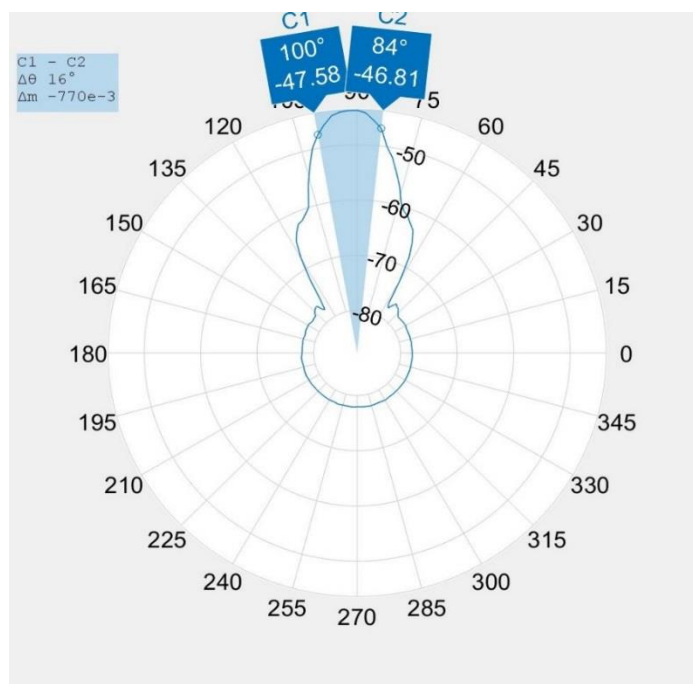


Figure 7-9 Measured corrugated horn polar diagram at 22GHz.

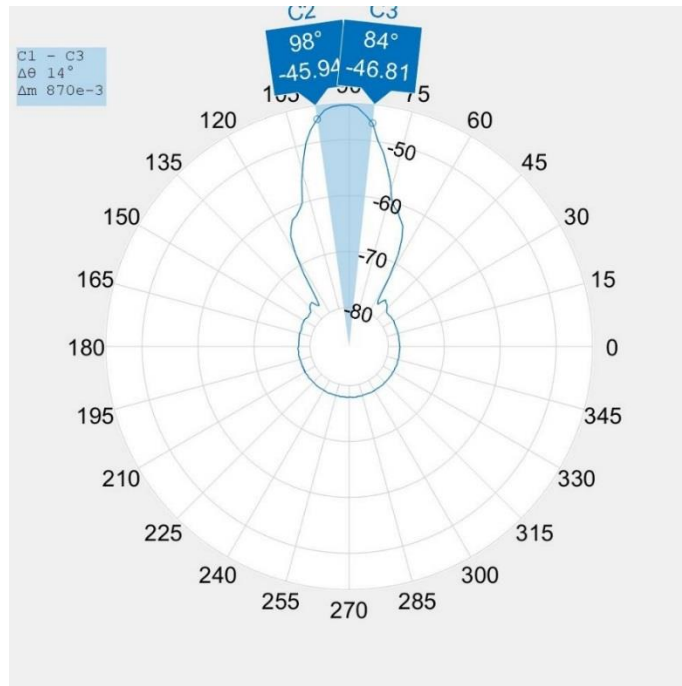


Figure 7-10 Measured corrugated horn polar diagram at 26GHz.

Figure 7-8, Figure 7-9 and Figure 7-10 show the corrugated horn antenna's polar diagram for 18, 22 and 26 GHz. The lines radiating from the centre of the plot intersect the horns beam shape at the -3dB points and indicate the beam width at that measured frequency. The gain calculated using equation 7-4, where θ_B and Φ_B are the azimuth and elevation half power beam widths, which are both the same due to the horn being conical. This equation is an approximation.

Horn gain as a function of beamwidth [97]:

$$G_{dBi} = 10 \cdot \text{Log}_{10} \left(\frac{29000}{\theta_B \Phi_B} \right) \quad (7-4)$$

Horn polarisation isolation (cross-polarisation) was performed by rotating the corrugated horn through 90 degrees relative to the rectangular standard gain horn. The horns measurement results presented in Table 7-1.

Frequency (GHz)	Measured full 3dB beamwidth (degrees)	Gain (dBi)	Isolation (cross polarisation) (dB)	Mean cross polarisation error (%)
18 GHz	20	19	-33	0.0455
22 GHz	16	21	-37	0.0204
26 GHz	14	22	-30	0.0893

Table 7-1 Horn measurement results

7.6 Conclusion

The measured return loss differs slightly from the HFSS model presented earlier in this chapter but is still acceptable for the application required. The horn antenna has unwanted side lobes, which are regions off-axis where the antenna has unwanted gain. These kept minimal with this antenna design due to the corrugations. The polar diagrams presented in Figure 7-8, Figure 7-9 and Figure 7-10 show that the measured sidelobe levels are very low for each measured frequency. From the table, at 22 GHz, the measured horn gain agrees with the calculation presented earlier in this chapter, the beamwidth is slightly different. The polarisation isolation (cross polarisation) error is very low for both polarisations.

Chapter 8 Turnstile Orthomode Transducer

8.1 Introduction

Chapter 5 presents a block diagram (Figure 5-1) of the proposed radar comprising a corrugated horn antenna, orthomode transducer (OMT) and a VNA acting as the source and receiver. This radar uses an OMT to produce the orthogonal polarisation required for full polarimetric measurements. A review of millimetre wave radar technology and techniques (chapter 3) compared several different OMT designs, including the Turnstile type chosen.

The Turnstile OMT used for this research was designed and developed by Navarrini and Plambeck [60], offering broadband operation covering the required 18 to 26 GHz band. This waveguide OMT performs polarisation separation with minimal transmission loss, low input return loss and excellent channel isolation (minimal cross-polarisation). The design uses split block construction to simplify the manufacturing process using a standard computer numerical control CNC milling machine (Figure 8-3 and Figure 8-4).

The OMT is a three-port device with two (WR42) rectangular waveguide ports and one circular port for the orthogonal polarisations (Figure 8-1).

The rectangular waveguide for channel 1 (Pol1) is visible on the block's lower left face. The rectangular waveguide for channel 2 (Pol2) is visible on the block's lower right face.

In the centre of the top of the polariser can be seen the circular port (Figure 8-2). This port connected to a conical corrugated horn antenna (Figure 7-4) for radar measurements.

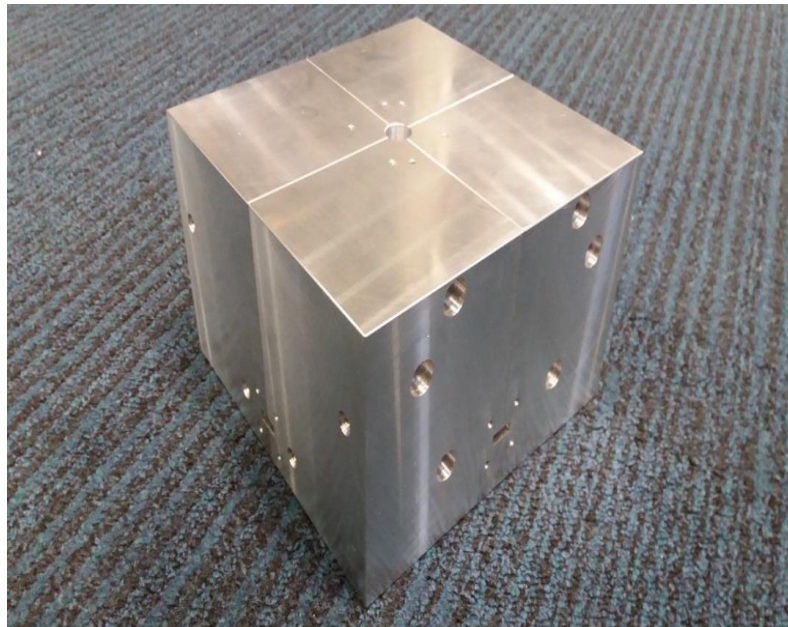


Figure 8-1 Assembled Turnstile polariser.

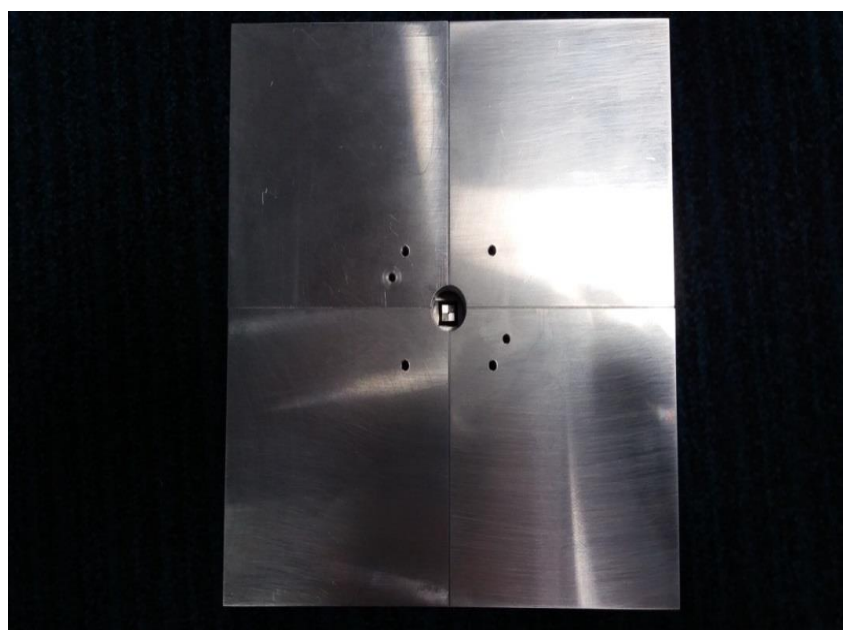


Figure 8-2 Polariser circular waveguide aperture.

8.2 Design overview

Figure 8-3 shows an exploded view of the polariser revealing the internal waveguide structure whilst, Figure 8-4 shows a close up of block 1, located at the top of the picture (Figure 8-3). A quarter of the circular waveguide is visible at the top of the block. The tuning stub visible just below this, please also refer to Figure 8-5 and Figure 8-6.

A wave entering the circular waveguide from the top and polarised in alignment with arrow Pol 1 is split by the turnstile junction exiting opposite waveguide pairs with a

180° phase shift (Figure 8-5 and Figure 8-6). The signals then recombined with an E-plane Y- junction power combiner that provides another 180° phase shift. The signal then passes through a tapered section that matches the power combiner to the standard WR42 waveguide size. The signal appears at the pol 1 (CH1) rectangular port shown in Figure 8-6. The same process applies to pol 2 except this time the signal appears out of the pol 2 (CH2) rectangular waveguide output.

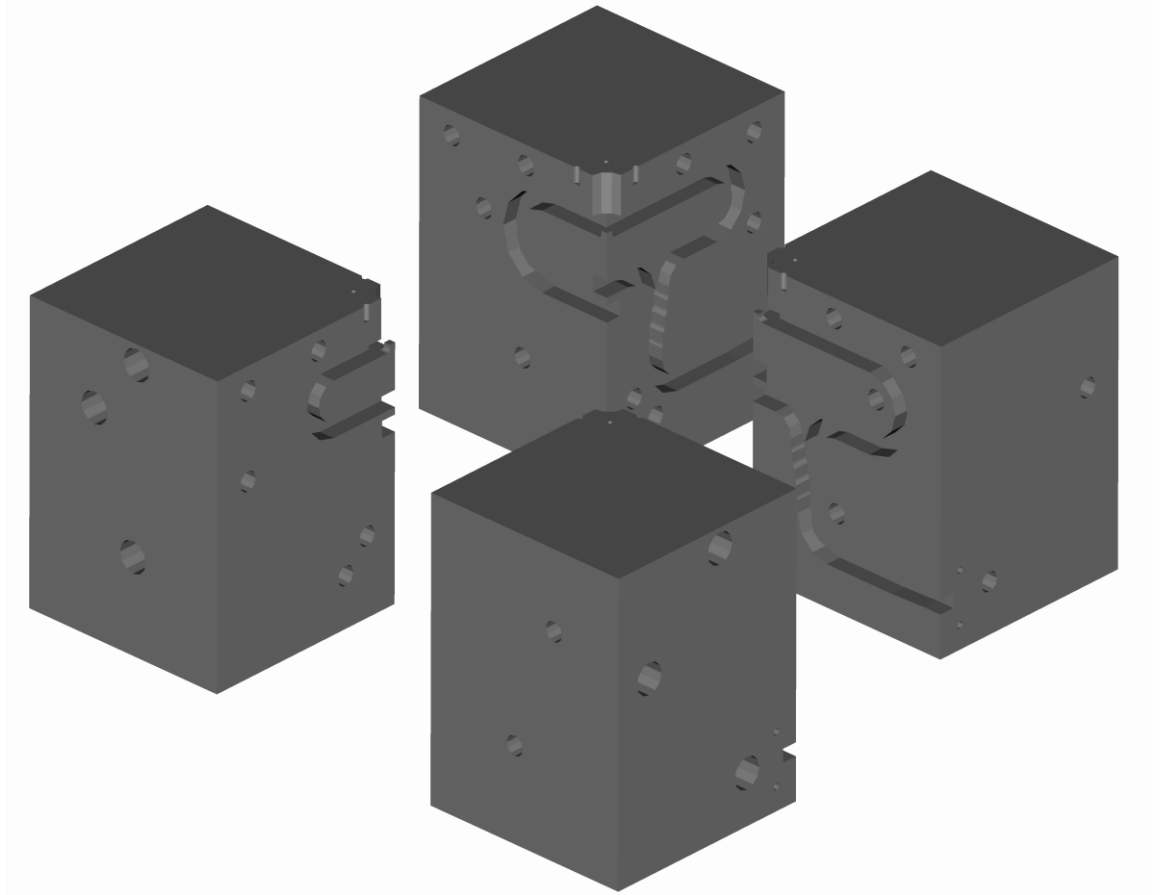


Figure 8-3 Exploded view of the polariser [60].

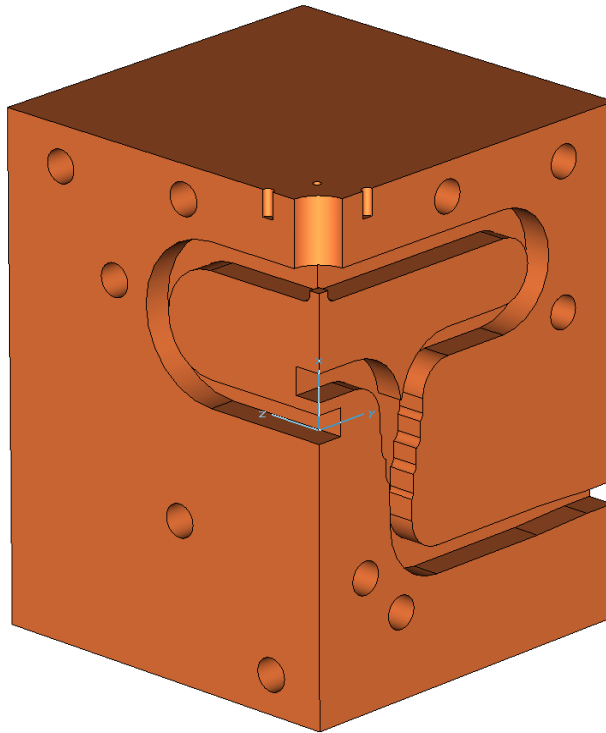


Figure 8-4 Polariser block 1 close up [60].

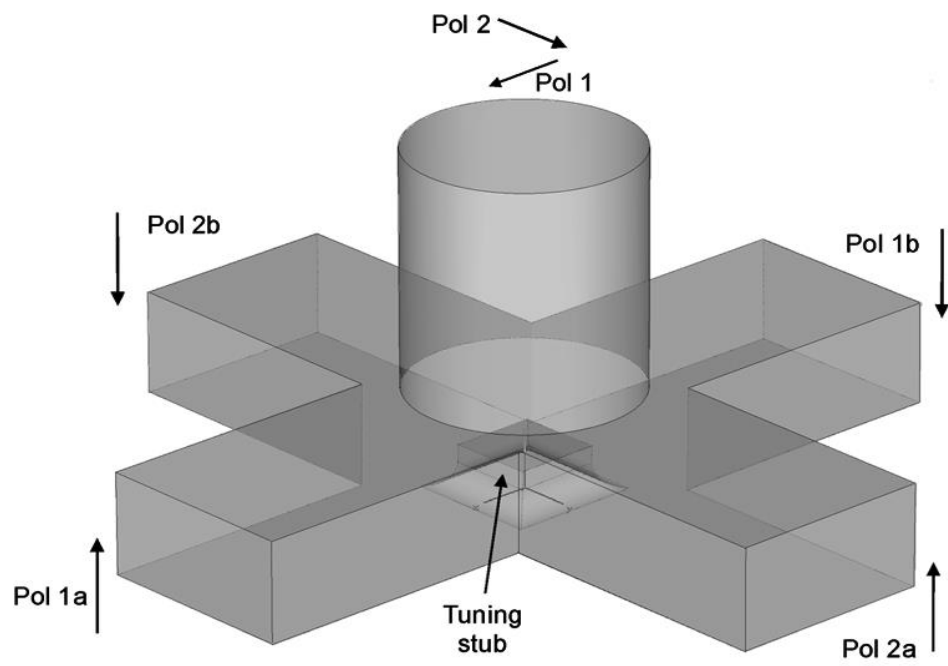


Figure 8-5 The turnstile junction [60].

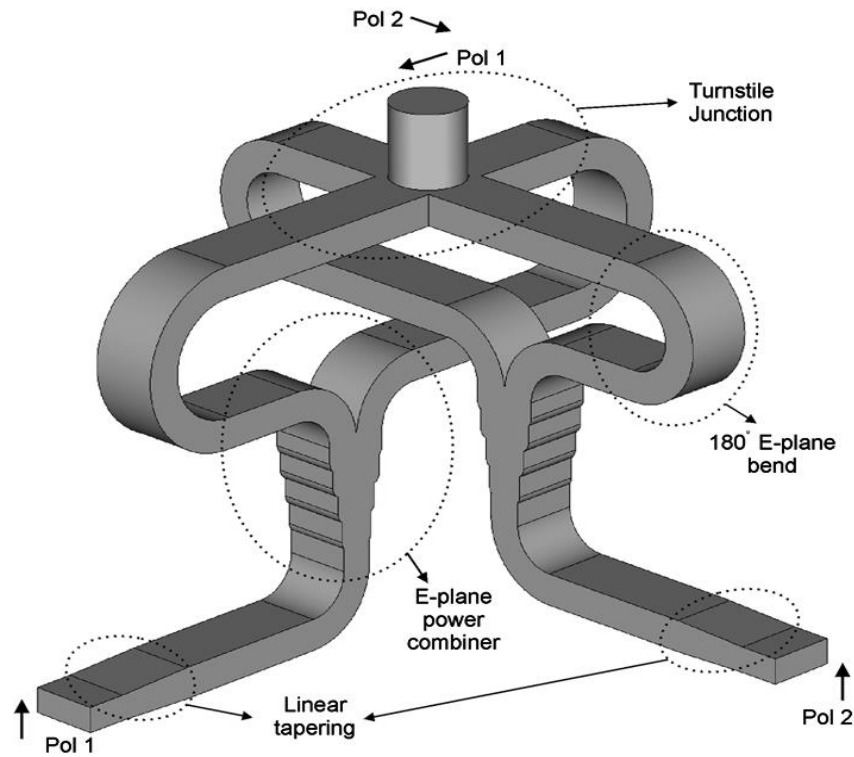


Figure 8-6 Turnstile junction and combiner arrangement [60].

8.3 Measurement procedure

Measurements of the OMT were taken using an Anritsu 37397A vector network analyser (Figure 8-7). Calibration performed using the standard short, open, load, through (SOLT) calibration method. The SOLT method used was of the coaxial type and served the same function as the TRL calibration detailed in chapter 6. The SOLT calibration standards were the only ones available at the time of testing.

The following procedure was used to measure the match (return loss) of the circular and rectangular waveguide ports on the OMT and the transmission loss for each polarisation. Note the unused rectangular waveguide (WR42) port is terminated with a Flann microwave 50Ω load to prevent unwanted reflection from the unused port. Figure 8-9 shows the experimental set up used to measure polarisation 1 (pol 1), and Figure 8-10 shows the set up for measuring polarisation 2 (pol 2). The circular to rectangular transition Figure 8-8 is a Flann model 20644.

1. Connect port 1 on the VNA to the circular port on the OMT via a circular to rectangular transition (Figure 8-8). Excitation of the correct polarisation occurs when the test port cable is aligned towards the relevant rectangular (WR42) port on the OMT (Figure 8-9 and Figure 8-10).

2. Connect port 2 on the VNA to the relevant rectangular (WR42) port on the OMT (Figure 8-9 and Figure 8-10).

The OMT isolation was measured using the above procedure except the circular to rectangular transition is set for the opposite polarisation (Figure 8-11).



Figure 8-7 Anritsu 37397A VNA used to measure the OMT (port 1 left, port 2 right)



Figure 8-8 Circular to rectangular waveguide transition

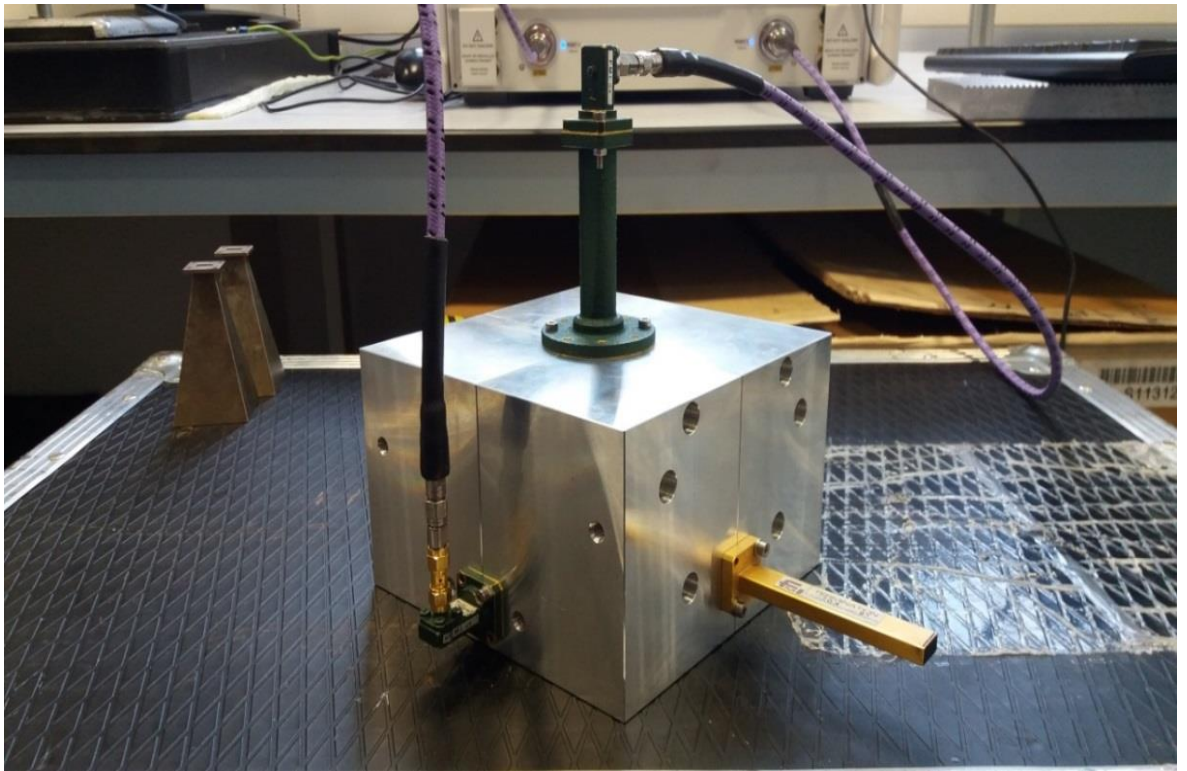


Figure 8-9 Measurement set up for pol1 transmission and return loss.

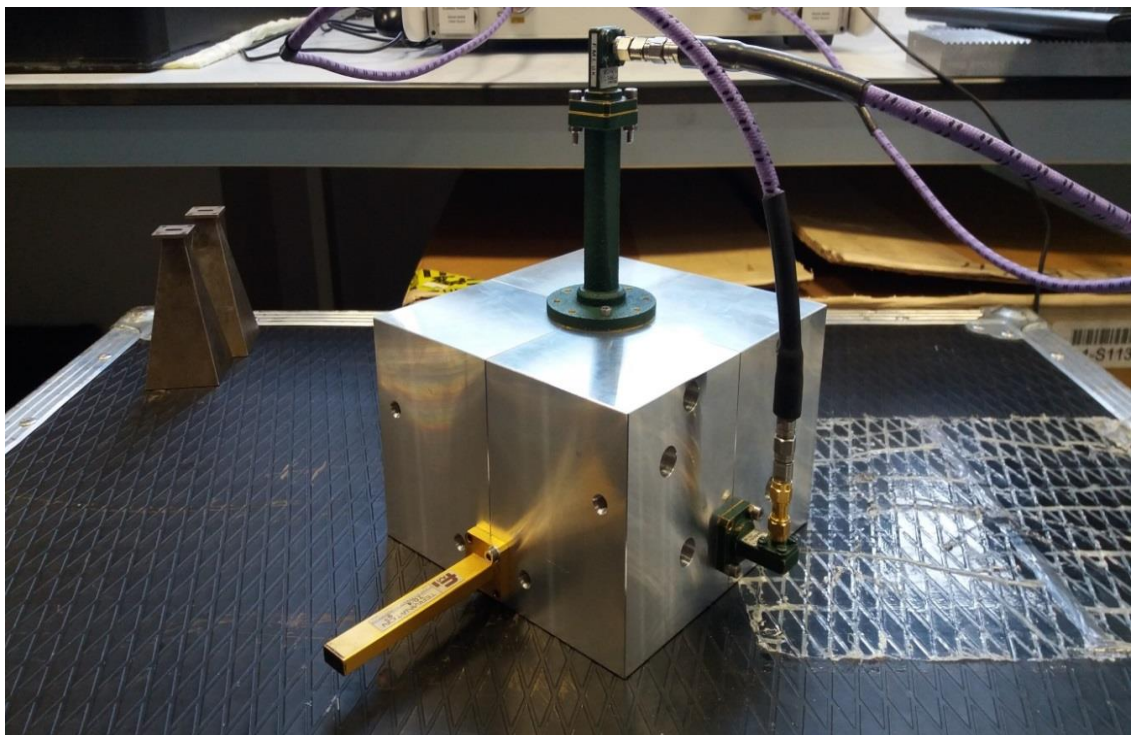


Figure 8-10 Measurement set up for pol 2 transmission and return loss.

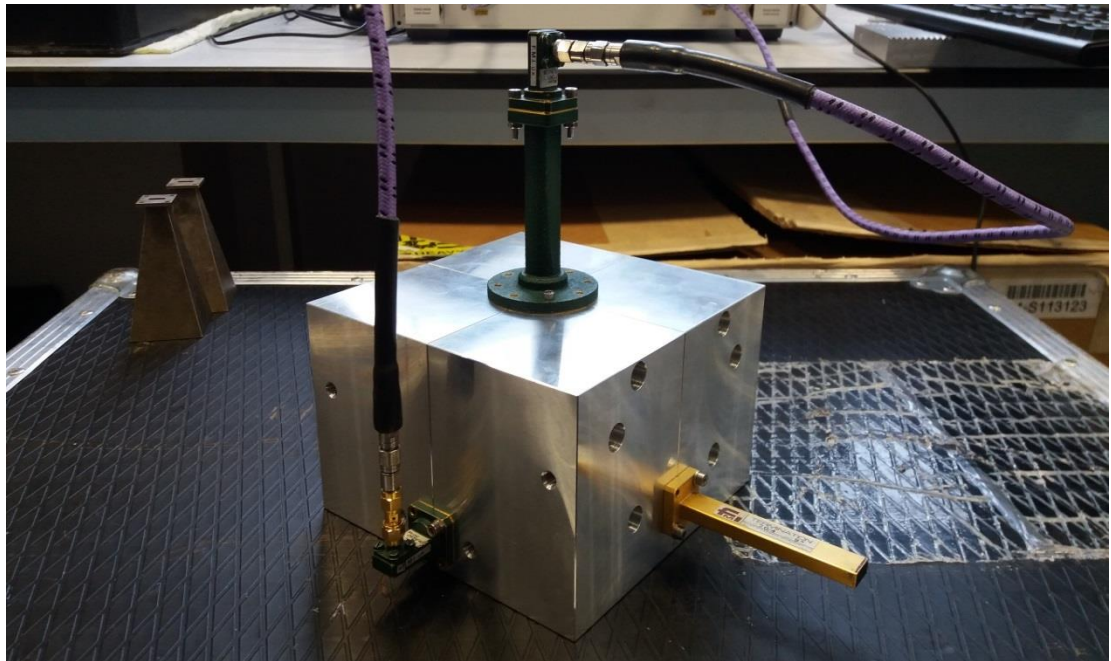


Figure 8-11 Measurement set up for cross-polarisation (Isolation).

8.4 Experimental Results

The following section examines via experimental evaluation the turnstile OMT manufactured in the mechanical engineering workshop at Manchester Metropolitan University to the Navarrini and Plambeck design comparing its measured performance to the modelled presented in Navarrini and Plambeck paper [60].

OMT measurement parameters include:

- Return loss for the circular port.
- Return loss for each rectangular (WR42) waveguide pol 1 and pol 2.
- Forward Transmission loss for each channel.
- Isolation.

Figure 8-12 to Figure 8-16 show the simulated and measured OMT responses taken from Navarrini and Plambeck's paper [60]. The return loss for the circular and rectangular ports (Figure 8-12, Figure 8-13 and Figure 8-14) are below -19dB. Measured and simulated return loss can also be seen in the same figures and almost identical at rectangular and circular ports.

Figure 8-15 and Figure 8-16 from Navarrini and Plambeck's paper [60] show the measured and simulated transmission loss. The average transmission loss measured for the OMT with the loss of the circular to rectangular transition being

removed from the measurement across the 18 to 26 GHz band being around -0.15dB.

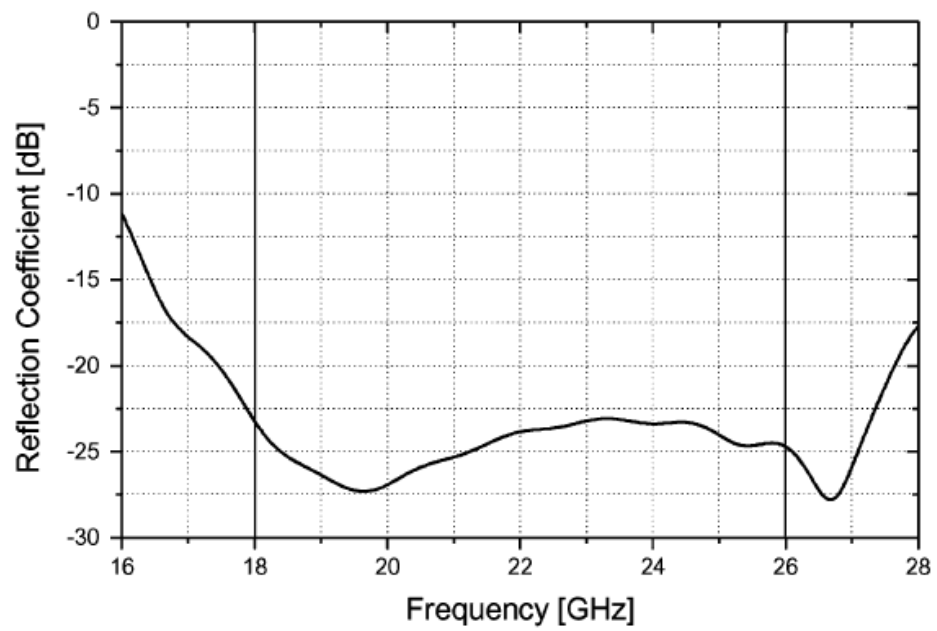


Figure 8-12 Simulated Circular Waveguide return loss [60].

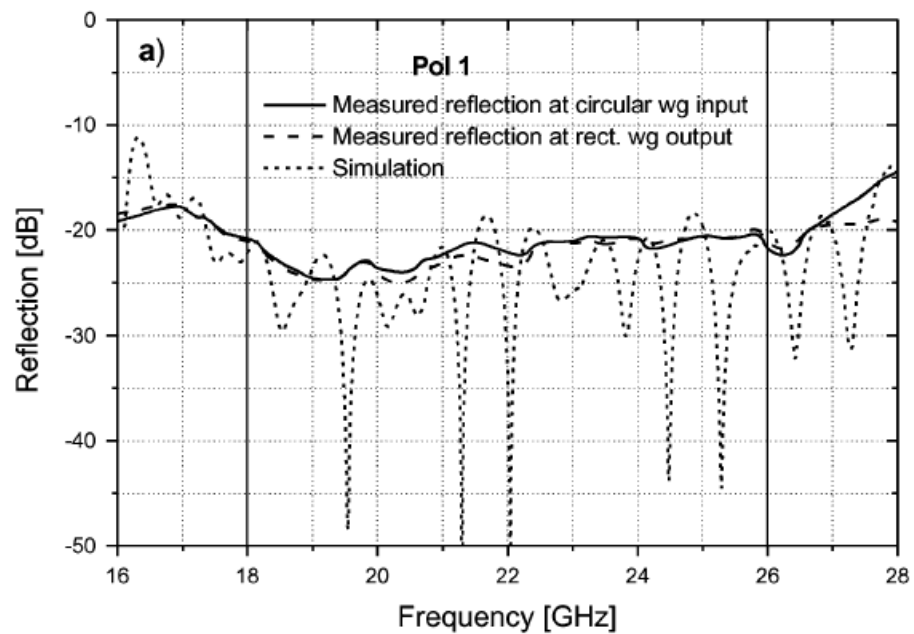


Figure 8-13 Polarisation 1 Measured and simulated input return loss for the prototype polariser designed and produced by A. Navarrini and R. L Plambeck [60].

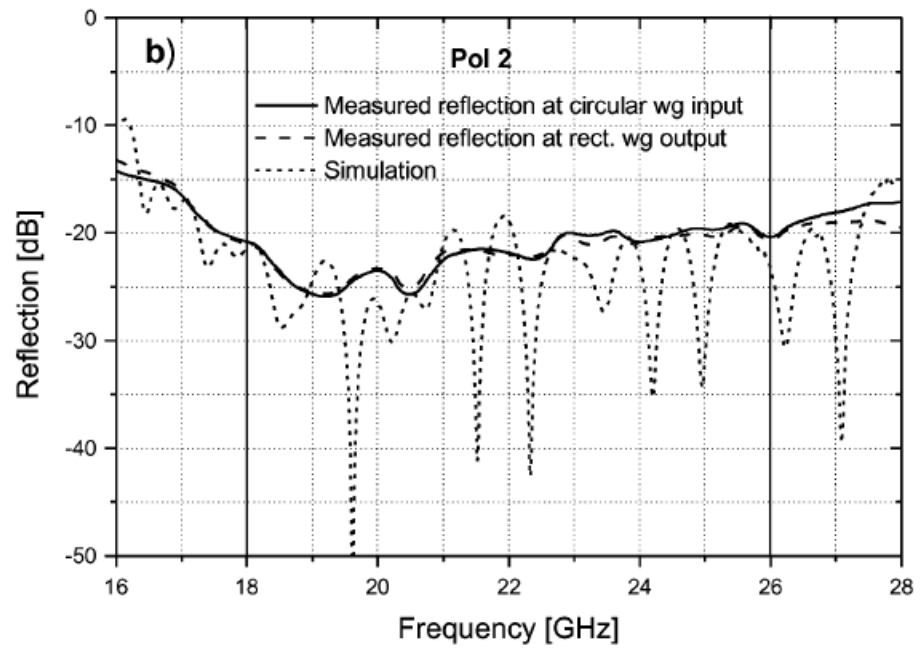


Figure 8-14 Polarisation 2 measured and simulated for the prototype polariser designed and produced by A. Navarrini and R. L Plambeck [60].

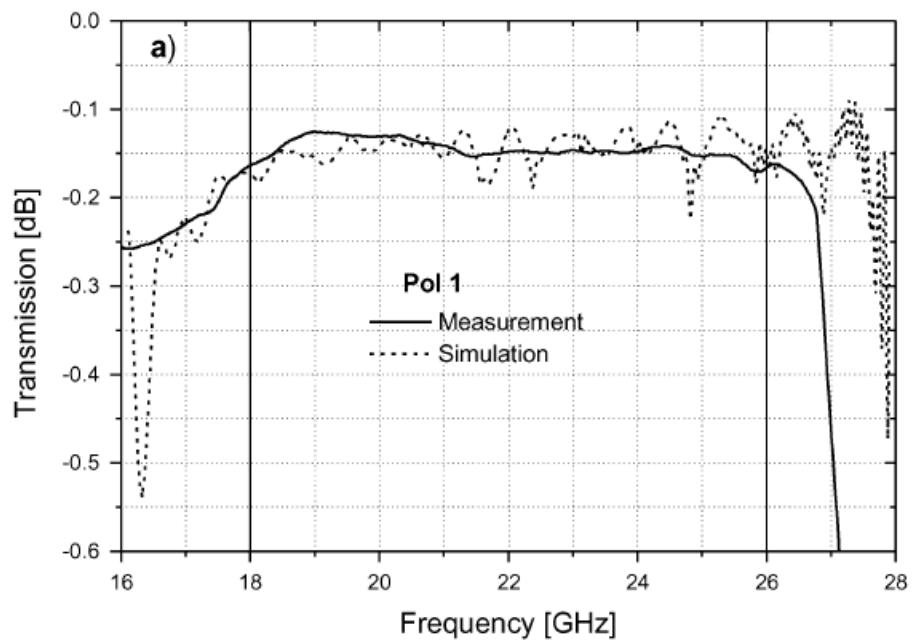


Figure 8-15 Measured and simulated polarisation 1 transmission loss for the prototype polariser designed and produced by A. Navarrini and R. L Plambeck [60].

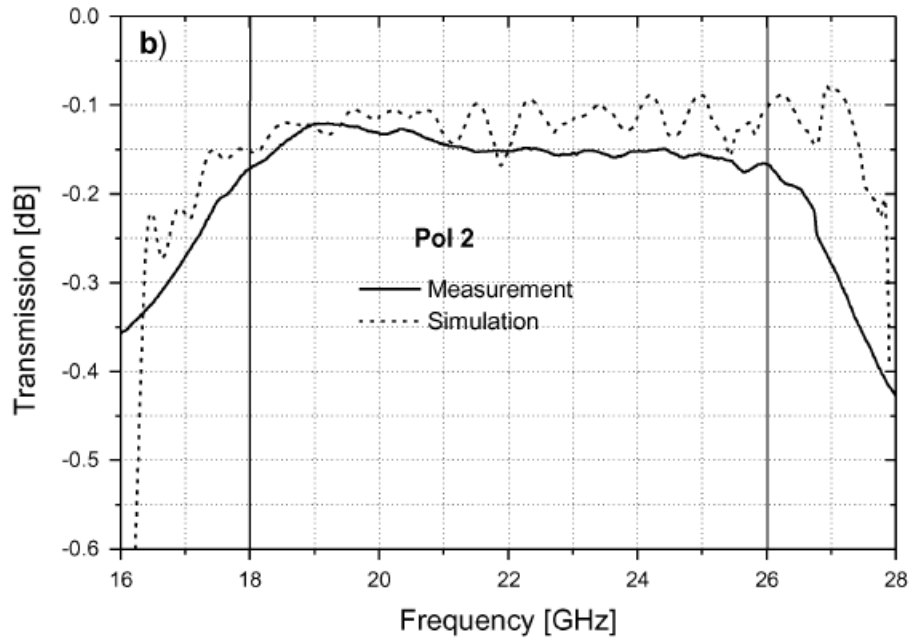


Figure 8-16 Measured and simulated polarisation 2 transmission loss for the prototype polariser designed and produced by A. Navarrini and R. L Plambeck [60].

The next sequence of figures represents the measured results for the OMT used for the radar trials documented in this thesis.

Figure 8-17 and Figure 8-20 show the measured OMT return loss for the circular and rectangular ports being better than -15dB.

Figure 8-21 and Figure 8-22, show the average transmission loss for polarisation 1 at 0.3 dB and 0.26 dB for polarisation 2, including the transmission loss of the circular to rectangular transition of 0.1 dB. The cause of the peak at the top of the band is unknown.

Figure 8-23 shows the measured isolation between polarisations from Navarrini and Plambeck's paper [60]. The isolation is lower than -48dB across the band for both polarisations.

Figure 8-24 and Figure 8-25 show the measured cross polarisation for both polarisations, which are lower than -35dB. The measured cross polarisation average for polarisation 1 and 2 are both -37 dB.

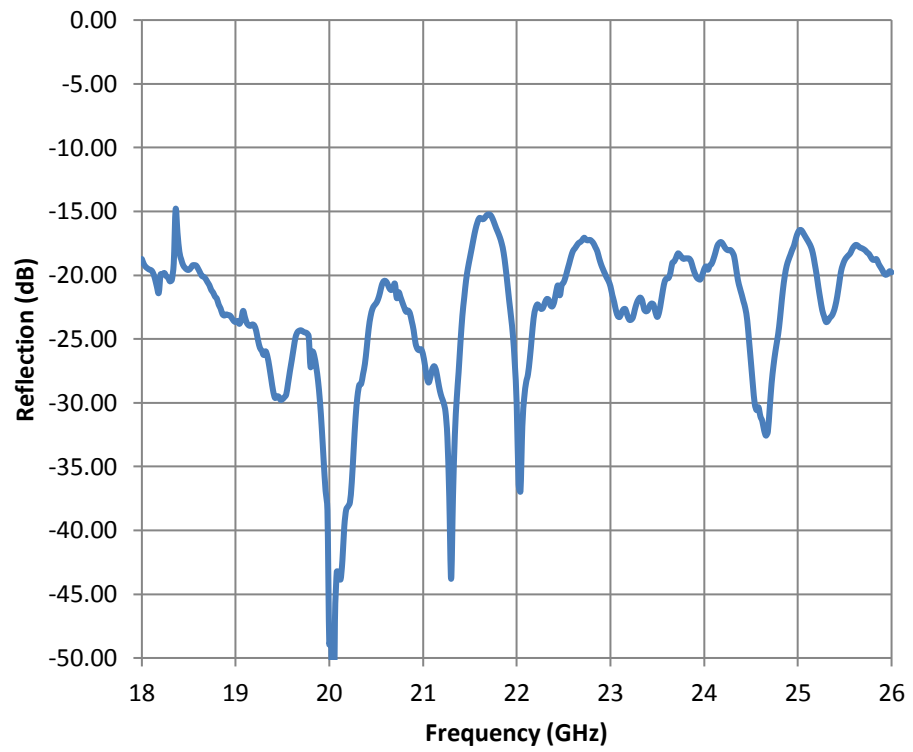


Figure 8-17 Measured polarisation 1 circular waveguide return loss.

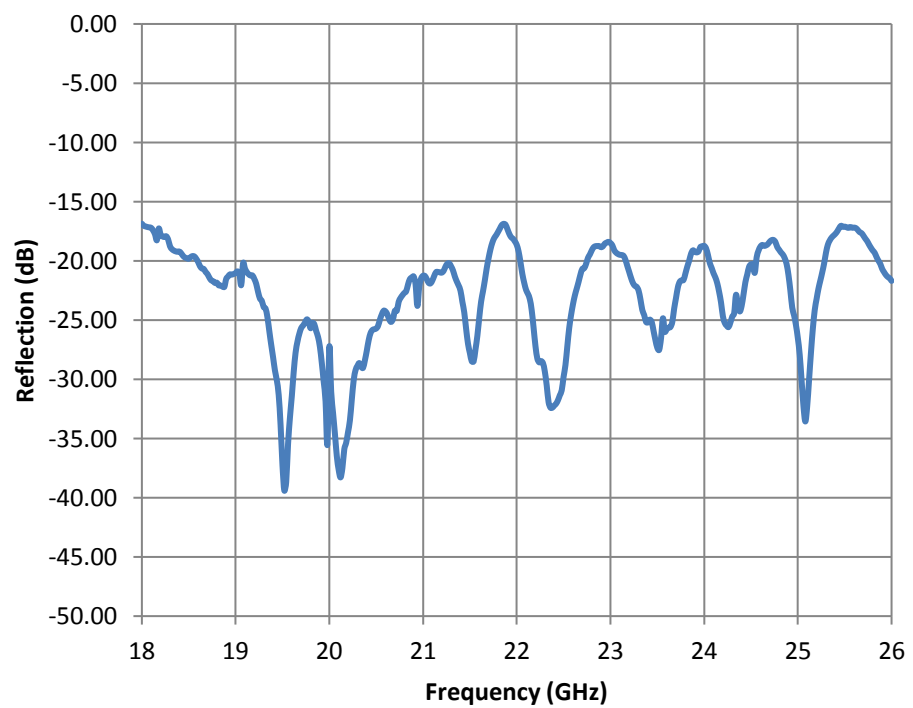


Figure 8-18 Measured polarisation 2 circular waveguide return loss.

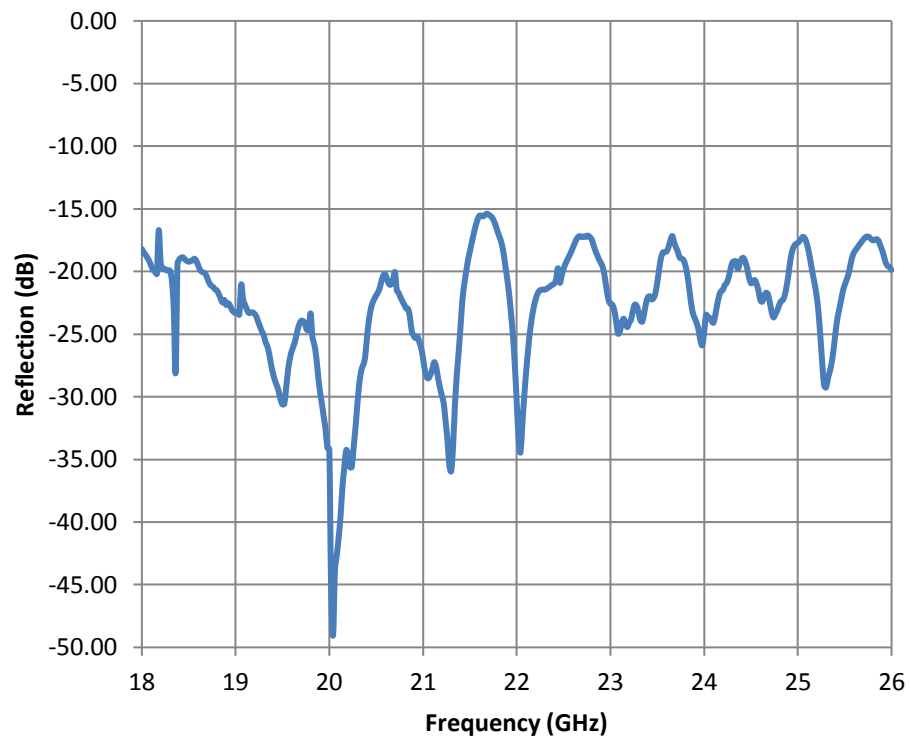


Figure 8-19 Measured polarisation 1 rectangular (WR42) port return loss.

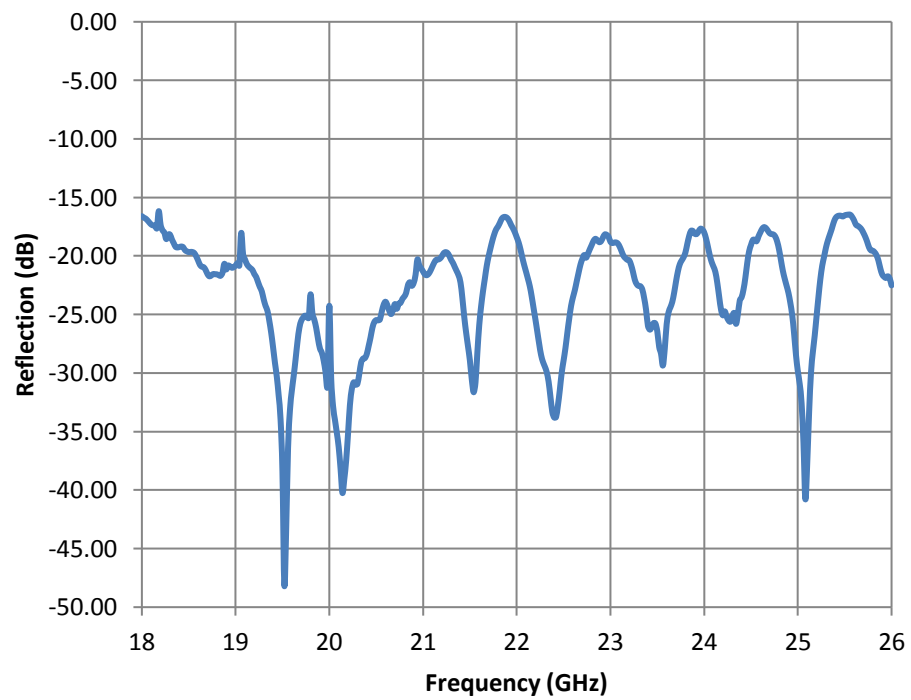


Figure 8-20 Measured polarisation 2 rectangular (WR42) port return loss.

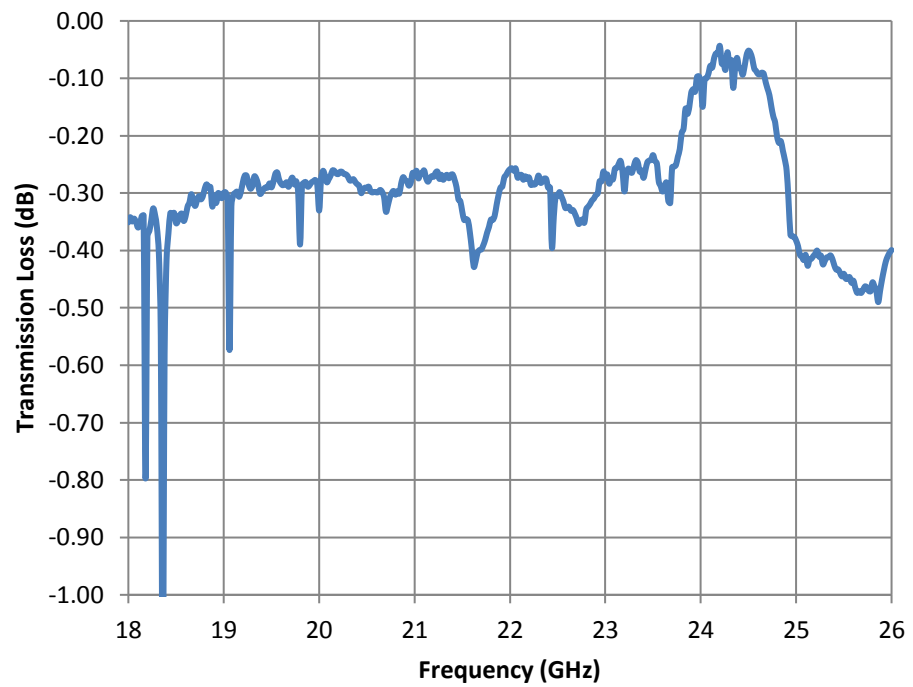


Figure 8-21 Measured polarisation 1 transmission loss.

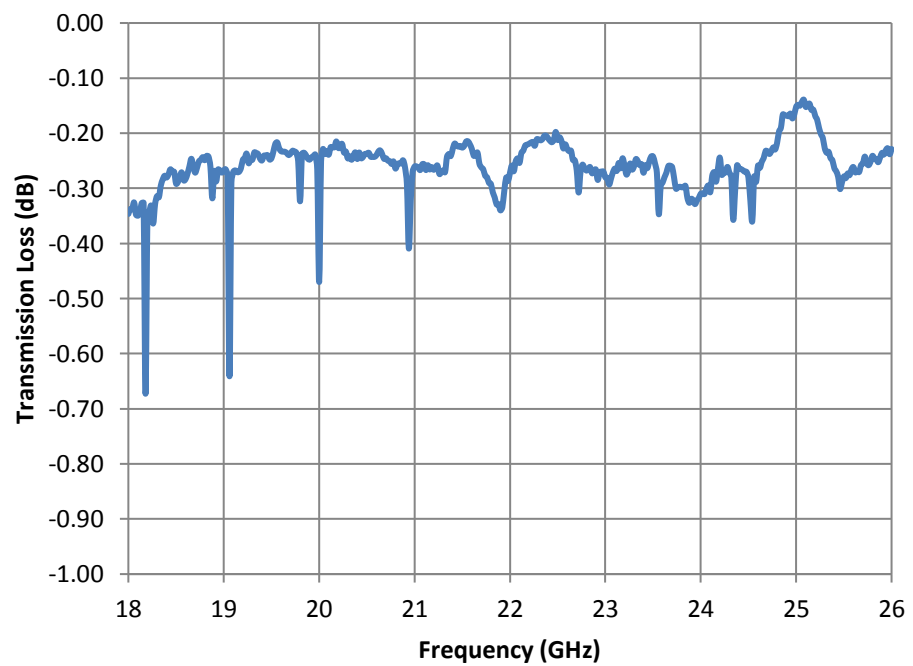


Figure 8-22 Measured Polarisation 2 Transmission loss.

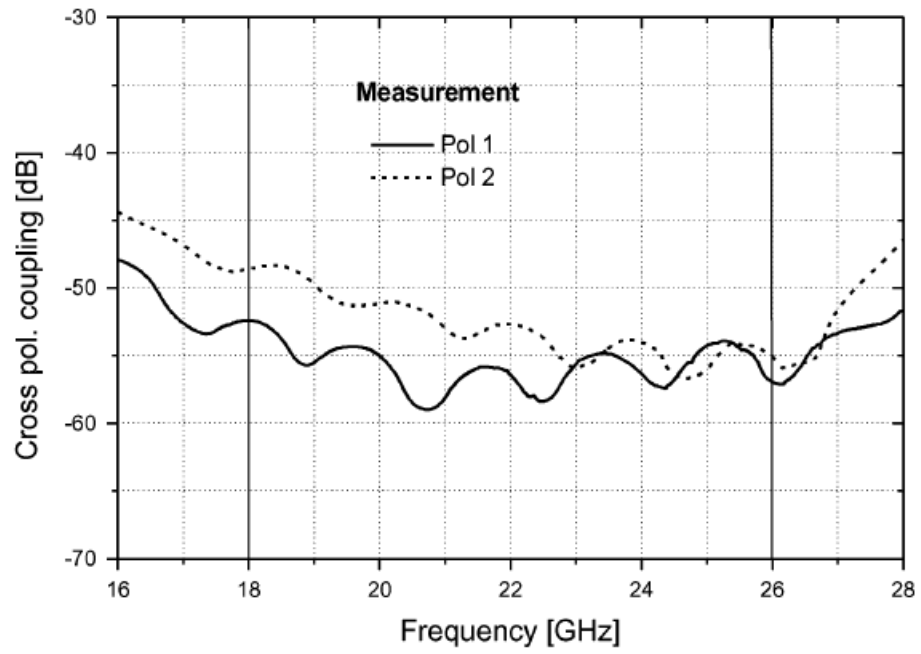


Figure 8-23 Measured OMT cross-polarisation (isolation) [60].

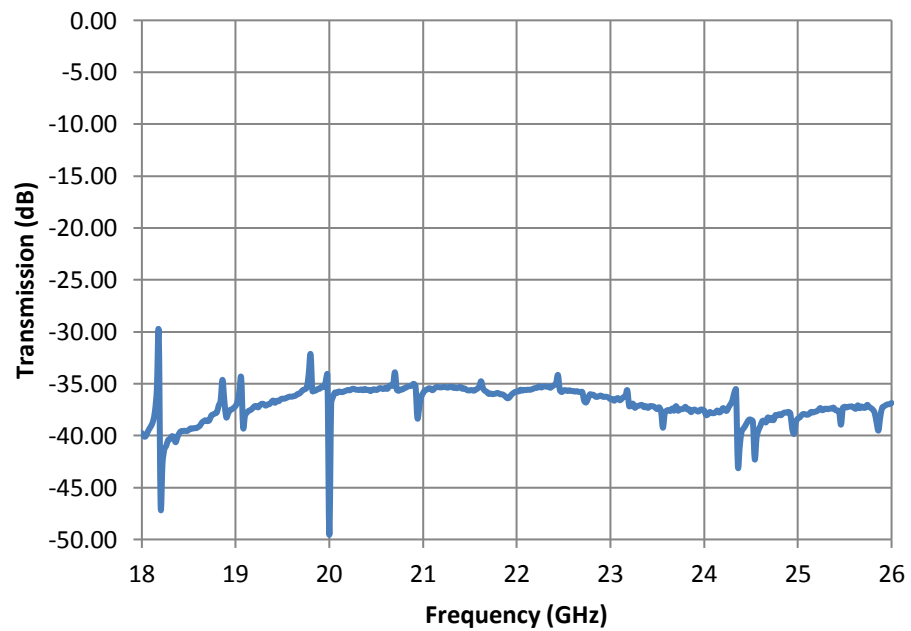


Figure 8-24 Measured OMT polarisation 1 cross-polarisation (isolation).

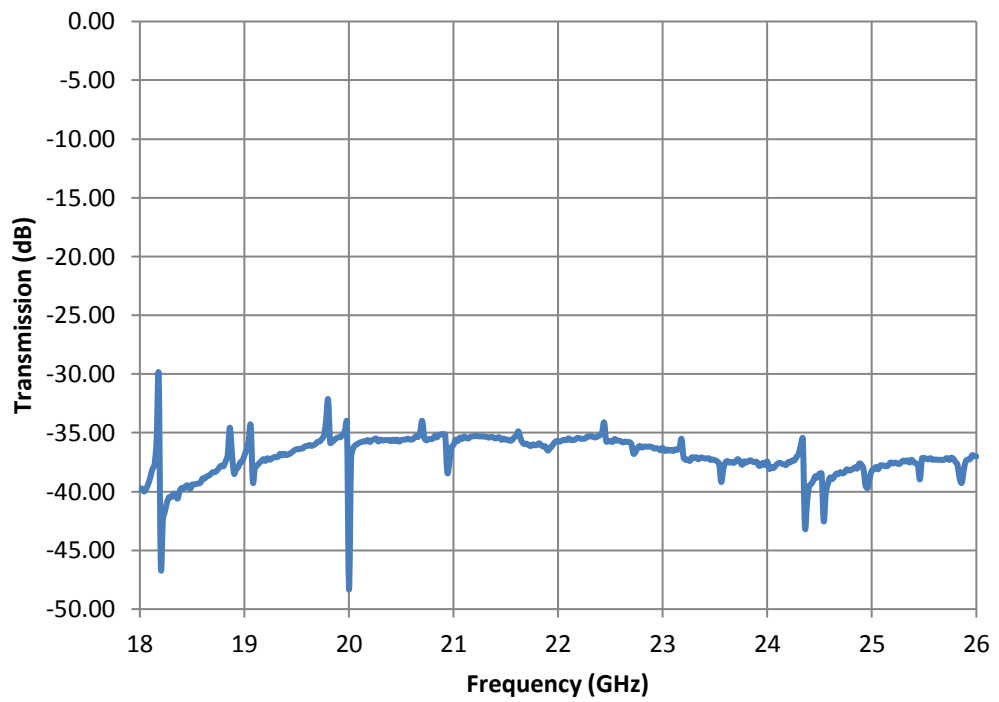


Figure 8-25 Measured polarisation 2 cross-polarisation (isolation).

	Input Return Loss (dB) Av	Worst case Input Return Loss (dB)	Transmiss ion Loss (dB) Av	Cross- polarisation (dB) (AV)	Mean cross- polarisat ion error (%)
CH1	-23	-15	-0.2	-37	0.0198
CH2	-23	-17	-0.16	-37	0.0197
Circular Port	-23	-15			

Table 8-1 Measured turnstile polariser return loss, transmission loss and isolation.

8.5 Conclusion

Initial testing of the OMT manufactured for the radar showed that one polarisation channel had slightly worse transmission loss. The cross-polarisation performance was also not as good as the design suggested. Performance improved after grinding the mating surface of each block on a surface plate with fine sandpaper attached. The blocks then cleaned with an ultrasonic cleaner to remove any cutting fluid and metal particles.

The only issue remaining is the resonances present in the transmission loss of both polarisations. Navarrini and Plambeck's paper states that these are caused by differences in the sidearm lengths leading to reflection from the power combiner. However, this does not affect the performance of the radar once calibrated.

Performance detailed in Table 8-1 indicates that return loss, transmission loss, and cross-polarisation levels are all good. The OMT although not as good as the one produced by Navarrini and Plambeck is still perfectly acceptable for the radar trials.

Chapter 9 Radar Calibration via Measurement of canonical targets

9.1 Introduction

The purpose of calibration is to extract the Sinclair matrix produced by the target. However, elements of the radar, including the horn antenna and OMT, create unwanted differential phase delay between orthogonal polarisations, and unwanted cross polarisation [98].

The radar receives a combination of the targets Sinclair matrix and the corruptive distortion produced by the radar on its transmission and reception cycles. Therefore, the radar receives what could be called the measured [M] matrix, also known as the observed matrix [O]. Calibration enables the extraction of the target Sinclair matrix from the measured matrix.

For the work presented in this thesis, calibration is a two-stage process; the first an internal calibration performed by calibrating the VNA up to the end of the test leads with a waveguide calibration kit utilising the standard through, reflect, line (TRL) approach covered in detail in chapter 6.

The second reduces the errors that are primarily generated by the horn and polariser. The calibration process aims to reduce these errors and enable an undistorted measurement of the targets Sinclair matrix.

This second calibration is done via the careful measurement using the radar of a set of calibration targets [99] [19] comprising;

- A sphere or flat metal plate (all of the measurements presented in this thesis a flat metal plate was used for calibration with a radar cross-section = 20951m^2 at 22 GHz, the sphere not used).
- A dihedral reflector orientated at 45° between orthogonal polarisations. Dihedral with a radar cross-section = 17033m^2 at 22 GHz used for the work presented in this thesis.
- One of the calibration strategies tried a vertical dihedral with the dimensions shown above.
- A wall of radar-absorbent material (RAM).

To remove the effects of impedance mismatches present between the polariser, horn and measurement system all targets including the flat metal plate, dihedral and

any other targets measured have their responses subtracted from the measured background of radar-absorbent material (RAM).

The measurement of all targets is taken in the frequency domain.

To summarise the corruptive distortions that affect the single antenna (monostatic) polarimetric radar are listed below;

1. Reflections arising from impedance mismatches
2. Polarisation conversion taking place within the horn and polariser.
3. Phase delay between the horizontal and vertical channels; dispersion is different for the two polarisations.
4. Dispersion in the waveguides.

This chapter presents three different radar calibration methods.

9.2 Radar cross polarisation errors

From chapters 8 and 9 Table 8-1 and Table 9-1, both the horn and OMT have a low cross-polarisation level. The tables present the results for signal propagation in just one direction, however for the radar both signal transmission and reception occurs; hence, the losses presented in Table 8-1 and Table 9-1 have to have their values doubled. The calculation of cross-polarisation errors for the horn and OMT combined are found using equation 9-1.

$$\text{cross - polarization Error} = \sqrt{(2 \times \text{horn error})^2 + (2 \times \text{OMT error})^2} \quad (9-1)$$

Table 9-1 presents from left to right the radars mean horn cross-polarisation, OMT cross-polarisation for each channel and total cross-polarisation error for each channel for both horn and OMT combined.

Mean Horn Cross- polar error (%)	Mean CH1 OMT Cross- polar error (%)	Mean CH2 OMT Cross- polar error (%)	Total CH1 Cross-polar error (%)	Total CH2 Cross- polar error (%)
0.3104	0.0396	0.0394	0.3129	0.3129

Table 9-1 Radar cross-polarisation Errors

9.3 Clutter

Clutter is any unwanted reflection from objects located in the target scene that can make the detection of the target of interest more difficult. Figure 9-1 shows a raw un-calibrated measurement of the wall of microwave absorber located at the end of the target range with no target present in the measurement.

In all four of the plots reflection from the horn and polariser are visible as large peaks finishing toward the centre of the plots at 2.5 ns. As this is the return time (microwave radiation to and back from the scene), the actual time the microwaves finish propagating through the horn and polariser is half this at 1.25 ns. A time of 1.25 ns gives a path length through polariser and horn of 37.5 cm, the horn antenna is 30 cm long, and the internal waveguide within the polariser is around 7.5 cm. The calibration process removes the effects of the reflections caused by the horn and polariser. From 2.5 ns to 100ns the reflections from objects in the target scene are visible and reduce in magnitude with increasing range, this is the clutter.

Clutter removal for the work presented in this thesis took place before calibration.

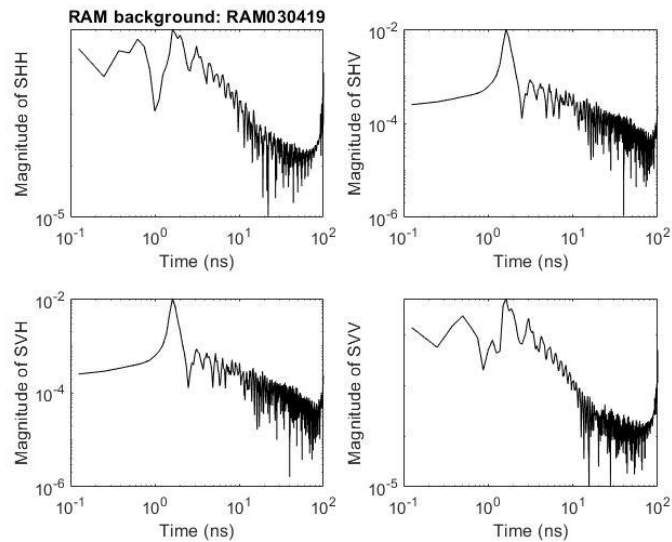


Figure 9-1 Measurement of clutter in the target range

A less obvious clutter source identified after analysing the measured data from a dihedral reflector orientated at 45° to the horizontal turned out to be produced by the radar.

Illumination of the dihedral at 45° with horizontal or vertical polarisation produces conversion into its orthogonal state upon reflection.

When this reflection arrives back at the radar, the radar then reflects radiation back towards the dihedral in the same polarisation state as that received. Once this

reflection arrives back at the dihedral, its polarisation state is again converted into its orthogonal state, finally coming back to the radar as clutter appearing as a co-polar response. Visible as black peaks in S_{HH} and S_{VV} Figure 9-2.

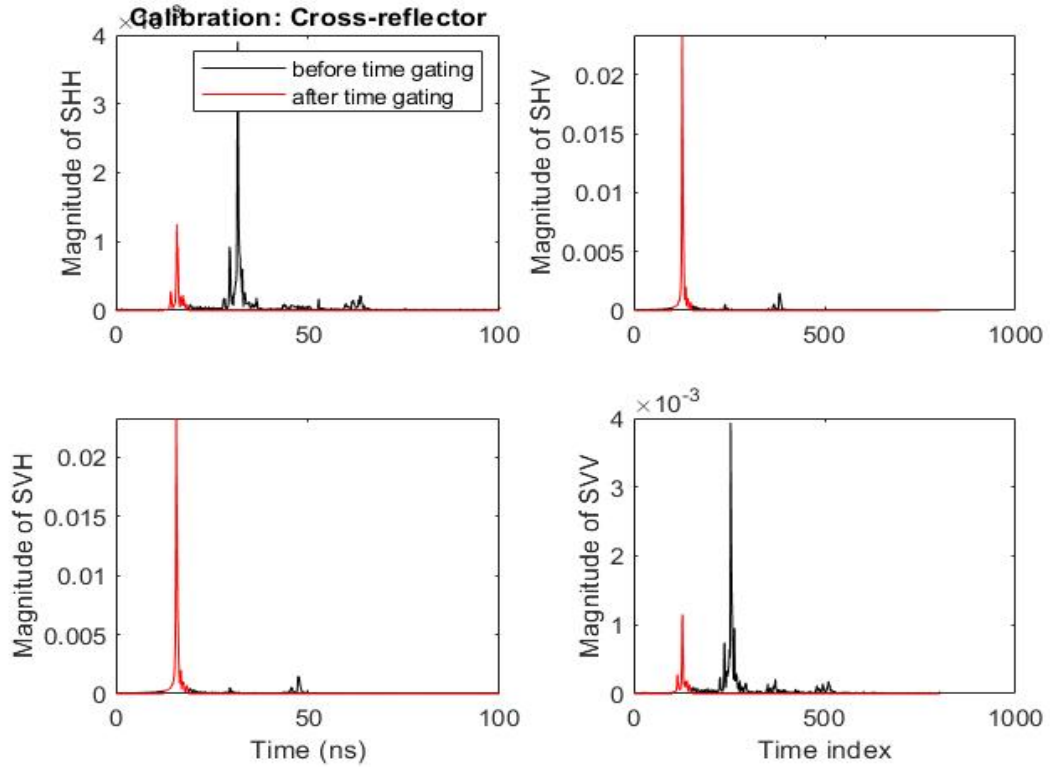


Figure 9-2 Measured response of a dihedral reflector orientated at 45°

9.4 Range Gating

The techniques in this thesis are concerned with the analysis of data in the frequency domain. However, by moving data into the time domain, a convenient clutter rejection technique can be implemented. By taking the inverse Fourier transforms of the s-parameters of the signal and calibration data (after background subtraction) a magnitude of the signal returns can be plotted out as a function of time. This transformation enables data that was reflected by objects in the vicinity of the target to be rejected simply by time gating out the signal returned from only the target. The time gating window around the target corresponded to ranges from 2.1 m to 2.3 m. After gating out all other data in the time domain, the signal can then be Fourier transformed back into the frequency domain. The improvement in the signal quality is evident, as shown by the removal of the black clutter traces leaving just the red traces in Figure 9-2.

9.5 Radar Calibration

This chapter presents three calibration methods and compares two of them to ascertain, which is most suitable for the radar presented in this thesis. A first basic approach is shown in equation 9-14 secondly, a method developed by Papathanassiou (1998a) and Kimura (2004) [100] [101] and thirdly a technique developed by Nesti and Hohmann [102]. The third calibration method not compared.

The radar's linear response has its co-polar calibration performed using a flat metal plate (or sphere), which produces a strong co-polar reflection when illuminated with linearly polarised radiation, correcting for channel phase and magnitude imbalance. A trihedral could also have performed the same operation; however, the sphere generally preferred in lab measurements due to its aspect independence and easily computable scattering matrix.

The sphere or plate, provide the measurements phase reference with the phase referenced to the centre of the sphere or when using the plate to its surface. The sphere and plate properties make them ideal for laboratory measurements where accurate phase and amplitude are required [102].

In the lab-based environment, a flat metal plate provided the co-polar calibration target for all of the measurements presented in this thesis. The cross-polar calibration performed using a dihedral reflector oriented at an angle of 45°; the dihedral reflector at 45° converts linear polarisation into its orthogonal counterpart.

Accurate alignment of targets, particularly the dihedral in the radar beam, is essential to avoid significant errors in the measured response [102]. Alignment of all targets performed using a laser pointer, tape measure and protractor.

When the background and stray phase effects of the radar have been removed, that which remains is the calibrated Sinclair matrix of the target alone. Given the radar configuration (Figure 5-1), the resulting s-parameters from the VNA are equivalent to the Sinclair parameters. These parameters produced by the target are linearly polarised, equation 9-2.

Calibration is made in the frequency domain, so there are many nominally different Sinclair matrices.

$$S = \begin{bmatrix} S_{11} & S_{12} \\ S_{21} & S_{22} \end{bmatrix} = \begin{bmatrix} S_{HH} & S_{HV} \\ S_{VH} & S_{VV} \end{bmatrix} \quad (9-2)$$

9.5.1 System Distortion Matrices

The following equations show how the radars system distortion matrices are derived and how ultimately the target's Sinclair matrix is extracted.

The backscattered electric field produced by a target is given by [98] [99] [103];

$$E^{bs} = \left(\frac{e^{-jkR_r}}{R_r} \right) S E^i \quad (9-3)$$

Where;

E^{bs} = The backscattered electric field produced by reflection from the target.

R_r = The range between the radar and the target.

E^i = The electric field incident upon the target from the radar.

$k = 2\pi/\lambda$.

S = The Sinclair matrix.

For the vertically polarised transmit mode [98] [99];

$$E^r = \begin{bmatrix} E_{vv}^r \\ E_{hh}^r \end{bmatrix} = e^{-2kR_r} \frac{K}{R_r^2} \begin{bmatrix} R_{vv} & R_{vh} \\ R_{hv} & R_{hh} \end{bmatrix} \begin{bmatrix} S_{vv} & S_{vh} \\ S_{hv} & S_{hh} \end{bmatrix} \begin{bmatrix} T_{vv} \\ T_{hh} \end{bmatrix} \quad (9-4)$$

For the horizontally polarised transmit mode [98] [99];

$$E^r = \begin{bmatrix} E_{vh}^r \\ E_{hh}^r \end{bmatrix} = e^{-2kR_r} \frac{K}{R_r^2} \begin{bmatrix} R_{vv} & R_{vh} \\ R_{hv} & R_{hh} \end{bmatrix} \begin{bmatrix} S_{vv} & S_{vh} \\ S_{hv} & S_{hh} \end{bmatrix} \begin{bmatrix} T_{vh} \\ T_{hh} \end{bmatrix} \quad (9-5)$$

Where;

E_r = The received electric field.

The R_{vv} and R_{hh} elements represent the amplitude and phase distortion produced by the receive antenna and polariser combination.

The R_{vh} and R_{hv} elements represent the cross-polarisation produced by the receive antenna and polariser combination.

With;

$$K = K_1^2 \sqrt{\left(\frac{G_t G_r \lambda^2}{(4\pi)^2} \right)} E_0 \quad (9-6)$$

Where;

K_1 is a constant related to the antenna's effective area and its transmission losses.

E_0 is the transmitted electric field.

Equations 9-4 and 9-5 can be written in a compact form [98] [99];

$$E^r = e^{-j2kR_r} \frac{K}{R_r^2} RSTp^t \quad (9-6)$$

Where the received electric field with vertically and horizontally polarised transmission states are given by [98] [99];

$$E^r = \begin{bmatrix} E_{vv}^r \\ E_{hh}^r \end{bmatrix}, p^t = \begin{bmatrix} 0 \\ 1 \end{bmatrix} \quad \text{vertical transmission} \quad (9-7)$$

$$E^r = \begin{bmatrix} E_{vh}^r \\ E_{hv}^r \end{bmatrix}, p^t = \begin{bmatrix} 0 \\ 1 \end{bmatrix} \quad \text{horizontal transmission} \quad (9-8)$$

Where the distortion matrices are given by;

$$R = \begin{bmatrix} R_{vv} & R_{vh} \\ R_{hv} & R_{hh} \end{bmatrix} \quad (9-9)$$

$$T = \begin{bmatrix} T_{vv} & T_{vh} \\ T_{hv} & T_{hh} \end{bmatrix} \quad (9-10)$$

Equation 9-6 can be re-written for both the vertical and horizontal transmission states [98] [99];

$$\begin{bmatrix} E_{vv}^r & E_{vh}^r \\ E_{hv}^r & E_{hh}^r \end{bmatrix} = e^{-j2kR_r} \frac{K}{R_r^2} \begin{bmatrix} R_{vv} & R_{vh} \\ R_{hv} & R_{hh} \end{bmatrix} \begin{bmatrix} S_{vv} & S_{vh} \\ S_{hv} & S_{hh} \end{bmatrix} \begin{bmatrix} T_{vv} & T_{vh} \\ T_{hv} & T_{hh} \end{bmatrix} \quad (9-11)$$

In compact form [98] [99];

$$\begin{bmatrix} E_{vv}^r & E_{vh}^r \\ E_{hv}^r & E_{hh}^r \end{bmatrix} = e^{-j2kR_r} \frac{K}{R_r^2} RST \quad (9-12)$$

Via matrix inversion the Sinclair matrix can then be obtained [98] [99];

$$S = \left(\frac{R_r^2}{K} e^{j2kR_r} \right) R^{-1} \begin{bmatrix} E_{vv}^r & E_{vh}^r \\ E_{hv}^r & E_{hh}^r \end{bmatrix} T^{-1} \quad (9-13)$$

9.5.2 Deconvolution Calibration Technique

For this method to remove the dispersion in the polariser and horn assembly, the target response is divided by the responses of the flat metal plate (or sphere) and a dihedral reflector angled at 45° between orthogonal polarisations. Dispersion in the polariser and the horn antenna cause waves at some frequencies to travel faster through the system than others meaning the effect of a delta function in the time domain is that it becomes broadened. This broadening is the convolution of a delta function with the system delta function response. Since convolution in the time

domain is multiplication in the frequency domain, the deconvolution can be achieved by dividing the target measured parameters by the measured parameters from the metal plate and dihedral. Any internal reflections produced by the horn and OMT get removed from the target, plate and dihedral parameters by subtracting the parameters from just the RAM background measurement with no target present. After calibration, the result is the Sinclair parameters for the target.

A basic method of calibration is presented in (equation 9-14);

$$\text{Calibrated Target} = \frac{(\text{Target}-\text{RAM})}{(\text{DH45}^\circ-\text{RAM})+(\text{Plate}-\text{RAM})} \quad (9-14)$$

9.5.3 Papathanassiou and Kimura Calibration

Equation 9-14 presents, a simple method of calibration that gave good results, however an alternative approach developed by Papathanassiou (1998a) and Kimura (2004) [100] [101], presented below (equation 9-15) is widely accepted as the standard method for polarimetric radar calibration [51]:

$$[O] = \begin{bmatrix} r_{11} & r_{12} \\ r_{21} & r_{22} \end{bmatrix} \begin{bmatrix} S_{11} & S_{12} \\ S_{21} & S_{22} \end{bmatrix} \begin{bmatrix} t_{11} & t_{12} \\ t_{21} & t_{22} \end{bmatrix} + \begin{bmatrix} n_{11} & n_{12} \\ n_{21} & n_{22} \end{bmatrix}$$

$$[O] = [R][S][T] + [N] \quad (9-15)$$

Where;

[O] = The observed (measured [M] matrix.

[R] = Distortion (convolution) produced by OMT and antenna.

[T] = Distortion (convolution) produced by OMT and antenna.

[S] = The scattering matrix produced by the target.

[N] = The unwanted noise produced by the target scene (clutter) and thermal noise in the radars receiver.

Calibration via the estimation of unwanted systematic cross polarisation and differential phase difference between channels H and V (ignoring noise) can be reduced by performing matrix inversion as shown;

$$[S] = [R]^{-1}[O][T]^{-1} \quad (9-16)$$

In equations 9-15 and 9-16, the convolution caused in the transmission and reception cycles are shown as separate matrices, simplification of this by combining

the two matrices and ignoring noise leads to the scattering vector distortion matrix [Z]:

$$k_{obs} = \begin{bmatrix} O_{HH} \\ O_{HV} \\ O_{VH} \\ O_{VV} \end{bmatrix} = [Z]k_s = \begin{bmatrix} r_{11}t_{11} & r_{11}t_{21} & r_{12}t_{11} & r_{12}t_{21} \\ r_{11}t_{12} & r_{11}t_{22} & r_{12}t_{12} & r_{12}t_{22} \\ r_{21}t_{11} & r_{21}t_{21} & r_{22}t_{11} & r_{22}t_{21} \\ r_{21}t_{12} & r_{21}t_{22} & r_{22}t_{12} & r_{22}t_{22} \end{bmatrix} \cdot \begin{bmatrix} S_{HH} \\ S_{HV} \\ S_{VH} \\ S_{VV} \end{bmatrix}$$

$$\Rightarrow k_s = [Z]^{-1} k_{obs} \quad (9-17)$$

Equation 9-17 applies to the bistatic or pseudo monostatic case where the cross-polar terms are non-reciprocal. For the monostatic case where $S_{HV} = S_{VH}$, the distortion matrix becomes rectangular as can be seen in equation 9-18:

$$k_{obs} = \begin{bmatrix} O_{HH} \\ O_{HV} \\ O_{VH} \\ O_{VV} \end{bmatrix} = [Z]k_s = \begin{bmatrix} r_{11}t_{11} & r_{11}t_{21} + r_{12}t_{11} & r_{12}t_{21} \\ r_{11}t_{12} & r_{11}t_{22} + r_{12}t_{12} & r_{12}t_{22} \\ r_{21}t_{11} & r_{21}t_{21} + r_{22}t_{11} & r_{22}t_{21} \\ r_{21}t_{12} & r_{21}t_{22} + r_{22}t_{12} & r_{22}t_{22} \end{bmatrix} \cdot \begin{bmatrix} S_{HH} \\ S_{HV} \\ S_{VV} \end{bmatrix}$$

$$k_s = (Z^{*T}Z)^{-1}Z^{*T}k_{obs} \quad (9-18)$$

Unwanted systematic cross-polarisation is reduced via calibration using a dihedral reflector orientated at 45° , values measured representing the [Z] matrix $r_{11} t_{22}$ and $r_{22} t_{11}$. The differential phase difference between channels is reduced via calibration using a flat metal plate, values measured representing the elements of the [Z] matrix $r_{11} t_{11}$ $r_{22} t_{22}$. All targets measured, including calibration targets, have their responses subtracted from a background measurement of microwave absorber as before.

A special case can be applied to the [Z] matrix when the systematic cross-polarisation is better than -30dB, which is the case for the radar presented in this thesis. With cross-polarisation better than -30 dB, all off-diagonal elements of the [Z] matrix can be set to zero [51] as can be seen in equation 9-19:

$$[Z] = r_{11}t_{11} \begin{bmatrix} 1 & 0 & 0 \\ 0 & t_{22}/t_{11} & 0 \\ 0 & r_{22}/r_{11} & 0 \\ 0 & 0 & r_{22}t_{22}/r_{11}t_{11} \end{bmatrix} \quad (9-19)$$

9.5.4 Nesti and Hohmann Calibration

This calibration technique uses three targets, a sphere, a vertical dihedral and a dihedral orientated at 45° . The co-polar response of the sphere or plate provides an absolute calibration reference, with which other targets can be compared. Alignment of the plate and dihedral is critical as misalignment manifests itself as cross-polar coupling.

Calibration procedure;

1. Co-polar calibration is performed via measurement of a metal sphere.
2. Calibrated measurement of a vertical dihedral is performed.
3. From measurements made in 1 and 2, the cross-polar response of the tilted dihedral is evaluated.
4. The radars cross-polar response is then calibrated via the measurement of the dihedral reflector at 45°.

Assuming the cross-polar coupling in the antenna and polariser are at least -20dB or lower in both transmitting and reception modes then $S_{HV} = S_{VH}$ and a simplified matrix can be used to define the measured response produced by a target:

$$M = [C].S \quad (9-20)$$

Where;

M = the complex vector of the measured response produced with the radar when illuminating a target.

$$M = \begin{bmatrix} M_{vv} \\ M_{hh} \\ M_{hv} \end{bmatrix} \quad (9-21)$$

S = the target scattering vector.

$$S = \begin{bmatrix} S_{vv} \\ S_{hh} \\ S_{hv} \end{bmatrix} \quad (9-22)$$

C = the (3x3) distortion matrix produced by the horn and OMT in both transmission and reception cycles.

The scattering vectors for the three targets are given by:

S1=(S1vv, S1hh, 0), Sphere

S2=(S2vv, S2hh, 0), Vertical dihedral

S3=(S3vv, S3hh, S3hv), Dihedral at 45°

The measured response from each target as can be seen in equation 1 contains the desired Sinclair matrix distorted by the horn and polarisers stray parasitic cross polarisation and phase mismatch.

The measured responses of each of the targets are related to the distortion and Sinclair vectors by the following equations;

Sphere;

$$M1_{vv} = C11.S1_{vv} \quad (9-23)$$

$$M2_{hh} = C22.S1_{hh} \quad (9-24)$$

$$M1_{hv} = C31.S1_{vv} + C32.S1_{hh} \quad (9-25)$$

Vertical dihedral;

$$M2_{vv} = C11.S2_{vv} \quad (9-26)$$

$$M2_{hh} = C22.S2_{hh} \quad (9-27)$$

$$M2_{hv} = C31.S2_{vv} + C32.S2_{hh} \quad (9-28)$$

Dihedral at 45°;

$$M3_{vv} = C11.S3_{vv} + C13.S3_{hv} \quad (9-29)$$

$$M3_{hh} = C22.S3_{hh} + C23.S3_{hv} \quad (9-30)$$

$$M3_{hv} = C31.S3_{vv} + C32.S3_{hh} + C33.S3_{hv} \quad (9-31)$$

$$C11 = M1_{vv}/S1_{vv} \quad (9-32)$$

$$C22 = M1_{hh}/S1_{hh} \quad (9-33)$$

$$S2_{vv} = M2_{vv}/C11 \quad (9-34)$$

$$S2_{hh} = M2_{hh}/C22 \quad (9-35)$$

$$S3_{hh} = S3_{vv} = 0.5(S2_{vv} + S2_{hh}) \quad (9-36)$$

$$S3_{hv} = S3_{vh} = 0.5(S2_{hh} - S2_{vv}) \quad (9-37)$$

C31 and C32 are found by solutions to simultaneous equations 9-25 and 9-28 (step 4).

$$C31 = (M2_{hv}.S1_{hh} - M1_{hv}.S2_{hh}) / (S2_{vv}.S1_{hh} - S1_{vv}.S2_{hh}) \quad (9-38)$$

$$C32 = (M1_{hv}.S2_{vv} - M2_{hv}.S1_{vv}) / (S2_{vv}.S1_{hh} - S1_{vv}.S2_{hh}) \quad (9-39)$$

$$C13 = (M3_{vv} - C11.S3_{vv}) / S3_{hv} \quad (9-40)$$

$$C23 = (M3_{hh} - C22.S3_{hh}) / S3_{hv} \quad (9-41)$$

$$C33 = (M3_{hv} - C31.S3_{vv} - C32.S3_{hh}) / S3_{hv} \quad (9-42)$$

From the above the distortion matrix is formed;

$$C = \begin{bmatrix} C_{11} & 0 + 0j & C_{13} \\ 0 + 0j & C_{22} & C_{23} \\ C_{31} & C_{32} & C_{33} \end{bmatrix} \quad (9-43)$$

The calibrated Sinclair matrix can then be found using equation (9-44);

$$S = [C]^{-1} \cdot M \quad (9-44)$$

9.5.5 Comparison of Calibration Techniques

To compare the basic calibration with that of Papathanassiou and Kimura calibration technique plots are presented for each technique using the Huynen polarisation fork and plotted on the Poincaré sphere. An evaluation of the Huynen polarisation fork and its associated parameters explained in more depth in chapters 4 and 10.

The polarisation fork has been used to provide a graphical comparison of each calibration technique and is used extensively later in the thesis.

On the plots, the green 'o's represent co-polar nulls and the blue 'x's, and red '+'s represent cross-polar nulls, description of their meaning explained further in chapters 4 and 10.

The plots presented in the next figures are of three basic radar targets;

1. A flat metal plate.
2. A dihedral reflector orientated at 45° to the horizontal.
3. A horizontal dipole array.

The best calibration is indicated by the lowest distribution (highest concentration) of co-polar nulls and the lowest spread of cross-polar nulls for targets presented.

The figures below present the basic calibration (left) and the Papathanassiou and Kimura calibration (right).

The flat metal plate response can be seen in Figure 9-3, the dihedral at 45° in Figure 9-4, and the horizontal dipole in Figure 9-5.

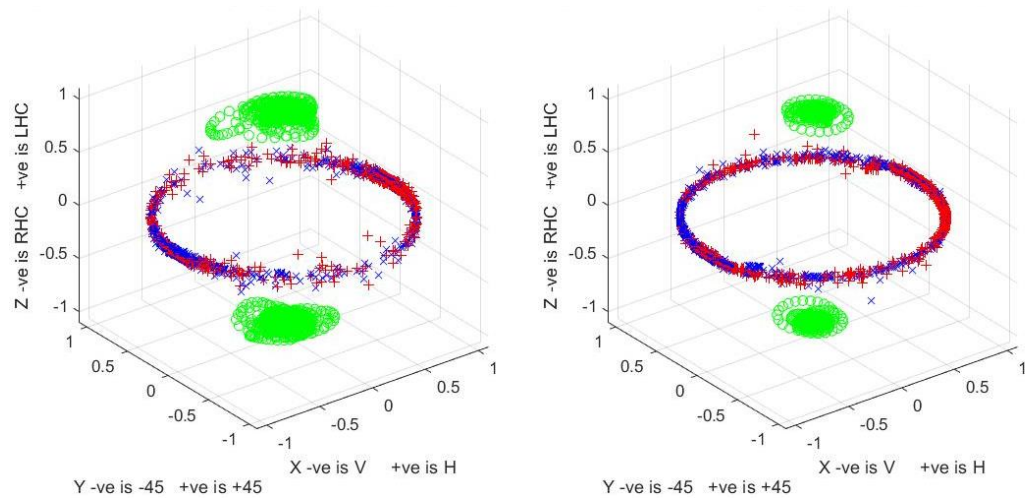


Figure 9-3 Huynen polarisation fork plot from the measurement of a flat metal plate, basic calibration (left), Papathanassiou and Kimura calibration (right)

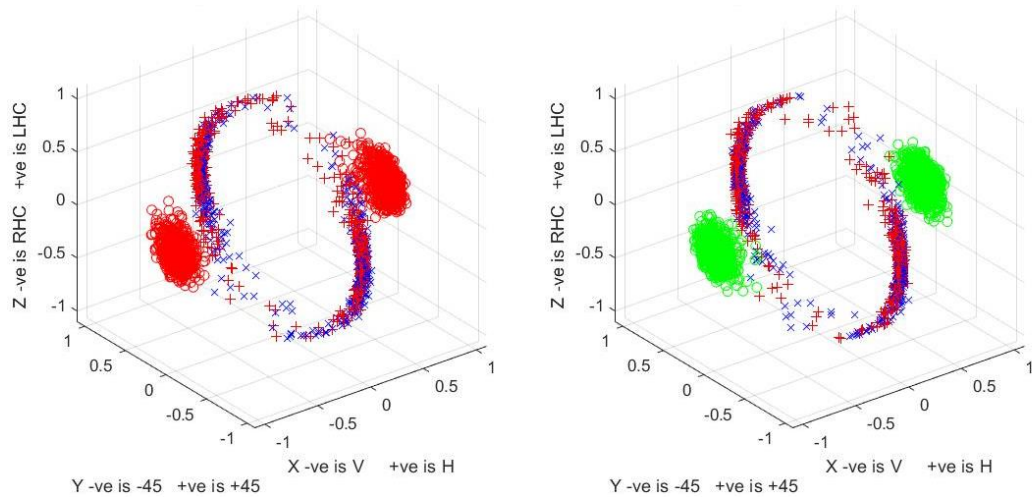


Figure 9-4 Huynen polarisation fork plot from the measurement of a Dihedral reflector at 45°, basic calibration routine (left), Papathanassiou and Kimura calibration (right)

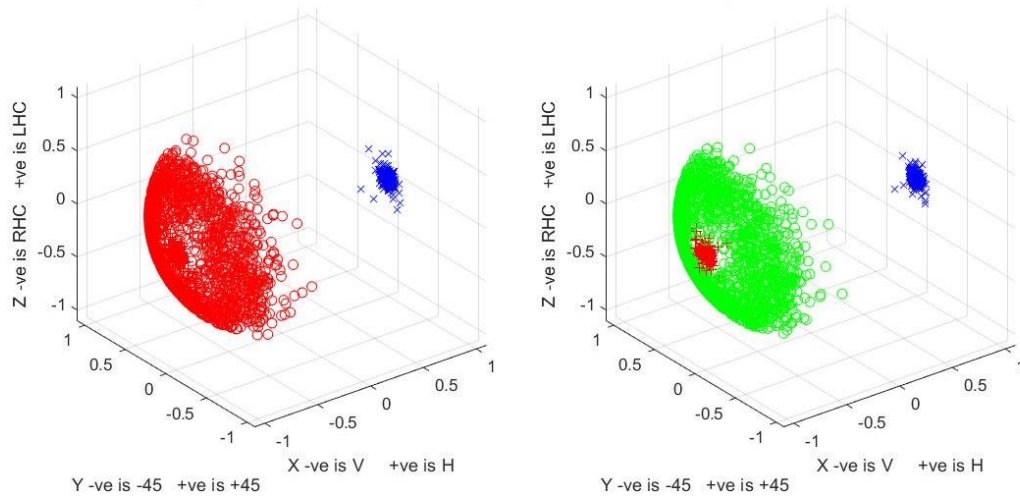


Figure 9-5 Huynen polarisation fork plot from the measurement of a horizontal Dipole array, basic calibration routine (left), Papathanassiou and Kimura calibration (right)

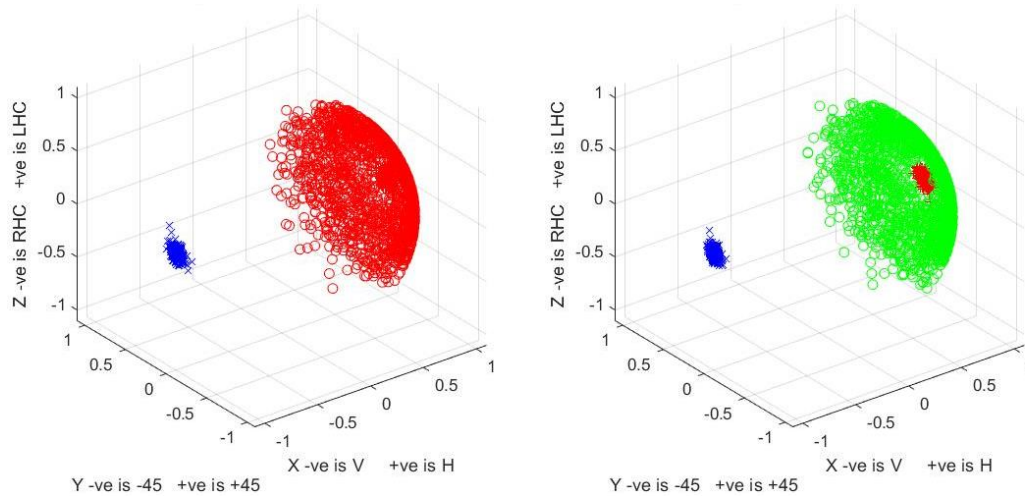


Figure 9-6 Huynen polarisation fork plot from the measurement of a vertical Dipole array, basic calibration routine (left), Papathanassiou and Kimura calibration (right)

9.6 Modelling of Target Sinclair Matrices

Modelling the target Sinclair matrix for a target is a good way to understand how targets reflect (or scatter) coherent waves from a full polarimetric radar. A validated model has value in that it enables the modelling of sophisticated targets and scenarios, which may be too costly to measure either in the laboratory or in-situ.

The simplest targets to begin modelling are the canonical targets of the odd-bounce (plane surface, sphere, trihedral) the even-bounce (the dihedral or roof-top), the dipole (straight wire or polariser) reflector and helix (right or left-handed). Considering the reflection from these and disregarding any phase effects to due

path lengths to the radar, the Sinclair matrix for the reflectors are for the odd-bounce [83]:

$$S_{SS} = \begin{bmatrix} 1 & 0 \\ 0 & 1 \end{bmatrix} \quad (10-1)$$

The even-bounce with an edge at an angle δ to the horizontal (the second equality for $\delta=0$):

$$S_{DS} = \begin{bmatrix} \cos 2\delta & \sin 2\delta \\ \sin 2\delta & -\cos 2\delta \end{bmatrix} = \begin{bmatrix} 1 & 0 \\ 0 & -1 \end{bmatrix} \quad (10-2)$$

The straight wire (dipole) orientated at α to the horizontal (the second equality for $\alpha=0$):

$$S_{Dip} = \begin{bmatrix} \cos^2 \alpha & \cos \alpha \sin \alpha \\ \cos \alpha \sin \alpha & \sin^2 \alpha \end{bmatrix} = \begin{bmatrix} 1 & 0 \\ 0 & 0 \end{bmatrix} \quad (10-3)$$

The helix, where \pm refers to the right or left-handedness of the helix:

$$S_{Helix} = \begin{bmatrix} 1 & \pm j \\ \pm j & -1 \end{bmatrix} \quad (10-4)$$

The quarter-wave plate [104], where \mp refers to $+90^\circ$ phase advance in the vertical polarisation and the minus to a 90° retardation in the phase:

$$S_{\lambda/4} = \begin{bmatrix} 1 & 0 \\ 0 & \mp j \end{bmatrix} \quad (10-5)$$

Further target descriptions can be found in the PhD by Huynen [105]. More complex targets can be described by using linear combinations of these basic targets.

Target type	Linear (HV) response	Circular (RL) response
Plate/sphere	$\begin{bmatrix} 1 & 0 \\ 0 & 1 \end{bmatrix}$	$\begin{bmatrix} 0 & 1 \\ 1 & 0 \end{bmatrix}$
Dihedral at 45°	$\begin{bmatrix} 0 & 1 \\ 1 & 0 \end{bmatrix}$	$\begin{bmatrix} 1 & 0 \\ 0 & 1 \end{bmatrix}$
Dihedral (horizontal and vertical)	$\begin{bmatrix} 1 & 0 \\ 0 & 1 \end{bmatrix}$	$\begin{bmatrix} 1 & 0 \\ 0 & 1 \end{bmatrix}$
Horizontal dipole	$\begin{bmatrix} 1 & 0 \\ 0 & 0 \end{bmatrix}$	$\begin{bmatrix} 1 & 1 \\ 1 & 1 \end{bmatrix}$
Vertical dipole	$\begin{bmatrix} 0 & 0 \\ 0 & 1 \end{bmatrix}$	$\begin{bmatrix} 1 & 1 \\ 1 & 1 \end{bmatrix}$
Helical (right hand)	$\begin{bmatrix} 1 & 1 \\ 1 & 1 \end{bmatrix}$	$\begin{bmatrix} 1 & 0 \\ 0 & 0 \end{bmatrix}$
Helical (Left hand)	$\begin{bmatrix} 1 & 1 \\ 1 & 1 \end{bmatrix}$	$\begin{bmatrix} 0 & 0 \\ 0 & 1 \end{bmatrix}$

Table 9-1 Theoretical Linear (HV) and Circular (RL) basis Sinclair matrices for simple canonical radar targets

9.7 Measurement results

The following results show the measured delta function responses representing multiple Sinclair matrices produced from the calibrated temporally resolved radar responses to some classical targets including the calibration targets;

1. Flat metal plate.
2. Dihedral reflector angled at 45° between orthogonal polarisations.
3. Dihedral reflector orientated horizontally between orthogonal polarisations.
4. Dihedral reflector orientated vertically between orthogonal polarisations.
5. A metal sphere
6. Long horizontal wires (referred to as the dipole)
7. Helical coils

8. Wall of microwave absorber.

Target responses are presented in both the linear and via a unitary transform circular formats using equation 2-3.

Each linear plot has four separate graphs indicating the magnitude of reflection (S_{HH} , S_{HV} , S_{VH} and S_{VV}). The S_{HH} graph indicates the magnitude of the horizontal polarisation reflected from the target when it is illuminated with horizontal polarisation. Conversely, the same applies to the S_{VV} graph but for vertical polarisation. The S_{HV} graph indicates that vertical polarisation gets reflected from the target when it is illuminated with horizontal polarisation. Conversely, the S_{VH} graph shows that horizontal polarisation gets reflected when the target is illuminated with vertical polarisation.

Each circular polarisation plot has four separate graphs indicating the magnitude of reflection (S_{RR} , S_{RL} , S_{LR} and S_{LL}). The S_{RR} graph indicates the magnitude of right-hand circular (RHC) polarisation reflected from the target when the target is illuminated with RHC polarisation. Conversely the same applies to the S_{LL} graph but for left-hand circular (LHC) polarisation. The S_{RL} graph indicates that LHC polarisation is reflected from the target when illuminated with RHC polarisation. Conversely, the S_{LR} graph RHC polarisation is reflected when the target is illuminated with LHC polarisation.

Figure 9-7 shows the response for a flat metal plate. The measurement indicates that a flat metal plate produces no change in the orientation of linearly polarised radiation, horizontal or vertically polarised target illumination gets reflected with the same polarisation orientation. However, circular polarisation gets transformed into its orthogonal state upon reflection, RHC target illumination gets reflected as LHC and vice versa.

Figure 9-8 presents a dihedral reflector's response with its ridge located at 45° to the horizontal. The results indicate that linear polarisation gets converted into its orthogonal states upon reflection. But no conversion occurs for circular polarisation.

Figure 9-9 presents the dihedral with its ridge orientated horizontally and orientated vertically in Figure 9-10. Both horizontal and vertical orientations produce no polarisation conversion for both the linear and circular cases.

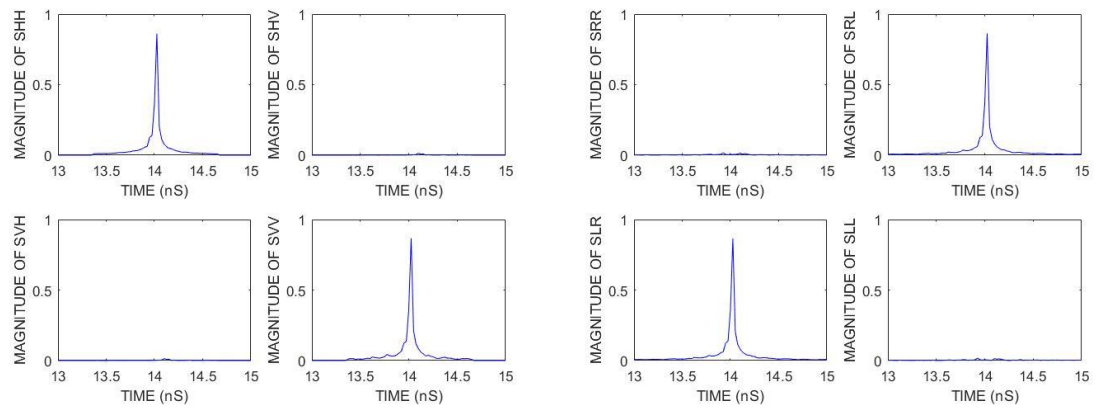
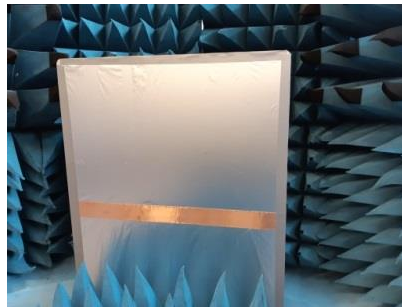


Figure 9-7 Flat metal plate (top), measured linear polarisation (bottom left), circular polarisation (bottom right).

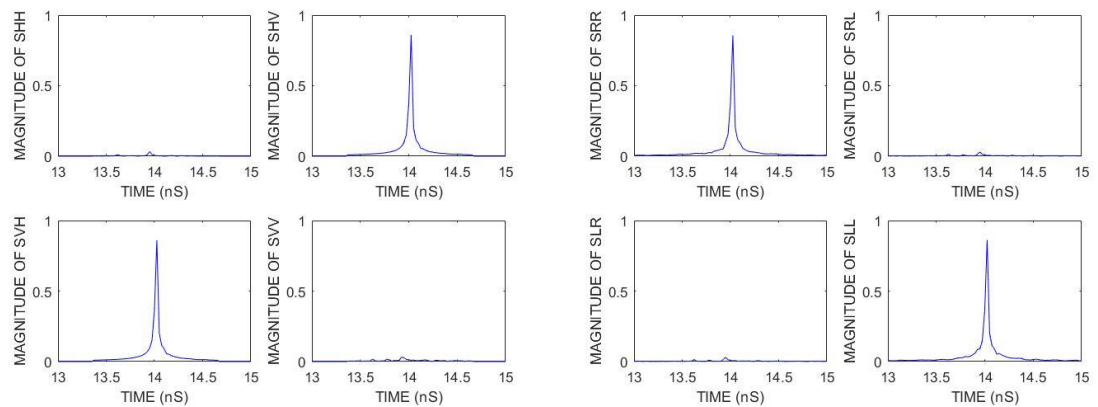
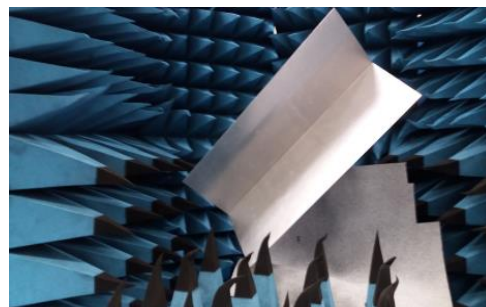


Figure 9-8 Dihedral reflector at 45° (top), measured linear polarisation (bottom left), circular (bottom right).

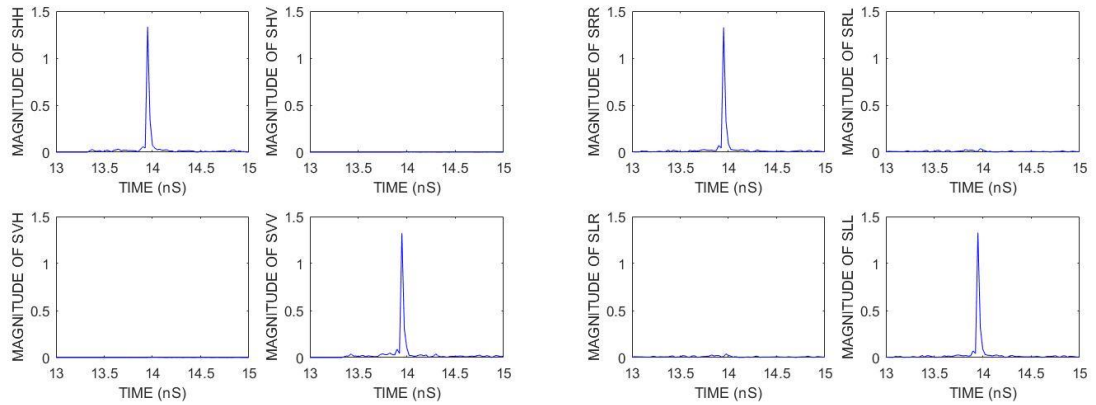


Figure 9-9 Horizontal dihedral reflector (top), measured linear polarisation (bottom left), circular (bottom right)

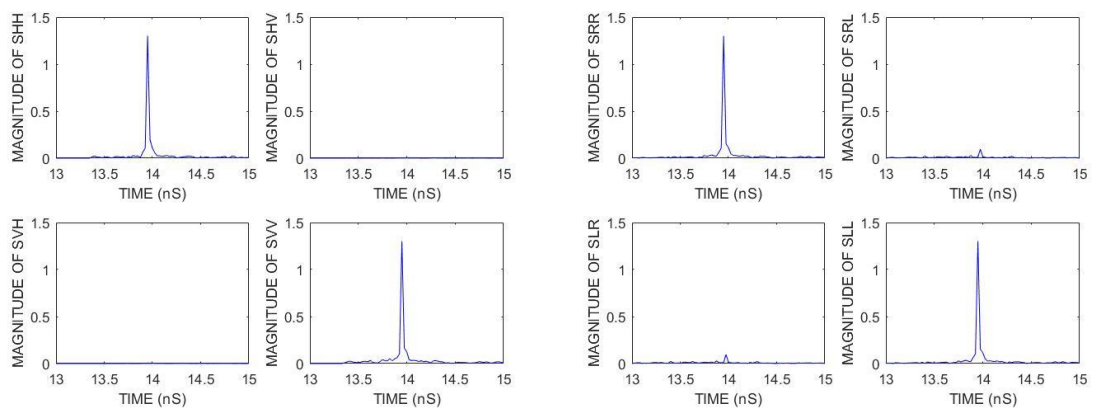
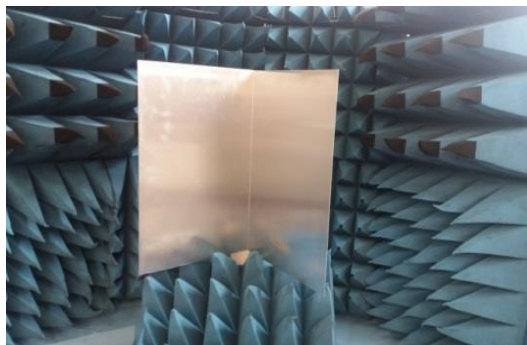


Figure 9-10 Vertical dihedral reflector (top), measured linear polarisation (bottom left), circular (bottom right)

Figure 9-12 presents a 6.5 cm diameter stainless steel sphere suspended in the beam of the radar. Linear polarisation gets transformed into the orthogonal states upon reflection, whilst circular remains unchanged. The response is the same as the metal plate; however, unlike the plate, the sphere is aspect independent.

The sphere has depth, the waves wrap around it, with part of the radiation being delayed by up to 1ns. This response is consistent with the creeping wave [106], Figure 9-11 [107] whereby some portion of the radiation travels around the sphere before being re-radiated back towards the antenna. This effect is responsible for the secondary and tertiary peaks visible in both the linear and circular plots. Literature states that this effect is most prevalent when the sphere's circumference is approximately equal to λ [107]. However, evidence of the creeping wave was noted in the measurements taken of spheres of different diameters.

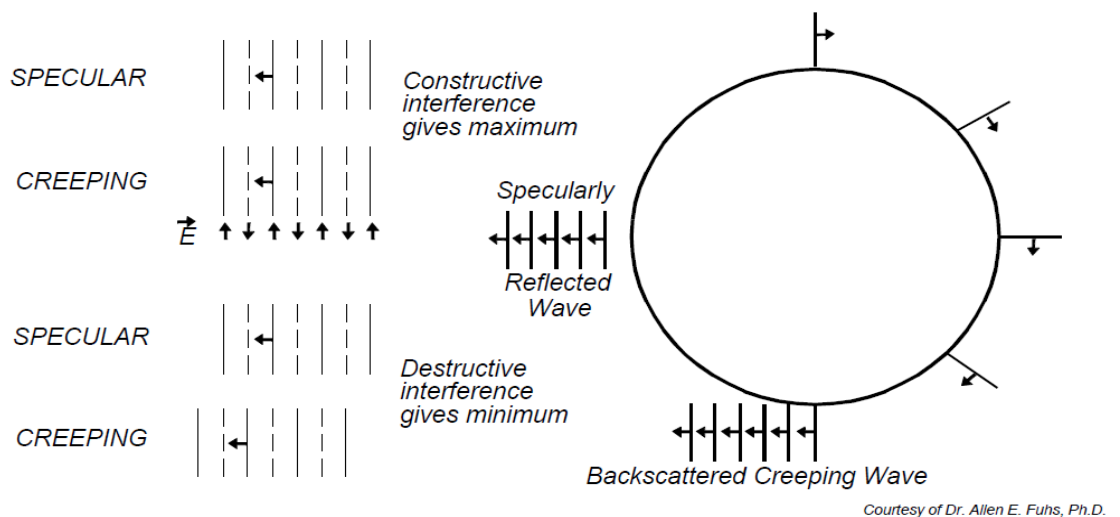


Figure 9-11 Addition of specular and creeping waves [107].

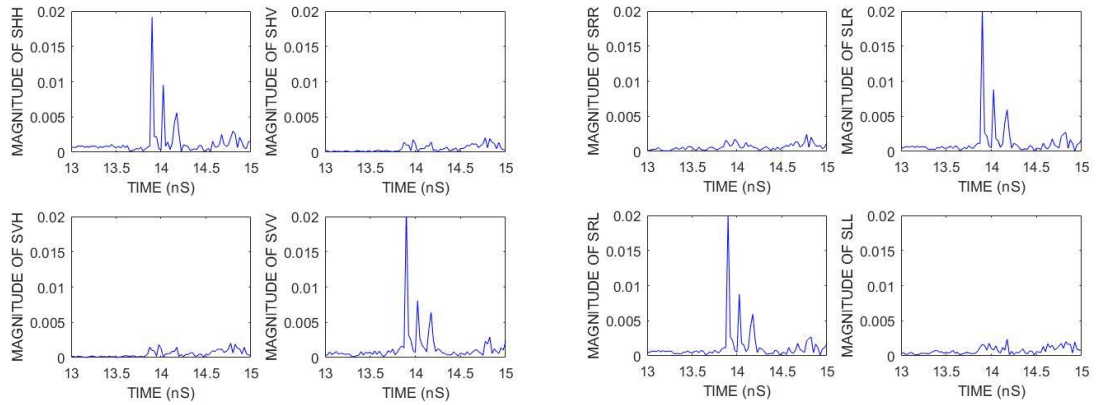
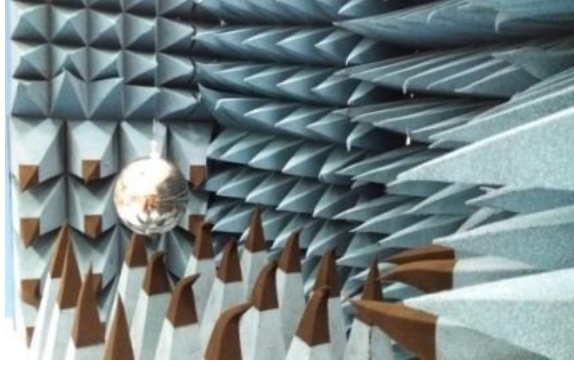


Figure 9-12 8.6 cm diameter sphere (top), measured linear polarisation (bottom left), circular (bottom right)

Figure 9-13 presents a horizontal dipole along with its associated Sinclair responses. The target is formed from an array of thin copper wires to increase its radar cross-section.

The S_{HH} response peak indicates that horizontal illumination results in horizontal reflection; conversely vertical illumination produces far less reflection because of the dipole orientation.

The circular polarisation states all have the same magnitude because the dipole has no defined orientation when illuminated with circular polarisation.

Figure 9-14 presents the same dipole but vertically orientated. The S_{VV} response peak indicates that vertical illumination results in vertical reflection; conversely, horizontal illumination produces far less reflection because of the dipole orientation.

The circular polarisation states all have the same magnitude because the dipole has no defined orientation when illuminated with circular polarisation.

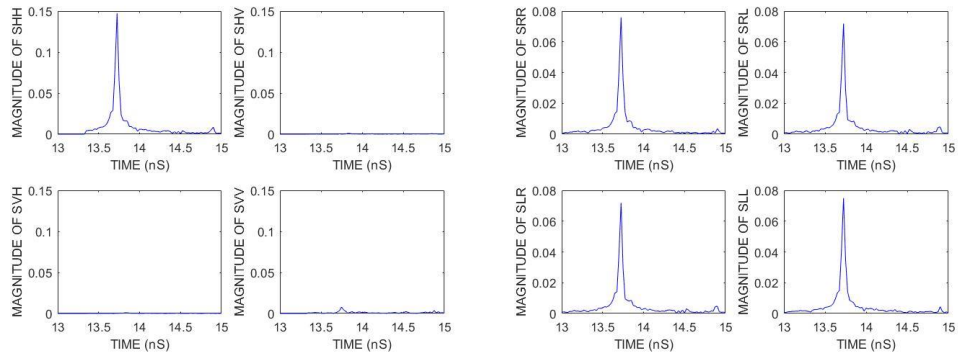


Figure 9-13 Horizontal dipole array (top), measured linear polarisation (bottom left), circular (bottom right)

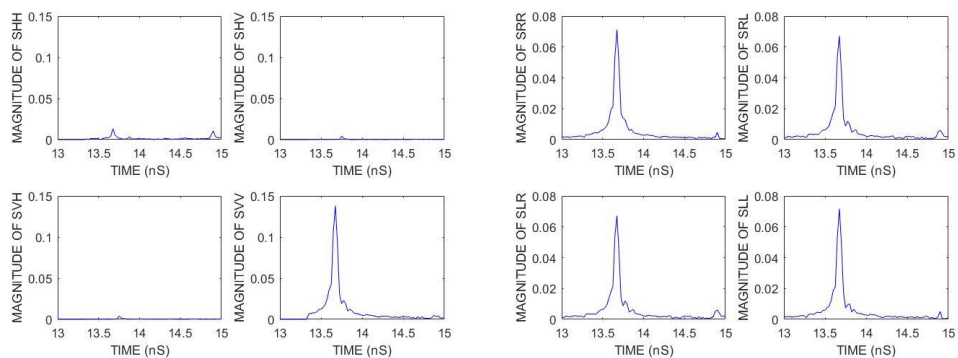


Figure 9-14 Vertical dipole array (top), measured linear polarisation (bottom left), circular (bottom right)

Figure 9-15 presents an array of ten helical antennas arranged in a hexagonal arrangement in the radar beam. Each helix has five turns wound in the same

direction and are tuned to work at K band in axial radiation mode. Note the largest response occurs in the S_{RR} component of the Sinclair matrix, as would be expected as this is the wind direction of the helix.

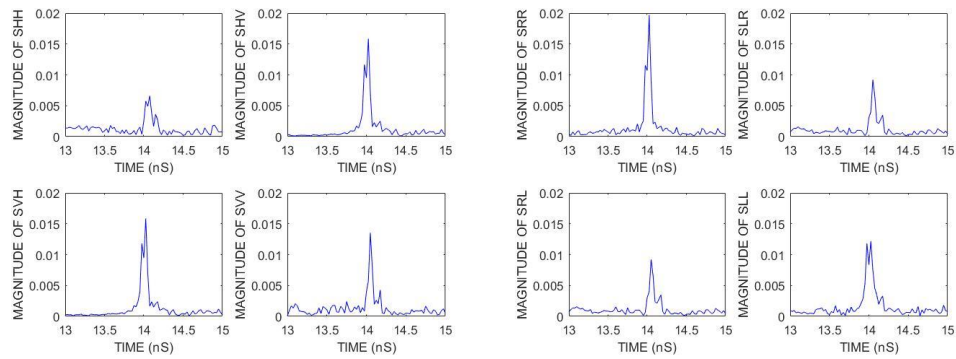


Figure 9-15 Array of helical antennas (top), measured linear polarisation (bottom left), circular (bottom right)

9.8 Conclusion

Calibration took place in two stages; VNA calibration using TRL standards (chapter 6) followed by radar calibration. Radar calibration compensates for cross polarisation and dispersion in the horn and OMT assembly. Radar calibration used a flat metal plate to provide the co-polar calibration, dihedral (corner) reflector at 45° for the cross-polar and a wall of microwave absorber to remove unwanted internal reflections.

Three calibration techniques were presented with two reviewed by comparing the measurement of three radar targets (plate, dihedral at 45° and a dipole (vertical and horizontal), Figure 9-3 to Figure 9-6. Both calibration techniques gave similar results, but the Papathanassiou and Kimura calibration was slightly better, producing the lowest distribution of co and cross-polar nulls. The Papathanassiou

and Kimura calibration was chosen as the calibration technique for all measurements presented.

This chapter presented an introduction to simulations as a potential means to understand how targets scatter coherent waves from the radar. Simulation of simple radar targets matched theory, it may be possible to simulate more complicated targets by combining these simple targets. Simulations could be a cost-effective wave to determine a targets response.

Measurements for a set of classical radar targets with calibration applied produced results that closely matched the theory. Each measurement produced sets of 801 Sinclair matrices (one for each spectral increment). Measurements were taken in the linear polarisation basis. Conversion to the circular polarisation basis was performed using a unitary transformation.

Chapter 10 Measurement of the Huynen Polarisation fork

10.1 Introduction

Chapter 10 applies the Huynen polarisation fork technique introduced in chapter 4. Measured responses of a set of simple canonical radar targets are analysed using the polarisation fork technique, the responses then compared to theory.

10.2 Measurement results

Table 10-1 provides details of physical target dimensions for reference. The results presented are plotted on the Poincaré sphere, a descriptive representation of which can be seen in Figure 2-4 and Figure 4-1. For the measured results the cross-polar null X2 (the handle of the fork) is represented by blue (X)'s, the X1 nulls (central prong of the fork) are represented by red (+)'s, the co-polar nulls (C1 and C2) are shown as green (O)'s for the measured responses presented below.

1. Flat metal plate. Figure 10-2 (left).
2. Vertical and horizontal dihedral reflectors. Figure 10-7
3. Dihedral reflector angled at 45° between orthogonal polarisations Figure 10-2 (right).
4. Vertical and horizontal dipoles. Figure 10-12.
5. Metal sphere. Figure 10-19 (left).
6. Wave plate with integral reflector (wires horizontal) (1mm spacing between wires and reflector), Figure 10-22
7. Wax blocks, Figure 10-26

The Huynen polarisation fork plots associated with each target are multispectral. There are 801 points between 18 to 26 GHz because of the stepped frequency radar used. Each spectral point produces a fork response that is in a slightly different position to the previous one resulting in the distribution of the co and cross-polar nulls about the Poincaré sphere.

Target type	Length(cm)	Width(cm)	Details
Flat plate	10.5	10.5	$\sigma=8.21\text{m}^2$ at 22 GHz
Dihedral	50	50 (aperture)	2 sides 35.5 cm with 90° bend in middle. $\sigma=17033\text{m}^2$ at 22 GHz
Dipole	50		(wires 0.4mm diameter x 20) 1λ separation at 22 GHz.
Sphere			10.5cm diameter stainless steel.
Wave plate	10	10	(Copper wires 0.5mm diameter x 74) 1mm separation between plate reflector and wires.
Wax blocks			2cm thick and 3.8 cm thick, 18 cm diameter.

Table 10-1 Target physical dimensions.

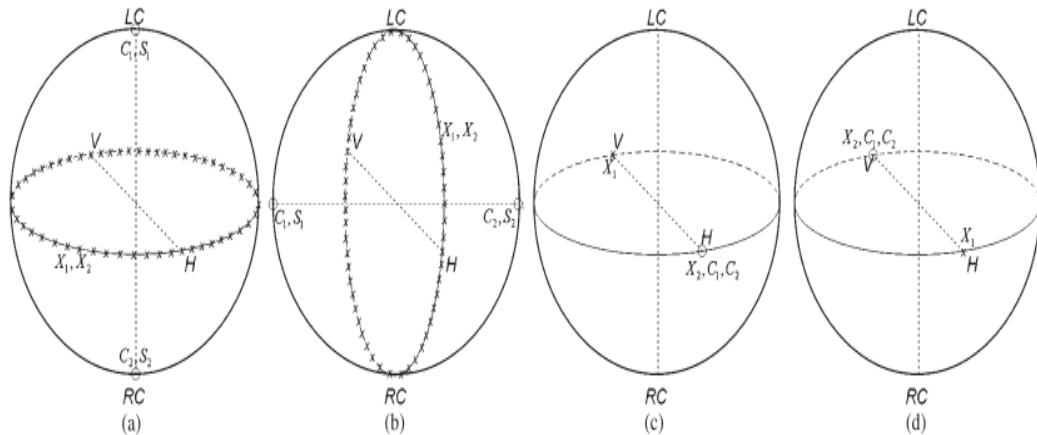


Figure 10-1 (a) Flat plate, (b) Dihedral at 45° , (c) Vertical dipole, (d) Horizontal dipole [69].

10.2.1 Flat metal plate and dihedral (corner) reflector at 45°

The flat plate and a dihedral reflector orientated at 45° and their associated fork plots via measurement are presented in Figure 10-2 and via simulation Figure 10-3.

Figure 10-2 left presents the Huynen polarisation fork of the flat plate. The cross-polar nulls located around the Poincaré sphere's equator indicate no conversion occurs for the linear polarisation states. The co-polar nulls located at the zenith and nadir show that transformation occurs for the circular polarisation states.

Figure 10-2 right presents the Huynen polarisation fork of the dihedral at 45°. The cross-polar nulls circumvent the zenith and nadir, indicating that polarisation conversion does not take place for the circular polarisation states. The co-polar nulls located at the vertical and horizontal linear polarisation points on the Poincaré sphere indicate that conversion is taking place for these polarisation states.

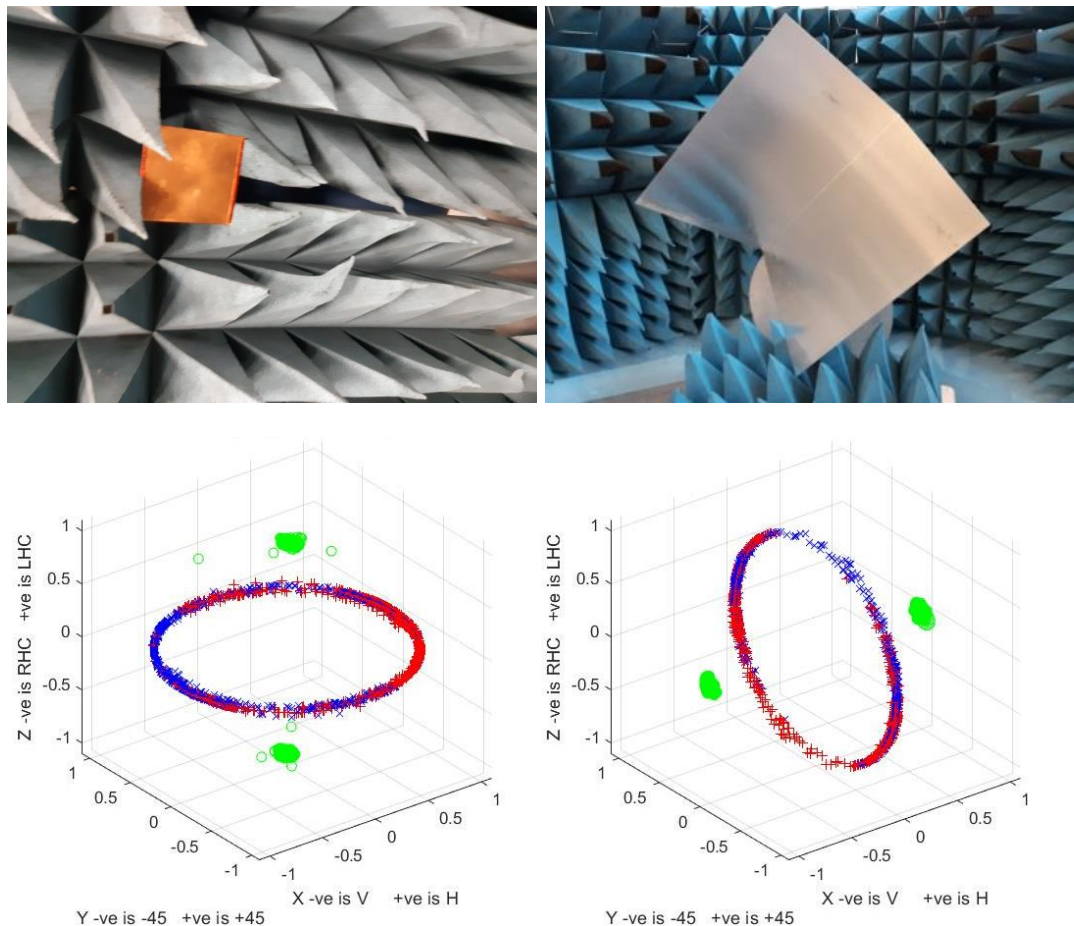


Figure 10-2 Flat plate reflector (top left), Dihedral reflector angled at 45° (top right), measured responses, Flat plate (bottom left), Dihedral 45° (bottom right).

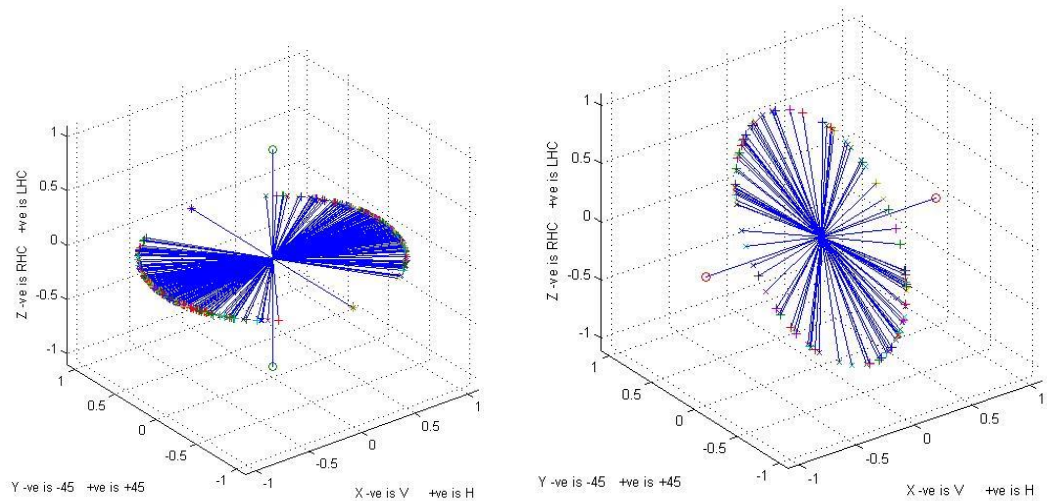


Figure 10-3 Simulated responses for Flat plate (left), Dihedral at 45°(right).

The orientation angle Figure 10-4 (left) for the plate shows a chaotic response due to the plate having no defined orientation, unlike the dihedral at 45° Figure 10-4 (right), which is $\pm 45^\circ$ on the plot. The skip angle for the plate visible in Figure 10-5 (left) at 0° indicates a single (odd) bounce reflection, whilst the dihedral at 45° Figure 10-5 (right) has a skip angle of $\pm 45^\circ$ indicating a double (even) bounce reflection is taking place. The fork angle for both plate and dihedral is 45° Figure 10-6 and are both in agreement with theory and via simulation. These relatively simple targets change little between each measured spectral point.

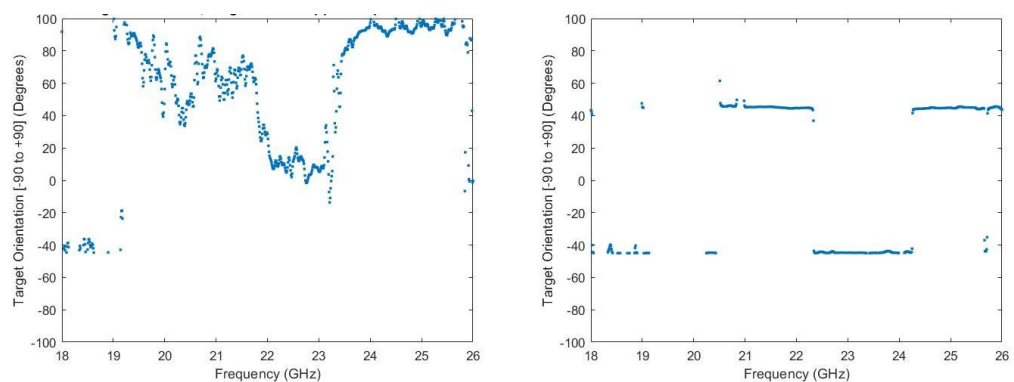


Figure 10-4 Measured orientation angle. Plate (left), Dihedral at 45° (right)

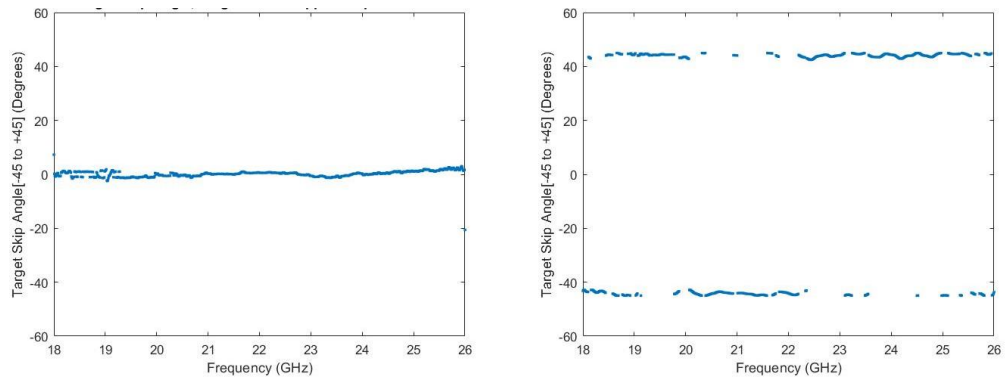


Figure 10-5 Measured skip angle. Plate (left), Dihedral at 45° (right)

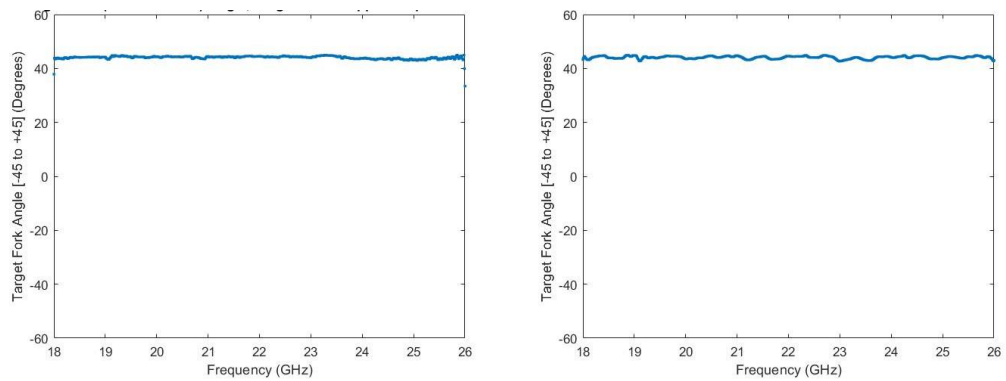


Figure 10-6 Measured fork angle. Plate (left), Dihedral at 45° (right)

10.2.2 Vertical and horizontal dihedral (corner) reflectors

Figure 10-7 presents the vertically and horizontally orientated dihedral along with associated fork plots.

Figure 10-8 presents the orientation angle, which is transiting between 0° and 90°. The helicity angle Figure 10-9 indicates that the dihedral in both vertical and horizontal orientations is at 0° with a small amount of conversion into helical orientation upon reflection due to target imperfections.

The dihedral is a double (even) bounce reflector, indicated by the skip angle shown in Figure 10-10, transiting between $\pm 45^\circ$. The fork angle (Figure 10-11) is 45° the same as for the dihedral orientated at 45° and the plate.

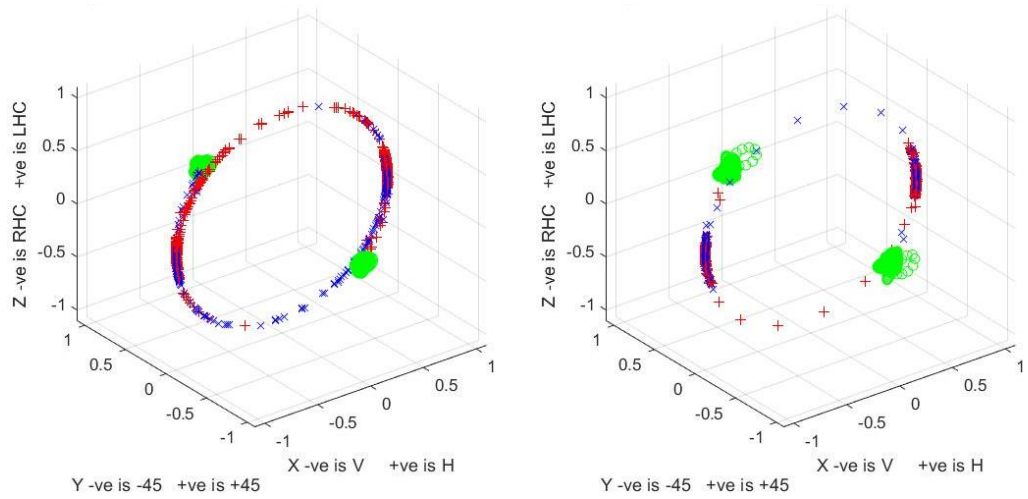


Figure 10-7 Vertical dihedral reflector (top left), Horizontal dihedral reflector (top right). Measured responses, vertical dihedral (bottom left), horizontal dihedral (bottom right).

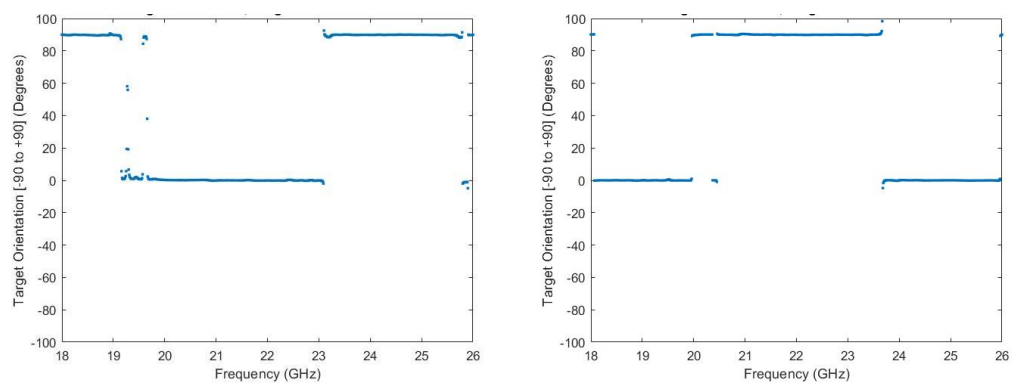


Figure 10-8 Measured orientation angle, Vertical dihedral (left), Horizontal dihedral (right)

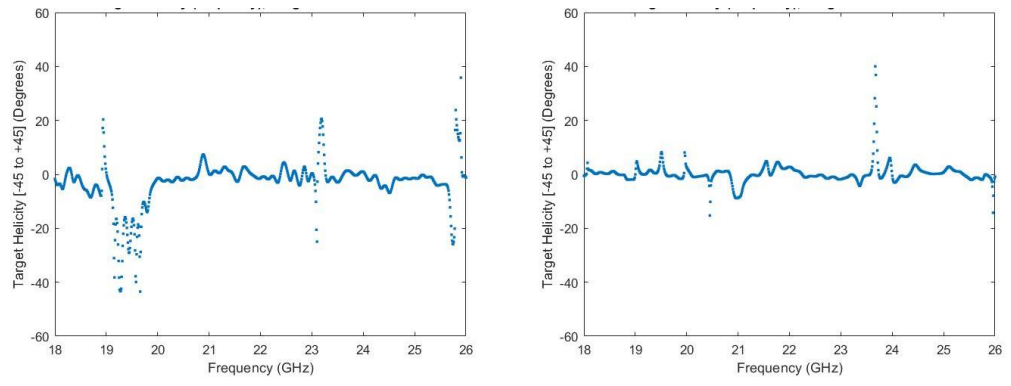


Figure 10-9 Measured helicity angle, Vertical dihedral (left), Horizontal dihedral (right)

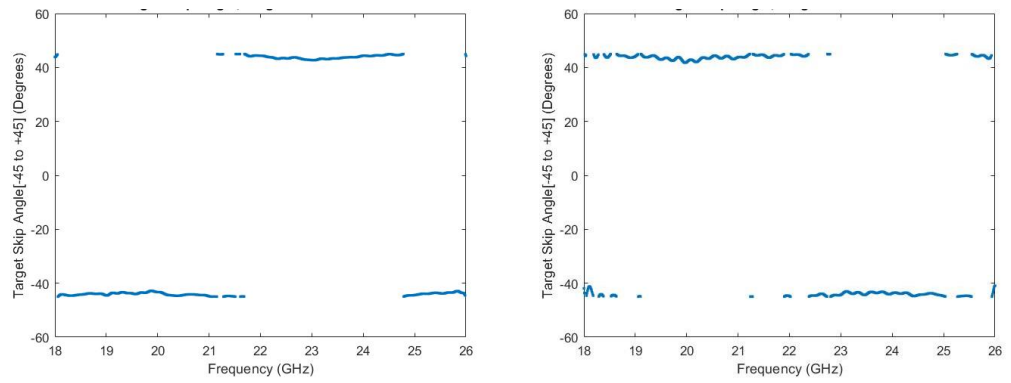


Figure 10-10 Measured skip angle, Vertical dihedral (left), Horizontal dihedral (right)

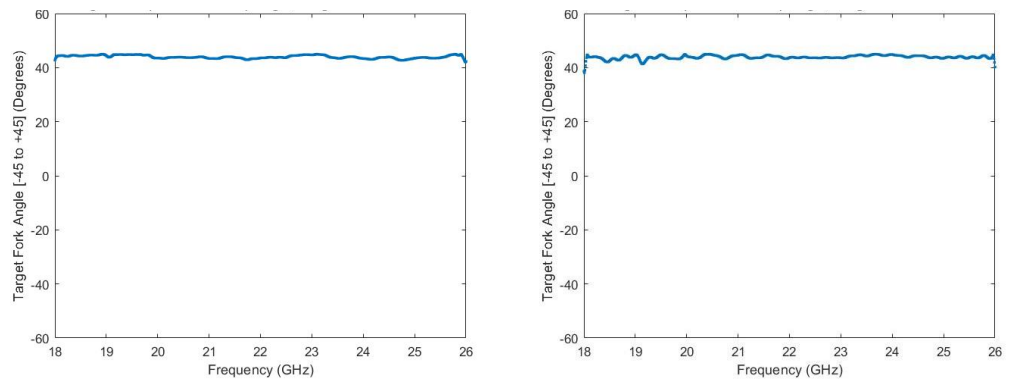


Figure 10-11 Measured fork angle, Vertical dihedral (left), Horizontal dihedral (right)

10.2.3 Vertical and horizontal dipoles

Figure 10-12 presents the dipole in vertical and horizontal orientations, measured response with vertical orientation (left) and horizontal (right), and associated fork plots.

Figure 10-13 presents the dipole's simulated response with vertical orientation (left), horizontal (right). The measured fork plot reveals a cone-shaped distribution of co-polar nulls around the X2 cross-polar null (the handle of the fork), caused by target imperfection.

Figure 10-14 presents the simulated response for the dipole at 45°. Measurements were not taken at these angles.

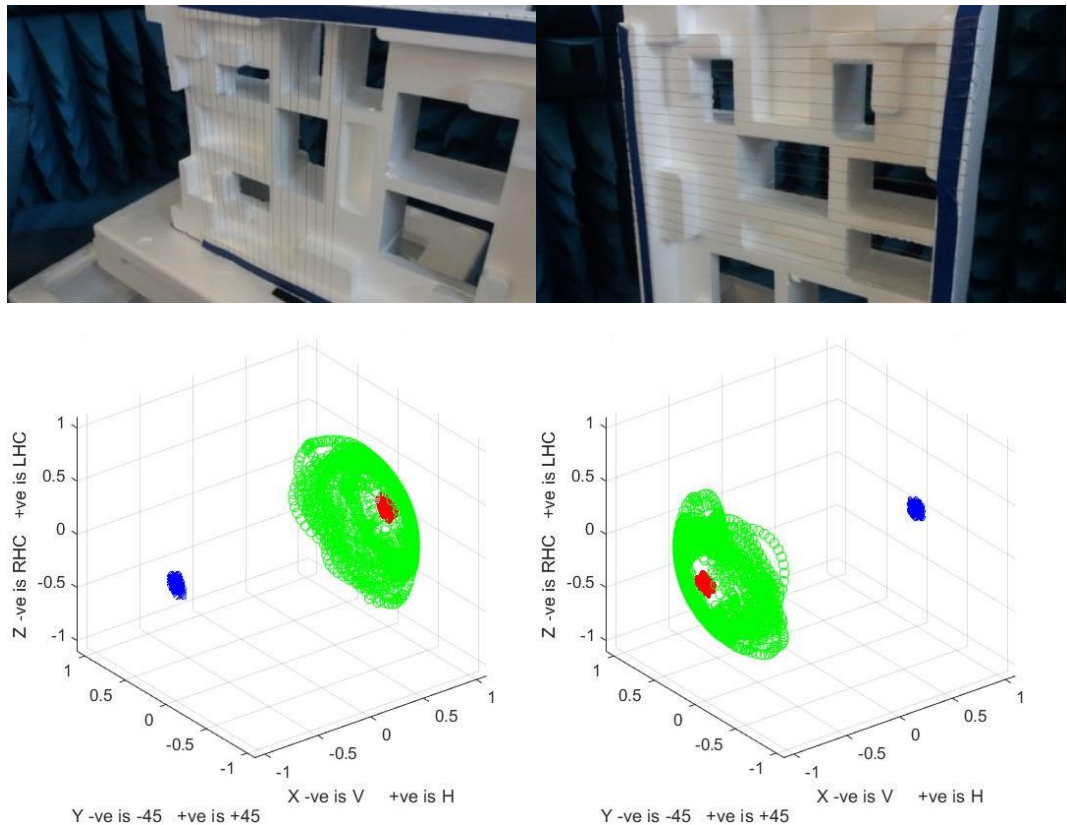


Figure 10-12 Vertical dipole (top left), Horizontal dipole (top right), Measured responses, Vertical dipole (bottom left), Horizontal dipole (bottom right).

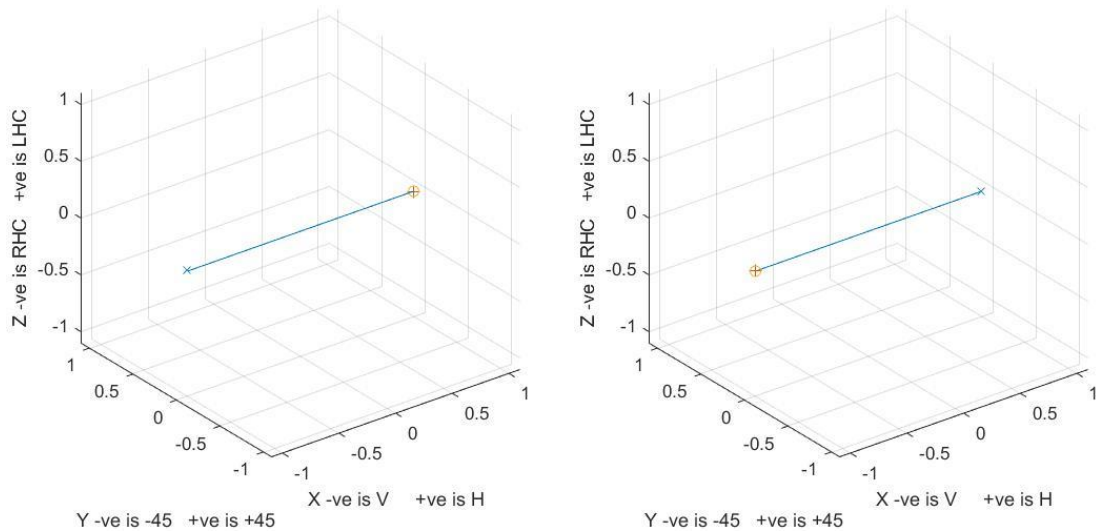


Figure 10-13 simulated responses for Vertical dipole (left), Horizontal dipole (right).

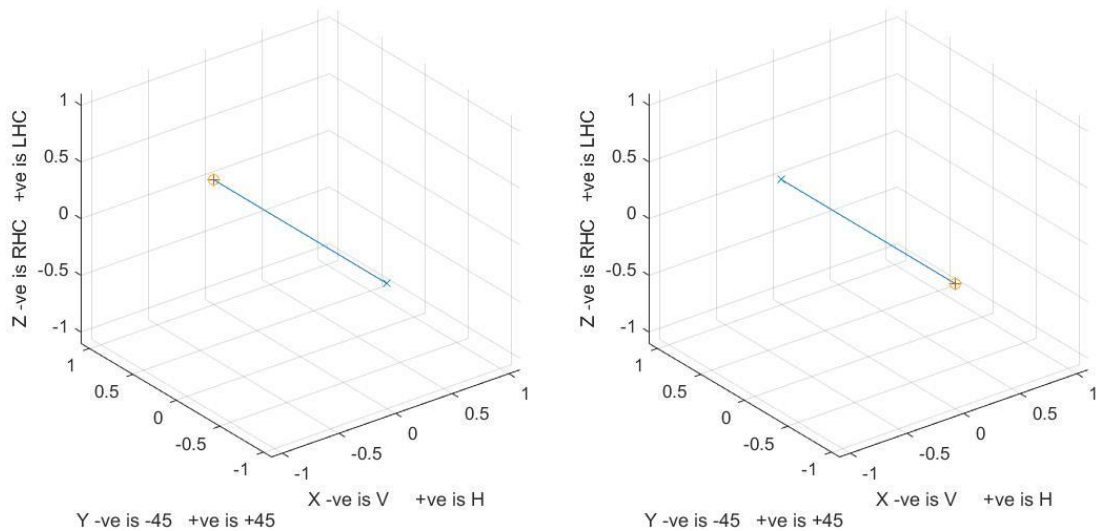


Figure 10-14 simulated Dipole responses at 45° (left), Dipole at -45° (right).

Figure 10-15 shows the Huynen target orientation angle for the dipole with vertical being at 90° (left) and horizontal at 0° (right) calculated using equation 4-22.

The target helicity (Figure 10-16) is around 0° for both horizontal and vertical orientations, indicating minimal helical conversion.

The skip angle (Figure 10-17) shows a variation proportional to frequency, transiting between $\pm 45^\circ$. A regular change with frequency suggests a path length effect might be responsible for this behaviour. This target is a composite target formed of multiple thin wires to increase the radar cross-section. However, reflection is taking place between the individual wires. For a single wire dipole, this angle would be 0°. Note the difference between plots in this figure between vertical and horizontal

orientation. Assuming the variation with angle arises from the array's path length, then equation 10-1 could be used to predict the distance (d) that would give rise to this effect. As the periodicity in the skip angle plots is around 308 MHz, equation 10-1 shows the distance (d) of 0.5 meters assuming the refractive index (n) to be unity suggesting part of the wave travels into the array and then back out.

The fork angle Figure 10-18, for the ideal single wire dipole, would be 0° . However, for this composite target, its values are distributed between 0° and 20° forming the cone-shaped distribution of co-polar nulls around the co-polar sub maximum (co-polar null) Figure 10-12.

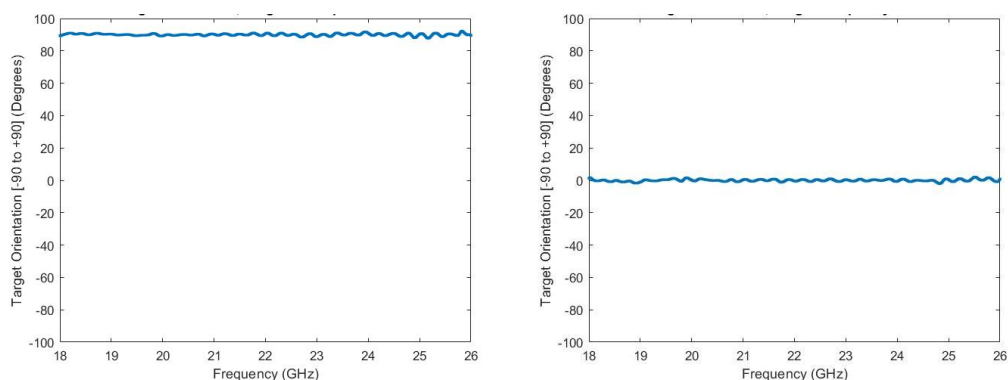


Figure 10-15 Measured orientation angle vertical left, horizontal right

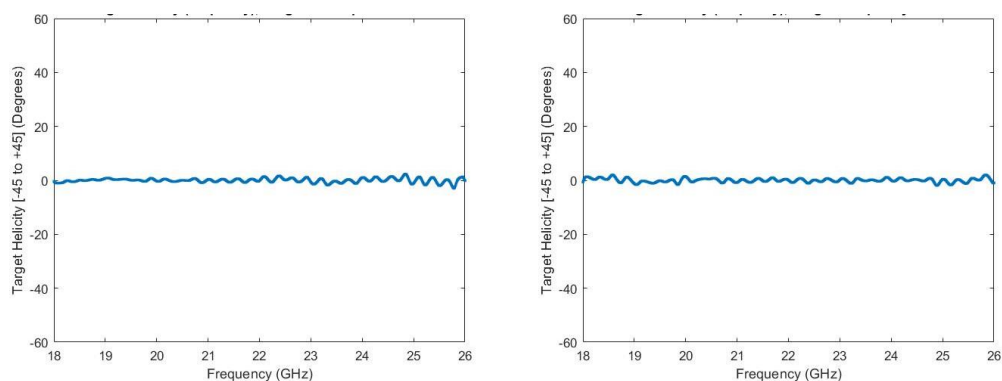


Figure 10-16 Measured helicity vertical left, horizontal right

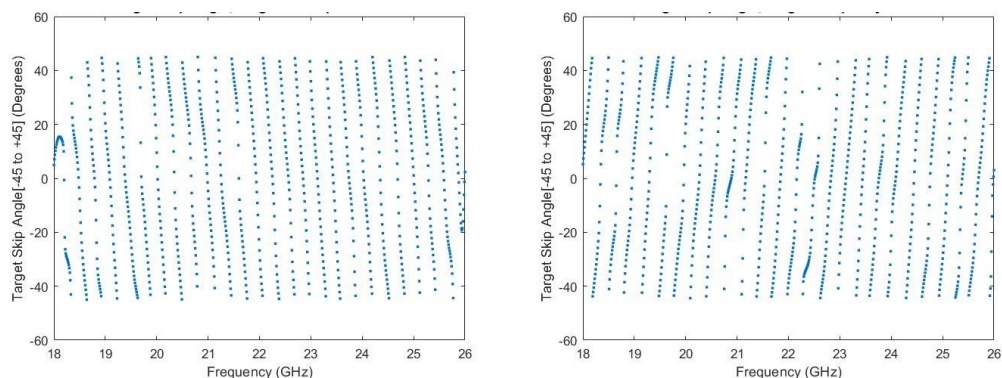


Figure 10-17 Measured skip angle vertical left, horizontal right

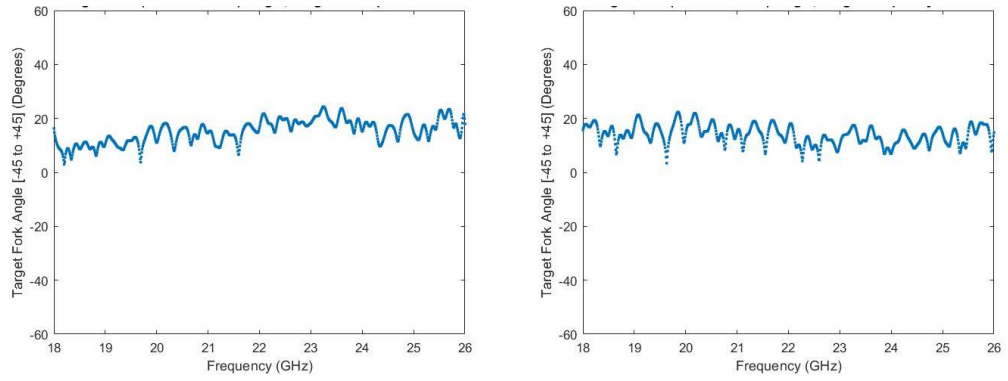


Figure 10-18 Measured fork angle vertical left, horizontal right

10.2.4 Metal sphere

Figure 10-19 shows a 10.5cm diameter stainless steel sphere (left) and its associated fork plot (right). The response is the same as that of the flat plate.

The orientation angle (Figure 10-20 left) is indeterminate as the sphere has no defined orientation. The helicity angle (Figure 10-20 right) is at around 0° indicating minimal helical conversion is taking place.

The skip angle (Figure 10-21 left) is at around 0° , indicating that only a single (odd) bounce reflection occurs. The fork angle (Figure 10-21 right) is at approximately 45° as theory dictates.

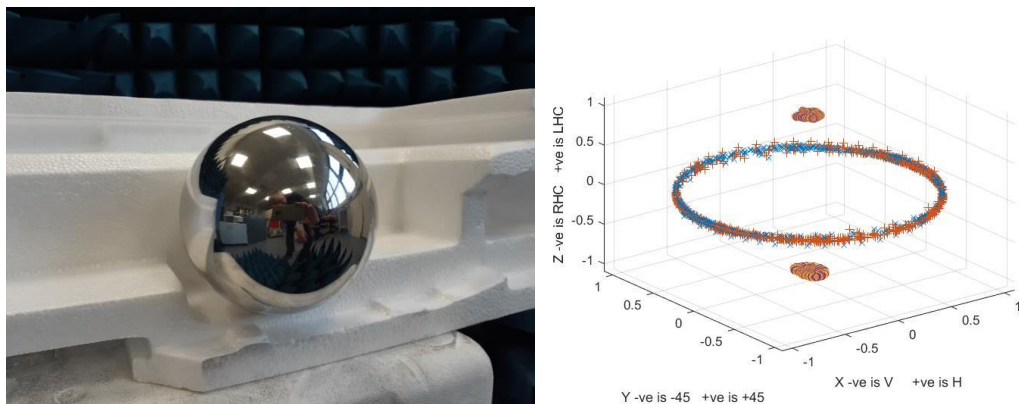


Figure 10-19 10.5 cm diameter sphere (left), Measured Huynen fork plot (right)

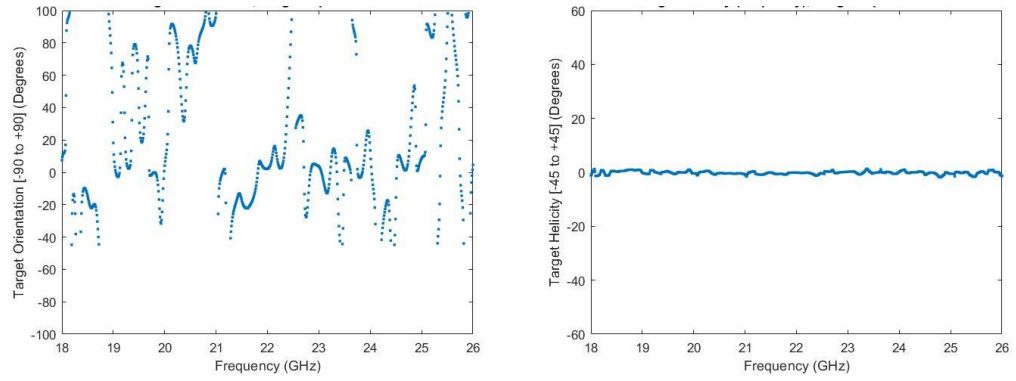


Figure 10-20 Measured orientation angle (left), Helicity angle (right)

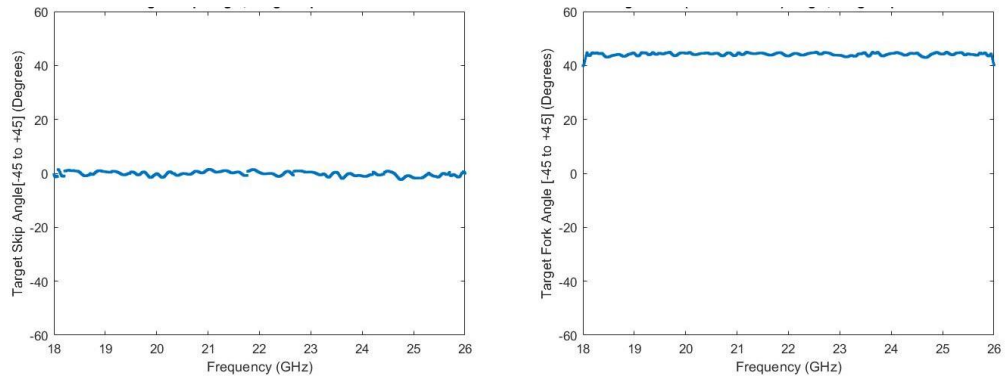


Figure 10-21 Measured skip angle (left), Fork angle (right)

10.2.5 Waveplate with integral reflector

Figure 10-22 presents a waveplate with integral reflector along with its associated fork plots. The waveplate retards one linear component of the polarisation (known as the slow axis) to its orthogonal component (known as the fast axis).

From the fork plots presented in Figure 10-22, the fork response is similar to that of the flat plate or sphere. However, the response is skewed with the co polar nulls offset from the zenith and nadir axis and the cross-polar nulls circumventing the Poincaré sphere in such a way as to indicate that helical conversion is taking place. The helicity angle presented in Figure 10-23 agrees with this.

The skip angle Figure 10-24 indicates the angle is positive increasing as a function of frequency for the horizontal plot and negative becoming more negative as a function of frequency for the vertical orientation due to the separation between the plate and the array of wires.

The fork angle (Figure 10-25) remains relatively constant at 45° across the band the same as the plate and sphere.

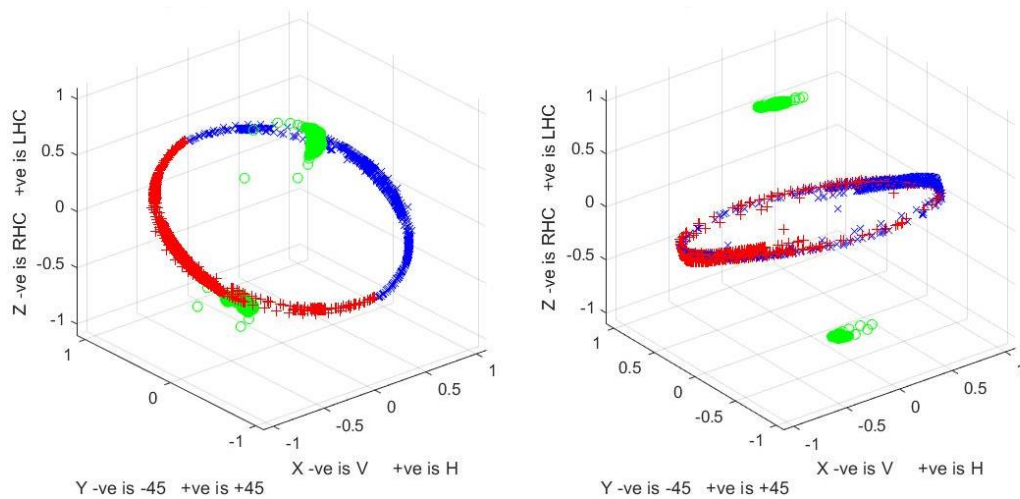
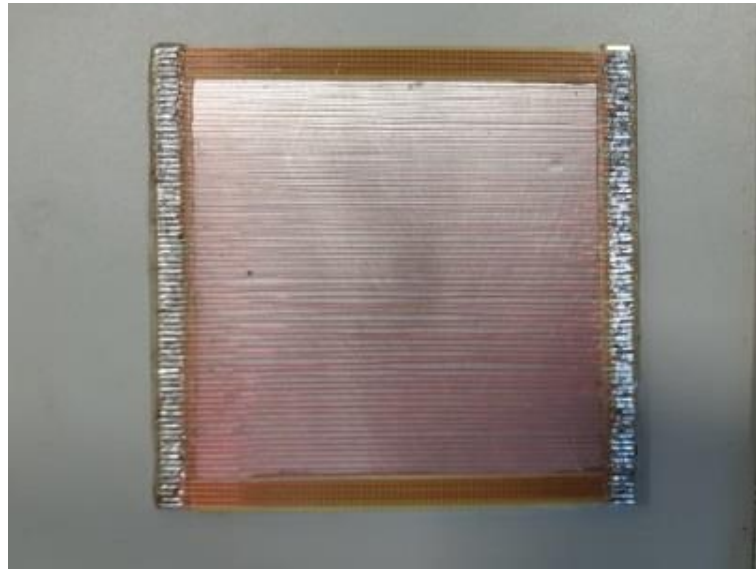


Figure 10-22 Wave plate with integral reflector, wires horizontal (top), Measured responses, wires horizontal (bottom left), vertical (bottom right).

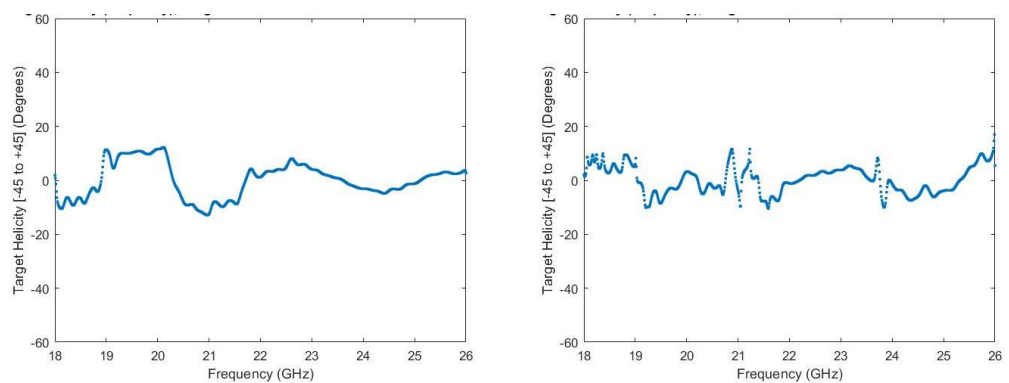


Figure 10-23 Measured helicity angle horizontal left, vertical right

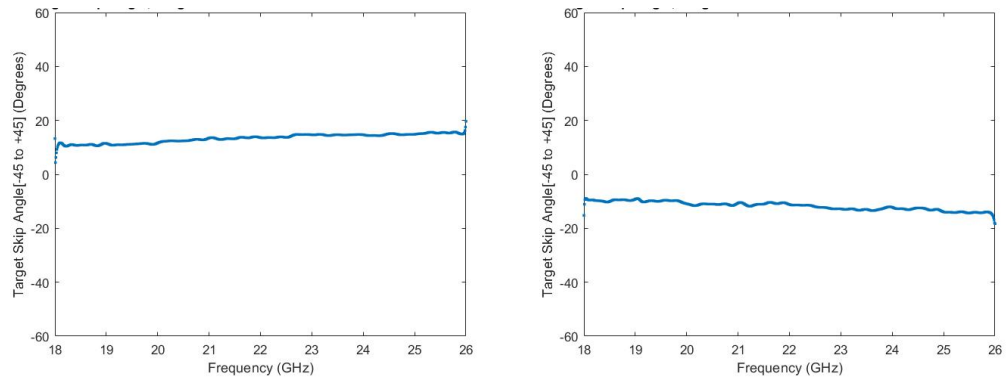


Figure 10-24 Measured skip angle horizontal left, vertical right

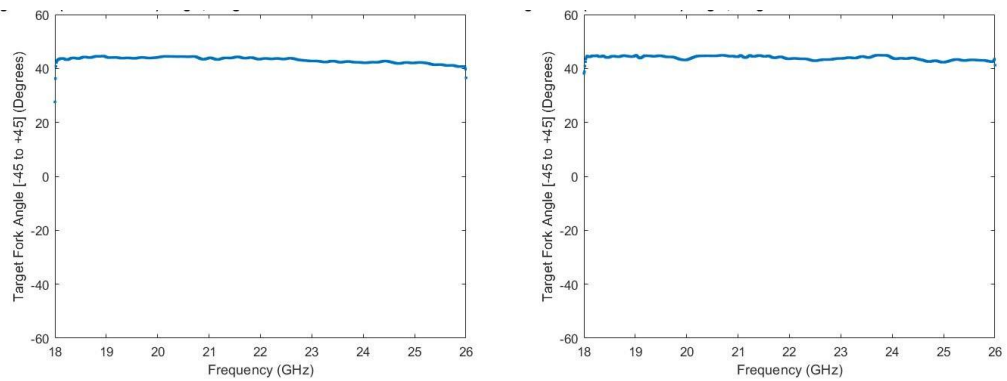


Figure 10-25 Measured fork angle horizontal left, vertical right

10.2.6 Wax block

Figure 10-26 shows two blocks made of beeswax, the left is 2 cm thick whilst the right is 3.8-cm. Beeswax is a useful material that has similar microwave properties to explosives used in PBIED's. The measured Huynen fork plot for the 3.8 cm thick wax block is shown in Figure 10-27. The measured fork response is identical to that for the flat plate previously shown; however, the Huynen polarisation parameters contain further information about the target as shown next.



Figure 10-26 2 cm thick wax block pictured left, 3.8 cm right.

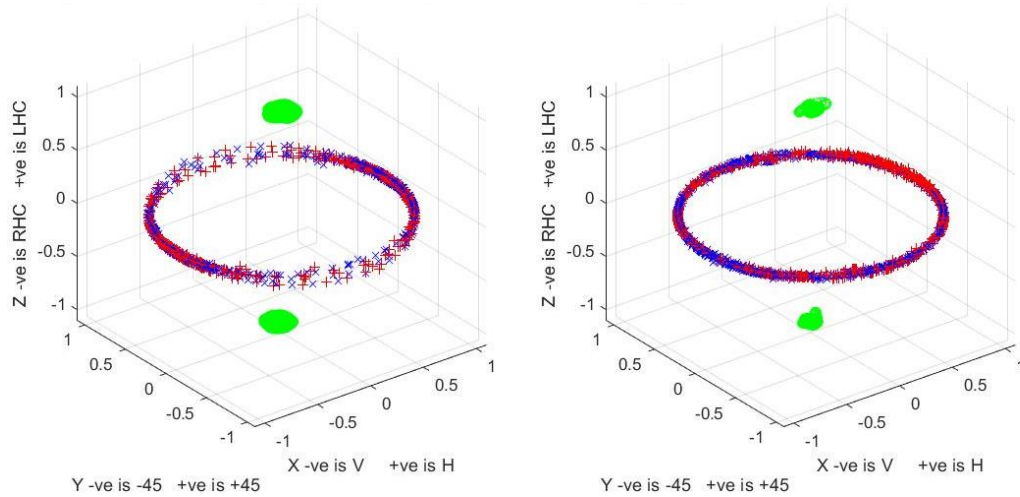


Figure 10-27 Huynen fork plots from the measurement of a 2cm thick wax block left, 3.8 cm right.

The Huynen target size for both wax blocks (Figure 10-28 and Figure 10-29) show a succession of peaks and troughs. The period for the 2-cm wax block is 6 GHz whilst for the 3.8-cm block is 2.56 GHz.

This frequency known as the fringe frequency Δf results from waves adding and subtracting due to reflection off the blocks front face combined with a delayed reflection from the blocks back face producing a phase shift imparted by the velocity delay caused by the dielectric properties of the block.

Equation 10-1 [108] enables calculation of the fringe frequency, given the dielectric thickness, the refractive index and c is the speed of light. Assuming the block thickness to be unknown as in a PBIED, simple transposition enables the determination of the dielectric thickness d , knowing the refractive index and measured fringe frequency. Assuming the dielectric constant for beeswax to be 1.47, and the measured fringe frequency for the thicker wax block to be 2.56 GHz then the dielectric thickness by calculation is 3.8cm which the block is in this case.

$$\Delta f = \frac{c}{2.d.n} \quad (10-1)$$

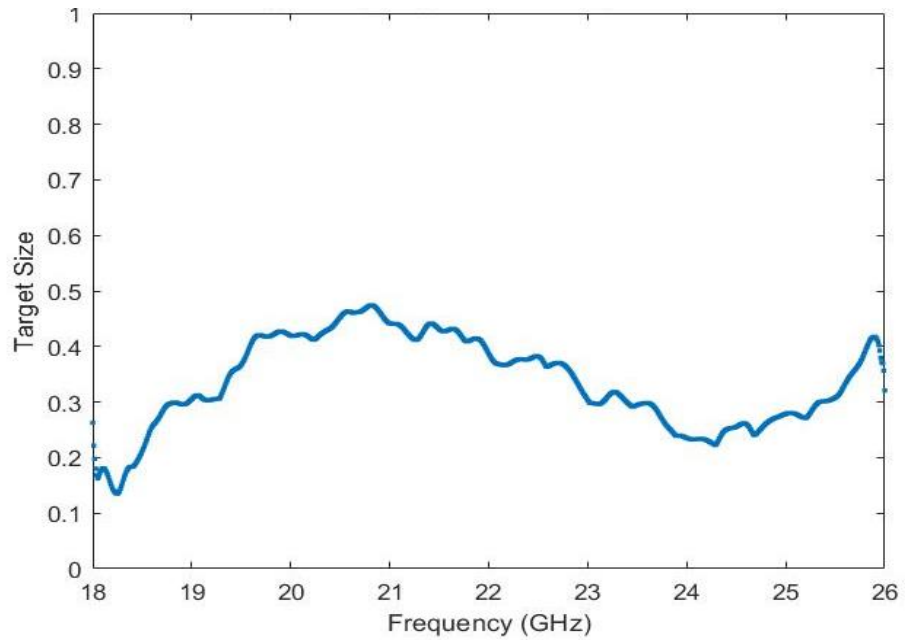


Figure 10-28 Measured Huynen target size (m) (cavity fringes) 2cm thick wax block, $n=1.47$

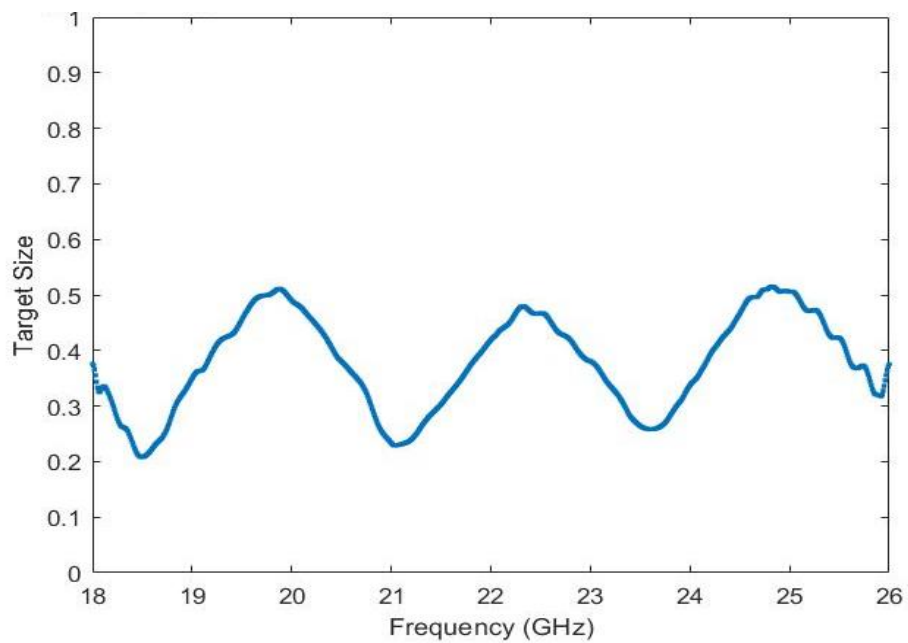


Figure 10-29 Measured Huynen target size (m) (cavity fringes) Wax block 3.8cm thick, $n=1.47$

For both blocks, the orientation angle (Figure 10-30), the helicity angle (Figure 10-31), the skip angle (Figure 10-32) and the fork angle (Figure 10-33) are the same as for the sphere and flat plate.

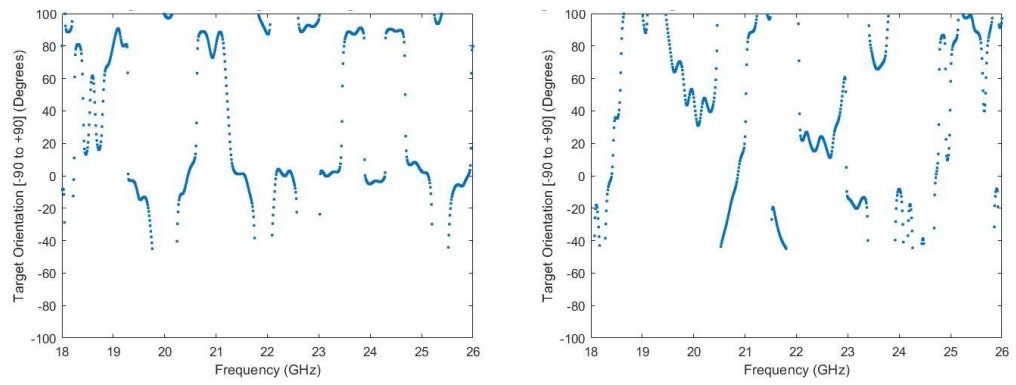


Figure 10-30 Measured orientation angle 2cm wax block left, 3.8cm right

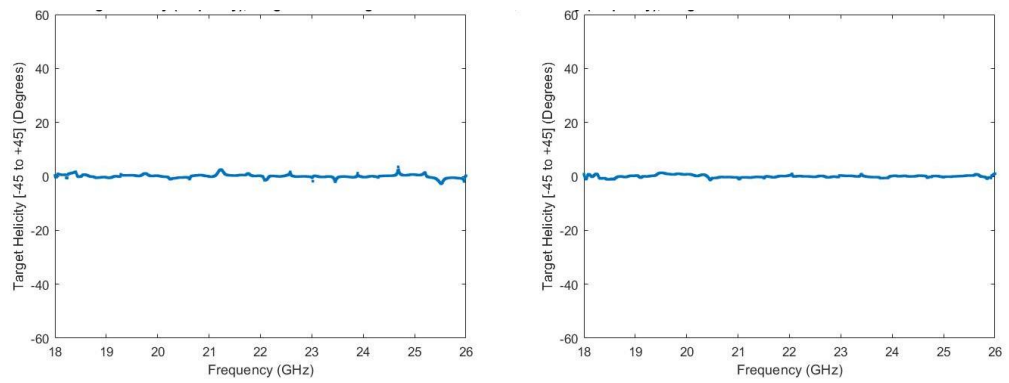


Figure 10-31 Measured helicity angle 2cm wax block left, 3.8cm right

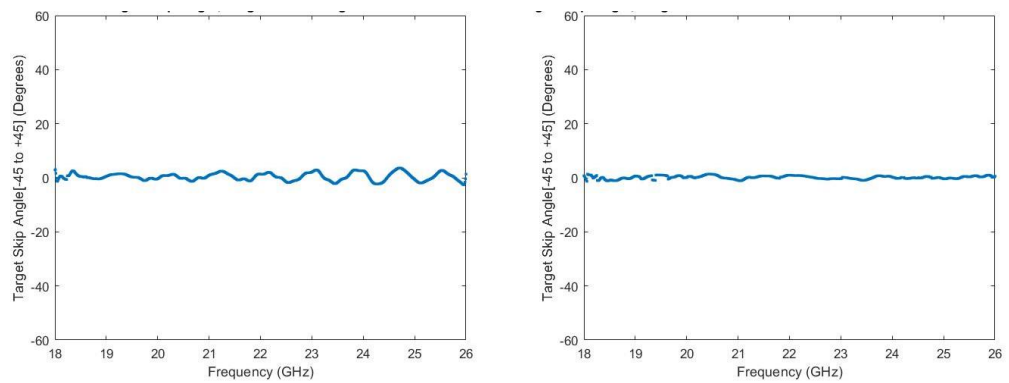


Figure 10-32 Measured skip angle 2cm wax block left, 3.8cm right

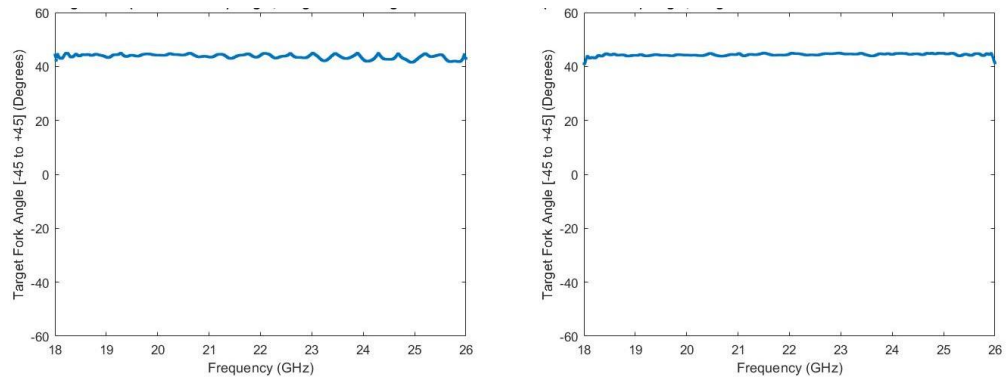


Figure 10-33 Measured fork angle 2cm wax block left, 3.8cm right

10.3 Conclusion

In this chapter, the measured responses of several simple canonical radar targets have been presented. The flat plate, dihedral reflector at 45° and vertical and horizontal dipoles all show agreement with the theoretical responses shown in Figure 10-1 [69], [109] and via simulation. The dipole's measured response in these orientations shows a distribution of the co-polar nulls forming a cone around the X2 cross-polar null (the handle of the fork) due to target imperfections. The array of thin wires used in the dipole interact with one another leading to a non-ideal response.

The delay caused by the waveplates fast and slow axes converts linear polarisation into helical upon reflection.

The Huynen polarisation parameter of target size enables the determination of dielectric thickness as in a PBIED. In total, seven pieces of target information are available for each spectral increment the radar measures.

Chapter 11 Characterisation of the effects of depolarisation

11.1 Introduction

De-polarisation is a change in the measured Sinclair parameters of a target caused by the target and or platform relative motion, or interaction with the environment involving secondary reflections. It may be related to speckle, and the changes may take place faster or slower than the system can measure.

Most radar scattering occurs when either the target, radar or both have some degree of motion. Motion can cause coherent illumination from the radar to have an uncontrolled phase shift when backscattered from the target, leading to incoherence in the scattering matrices. This effect is particularly prevalent in remote sensing where target motion and position can be continually varying.

The process is stochastic. In the lab-based scenario and with static targets detailed in this thesis depolarisation did not manifest itself, it only occurred when target motion was present.

For the monostatic radar presented in this thesis, the coherency matrix was implemented. The coherency matrix performs time averaging which, has the effect of removing speckle effects from the data. The coherency matrix makes an average of conjugate cross-products for the off diagonals and the self-conjugate on the diagonals. Doing so removes data that is not similar between sweeps and retains data of a similar nature. In looking at the individual Sinclair parameters from trace to trace, from say a person, you will see a large variation, which is the speckle. The target will remain pretty much the same. These differences are averaged out by the coherency matrix, as they are different from trace to trace. However, the signal from the target will remain unchanged.

With a perfectly stationary target, it may be possible to average the Sinclair parameters to remove noise. However, if the target moves and you try to average the Sinclair parameters, you will remove your target signal. However, when averaging the coherency matrix, this does not happen. Any similarities in the cross-products are retained whilst removing any that change and that are not correlated.

The mathematics presented in this chapter enable a coherent decomposition method to be used in the presence of depolarisation. The covariance and coherency matrices relate to spatial power received from a target and provide a method to recover the polarimetric target scattering information when depolarisation is present. These matrices are composed of an average of many measurements of the Sinclair matrix indicated by $\langle \dots \rangle$.

The following equations are taken from the 'Basics of SAR Polarimetry' [53].

11.2 Bistatic case

For the bistatic case, the Sinclair matrices can be converted into the lexicographic and Pauli covariance matrices. These 4 x 4 matrices the lexicographic form visible in equation 11-3 contain 16 elements where the $\langle \dots \rangle$ indicate averages of many values. Elements of the covariance matrices can be derived via application of the Lexi and Pauli feature vectors (equations 11-1 and 11-2) followed by a Kronecker multiplication of the feature vector with its conjugate transpose as can be seen in equations 11-3 and 11-4. Conversion of the Sinclair matrix to the Covariance matrix via the Lexicographic and Pauli feature vectors:

11.2.1 Lexicographic feature vector (f_{4L})

The Lexicographic feature vector obtained by a Lexicographic expansion of [S] (Page 1-32, equation 3.37 [53]);

$$f_{4L} = [S_{HH} \ S_{HV} \ S_{VH} \ S_{VV}]^T \quad (11-1)$$

11.2.2 Polarimetric correlation phase preserving Pauli feature vector (f_{4P})

(Page 1-32, equation 3.39 [53])

$$f_{4P} = \frac{1}{\sqrt{2}} [(S_{HH} + S_{VV}) \ (S_{VV} - S_{HH}) \ (S_{HV} + S_{VH}) \ j(S_{HV} - S_{VH})]^T \quad (11-2)$$

11.2.3 The lexicographic covariance (C_{4L}) matrix

(Page 1-34, equations 3.48 and 3.49 [53])

$$[C_{4L}] = \langle f_{4L} \cdot f_{4L}^\dagger \rangle \quad (11-3)$$

$$[C_{4L}] = \begin{bmatrix} \langle |S_{HH}|^2 \rangle & \langle S_{HH} S_{HV}^* \rangle & \langle S_{HH} S_{VH}^* \rangle & \langle S_{HH} S_{VV}^* \rangle \\ \langle S_{HV} S_{HH}^* \rangle & \langle |S_{HV}|^2 \rangle & \langle S_{HV} S_{VH}^* \rangle & \langle S_{HV} S_{VV}^* \rangle \\ \langle S_{VH} S_{HH}^* \rangle & \langle S_{VH} S_{HV}^* \rangle & \langle |S_{VH}|^2 \rangle & \langle S_{VH} S_{VV}^* \rangle \\ \langle S_{VV} S_{HH}^* \rangle & \langle S_{VV} S_{HV}^* \rangle & \langle S_{VV} S_{VH}^* \rangle & \langle |S_{VV}|^2 \rangle \end{bmatrix} \quad (11-4)$$

11.2.4 The Pauli covariance (C_{4P}) matrix

(Page 1-34, equation 3.50, [53])

$$[C_{4P}] = \langle f_{4P} \cdot f_{4P}^\dagger \rangle \quad (11-5)$$

11.3 Monostatic reciprocal case

In the monostatic case $S_{HV}=S_{VH}$ enabling the four-dimensional f_4 feature vectors to be reduced to the three-dimensional f_3 feature vectors leading to the covariance and coherency matrices which completely describe the reciprocal scatterer;

11.3.1 Lexicographic feature vector (f_{3L})

(Page 1-35, equation 3.53, [53])

$$f_{3L} = [S_{HH} \quad \sqrt{2S_{HV}} \quad S_{VV}]^T \quad (11-6)$$

11.3.2 The Pauli feature vector (f_{3P})

The Pauli feature vector obtained from the Pauli spin matrix set (Page 1-35, equation 3.55 [53]):

$$f_{3P} = \frac{1}{\sqrt{2}} [(S_{HH} + S_{VV}) \quad (S_{HH} - S_{VV}) \quad 2S_{HV}]^T \quad (11-7)$$

11.3.3 The Lexicographic coherency (C_{3L}) matrix

(Page 1-36, equation 3.61, [53])

$$[C_{3L}] = \langle f_{3L} \cdot f_{3L}^\dagger \rangle = \begin{bmatrix} \langle |S_{HH}|^2 \rangle & \sqrt{2}\langle S_{HH} S_{HV}^* \rangle & \langle S_{HH} S_{VV}^* \rangle \\ \sqrt{2}\langle S_{HV} S_{HH}^* \rangle & 2\langle |S_{HV}|^2 \rangle & \sqrt{2}\langle S_{HV} S_{VV}^* \rangle \\ \langle S_{VV} S_{HH}^* \rangle & \sqrt{2}\langle S_{VV} S_{HV}^* \rangle & \langle |S_{VV}|^2 \rangle \end{bmatrix} \quad (11-8)$$

11.3.4 The Pauli coherency (C_{3P}) matrix

(Page 1-36, equation 3.62 [53])

$$[C_{3P}] = \langle f_{3P} \cdot f_{3P}^\dagger \rangle \quad (11-9)$$

$$= \frac{1}{2} \begin{bmatrix} \langle |S_{hh} + S_{vv}|^2 \rangle & \langle (S_{hh} + S_{vv})(S_{hh} + S_{vv})^* \rangle & 2\langle (S_{hh} + S_{vv})S_{hv}^* \rangle \\ \langle (S_{hh} - S_{vv})(S_{hh} + S_{vv})^* \rangle & \langle |S_{hh} - S_{vv}|^2 \rangle & 2\langle (S_{hh} - S_{vv})S_{hv}^* \rangle \\ 2\langle S_{hv}(S_{hh} + S_{vv})^* \rangle & 2\langle S_{hv}(S_{hh} + S_{vv})^* \rangle & 4\langle |S_{hv}|^2 \rangle \end{bmatrix} \quad (11-10)$$

11.4 Measurement results

Figure 11-1 shows the Huynen fork response of a dihedral reflector orientated at 45° to the incident beam of the radar moving ± 5.5 cm in the range dimension of the radar, produced via the averaging of 100 Sinclair matrices for each spectral increment. Figure 11-2 shows the same target; this time, the plot is produced via the application of the coherency matrix. It can be seen that the plot produced via the coherency matrix has recovered the target information and is exhibiting a lower distribution of the co and cross-polar nulls than for that using the average Sinclair.

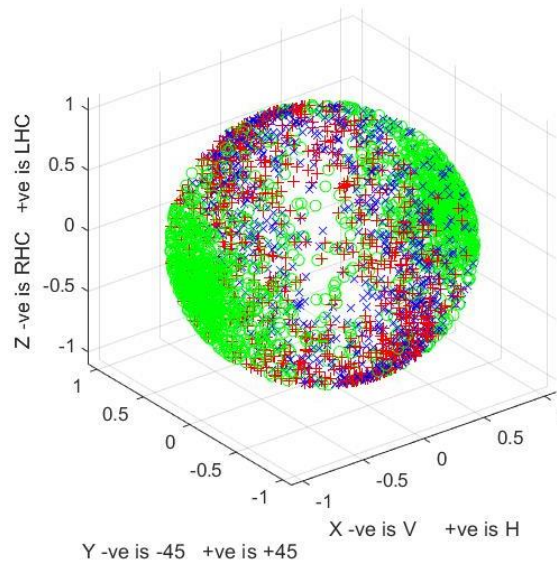


Figure 11-1 Huynen fork plot from the measurement of a moving dihedral reflector via averaged Sinclair

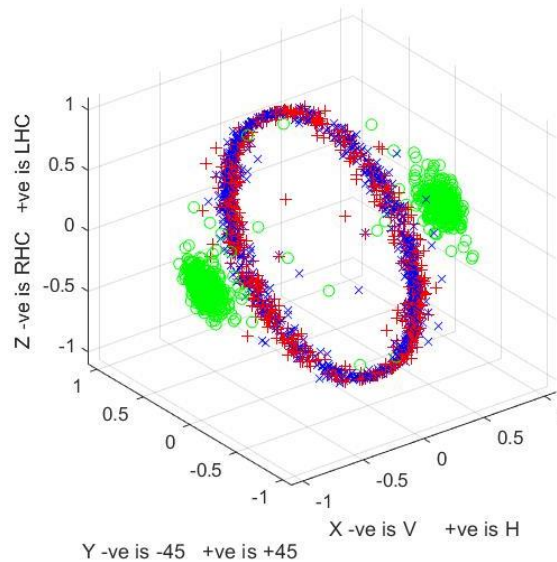


Figure 11-2 Huynen fork plot from the measurement of a moving dihedral reflector via the Coherency matrix

11.5 Conclusion

Depolarisation is a stochastic process produced by target motion relative to the radar or the environment which generates phase and amplitude changes in the Sinclair matrix components.

The phenomenon is most apparent when a target or the radar moves in range because of increased phase change. Cross-range motion causes less change.

The effects of depolarization can be seen by the increased distribution of the co and cross-polar nulls shown on the Huynen polarisation fork plot (Figure 11-1). The application of the coherency matrix approach to the same target data shows a reduction in the distribution of the co and cross-polar nulls as can be seen in Figure 11-2. However, the effects of depolarisation can be reduced via the application of the mathematics presented in this chapter.

Chapter 12 Characterisation of threat and non-dangerous items

12.1 Introduction

In this chapter, the radar signatures of threat and non-dangerous items are investigated to identify characteristics that could be used to recognise target features using the Huynen polarisation fork and associated parameters. Please refer to chapters 4 and 10 for a detailed description of the Huynen polarisation fork technique. The plots show the Huynen polarisation fork on the Poincaré sphere and parameters plotted for each of the 801 spectral increments between 18 to 26 GHz.

The radar signatures of a variety of threat and non-threat targets on their own including the polarimetric response of two knives of different sizes analysed.

The human torso on its own for two individuals is presented, followed by selected targets placed against the torso.

Targets present an aspect dependent signature that is unique to that particular target. Understanding these signatures could enable identification, particularly when targets are placed against the human body.

12.2 Measurement results

The Huynen fork is presented for each target with selected Huynen parameter plots included demonstrating key features of targets. Complete sets of the Huynen target parameters for each target are available in Appendix-B.

Table 12-1 provides details of target dimensions and materials.

Targets measured:

- Metal triangle (symmetric target).
- Small vertical and horizontal knives.
- Long vertical and horizontal knives.
- Long horizontal and 45° orientated knives.
- Small knife at 45° blade spine leading edge compared with blade edge.
- Long vertical and horizontal knives edge-on.
- Brass gun horizontal and at 45° orientations.

- Shrapnel target.
- Human torso perpendicular to the radar beam with hands above head.
- Human torso perpendicular to the beam of the radar with hands at the side.
- Human torso presented side on to the beam of the radar with hands above the head compared to hands at the side.
- Small knife vertical and horizontal on the human torso.
- Long vertical and horizontal knives on the human torso.
- Vertical and horizontal guns on the human torso.
- Shrapnel placed against the human torso.
- Smartphone
- Keys.

Target type	Length (cm)	Width (cm)	Thickness (cm)	Details
Long knife	45	4	0.2	Aluminium strip, no sharp edge.
Small knife	12.5	2	0.5	Plastic blade with an edge, covered with copper tape.
Brass gun				Brass blocks soft soldered to a copper tube barrel.
Shrapnel Target	31.5	12	2.2	Galvanised steel felt nails (2cm long) embedded in a paraffin wax matrix (random orientation).
Human torso	72	42	24	
Mobile phone	15	7	1	Smartphone with aluminium frame.
Keys				Various sized keys joined via 3 metal rings randomly orientated.
Triangle			0.2	Sheet aluminium

Table 12-1 Target details

12.2.1 Symmetric target a metal triangle

Before examining the knife, the response of a flat metal dagger-shaped triangle is presented (Figure 12-1 left). This target represents a symmetric target in that it has roll symmetry and is symmetric at all aspect angles (Huynen's thesis [68] page 65).

Huynen indicates in his thesis that the Sinclair matrix for this target is:

$$S_{sym} = \begin{bmatrix} 2^{2iv} & 0 \\ 0 & \tan^2 \gamma e^{-2iv} \end{bmatrix} \quad (12-1)$$

Where the targets Huynen parameters;

Target orientation angle $\phi_m = 0^\circ$

Target Helicity (ellipticity) angle $\tau_m = 0^\circ$

Target skip angle $\nu = 0^\circ$

The Huynen fork plot for this target can be seen in Figure 12-1 (right) and Figure 12-2 (left and right) viewed from $\phi=90^\circ$ (vertical linear position). The fork plot is the same as that of a flat metal plate or sphere with cross-polar nulls located around the equator on the Poincaré sphere and co polar nulls located at zenith and nadir. No helical conversion is visible in the plots.

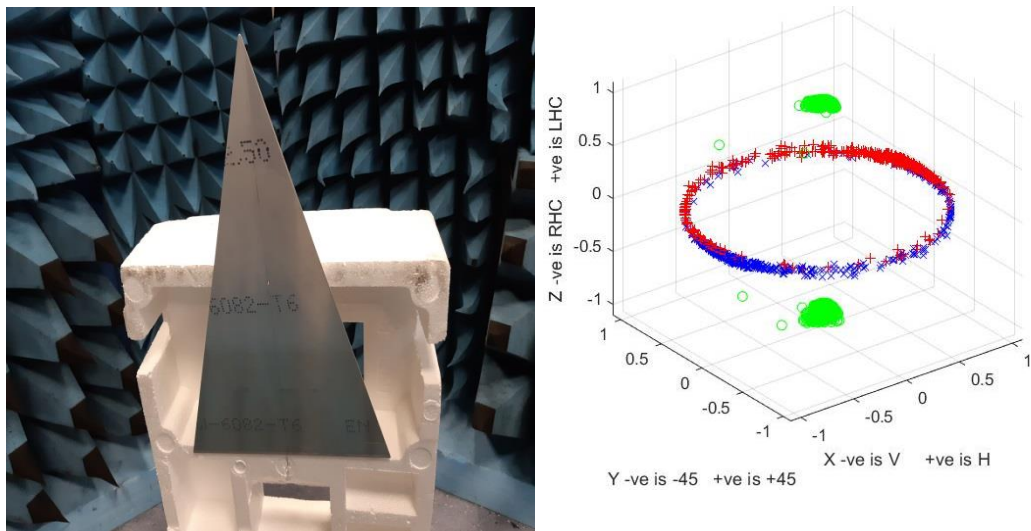


Figure 12-1 Metal triangle left, measured fork plot right

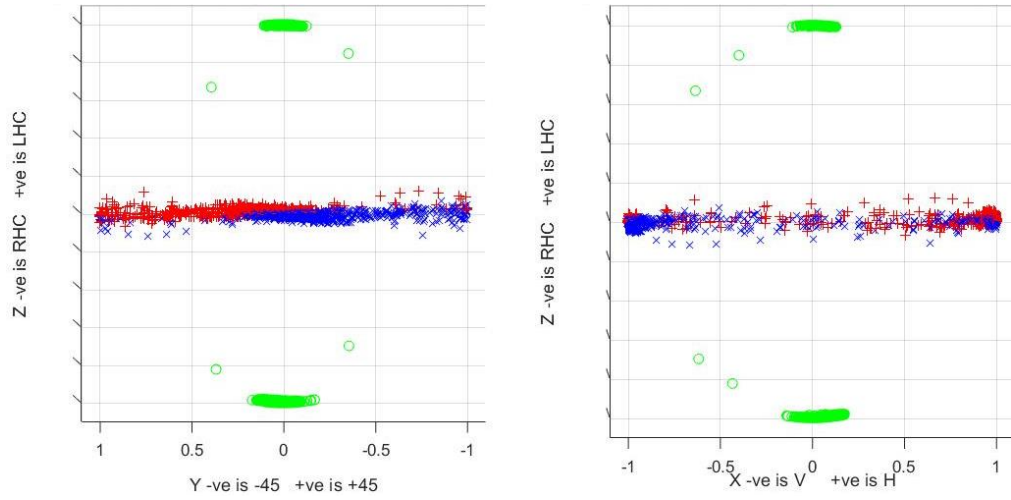


Figure 12-2 Metal triangle fork plots via measurement viewed from the vertical polarisation position left, and from the -45° polarisation position (right)

12.2.2 Knife measurements

The response of a metal triangle a symmetric target produced a response similar to that of a flat metal plate or sphere, however, unlike the triangle the knife is an asymmetric target due to the curved blade edge. The blades curved edge forms a section of a helix.

Huynen in his thesis ([68] page 68) describes the helix as a non-symmetric target where a right-hand helix has Huynen target parameters of;

Target orientation angle $\phi_m = 0^\circ$

Target Helicity (ellipticity) angle $\tau_m = 45^\circ$

Target skip angle ν is arbitrary

Target characteristic (fork) angle $\Upsilon = 0^\circ$

Its Sinclair matrix is given by;

$$S_{RH} = \begin{bmatrix} 1 & -i \\ -i & -1 \end{bmatrix} \quad (12-2)$$

A left-hand helix has target parameters of;

Target orientation angle $\phi_m = 0^\circ$

Target Helicity (ellipticity) angle $\tau_m = -45^\circ$

Target skip angle ν is arbitrary

Target characteristic (fork) angle $\Upsilon = 0^\circ$

Its Sinclair matrix is:

$$S_{RH} = \begin{bmatrix} 1 & i \\ i & -1 \end{bmatrix} \quad (13-3)$$

12.2.3 Small vertical and horizontal knives

The first measurements show a small metallised plastic knife in Figure 12-3 in both vertical and horizontal orientations. The Huynen fork plots (Figure 12-4) show orientation information is available for the horizontal case as indicated by the blue cross-polar null's location on the Poincaré sphere. The vertical case orientation definition is less apparent because the blade's side is almost perfectly perpendicular to the antenna's boresight and not presenting a leading edge to the radar. Orientation angle plots are visible in Figure 12-6. The knife orientated horizontally has its spine (non-sharp edge) offering a leading-edge for this measurement.

Figure 12-5 Huynen fork plot viewed from the $\phi=90^\circ$ (vertical linear position) on the Poincaré sphere indicates a visible increase in helicity for both blade orientations, produced by the curved blade edge. Figure 12-7 presents the resulting helicity angle. The knife a non-symmetric target produces helicity.

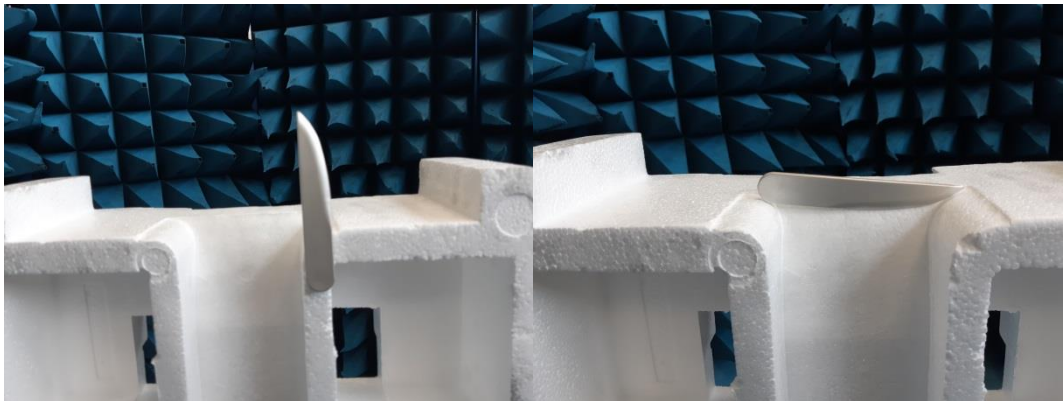


Figure 12-3 Small vertical knife (left), horizontal knife (right).

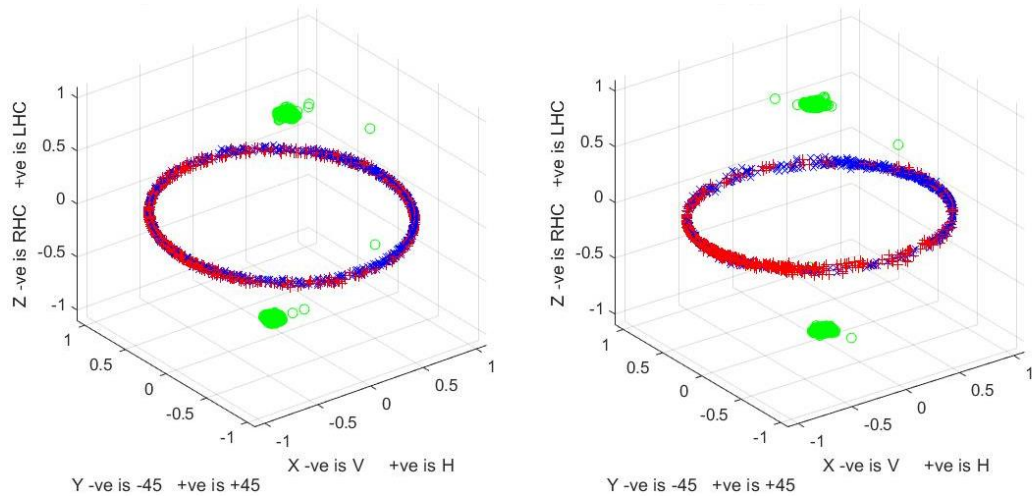


Figure 12-4 Small knife fork plot via measurement, vertical left, horizontal right

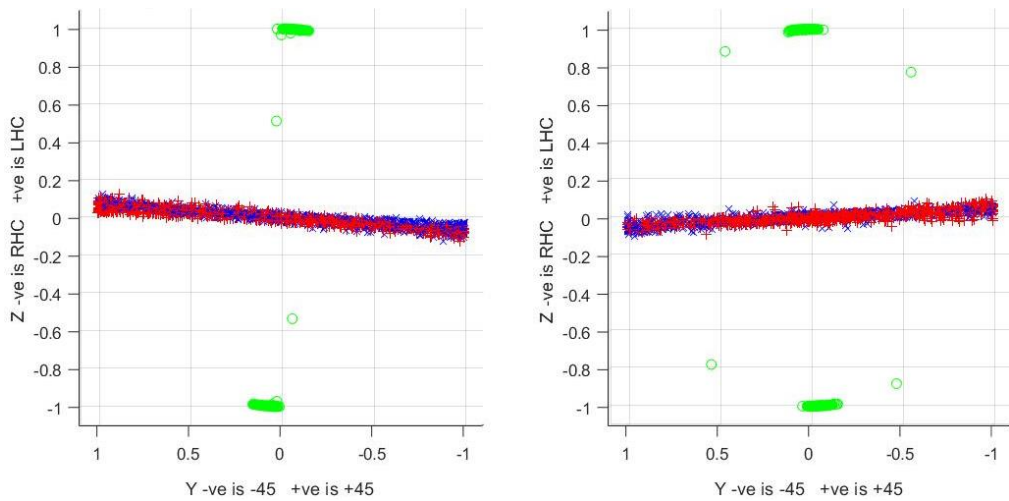


Figure 12-5 Small knife fork plot via measurement side view vertical left, horizontal right

Figure 12-6 presents the Huynen target orientation angle indicating a predominance of vertical orientation (left plot) whilst the right plot shows horizontal. This angle matches the physical orientation of the knife.

Figure 12-7 presents the Huynen helicity (ellipticity) angle. This angle is not zero indicating that the knife in both orientations produces some conversion from linear to helical polarisation upon reflection. The non-symmetrical nature of the target causes this conversion.

The knife is behaving as a combination of single bounce (flat plate) combined with a helical structure caused by the blade's curved edge with orientation information produced when the knife presents a leading edge to the radar's boresight.

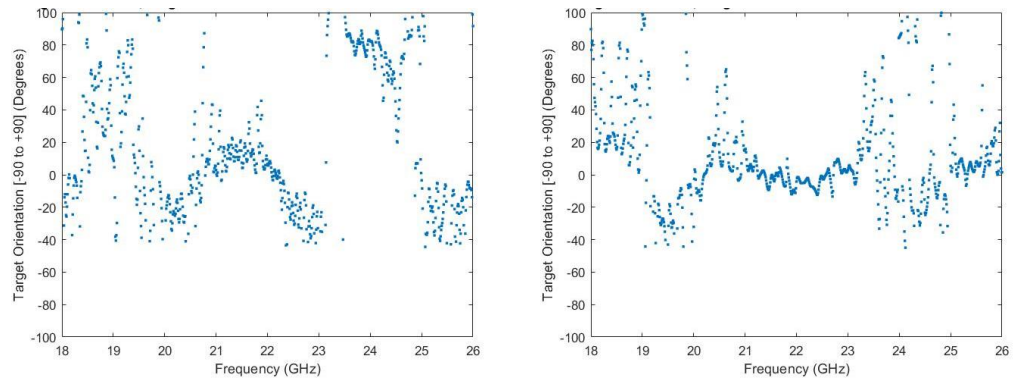


Figure 12-6 Small knife measured orientation angle vertical left, horizontal right

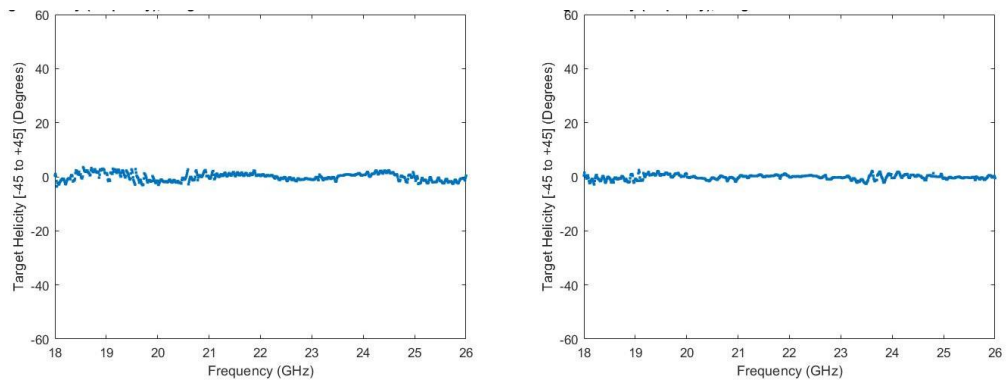


Figure 12-7 Small knife measured helicity angle vertical left, horizontal right

12.2.4 Long vertical and horizontal knives

Figure 12-8 shows a long aluminium knife-shaped target in vertical and horizontal orientations and again with the blade spine presenting a leading edge.

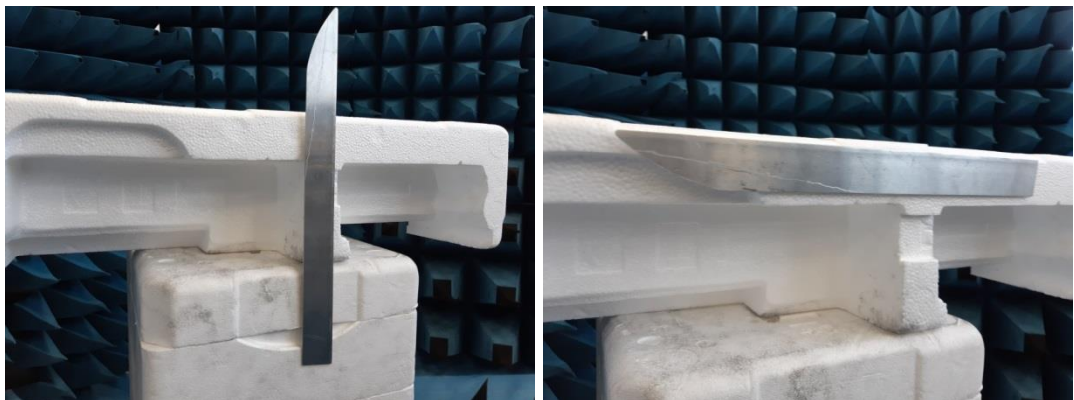


Figure 12-8 Vertical Long Knife left, horizontal right.

Orientation information is available for the horizontal orientation in Figure 12-9 (right) and Figure 12-11 (right). Orientation information is far less evident for the vertical knife due to the blade in this orientation not presenting a leading edge to the radar's

boresight leading to a response similar to that of a flat plate or sphere. However, in Figure 12-10 of the fork plot for each knife orientation, some conversion occurs from linear polarisation to helical upon reflection. The helicity being opposite for vertical and horizontal orientations. Figure 12-12 shows the Huynen orientation angle.

The long knife is behaving similarly to that of the small knife previously shown as a combination of single bounce (flat plate) combined with a helical structure caused by the blade's curved edge with orientation information produced when the knife presents a leading edge to the boresight of the radar.

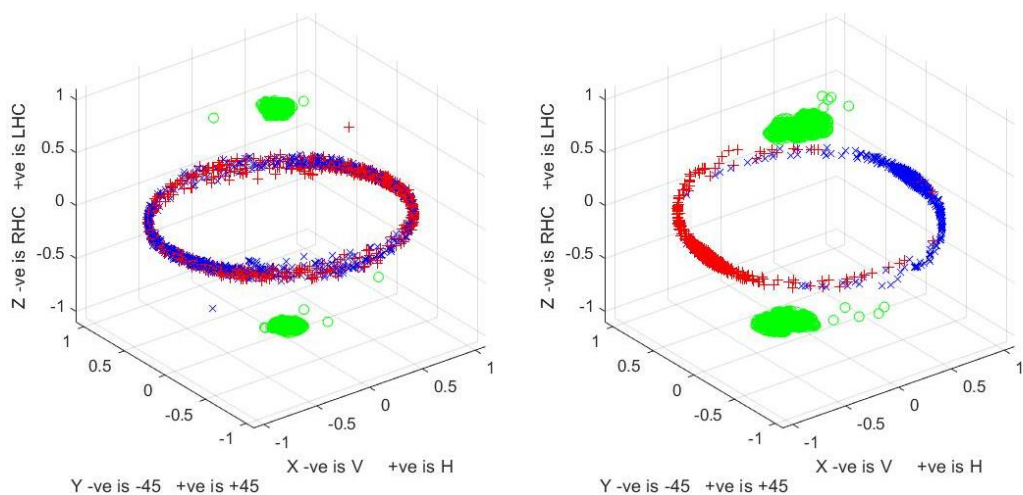


Figure 12-9 Long knife fork plot via measurement vertical left, horizontal right

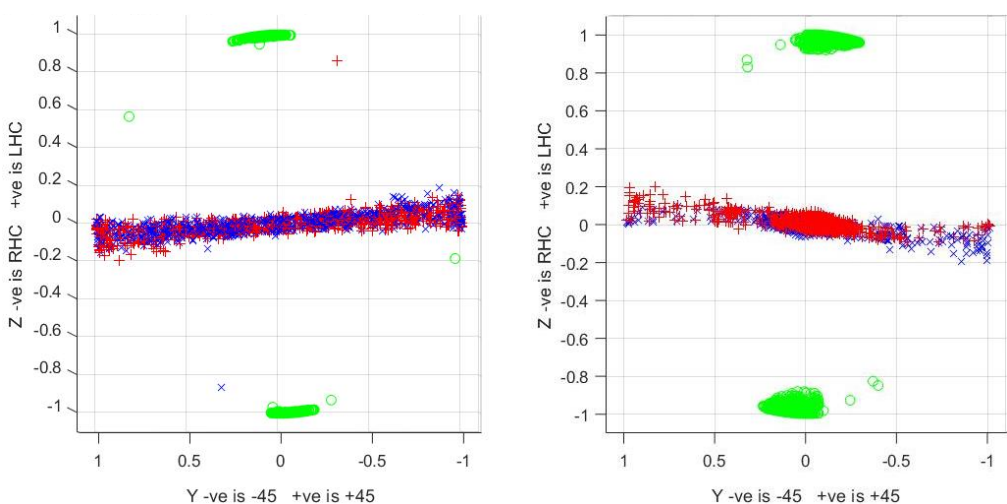


Figure 12-10 Long knife fork plot via measurement vertical left, horizontal right
(Viewed from the vertical polarisation position)

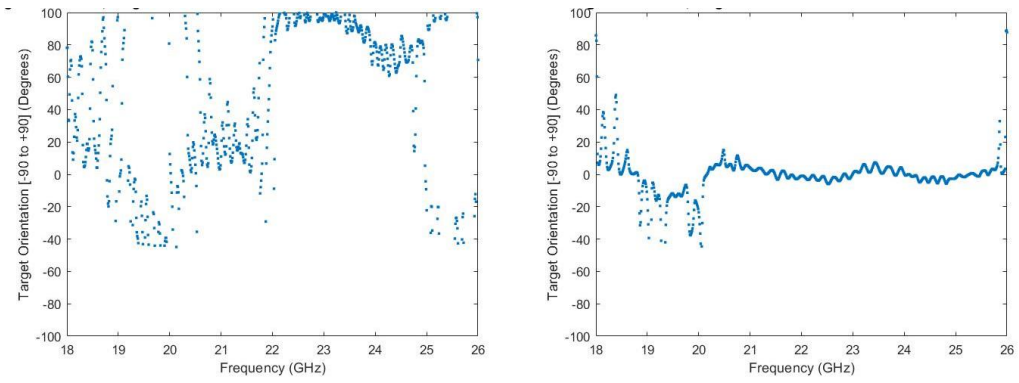


Figure 12-11 Long knife measured orientation angle vertical left, horizontal right

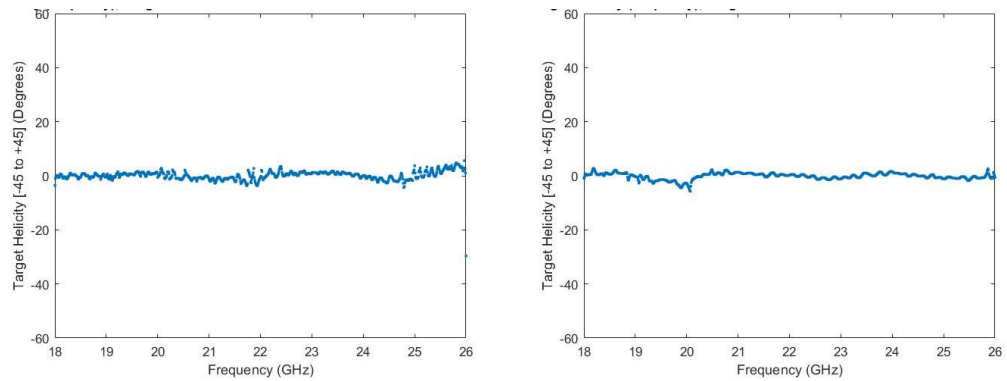


Figure 12-12 Long knife measured helicity angle vertical left, horizontal right

12.2.5 Long horizontal and 45° oriented knives

Figure 12-13 presents the long knife positioned horizontally and at 45°. This time the blades sharp edge is providing the leading edge to the beam of the radar.

The fork plot for both horizontal and vertical alignments shown in Figure 12-14 provides orientation information visible in both plots. Figure 12-15 provides the Huynen orientation angle for both orientations being predominantly 0° for horizontal and at -45° for the knife orientated at 45°.

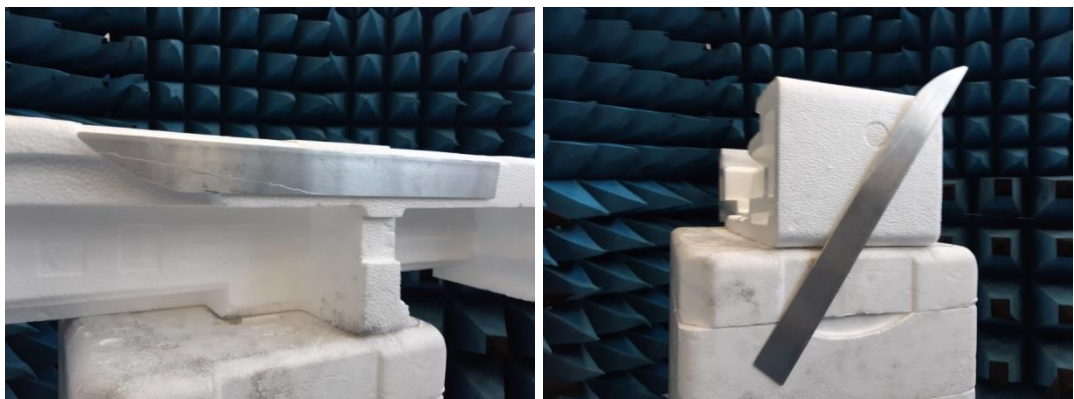


Figure 12-13 Long horizontal knife left, at 45° right

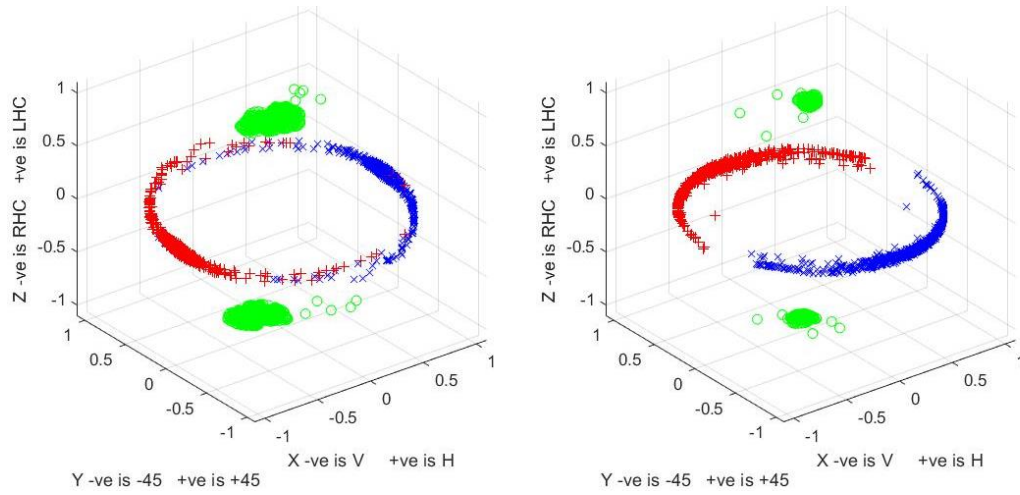


Figure 12-14 Long knife fork plot via measurement horizontal left, 45° right

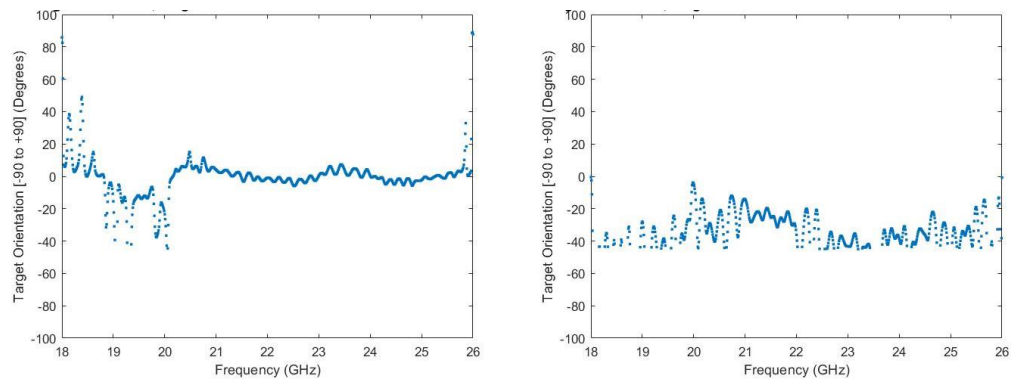


Figure 12-15 Long knife measured orientation angle horizontal left, 45° right

12.2.6 Small knife at 45°, blade spine leading-edge compared with the blade edge

Figure 12-16 shows the small metallised knife at 45° orientation with its associated fork plot visible in Figure 12-17. This measurement compares the blade spine to the blades sharp edge, both facing the radars boresight.

From the fork plot (Figure 12-17), orientation switches direction from +45° for the blade spine leading to -45° for the sharp edge. This effect is due to the orientation of the blades sharp curved edge. The blade edge forming part of a helix where the right-hand RH helix gives an orientation angle (τ_m) of +45°, and a left-hand LH helix gives an orientation angle of -45°. Figure 12-18 shows the orientation angle as a function of frequency.

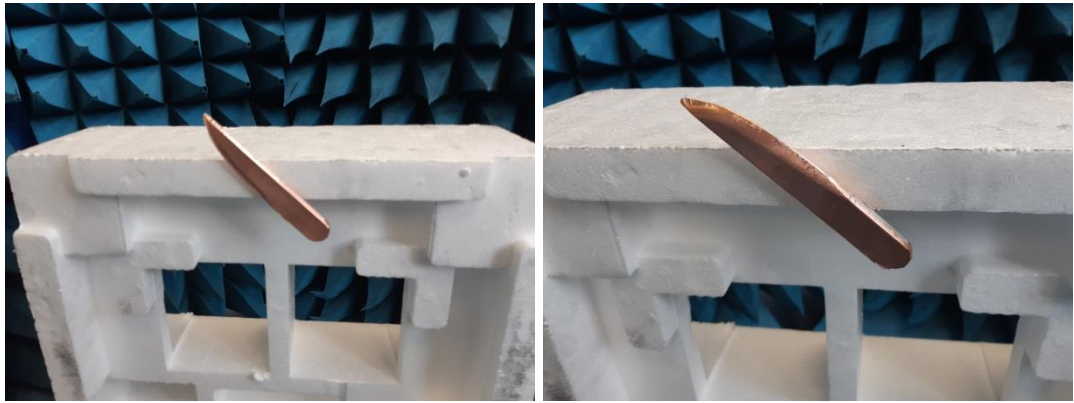


Figure 12-16 small knife at 45° spine leading left, blade edge leading right

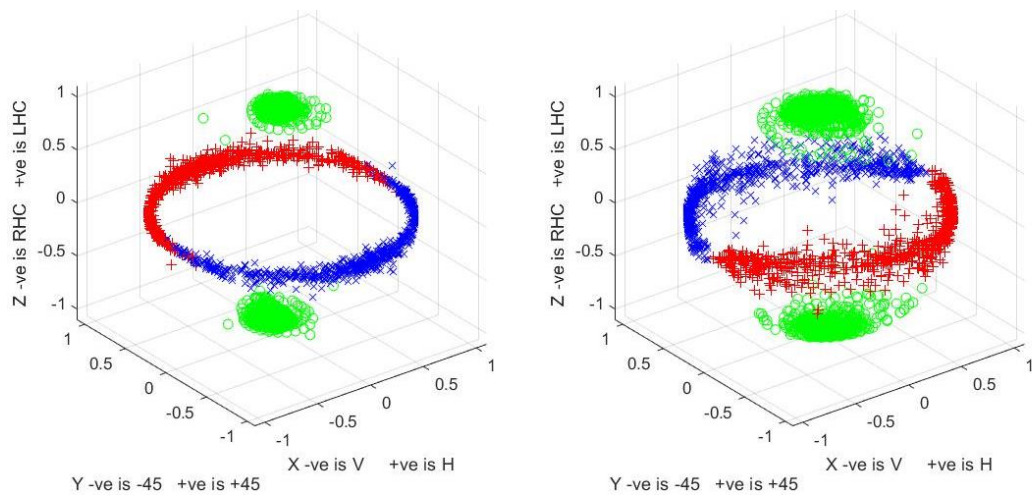


Figure 12-17 Small knife at 45° fork plot via measurement blade spine leading left, sharp edge right

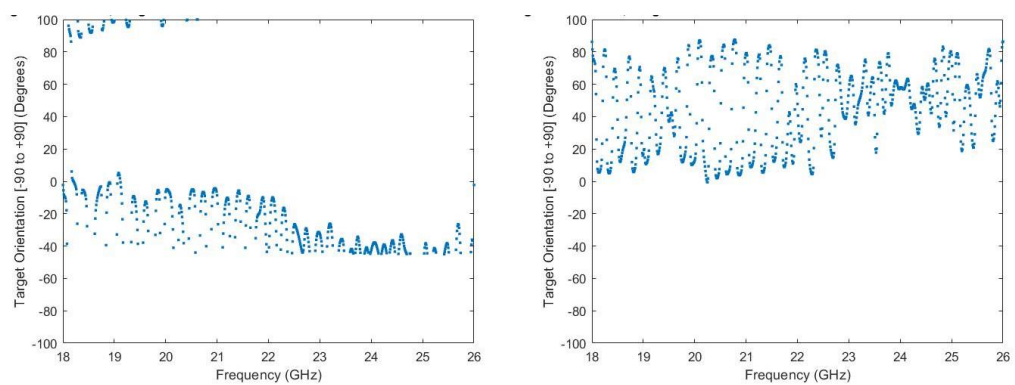


Figure 12-18 Small knife at 45° measured orientation angle blade spine leading left, sharp edge right

12.2.7 Long vertical and horizontal knives edge-on

The long knife positioned edge-on to the radar's boresight in both vertical and horizontal orientations produced the fork plots visible in Figure 12-20. The knife response is similar to that of the dipole presented in chapter 10. The blue cross-polar nulls indicate the orientation. The green co-polar nulls clustering around the red cross-polar nulls (co-polar sub maximum points) as in the dipole presented earlier.

Figure 12-20 presents a side view of the Poincaré sphere viewed from $\phi=0^\circ$ (vertical linear position) and clearly shows the helicity caused by the curved blade edge visible as the blue and red diagonal distribution cross-polar nulls. The green co-polar nulls have also moved away from the zenith and nadir. Figure 12-22 also shows an increase in helicity.

Figure 12-21 presents the knife's orientation angle with a vertical orientation in the left plot at around 90° and horizontal (right plot) at about 0° .

Figure 12-23 presents the targets skip angle. This Huynen target parameter represents the number of reflections taking place. It might be expected to be zero; however, the plot shows a skip angle similar to that for a dihedral target.

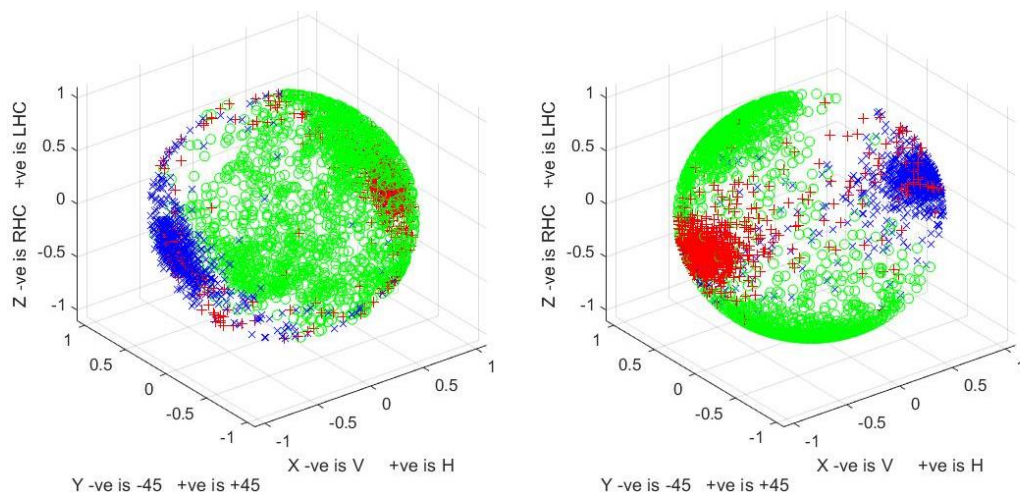


Figure 12-19 Huynen fork plot via measurement for a long knife edge-on vertical left, horizontal right

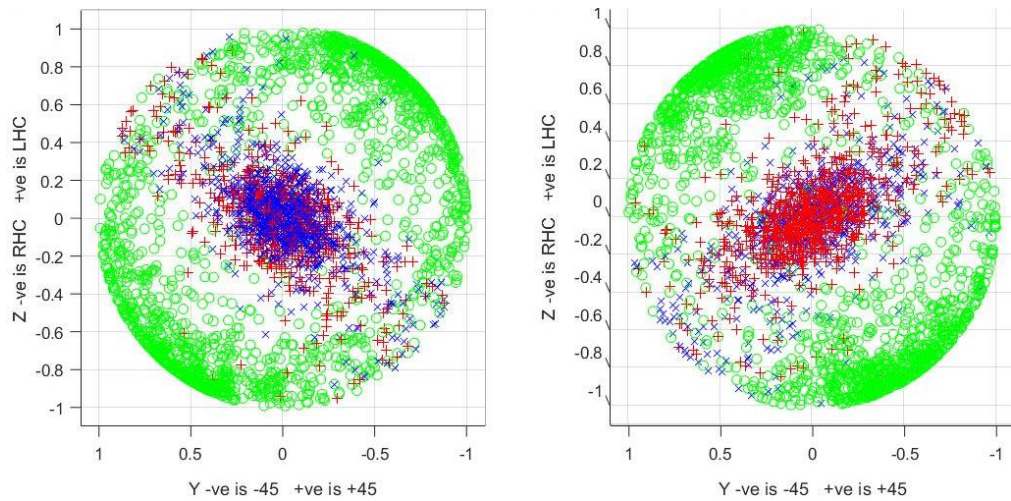


Figure 12-20 Huynen fork plot via measurement for a long knife edge-on vertical
left, horizontal right

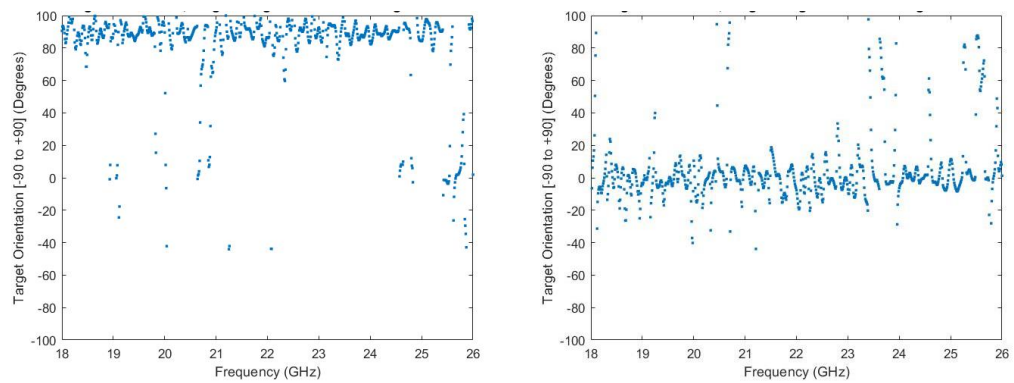


Figure 12-21 Measured orientation angle for a long knife edge-on vertical left,
horizontal right

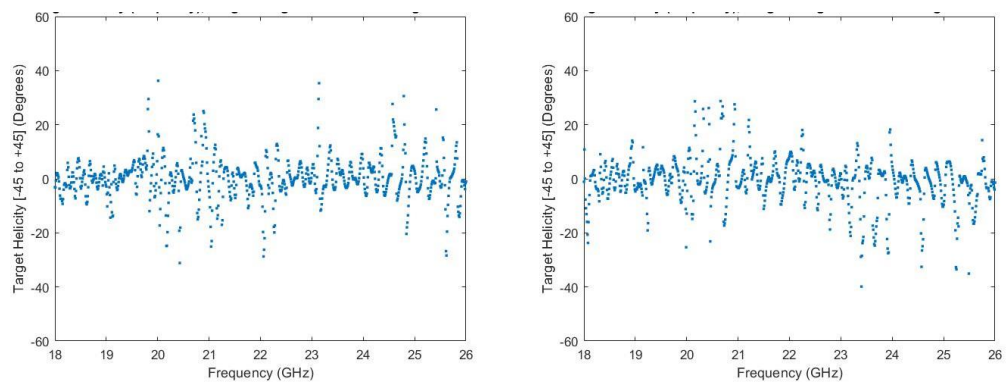


Figure 12-22 Measured helicity angle for a long knife edge-on vertical left,
horizontal right

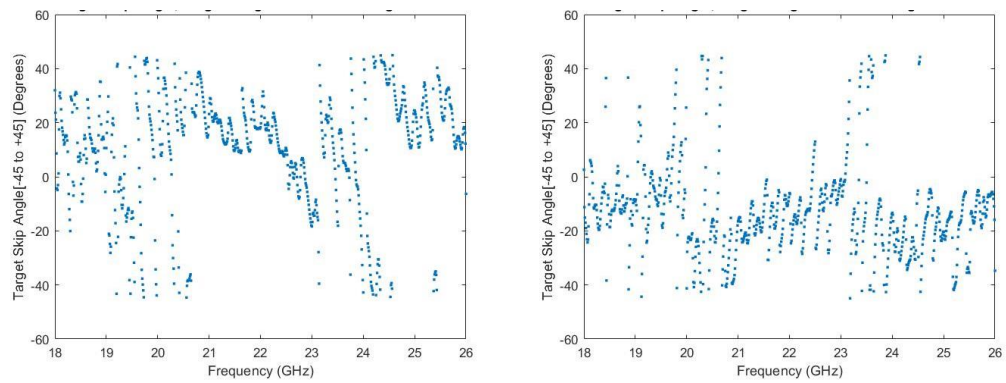


Figure 12-23 Measured skip angle for a long knife edge-on vertical left, horizontal right

12.2.8 Brass gun

Figure 12-24 shows a gun-shaped object manufactured from brass blocks and a copper tube for the barrel joined with soft solder. The structure, although basic, has a geometry similar to that of a handgun.

Figure 12-24 presents the gun barrel orientated in horizontal and vertical orientations with associated fork plots in Figure 12-25. Some orientation information is visible in the fork plot for the gun orientated vertically, however less so for the horizontal orientation, Figure 12-26 presents the Huynen orientation angle plots.

The gun barrel orientated horizontally produces both horizontal and vertically polarised reflections indicating that reflection is taking place from more than one edge of the gun. The orientation angle is 0° produced by a leading-edge provided by the horizontal handle for the gun aligned with the barrel vertical.

Figure 12-27 indicates that the gun produces a helical response upon reflection caused by a double bounce reflection produced by the gun structure and shown as an increase in the skip angle (Figure 12-28).

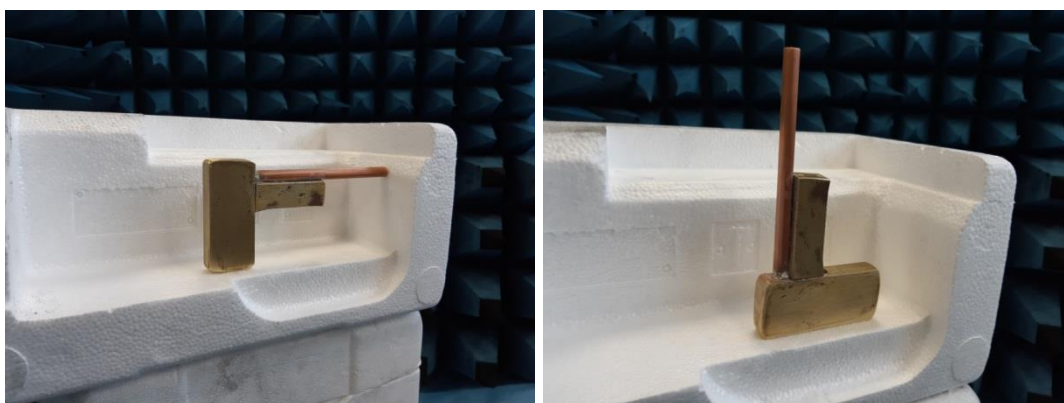


Figure 12-24 Brass Gun, horizontal barrel (left), vertical (right).

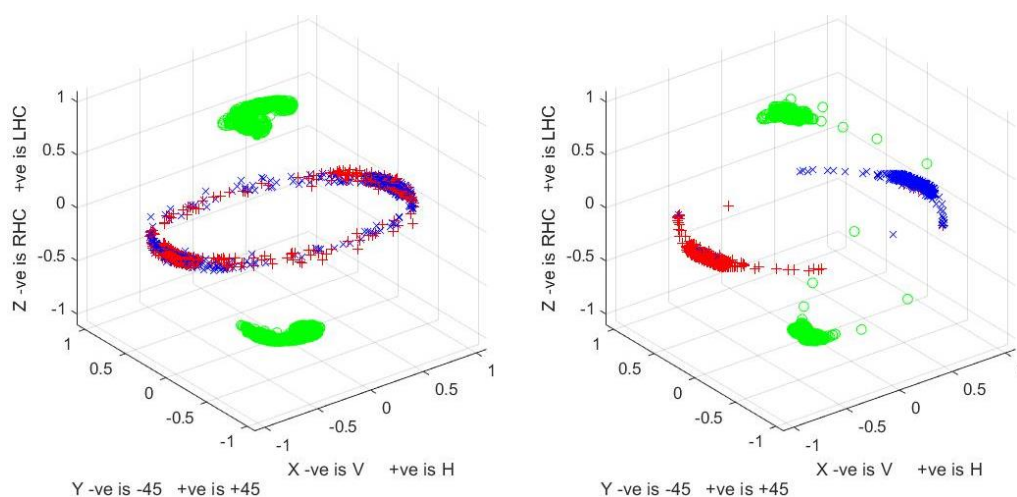


Figure 12-25 Brass gun fork plot via measurement horizontal left, vertical right

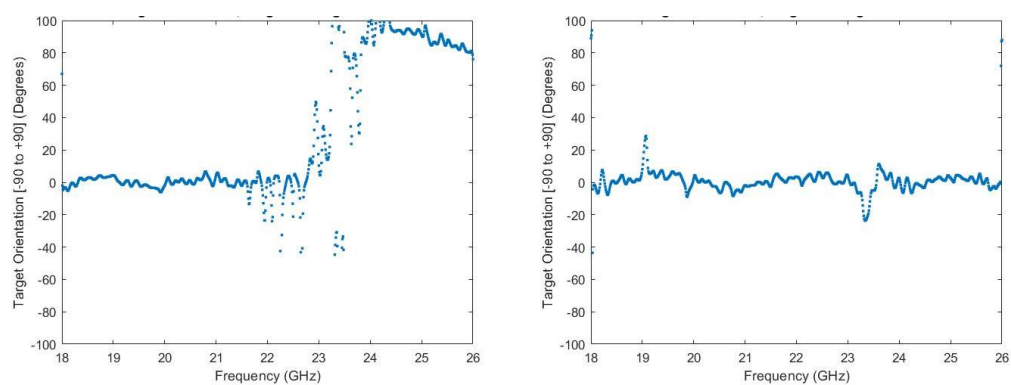


Figure 12-26 Brass gun measured orientation angle horizontal left, vertical right

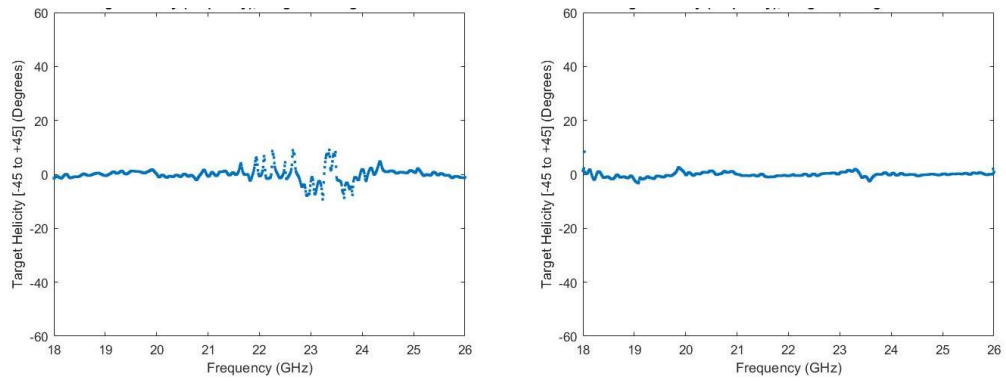


Figure 12-27 Brass gun measured helicity angle horizontal left, vertical right

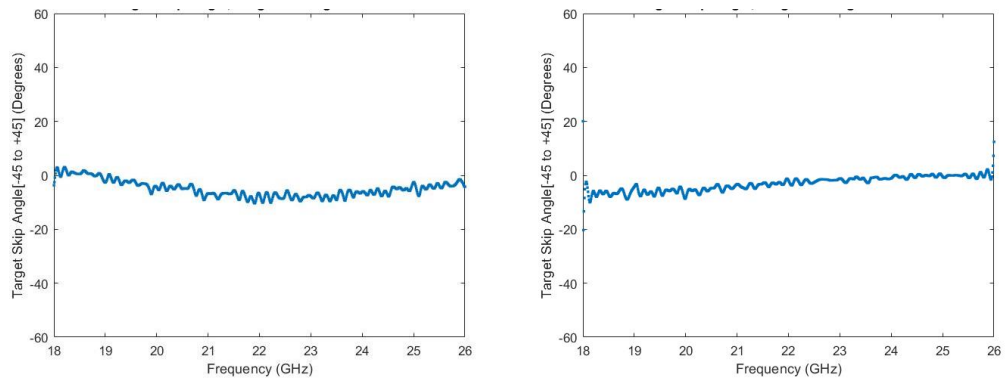


Figure 12-28 Brass gun measured skip angle horizontal left, vertical right

12.2.9 Brass gun horizontal and at 45° orientations

Figure 12-29 shows the gun positioned with barrel horizontally and at 45° with Figure 12-30 showing associated fork plots. Orientation information is visible in the fork plot for the 45° orientation, indicating that part of the gun is presenting a vertical leading edge to the radar beam. Orientation information in the fork plot for the horizontal barrel is far less distinct. However, the Huynen orientation angle visible in Figure 12-31 (left) shows that the gun has a predominance of horizontal orientation for the lower 50% of the spectral range. The upper 50% of the spectral range is indicating a predominance of vertical orientation. Additionally, the cross-polar nulls are separating on the Poincaré sphere plot of the gun orientated at 45°, the mechanism for causing this is unknown.

Multiple reflections occur between different gun parts visible as an increase in the skip angle (Figure 12-33), leading to a rise in helical conversion upon reflection back to the radar Figure 12-32.

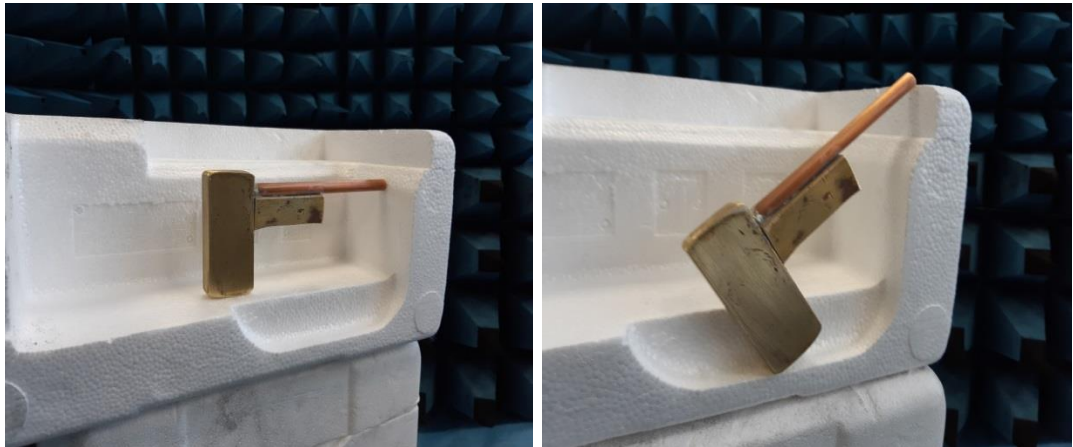


Figure 12-29 Brass gun horizontal orientation left, 45° right

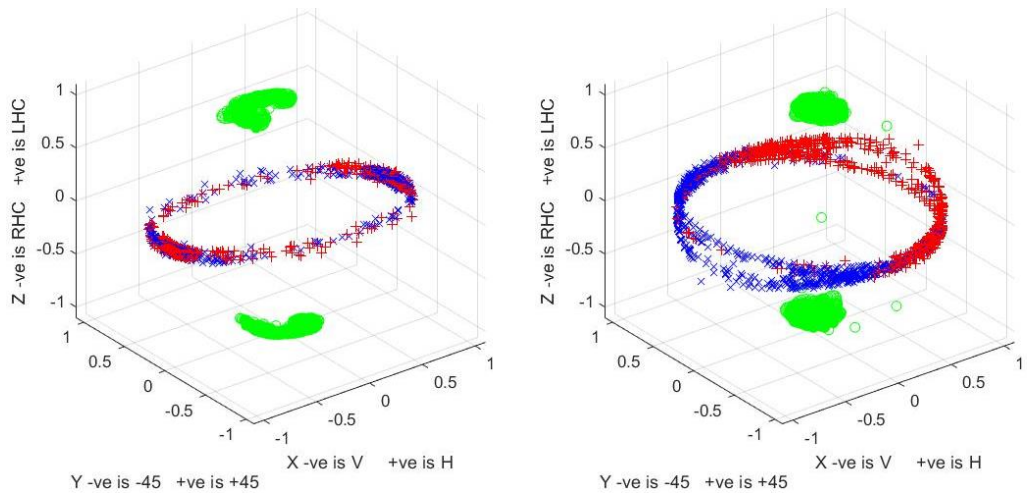


Figure 12-30 Brass gun fork plot via measurement horizontal left, 45° right

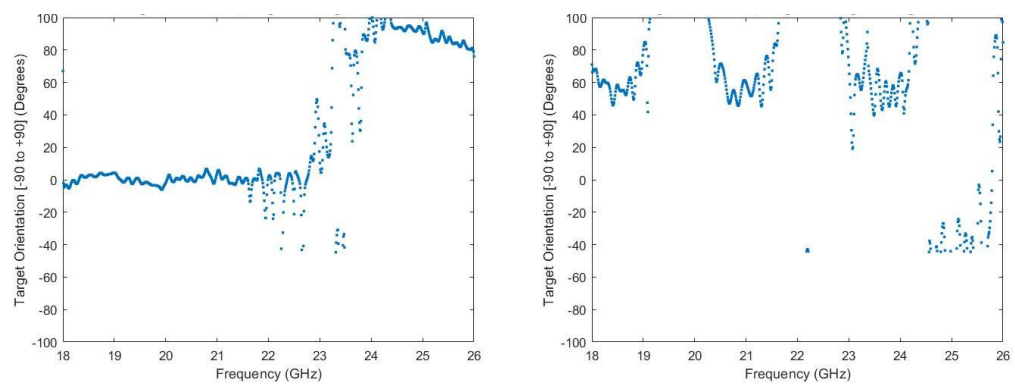


Figure 12-31 Brass gun measured orientation angle horizontal left, 45° right

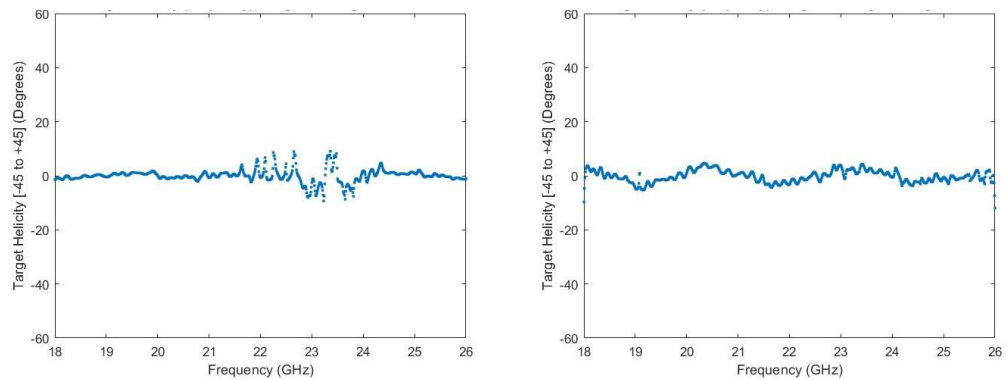


Figure 12-32 Brass gun measured helicity angle horizontal left, 45° right

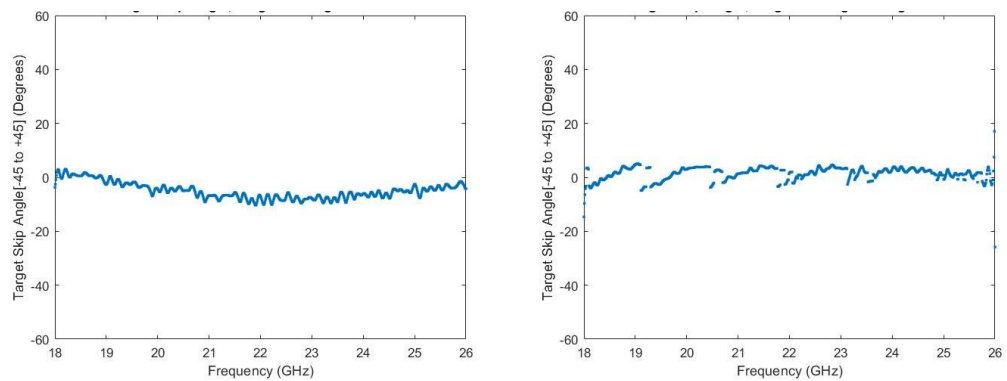


Figure 12-33 Brass gun measured skip angle horizontal left, 45° right

12.2.10 Shrapnel target

Figure 12-34 shows a shrapnel target produced with a mixture of roofing-felt nails embedded in a matrix of paraffin wax. The embedded shrapnel's random nature produces a slightly stochastic response as can be seen in the fork plot presented in Figure 12-34 (right). However, closer inspection indicates that some orientation information is visible as indicated by the position of the blue cross-polar nulls, which show a predominance of horizontally polarised reflection caused by the orientation of the rectangular wax block. Figure 12-35 (right) shows the Huynen orientation angle plot with a predominance of horizontal orientation. The target size (Figure 12-35 left) has ripples with a period of 1.3 GHz. Using equation 10-1 and assuming a dielectric constant of 2.2 for paraffin wax gives a wax block thickness of 5.2 cm. The measured thickness of the paraffin wax block is 2.5 cm. This discrepancy might be accounted for by the nails in the block, which would increase the effective refractive index [110], giving a value smaller than the predicted value of 5.2 cm.

Figure 12-36 (left) shows the helicity angle. It indicates that some conversion from the linear polarisation states to helical occurs upon reflection due to the shrapnel's multiple reflections. The shrapnel also produces an increase in skip angle Figure 12-36 (right).

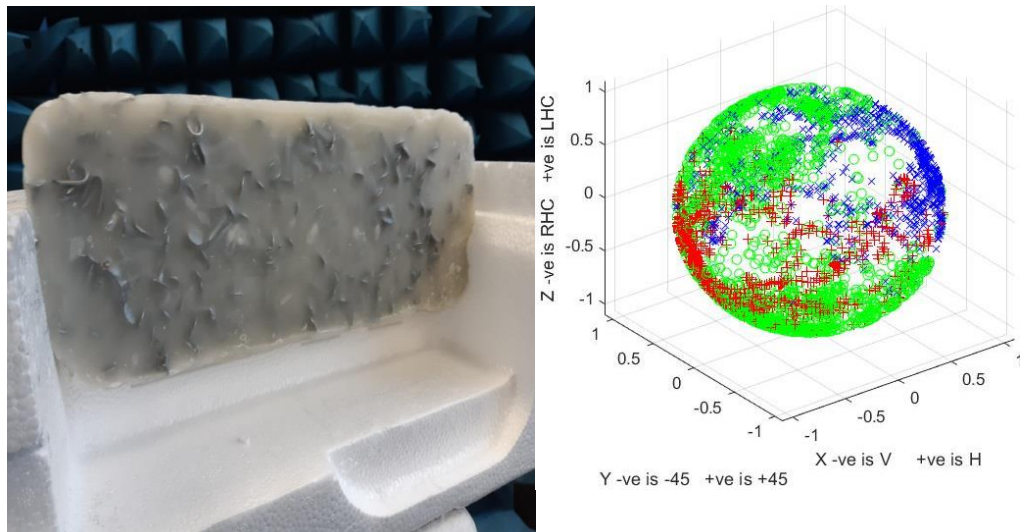


Figure 12-34 Shrapnel Target left, fork plot via measurement right

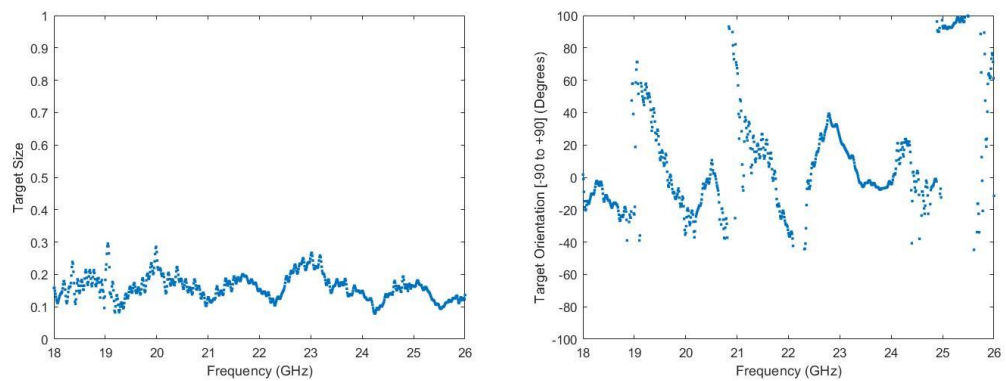


Figure 12-35 Measured shrapnel target size left, orientation angle right

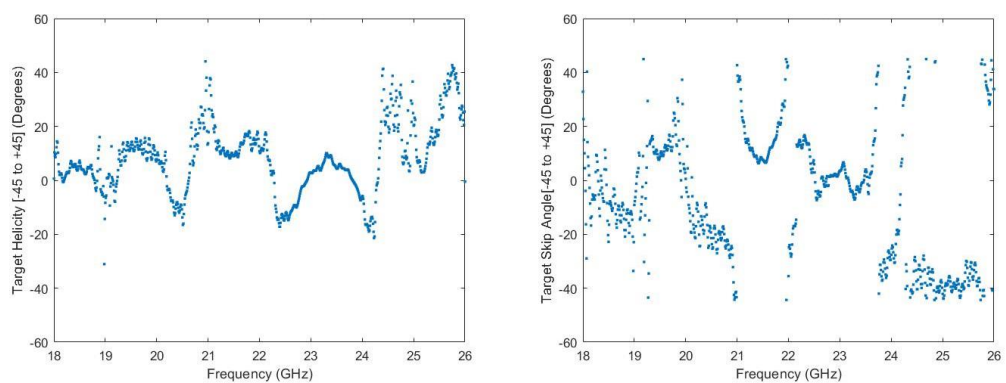


Figure 12-36 Measured shrapnel helicity angle left, skip angle right

12.2.11 The human torso

The detection of concealed weapons located on an individual tends to be complicated by the human torso's response, which tends to produce strong reflection when stimulated by radiation in the microwave region.

The torso's orientation in the radar beam and position of the arms and hands all affect the polarimetric response.

For static targets, the Sinclair parameters remain constant between consecutive measurements enabling direct calculation of the Huynen parameters as per chapters 4 and 10. However, if a target moves during measurement, then the Sinclair parameters can change significantly between consecutive measurements. Figure 12-37 shows a static dihedral reflector orientated at 45° on the right and a human torso with arms above the head on the left. The three sets of Sinclair matrices for the static dihedral are almost identical; however, the torso's Sinclair parameters are all noticeably different to one another because of movement of the torso between measurements. For this reason, the generation of the Huynen fork parameters needs to be calculated via application of the coherency matrix discussed in chapter 11 for moving targets.

The fork plots presented in Figure 12-38 compare the measurement of the torso of an individual with hands above head. The left plot shows the fork produced using the coherency matrix, the right via averaged Sinclair. It is evident with the averaged Sinclair that torso motion corrupts the measurement. The coherency matrix recovers this.

Movement of a target between measurements leads to speckle, even small movements caused by the action of a person breathing can cause this.

Measurements of two individual's torsos with no threat objects present and again with threat objects are compared.

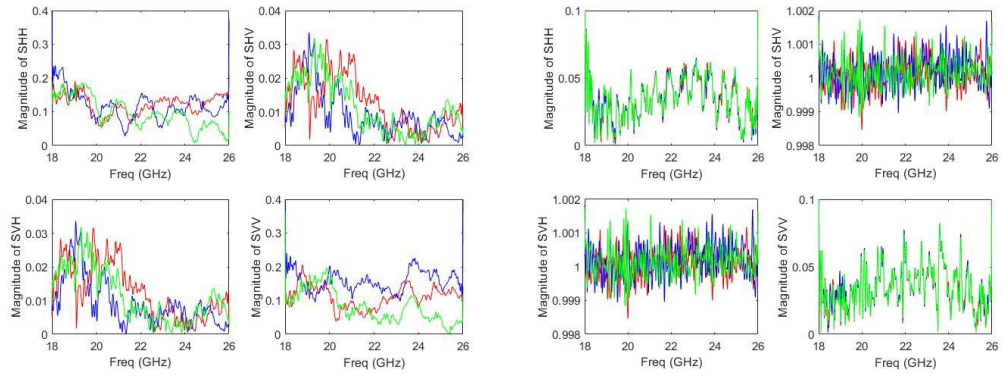


Figure 12-37 Consecutive delta function plots via measurement of the human torso with hands above head left, dihedral target at 45°right

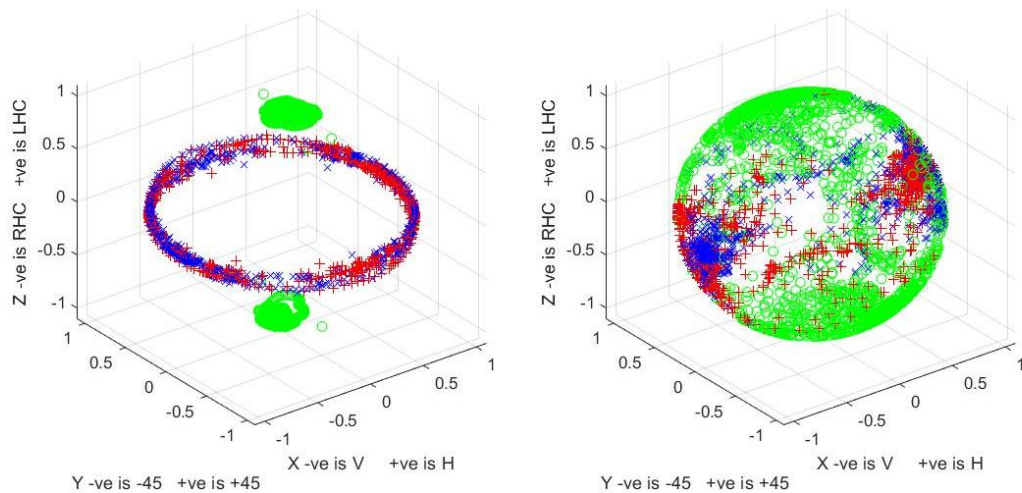


Figure 12-38 Fork plot from a measurement of the human torso with hands above head via coherency left, via average Sinclair right

12.2.12 Human torso perpendicular to radar beam with hands above head

The human torso aligned perpendicular to the radar's boresight with hands above the head produces a fork plot similar to that of a flat metal plate/sphere (Figure 12-39). The cross-polar nulls for the plate/sphere are located around the equator of the Poincaré sphere indicating that for the linear polarisation states no conversion takes place upon reflection and that conversion does take place for the circularly polarized states.

However, unlike the plate/sphere, the torso shown in the fork plot (Figure 12-39) indicates that some orientation information is present, characterised by the clustering of the blue cross-polar nulls particularly for subject 1. The difference in orientation between subjects 1 and 2 is unknown but could be caused by a zip or belt.

The Huynen target parameter is presented in Figure 12-40, showing the chaotic nature of the human torso's reflection.

Figure 12-41 indicates that a small amount of conversion into circular polarisation is taking place upon reflection. The skip angle (Figure 12-42) shows that a small amount of multi-bounce reflection is also taking place.

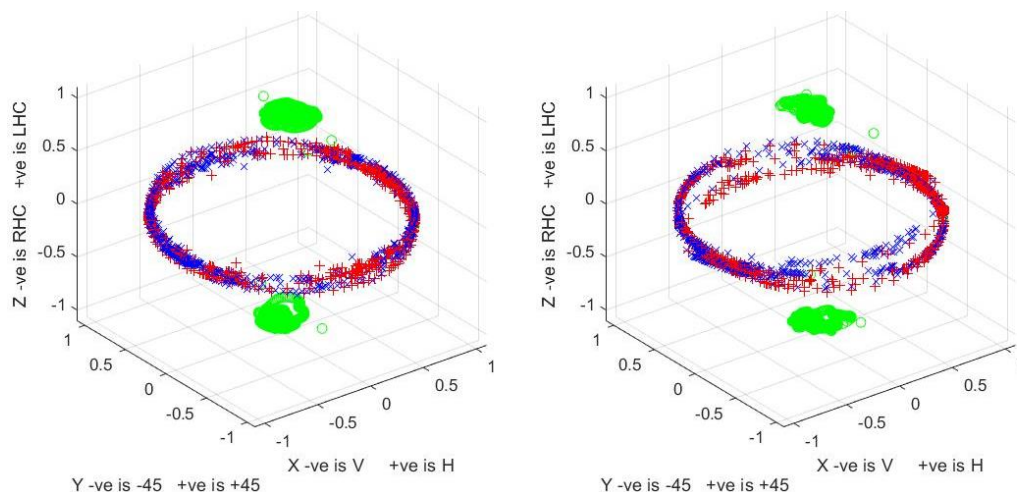


Figure 12-39 Hands above head fork plot via measurement of subject 1 left, subject 2 right

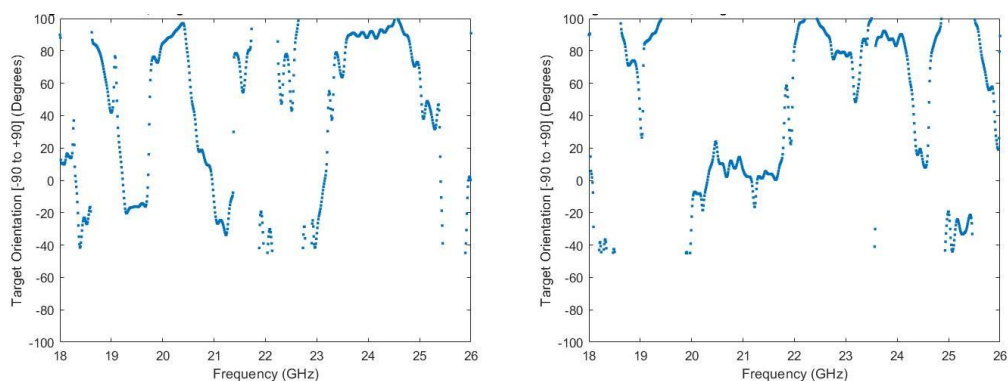


Figure 12-40 Hands above head measured orientation angle subject 1 left, subject 2 right

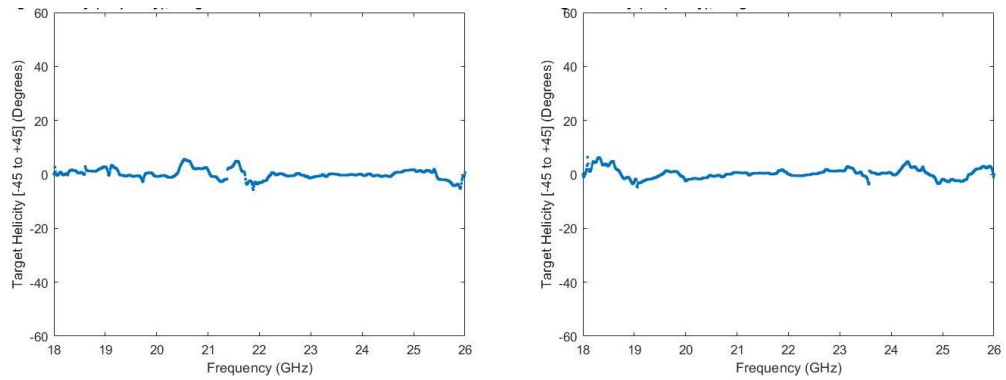


Figure 12-41 Hands above head measured helicity angle subject 1 left, subject 2 right

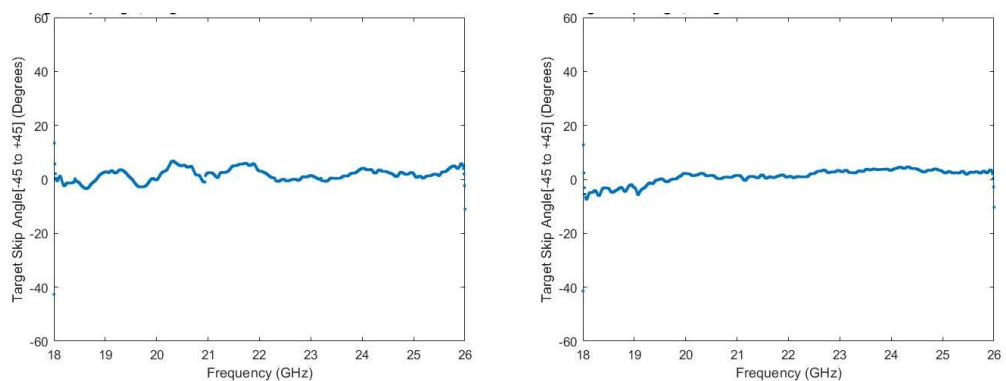


Figure 12-42 Hands above head measured skip angle subject 1 left, subject 2 right

12.2.13 Human torso perpendicular to the beam of the radar with hands at the side

Figure 12-43 shows the Huynen fork response produced by the torso facing the antenna's boresight; however, this time, the subject has hands and arms placed at the side. Subject 1 still shows some vertical orientation visible in the fork plot, possibly due to a belt or zip on the individual. The Huynen orientation plots can be seen in Figure 12-44 and show subject 1 having a predominance of vertical orientation.

From the fork plots (Figure 12-43) and the Huynen helicity parameter plots Figure 12-45, both subjects produce an increased helical response upon reflection; this is caused by the arms being present at the torso side.

The fork plot for the torso (hands above head) aligned boresight with the radar is very similar to that of the flat plate/sphere.

The torso causes the bulk of the reflection, the arms producing a small amount of double bounce reflection like that of the dihedral.

The response is also similar to that of the waveplate, with a delay between horizontal and vertical polarisation.

The skip angle for the torso with arms at the side is relatively low as can be seen in Figure 12-46, similar to that of the waveplate, the skip angle for a dihedral would be larger.

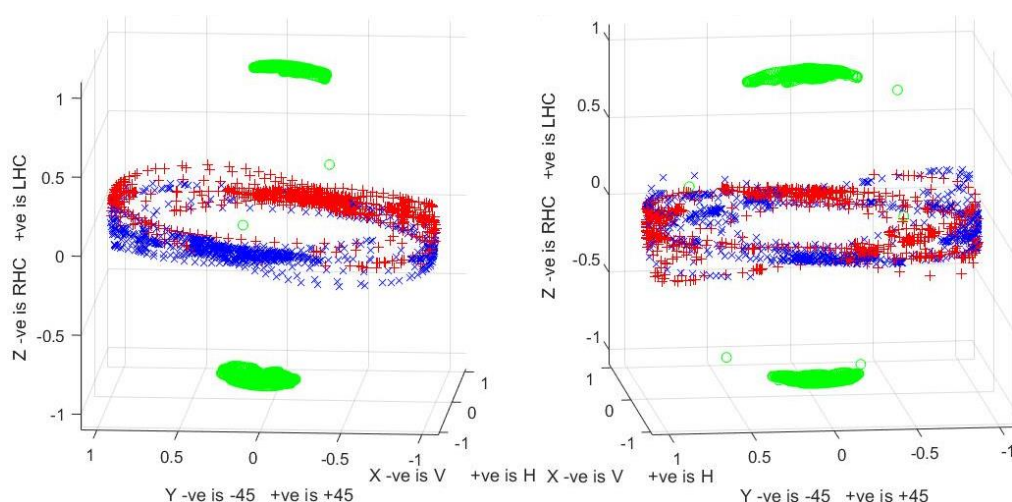


Figure 12-43 Hands at side fork plot via measurement subject 1 left, subject 2 right

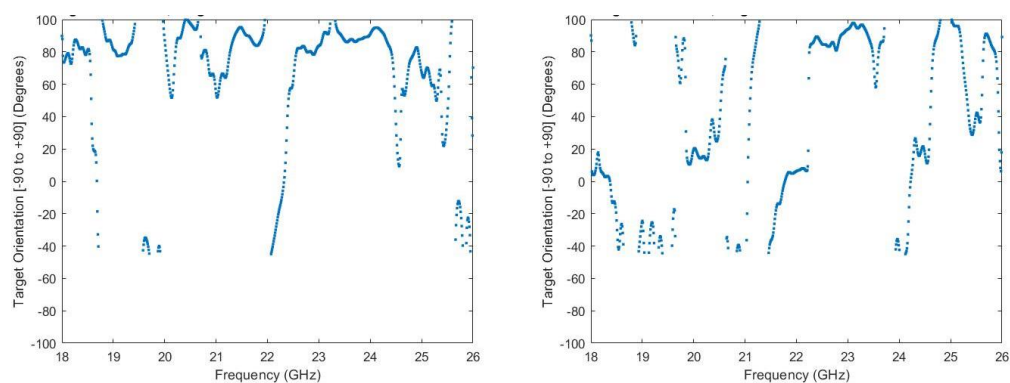


Figure 12-44 Hands at side measured orientation angle subject 1 left, subject 2 right

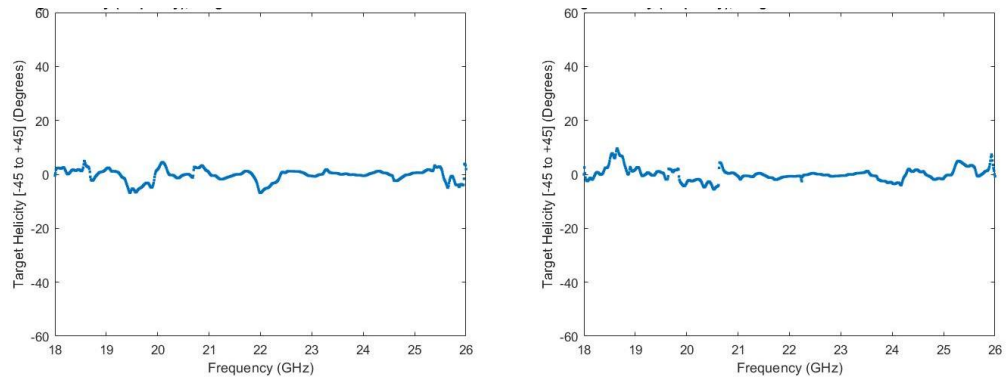


Figure 12-45 Hands at side measured helicity angle subject 1 left, subject 2 right

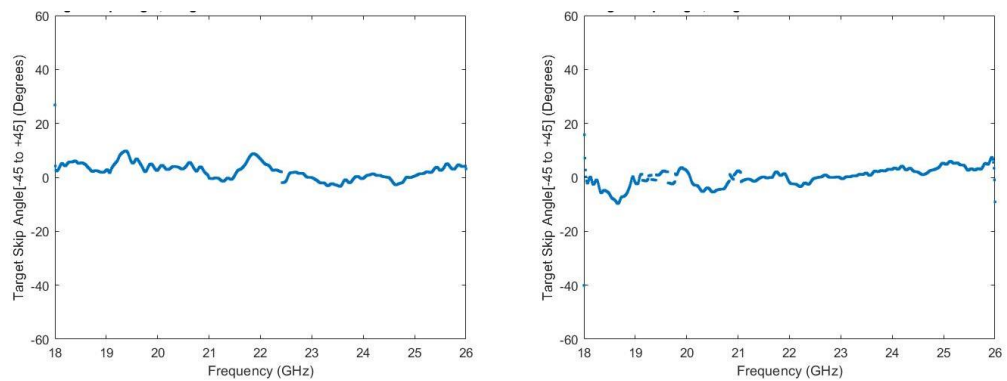


Figure 12-46 Hands at side measured skip angle subject 1 left, subject 2 right

12.2.14 Human torso presented side on to the beam of the radar with hands above the head compared to hands at the side

The next series of plots show subject 1's torso presented side on to the radar and compare the torso with arms and hands above the head and arms and hands at the side.

The fork response Figure 12-47 (left) shows the torso side on, but with the hands above the head. Again it is very similar to that of a flat plate but with some orientation information visible.

With the arms at the side (Figure 12-47 right) the response remains similar to the response with the arms above the head. The helicity angle Figure 12-49 remains relatively low for both torsos with arms in either position.

The skip angle (Figure 12-50) is low for the measurement with the arms above the head, increasing slightly for the arms at the side, showing reflections between torso and arms.

The target size (Figure 12-48 left) remains relatively constant across the band with the arms above head. The right plot in the figure presents a measurement with the arms at the side. This time ripples are present with a periodicity of around 1.5 GHz. The ripple relates to a distance of 10 cm caused by the arms and torso.

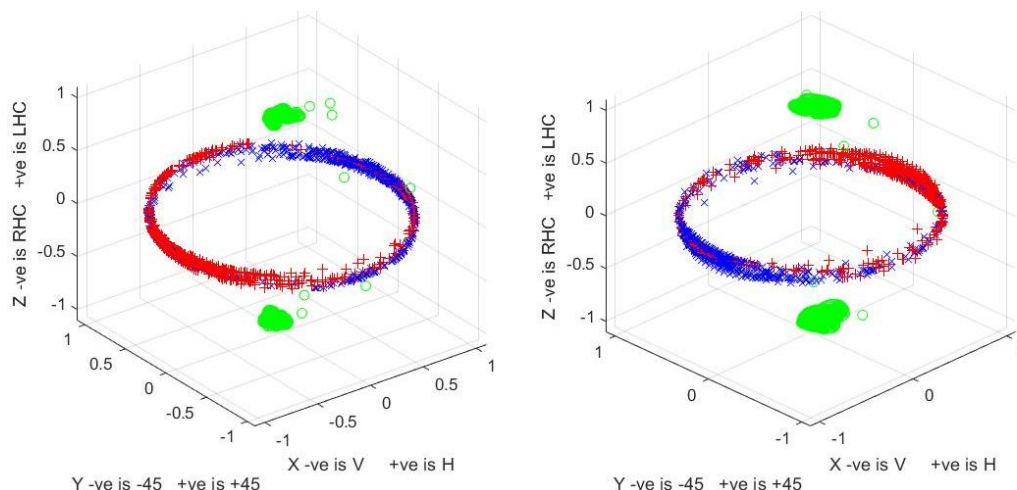


Figure 12-47 Subject 1 side on fork plot via measurement hands above head left, hands at the side right

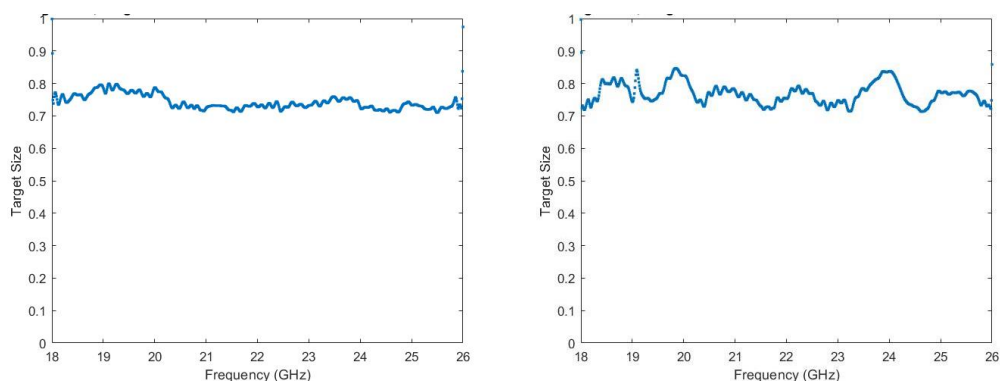


Figure 12-48 Subject 1 side on measured target size hands above head left, hands at the side right

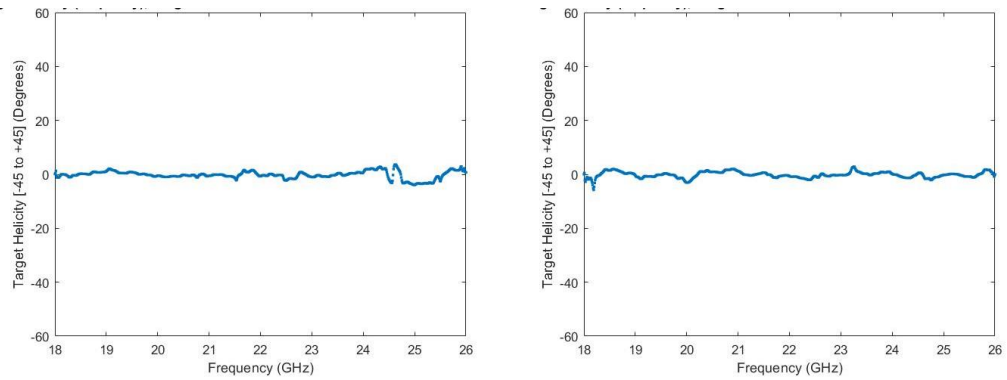


Figure 12-49 Subject 1 side on measured helicity angle hands above head left, hands at the side right

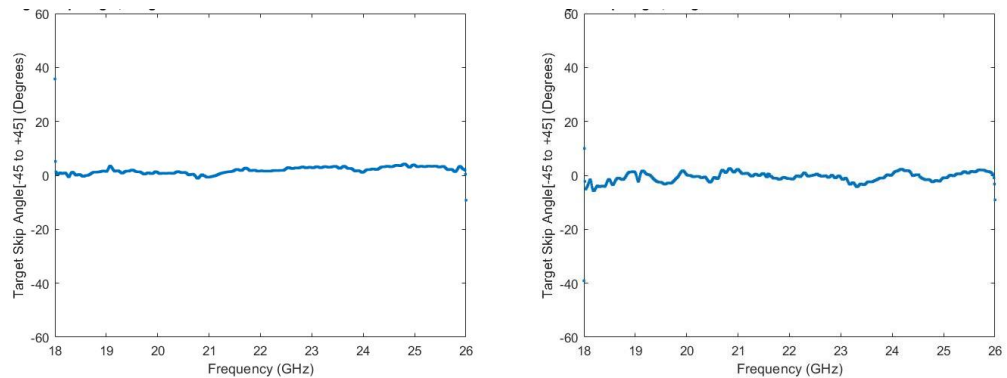


Figure 12-50 Subject 1 side on measured skip angle hands above head left, hands at the side right

12.2.15 Knife placed against the human torso

The knife on its own presented earlier in this chapter behaves like a flat plate reflector providing orientation information only when it offers a leading edge to the radars boresight but being a non-symmetrical target also produces helicity. The same applies when placed against the human torso. The torso on own with arms above the head has a minimal helical conversion.

12.2.16 Small knife vertical and horizontal on the human torso

Figure 12-51 shows a small knife placed against the human torso with its associated fork plot presented in Figure 12-52. The arms and hands were above the head.

Figure 12-53 viewed from the side $\phi=90^\circ$ (vertical linear position) presents the fork plot showing helicity produced by the knife's curved blade edge. The increase in helicity can also be seen in Figure 12-54.

Figure 12-55 shows the targets skip angle, indicating that multiple reflections are taking place in this case between the knife and torso.



Figure 12-51 Short knife on the human torso vertical left, horizontal right

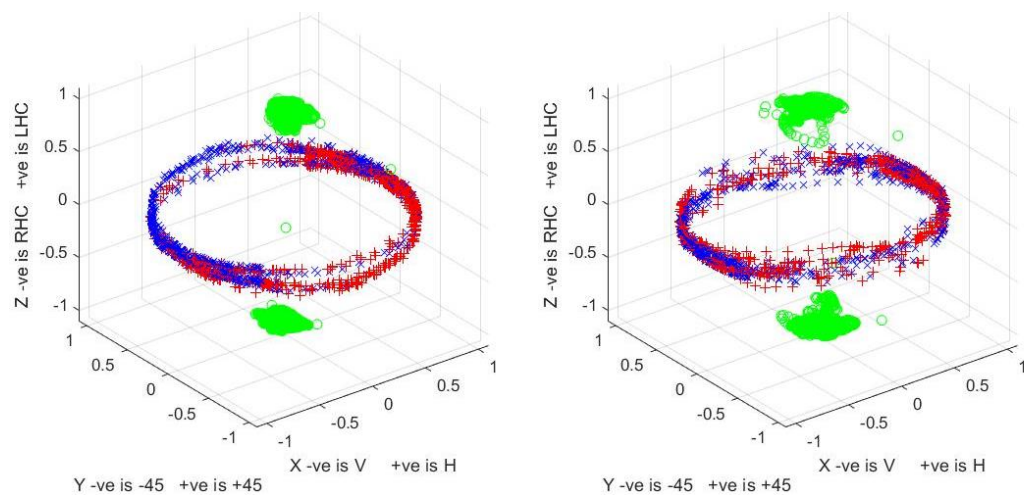


Figure 12-52 Fork plot via measurement of a short knife placed against the human torso vertical left, horizontal right

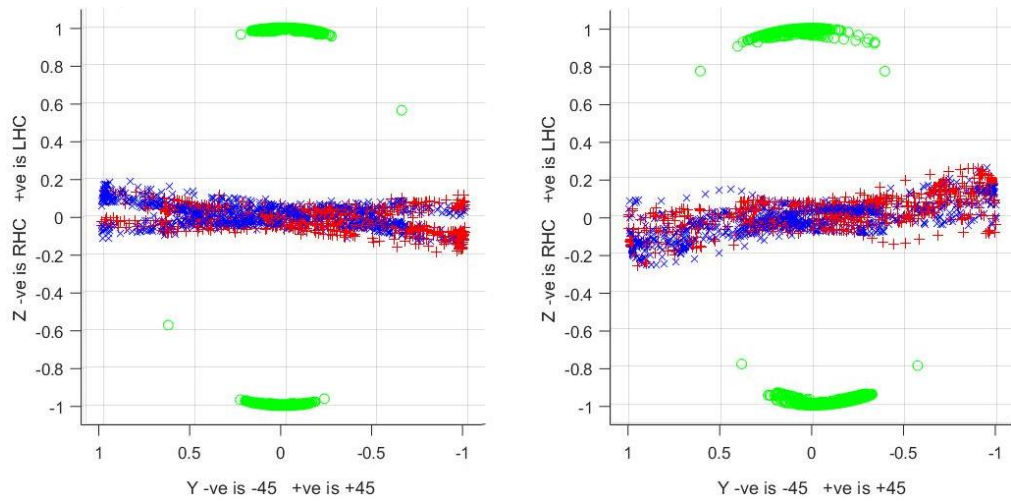


Figure 12-53 Fork plot (side view) via measurement of a short knife placed against the human torso vertical left, horizontal right

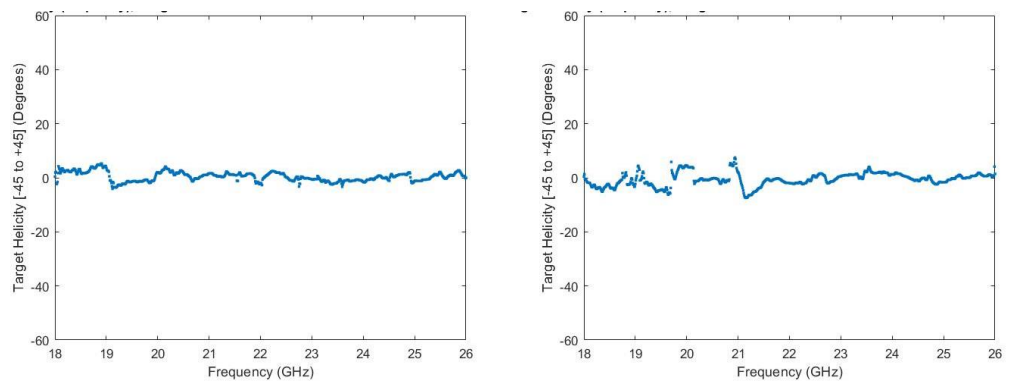


Figure 12-54 Measured helicity angle of a short knife placed against the human torso vertical left, horizontal right

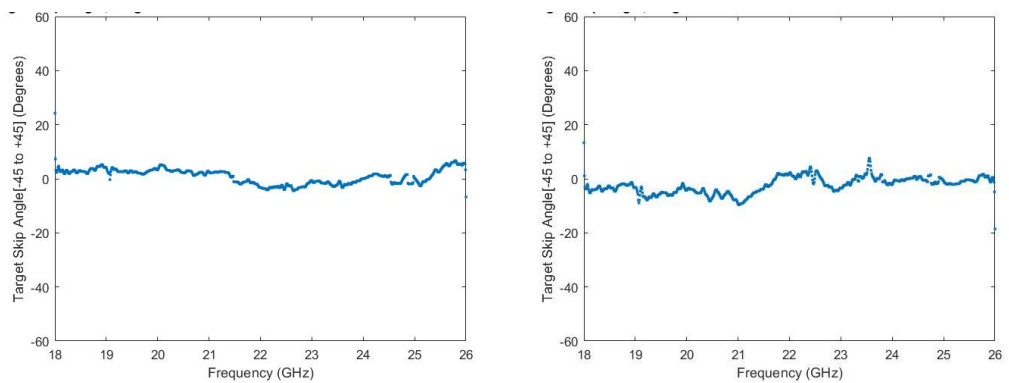


Figure 12-55 Measured skip angle of a short knife placed against the human torso vertical left, horizontal right

12.2.17 Long vertical and horizontal knives on the human torso

Figure 12-56 shows the knife held in position against the torso with one hand whilst the other arm and hand are at the torso side. With the arms at the side of the torso leads to an increase in helicity as previously shown.

Figure 12-57 shows the fork response for the vertical knife on the left and horizontal right. Figure 12-58 presents a side view of the Poincaré sphere from the vertical linear position ($\phi=90^\circ$).

The fork plot for the vertical knife shows a notable increase in helicity in Figure 12-59. The vertical knife's skip angle is also indicating an increase in multiple reflections because the arm is positioned slightly away from the torso for this measurement.

The horizontal knife exhibits far less helicity visible in the fork and helicity angle plots. There is still a small amount of helicity present, but this time it's in the opposite direction to the vertical knife.

The vertical knife produces a helicity angle with the same sign as the torso with the arms at the side, increasing the effective helicity angle.

The horizontal knife produces a helicity angle with a sign in the opposite direction to the torso. The knife in this orientation has the effect of reducing the torso's helicity. The skip angle (Figure 12-60) shows that very few multiple reflections are taking place.

Some orientation information is visible in the fork plots.

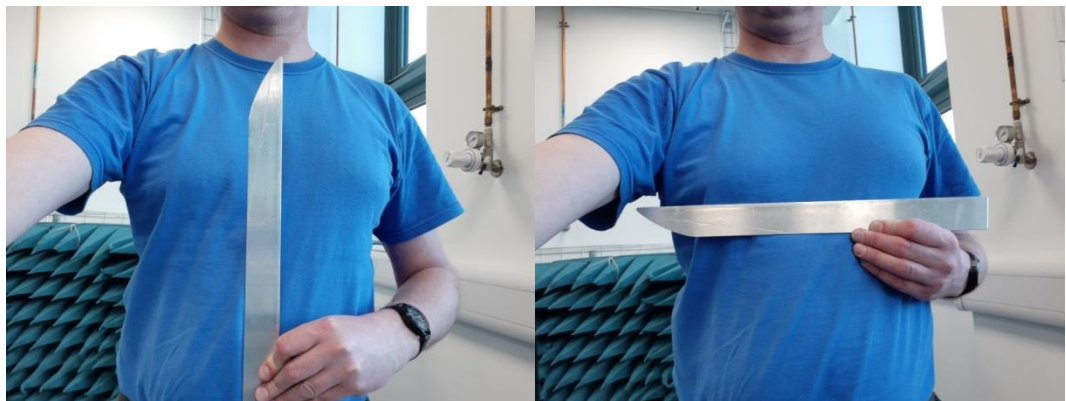


Figure 12-56 Human torso with a long vertical knife left, horizontal right.

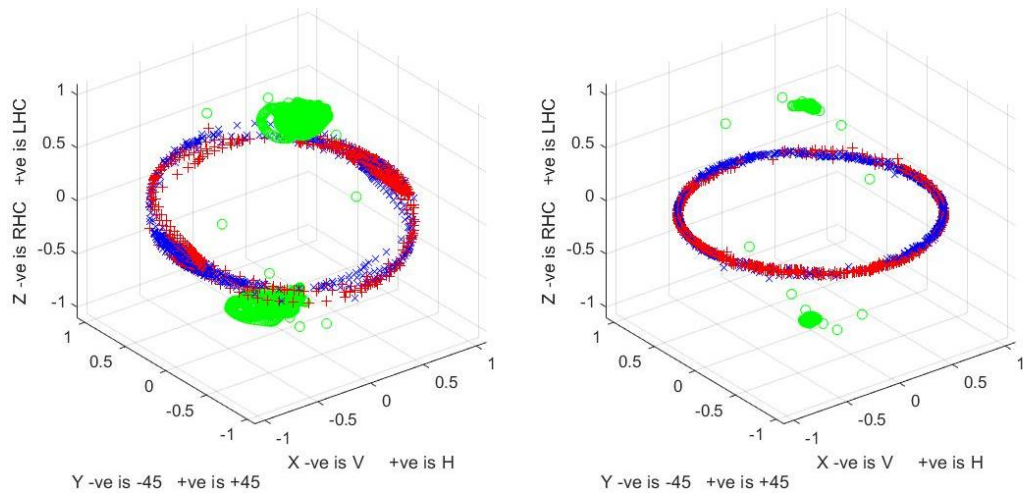


Figure 12-57 Fork plot via measurement of the human torso with a long vertical knife left, horizontal right

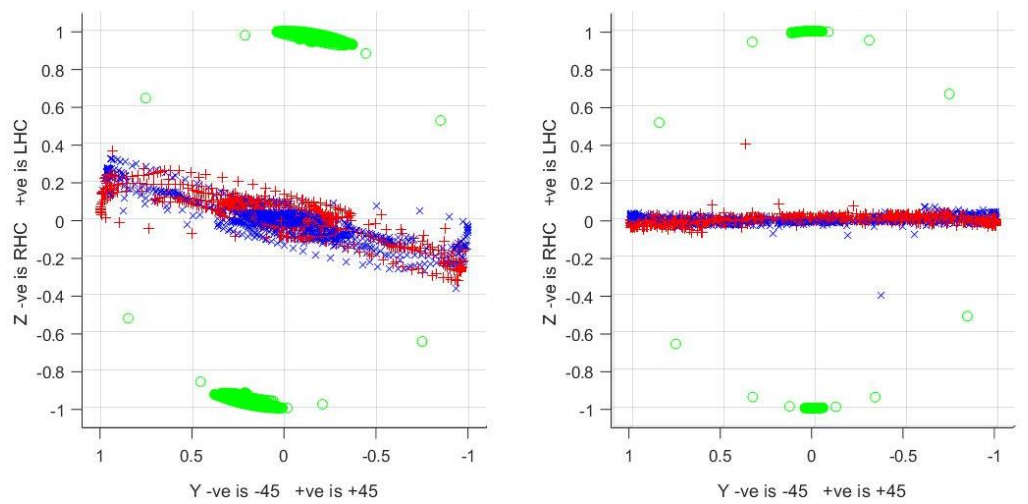


Figure 12-58 Side view of the fork plot via measurement of the human torso with a long vertical knife left, horizontal right

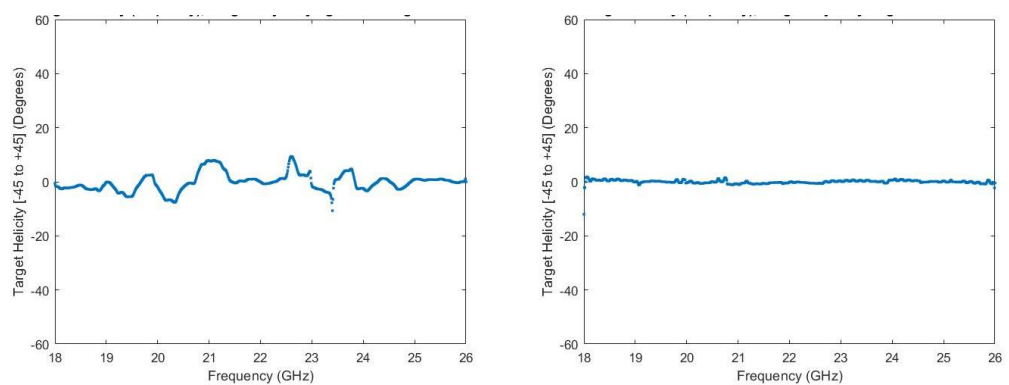


Figure 12-59 Measured helicity angle of the human torso with a long vertical knife left, horizontal right

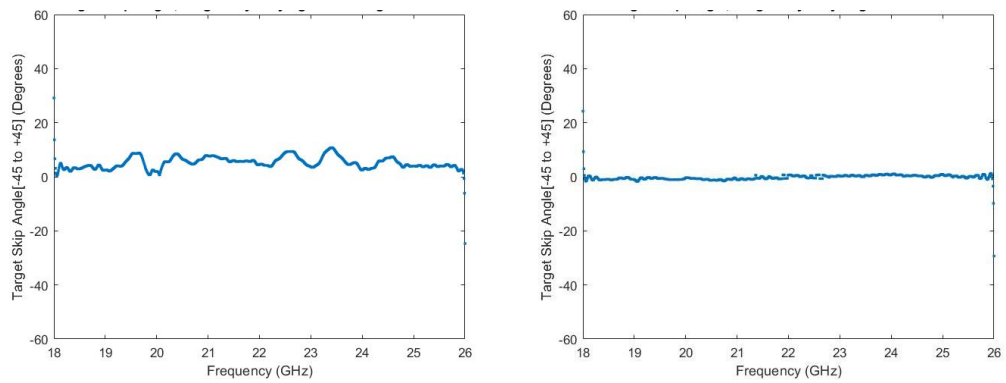


Figure 12-60 Measured skip angle of the human torso with a long vertical knife left, horizontal right

12.2.18 Vertical and horizontal guns on the human torso

Figure 12-61 shows the gun held against the torso of subject 1 in both vertical and horizontal orientations. In both cases, the gun held with the individual's left arm was at the torso side.

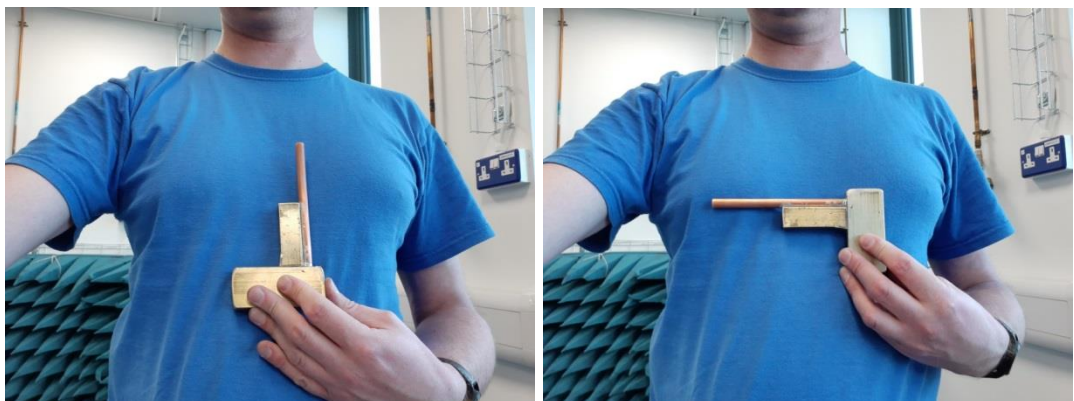


Figure 12-61 Human torso with a vertical brass gun left, horizontal right.

Both the human torso and gun represent plane surface reflectors when measured on their own. However, when the arms are at the torso's side, an increase in helicity occurs.

Suppose a plane reflector such as a knife perpendicular to the radars boresight presents leading edge. In that case, orientation information will be provided on the fork plots by this edge. The same applies to the gun.

The measured responses of vertically and horizontally orientated guns provide orientation information visible in the Huynen fork plots, (Figure 12-62 and Figure 12-64).

The co-polar nulls have moved away from the zenith and nadir and towards the fork's central prong (X2) (red crosses) (Figure 12-64 and Figure 12-65). The co-polar nulls for a dipole form around the fork's central prong, so the measured response indicates that the gun on the torso is a combination of flat plate and a small amount of dipole.

The blue cross-polar nulls (X1) representing the fork's handle indicate that when the gun barrel is vertical, parts of the gun produce a horizontal response on the Poincaré sphere.

When the barrel is horizontal, the fork response and orientation angle (Figure 12-66) indicates vertical orientation. The gun handle, in this case, is providing the orientation information.

Figure 12-63 shows the Huynen fork viewed from the vertical polarisation position on the Poincaré sphere, indicating that the target forms multiple fork plots in this orientation. An increase in helicity is also apparent from the fork and helicity plot (Figure 12-67). This effect is caused by reflection between the arms at the side of the torso and the gun. The skip angle indicates multiple reflections (Figure 12-68).

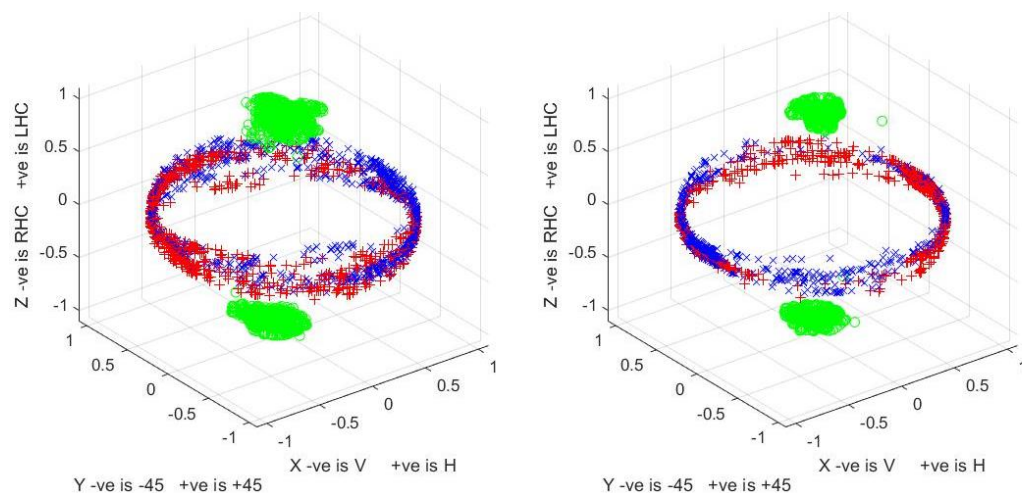


Figure 12-62 Fork plot via measurement of the human torso with a vertical gun left, horizontal right

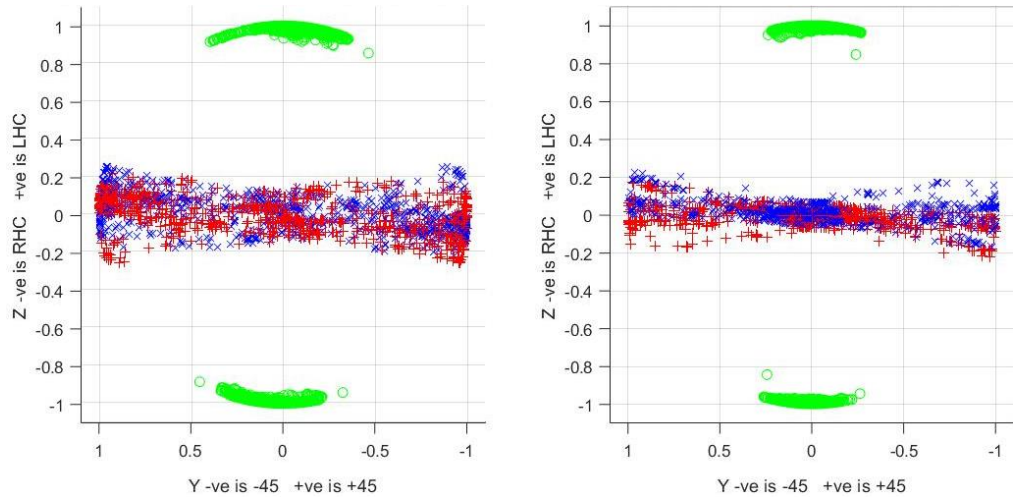


Figure 12-63 Fork plot via measurement of the human torso with a vertical gun left, horizontal right (viewed from the vertical position)

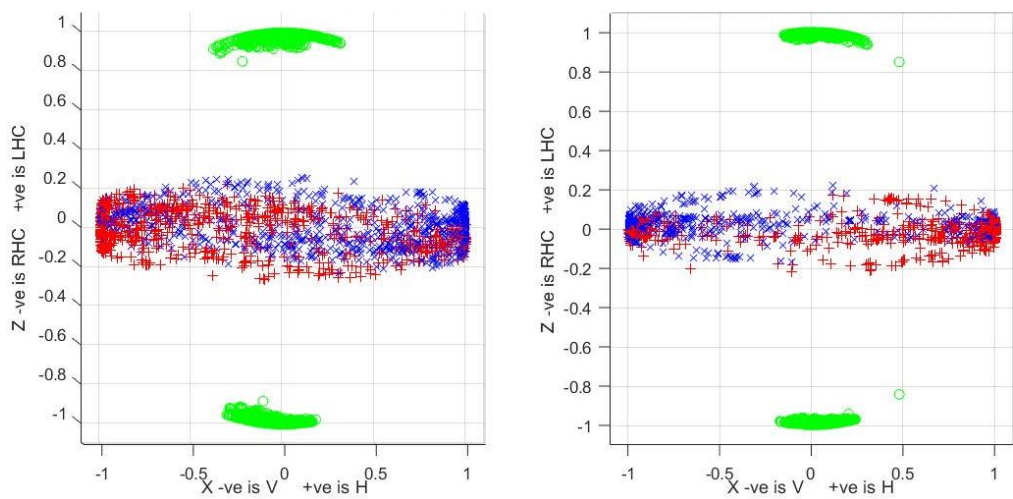


Figure 12-64 Fork plot via measurement of the human torso with a vertical gun left, horizontal right (viewed from the -45° position)

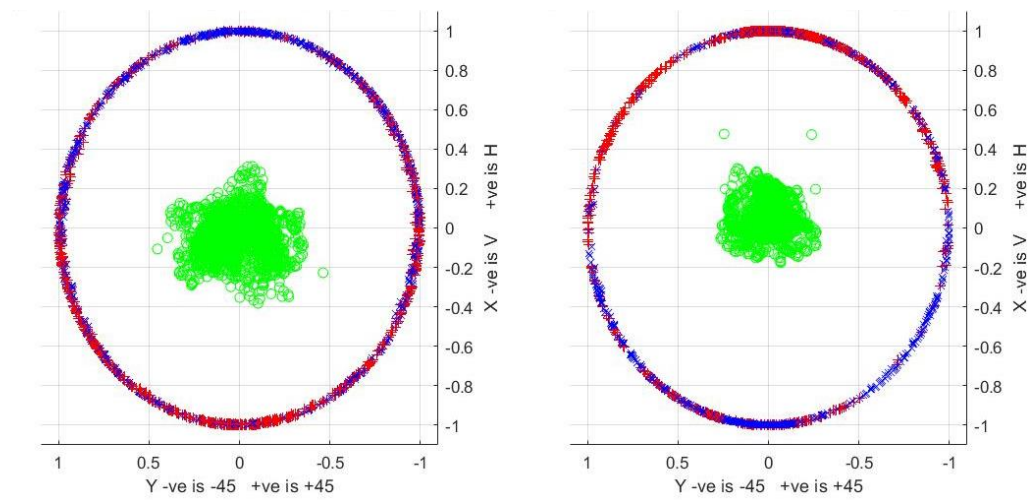


Figure 12-65 Fork plot via measurement of the human torso with a vertical gun left, horizontal right (viewed from the zenith)

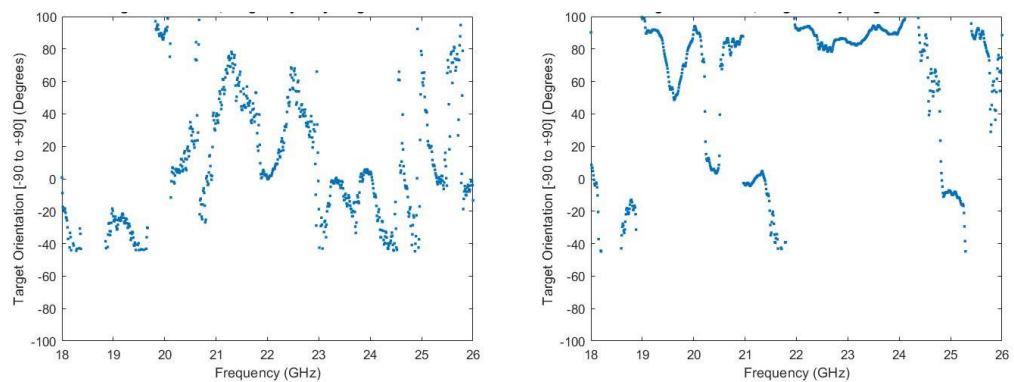


Figure 12-66 Measured orientation angle of the human torso with a vertical gun left, horizontal right

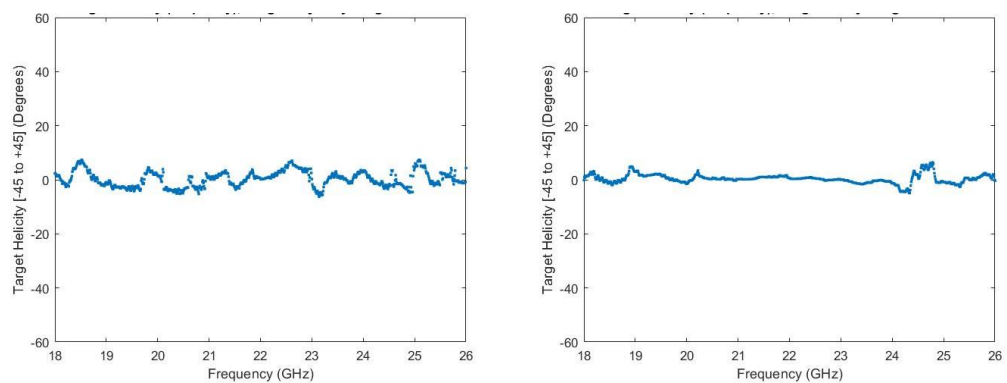


Figure 12-67 Measured helicity angle of the human torso with a vertical gun left, horizontal right

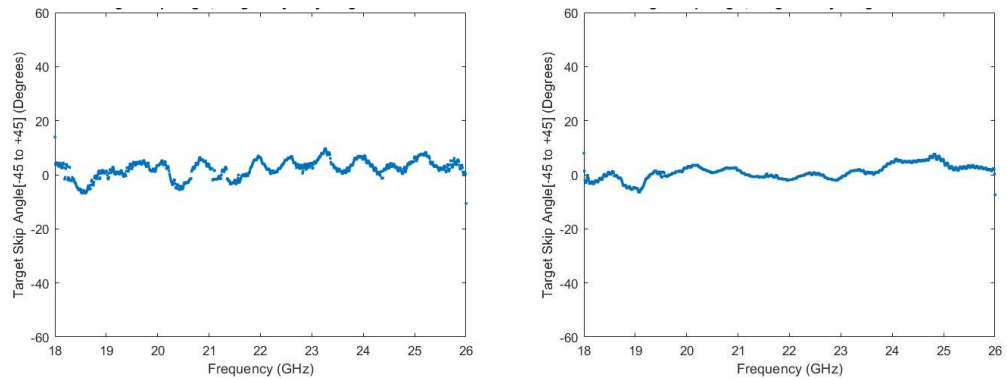


Figure 12-68 Measured skip angle of the human torso with a vertical gun left, horizontal right

12.2.19 Shrapnel placed against the human torso

The following series of figures compare the same shrapnel target, as shown earlier in this chapter. Measurements compare the shrapnel target on its own, to that of the shrapnel located on the torso of subject two.

Figure 12-69 and Figure 12-71 indicate that some orientation information is present in the shrapnel measurements both on its own and when placed against the torso indicated by the blue cross-polar nulls. The orientation angle plot Figure 12-73 also shows a predominance of vertical orientation.

The shrapnel target on its own Figure 12-70 (left) indicates a conversion to helical polarisation is taking place upon reflection, also visible in the right plot of this figure. However, the helicity is slightly lower in the right plot. For this measurement, one arm was at the torso's side whilst the other was holding the shrapnel target. The helicity produced by the torso has reduced the effects of the helicity produced by the shrapnel target Figure 12-74.

Figure 12-72 presents the Huynen fork viewed from the vertical polarisation position on the Poincaré sphere, comparing the measurement of subject 2s torso on its own with a measurement of the same subject but with the shrapnel target held against the torso.

Both plots show an increase in helicity, with the torso on its own producing an apparent spread of multiple fork responses orientated about the horizontal-vertical axis on the Poincaré sphere.

The torso with the shrapnel present shown in the figure's right plot shows the red and blue cross-polar nulls forming arcs also visible in Figure 12-70 (left) and is characteristic of the shrapnel target.

The skip angle Figure 12-75 compares the shrapnel's measurement on its own (left plot in the figure) with the shrapnel located on subject 2's torso (right plot in the figure).

The shrapnel on its own shown in the figure indicates that multiple reflections are taking place between the metal particles in the wax matrix.

The shrapnel response on the torso becomes suppressed by the dominant nature of the torso's response.

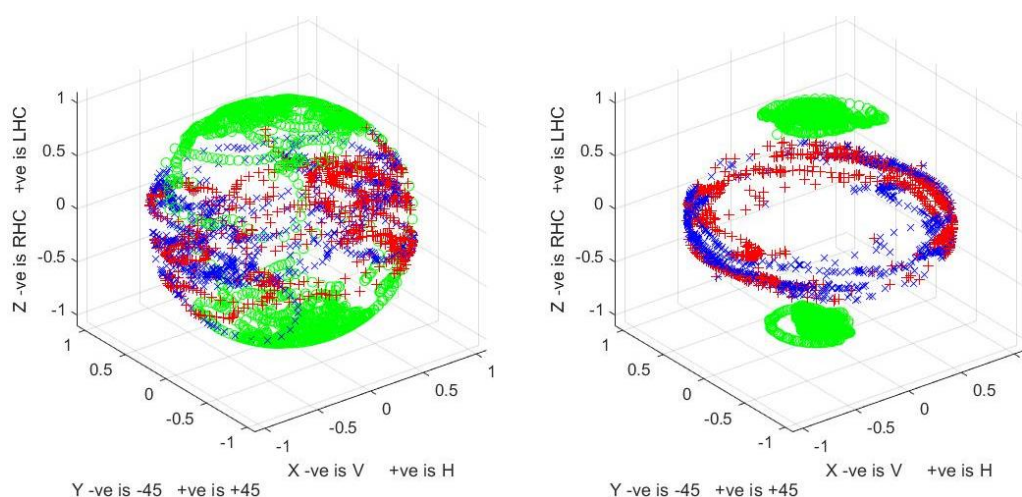


Figure 12-69 Fork plot via measurement of shrapnel on its own left, located on subject 2 torso right

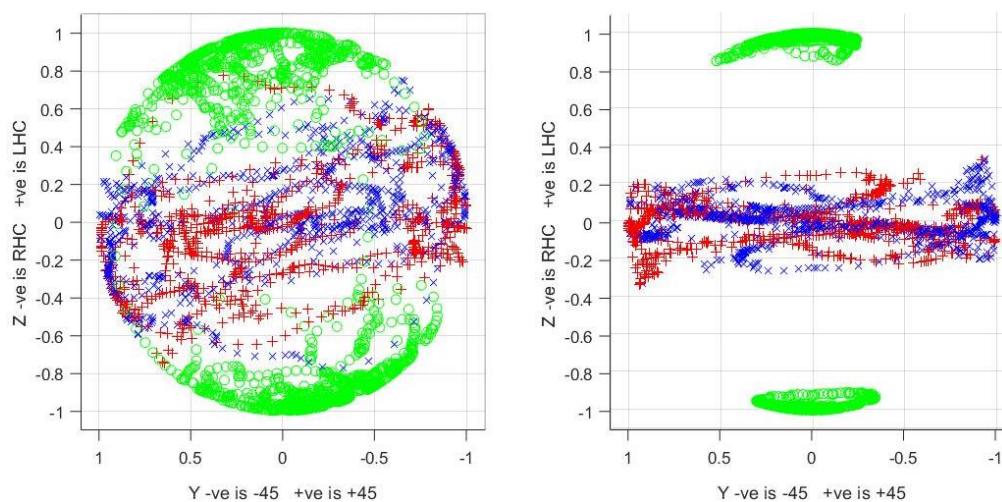


Figure 12-70 Fork plot via measurement of shrapnel on its own left, located on subject 2 torso right (viewed from the vertical polarisation position)

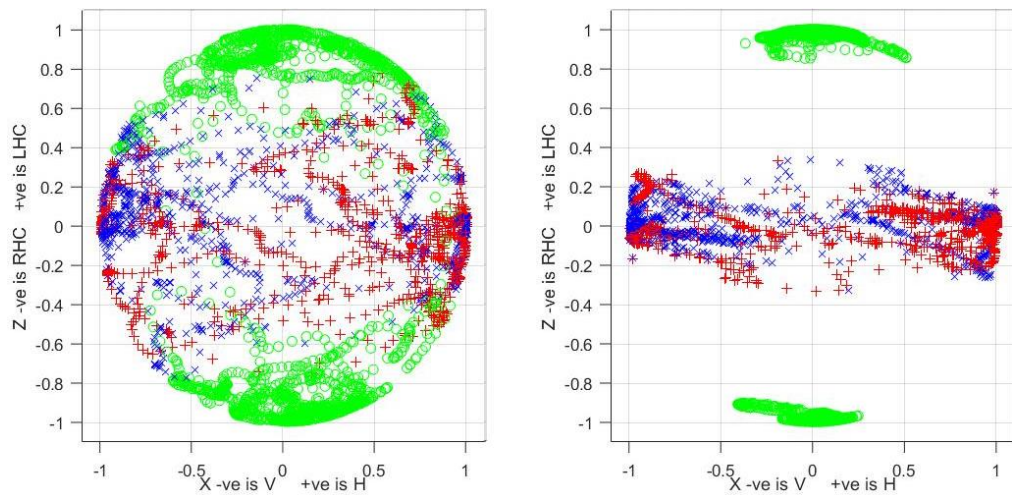


Figure 12-71 Fork plot via measurement of shrapnel on its own left, located on subject 2 torso right (viewed from the -45° polarisation position)

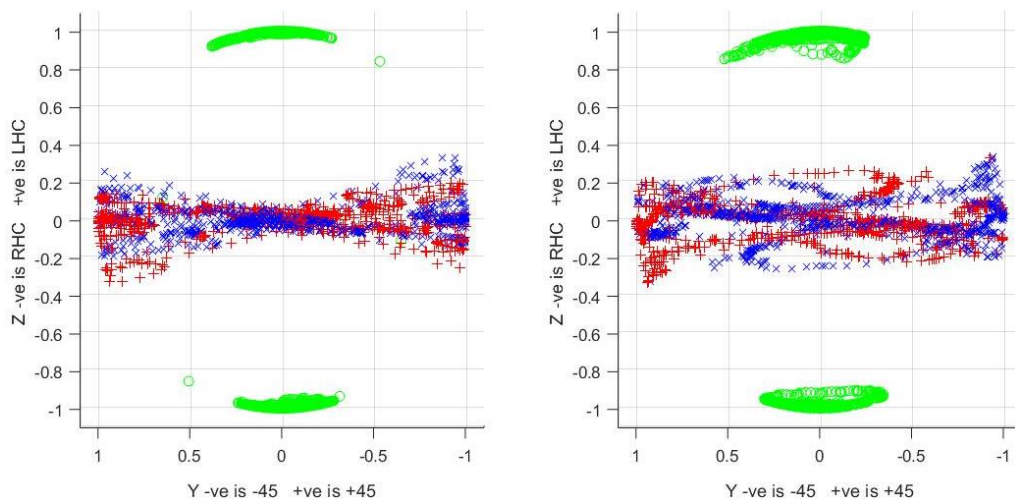


Figure 12-72 Fork plot via measurement of subject 2's torso with hands at side left, shrapnel on subject 2 right (viewed from the vertical polarisation position)

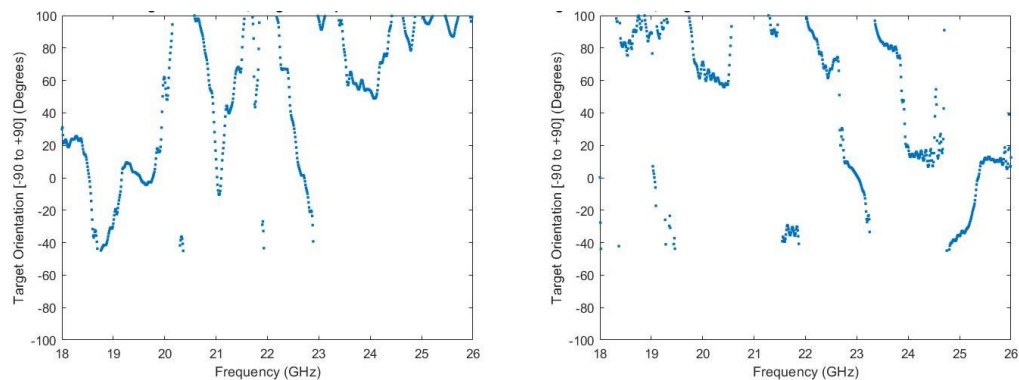


Figure 12-73 Measured orientation angle of shrapnel on its own left, located on subject 2 torso right

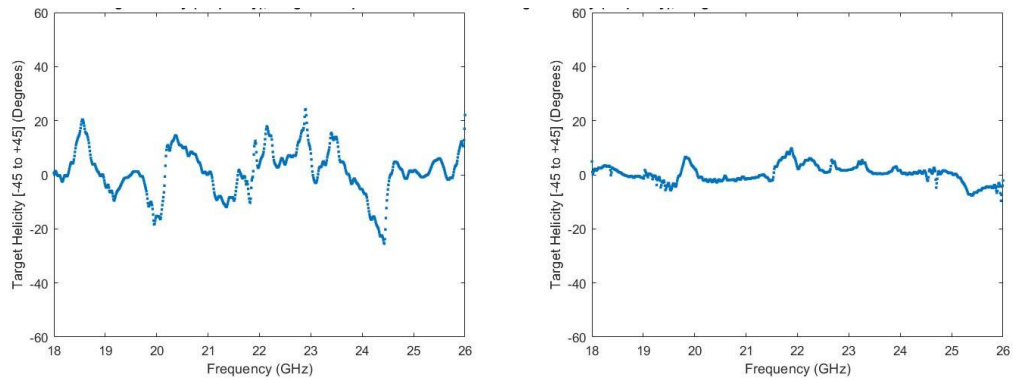


Figure 12-74 Measured helicity angel of shrapnel on its own left, located on subject 2 torso right

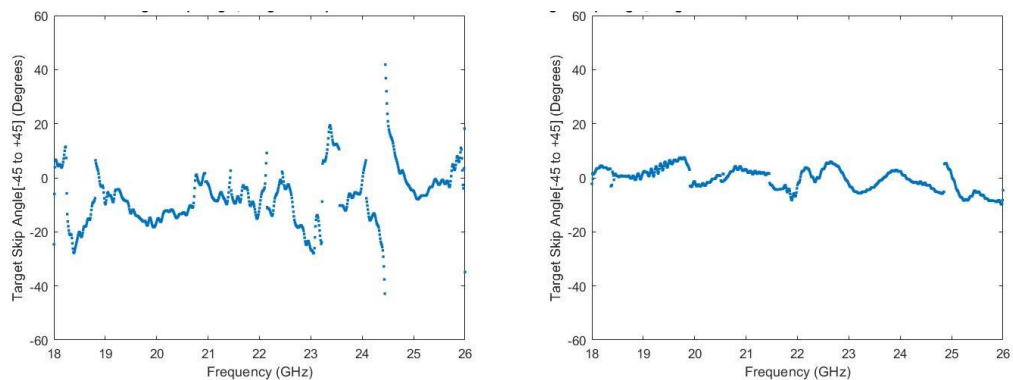


Figure 12-75 Measured skip angle of shrapnel on its own left, located on subject 2 torso right

12.2.20 Smartphone

There are many benign objects carried by individuals, one such item being a smartphone. The phone used for the measurements is visible in Figure 12-76 with its orientation being horizontal when measured. The fork plot Figure 12-77 and Figure 12-78 indicates a combination of flat plate and dipole response is taking place with orientation information being visible. The blue cross-polar nulls indicating a predominance of horizontal orientation and the co-polar nulls (green circles) have moved away from the zenith and nadir locations moving toward the fork's central prong (red cross-polar nulls), as for the dipole previously shown. Orientation angle in Figure 12-79 (left) being at 0° across most of the band. The phone measured has a frame manufactured from aluminium, and this frame is providing the orientation information.

The smartphone also produces a helical response upon reflection (Figure 12-77 right and Figure 12-79 right). This effect caused by the capacitive touchscreen, which is composed of a grid of minute conductive wires similar to a wave plate.

The smartphones skip angle Figure 12-80 indicates that multiple reflections are taking place. This target is a combination of a wave plate with a dipole.



Figure 12-76 Smartphone.

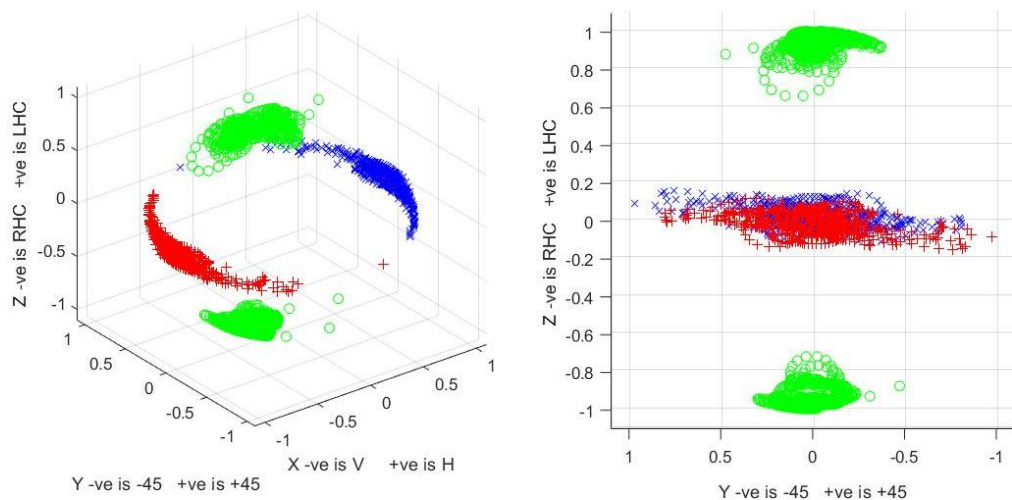


Figure 12-77 Huyen fork plot via measurement of a smartphone on its own (left).
Viewed from the vertical polarisation position (right)

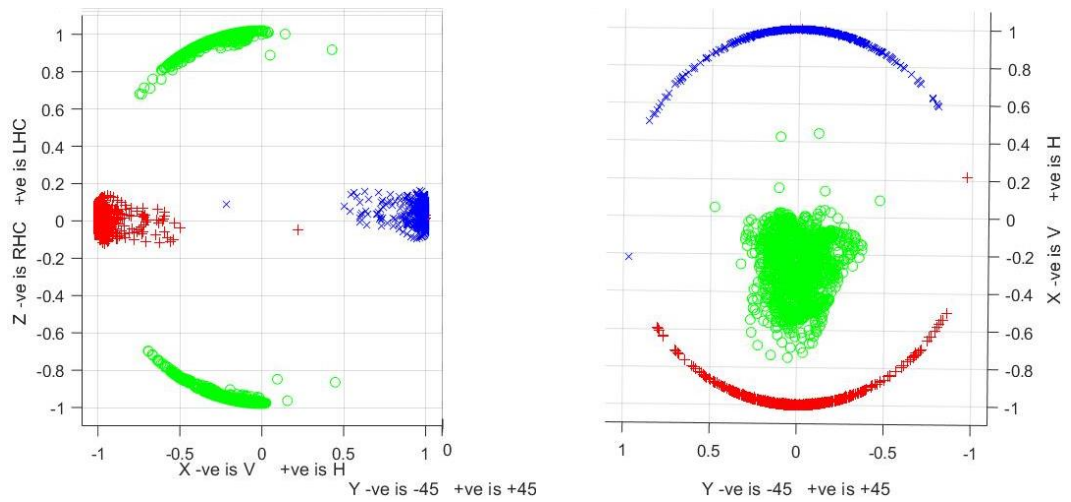


Figure 12-78 Huyen fork plot via measurement of a smartphone on its own from the -45° polarisation position (left), the zenith (right)

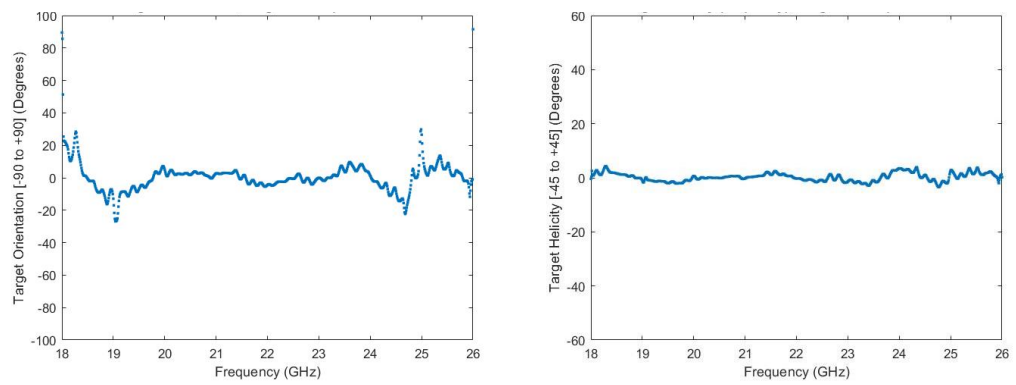


Figure 12-79 Smartphone measured orientation angle left, helicity angle right

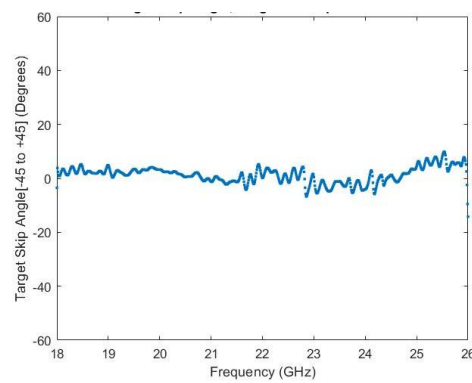


Figure 12-80 Smartphone measured skip angle left.

12.2.21 Keys

Another benign and commonly carried item is a set of keys. A typical set presented in Figure 12-81 and used in the following measurements.

Some orientation information is visible in the fork plot (Figure 12-83) and the Huynen orientation angle plots (Figure 12-84), showing a horizontal orientation's predominance due to the keys position on a flat surface. Like the dipole, the green co-polar nulls are moving toward the central prong of the fork indicated by the red cross-polar nulls (Figure 12-82 (left) and Figure 12-83 (left)).

Helical conversion is present in Figure 12-82 (left) and is caused similarly to that of the dihedral by double bounce reflection between some of the keys. This mechanism also indicated by the increase in skip angle Figure 12-85 right.

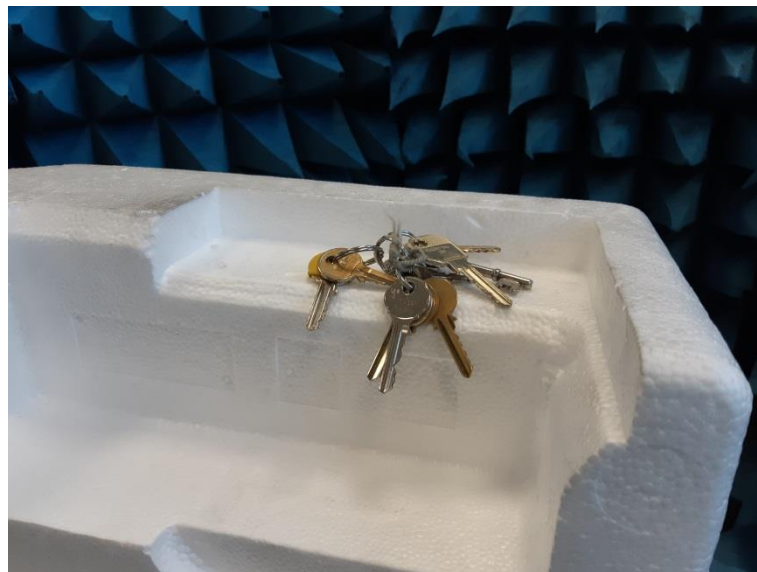


Figure 12-81 Set of keys measured on own.

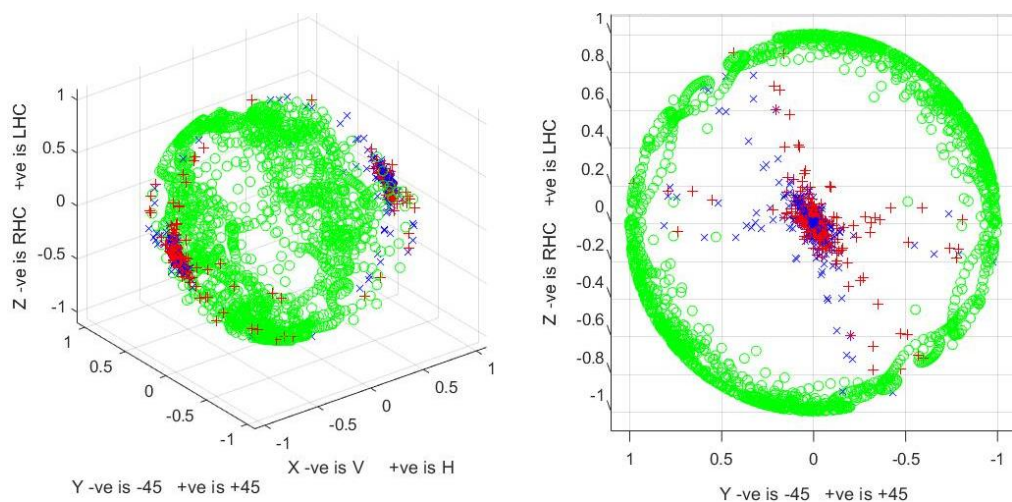


Figure 12-82 Keys fork plot via measurement, viewed from the vertical polarisation position (right)

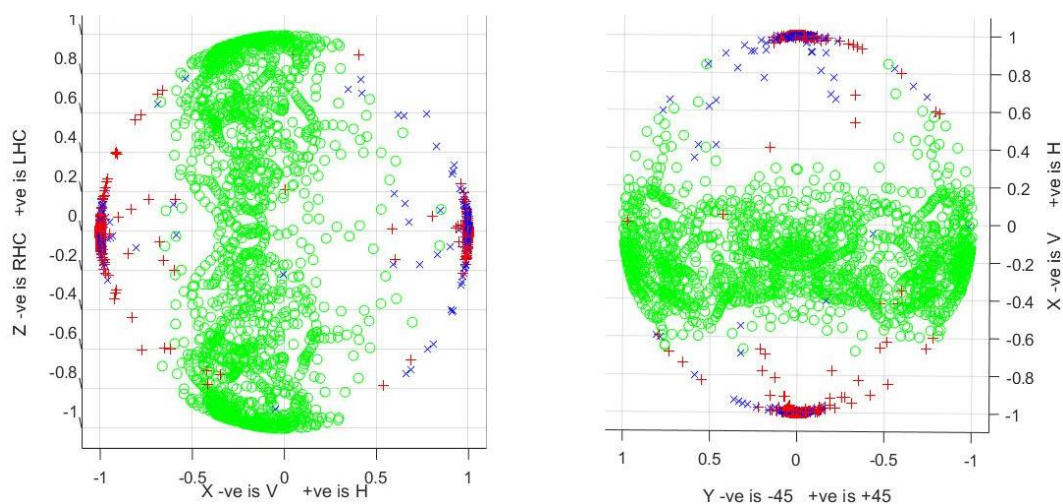


Figure 12-83 Keys fork plot via measurement viewed from the -45° polarisation position (left), from the zenith right

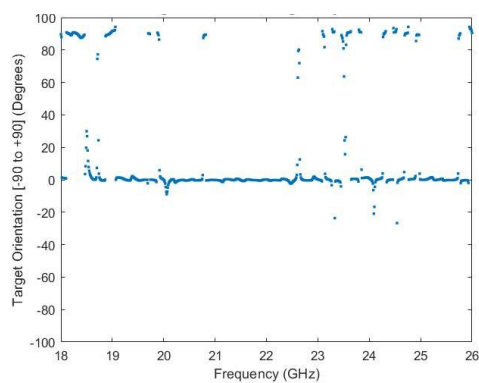


Figure 12-84 Measured orientation angle

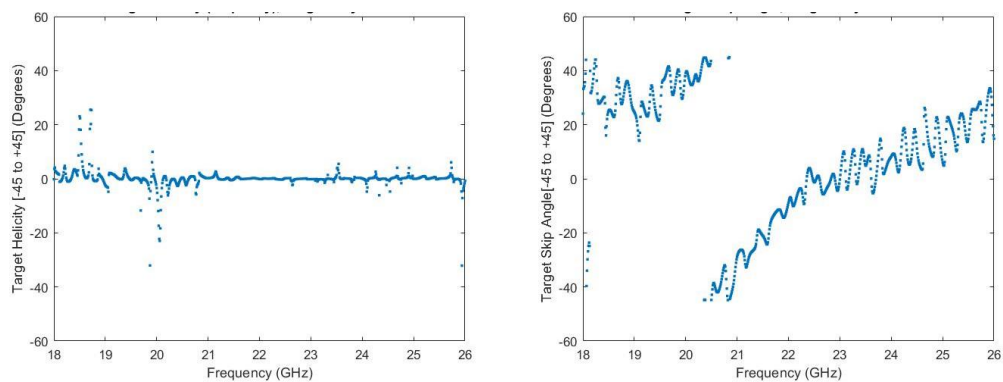


Figure 12-85 Helicity angle left, skip angle right both via measurement

12.3 Conclusion

When targets have their responses represented using the Huynen fork technique and plotted on the Poincaré sphere, the leading edge presented by an object such as a knife blade provides the orientation information.

A flat plate object such as a metal plate, wax block or the human torso with arms above head aligned perpendicular to the radars boresight tends to produce only a single bounce (co-polar) reflection with minimal conversion into helical polarisation states.

A knife perpendicular to the radars boresight with no leading-edge presented produces a Huynen fork response is similar to that of a flat plate, cross-polar nulls distributed about the equator on the Poincaré sphere with no defined orientation. A knife that presents a leading edge to the radars boresight produces a Huynen fork response with orientation information similar to the dipole. The curved edge of the blade produces helicity.

Objects that delay one linear (HV) polarisation relative to its orthogonal counterpart caused by reflection or diffraction between surfaces on the target convert the linear polarisation into helical polarisation upon reflection. This effect is evident in the gun and human torso's measurements aligned boresight with the antenna and with hands at the side.

The torso presented side on to the antenna produces a flat plate response regardless of the hand's position. However, the Huynen target size parameter shows ripples across the spectral range that measurements were taken over the spacing between peaks and troughs becoming closer with the hands at the side of the torso.

Complicated targets such as PBIED's with embed shrapnel and benign objects such as keys tend to produce a stochastic response when their responses are represented using the Huynen fork technique and plotted on the Poincaré sphere. The associated Huynen target parameters for these objects reveal that a lot of information is contained in the radiometric bandwidth that the radar operates over.

Chapter 13 H/α decomposition

13.1 Introduction

This chapter looks at the H/α signatures of the same array of targets previously analysed using the Huynen polarisation fork technique and its associated parameters.

The H/α decomposition technique developed by S. R. Cloude and E. Pottier in 1997 extracts the average target parameters based on second-order statistics. This incoherent technique is based on the eigenvector analysis of the 3 x 3 coherency matrix [T]. The eigenvectors providing information about the type of scattering taking place (Surface (Bragg), volume, double bounce) whilst the eigenvalues provide their relative magnitudes [49].

13.2 The Pauli feature vector (f_{3P})

The Pauli feature vector equation 13-1 is derived from the elements of the Sinclair matrix. The first element provides information about the targets single (odd, surface) bounce scattering the second element indicates the even bounce (dihedral) characteristics whilst the last element describes the cross polarised (diffuse) scattering [111]. (Page 1-35, equation 3.55 [53])

$$f_{3P} = \frac{1}{\sqrt{2}} [(S_{HH} + S_{VV}) \ (S_{HH} - S_{VV}) \ 2S_{HV}]^T \quad (13-1)$$

13.3 The Pauli coherency (C_{3P}) (T) matrix

The Pauli coherency matrix relates to the spatial power received from a target. The elements of this 3 x 3 matrix are composed of averages of multiple measurements denoted by the brackets $\langle \rangle$. It is formed from Pauli feature vector multiplied by its Hermitian transpose equation 13-2.

(Page 1-36, equation 3.62, [53])

$$[C_{3P}] = [T] = \langle f_{3P} \cdot f_{3P}^\dagger \rangle \quad (13-2)$$

$$[T] = \frac{1}{2} \begin{bmatrix} \langle |S_{hh} + S_{vv}|^2 \rangle & \langle (S_{hh} + S_{vv})(S_{hh} + S_{vv})^* \rangle & 2\langle (S_{hh} + S_{vv})S_{hv}^* \rangle \\ \langle (S_{hh} - S_{vv})(S_{hh} + S_{vv})^* \rangle & \langle |S_{hh} - S_{vv}|^2 \rangle & 2\langle (S_{hh} - S_{vv})S_{hv}^* \rangle \\ 2\langle S_{hv}(S_{hh} + S_{vv})^* \rangle & 2\langle S_{hv}(S_{hh} + S_{vv})^* \rangle & 4\langle |S_{hv}|^2 \rangle \end{bmatrix} \quad (13-3)$$

Equation 13-3 can be decomposed into a set of real eigenvalues ($\lambda_1, \lambda_2, \lambda_3$) and their corresponding eigenvectors (u_1, u_2, u_3) [111] leading to equation 13-4:

$$[T] = [U_3] \begin{bmatrix} \lambda_1 & 0 & 0 \\ 0 & \lambda_2 & 0 \\ 0 & 0 & \lambda_3 \end{bmatrix} [U_3]^{-1} = [u_1 \quad u_2 \quad u_3] \begin{bmatrix} \lambda_1 & 0 & 0 \\ 0 & \lambda_2 & 0 \\ 0 & 0 & \lambda_3 \end{bmatrix} [u_1 \quad u_2 \quad u_3]^{-1} \quad (13-4)$$

Where the eigenvalues are parametrized as in equation 13-5:

$$U_3 = \begin{bmatrix} \cos \alpha_1 & \cos \alpha_2 & \cos \alpha_3 \\ \sin \alpha_1 \cos \beta_1 e^{j\delta_1} & \sin \alpha_2 \cos \beta_2 e^{j\delta_2} & \sin \alpha_3 \cos \beta_3 e^{j\delta_3} \\ \sin \alpha_1 \sin \beta_1 e^{j\gamma_1} & \sin \alpha_2 \sin \beta_2 e^{j\gamma_2} & \sin \alpha_3 \sin \beta_3 e^{j\gamma_3} \end{bmatrix} \quad (13-5)$$

The Entropy (H) provides information about the degree of statistical disorder in the scattering, with values ranging from 0 for no depolarisation to 1 for complete depolarisation (please refer to Figure 13-1):

$$H = -\sum_{n=1}^{n=3} P_n \log_3(P_n) \quad (13-6)$$

The Alpha (α) anisotropy indicates the type of scattering taking place (surface, volume and double bounce reflection) with values ranging from 0° to 90° (please refer to Figure 13-1);

$$\alpha = \sum_{n=1}^{n=3} P_n \alpha_n \quad (13-7)$$

Where P_i is the probability associated with the eigenvalues λ_i of the Coherency matrix, defined as;

$$P_i = \frac{\lambda_i}{\sum_{j=1}^{j=3} \lambda_j} \quad (13-8)$$

13.4 Measurement results

The following figures represent the H/α responses of various measured targets, referring to Figure 13-1 and Table 13-1 to describe the types of scattering shown.

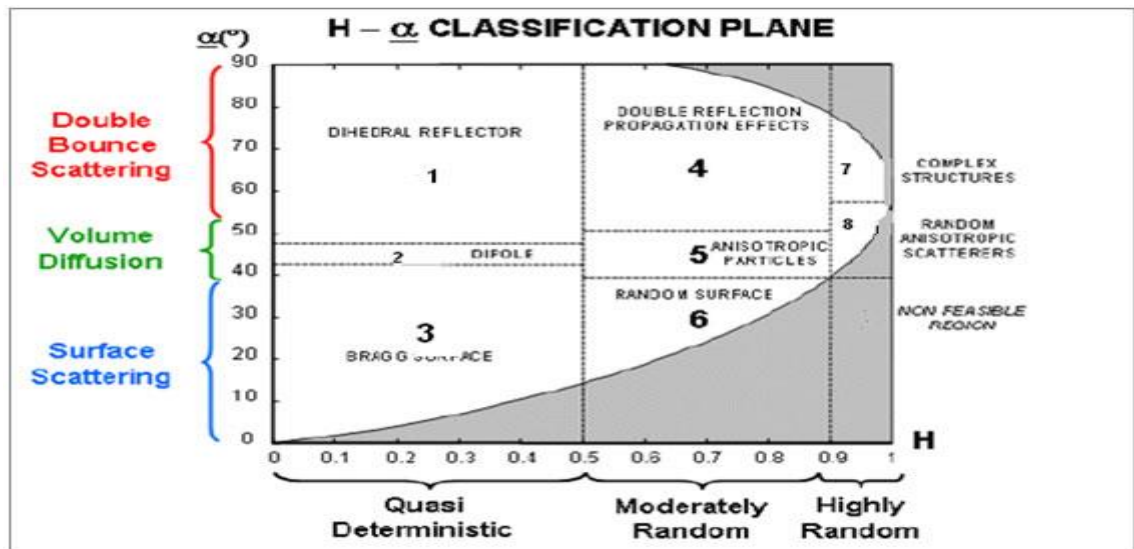


Figure 13-1 Graph showing Wishart classification [75] [76]

Class	Description	Criteria
1	Low entropy (double bounce) scattering	$\alpha > 48, H < 0.5$
2	Low entropy (dipole) scattering	$\alpha > 42 \leq 48, H \leq 0.5$
3	Low entropy (surface) scattering	$\alpha \leq 42, H = 0.5$
4	Medium entropy (multiple) scattering	$\alpha \geq 50, H = 0.5 \text{ to } 0.9$
5	Medium entropy (dipole) scattering	$\alpha \geq 40 \leq 50, H = 0.5 \text{ to } 0.9$
6	Medium entropy (surface) scattering	$\alpha \leq 40, H = 0.5 \text{ to } 0.9$
7	High entropy (double bounce) scattering	$\alpha \geq 55, H > 0.9$
8	High entropy (multi target) scattering	$\alpha \geq 40 \leq 55, H > 0.9$

Table 13-1 H/α class descriptions [75] [76].

13.4.1 Plate and Sphere

Figure 13-2 compares the flat-plate reflector with the 10.5 cm diameter sphere (top left and right) with associated H/α responses shown bottom left and right.

The anisotropy (α) is lower for the plate at between 0° and 11° , for the sphere it is between 0° and 50° , in both cases indicating that single 'odd' bounce (Bragg surface) scattering is taking place.

The plate's entropy is low at up to 0.01 but for the sphere is up to 0.15. Higher anisotropy (α) and entropy for the sphere are due to the target's slight motion during the measurements.

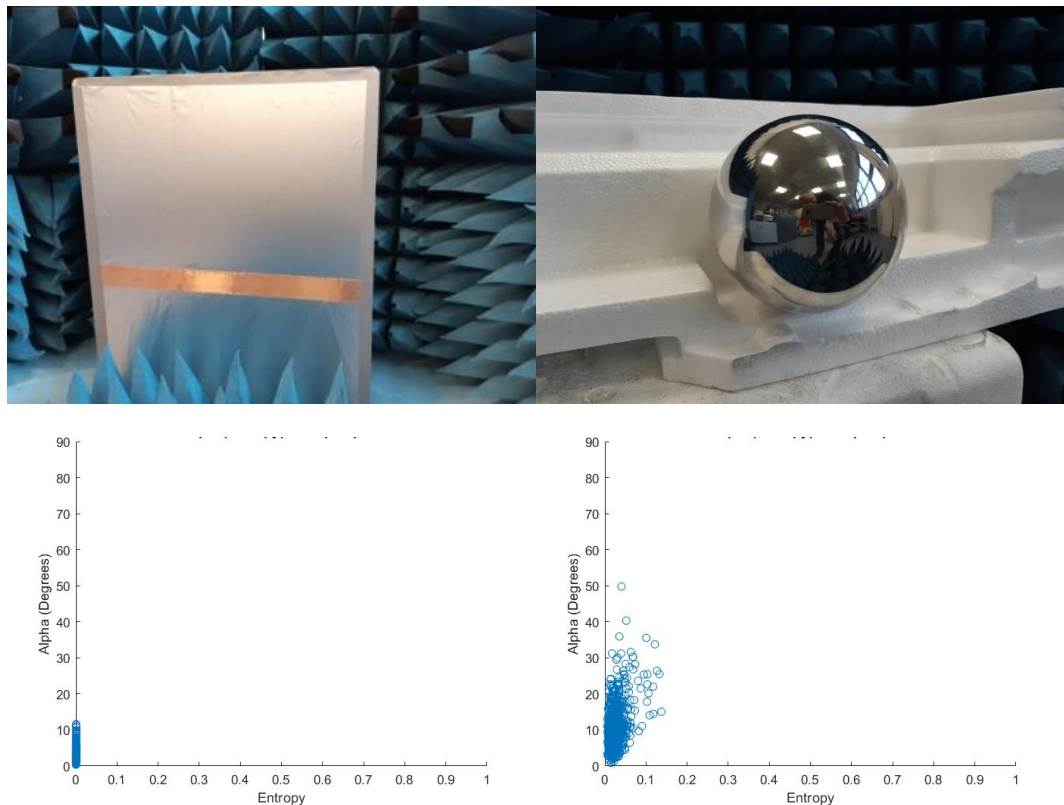


Figure 13-2 Flat Plate (left top), Sphere (top right), Flat Plate H/α response (bottom left), Sphere H/α response (bottom right) both via measurement

13.4.2 Dihedral at 45°

Figure 13-3 shows the dihedral reflector orientated at 45° to the incident beam of the radar. This double bounce reflector orientated at 45° produces polarisation state conversion for the linear polarisation states. The associated H/α plot presented on the right of the figure. From the H/α plot, the entropy is visibly low at around 0.01. The alpha angle ranges from 30° to 90° showing a predominance of double bounce scattering is taking place and some dipole scattering caused by edge effects.

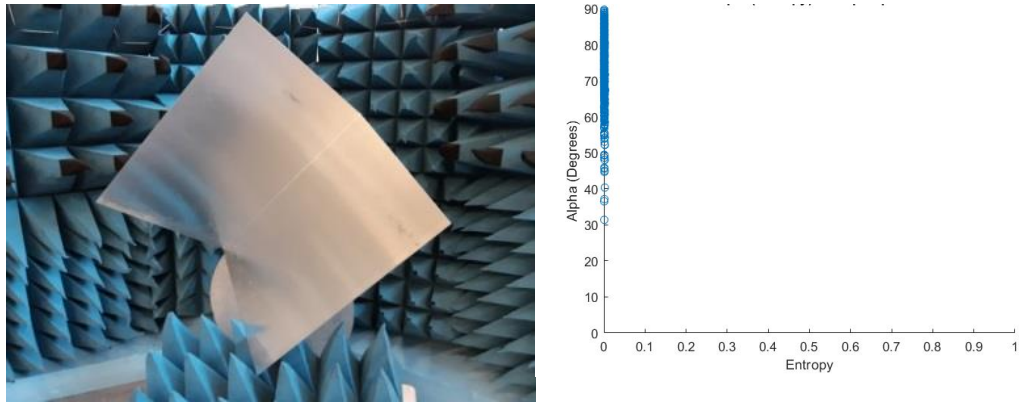


Figure 13-3 Dihedral (double bounce) at 45° (left), Measured H/ α response (right)

13.4.3 Horizontal Dipole

Figure 13-4 shows a horizontal array of thin copper wires referred to as a dipole (left in the figure) with its associated H/ α plot on the figure's right. The anisotropy (alpha) in the H/ α plot clearly shows that the scattering is that of a dipole, some surface and double bounce scattering are also visible on the plot with values ranging from 30° up to 60°. An interaction between the thin wires causes this distribution of the anisotropy (alpha) value.

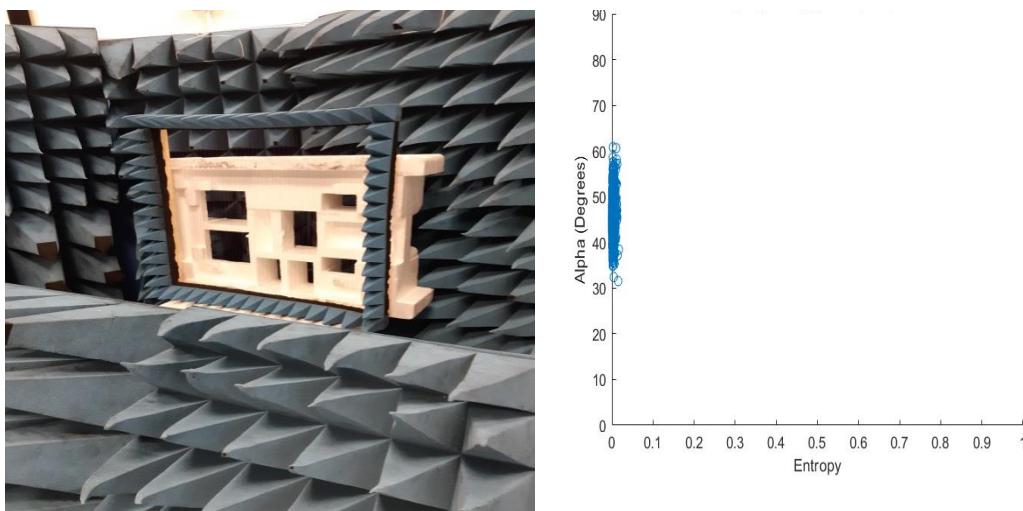


Figure 13-4 Horizontal Dipole (left), Measured H/ α response (right)

13.4.4 Wax block

Figure 13-5 and Figure 13-6 show a 3.8 cm thick wax block with a smooth burnt side and a rippled (textured) side along with associated H/ α responses. The H/ α plot for the smooth burnt side (Figure 13-5 right) has an anisotropy (alpha) ranging from 0°

to 10° , with entropy ranging from 0 to 0.03. The textured side (Figure 13-6 right) has an anisotropy (alpha) ranging from 0° to 67° , with entropy ranging from 0 to 0.53.

Both sides of the target indicate that single bounce (Bragg surface) scattering is present, the same as for the flat metal plate and sphere. The increased anisotropy (alpha) angle and entropy for the textured side are likely due to the target moving during measurements.

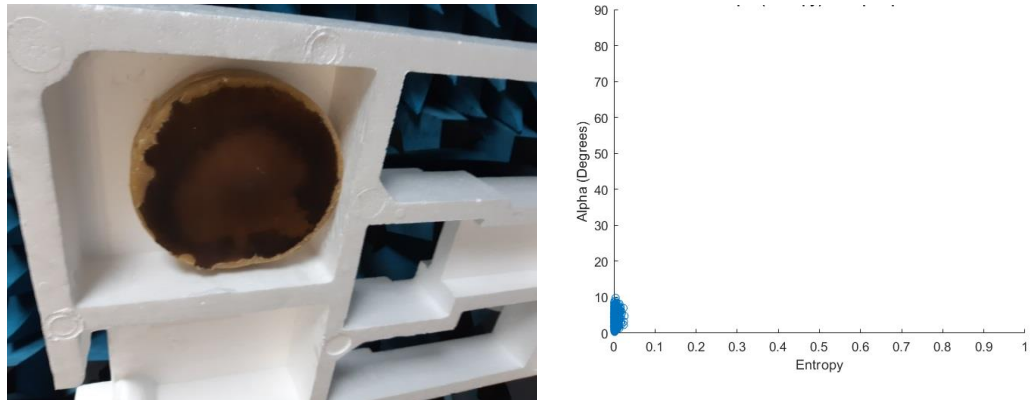


Figure 13-5 A 3.8cm thick wax block (smooth burnt side to beam) (left), measured H/α response (right)

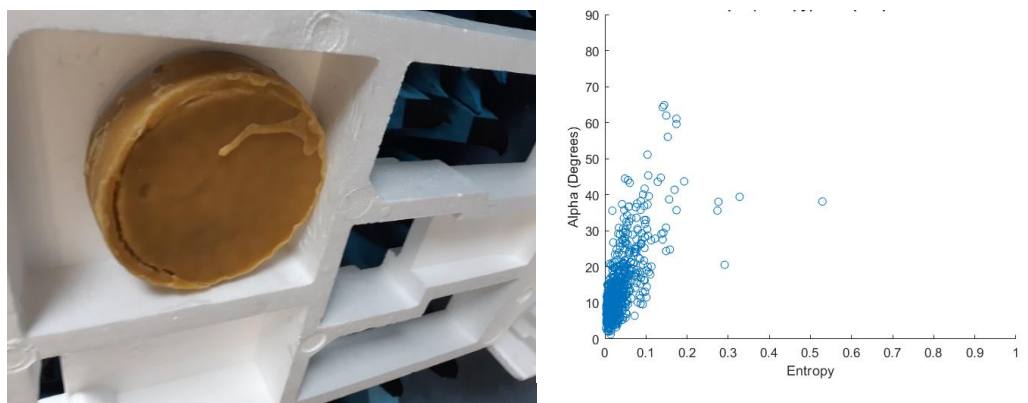


Figure 13-6 3.8cm thick wax block (textured side to beam) (left), measured H/α response (right)

13.4.5 Knife perpendicular to the radar beam

Figure 13-7 left shows a small metallised plastic knife perpendicular to the radars boresight with no leading-edge presented. Figure 13-7 right shows the targets H/α response. When aligned perpendicular to the radars boresight and with no leading-edge, the anisotropy (alpha) displayed on the H/α plot is that of a single bounce flat

plate/sphere reflector as shown in Figure 13-2. The entropy is low (0 and 0.06) due to the target being stationary.

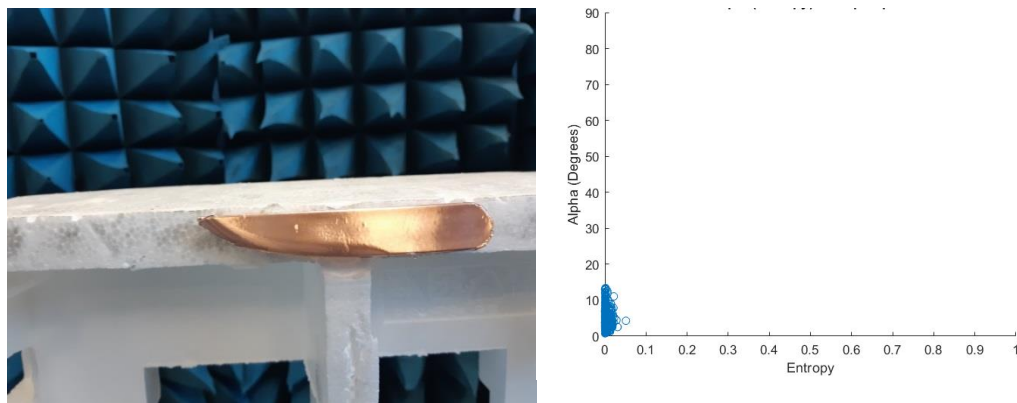


Figure 13-7 Small metallised plastic knife (left) horizontal no dominant leading-edge, measured H/α response (right)

13.4.6 Small knife at 45° blade spine leading compared to blade edge leading

Figure 13-8 shows a metallised plastic knife orientated at 45° with the leading-edge provided by the blade's spine (left) and the blade's sharp edge (right). Figure 13-9 presents the associated H/α plots.

The H/α plot with the blade's spine leading has anisotropy (alpha) ranging from 0° to 50°. With the sharp edge leading anisotropy (alpha) ranges from 0° to 75°. The entropy ranges from 0 to 0.35 for the spine leading with the sharp edge leading is from 0 to 0.45.

The higher anisotropy (alpha) for both targets is due to the leading edge producing a dipole effect. The increased entropy is due to target motion during measurement.

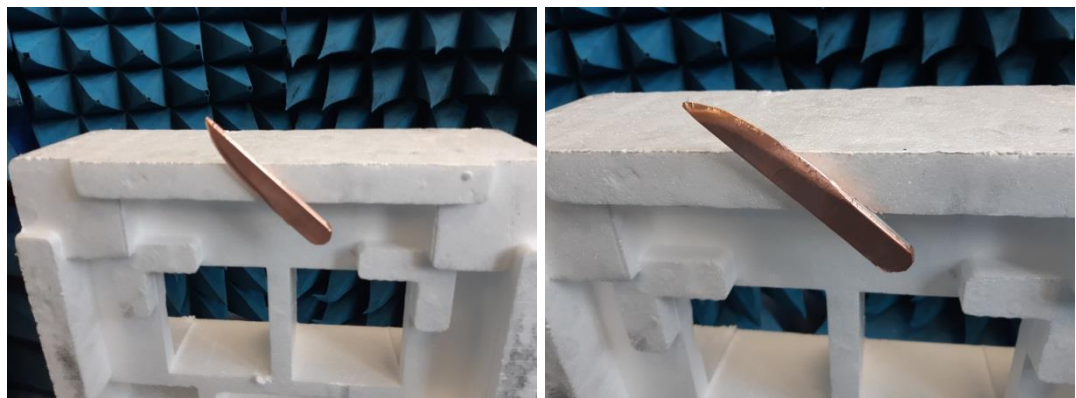


Figure 13-8 small knife at 45° spine leading left, blade edge leading right

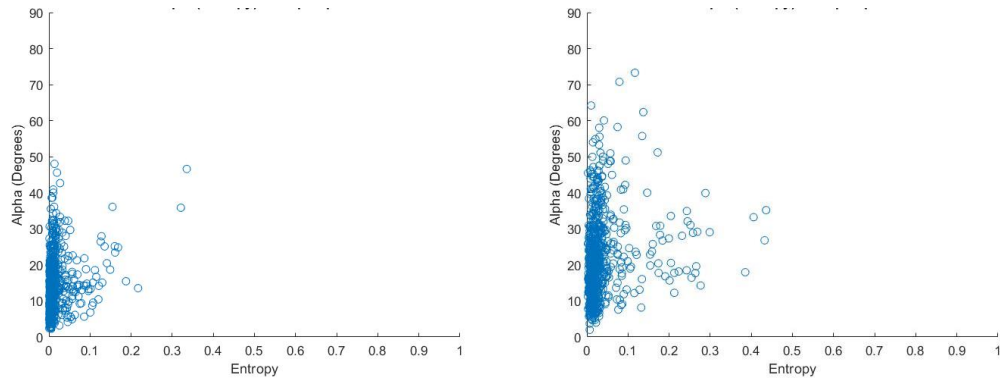


Figure 13-9 Small metallised plastic knife at 45°, blade spine presenting leading edge (left), blade edge presenting the leading edge (right), measured H/α responses

13.4.7 Long knife edge-on

Figure 13-10 shows the H/α response produced by a long knife edge-on with the sharp edge facing the radar's boresight with both vertical and horizontal orientations shown.

The H/α response for both orientations is very similar as might be expected. The alpha angle indicates that a small amount of surface scattering occurs; however, the dominant scattering mechanism is of dipole because the knife is presented edge on to the radar's boresight.

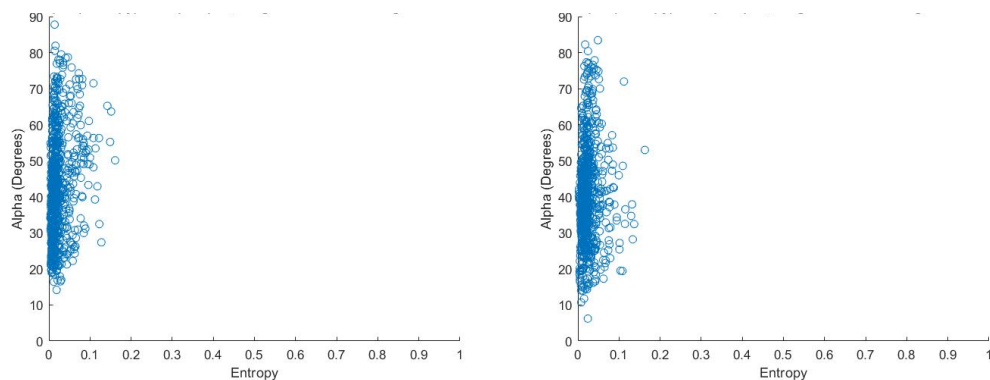


Figure 13-10 long knife edge-on, vertical left, horizontal right. Measured H/α responses

13.4.8 Horizontal and vertical Brass Gun

Figure 13-11 shows a brass gun with its barrel orientated horizontally top left and vertically top right with associated H/α plots bottom left and right. The anisotropy

(alpha) ranges from approximately 0° to 30° , as shown in both H/ α plots indicating that predominantly surface scattering occurs. The entropy is relatively low, ranging from 0 to 0.1 for both orientations.

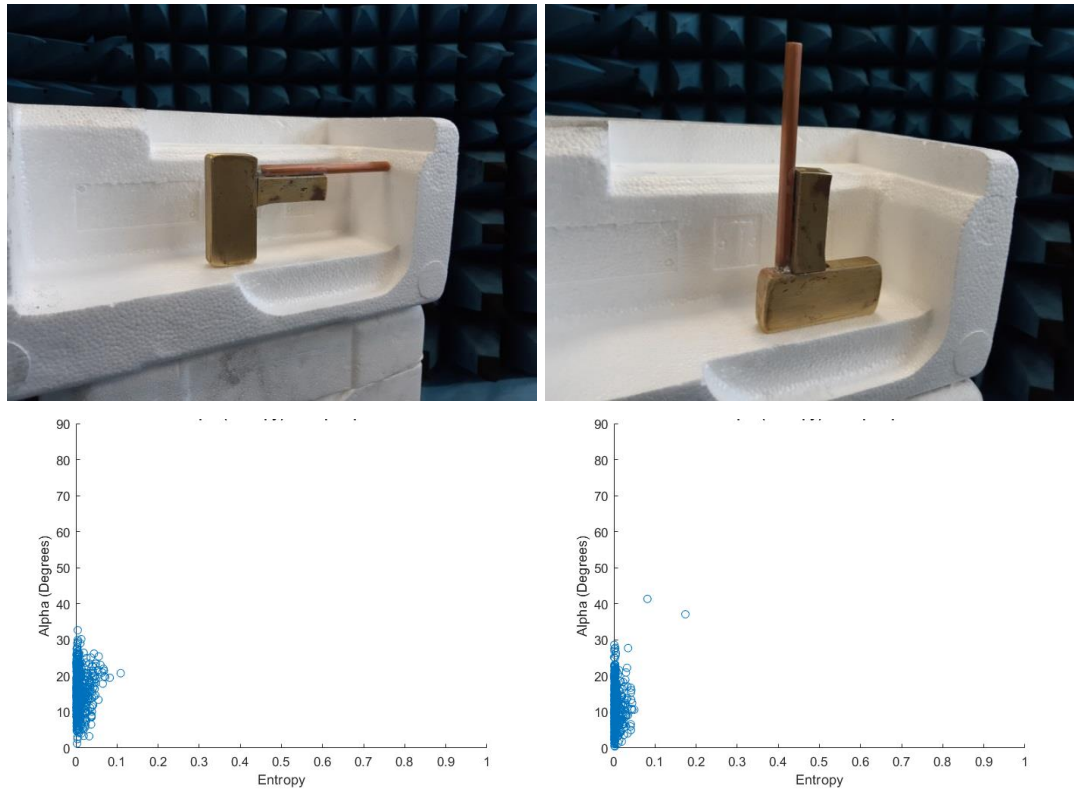


Figure 13-11 Horizontal brass gun (left), Vertical brass gun (right), Horizontal brass gun measured H/ α response (bottom left), Vertical brass gun measured H/ α response (right)

13.4.9 Brass Gun at 45°

The brass gun in Figure 13-12 has its barrel orientated at 45° (left), with its H/ α plot visible on the right. Relatively low anisotropy (alpha) between 0° and 20° indicates that the scattering mechanism is predominantly that of a flat surface with values of entropy between 0 and 0.1.

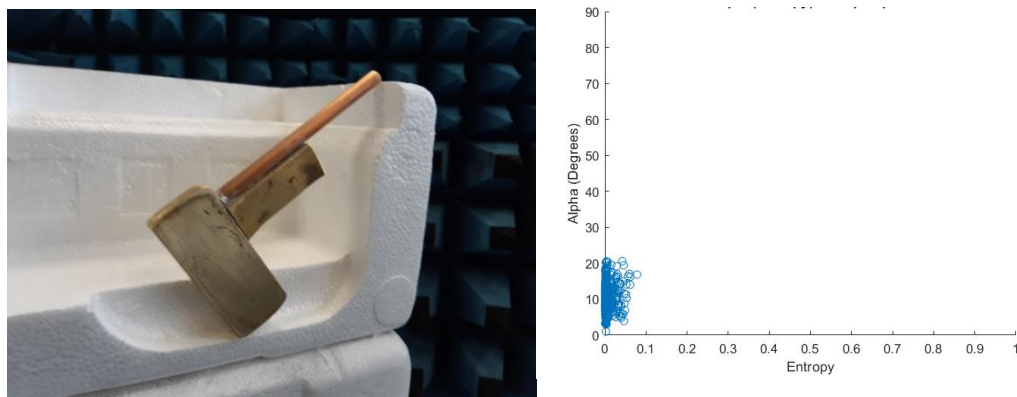


Figure 13-12 Brass gun on its own at 45° (left), measured H/ α response (right)

13.4.10 Human torso with hands above head

Figure 13-13 shows the response of the torso's of two individual's perpendicular to the radar's boresight with arms and hands above the head. The H/α response of the first individual presented in the left of the figure whilst the second individual is on the right. The values of anisotropy (alpha) for both responses are very similar, ranging from 5° to 30° and behaving predominantly as a surface reflector including a small amount of random surface scattering. The entropy is higher at 0.15 to 0.6 due to breathing and involuntary motion. Movement of the chest caused by breathing is taking place in the radars range dimension, affecting the phase of the reflected response.

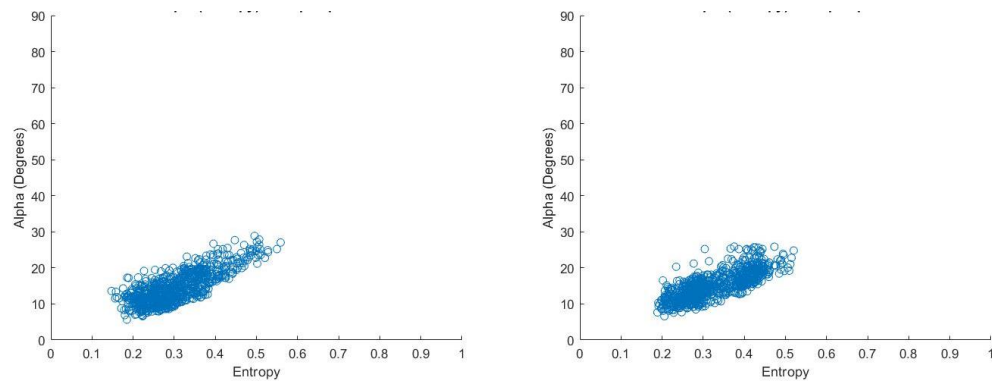


Figure 13-13 Subject 1 (Left), Subject 2 (right) torso on its own perpendicular to beam hands above head measured H/α responses

13.4.11 Human torso with hands at the side

Figure 13-14 shows the H/α responses of the same two individuals presented in the previous measurement, however this time with arms and hands at the side.

The H/α plot shown is very similar to that of the torso with the arms and hands above the head with the anisotropy (alpha) indicating a predominantly surface and a small amount of random surface scattering. The distribution of points is now more scattered with increased levels of entropy. The increase in entropy again effected by the motion of the chest due to breathing.

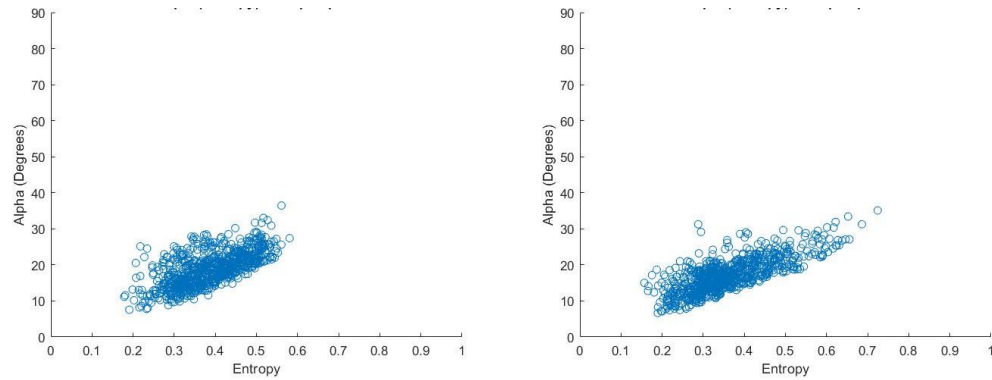


Figure 13-14 Subject 1 (Left), Subject 2 (right) torso on its own perpendicular to beam hands at side measured H/ α responses

13.4.12 Human torso presented side on to the beam of the radar with hands above head

Figure 13-15 shows the H/ α responses of both subjects, with their sides facing the radar, hands are above the head.

The anisotropy (alpha) ranges from around 5° to 20° and the entropy from 0.2 to 0.46 for subject 1, and from 0.1 to 0.36 for subject 2.

Entropy is lower for the measurements taken with the torso side facing the radar than the torso perpendicular. This effect is because the chest movement varies in the radars cross-range dimension for the side-on orientation, compared to the torso perpendicular where chest movement is in the range dimension and has a much larger effect on the phase.

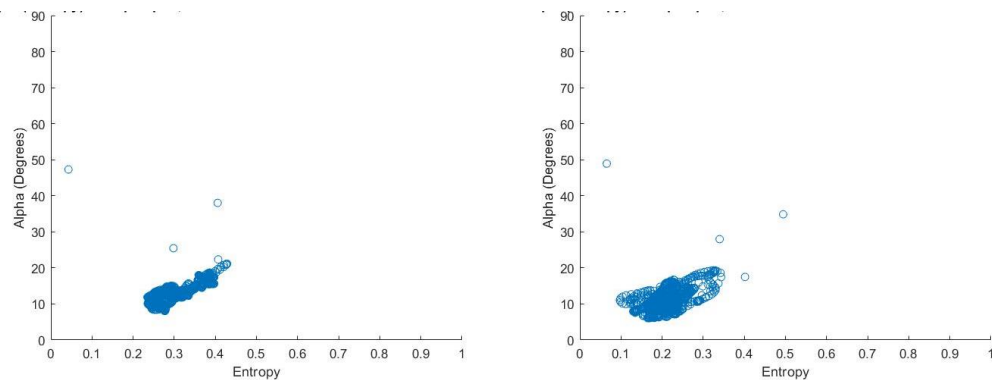


Figure 13-15 Subject 1 side on hands above head left, hands at side right measured H/ α responses

13.4.13 Small knife located on the human torso (hands above head)

Figure 13-16 shows a small metallised plastic knife on the torso of subject 1 in both vertical and horizontal orientations. The subject had hands above the head during the measurements. The anisotropy (α) shown in the H/α responses of Figure 13-17 range from 10° to 30° for vertical and 10° to 40° for horizontal orientations, both indicate surface scattering but with increased levels of random scattering compared to the torso on its own. The entropy ranges from 0.2 to 0.55 for subject 1 and 0.2 to 0.7.



Figure 13-16 Short knife on the human torso vertical left, horizontal right

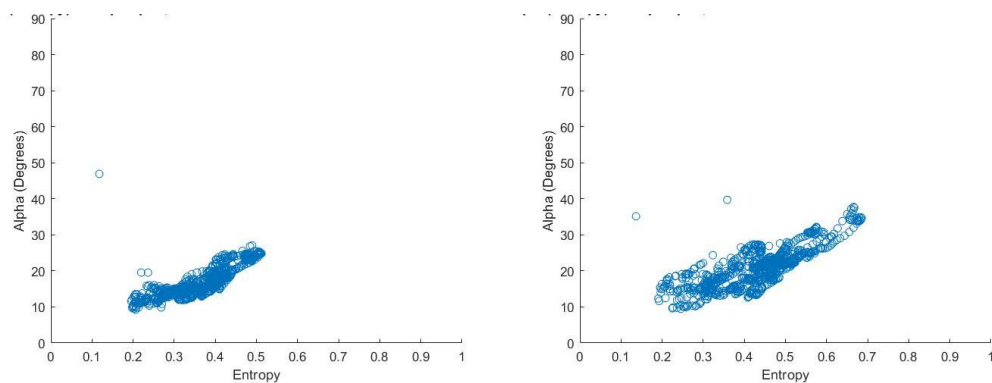


Figure 13-17 Measured H/α response for a small metallised plastic knife against the human torso (subject 1). Vertical orientation left, horizontal right

13.4.14 Long knife located on the human torso

The following plots show a comparison of a long knife orientated horizontally on the torso facing the radar with hands located at the torso side for one measurement and hands above the head for the other.

Figure 13-18 shows the H/α responses for the horizontal knife on the torso with hands above head on the left of the figure and hands at the side on the right.

The anisotropy (alpha) is low for both plots ranging from 2° to 20° indicating that only surface scattering is taking place, meaning that the knife has no leading-edge present due to the lack of dipole scattering. The entropy is higher than for the same knife on its own, ranging from 0.1 to 0.3 due to torso motion.

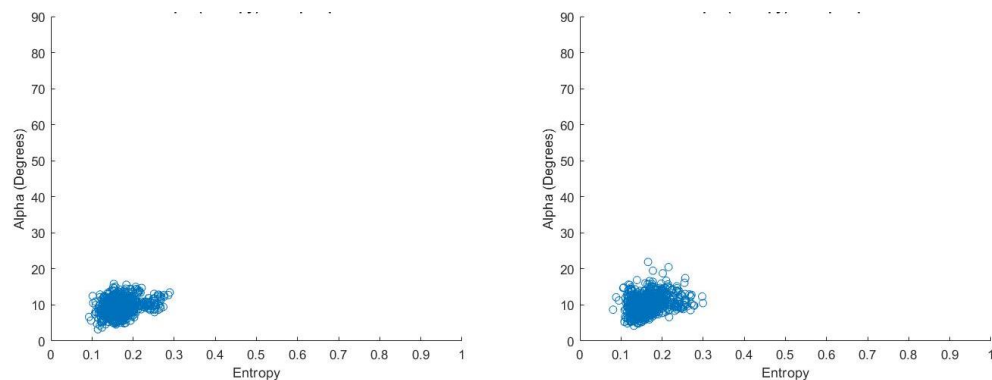


Figure 13-18 Subject 1 with a long horizontal knife on torso hands above head (left), hands at the side (right) measured H/α responses

Figure 13-19 presents the same measurement; however, this time, the knife is orientated vertically on the torso.

The dominant scattering mechanism is again that of a flat surface. The anisotropy (alpha) angle ranges from 5° to 25°, slightly higher than when the knife was orientated horizontally. For this measurement, the knife presented a leading edge to the radars boresight, entropy for this measurement ranging from 0.2 to 0.4.

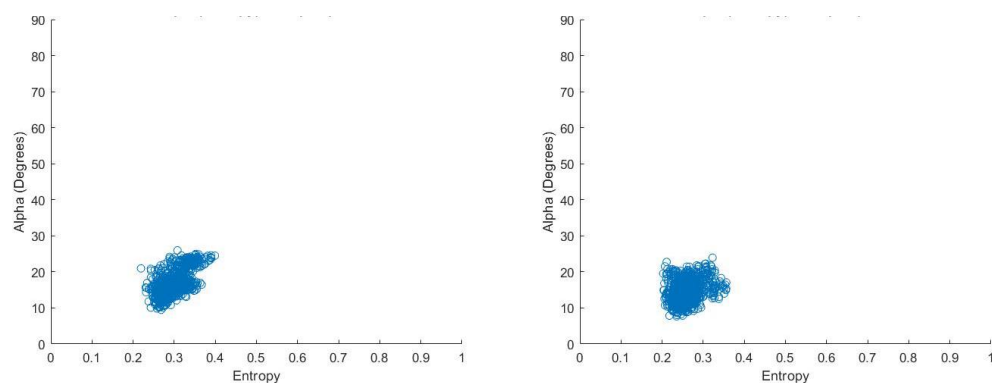


Figure 13-19 Subject 1 with a long vertical knife on torso hands above head (left), hands at the side (right) measured H/α responses

13.4.15 Gun on the human torso

Figure 13-20 shows subject 1 with a gun with a vertical barrel (left) and horizontal barrel (right). Figure 13-21 shows the associated H/ α response for each orientation.

The anisotropy (α) indicates that the dominant scattering mechanism is that of the surface type but with some random surface scattering, with values from 10° to 35° for both orientations. Entropy is ranging from 0.2 to around 0.6 for both orientations.

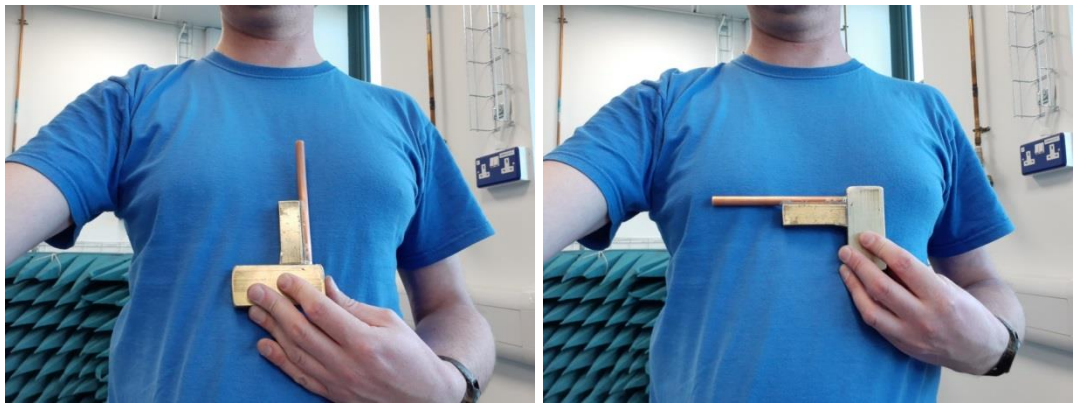


Figure 13-20 Human torso with a vertical brass gun left, horizontal right.

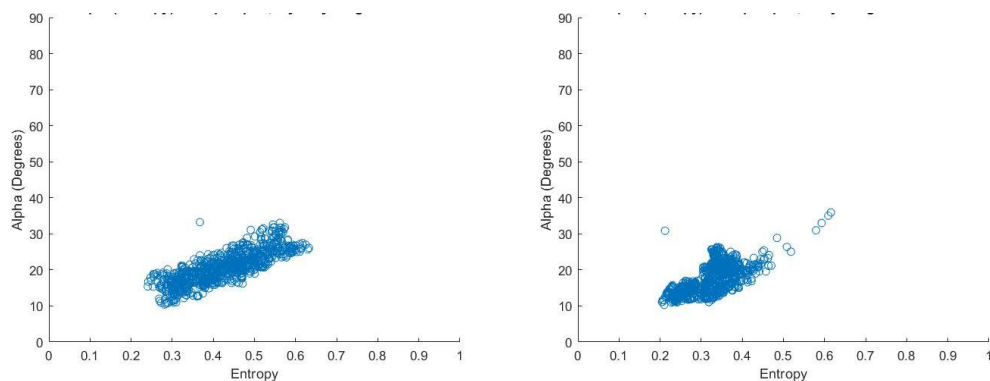


Figure 13-21 Human torso with vertical gun left, horizontal right measured H/ α responses.

13.4.16 Shrapnel target (located on and off the torso)

Figure 13-22 shows a shrapnel target (left) and its associated H/ α response on the right. The anisotropy (α) ranges from 10° to 90° indicating that plane (surface, dipole and dihedral) scattering occurs. Entropy is ranging from 0 to 0.03.

Figure 13-23 shows the shrapnel target placed against the torso of subject 2 (left) and held 40cm in front of subject 2's torso (right). The shrapnel against the torso

has anisotropy (alpha) ranging from 10° to 46° and an entropy ranging from 0.3 to 0.8. The scattering mechanisms in this configuration produce plane and random (surface) and anisotropic particle scattering.

Shrapnel held 40cm away from the torso has anisotropy (alpha) ranging from 25° to 70° and an entropy ranging from 0.3 to 0.9. The scattering mechanisms for this configuration produce plane and random (surface), anisotropic particle scattering, and double reflection propagation effects.

Figure 13-24 shows the shrapnel target placed on the torso of subject 2, who rotated their body from left to right whilst measurements were taking place. The anisotropy (alpha) ranges from 30° to 60° and entropy from 0.4 to 1. Indicating that plane and random surface scattering, anisotropic particle, random anisotropic and double reflection propagation effects occur.

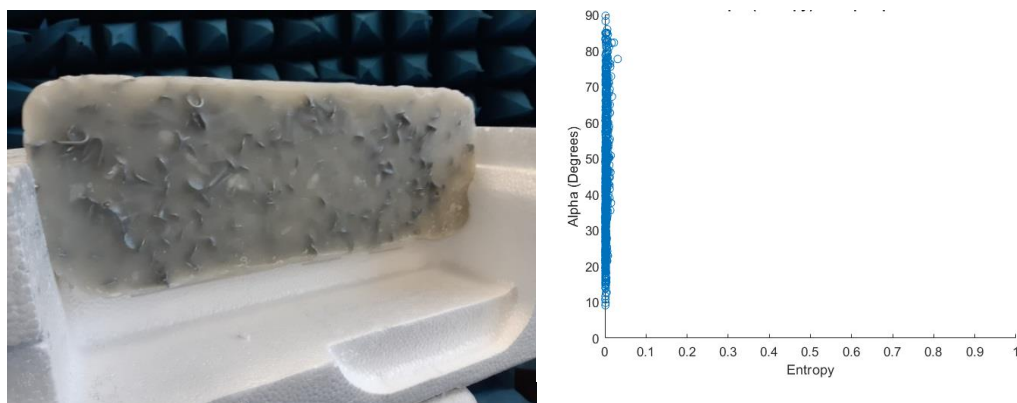


Figure 13-22 Horizontal Shrapnel target (left), measured H/α response (right)

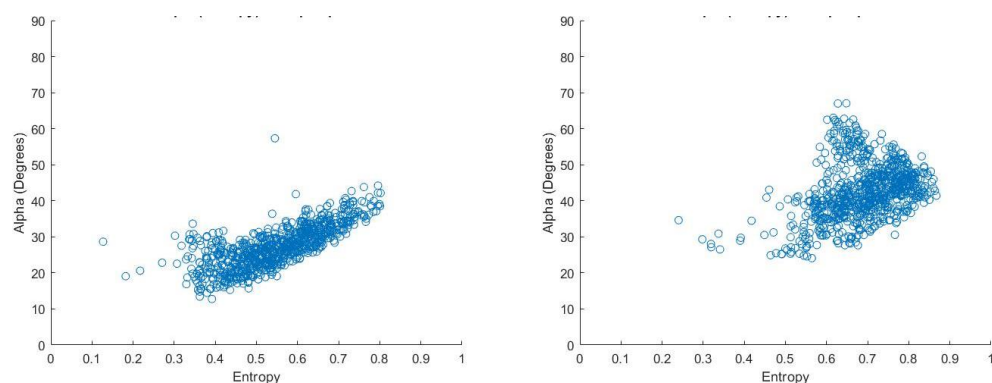


Figure 13-23 Horizontal shrapnel on subject 2 (left), Horizontal shrapnel 40cm in front of subject 2, measured H/α responses

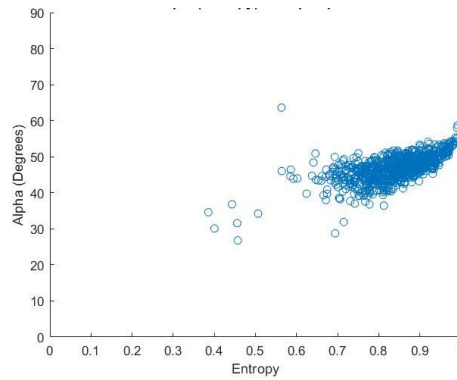


Figure 13-24 Horizontal shrapnel on subject 2 torso whilst torso rotating from left to right, measured H/ α response

13.4.17 Smartphone

Figure 13-25 shows a mobile phone (left) and its H/ α plot on the figure's right. The anisotropy (α) ranges from 0° to 65°, entropy from 0 to 0.25. It indicates that a predominance of surface scattering occurs but with some dipole and dihedral scattering taking place. The dipole scattering and dihedral scattering are caused by the wires built into the phone's touchscreen display. The increase in entropy is due to target motion during measurement.

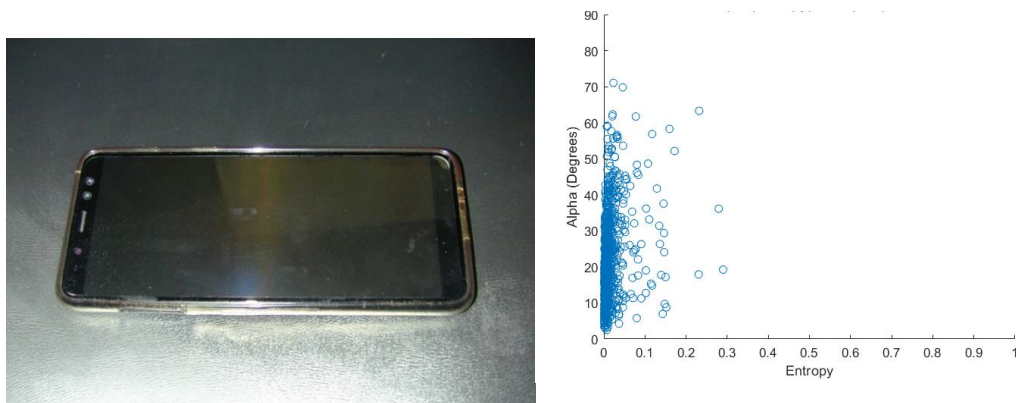


Figure 13-25 Smartphone on own (left), measured H/ α response (right)

13.4.18 Keys

Figure 13-26 shows a set of keys (left) along with its H/ α plot right. This target is composed of keys with random sizes and orientations. The anisotropy (α) ranges from 0° to 90° and entropy from 0 to 0.5 indicating plane (surface), dipole and dihedral scattering.

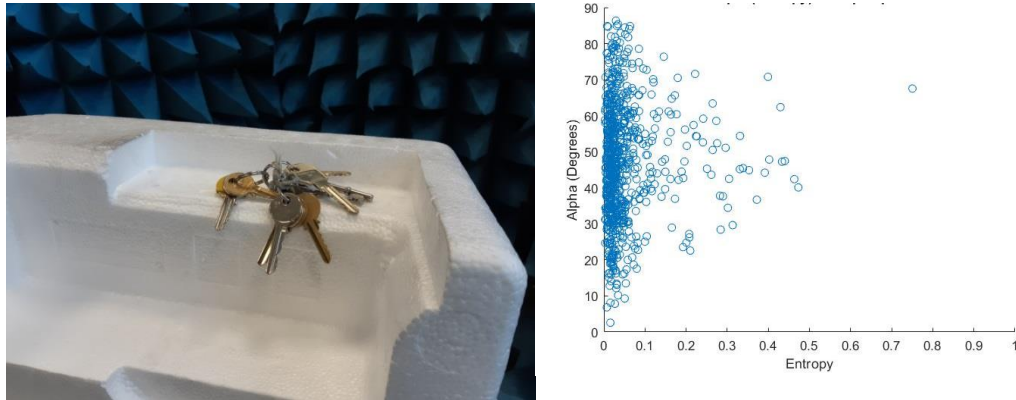


Figure 13-26 Keys on own (left), measured H/ α response (right)

13.5 Conclusion

The H/ α decomposition technique provides a role invariant method for extracting the key scattering mechanisms produced by targets.

Static targets with no leading edges presented to the boresight of the radar produce surface (Bragg) scattering the plate and sphere being classic examples. However, in this chapter, it has been shown that targets such as a knife, a wax block, gun, a smartphone and even the human torso when presented perpendicular to the radar's boresight also tend to produce surface scattering.

Measurements presented of an array of thin wires referred to as the dipole shows a predominance of dipole scattering on the H/ α plot. However, some dihedral (double bounce) scattering noted caused by reflection between the wires, and some surface scattering is also present. The smartphone produced predominantly surface scattering, but the array of fine conducting wires forming the touch screen added a dipole component to the response.

Targets that present a leading edge to the radar's boresight tend to produce plane (surface) scattering but with increased dipole scattering levels. The dipole response of the knife increases, as the knife is presented edge on to the radar.

Measurements of a shrapnel target on its own tended to produce surface, dipole and dihedral scattering. The surface scattering is coming from the wax block's surface, dipole scattering from the orientation of an edge on the wax block.

Measurements of the human torso showed that it produces a predominance of surface scattering. The entropy was always higher than for static targets due to the target's involuntary movement during measurement, including breathing.

The entropy was higher when the torso was perpendicular to the radar's boresight because breathing moves the chest in the range dimension affecting phase.

Torso presented side on produced lower entropy because the chest movement due to breathing is now taking place in the radars cross-range dimension, which has a much smaller effect on the reflected wavefront phase.

All targets presented against the human torso exhibited increased entropy levels compared to the targets measured on their own, increasing entropy caused by torso movement.

Both knife and gun produce predominantly surface scattering when measured on their own, this still found to be the case when located on the torso, but the entropy increased due to torso motion.

The shrapnel target on its own exhibited low entropy levels ranging from 0 to 0.03, producing surface, dipole and dihedral scattering.

The same target placed on the body caused entropy to increase to between 0.3 to 0.8. The scattering mechanisms changed to plane and random (surface) and anisotropic particle scattering.

The shrapnel 40cm away from the torso produced entropy ranging from 0.3 to 0.9. The scattering became plane and random (surface), anisotropic particle scattering, and double reflection propagation effects.

The shrapnel target placed against the torso rotating in the radar beam produced an entropy increase ranging from 0.4 to 1. The scattering mechanisms became plane and random surface scattering, anisotropic particle, random anisotropic and double reflection propagation effects.

With shrapnel on it, the torso caused entropy to increase significantly due to involuntary torso motion, including breathing, the scattering mechanisms becoming increasingly random as torso motion increases.

The keys had entropy ranging from 0 to 0.5 with scattering mechanisms of a plane (surface), dipole and dihedral scattering. Dipole scattering caused by an edge of the wax block, dihedral scattering caused by reflection between fragments.

Some of the targets measured on their own produced unexpected increased entropy levels due to decaying simple harmonic motion of the target on its stand during the measurement. The wax block's textured side also showed an increase in entropy, which might be partly due to volumetric scattering from the targets rough surface.

Chapter 14 Conclusion and Future Work

14.1 Conclusion

Potential threats carried by individuals tend to have a smaller physical size than that of the diffraction-limited beam size of a radar's antenna (λ/D), where D is the aperture size. For an imaging sensor, this constitutes a single-pixel making spatial information challenging to obtain; therefore, an alternative approach is required. Two such options are to increase the bandwidth of the radar and to use full polarimetry.

Increase in bandwidth is obtainable using a narrow pulse in the case of the pulsed radar. The FMCW radar and stepped frequency radar can be designed to operate over a larger bandwidth by operating at higher frequencies. However, there are limitations here, particularly when moving above 300 GHz, as increased atmospheric attenuation and scattering from clothing tends to reduce the magnitude of radar reflections.

Full polarimetric techniques where both the phase and amplitude are measured for the co and cross-polar reflections from targets enable the population of the elements of the (2x2) Sinclair scattering matrix. This technique provides the maximum amount of polarimetric information about a target. In a monostatic configuration, the measured Sinclair matrix contains five separate pieces of information about the target. The cross-polar elements $S_{HV} = S_{VH}$ are identical with the sixth piece of information being the phase (effectively the target range). The combination of VNA, OMT and horn antenna enables the extraction of the full polarimetric signature.

The radar presented in this thesis when un-calibrated produces sets of measured (observed) matrices that contain both target-related information and corruptive distortions created by the OMT, horn antenna and VNA. These components all have unwanted levels of cross-polarisation and phase difference between channels. This corruption takes place both on the radar's transmission and reception cycles. These corruptions require removal to enable extraction of the target Sinclair matrices; effectively, the system needs a calibration. Calibration comprises two parts, the internal calibration of the VNA (to the ends of the coaxial cables to the OMT) and the external calibration (of the OMT and the antenna).

Several techniques are available for the VNA internal calibration. The standard through reflect line (TRL) calibration technique for the application presented produced good results.

For the assembled radar's external calibration, evaluation of the basic deconvolution calibration compared well with that of the more complicated Papathanassiou and Kimura technique. This similarity is likely due to the very low levels of system cross-polarisation (<30dB) enabling simplification of the scattering vector distortion matrix [Z] used by the Papathanassiou and Kimura technique.

Radar calibration occurs via measurement of canonical targets, these comprising a flat metal plate for the co-polar correction and a dihedral at 45° for the cross-polar correction. All measured target responses have the measured background of microwave absorber subtracted from them, to remove the effects of internal reflections produced within the OMT, horn antenna and from objects that are not part of the target. All measurements are taken in the frequency domain.

All radar measurement scenarios contain clutter, which proved to be the case for the lab-based measurements presented. Clutter removal occurs before calibration by converting the measured response into the time domain and applying time (i.e. range) gating using a simple rectangular window centred at the point of the target location. Conversion back to the frequency domain was then applied as target decomposition takes place in the frequency domain. Clutter if unremoved masks the response of the target.

The target decomposition theorem's application enables a target to be broken down into a set of simpler parameters representing aspects of a target's shape and size and aid classification. Target decomposition primarily developed by and for the remote sensing community can be either coherent or incoherent. Coherent decompositions work directly on the Sinclair matrix and are useful when the Sinclair matrix does not change between measurements. When the Sinclair matrix changes between measurements, perhaps due to movement, an incoherent decomposition is required. This interaction between the target and its environment is depolarisation and could also be a manifestation of speckle. Target information can be recovered using the coherency, covariance or Kennaugh matrices, as these matrices are related to target's physical properties, including depolarisation. In the presence of depolarisation, the Huynen fork can be retrieved using the phase-amplitude matrix. This matrix derived from the Coherency matrix's dominant eigenvalues and eigenvectors (chapters 11 and 12).

The stepped frequency radar presented took an appreciable amount of time to make measurements, not a problem when measuring static targets. However, any target motion led to notable levels of depolarisation. Huynen target parameters and the

fork could still be recovered using the coherency matrix. Target motion taking place in the radar's range dimension produced increased depolarisation levels, cross-range motion did not cause an issue.

Static measurements of some targets took place with the target resting on a piece of polystyrene. Some of the measurements produced an unexpected increase in entropy subsequently found to be caused by the polystyrene stand's simple harmonic motion as it settled after being adjusted. Additionally, the polystyrene stand will have produced a small amount of surface reflection appearing as clutter in the measurements. Careful choice of target stand material and application needs to be researched before taking further measurements.

The Huynen target size parameter revealed the thickness of a block of beeswax calculated from cavity fringing produced by reflection from the block's front and back surfaces along with the reduction in propagation velocity in the wax. This parameter could be a useful metric for the detection of high energy nitrogen-based explosives. Measurement of a paraffin wax block containing shrapnel produced cavity fringing in the same way; however, the thickness calculated from the fringing came out larger than the block's physical measurement. Most likely caused by an increase in the blocks refractive index due to the metal fragments. Cavity fringing measurements using the Huynen target size provides a possible method to detect PBIED's and shrapnel devices in a security screening scenario. The smooth surface of the block of beeswax produced a Huynen fork and H/α plot the same as that of a plane reflector. If the surface texture of the block facing the radar is rough, then the fork plot is chaotic with large variations of the Huynen parameter's with frequency, the entropy of the H/α remained low. Shrapnel particles in a wax block cause an increase in the Huynen helicity parameter and visible on the fork plot. The wax block placed on the human torso produced periodic variations in the Huynen target size caused by cavity fringing. The entropy increased significantly due to torso motion. The human torso with any target placed against it dominates the response.

The human torso represents unwanted clutter making detection of concealed weapons and PBIED's more complicated. The torso on its own produces a single bounce reflection. However, with arms at the side produces a double bounce reflection when the torso is perpendicular to the radar's boresight creating a helical conversion in the Huynen fork plots presented in chapter 12. It might be possible for these signatures to be subtracted from measurements made of individuals carrying concealed weapons, leaving the weapon's signature on its own.

Simulations of canonical targets closely matched that of the measured. More complicated targets, including that of the human torso, could be simulated by combining these simple targets. It would be advantageous to develop simulations as a low-cost method to assess complex target responses without expensive radar test equipment.

The torso perpendicular to the radar's boresight produced depolarisation. This effect manifested itself as an increase in entropy caused by the chest's motion due to breathing which occurred in the range dimension; this effect was less prevalent when the torso was aligned side on to the boresight.

The curved edge of a knife blade always caused an increase in the Huynen helicity parameter regardless of the knife's orientation. Side on and perpendicular to the radar's boresight the knife behaves like a plane reflector for both the Huynen and H/α decompositions. The knife, edge on acts as a dipole again visible using both Huynen and H/α .

The monostatic radar using full polarimetric techniques has the potential to provide the maximum amount of target-related information compared to that of passive systems and radar using single polarisation. Further work is required.

14.2 Future work

It would be advantageous to develop further a radar of the type presented in this thesis. Measurement speed produced one limitation as even the slightest target movement led to depolarisation. The VNA is not representative of the data gathering speed of FMCW radars, which can sweep over a radiation bandwidth of several GHz at the rate of milliseconds rather than seconds. Further work needs to be carried out to speed up measurements.

The radar development to work at higher frequency would benefit range resolution and beam size with attenuation constraint from the atmosphere and clothing. A narrower beam size would enable illumination of just the torso and reduce the arm's effects on the measurements.

Characterisation of threat devices measured on their own needs performing to ascertain key signatures. The work presented in this thesis has demonstrated that a knife blade always produces a helical response using the Huynen fork decomposition regardless of the blade orientation. Other targets are likely to have similar repeatable characteristics, and these might be subtle but significant to aid

detection. The human torso needs characterising in the same way but to assist the subtraction of its response from the torso carrying a threat device leaving just the threat device's response.

Further work into the development of simulations as a tool to simulate more complicated targets is required. Simulations have the potential to provide a low-cost approach to assessing the response of a threat device concealed on an individual. Complicated targets can be simulated via the combination of canonical targets such as the plate, dipole and dihedral.

Each decomposition produces its own set of unique parameters with some overlap between types. Further work is required to ascertain each decomposition's relative merits for the detection of each target type. One decomposition might be more suited to detect a knife, and another might be better at identifying a firearm.

Machine learning techniques would potentially offer a faster route to target identification. Use of the receiver operating characteristics would be an excellent method to assess the performance.

A summary of future work is listed below;

- Further measurements of threat devices in different orientations are required to assess characteristic polarimetric signatures that uniquely define them.
- Further measurements of the human body would be advantageous to reference its full polarimetric signature and remove its response from measurements made where targets are present.
- Development of a similar radar type operating at higher frequencies needs to be investigated. Working at a higher frequency would enable a narrower beam to be realised for a given aperture size. However, care would need to be taken to avoid the increased attenuation produced by clothing and the atmosphere at higher frequencies.
- Develop a radar with a narrower, pencil-like beam to reduce the arm's effects when measuring the torso. A narrow pencil beam could facilitate the scanning of sectors of the human body to reduce this.
- An investigation into removing the human body's signature from measurements made with threat targets placed on the body (the body representing clutter) needs to be performed; further processing is then required to remove the human torso's response leaving just the target's response.

- Further work is required to investigate simulation's application to see if targets can be simulated via a composite of canonical targets, reducing time and costs.
- Further evaluation and comparison of decomposition techniques are required to assess each type's relative merits and determine suitability for concealed weapons detection.
- Application of more than one decomposition technique would be advantageous. Each decomposition provides a set of phenomenological parameters relating to aspects of the target. Some parameters are the same between different decomposition types, so careful decomposition choice would need to be made to reduce this parameter overlap.
- An investigation into the application of machine learning is required to aid target detection and to enable identification automation, whilst protecting public privacy and providing a more rapid response to security officers.

Chapter 15 Bibliography

- [1] "Institute for Economics and Peace.," [Online]. Available: <http://economicsandpeace.org/>.
- [2] "National Consortium for the Study of terrorism," Department of Homeland Security, The University of Maryland., June 2015. [Online]. Available: <https://www.state.gov/documents/organization/239628.pdf>.
- [3] D. A. Q.C., "THE TERRORISM ACTS IN 2015," UK Government, London, 2015.
- [4] N. Stripe, "Crime in England and Wales: year ending December 2019," Office for National Statistics, 2020.
- [5] "Hyperspectral Imaging Technology for the Non-Scientist," Civil Air Patrol ARCHER Training, [Online]. Available: https://tests.capnhq.gov/ops/archer_training/archer_hsi_tech/Electromagnetic%20Radiation.cfm. [Accessed Wed Jan 2019].
- [6] H. D. Griffiths and C. J. Baker, "Radar Imaging For Combatting Terrorism," *Springer*, pp. 1-19, 2006.
- [7] D. M. Sheen, D. L. McMakin and T. E. Hall, "Speckle in active millimeter-wave and terahertz imaging and spectroscopy," in *"Speckle in activemillimeter-wave and terahertz imaging and spectroscopy," Proc. SPIE 6548, Passive Millimeter-Wave Imaging Technology X, 654809 (1 May 2007)*, Orlando, Florida, UnitedStates, 2007.
- [8] I. Ocket, B. Nauwelaers, J. Fostier, L. Meer, F. Olyslager, G. Koers, J. Stiens and R. Vounckx, "Characterization of speckle/despeckling in active millimeter wave imaging systems using a first order 1.5D model," in *Proceedings of SPIE Vol. 6194, Millimeter-Wave and Terahertz Photonics*, Andreas Stöhr, Univ. Duisburg-Essen (Germany), 2006.
- [9] H. Essen, H.-H. Fuchs, M. Hagelen, S. Stanko and D. Notel, "Concealed Weapon Detection with Active and Passive Millimeterwave Sensors, Two Approaches," 2001.
- [10] S. W. Harmer, N. Bowring, D. Andrews, N. D. Rezgui, M. Southgate and S. Smith, "A Review of Nonimaging Stand-Off Concealed Threat Detection with Millimeter-Wave Radar," *IEEE Microwave magazine*, vol. 13, no. 1, pp. 160 - 167, 2012.
- [11] D. A. Andrews, S. W. Harmer, N. J. Bowring, N. D. Rezgui and M. J. Southgate, "Active Millimeter Wave Sensor for Standoff Concealed Threat Detection," *IEEE SENSORS JOURNAL*, vol. 13, no. 12, 2013.
- [12] R. Appleby and R. N. Anderton, "Millimeter-Wave and Submillimeter-Wave Imaging for Security and Surveillance," *Proceedings of the IEEE*, vol. Vol. 95, no. No. 8, pp. 1683-1690, 2007.

- [13] D. A. Andrews, N. D. Rezgui, S. E. Smith, N. Bowring, M. Southgate and J. G. Baker, "Detection of concealed explosives at stand-off distances using wide band swept millimetre waves," in *Millimetre Wave and Terahertz Sensors and Technology*, Cardiff, 2008.
- [14] A. Cenanovic, F. Gumbmann and L. Schmidt, "Automated Threat Detection and Characterization with a Polarimetric Multistatic Imaging System," in *EUSAR 2012; 9th European on Synthetic Aperture Radar*, Nuremberg, Germany, 2012.
- [15] J. Randa, J. Lahtinen, A. Camps, A. J. Gasiewski, M. Hallikainen, D. M. L. Vine, M. Martin-Neira, J. Piepmeier, P. W. Rosenkranz, C. S. Ruf, J. Shiue and N. Skou, "Recommended Terminology for Microwave Radiometry," National Institute of Standards and Technology, Washington, DC, 2008.
- [16] N. Bowring, D. Andrews, N. D. Rezgui and S. Harmer, "Remote Detection and Measurement of Objects". United States of America Patent US 2010/0005044A1, 7th Jan 2010.
- [17] N. Bowring, D. Andrews, N. D. Rezgui and S. Harmer, "Remote Detection and Measurement of Objects". United States of America Patent US 2011/0181300A1, 28th Jul 2011.
- [18] N. Bowring, D. Andrews, N. D. Rezgui and S. Harmer, "Detection of Objects". United States of America Patent US 2012/0256786A1, 11th Oct 2012.
- [19] E. Blackhurst, N. Salmon and M. Southgate, "Full Polarimetric Millimetre Wave Radar for Stand-off Security Screening," in *SPIE Security + Defence, 2017*, Warsaw, Poland, 2017.
- [20] A. W. Doerry and F. M. Dickey, "Synthetic Aperture Radar," *Optical Society of America Optics and Photonics News*, pp. 28-33, Nov 2004.
- [21] M. Skolnic, *Introduction to Radar Systems*, McGraw-Hill, 1987.
- [22] "Radar Basic - Synthetic Aperture Radar," [radartutorial.eu](http://www.radartutorial.eu/20.airborne/ab07.en.html), [Online]. Available: <http://www.radartutorial.eu/20.airborne/ab07.en.html>. [Accessed 17th Dec 2018].
- [23] P. Millot and L. Casadebaig, "Ultra Wide X-Band Microwave Imaging of Concealed Weapons and Explosives Using 3D-SAR Technique," *International Journal of Antennas and Propagation*, vol. Volume 2015, 2015.
- [24] A. Zhuravlev, S. Ivashov, V. Razevig, I. Vasiliev and T. Bechtel, "Inverse synthetic aperture radar imaging for concealed object detection on a naturally walking person," in *Proc. SPIE 9074, Sensors, and Command, Control, Communications, and Intelligence (C3I) Technologies for Homeland Security and Homeland Defense XIII, 907402*, 2014.
- [25] H. Shi, S. Xia, Q. Qin, T. Yang and Z. Qiao, "Non-Stationary Platform Inverse Synthetic Aperture Radar Maneuvering Target Imaging Based on Phase Retrieval," *Sensors — Open Access Journal*, pp. 1 - 16, 2018.

- [26] A. Zhuravlev, S. Ivashov, V. Razevig, I. Vasiliev and T. Bechtel, "Inverse synthetic aperture radar imaging for concealed object detection on a naturally walking person," in *Sensors, and Command, Control, Communications, and Intelligence (C3I) Technologies for Homeland Security and Homeland Defense XIII*, 907402, 2014.
- [27] 3VGEOMATICS, "What is InSAR?," 3VGEOMATICS, [Online]. Available: <https://3vgeomatics.com/technology/what-is-insar/>. [Accessed 4th Oct 2019].
- [28] A. Government, "Interferometric Synthetic Aperture Radar," Australian Government, [Online]. Available: <https://www.ga.gov.au/scientific-topics/positioning-navigation/geodesy/geodetic-techniques/interferometric-synthetic-aperture-radar>. [Accessed 8th Oct 2019].
- [29] H. Shiqi, L. Zhiganga, Z. Qingmina and Y. Yia, "Extraction and Analysis of Polarimetric Interferometry Information of SAR Targets," *Procedia Engineering*, vol. 15, pp. 2057-2061, 2011.
- [30] Y. Zhen and Y. Ruliang, "Application of Polarimetric Synthetic Aperture Radar Interferometry," in *Proceedings of the 2002 IEEE Radar Conference (IEEE Cat. No.02CH37322)*, Long Beach, CA, USA, 2002.
- [31] "radartutorial.eu," [Online]. Available: <http://www.radartutorial.eu/02.basics/Pulse%20Radar.en.html>. [Accessed Wed 1 2019].
- [32] D. O'Reilly, "A Feasibility Study On The Application Of Polarimetric Decomposition Algorithms To The Detection Of Concealed Weapons," Manchester Metropolitan University, Manchester, 2015.
- [33] "radartutorial.eu," [Online]. Available: <http://www.radartutorial.eu/05.bistatic/bs04.en.html>. [Accessed 8th Jan 2019].
- [34] T. Johnsen and K. E. Olsen, "Bi- and Multistatic Radar," [Online]. Available: <https://www.sto.nato.int/publications/.../RTO-EN-SET.../EN-SET-086bis-04.pdf>. [Accessed 8th Jan 2019].
- [35] S. Harmer, D. Andrews, N. Bowring, N. Rezgui and M. Southgate, "Ultra wideband detection of on body concealed weapons using the out of plane polarized late time response," in *SPIE Security and Defence*, Berlin, 2009.
- [36] P. Nandi, S. Hutchinson and M. Fernando, "Multi Object Concealed Threat Detection by Late Time Response Analysis," in *16th Mediterranean Microwave Symposium (MMS)*, Abu Dhabi, United Arab Emirates, 2016.
- [37] W.C.Chen, *Radar Target Identification based on Complex Natural Resonances (Phd Thesis)*, Queensland, Australia: The University of Queensland, 2015.
- [38] N. Shuley and D. Longstaff, "Role of polarisation in automatic target recognition using resonance descriptions," *IEEE Electronics Letters*, vol. 40, pp. 268-270, 2004.

- [39] C. E. Baum, E. J. Rothwell, K. M. Chen and D. P. Nyquist, "The singularity expansion method and its application to target identification," *Proceedings of the IEEE*, vol. 79, pp. 1481-1492, 1991.
- [40] S. Hutchinson, *Investigation of late time response analysis for security applications*, Manchester: Manchester Metropolitan University, Manchester, UK, 2015.
- [41] S. W. Harmer, S. E. Cole, N. J. Bowring, N. D. Rezgui and D. Andrews, "ON BODY CONCEALED WEAPON DETECTION USING A PHASED ANTENNA ARRAY," *Progress In Electromagnetics Research*, vol. 124, p. 187–210, 2012.
- [42] J. J. McCombe, N. K. Nikolova, M. S. Georgiev and T. Thayaparan, "Clutter Removal in the Automatic Detection of Concealed Weapons with Late Time Responses," in *Proceedings of the 10th European Radar Conference*, Nuremberg, Germany, 2013.
- [43] D. D. O'Reilly, "A Feasibility Study On The Application Of Polarimetric Decomposition Algorithms To The Detection Of Concealed Weapons," Manchester Metropolitan University, Manchester, 2015.
- [44] P. K. M. Nkwari, S. Sinha and H. C. Ferreira, "Through-the-Wall Radar Imaging: A Review," *IETE Technical Review*, pp. 1-11, 2017.
- [45] Y. Ma, H. Hong and X. Zhu, "Interaction Multipath in Through-the-Wall Radar Imaging Based on Compressive Sensing," *Sensors — Open Access Journal*, 2018.
- [46] T. Fawcett, "An introduction to ROC analysis," *Elsevier*, pp. 861-874, 2005.
- [47] C. Wolff, "Synthetic aperture radar," [radartutorial.eu](http://www.radartutorial.eu), [Online]. Available: <http://www.radartutorial.eu/20.airborne/ab07.en.html>. [Accessed 8th Oct 2019].
- [48] A. Lipson, S. Lipson and H. Lipson, *Optical Physics*, Cambridge University Press, 2011.
- [49] E. Pottier, J. Lee and L. Ferro-Famil, "Polsarpro V3.0 Advanced Concepts," [Online]. Available: http://earth.esa.int/landtraining07/polsar_advanced_concepts.pdf. [Accessed 2nd Oct 2018].
- [50] a. D. H. T. Dallmann, "On the Connection between Jones Matrix and Sinclair Matrix," in *PIERS Proceedings*, Czech Republic, 2015.
- [51] S.R.Cloude, *Polarisation: Applications in Remote Sensing*, Oxford University Press, 2010.
- [52] a. R. J.J.Gil, *Polarized Light and the Mueller Matrix Approach*, CRC Press, 2016.
- [53] I. E. W. Kedel, E.Pottier, W-M.Boerner, S.R.Cloude, L.Ferro-Famil and J.-S. L., "NATO EN-SET-081 Radar Polarimetry and Interferometry Lecture Notes," 14-15 Oct 2004. [Online]. Available: <https://www.sto.nato.int/publications/STO%20Educational%20Notes/Forms/Document%20Set%20View.aspx?FolderCTID=0x0120D5200078F9E87043356C409A0D30823A>

FA16F60300099FA443AE6E08499A57A0FBE0134F20&View=%7Bb927897e-9dc2-4392-aa25-598b0c04b48e%7D&RootFolder=%2Fpubl. [Accessed 11th Jan 2019].

- [54] A. Xi and W. Boerner, "Determination of the characteristic polarization states of the radar target scattering matrix $[S(AB)]$ for the coherent monostatic and reciprocal propagation space by using the complex polarisation ratio p transformation formulation," *Opt. Soc. Am. A*, vol. 9, no. 3, pp. 437-455, 1992.
- [55] O. L. Daniyan, F. E. Opara, B. I. Okere and N. Aliyu, "Horn Antenna Design: The Concepts and Considerations," *International Journal of Emerging Technology and Advanced Engineering*, vol. 4, no. 5, pp. 706-708, 2014.
- [56] D. C. d. R. Bocio, "High performance horn antenna design (II)," [Online]. Available: <https://docplayer.net/23867652-High-performance-horn-antenna-design-ii-dr-carlos-del-rio-bocio-antenna-group-public-university-of-navarra.html>. [Accessed 9th Oct 2018].
- [57] G. Valente and A. Navarrini, "Design of Planar Orthomode Transducer for 84 - 116 GHz," in *24th International Symposium on Space Terahertz Technology*, Groningen, 2013.
- [58] P. Grimes, O. King, G. Yassin and M. Jones, "Compact broadband planar orthomode transducer," *astro-ph*, 2007.
- [59] G. Engargiola and R. Plambeck, "Tests of a planar L-band orthomode transducer in circular waveguide.," 2002.
- [60] N. Alessandro and P. R. L., "A Turnstile Junction Waveguide Orthomode Transducer," *IEEE TRANSACTIONS ON MICROWAVE THEORY AND TECHNIQUES*, 2006.
- [61] M. a. H.B.Goldberg, "Applications of the turnstile junction," *Microwave Theory Techniques*, pp. 40-55, 1955.
- [62] N. Alessandro, B. Alberto and P. R. L., "Test of 1 mm Band Turnstile Junction Waveguide Orthomode Transducer," in *17th International Symposium on Space Terahertz Technology*.
- [63] P. L. a. M. KASAL, "X Band Septum Polarizer as Feed for Parabolic Antenna," in *15th Conference on Microwave Techniques COMITE 2010*, Brno, Czech Republic, 2010.
- [64] S. R. Pottier and E. Cloude, "A Review of Target Decomposition Theorems in Radar Polarimetry," *IEEE Transactions on Geoscience and Remote Sensing*, vol. 34, no. 2, pp. 498-518, 1996.
- [65] "Polarimetric Decompositions," [Online]. Available: https://earth.esa.int/documents/653194/656796/Polarimetric_Decompositions.pdf. [Accessed 28th Sept 2018].

- [66] Alberga.V, Krogager.E and C. a. Wanielik.G, "Potential of coherent decompositions in SAR polarimetry and interferometry," in *Geoscience and Remote Sensing Symposium. IGARSS.Proceedings.*, Anchorage, Alaska, 2004.
- [67] E. M. Kennaugh, *Effects of type and polarization on echo characteristics*, Columbus, Ohio: Antennas Laboratory, The Ohio State University, 1949-1954.
- [68] J. Huynen, *Phenomenological theory of radar targets*, Drukkerij Bronder, Rotterdam, The Netherlands: Delft University of Technology, 1970.
- [69] A. Marino and S. Cloude, "A Polarimetric Target Detector Using the Huynen Fork," *IEEE Transactions on geoscience and remote sensing.*, vol. 48, no. 5, pp. 2357-2366, 2010.
- [70] W. Boerner, W. Yan and A. Xi, "On the Basic principles of Radar Polarimetry: Target Characteristic Polarisation State Theory of Kennaugh, Huynen's Polarization Fork Concept, and its Extension to the Partially Polarized Case," *Proceedings of the IEEE*, vol. 79, no. 10, pp. 1538-1550, 1991.
- [71] E. Kennaugh, "Polarization Properties of Radar Reflections, M. Sc. thesis," Ohio State University,, Columbus, 1952.
- [72] W. T. K. R. G. W. E. N. Baird, "Classification of targets using optimized ISAR Euler imagery," in *Radar Sensor Technology X, Proceedings of the SPIE Vol. 6210 (SPIE, Bellingham, WA) 62100A.*, Bellingham, WA, 2006.
- [73] "SAR Processing with Geomatica," 2012. [Online]. Available: <https://www.pcigeomatics.com/pdf/TrainingGuide-SAR-processing-with-Geomatica.pdf>. [Accessed 28th Sept 2018].
- [74] M. Ouarzeddine, B. Souissi and A. Belhadj-Aissa, "Target Detection and Characterization Using H/alpha Decomposition and Polarimetric Signatures," *IEEE*, pp. 395-400, 2006.
- [75] a. E. S.R Cloude, "An Entropy Based Classification Scheme for Land Applications of Polarimetric SAR," *IEEE TRANSACTIONS ON GEOSCIENCE AND REMOTE SENSING*, vol. 35, no. 1, pp. 68-78, 1997.
- [76] S. Lakshmi, S. Patra, J.Saibaba and G. Varadan, "Polarimetric SAR data analysis for identification and characterisation of ships," 16th April 2012. [Online]. Available: <https://www.geospatialworld.net/article/polarimetric-sar-data-analysis-for-identification-and-characterisation-of-ships/>. [Accessed 24th May 2019].
- [77] D. G. Corr and A. F. Rodrigues, "Alternative Basis Matrices for Polarimetric Decomposition," in *European conference; 4th, Synthetic aperture radar; EUSAR 2002*, Cologne, Germany, 2002.

- [78] J. Lee, D. L. Schuler and T. L. Ainsworth, "Polarimetric SAR Data Compensation for Terrain Azimuth Slope Variation," *IEEE TRANSACTIONS ON GEOSCIENCE AND REMOTE SENSING*, vol. 38, no. 5, pp. 2153-2163, 2000.
- [79] M.J.Rosker and H.B.Wallace, "Imaging Through the Atmosphere at Terahertz Frequencies," in *2007 IEEE/MTT-S International Microwave Symposium*, Honolulu, HI, USA, 2007.
- [80] C. Wolff, "radartutorial.eu," [Online]. Available: <http://www.radartutorial.eu/01.basics/Radar%20Cross%20Section.en.html>. [Accessed 29th Jan 2019].
- [81] Keysight, "Noise Figure Measurement Accuracy: The Y-Factor Method," [Online]. Available: <http://literature.cdn.keysight.com/litweb/pdf/5952-3706E.pdf>. [Accessed 3rd Oct 2019].
- [82] J. D. Kraus, Radio Astronomy 2nd edition, Ohio: McGraw-Hill, 1966.
- [83] Massonnet, D.; Soyris, J-C, Imaging with synthetic aperture radar, Lausanne: EPFL Press, 2008.
- [84] Keysight, "A Framework for Understanding: Deriving the Radar Range Equation.," [Online]. Available: <http://literature.cdn.keysight.com/litweb/pdf/5992-1386EN.pdf>. [Accessed Mon Sept 2019].
- [85] R. C. Harney, "Combat Systems," vol. 1, 2004.
- [86] V. S. Bagad, Microwaves and Radar, Pune: www.vtubooks.com, 2008.
- [87] D. Kissinger, Millimeter-Wave Receiver Concepts for 77 GHz Automotive Radar in Silicon-Germanium Technology, Springer, 2012.
- [88] RF Wireless World, [Online]. Available: <http://www.rfwireless-world.com/Tutorials/Vector-Network-Analyzer-VNA-tutorial.html>. [Accessed 23 Aug 2018].
- [89] K. Technologies, "Applying Error Correction to Vector Network Analyzer Measurements," Keysight, 28 Feb 2018. [Online]. Available: www.keysight.com/find/na. [Accessed 20 Aug 2018].
- [90] M. Hiebel, Fundamentals of Vector Network Analysis, Germany: Rohde and Schwarz GmbH and Co.KG, 2016.
- [91] "Microwaves 101," 12 Nov 2018. [Online]. Available: <https://www.microwaves101.com/encyclopedias/s-parameters>. [Accessed 12 Nov 2018].
- [92] B. C. Wadell, "VSWR, Reflection Coefficient, and Impedance.," in *Transmission Line Design Handbook*, Norwood, MA 02062, Artech House Inc, 1991, pp. 497-499.

- [93] Keysight, "Applying Error Correction to Vector Network Analyzer Measurements," 28th February 2018. [Online]. Available: <http://literature.cdn.keysight.com/litweb/pdf/5965-7709E.pdf>. [Accessed 24th May 2019].
- [94] J. Fleury and O. Bernard, "Designing and characterizing TRL fixture calibration standards for device modeling," [Online]. Available: <http://www.cel.com/pdf/press/TRL.pdf>. [Accessed 29th Jan 2019].
- [95] "Microwave horn antenna theory," Electronics notes, 5th July 2020. [Online]. Available: <https://www.electronics-notes.com/articles/antennas-propagation/horn-antenna/theory-equations.php>. [Accessed 5th July 2020].
- [96] C. A. Balanis, "Antenna Theory Third Edition," in *Antenna Theory Analysis and Design*, New Jersey, USA, Wiley, 2005, p. 35.
- [97] J. E. Hill, "Gain of Directional Antennas," 5th July 2020. [Online]. Available: http://www.cs.binghamton.edu/~vinkolar/directional/Direct_antennas.pdf. [Accessed 5th July 2020].
- [98] D. Long and F. Ulaby, "Calibration of Polarimetric Radars," in *Microwave Radar and Radiometric Remote Sensing*, Michigan, The University of Michigan, 2014, pp. 658-665.
- [99] F. T. U. Kamal Sarabandi, "Calibration of Polarimetric Radar Systems with Good Polarisation Isolation," *IEEE Transactions on Geoscience and Remote Sensing*, vol. 28, no. 1, pp. 70-75, 1990.
- [100] P. K.P and Z. M, "Polarimetric calibration of the airborne experimental SAR system of DLR," in *Proceedings of European SAR Conference, EUSAR 1998*, Friedrichshafen, Germany, 1998.
- [101] K. H, M. T, P. K.P and H. I, "Improvement of polarimetric SAR calibration based on the Quegan algorithm," in *Proceedings of the IEEE IGARSS 04 Symposium 1*, 2004.
- [102] G. Nesti and M. Hohmann, "A Efficient Calibration Procedure for Polarimetric Radar Systems," in *10th Annual International Symposium on Geoscience and Remote Sensing*, College Park, Maryland, USA, 1990.
- [103] D. Long and F. Ulaby, *Microwave Radar and Radiometric Remote Sensing*, Michigan: The University of Michigan Press, 2014.
- [104] Agrawal, A.P.; Boerner, W. M., "Redevelopment of Kennaugh's Target Characteristic Polarisation State Theory Using the Polarization Transformation Ratio Formalism for the Coherent Case," *IEEE Transactions on Geoscience and Remote Sensing*, vol. 27, no. 1, pp. 2-14, 1989.
- [105] Huynen, J.R, *Phenomenological theory of radar targets*, PhD dissertation, Drukkerij Bronder, Rotterdam, The Netherlands: Delft University of Technology, 1970.

- [106] M. C. a. B. Borden, Fundamentals of radar imaging, SIAM, 2009.
- [107] D. A. E. Fuhs, Electronic Warfare and Radar Systems Engineering Handbook, Point Mugu, CA 93042: Jeffrey Frank Jones, 2013.
- [108] E. Hecht and A. Zajac, Optics, Addison-Wesley, 1974.
- [109] A. Agrawal and W. M. Boerner, "Redevelopment of Kennaugh's Target Characteristic Polarisation State Theory Using the Polarization Transformation Ratio Formalism for the Coherent Case.," *IEEE Transactions on Geoscience and Remote Sensing*, vol. 27, no. 1, pp. 2-14, 1989.
- [110] A. R. Hippel, Dielectric Materials and Applications, John Wiley, 1954.
- [111] j. adametz and l.-p. schmidt, "Threat object classification with a close range polarimetric imaging system by means of H-a decomposition," *International Journal of Microwave and Wireless Technologies*, 2014.
- [112] H. a. S. Executive, "A guide to the Control of Electromagnetic Fields at Work Regulations 2016," July 2016. [Online]. Available: <http://www.hse.gov.uk/pubns/books/hsg281.htm>. [Accessed 20th Dec. 2018].
- [113] H. a. S. Executive, "A guide to the Control of Electromagnetic Fields at Work HSG281," 2016. [Online]. Available: <http://www.hse.gov.uk/pubns/priced/hsg281.pdf>. [Accessed 27th March 2019].

Chapter 16 Appendix A

RF Safety exposure limits

Unlike radiation from radioactive materials, microwave radiation is non-ionizing due to the energy levels being relatively low. However, microwave radiation can cause heating of body tissue if the power density is high enough. Guidelines set out for the exposure for electromagnetic radiation can be found in [112] [113] indicating a basic restriction of:

10W/m² of exposure.

The measurements presented in this thesis were taken at a range of 2 meters in a controlled laboratory environment. The calculation of radiation intensity can be seen below:

VNA source power is the power the internal source is set to inside the VNA, and this power appears at both port 1 and 2 on the VNA.

$$\text{VNA source power (P}_{\text{source}}) = 1 \text{ mW}$$

The Isotropic power density calculation provides the level of power that would be received at range R if the source power were to be radiated uniformly in all directions. The Isotropic power density is the source power density divided by the surface area of a sphere at a range R and is given by:

$$P_{\text{Isotropic}} = \frac{P_{\text{source}}}{4\pi R^2} \quad (16-1)$$

The radar is fitted with a conical horn antenna with a gain of 20.7 dB ($G_{\text{ratio}} = 117.5$) by calculation and a 3db beamwidth of 12.3° (Chapter 7). The antenna's gain concentrates the isotropic power density into a pencil beam, producing a spot size with an area of 0.146m² at a range of 2 meters. The power density with gain is given by:

$$P_{dg} = P_{\text{Isotropic}} \times G_{\text{ratio}} \quad (16-2)$$

$$P_{d(2m)} = \frac{P_{dg}}{\text{Area}} \quad (16-3)$$

The calculated power density for the VNA based radar at a range of 1 and 2 meters can be seen below and plotted in Figure 16-1:

$$P_{dg(1m)} = 218.17 \text{ mW/m}^2$$

$$P_{dg(2m)} = 1.99 \text{ mW/m}^2$$

This level is well within the guidelines set out in [112][113].

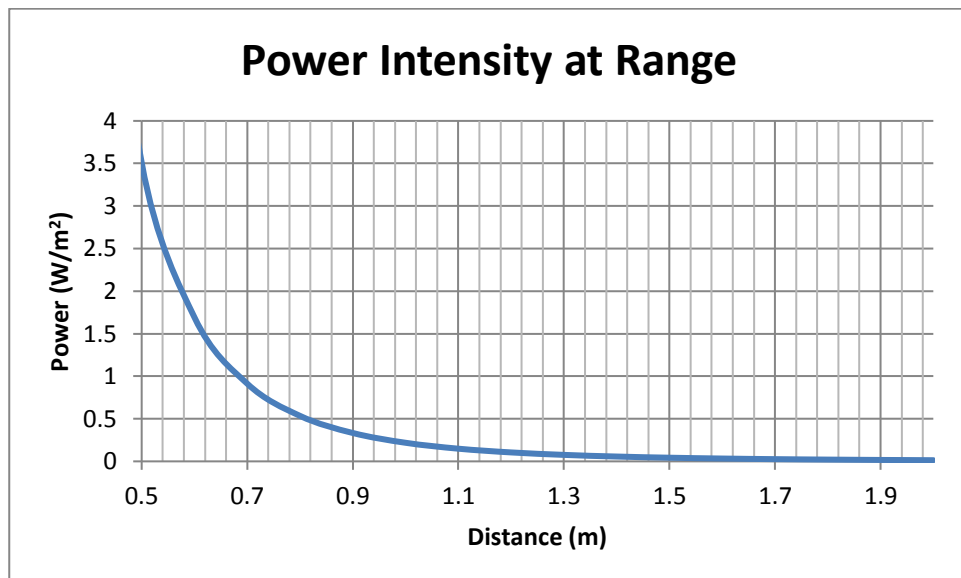


Figure 16-1 Power intensity at a range

Chapter 17 Appendix B

Huynen Target Parameters for selected targets

17.1 Flat plate and a dihedral reflector orientated at 45°

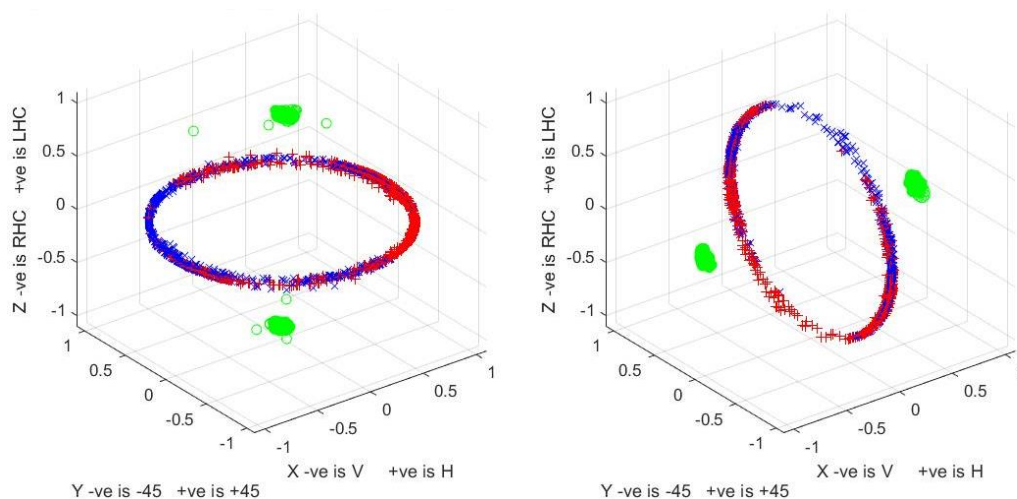


Figure 17-1 Flat plate reflector (top left), Dihedral reflector angled at 45° (top right). Measured fork plot responses, Flat plate (bottom left), Dihedral 45° (bottom right).

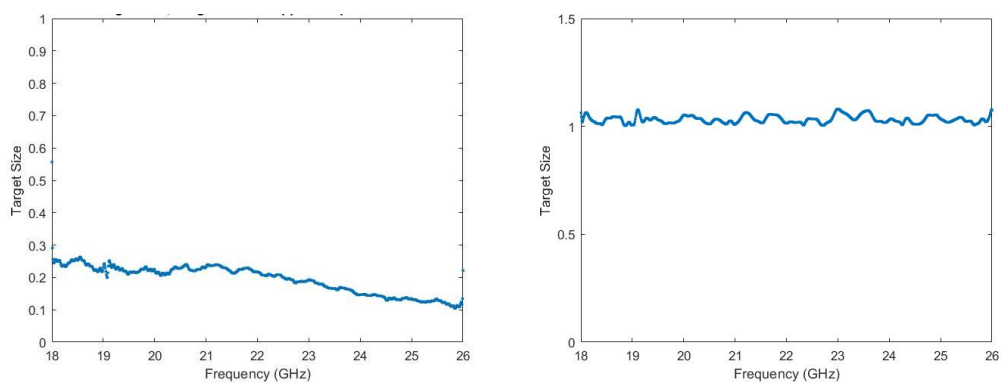


Figure 17-2 Measured target size. Plate (left), measured dihedral at 45° (right).

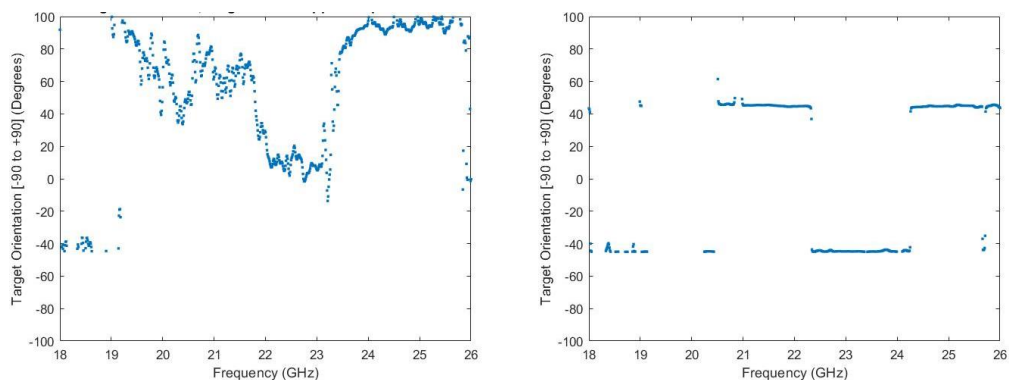


Figure 17-3 Measured orientation angle. Plate (left), Dihedral at 45° (right)

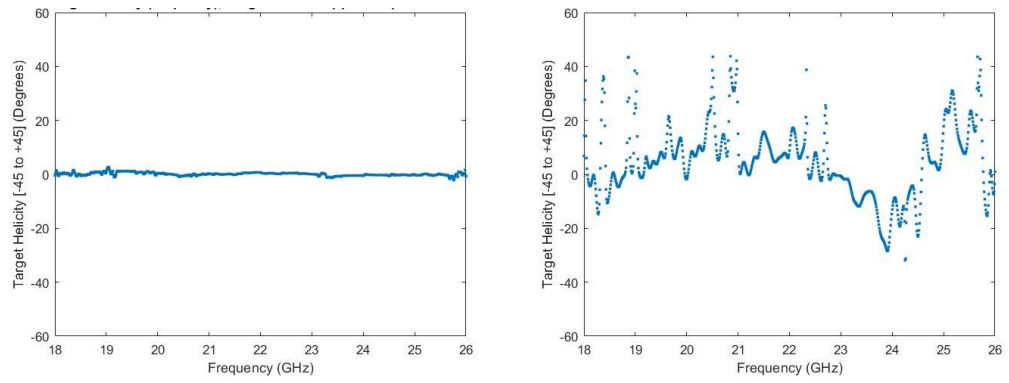


Figure 17-4 Measured helicity angle, Plate (left), Dihedral (right)

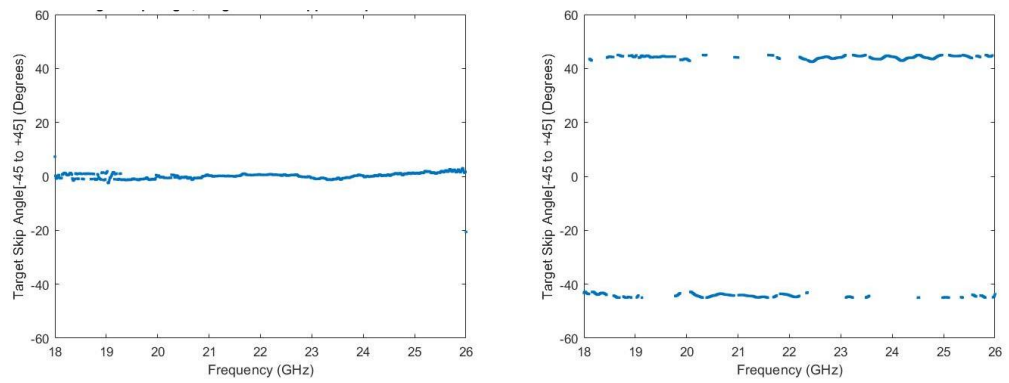


Figure 17-5 Measured skip angle. Plate (left), Dihedral at 45° (right)

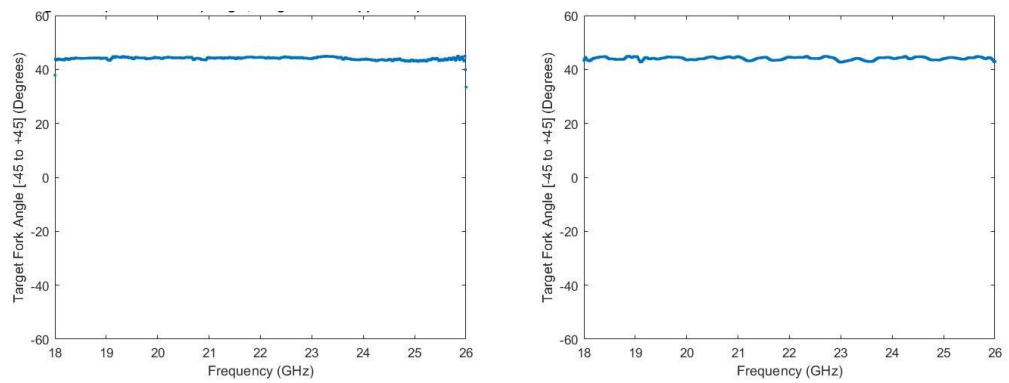


Figure 17-6 Measured fork angle. Plate (left), Dihedral at 45° (right)

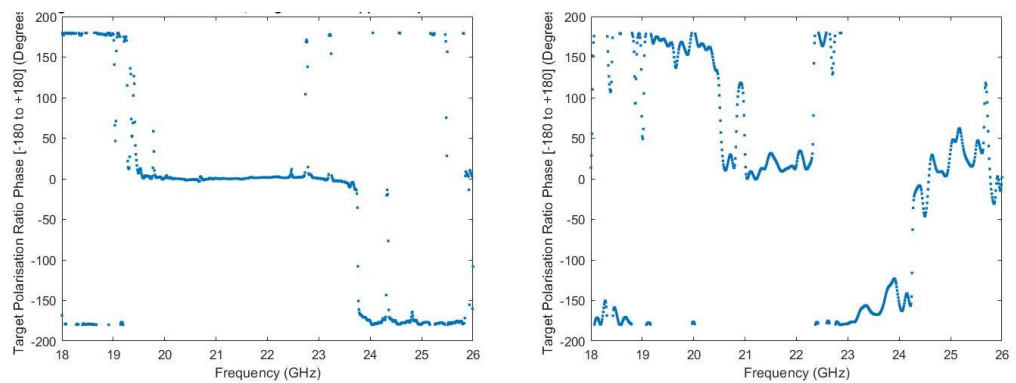


Figure 17-7 Phase of the polarisation ratio. Plate (left), Dihedral at 45° (right)

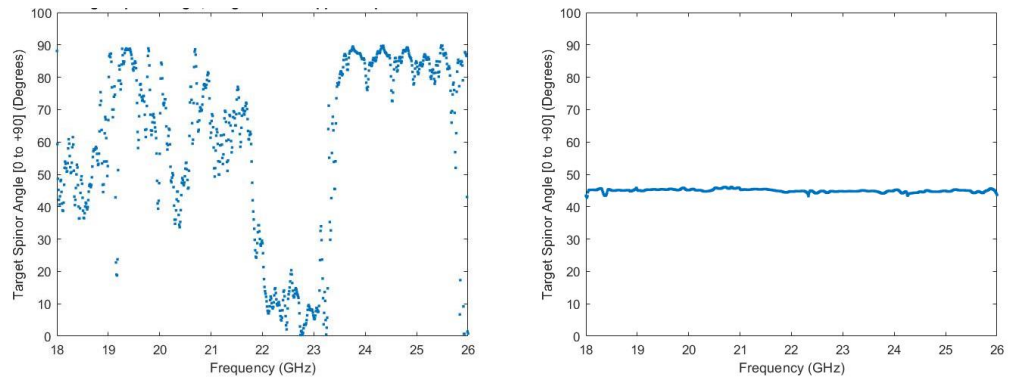


Figure 17-8 Measured spinor angle Plate. (left), Dihedral at 45° (right)

17.2 Vertical and horizontal dihedral

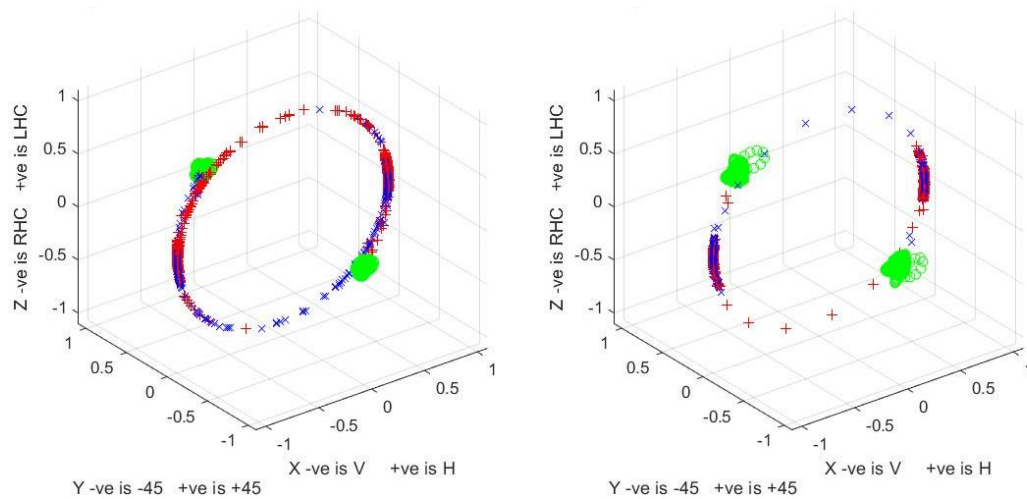
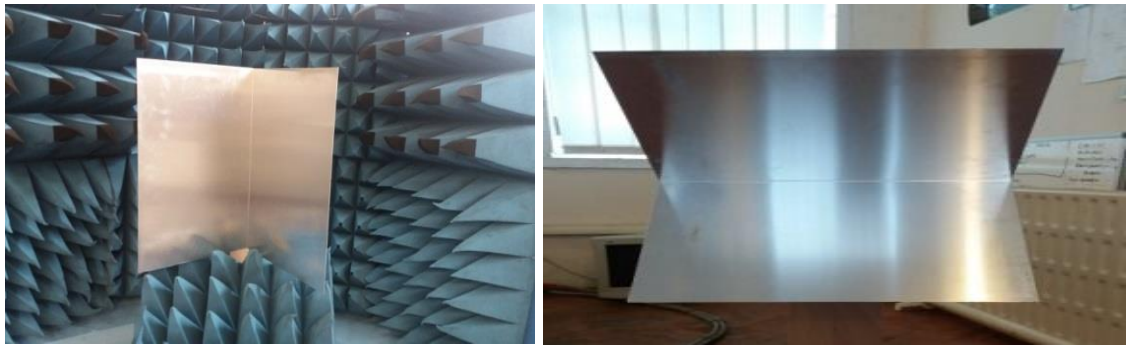


Figure 17-9 Vertical dihedral reflector (top left), Horizontal dihedral reflector (top right). Measured fork plot responses, vertical dihedral (bottom left), horizontal dihedral (bottom right).

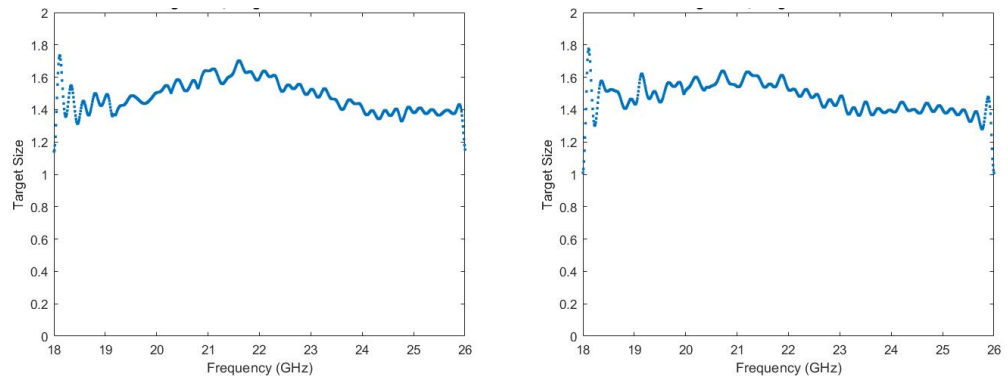


Figure 17-10 Measured target size, Vertical dihedral (left), Horizontal dihedral (right)

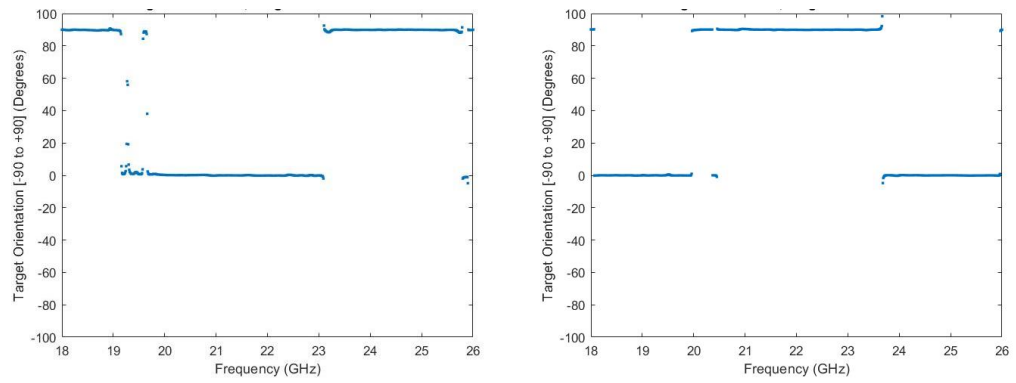


Figure 17-11 Measured orientation angle, Vertical dihedral (left), Horizontal dihedral (right)

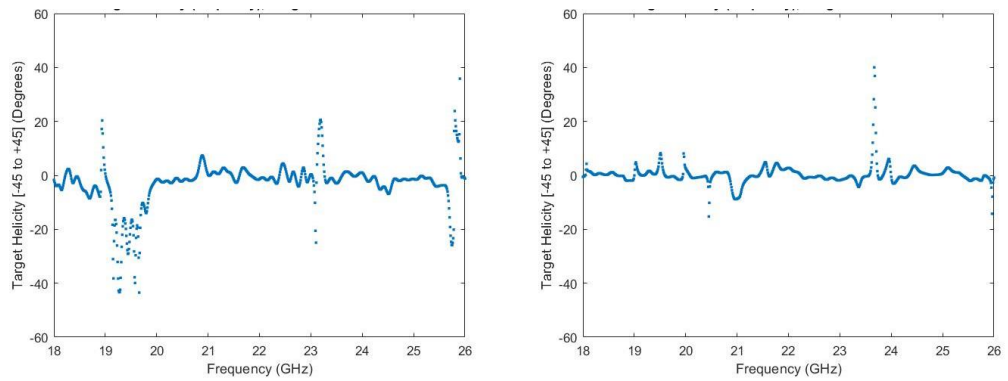


Figure 17-12 Measured helicity angle, Vertical dihedral (left), Horizontal dihedral (right)

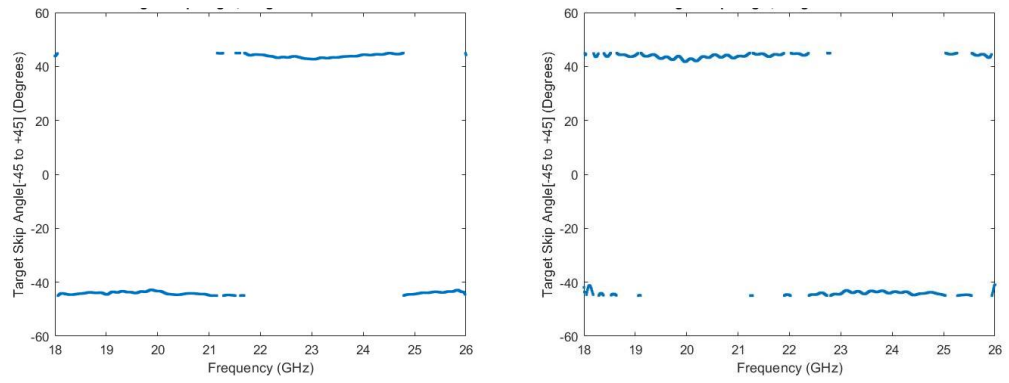


Figure 17-13 Measured skip angle, Vertical dihedral (left), Horizontal dihedral (right)

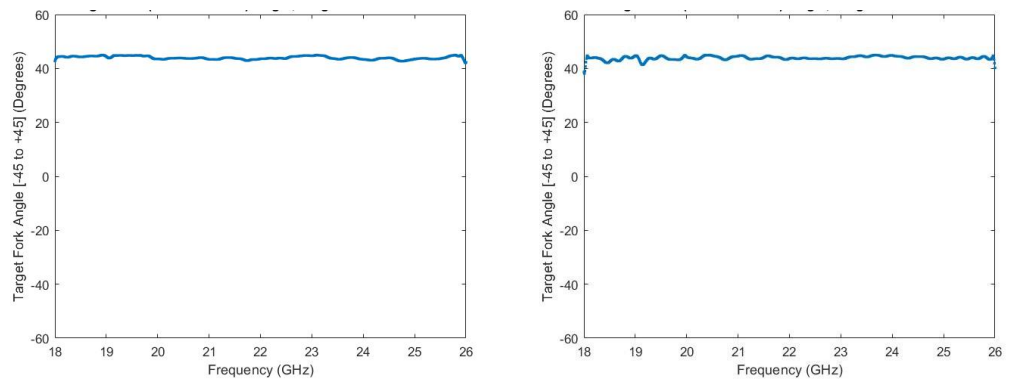


Figure 17-14 Measured fork angle, Vertical dihedral (left), Horizontal dihedral (right)

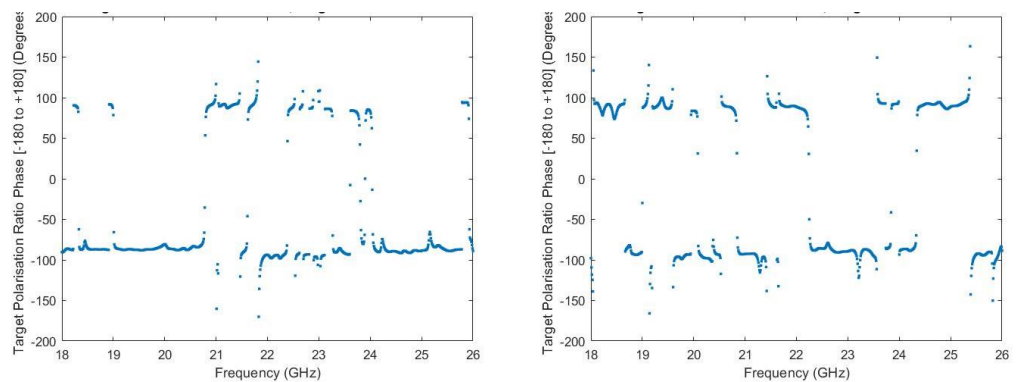


Figure 17-15 Measured phase of polarisation ratio, Vertical dihedral (left), Horizontal dihedral (right)

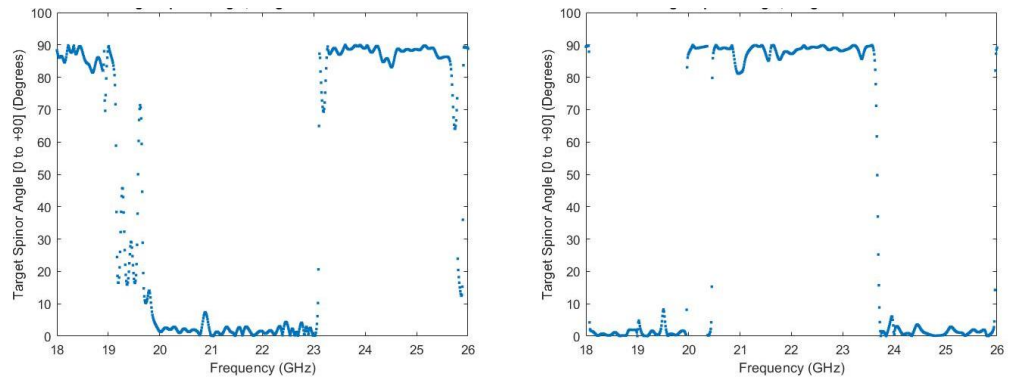


Figure 17-16 Measured spinor angle, Vertical dihedral (left), Horizontal dihedral (right)

17.3 Vertical and horizontal dipole

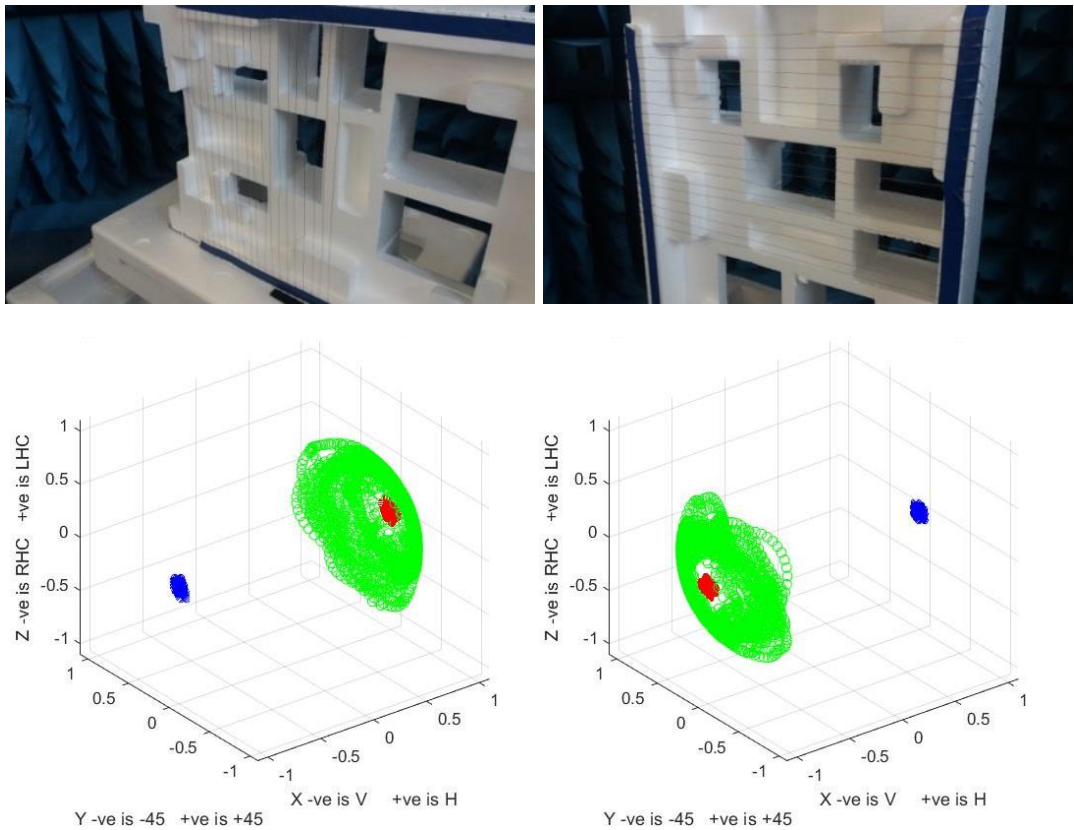


Figure 17-17 Vertical dipole (top left), Horizontal dipole (top right), Measured fork plot responses, Vertical dipole (bottom left), Horizontal dipole (bottom right).

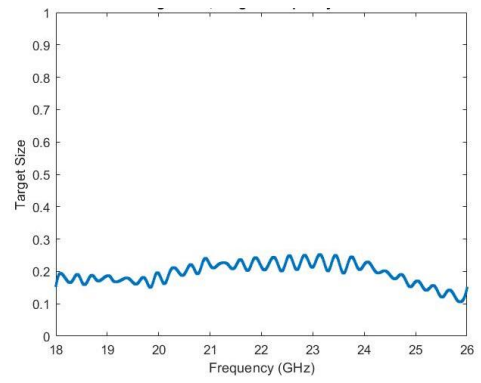
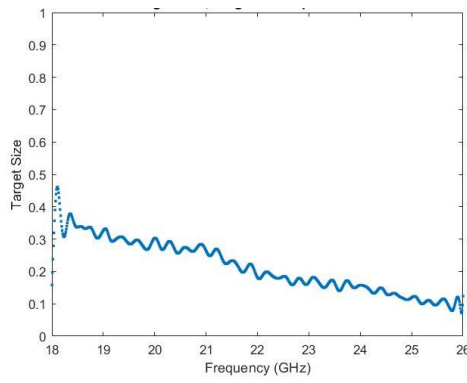


Figure 17-18 Measured target size vertical left, horizontal right

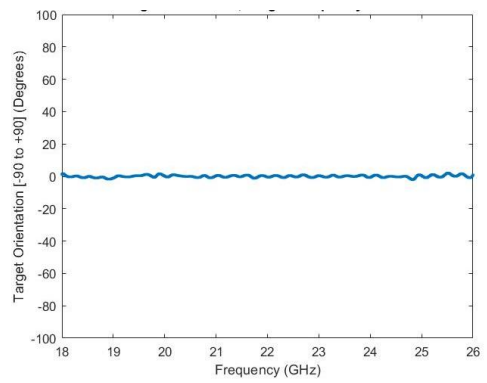
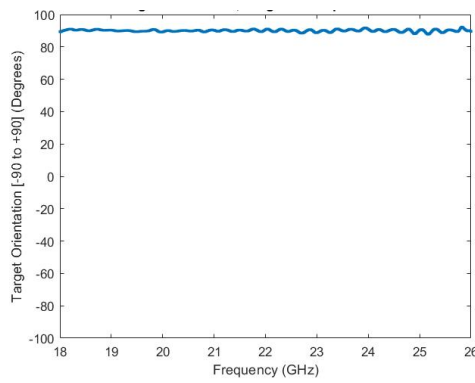


Figure 17-19 Measured orientation angle vertical left, horizontal right

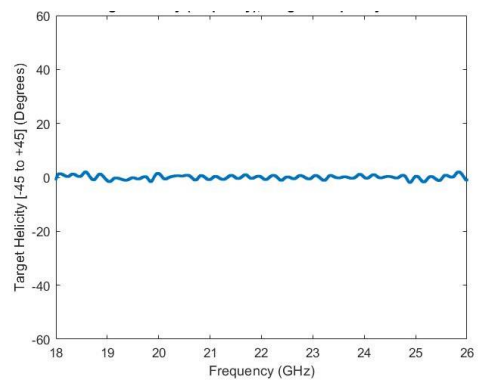
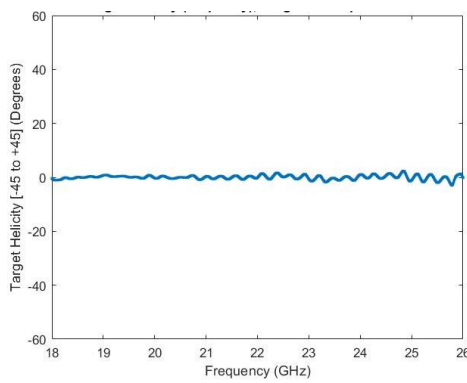


Figure 17-20 Measured helicity vertical left, horizontal right

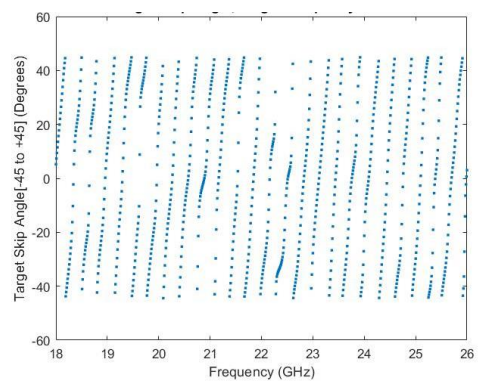
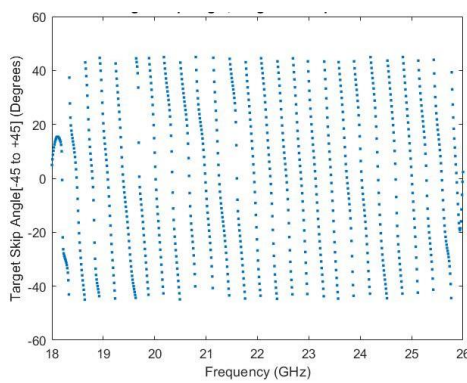


Figure 17-21 Measured skip angle vertical left, horizontal right

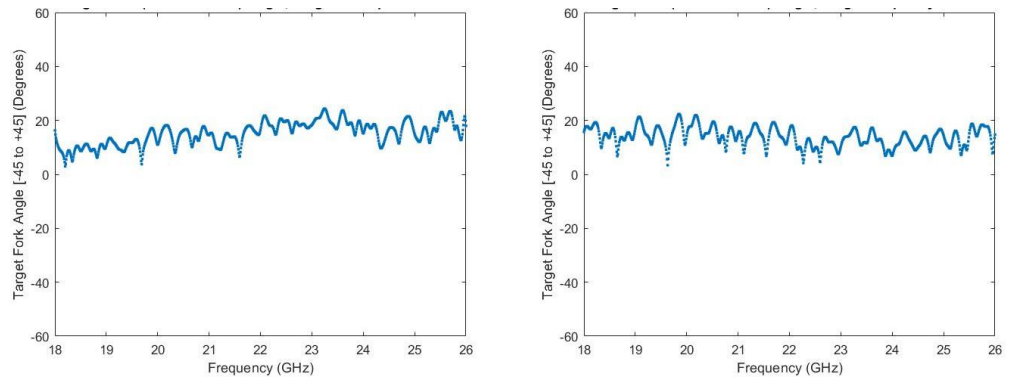


Figure 17-22 Measured fork angle vertical left, horizontal right

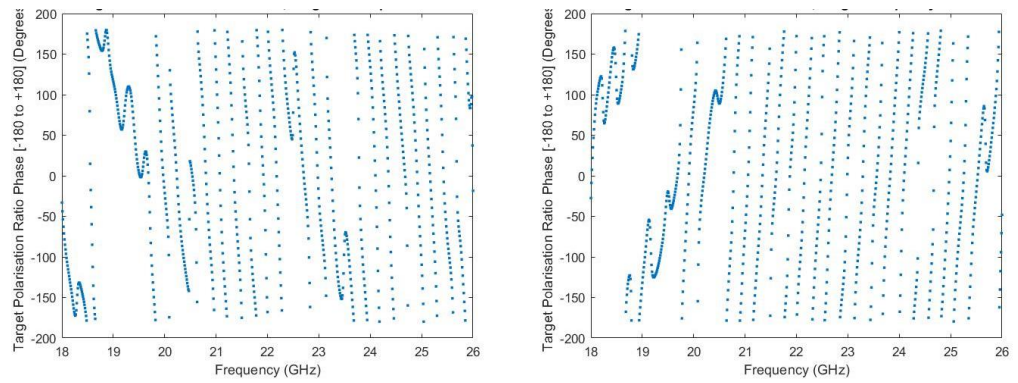


Figure 17-23 Measured polarisation phase ratio vertical left, horizontal right

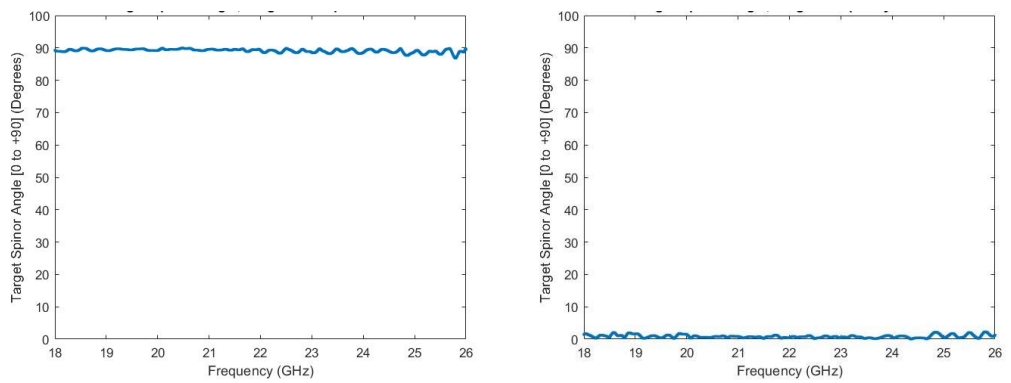


Figure 17-24 Measured spinor angle vertical left, horizontal right

17.4 Metal sphere



Figure 17-25 10.5cm in diameter sphere.

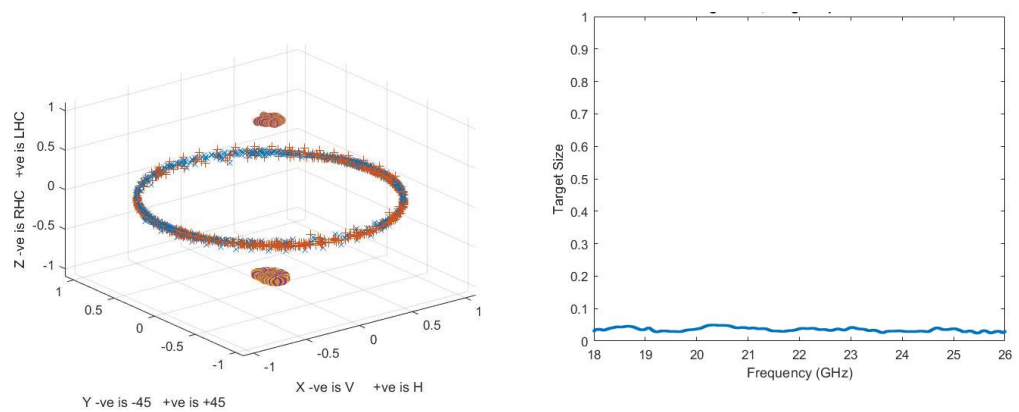


Figure 17-26 Huynen fork plot via measurement (left), measured target size (right)

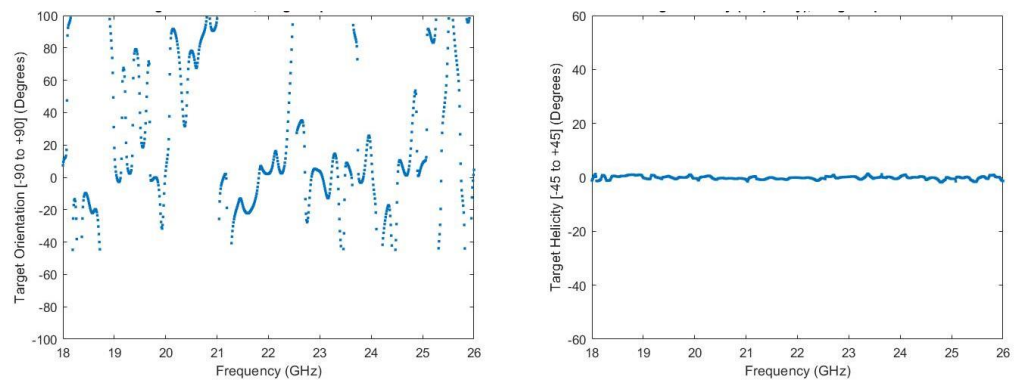


Figure 17-27 Measured orientation angle (left), Helicity angle (right)

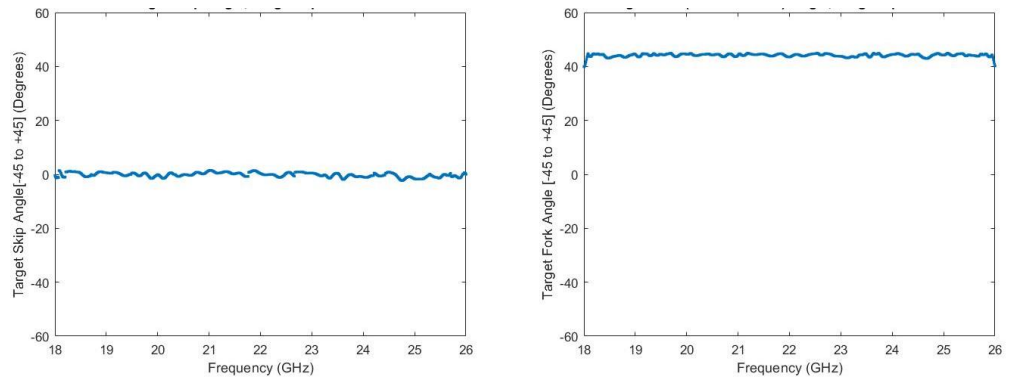


Figure 17-28 Measured skip angle (left), Fork angle (right)

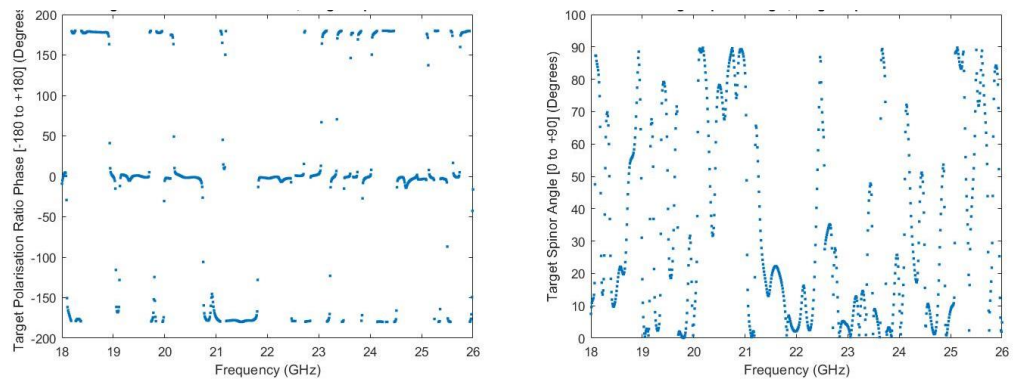


Figure 17-29 Measured polarisation phase ratio (left), Spinor angle (right)

17.5 Wave plate with integral reflector

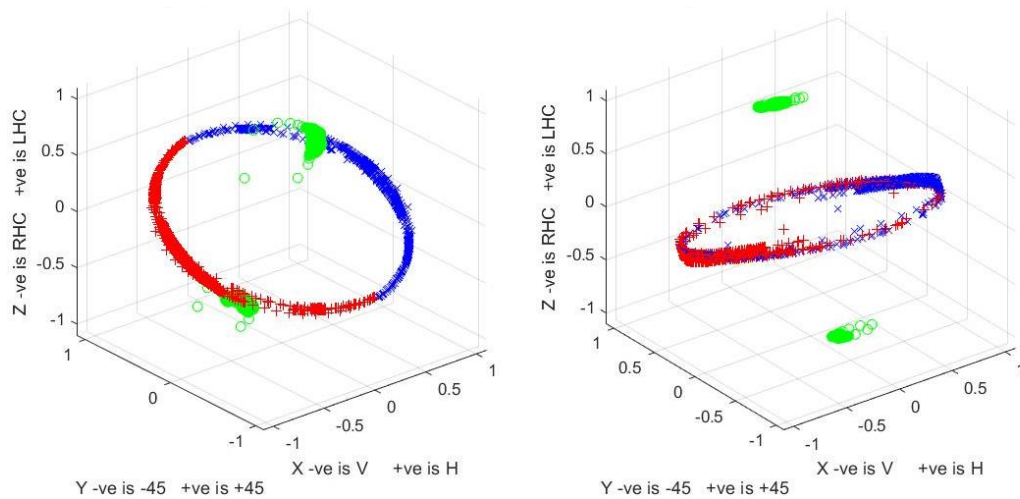
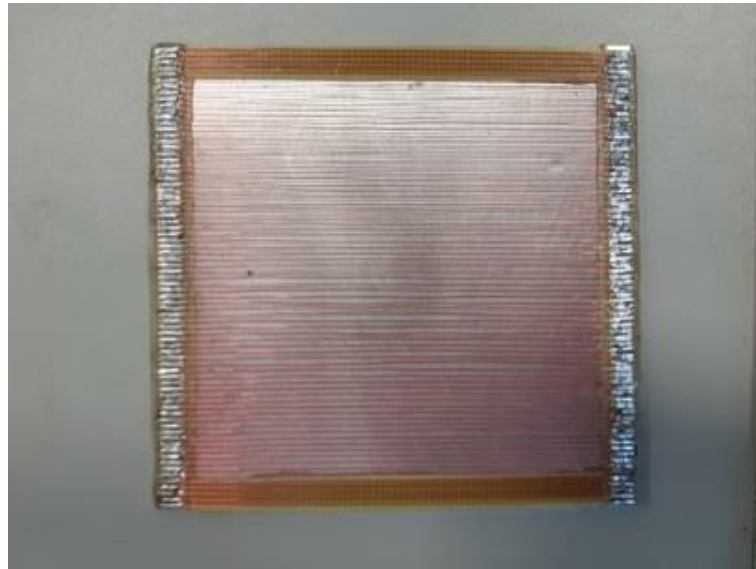


Figure 17-30 Wave plate with integral reflector, wires horizontal (top), Measured fork plot responses, wires horizontal (bottom left), vertical (bottom right).

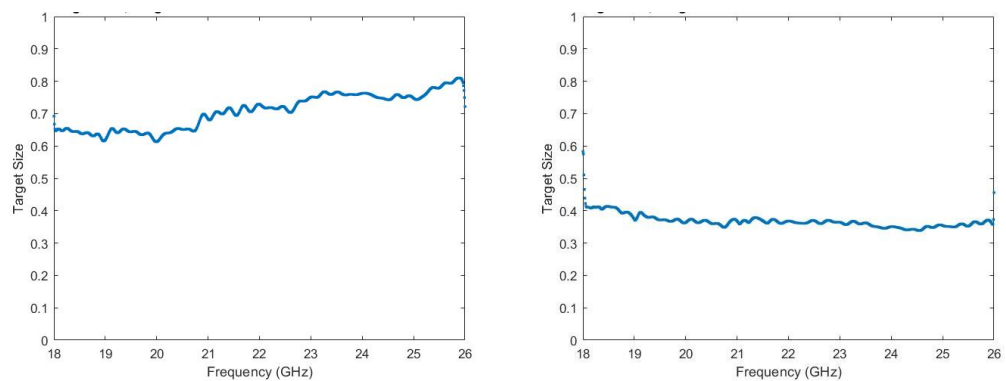


Figure 17-31 Measured target size horizontal left, vertical right

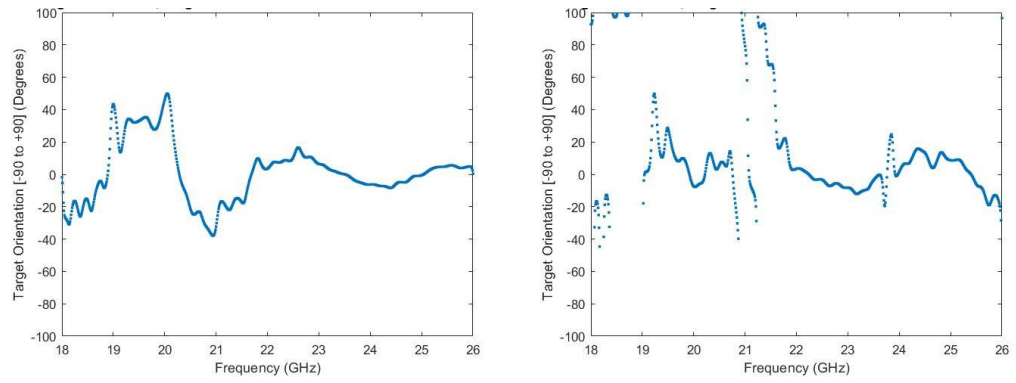


Figure 17-32 Measured orientation angle horizontal left, vertical right

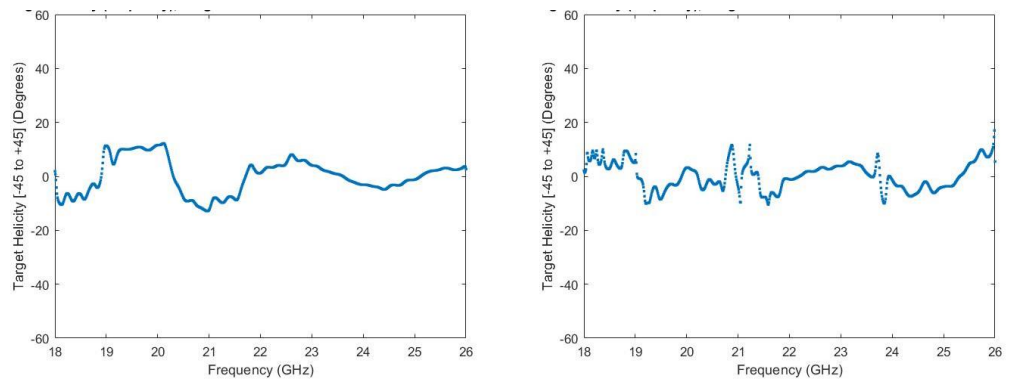


Figure 17-33 Measured helicity angle horizontal left, vertical right

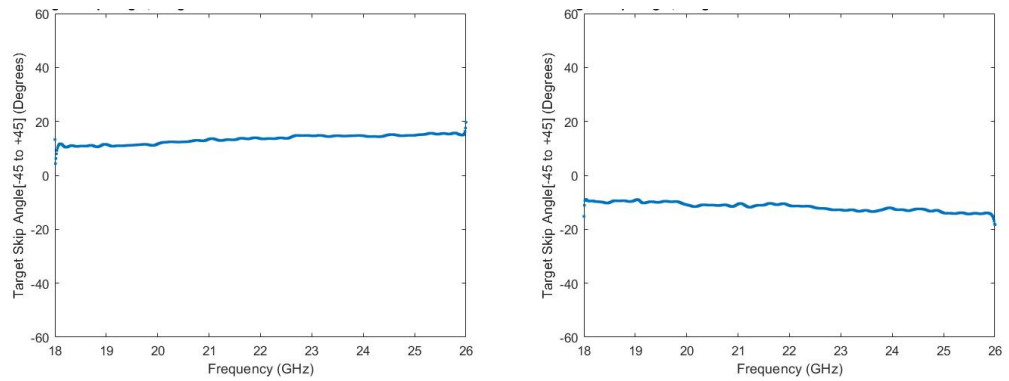


Figure 17-34 Measured skip angle horizontal left, vertical right

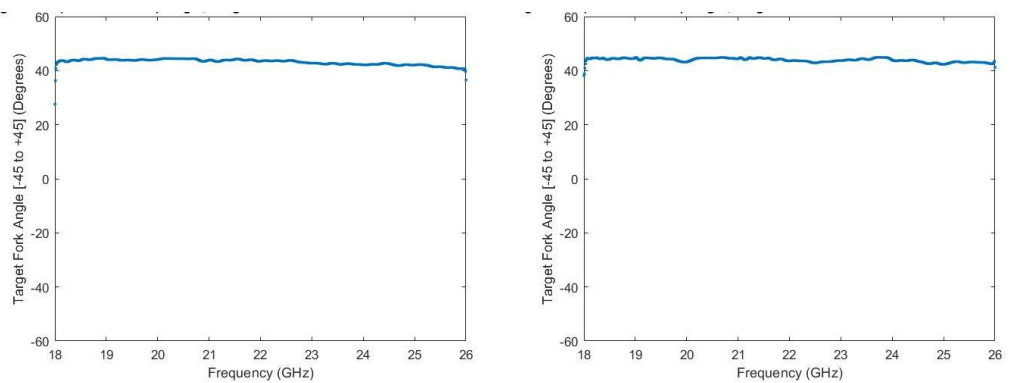


Figure 17-35 Measured fork angle horizontal left, vertical right

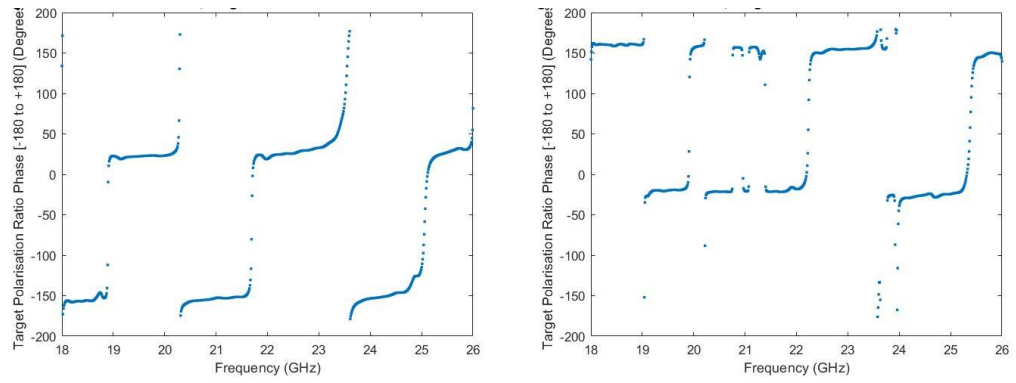


Figure 17-36 Measured polarisation phase ratio horizontal left, vertical right

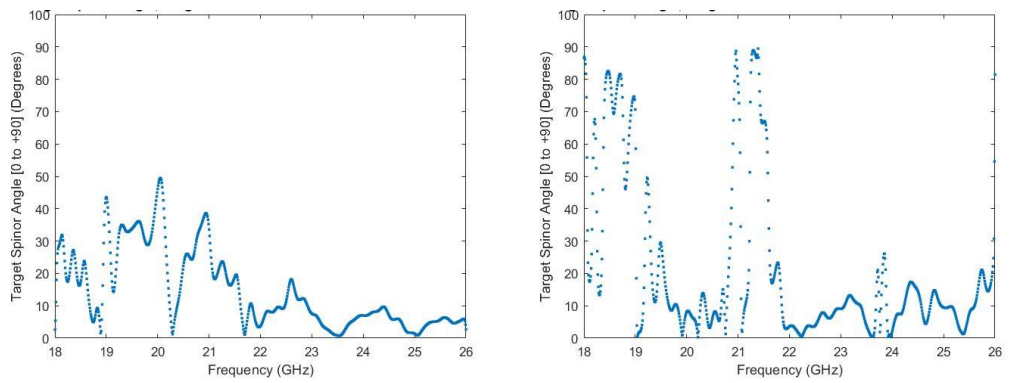


Figure 17-37 Measured spinor angle horizontal left, vertical right

17.6 Wax block



Figure 17-38 2 cm thick wax block pictured left, 3.8 cm right.

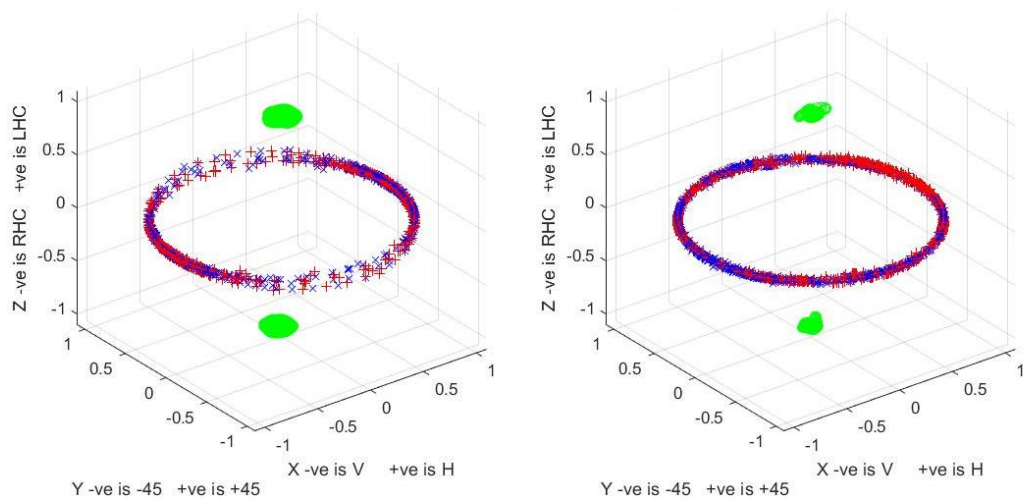


Figure 17-39 Measured fork plots, 2cm thick wax block left, 3.8 cm right

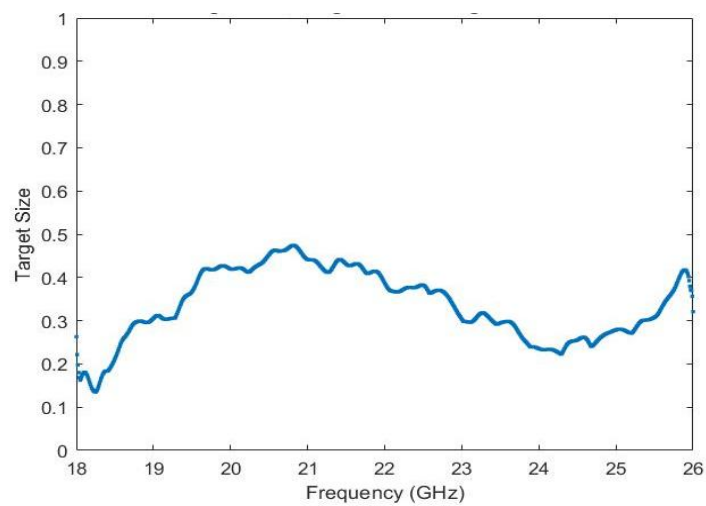


Figure 17-40 Measured Huynen target size (m) (cavity fringes) 2cm thick wax block, $n=1.47$

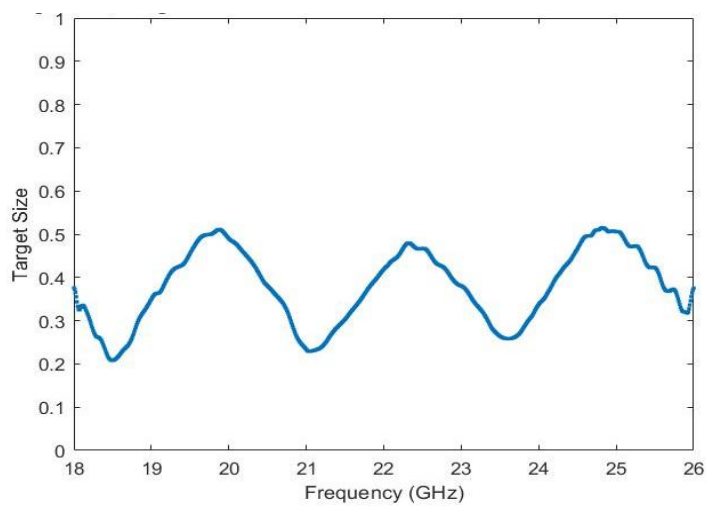


Figure 17-41 Measured Huynen target size (m) (cavity fringes) Wax block 3.8cm thick, $n=1.47$

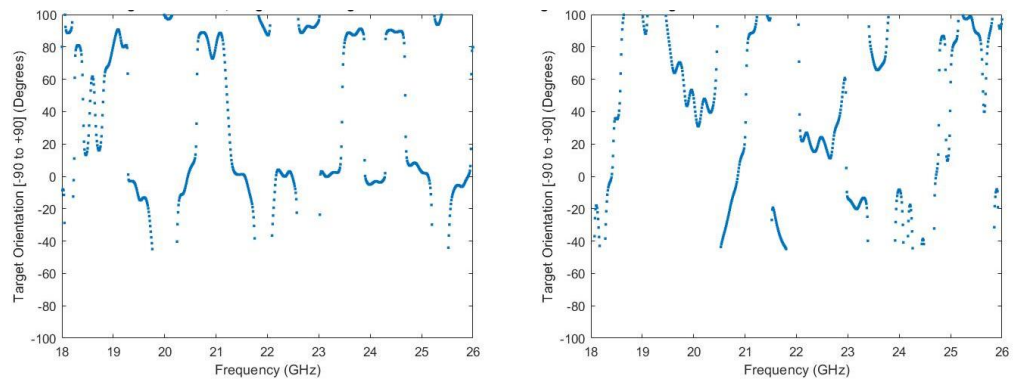


Figure 17-42 Measured orientation angle 2cm wax block left, 3.8cm right

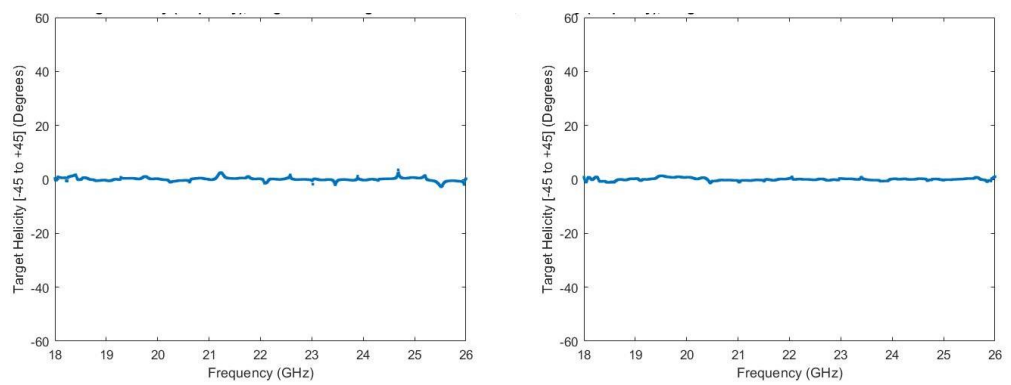


Figure 17-43 Measured helicity angle 2cm wax block left, 3.8cm right

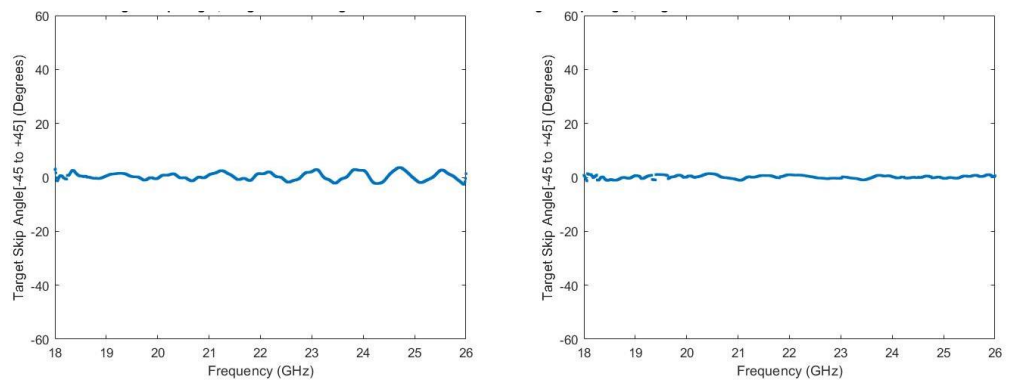


Figure 17-44 Measured skip angle 2cm wax block left, 3.8cm right

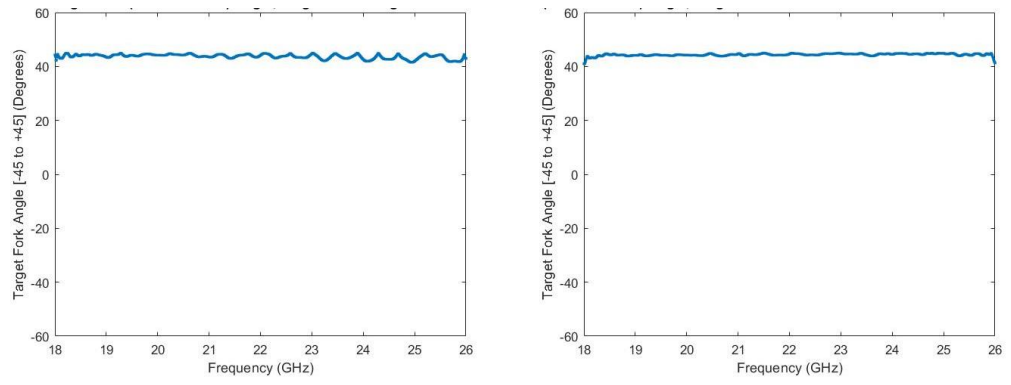


Figure 17-45 Measured fork angle 2cm wax block left, 3.8cm right

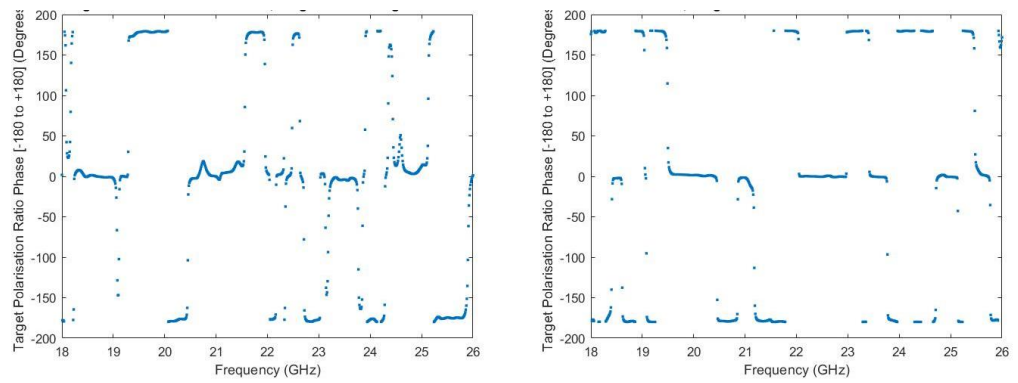


Figure 17-46 Measured polarisation phase ratio 2cm wax block left, 3.8cm right

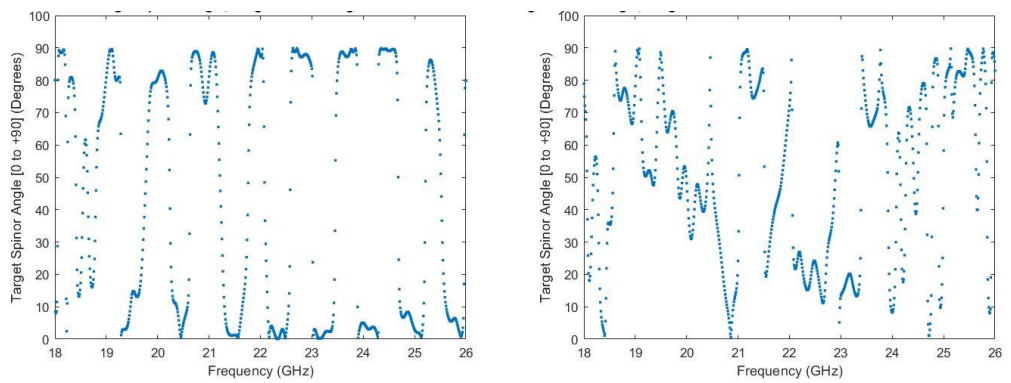


Figure 17-47 Measured spinor angle 2cm wax block left, 3.8cm right

17.7 Metal triangle

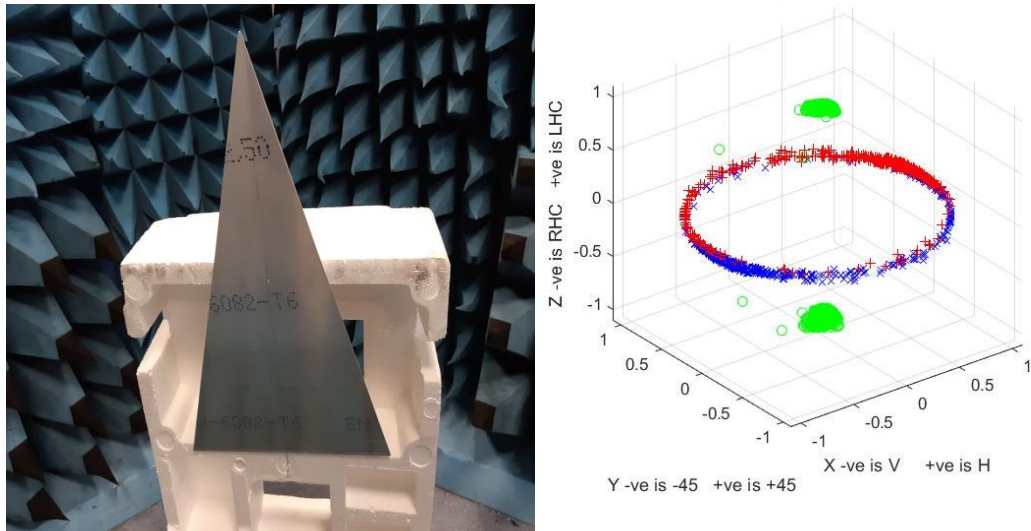


Figure 17-48 Metal triangle left, measured fork plot right

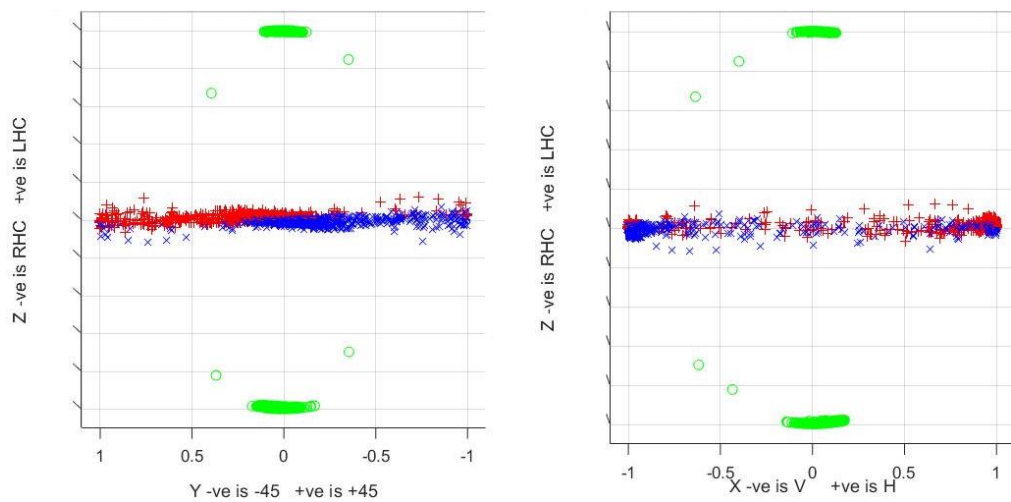


Figure 17-49 Metal triangle measured fork plots viewed from the vertical polarisation position left, and from the -45° polarisation position (right)

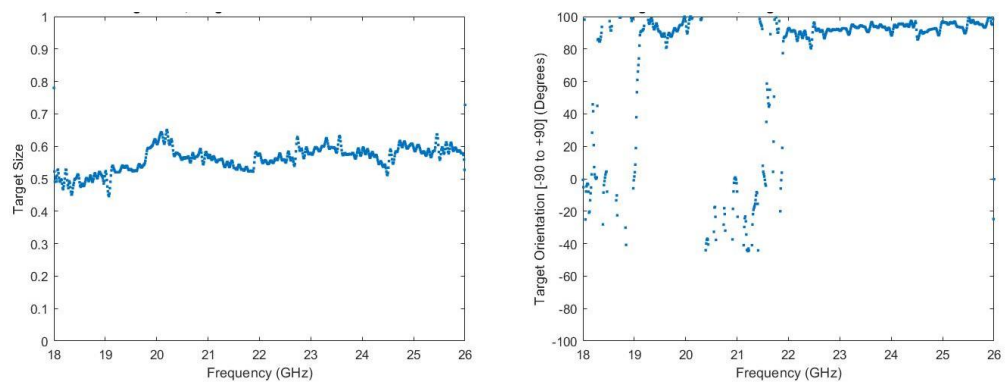


Figure 17-50 Metal triangle measured target size left, orientation angle right

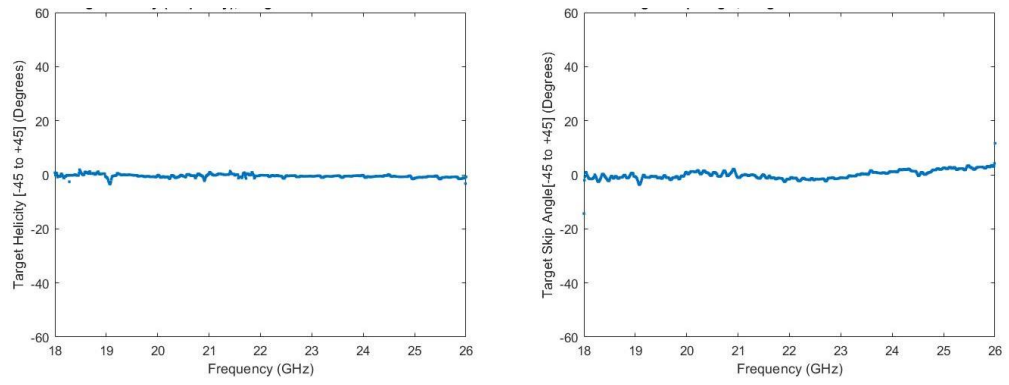


Figure 17-51 Metal triangle measured helicity angle left, skip angle right

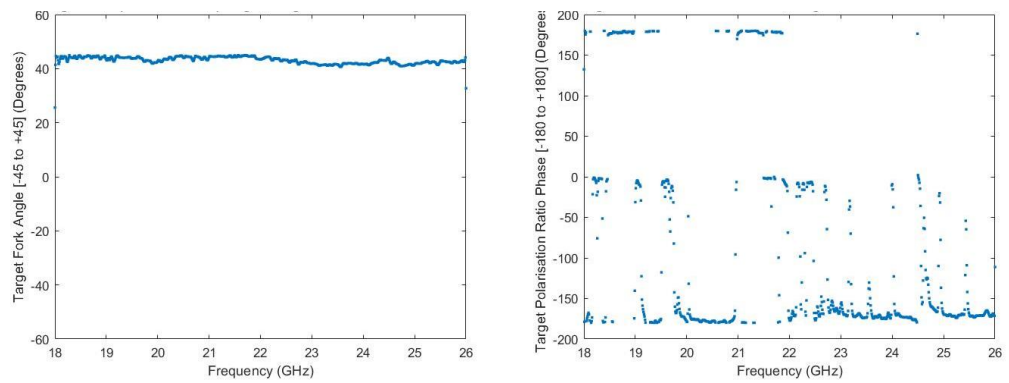


Figure 17-52 Metal triangle measured fork angle left, polarisation phase ratio right

17.8 Small vertical and horizontal knives

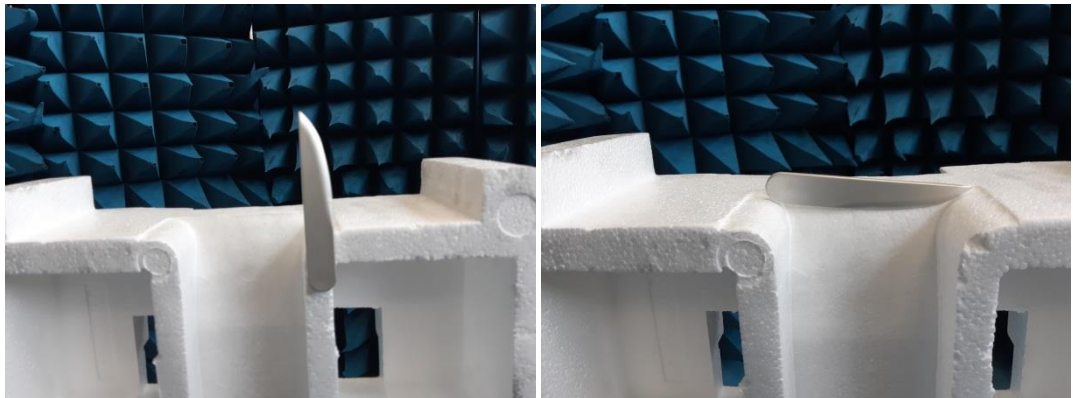


Figure 17-53 Small vertical knife (left), horizontal knife (right).

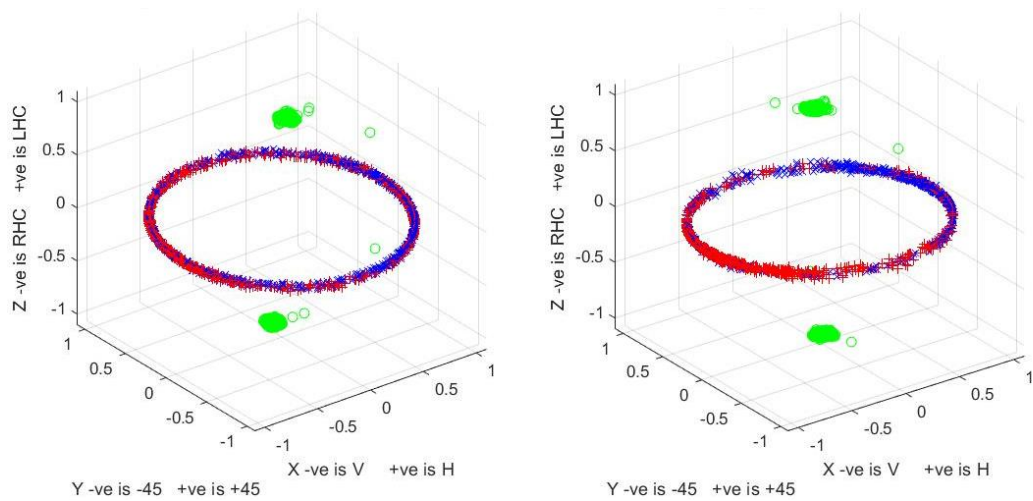


Figure 17-54 Small knife measured fork plots vertical left, horizontal right

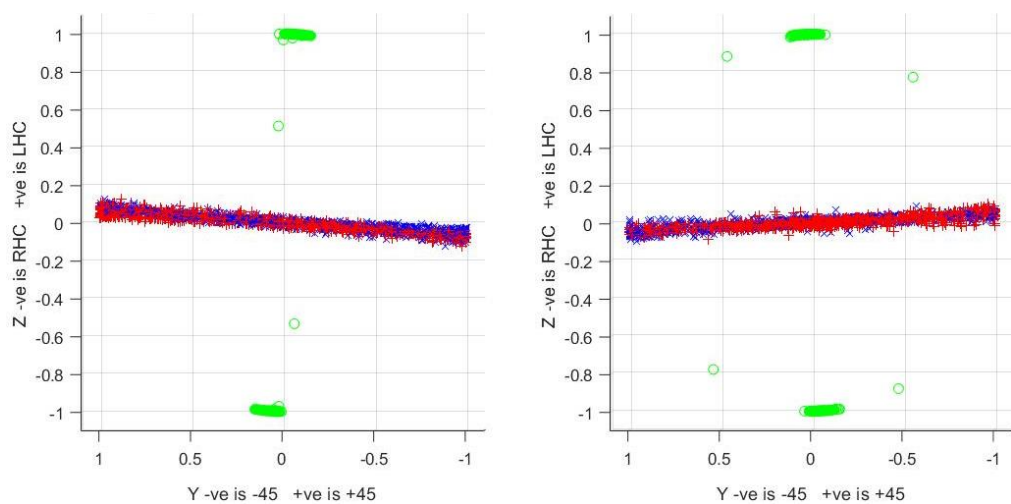


Figure 17-55 Small plastic knife measured fork plots side view vertical left, horizontal right

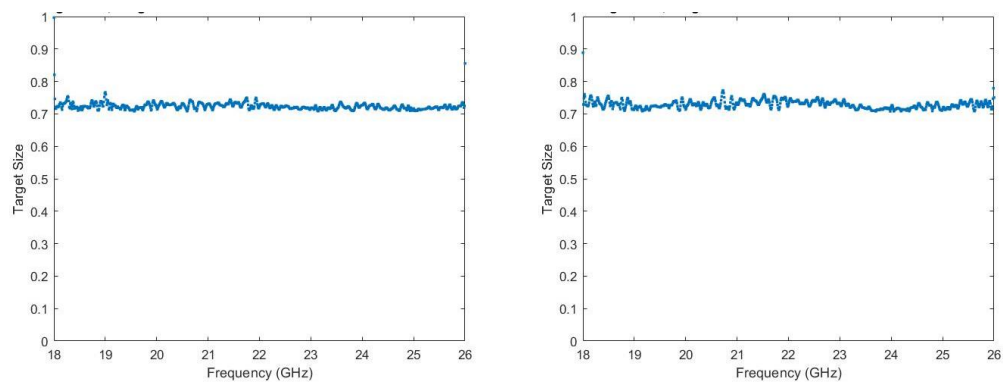


Figure 17-56 Small knife measured target size vertical left, horizontal right

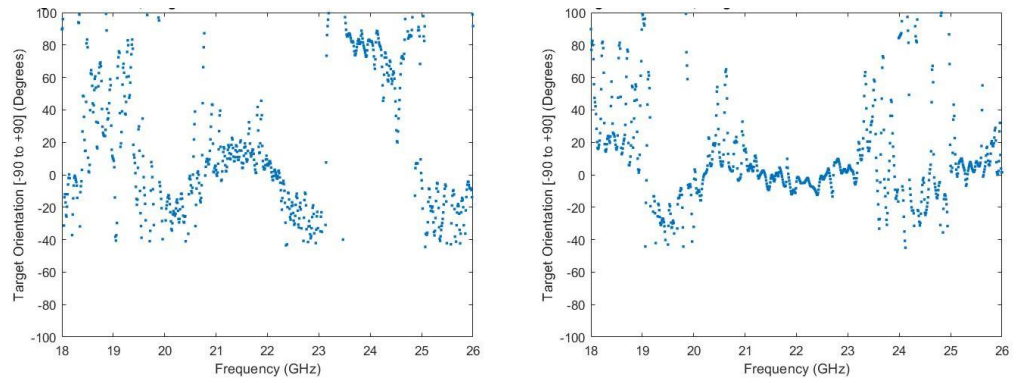


Figure 17-57 Small knife measured orientation angle vertical left, horizontal right

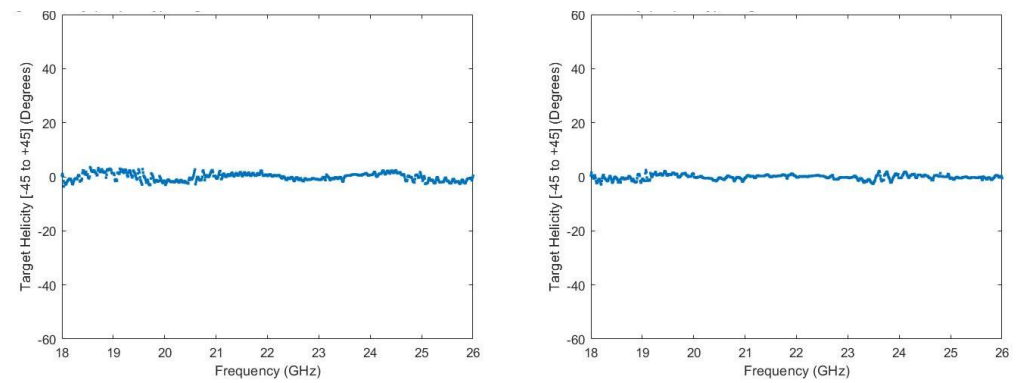


Figure 17-58 Small knife measured helicity angle vertical left, horizontal right

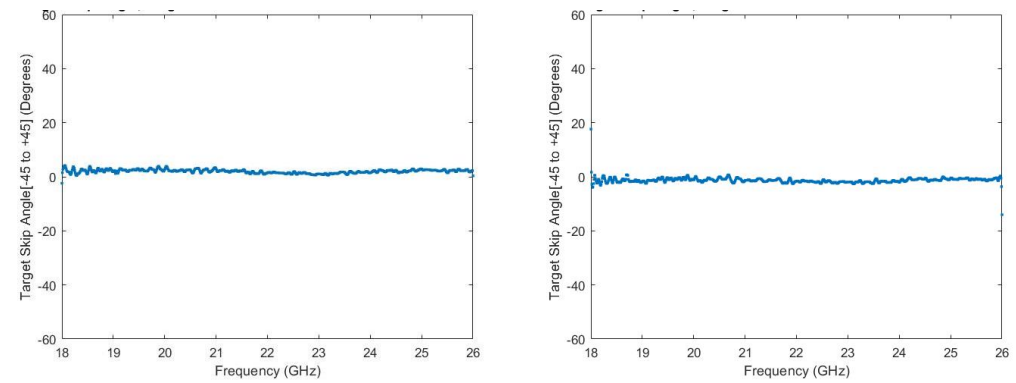


Figure 17-59 Small knife measured skip angle vertical left, horizontal right

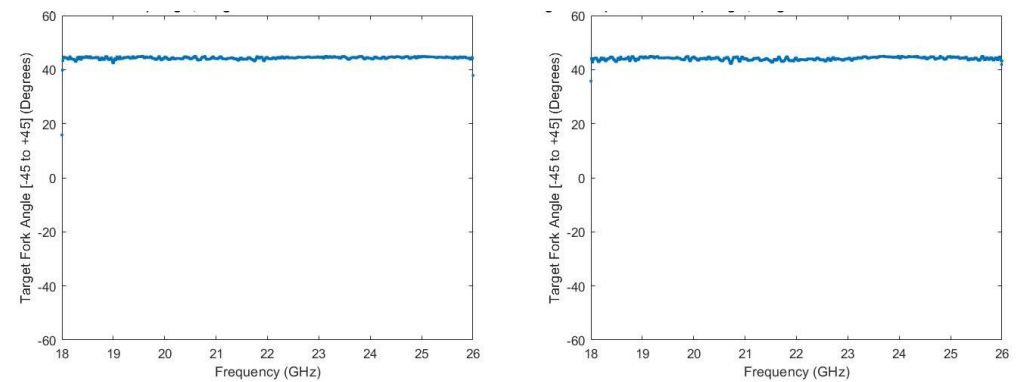


Figure 17-60 Small knife measured fork angle vertical left, horizontal right

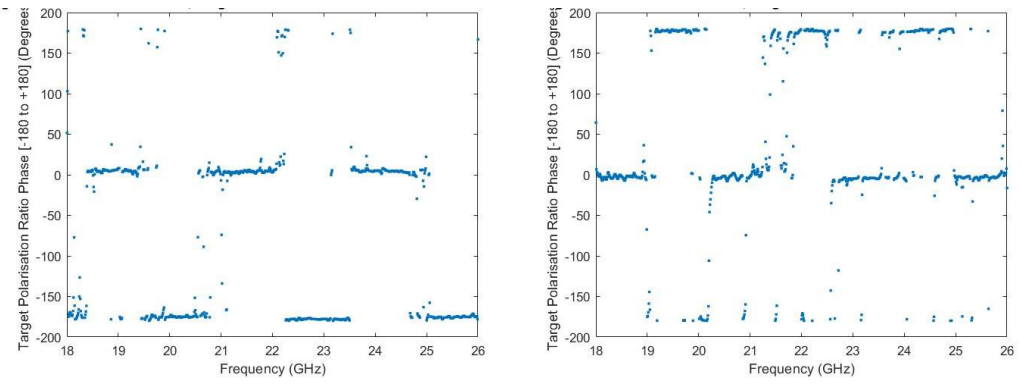


Figure 17-61 Small knife measured polarisation phase ratio vertical left, horizontal

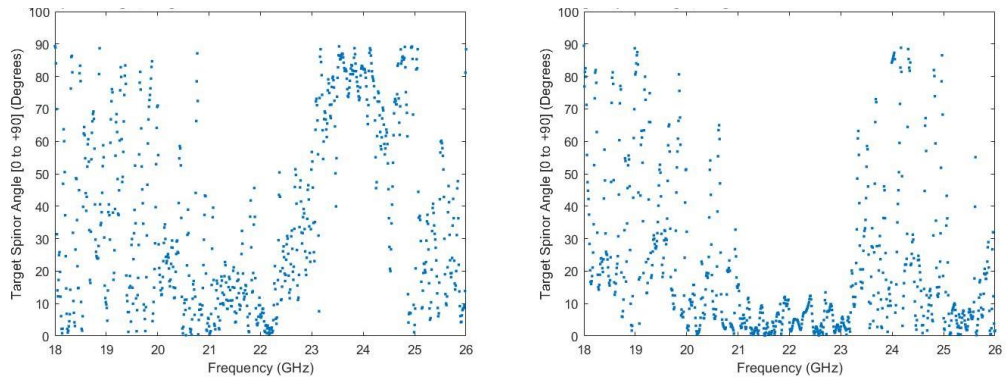


Figure 17-62 Small knife measured spinor angle vertical left, horizontal right

17.9 Long Knife in vertical and horizontal orientations

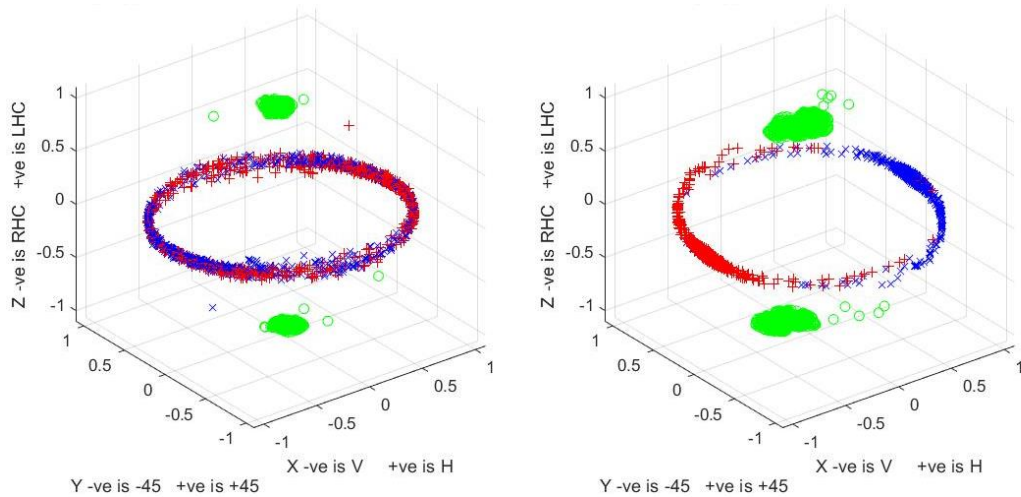


Figure 17-63 Long knife measured fork plots vertical left, horizontal right

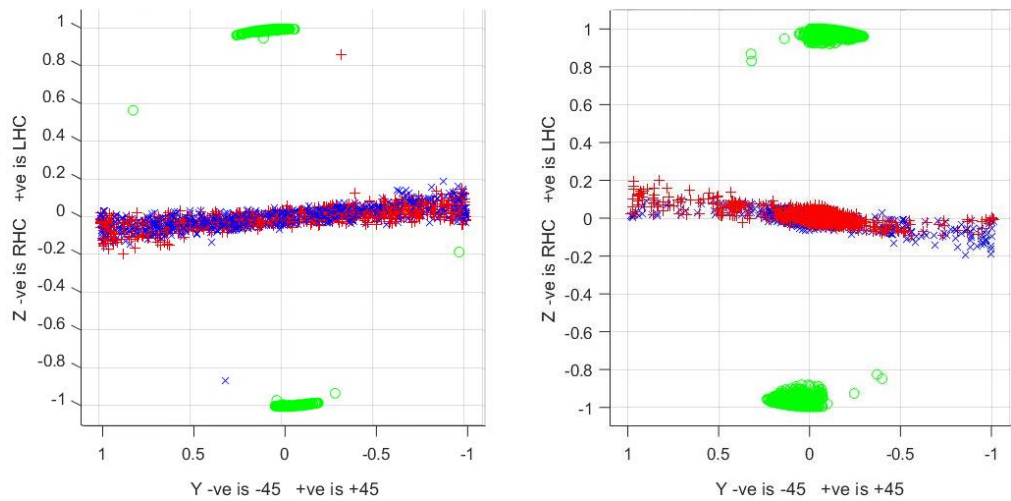


Figure 17-64 Long knife measured fork plots vertical left, horizontal right

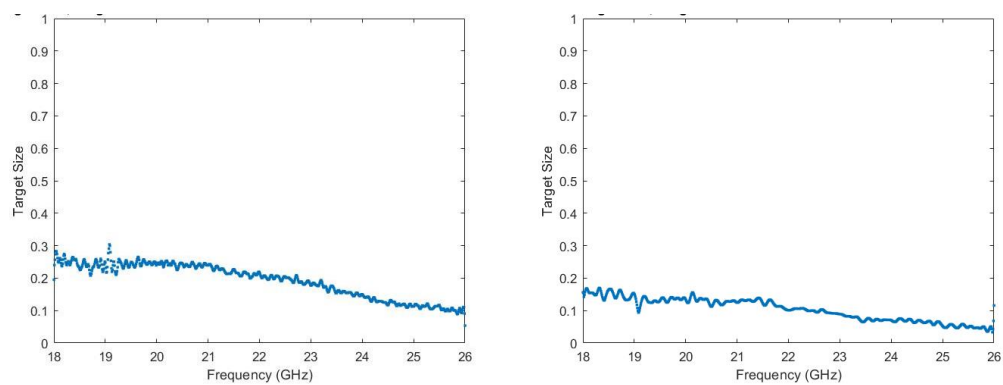


Figure 17-65 Long knife measured target size vertical left, horizontal right

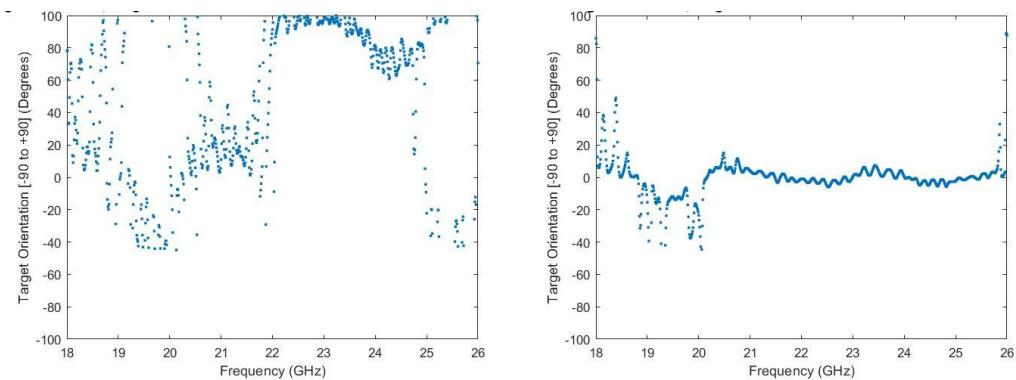


Figure 17-66 Long knife measured orientation angle vertical left, horizontal right

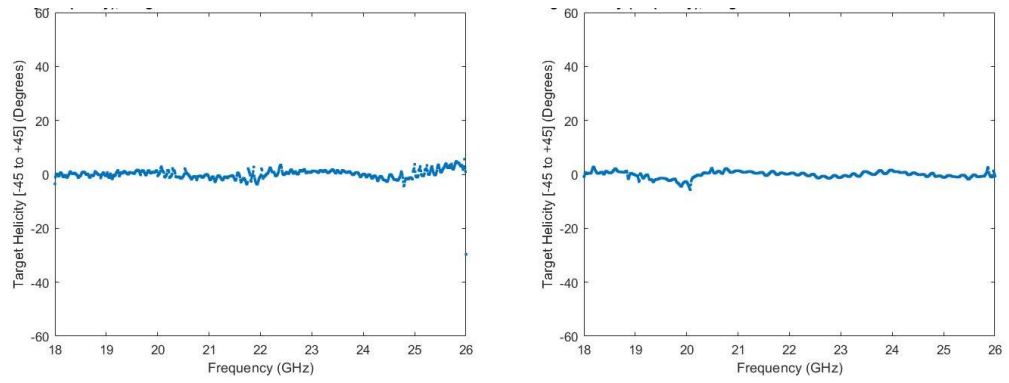


Figure 17-67 Long knife measured helicity angle vertical left, horizontal right

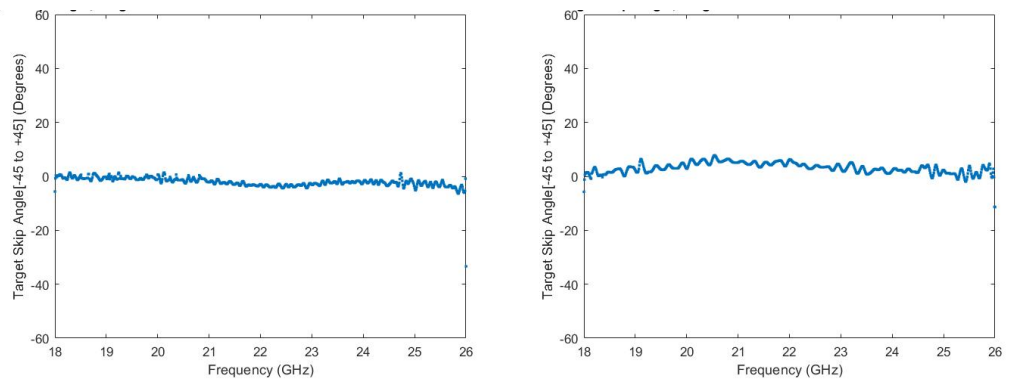


Figure 17-68 Long knife measured skip angle vertical left, horizontal right

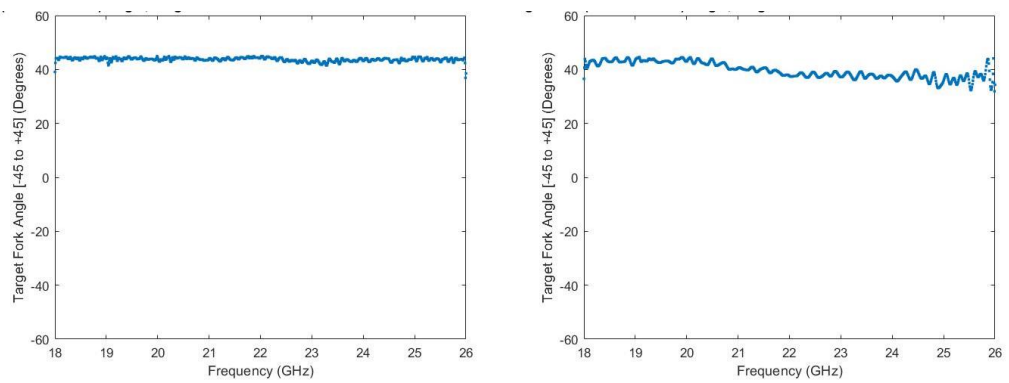


Figure 17-69 Long knife measured fork angle vertical left, horizontal right

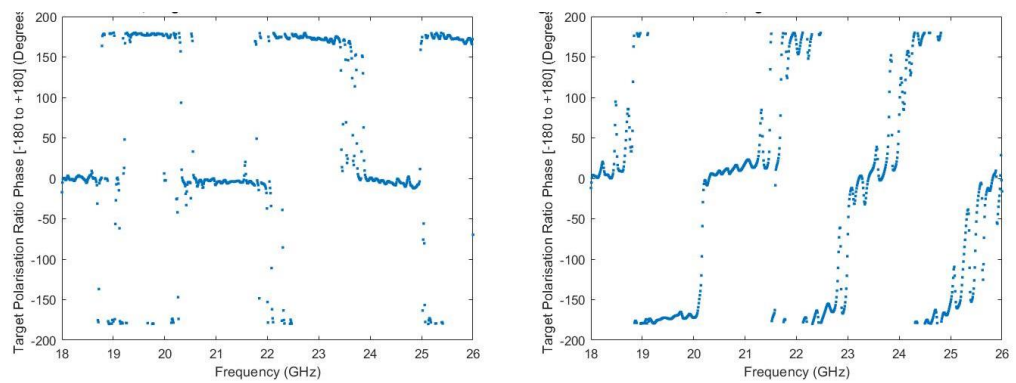


Figure 17-70 Long knife polarisation phase ratio vertical left, horizontal right

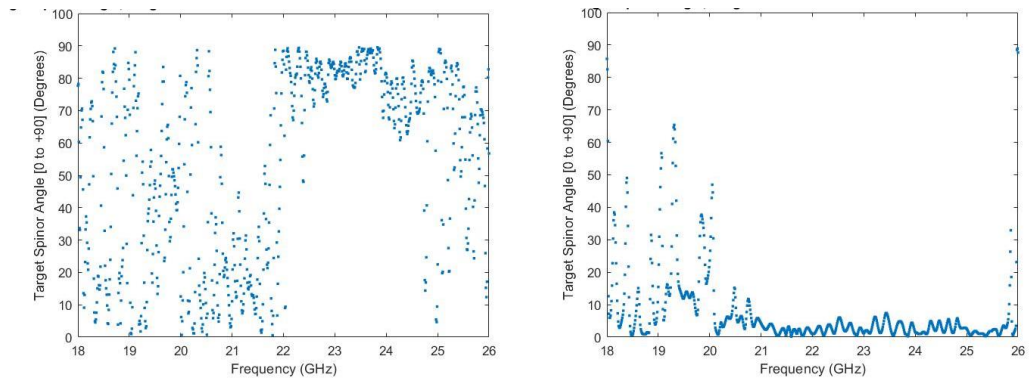


Figure 17-71 Long knife measured spinor angle vertical left, horizontal right

17.10 Long knife horizontal and 45° orientations



Figure 17-72 Long horizontal knife left, at 45° right

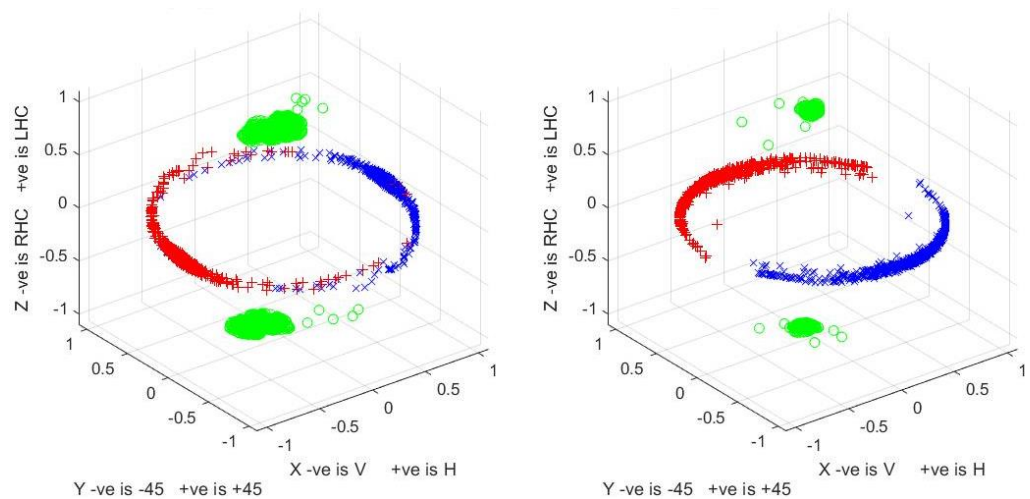


Figure 17-73 Long knife measured fork plots horizontal left, 45° right

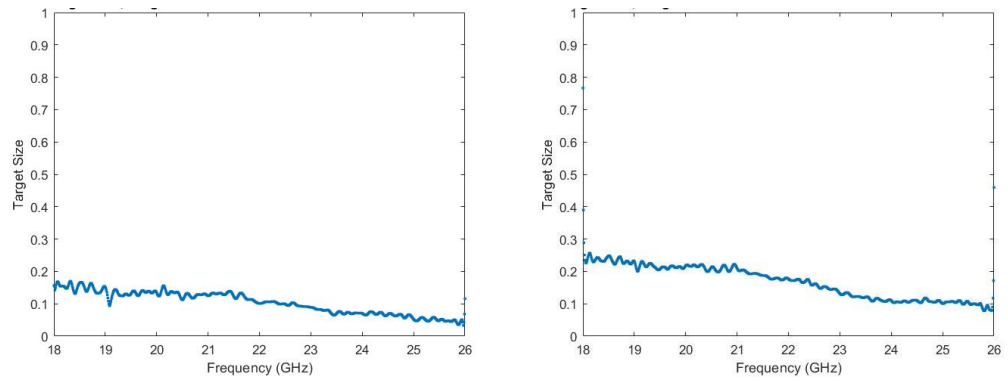


Figure 17-74 Long knife measured target size horizontal left, 45° right

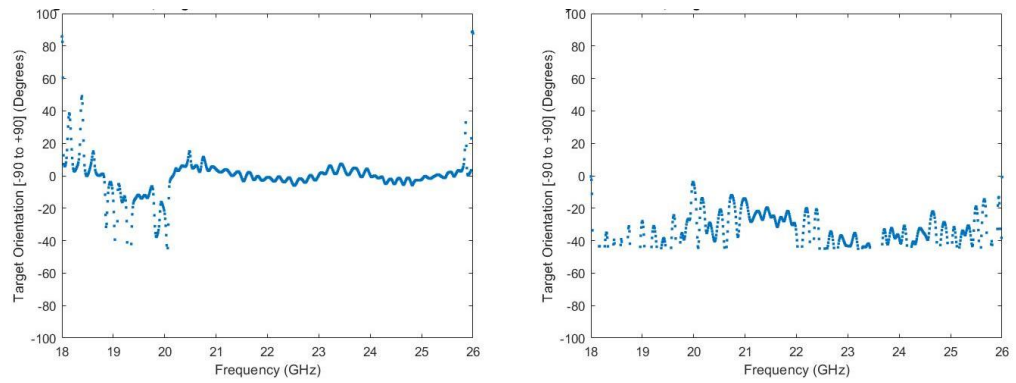


Figure 17-75 Long knife measured orientation angle horizontal left, 45° right

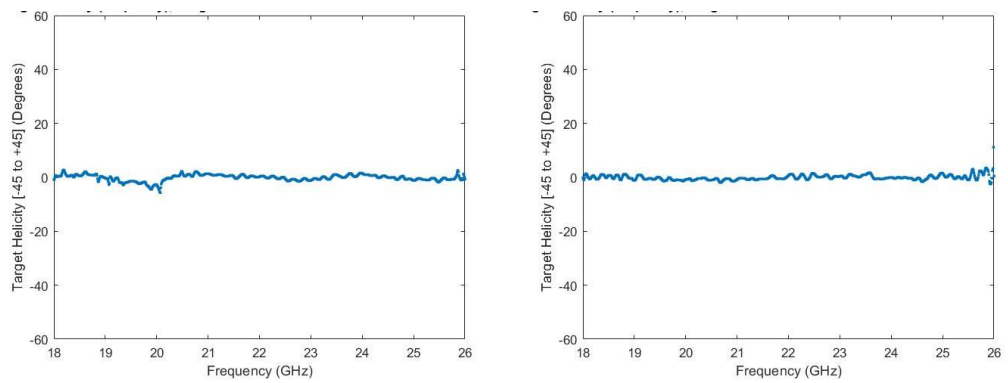


Figure 17-76 Long knife measured helicity angle horizontal left, 45° right

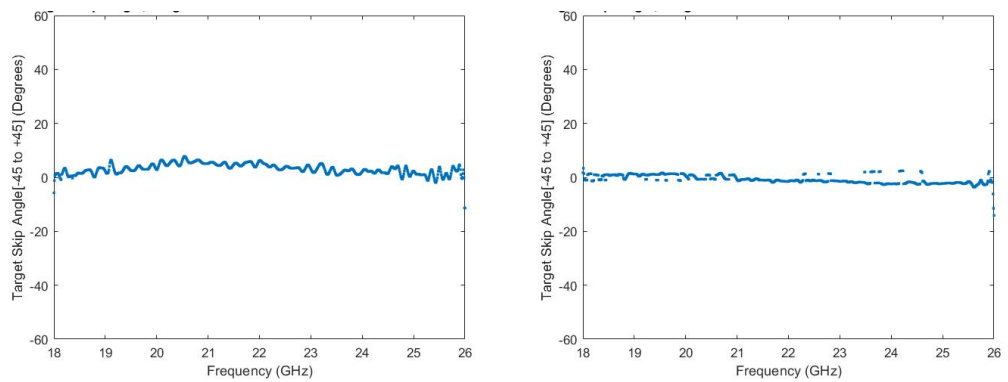


Figure 17-77 Long knife measured skip angle horizontal left, 45° right

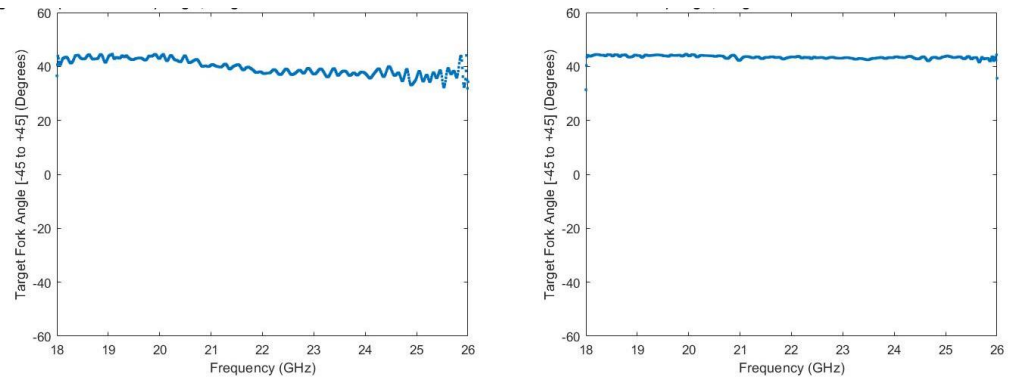


Figure 17-78 Long knife measured fork angle horizontal left, 45° right

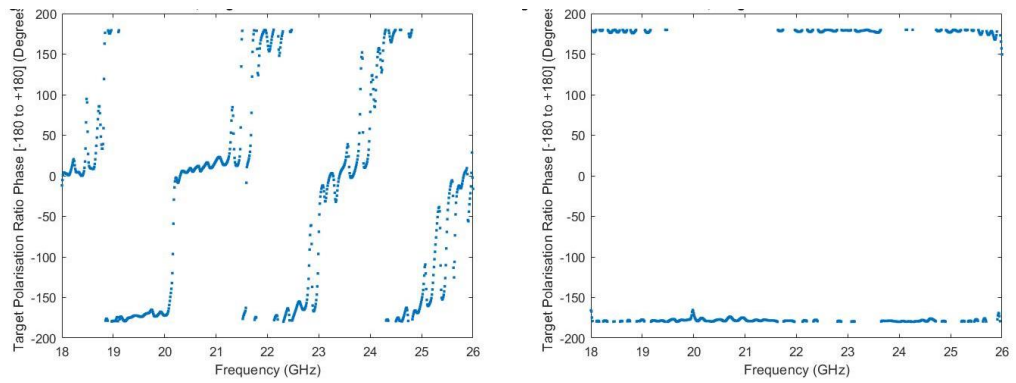


Figure 17-79 Long knife measured polarisation phase ratio horizontal left, 45° right

17.11 Short knife at 45° blade spine leading compared to the blade edge

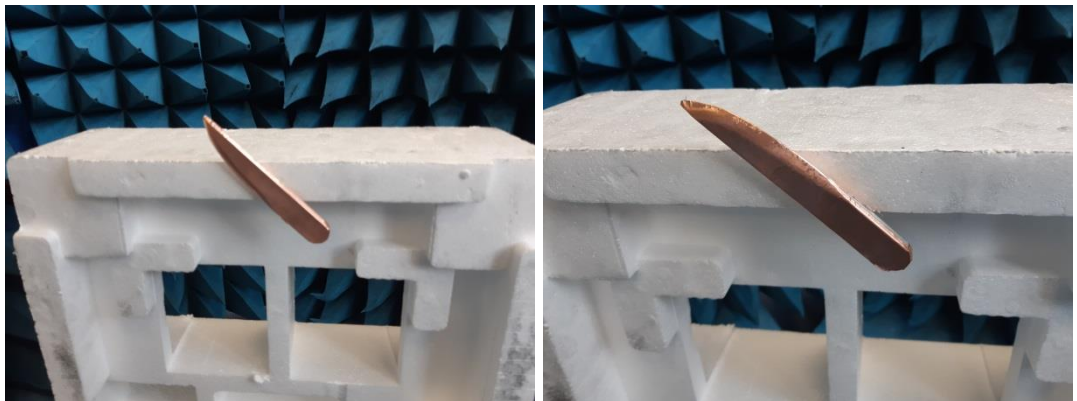


Figure 17-80 Small knife at 45° spine leading left, blade edge leading right

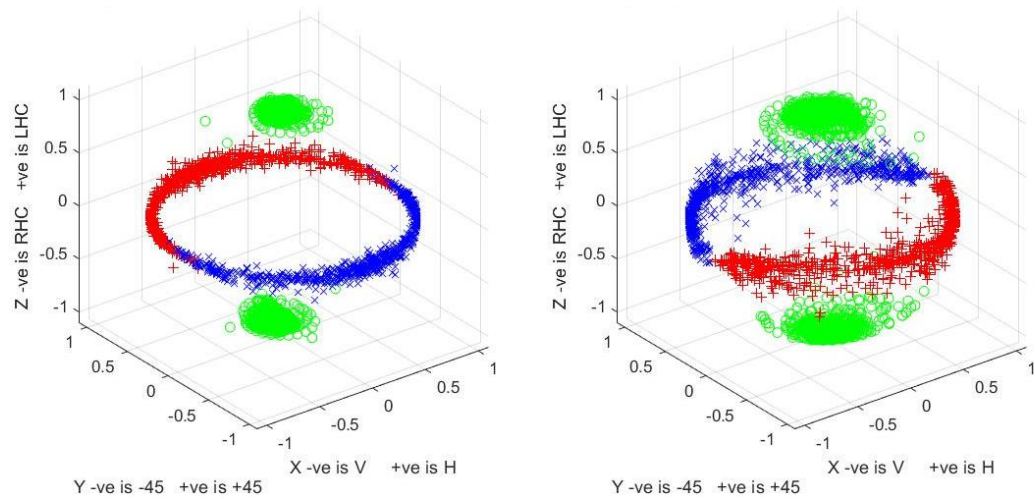


Figure 17-81 Small knife at 45° measured fork plots blade spine leading left, sharp edge right

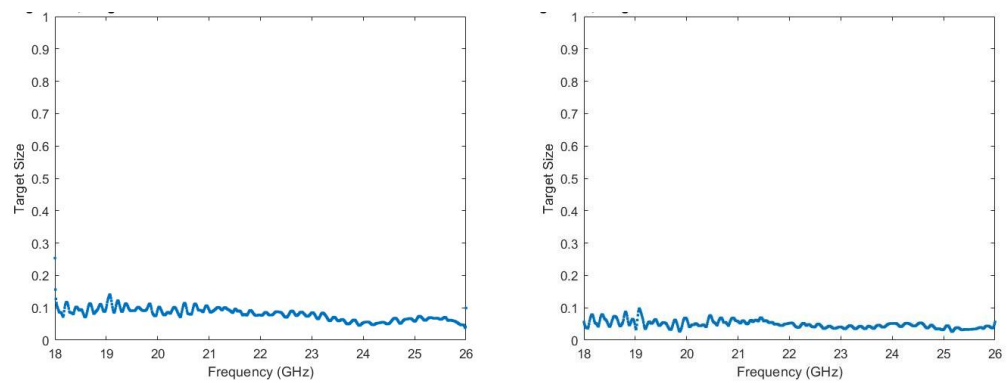


Figure 17-82 Small knife at 45° measured target size blade spine leading left, sharp edge right

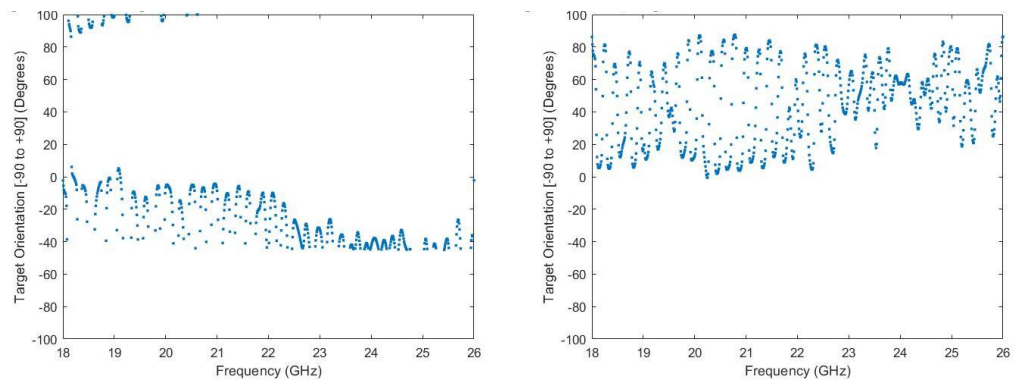


Figure 17-83 Small knife at 45° measured orientation angle blade spine leading left, sharp edge right

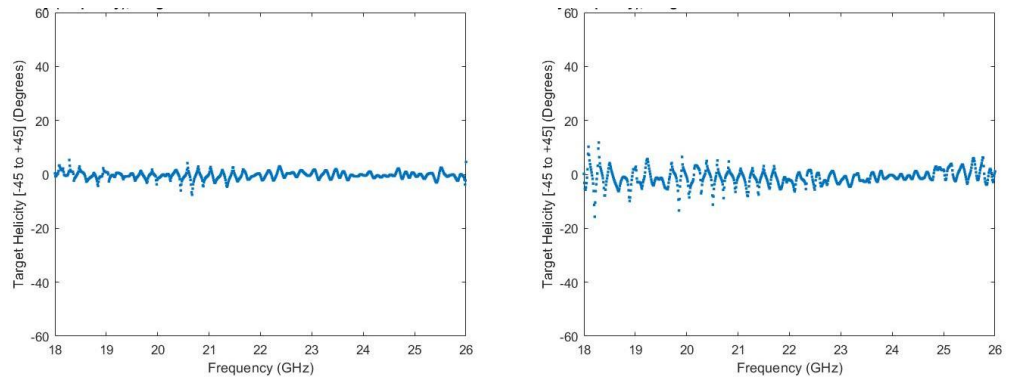


Figure 17-84 Small knife at 45° measured helicity angle blade spine leading left, sharp edge right

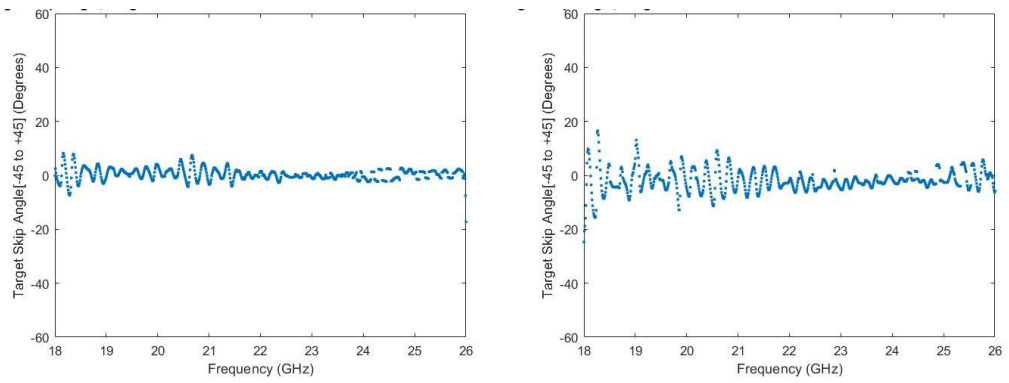


Figure 17-85 Small knife at 45° measured skip angle blade spine leading left, sharp edge right

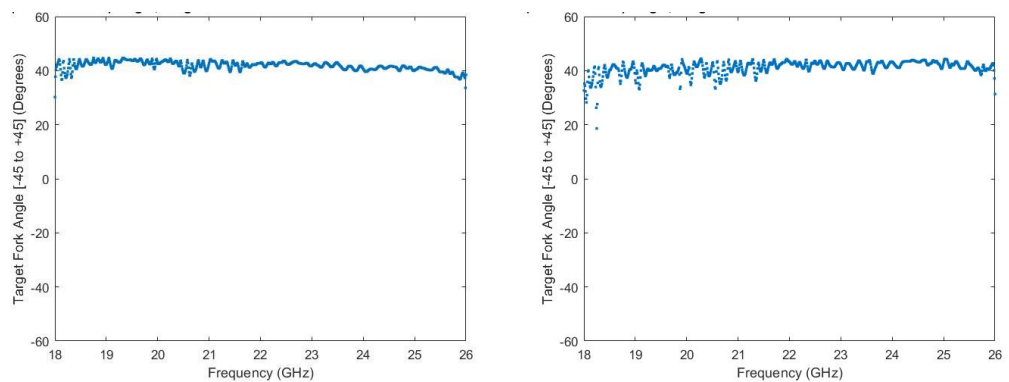


Figure 17-86 Small knife at 45° measured fork angle blade spine leading left, sharp edge right

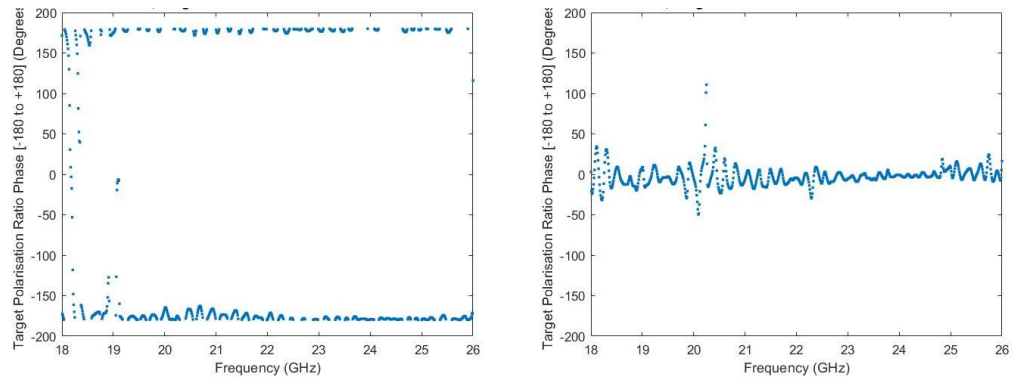


Figure 17-87 Small knife at 45° measured polarisation phase ratio blade spine leading left, sharp edge right

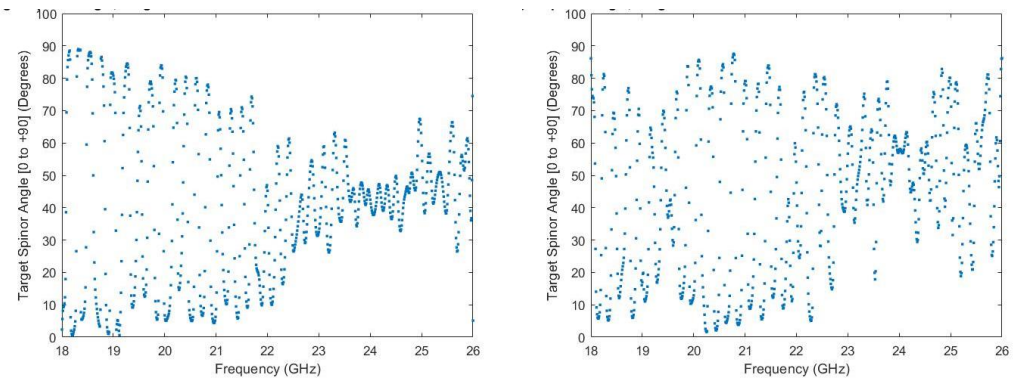


Figure 17-88 Small knife at 45° measured spinor angle blade spine leading left, sharp edge right

17.12 Long vertically and horizontally orientated knives edge on

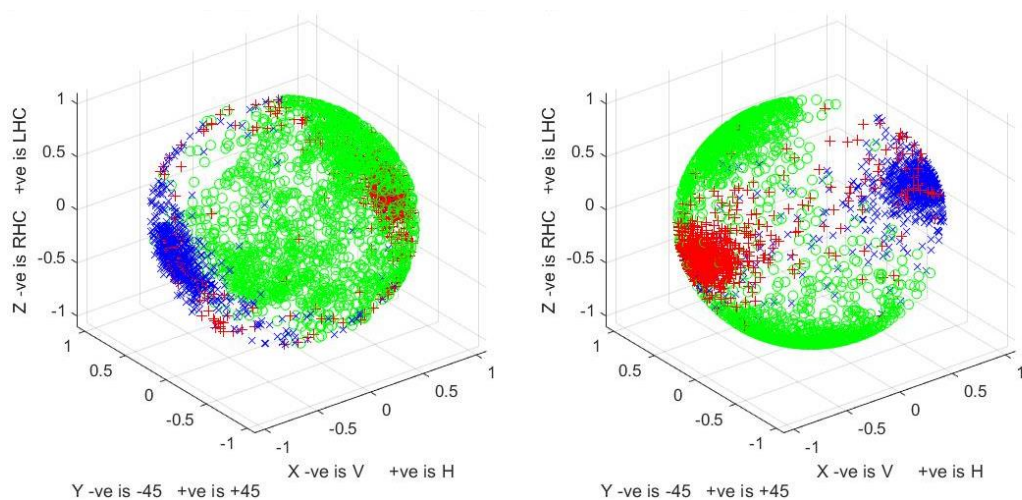


Figure 17-89 Measured Huygens fork plots for a long knife edge on vertical left, horizontal right

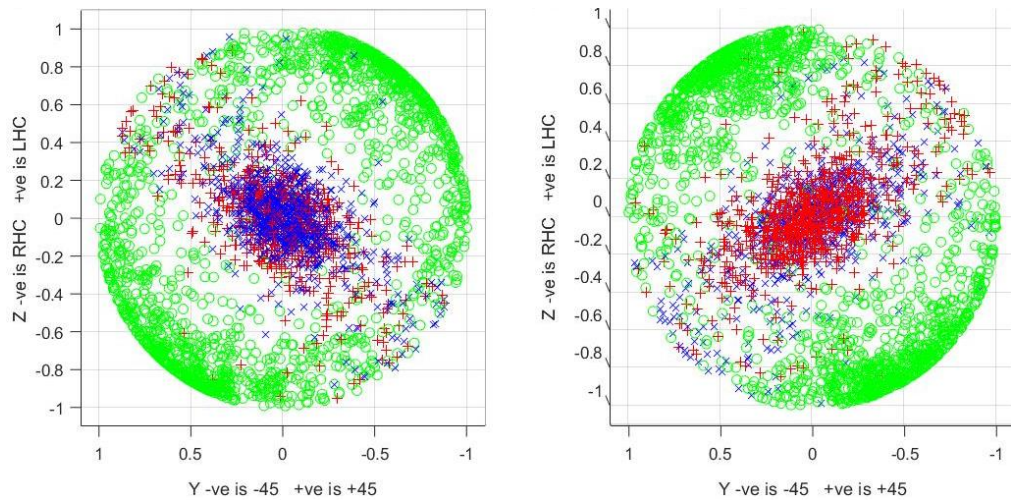


Figure 17-90 Measured Huygen fork plots for a long knife edge on vertical left, horizontal right

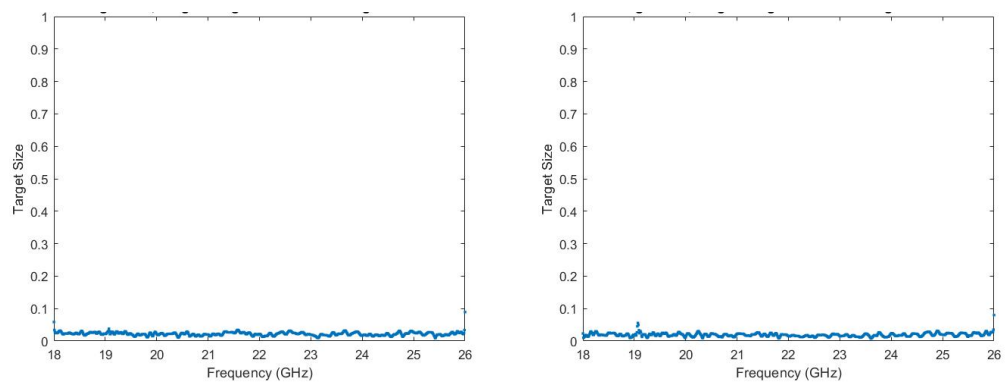


Figure 17-91 Measured target size for a long knife edge on vertical left, horizontal right

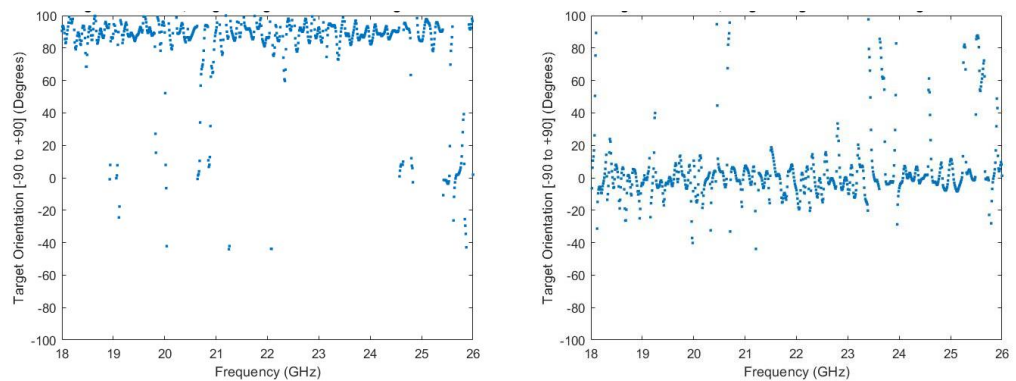


Figure 17-92 Measured orientation angle for a long knife edge on vertical left, horizontal right

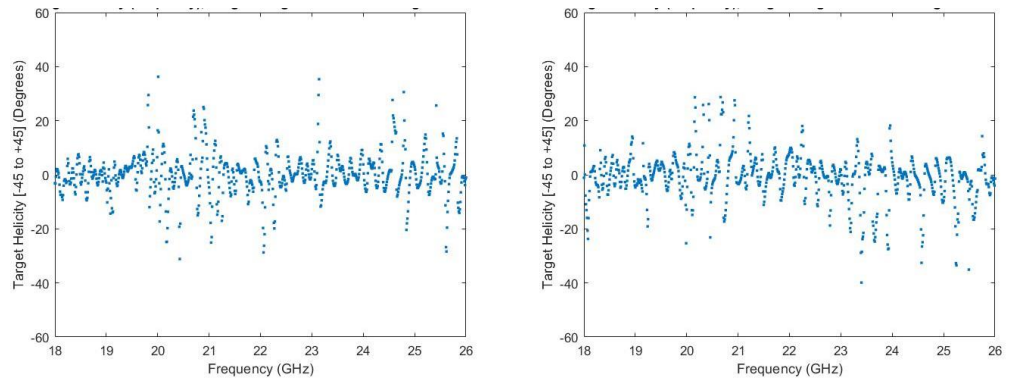


Figure 17-93 Measured helicity angle for a long knife edge on vertical left, horizontal right

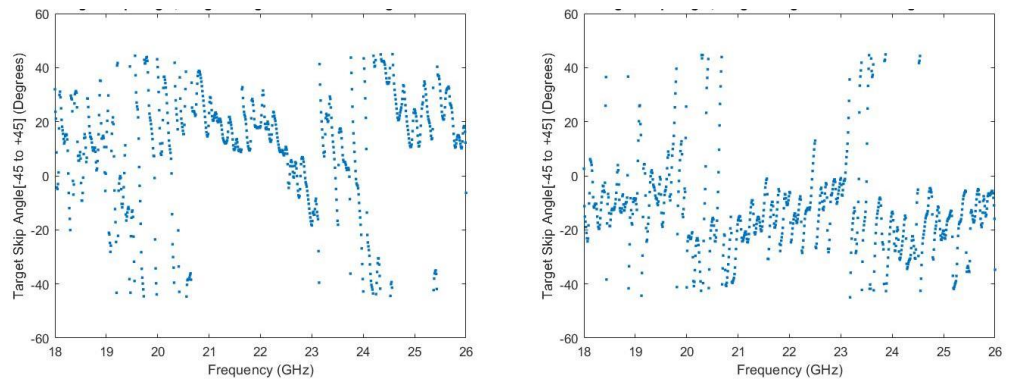


Figure 17-94 Measured skip angle for a long knife edge on vertical left, horizontal right

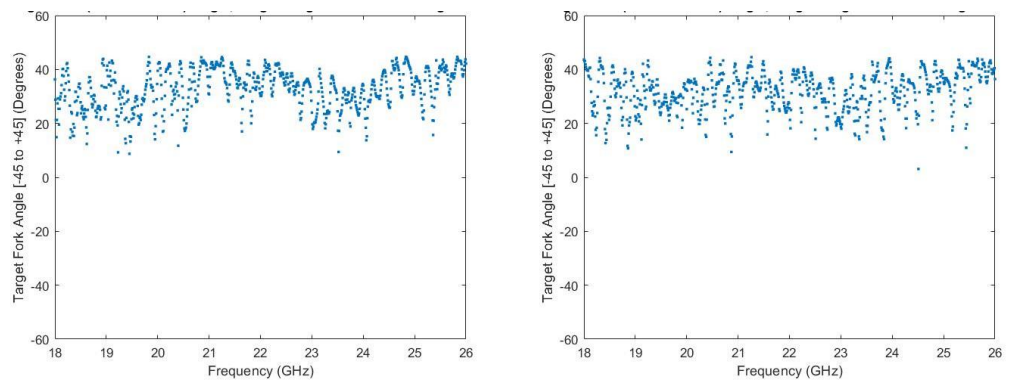


Figure 17-95 Measured fork angle for a long knife edge on vertical left, horizontal right

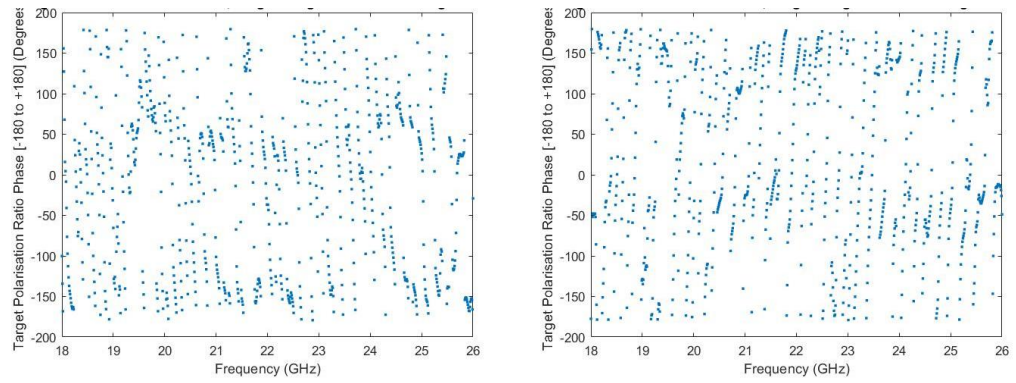


Figure 17-96 Measured polarisation phase ratio for a long knife edge on vertical left, horizontal right

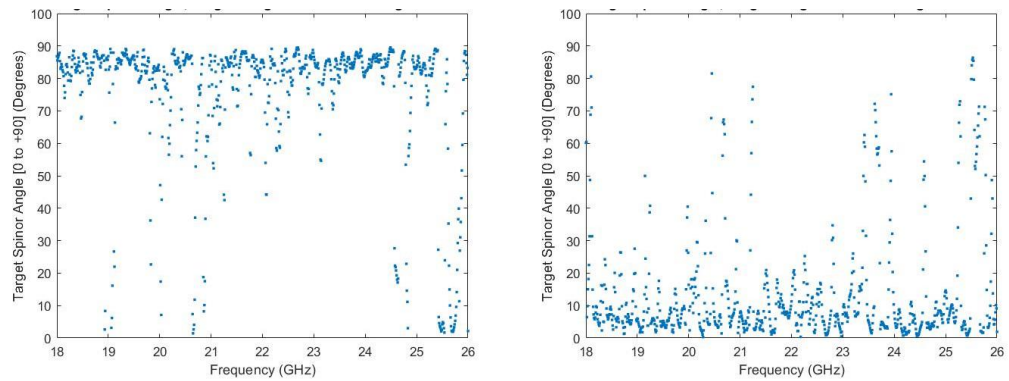


Figure 17-97 Measured spinor angle for a long knife edge on vertical left, horizontal right

17.13 Brass gun horizontal and vertical orientations

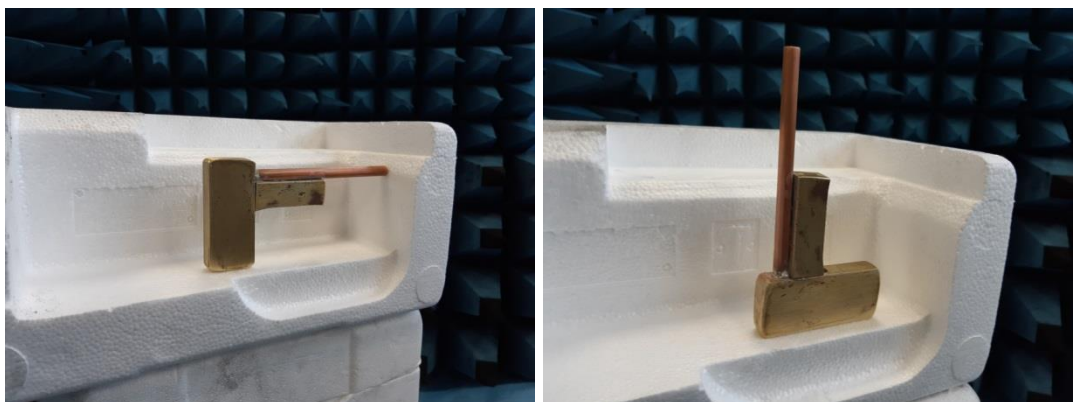


Figure 17-98 Brass Gun, horizontal barrel (left), vertical (right).

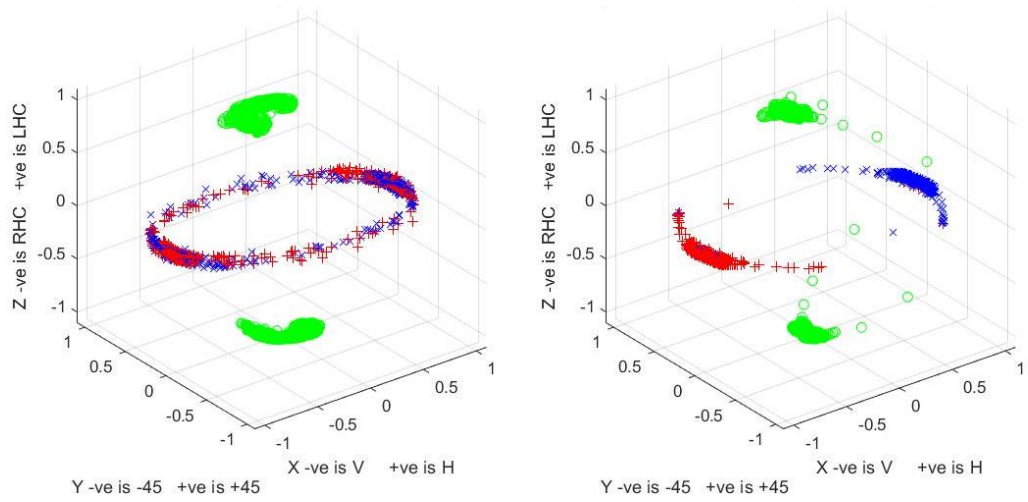


Figure 17-99 Brass gun measured fork plots horizontal left, vertical right

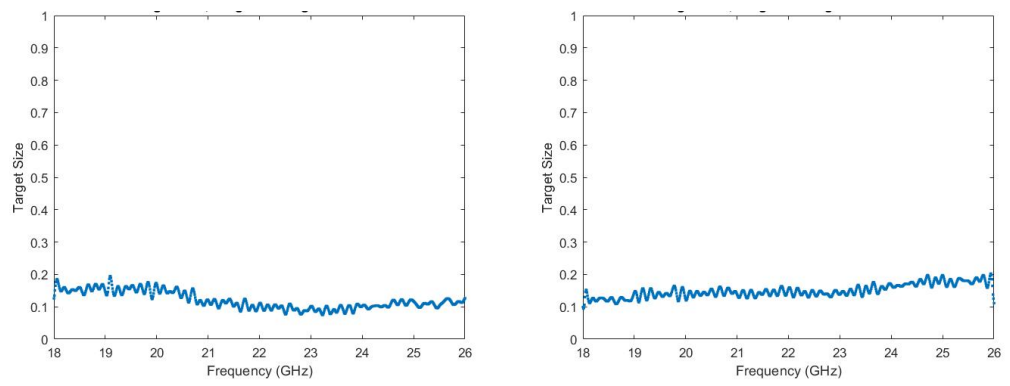


Figure 17-100 Brass gun measured target size horizontal left, vertical right

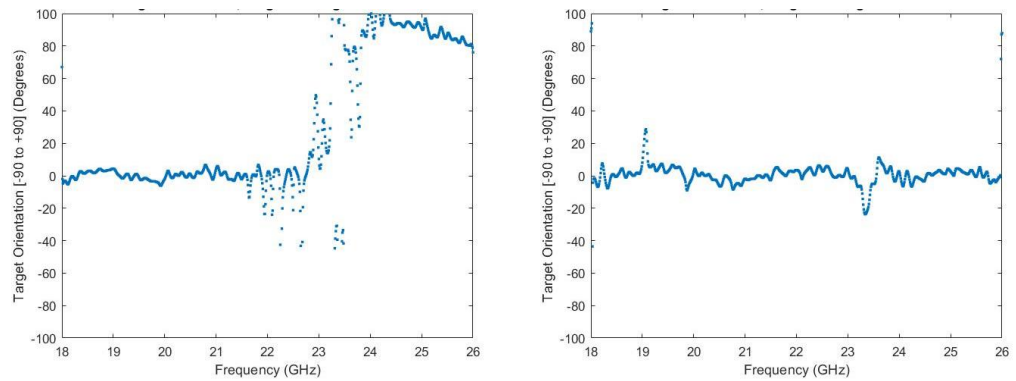


Figure 17-101 Brass gun measured orientation angle horizontal left, vertical right

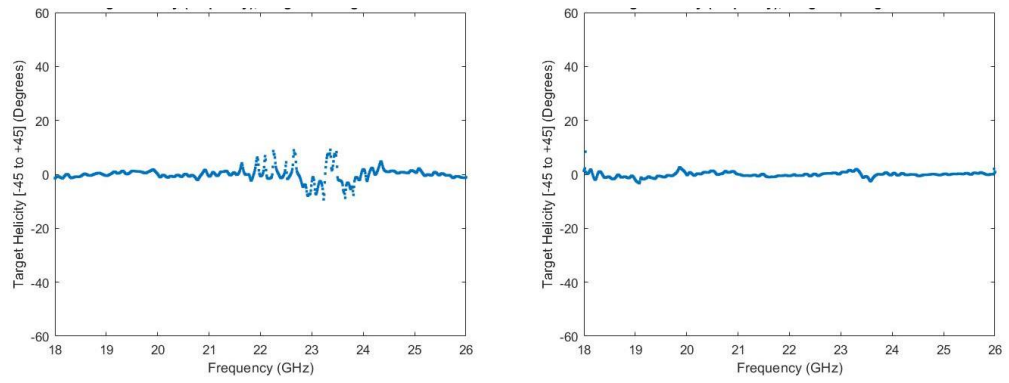


Figure 17-102 Brass gun measured helicity angle horizontal left, vertical right

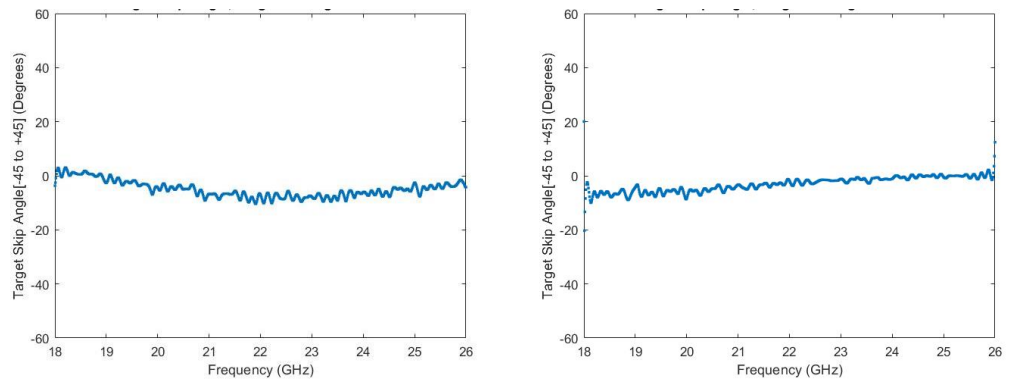


Figure 17-103 Brass gun measured skip angle horizontal left, vertical right

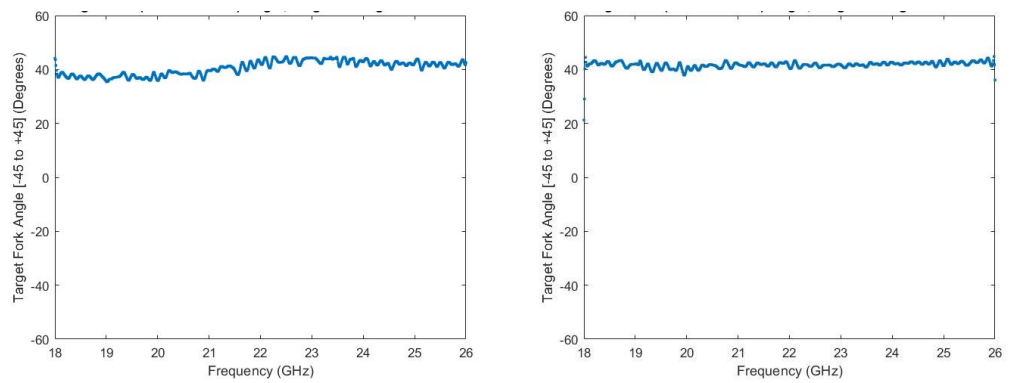


Figure 17-104 Brass gun measured fork angle horizontal left, vertical right

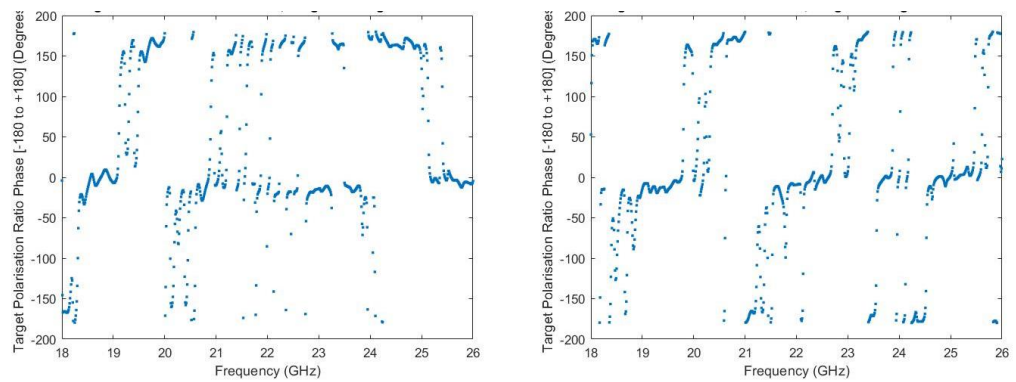


Figure 17-105 Brass gun polarisation ratio phase horizontal left, vertical right

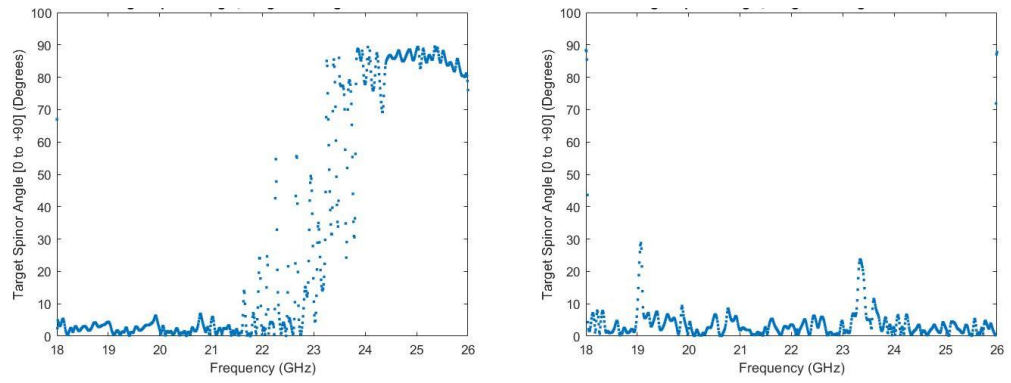


Figure 17-106 Brass gun measured spinor angle horizontal left, vertical right

17.14 Brass gun horizontal orientation left, 45° right

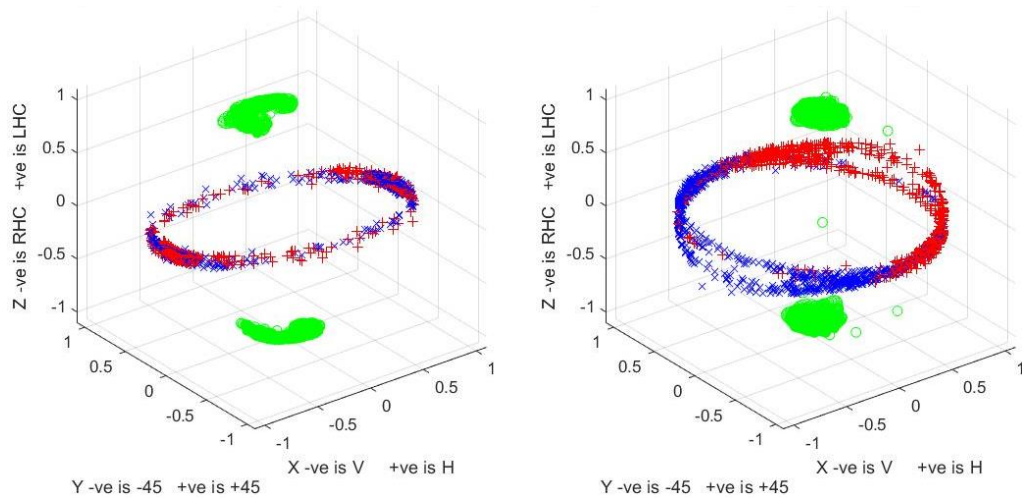


Figure 17-107 Brass gun measured forks plot horizontal left, 45° right

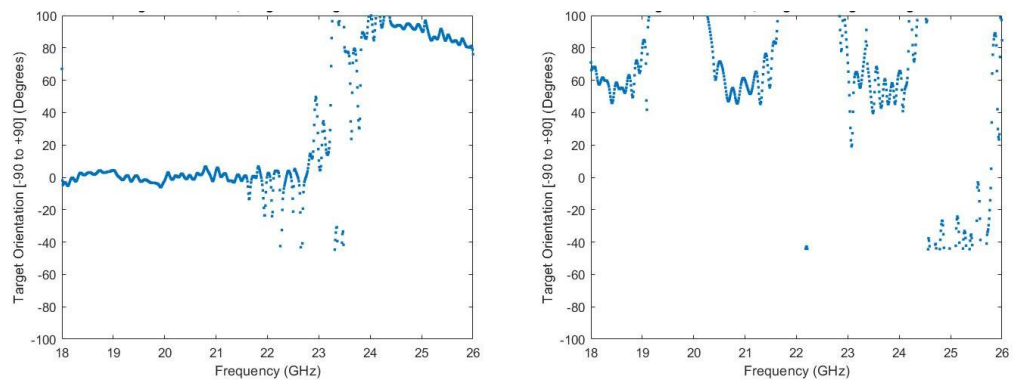


Figure 17-108 Brass gun measured orientation angle horizontal left, 45° right

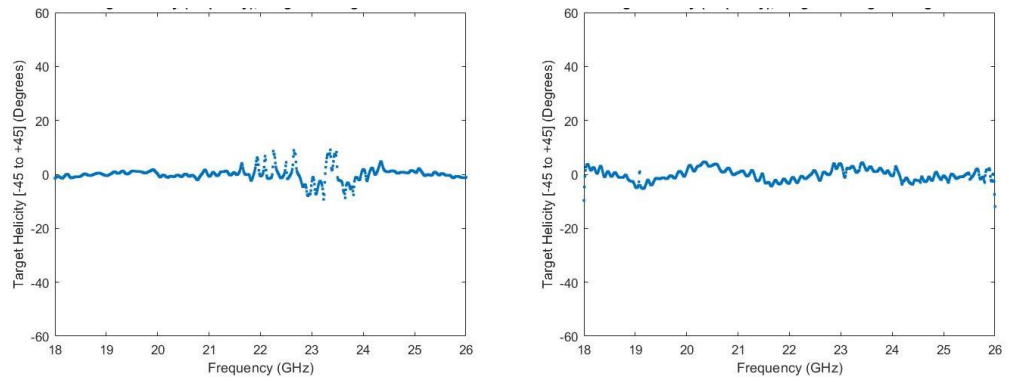


Figure 17-109 Brass gun measured helicity angle horizontal left, 45° right

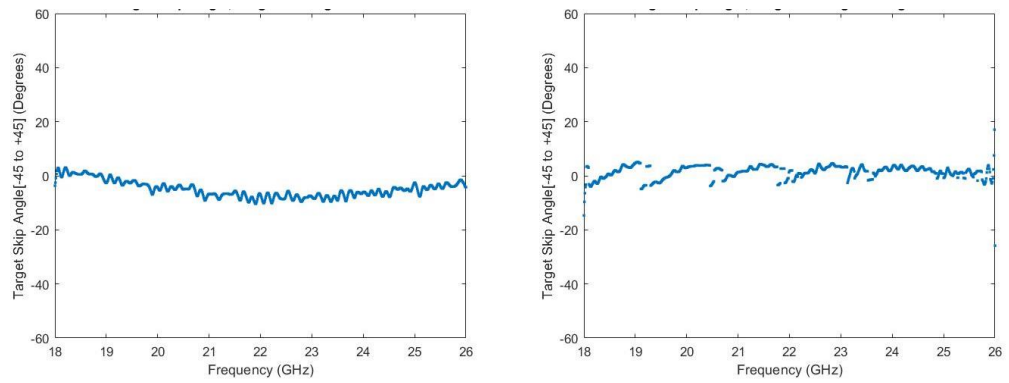


Figure 17-110 Brass gun measured skip angle horizontal left, 45° right

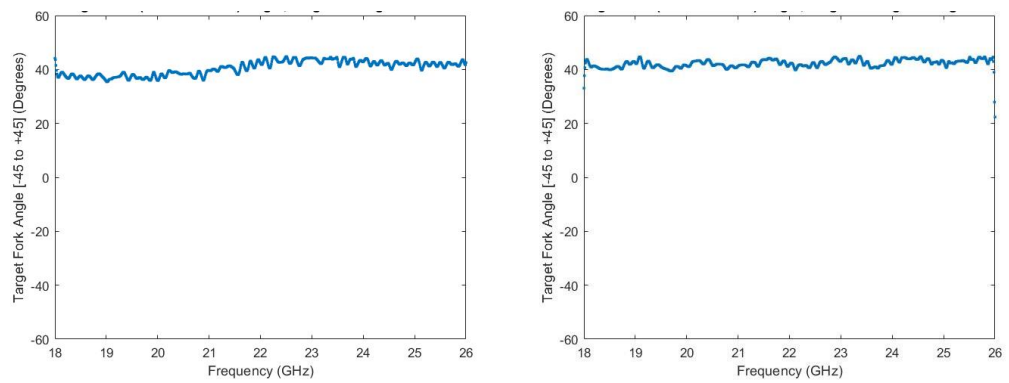


Figure 17-111 Brass gun measured fork angle horizontal left, 45° right

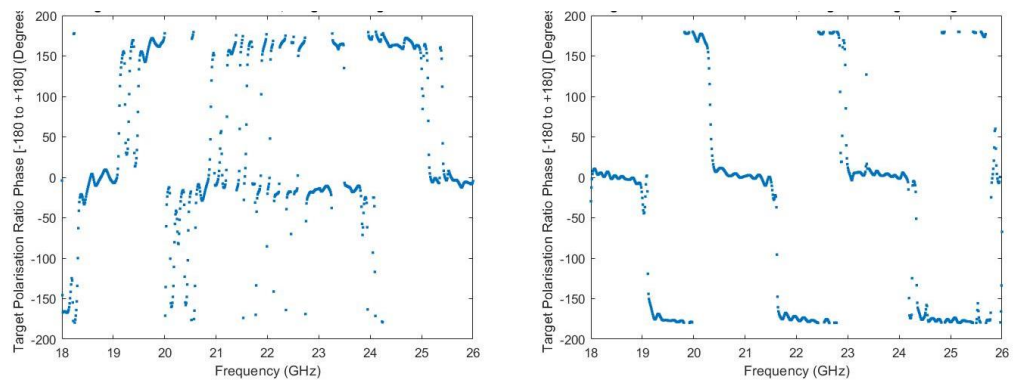


Figure 17-112 Brass gun polarisation ratio phase horizontal left, 45° right

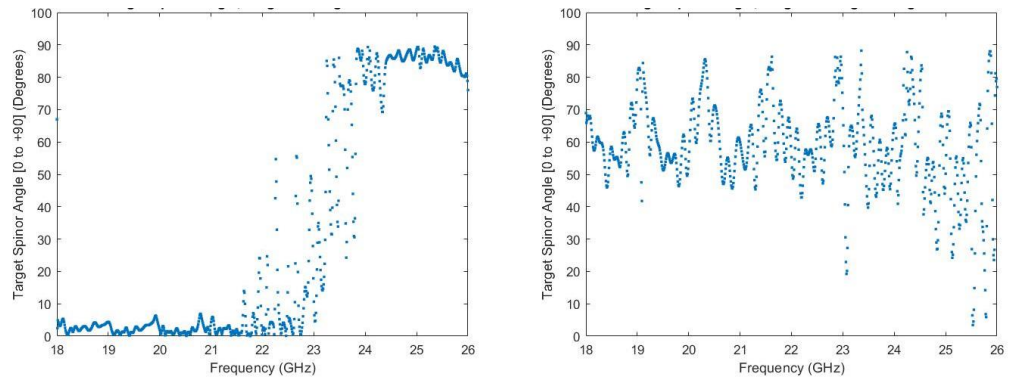


Figure 17-113 Brass gun measured spinor angle horizontal left, 45° right

17.15 Shrapnel target

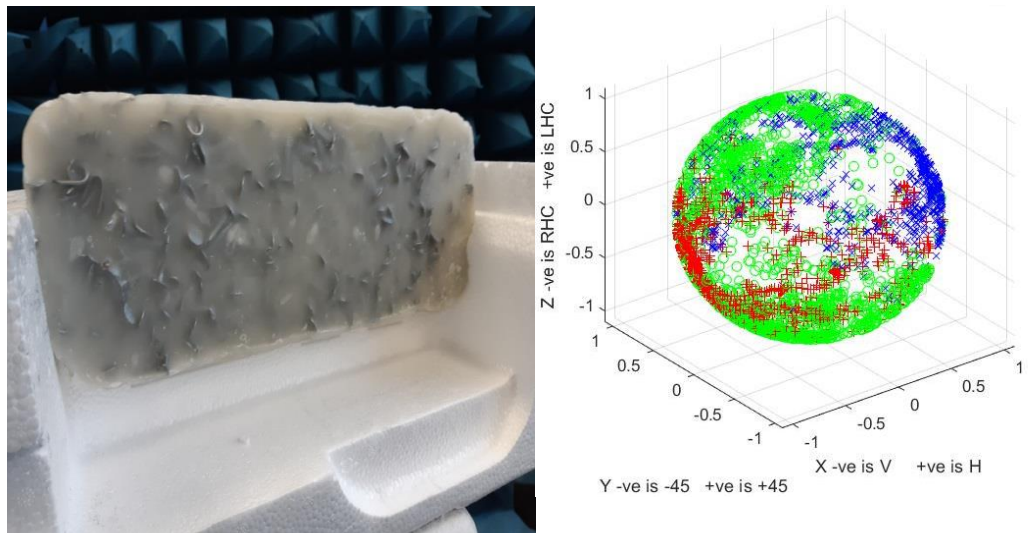


Figure 17-114 Shrapnel Target left, measured fork plot right

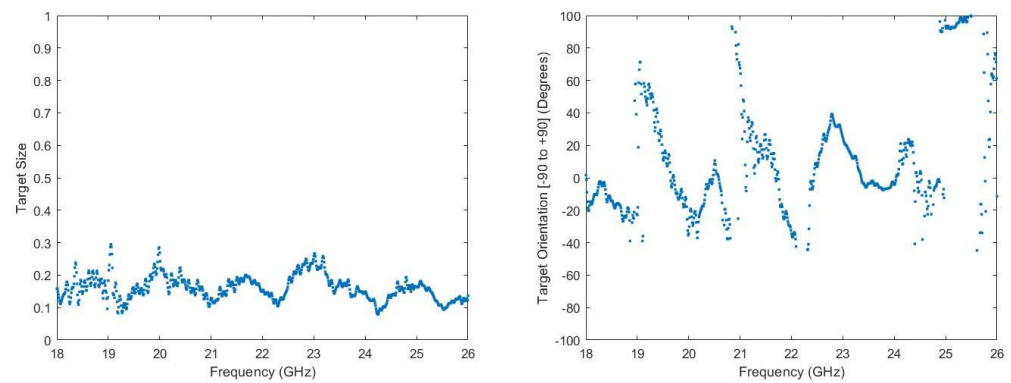


Figure 17-115 Shrapnel measured target size left, orientation angle right

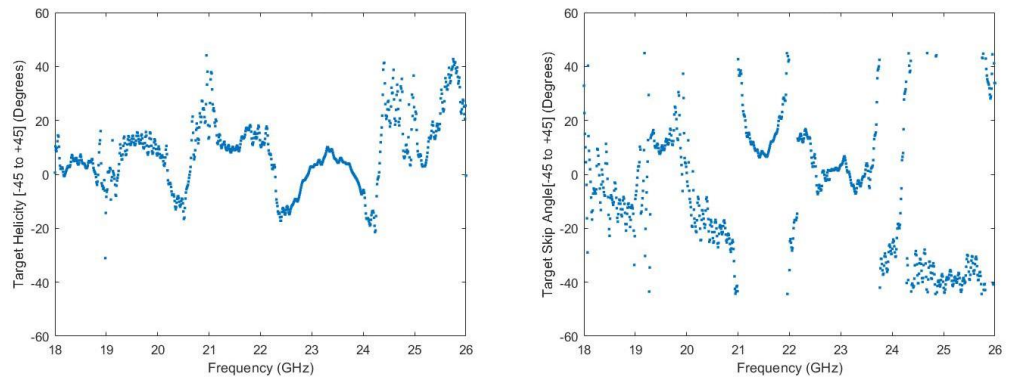


Figure 17-116 Shrapnel measured helicity angle left, skip angle right

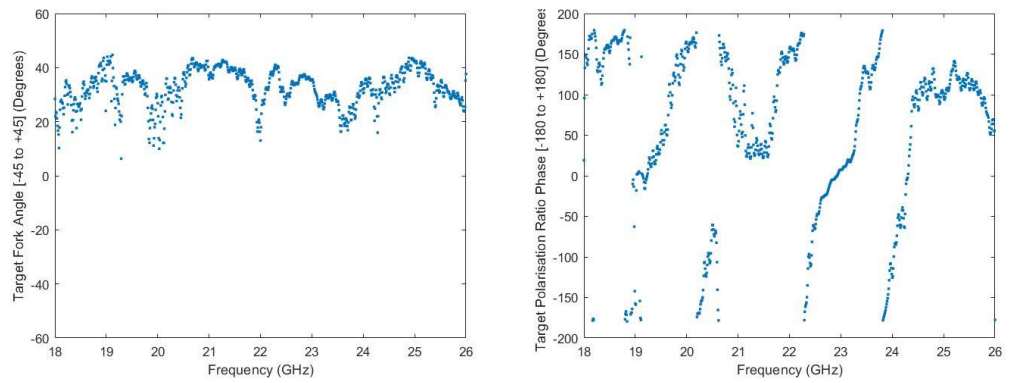


Figure 17-117 Shrapnel measured fork angle left, polarization phase ratio right

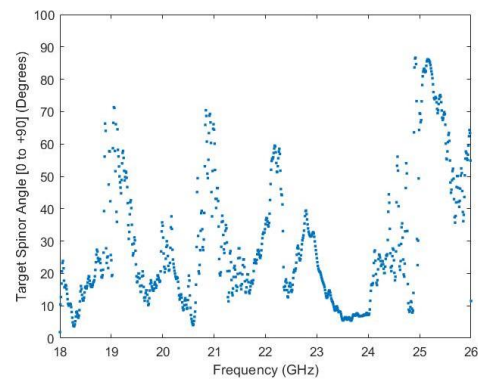


Figure 17-118 Shrapnel measured spinor angle

17.16 Human torso perpendicular to radar beam with hands above head

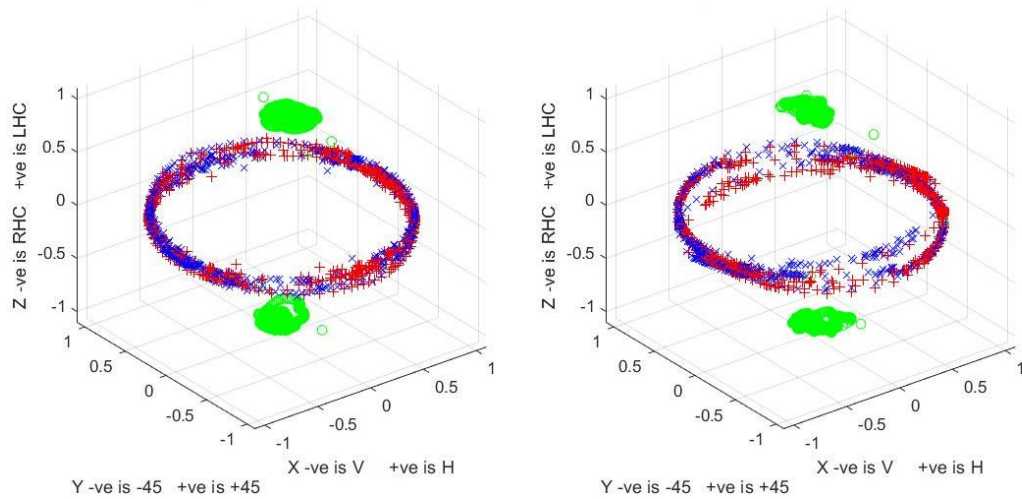


Figure 17-119 Hands above head measured fork plot subject 1 left, subject 2 right

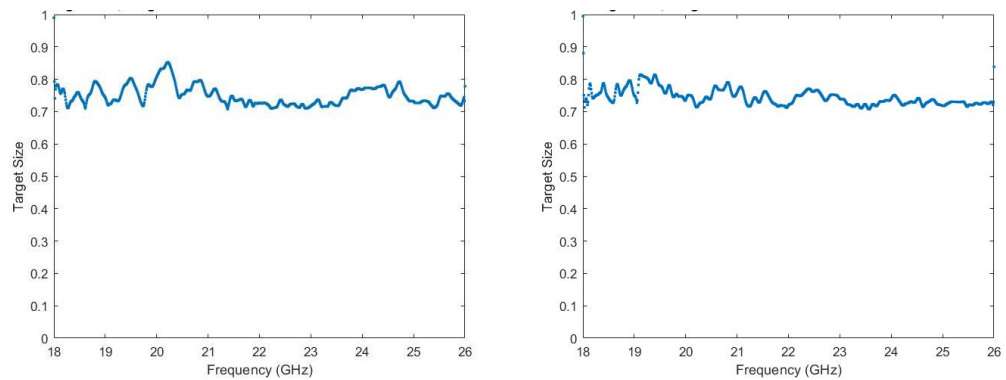


Figure 17-120 Hands above head measured target size subject 1 left, subject 2 right

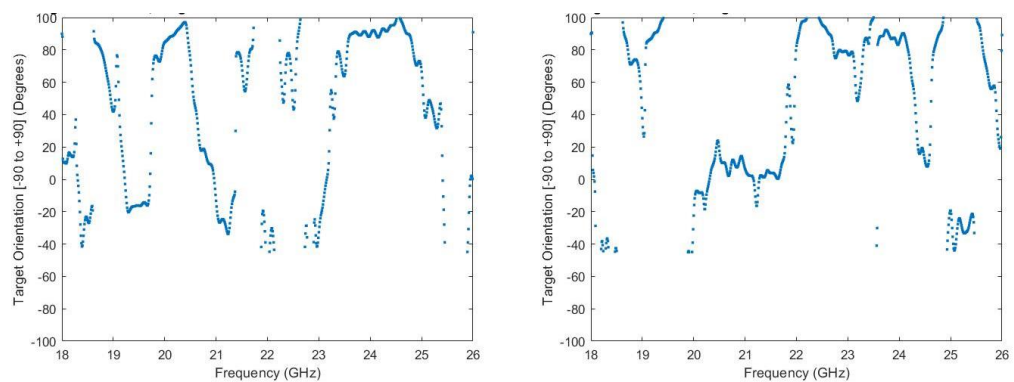


Figure 17-121 Hands above head measured orientation angle subject 1 left, subject 2 right

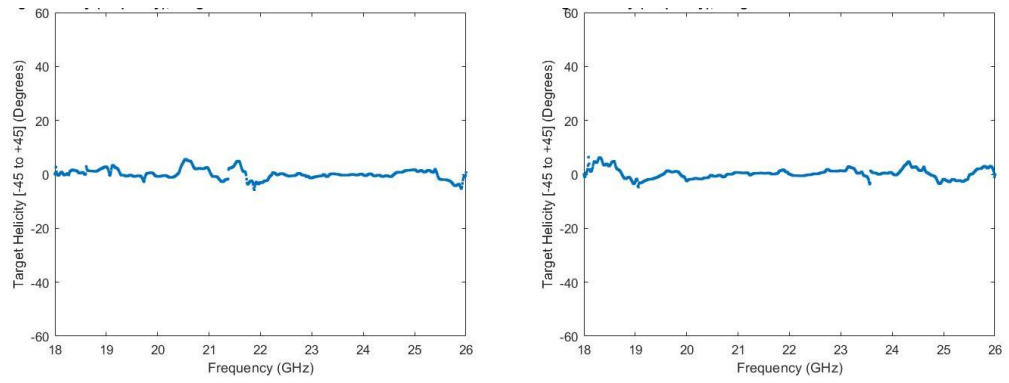


Figure 17-122 Hands above head measured helicity angle subject 1 left, subject 2
right

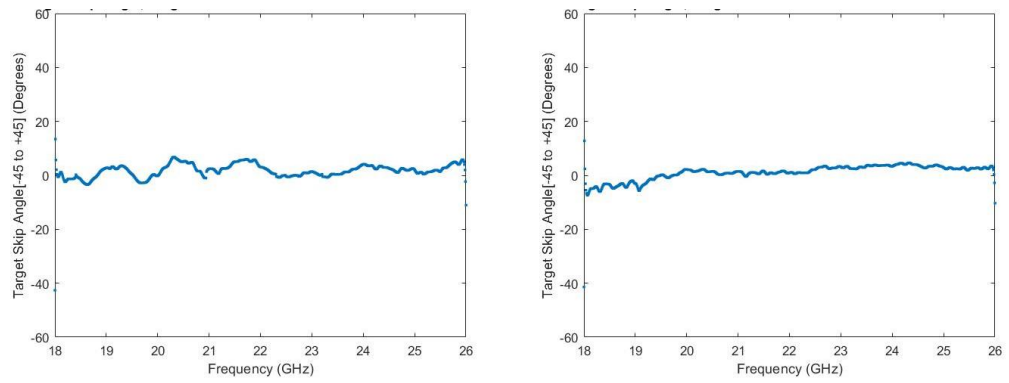


Figure 17-123 Hands above head measured skip angle subject 1 left, subject 2
right

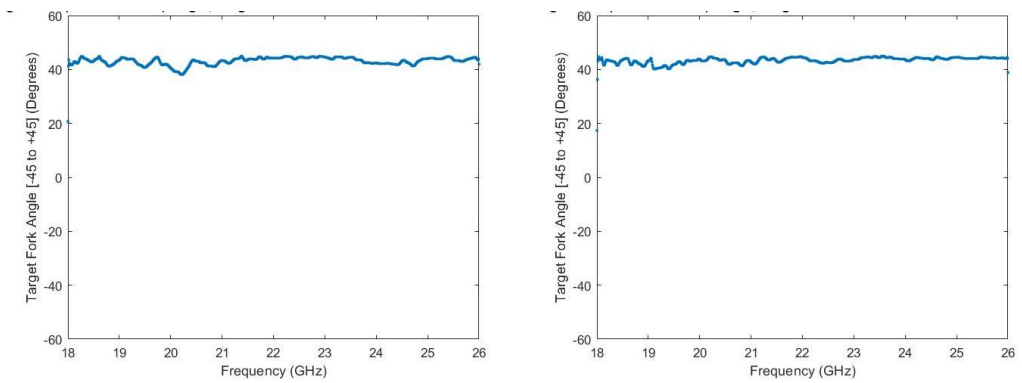


Figure 17-124 Hands above head measured fork angle subject 1 left, subject 2
right

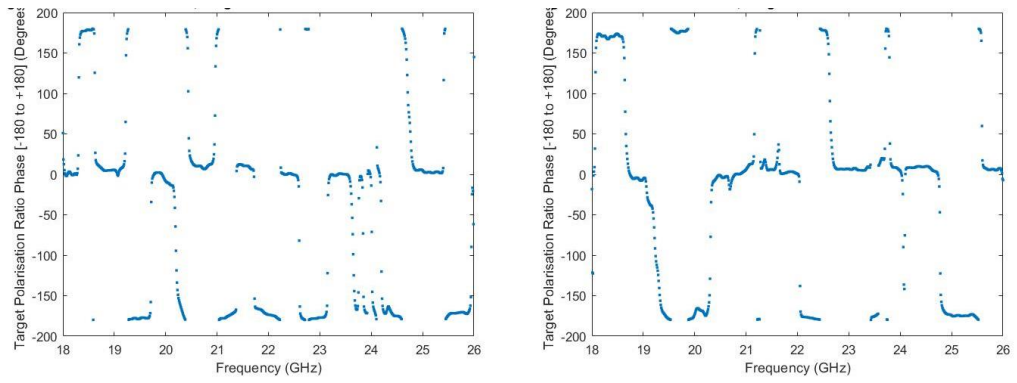


Figure 17-125 Hands above head measured polarisation phase ratio subject 1 left, subject 2 right

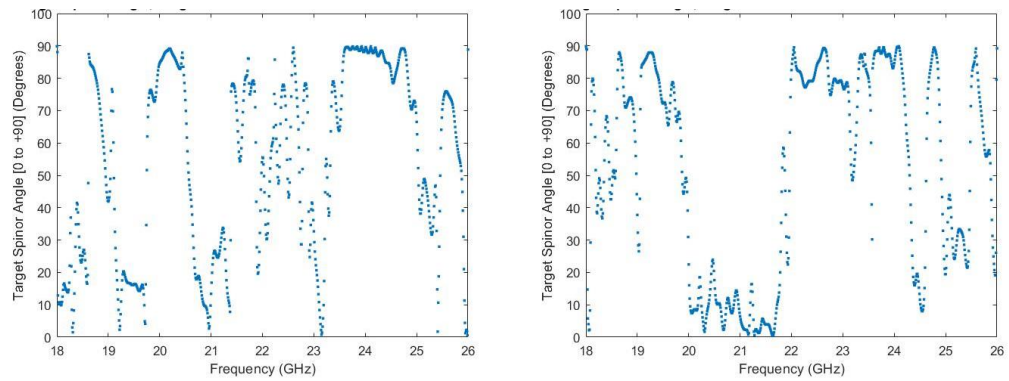


Figure 17-126 Hands above head measured spinor angle subject 1 left, subject 2 right

17.17 Human torso perpendicular to the beam of the radar with hands at the side

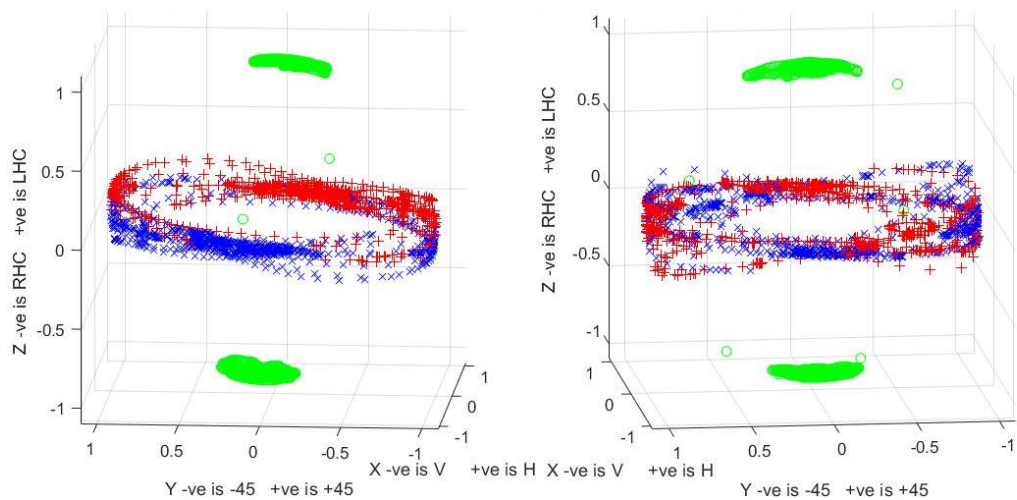


Figure 17-127 Hands at side measured fork plot subject 1 left, subject 2 right

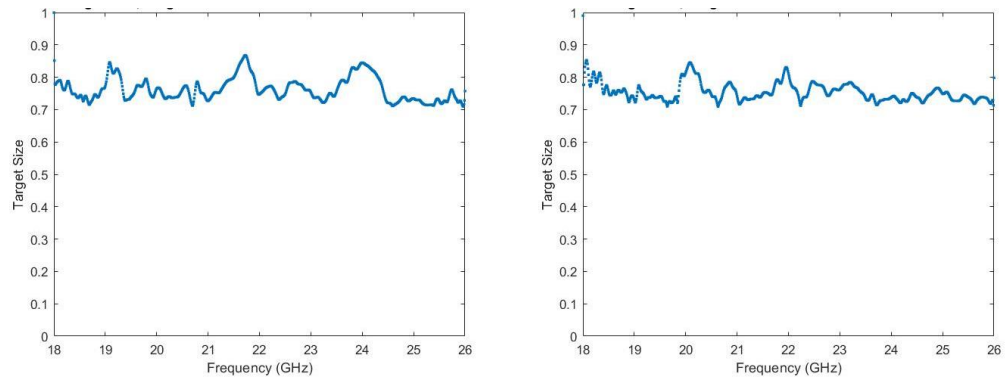


Figure 17-128 Hands at side measured target size subject 1 left, subject 2 right

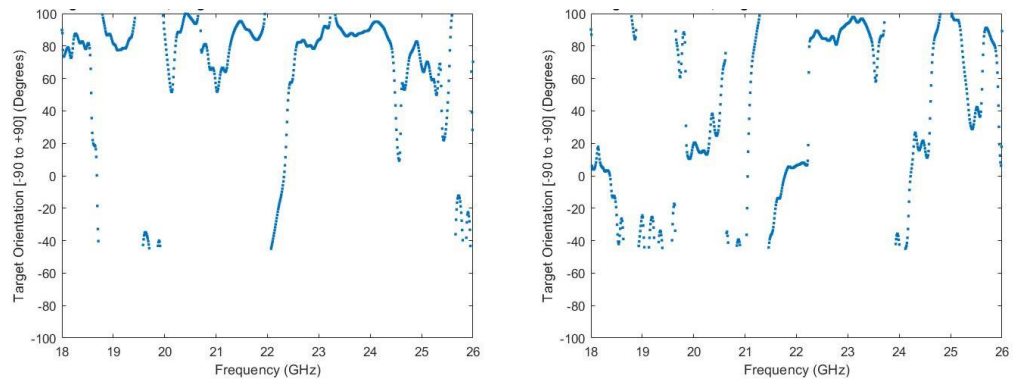


Figure 17-129 Hands at side measured orientation angle subject 1 left, subject 2 right

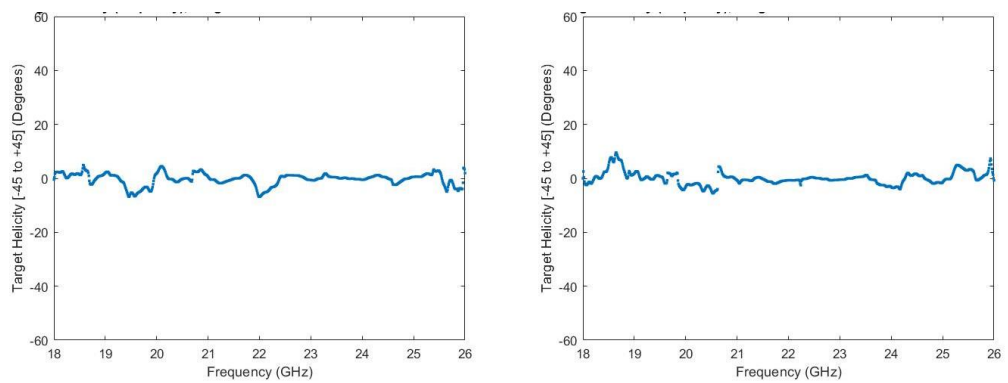


Figure 17-130 Hands at side measured helicity angle subject 1 left, subject 2 right

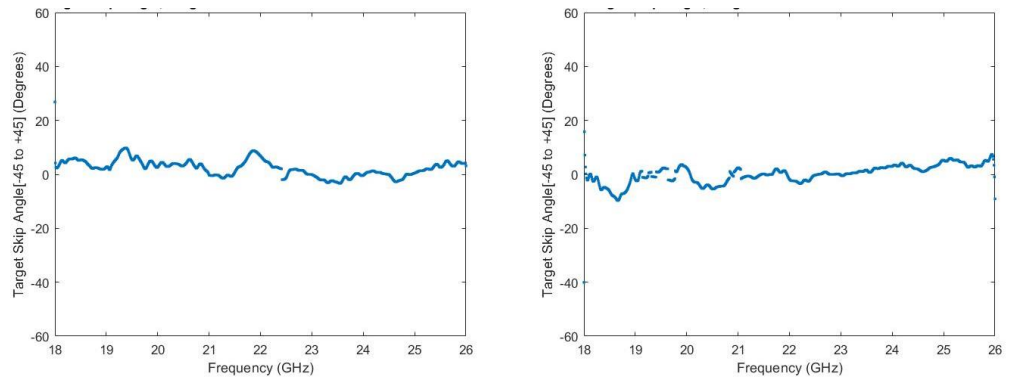


Figure 17-131 Hands at side measured skip angle subject 1 left, subject 2 right

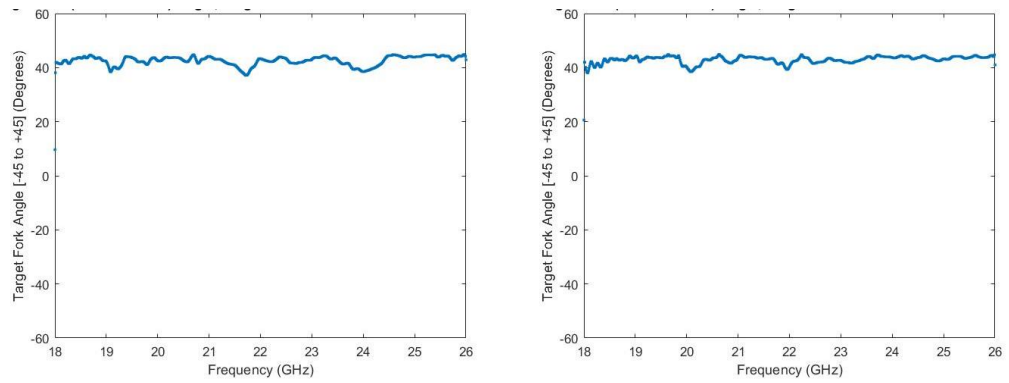


Figure 17-132 Hands at side measured fork angle subject 1 left, subject 2 right

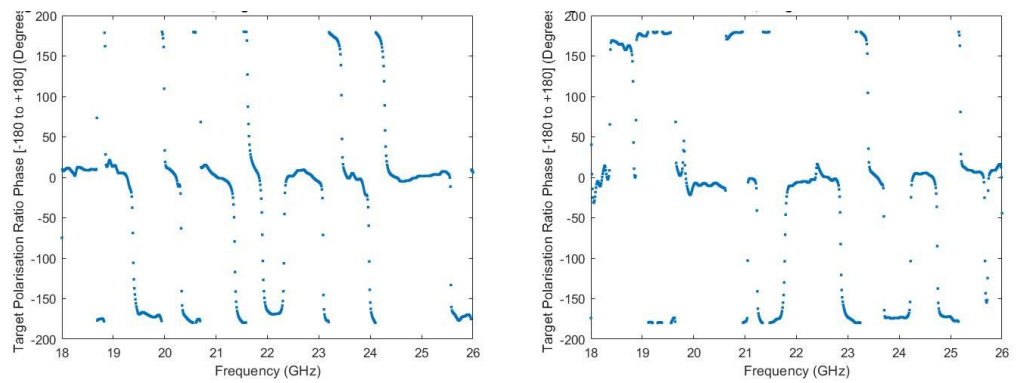


Figure 17-133 Hands at side polarisation phase ratio subject 1 left, subject 2 right

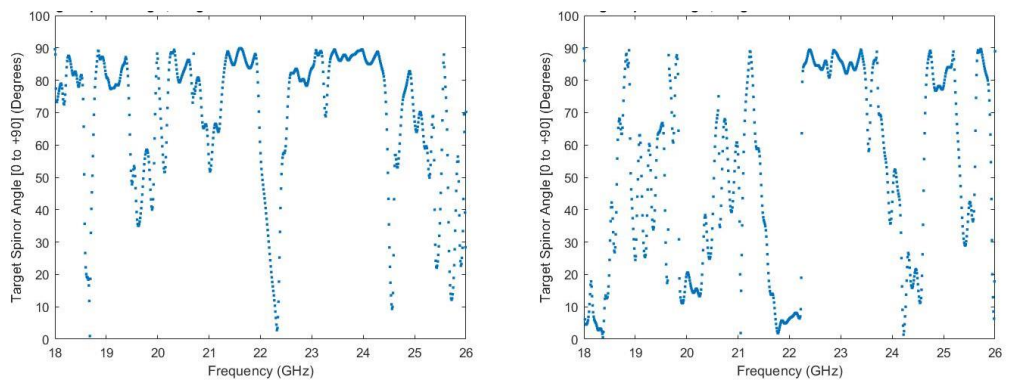


Figure 17-134 Hands at side measured spinor angle subject 1 left, subject 2 right

17.18 Human torso presented side on to the beam of the radar with hands above the head compared to hands at the side

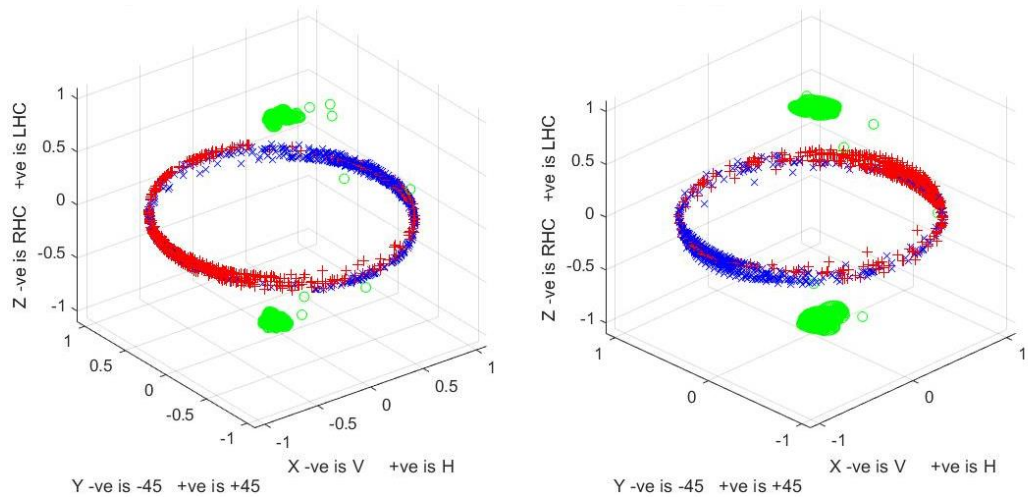


Figure 17-135 Subject 1 side on measured forks plot hands above head left, hands at the side right

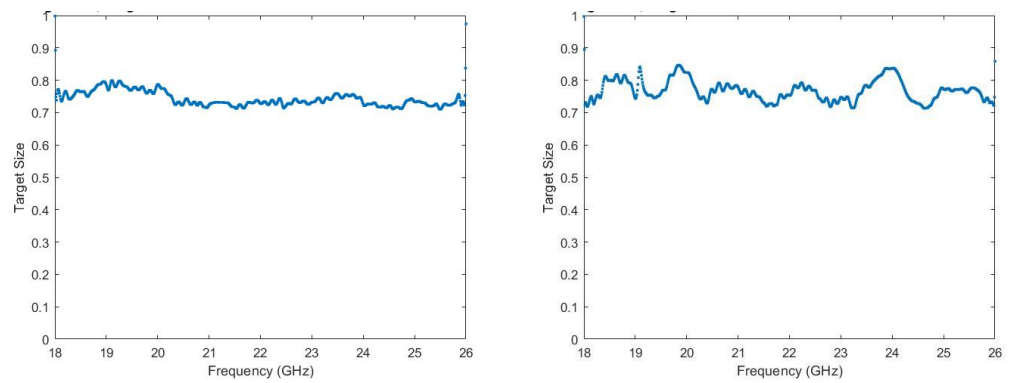


Figure 17-136 Subject 1 side on measured target size hands above head left, hands at the side right

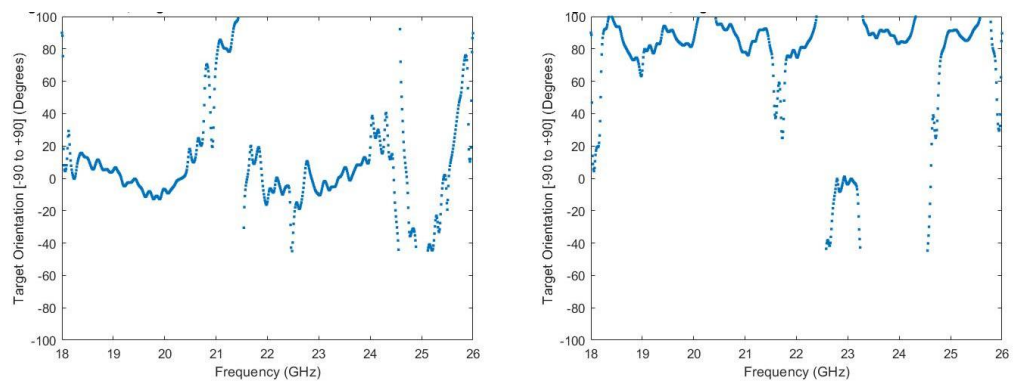


Figure 17-137 Subject 1 side on measured orientation angle hands above head left, hands at the side right

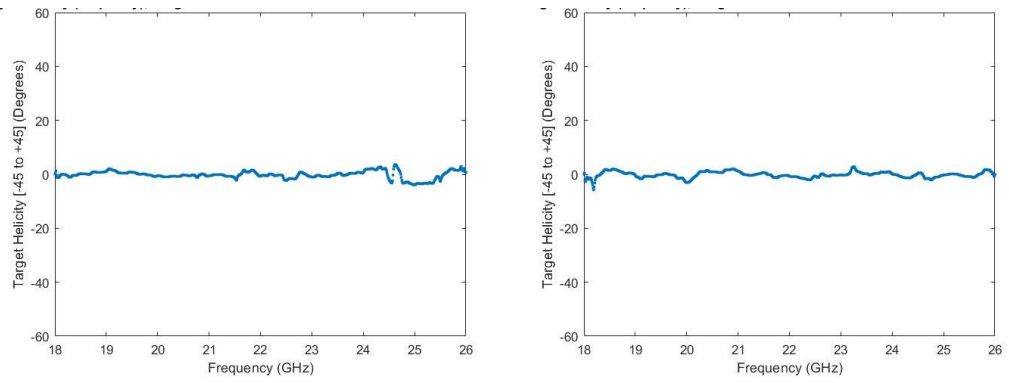


Figure 17-138 Subject 1 side on measured helicity angle hands above head left,
hands at the side right

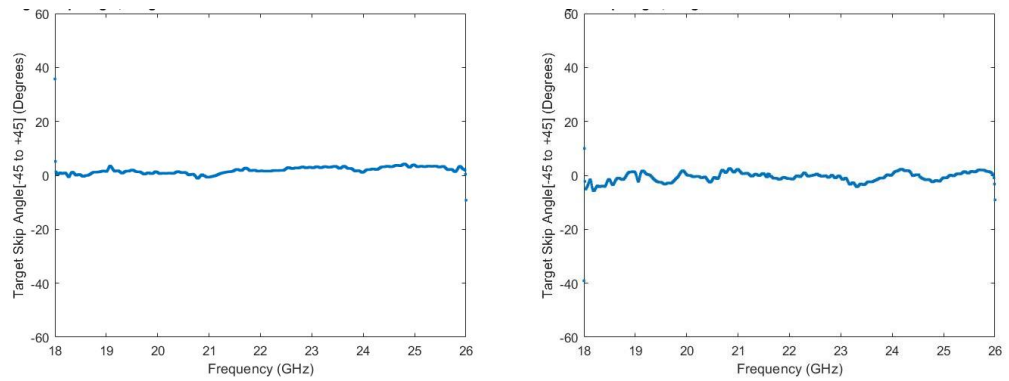


Figure 17-139 Subject 1 side on measured skip angle hands above head left,
hands at the side right

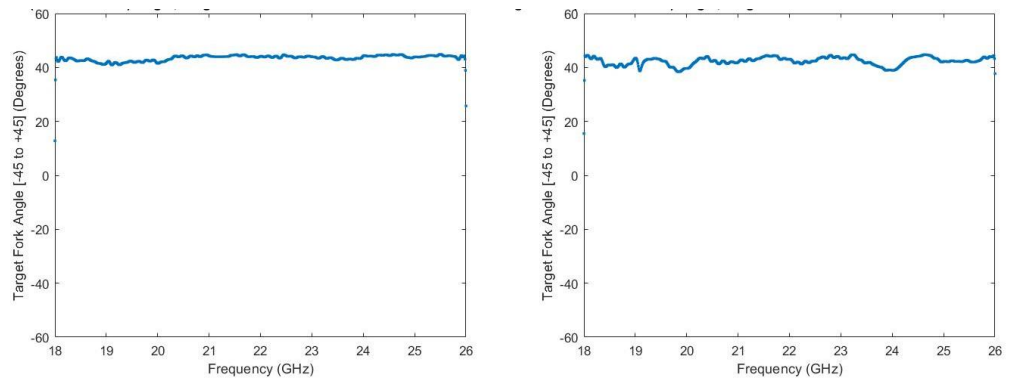


Figure 17-140 Subject 1 side on measured fork angle hands above head left,
hands at the side right

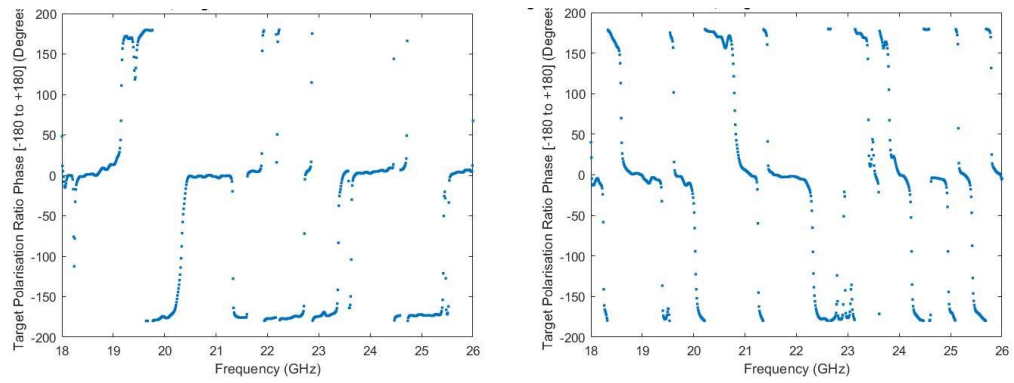


Figure 17-141 Subject 1 side on polarisation phase ratio hands above head left,
hands at the side right

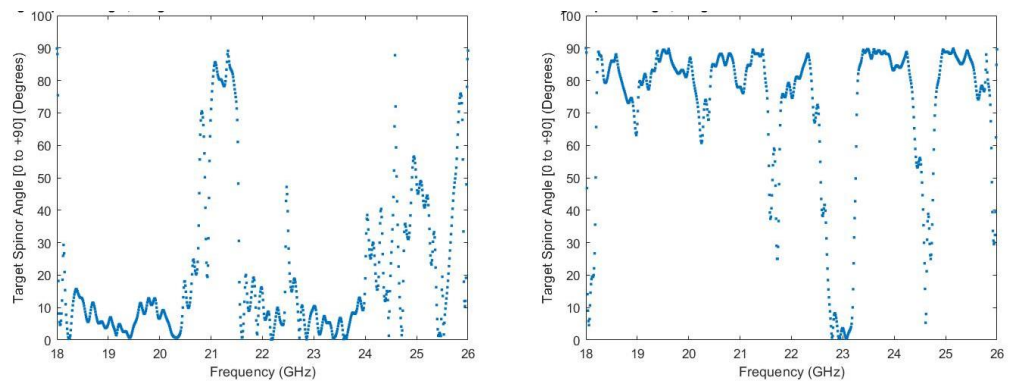


Figure 17-142 Subject 1 side on measured spinor angle hands above head left,
hands at the side right

17.19 Human torso presented side on to the beam of the radar with hands above the head compared to hands at the side

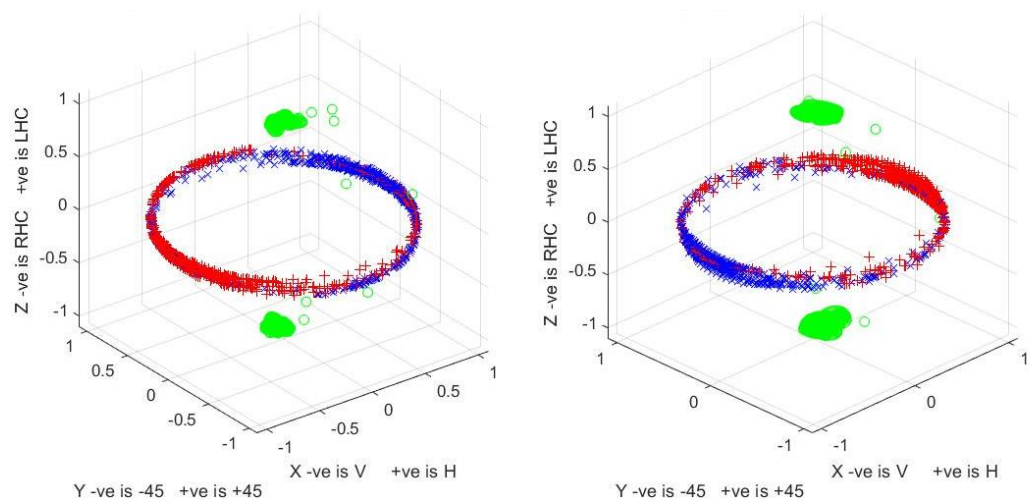


Figure 17-143 Subject 1 side on measured fork plots hands above head left,
hands at the side right

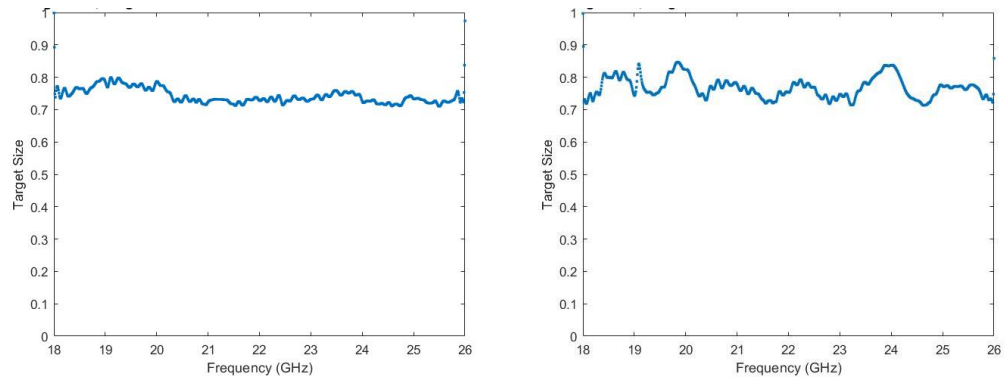


Figure 17-144 Subject 1 side on measured target size hands above head left,
hands at the side right

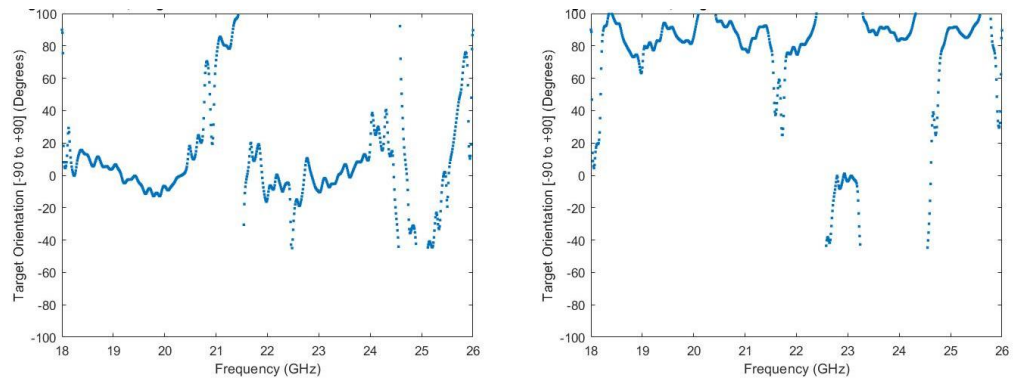


Figure 17-145 Subject 1 side on measured orientation angle hands above head
left, hands at the side right

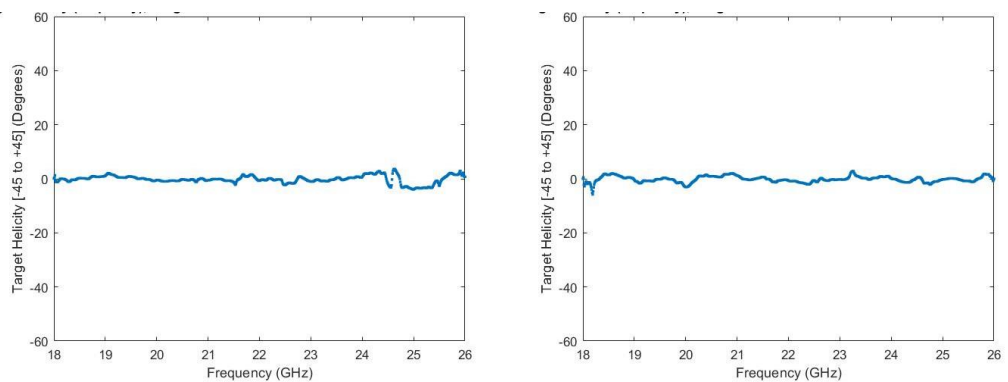


Figure 17-146 Subject 1 side on measured helicity angle hands above head left,
hands at the side right

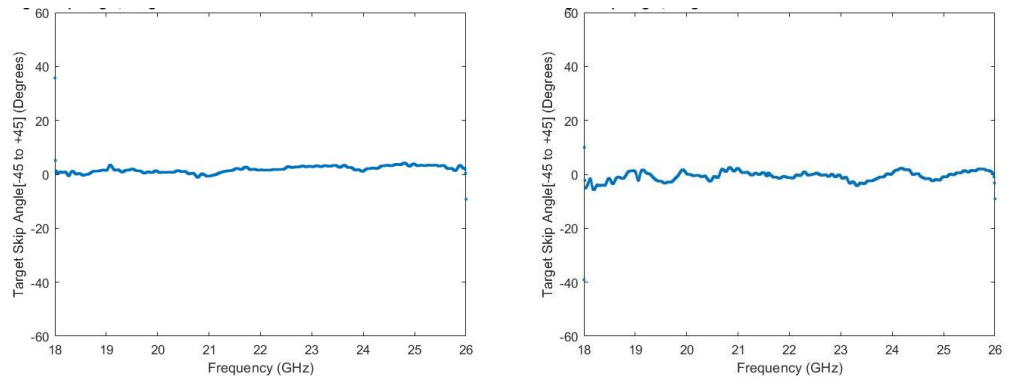


Figure 17-147 Subject 1 side on measured skip angle hands above head left, hands at the side right

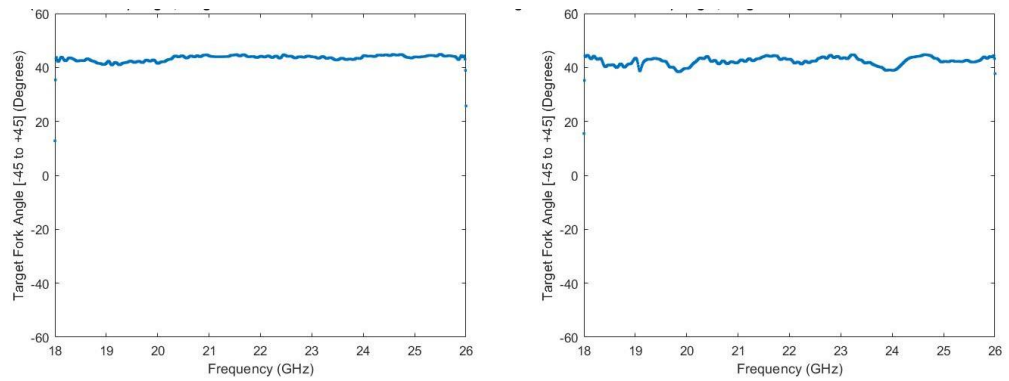


Figure 17-148 Subject 1 side on measured fork angle hands above head left, hands at the side right

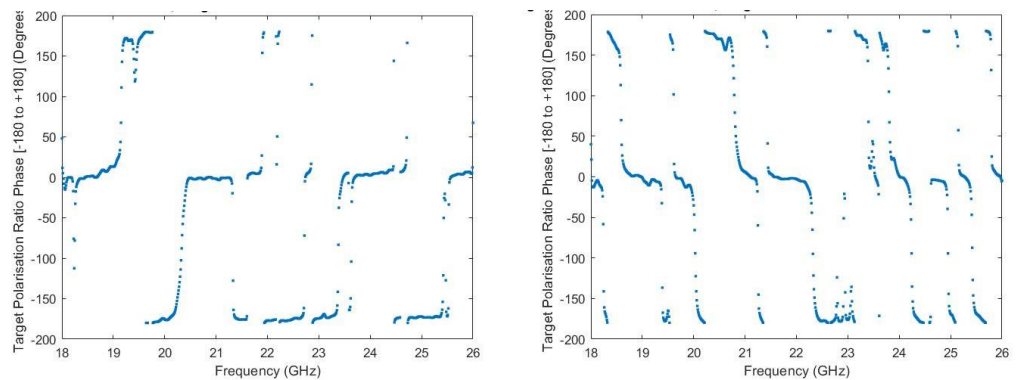


Figure 17-149 Subject 1 side on measured polarisation phase ratio hands above head left, hands at the side right

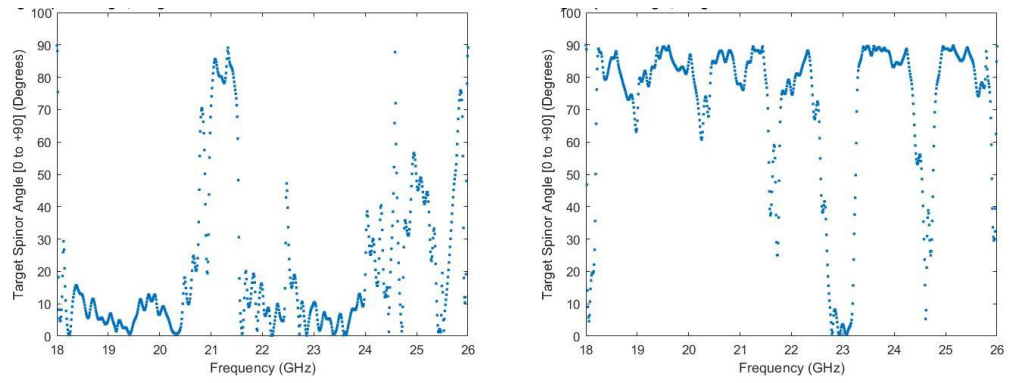


Figure 17-150 Subject 1 side on measured spinor angle hands above head left,
hands at the side right

17.20 Small knife vertical and horizontal on the human torso

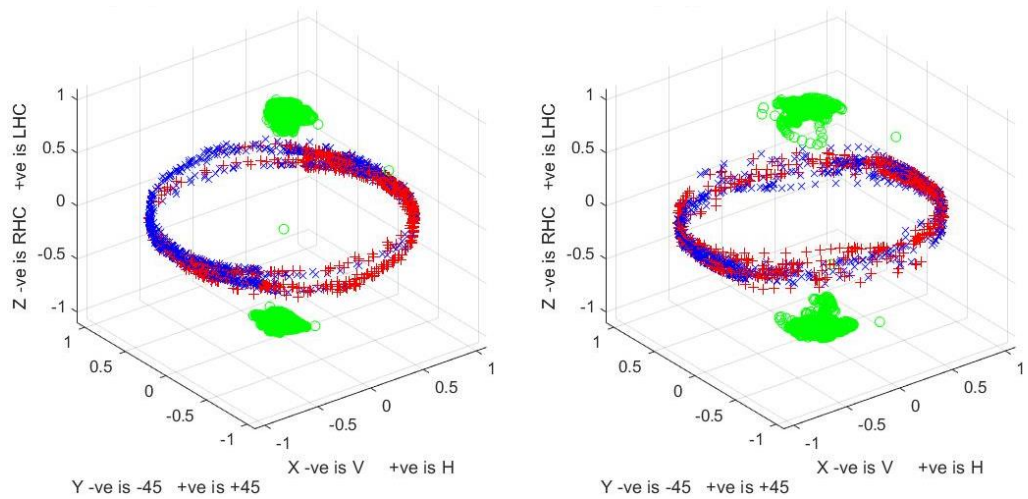


Figure 17-151 Fork plots measurement of a short knife placed against the human
torso vertical left, horizontal right

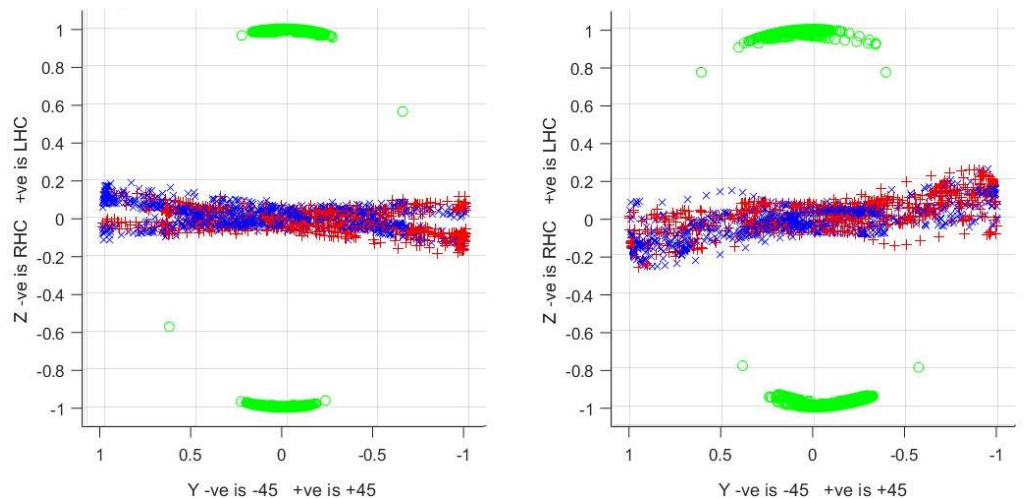


Figure 17-152 Fork plots (side view) measurement of a short knife placed against
the human torso vertical left, horizontal right

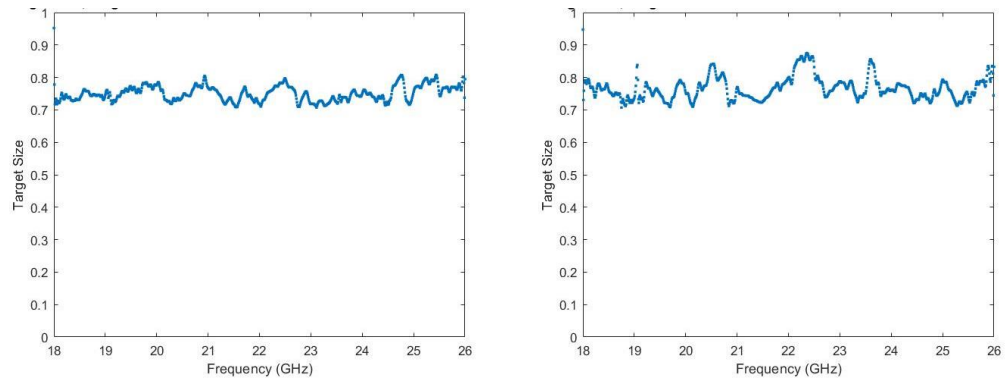


Figure 17-153 Measured target size of a short knife placed against the human torso vertical left, horizontal right

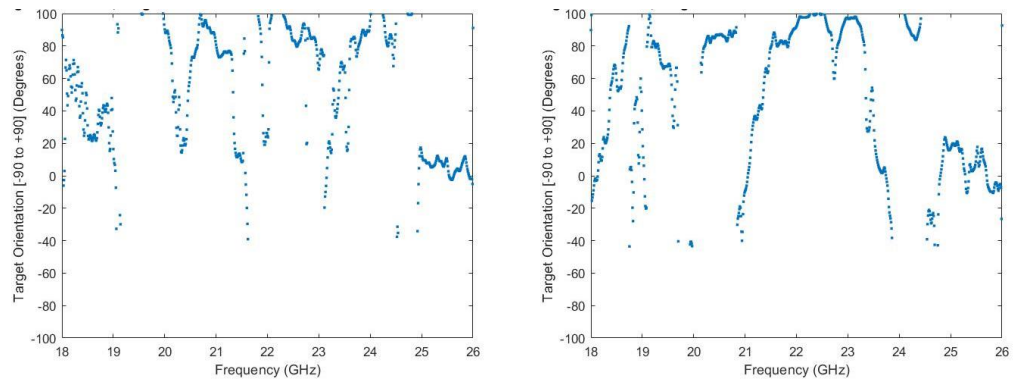


Figure 17-154 Measured orientation angle of a short knife placed against the human torso vertical left, horizontal right

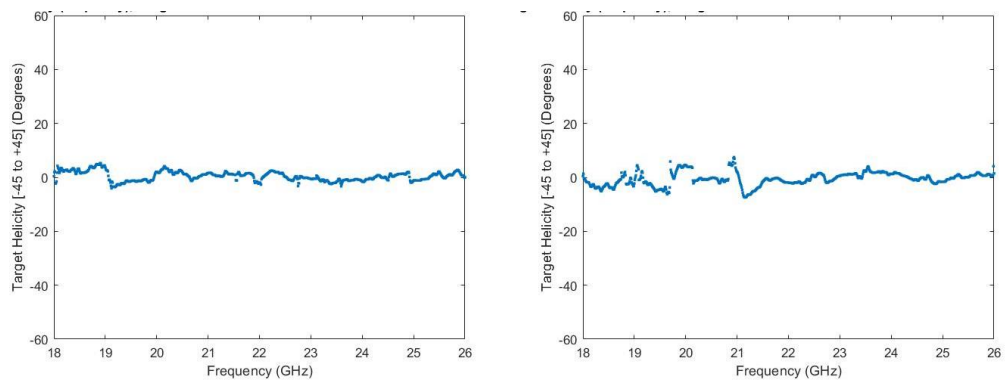


Figure 17-155 Measured helicity angle of a short knife placed against the human torso vertical left, horizontal right

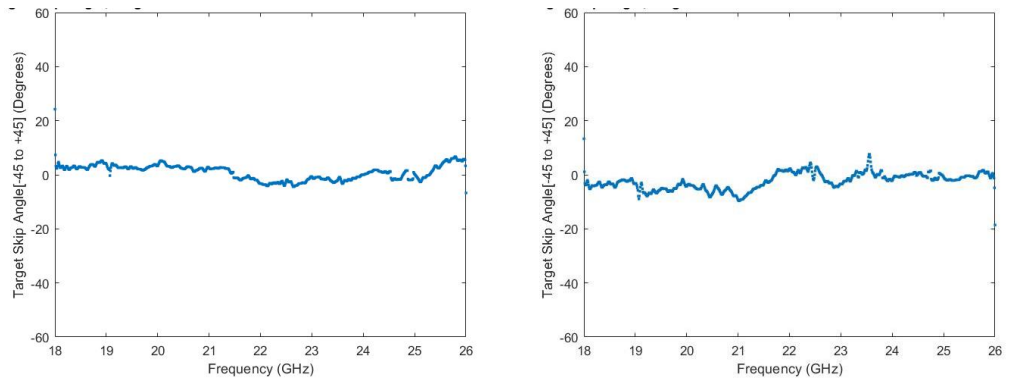


Figure 17-156 Measured skip angle of a short knife placed against the human torso vertical left, horizontal right

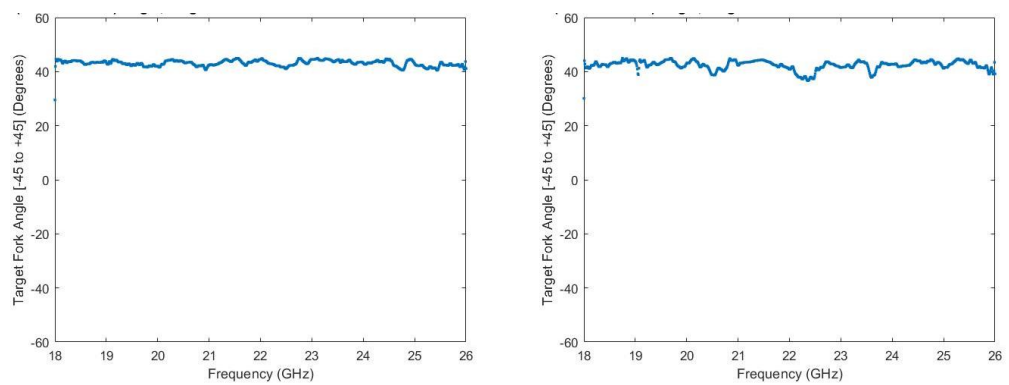


Figure 17-157 Measured fork angle of a short knife placed against the human torso vertical left, horizontal right

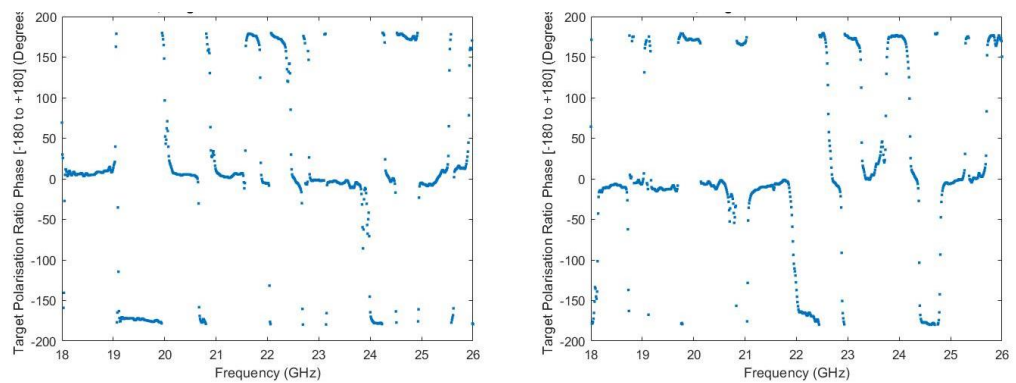


Figure 17-158 Measured polarisation phase ratio of a short knife placed against the human torso vertical left, horizontal right

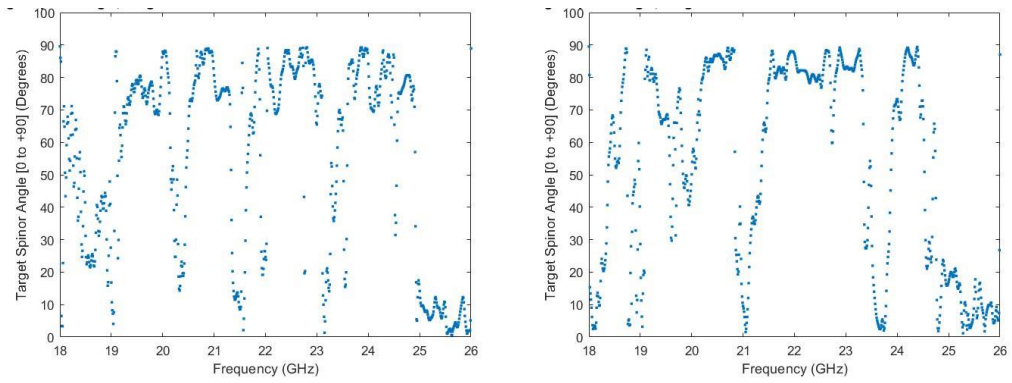


Figure 17-159 Measured spinor angle of a short knife placed against the human torso vertical left, horizontal right

17.21 Long vertical and horizontal knives on the human torso



Figure 17-160 Human torso with a vertical long knife left, horizontal right.

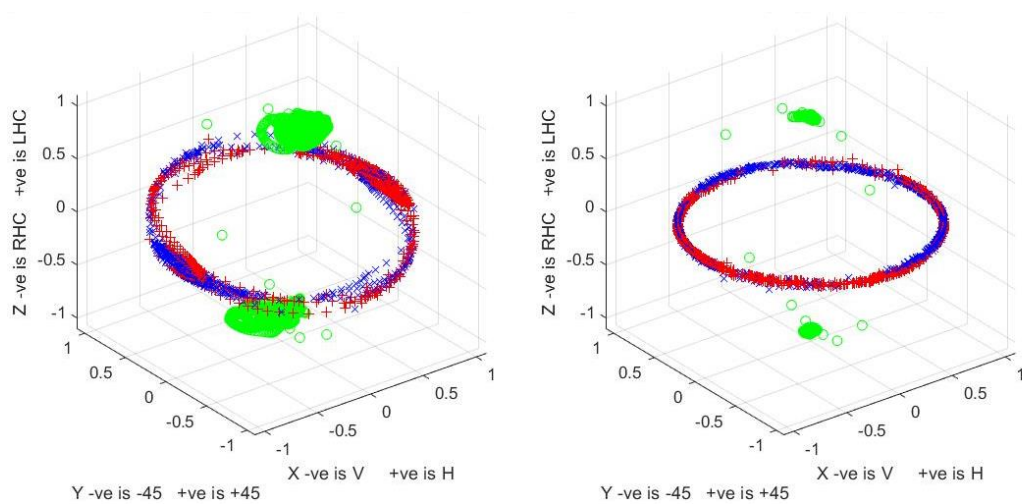


Figure 17-161 Fork plots via measurement of the human torso with a vertical long knife left, horizontal right

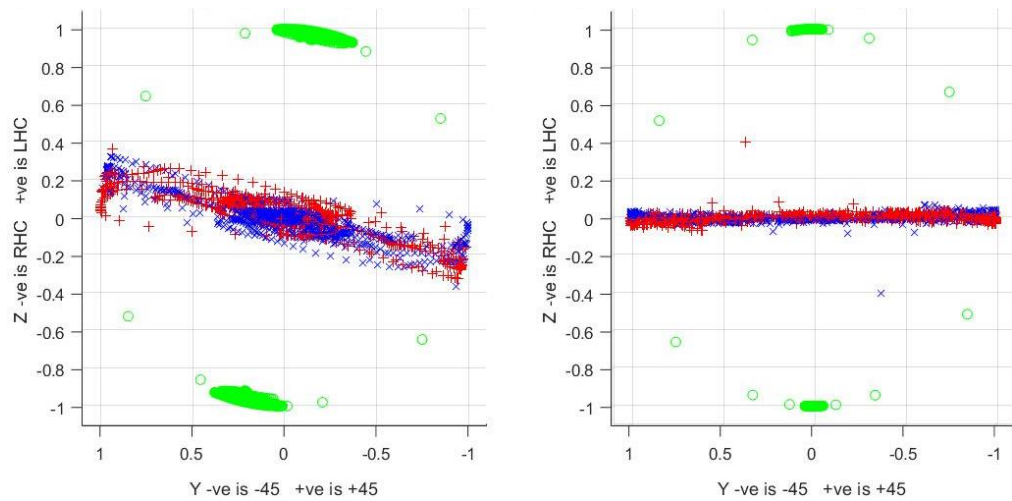


Figure 17-162 Fork plots of the human torso via measurement with a vertical long knife left, horizontal right

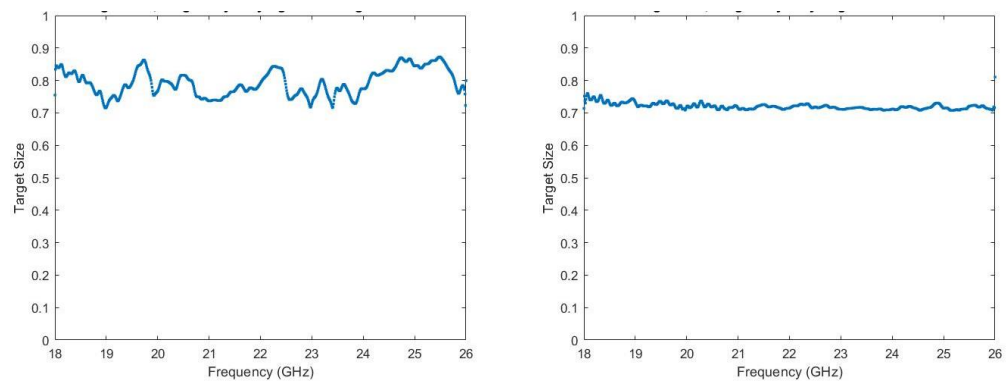


Figure 17-163 Measured target size of the human torso with a long vertical knife left, horizontal right

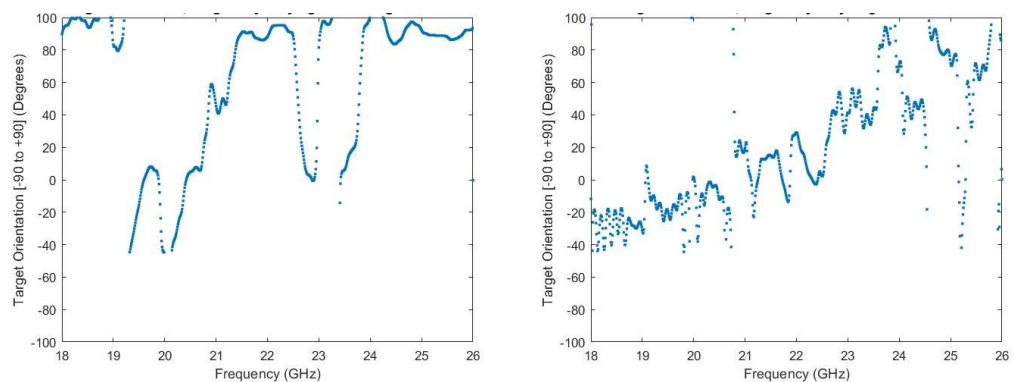


Figure 17-164 Measured orientation angle of the human torso with a vertical long knife left, horizontal right

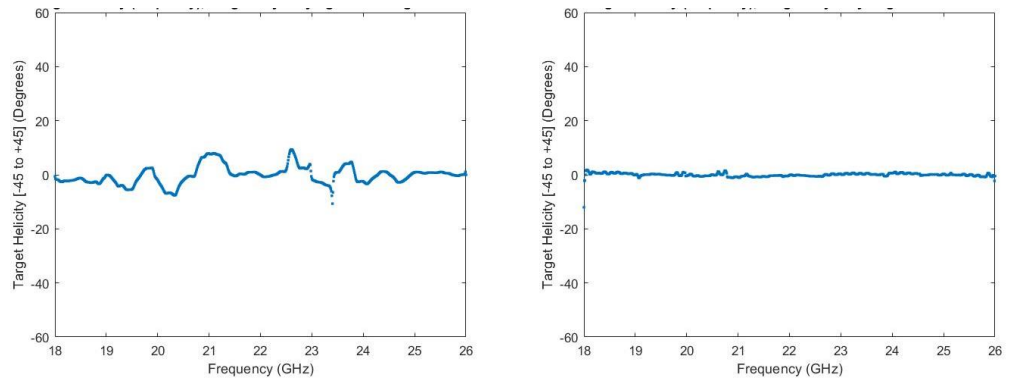


Figure 17-165 Measured helicity of the human torso with a vertical long knife left, horizontal right

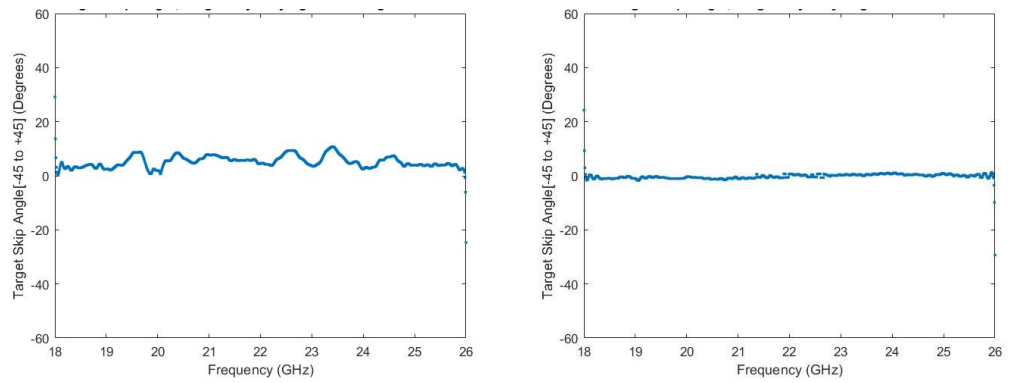


Figure 17-166 Measured skip angle of the human torso with a vertical long knife left, horizontal right

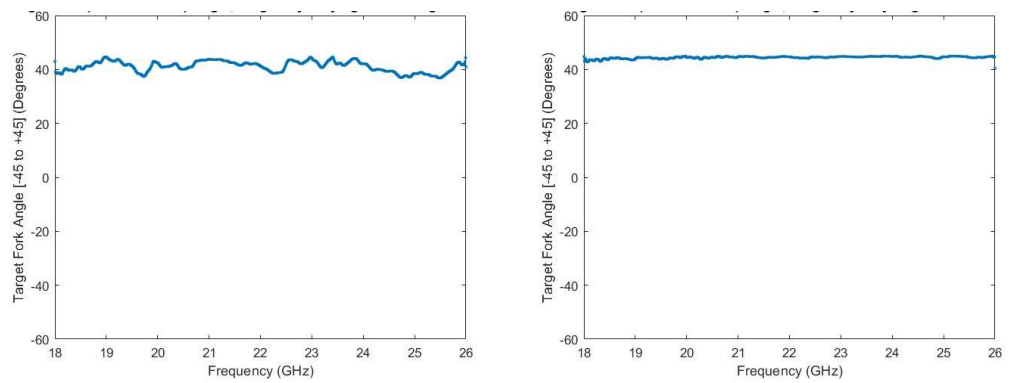


Figure 17-167 Measured fork angle of the human torso with a vertical long knife left, horizontal right

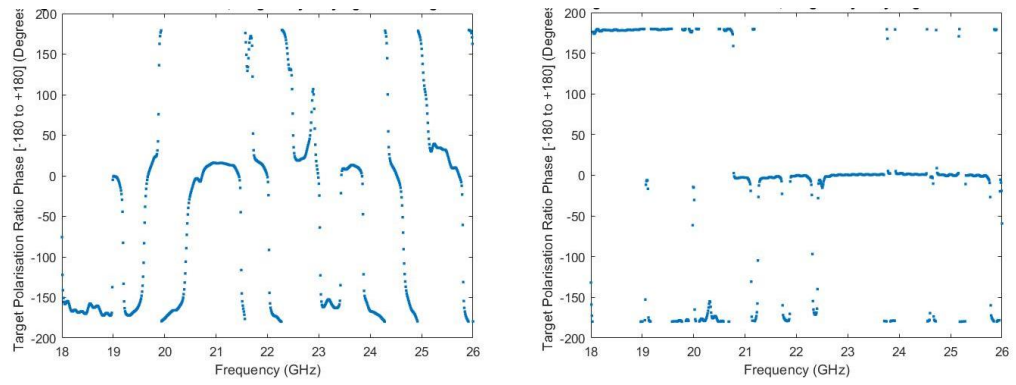


Figure 17-168 Measured polarisation phase ratio for the human torso with a vertical long knife left, horizontal right

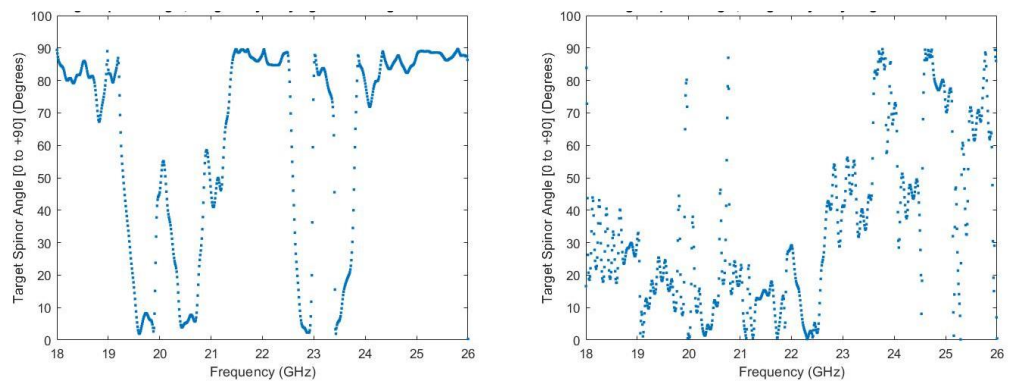


Figure 17-169 Measured spinor angle for the human torso with a vertical long knife left, horizontal right

17.22 Vertical and horizontal guns on the human torso



Figure 17-170 Human torso with a vertical brass gun left, horizontal right.

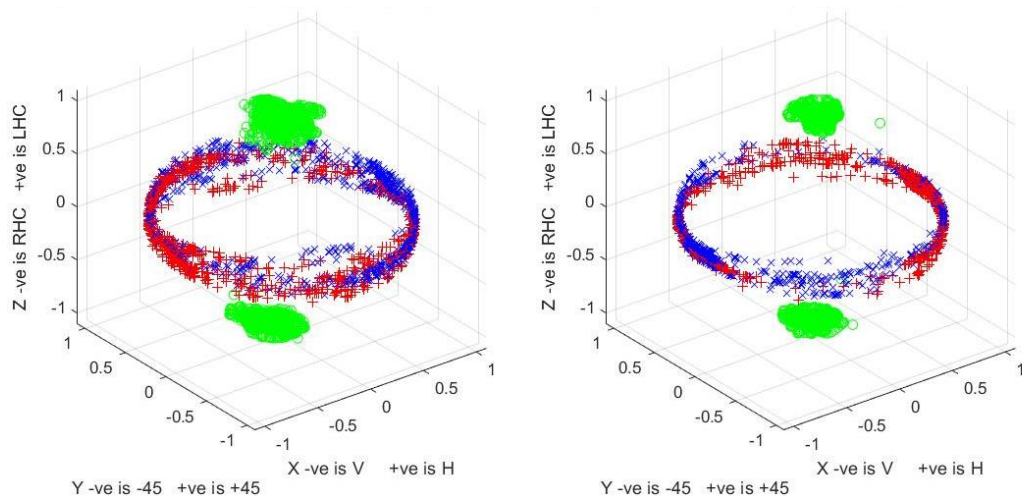


Figure 17-171 Fork plots via measurement of the human torso with a vertical gun left, horizontal right

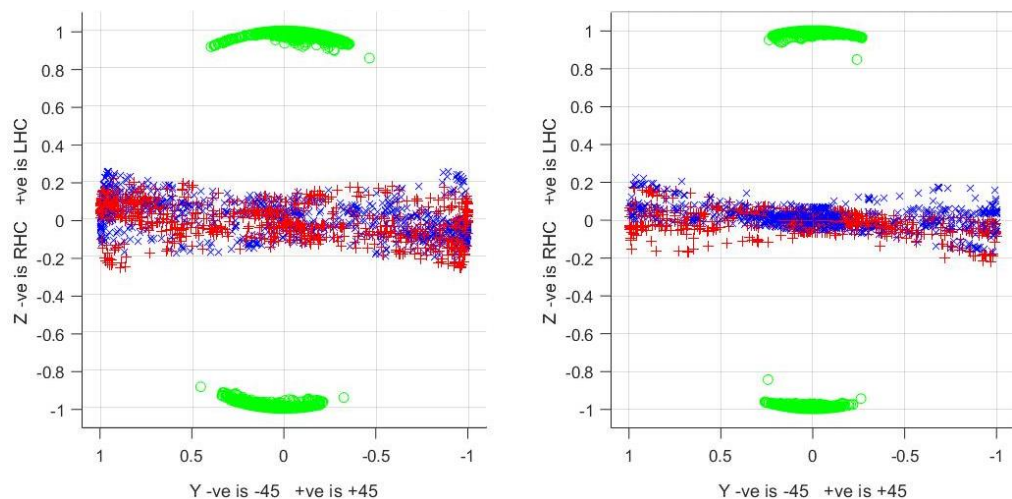


Figure 17-172 Fork plots of the human torso via measurement with a vertical gun left, horizontal right (viewed from the vertical position)

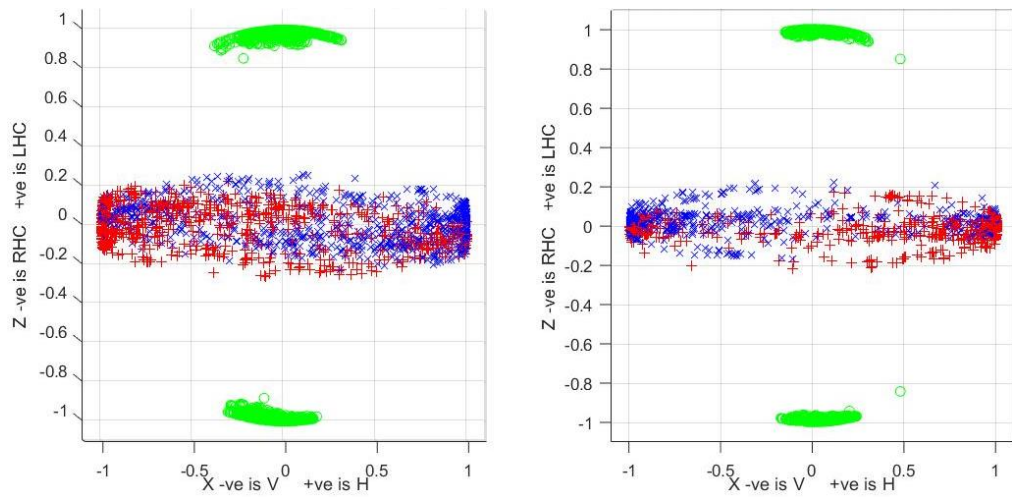


Figure 17-173 Fork plots of the human torso via measurement with a vertical gun
left, horizontal right (viewed from the -45° position)

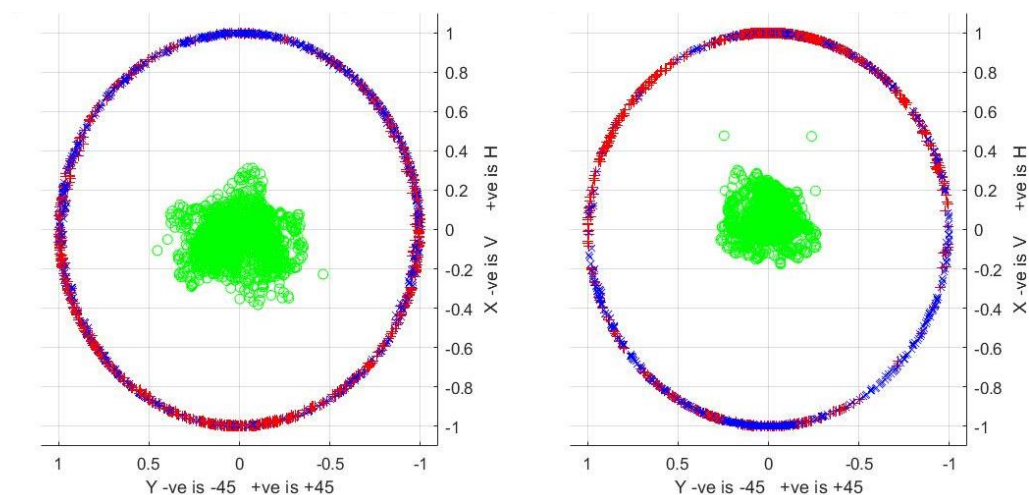


Figure 17-174 Fork plots of the human torso via measurement with a vertical gun
left, horizontal right (viewed from the zenith)

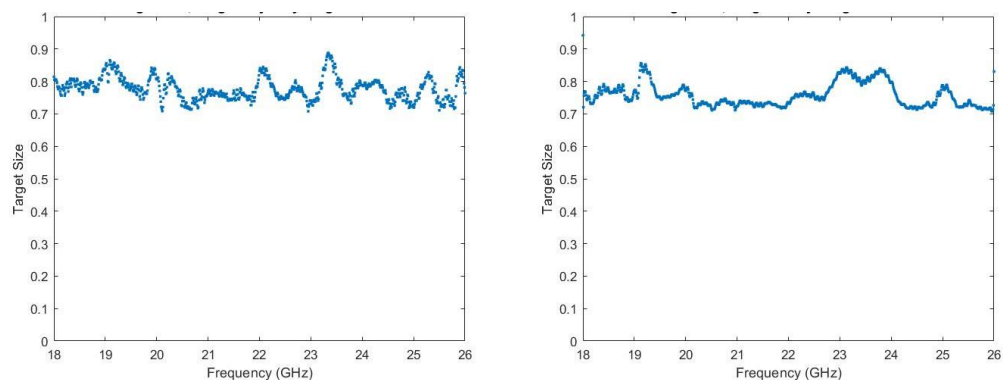


Figure 17-175 Measured target size of the human torso with a vertical gun left,
horizontal right

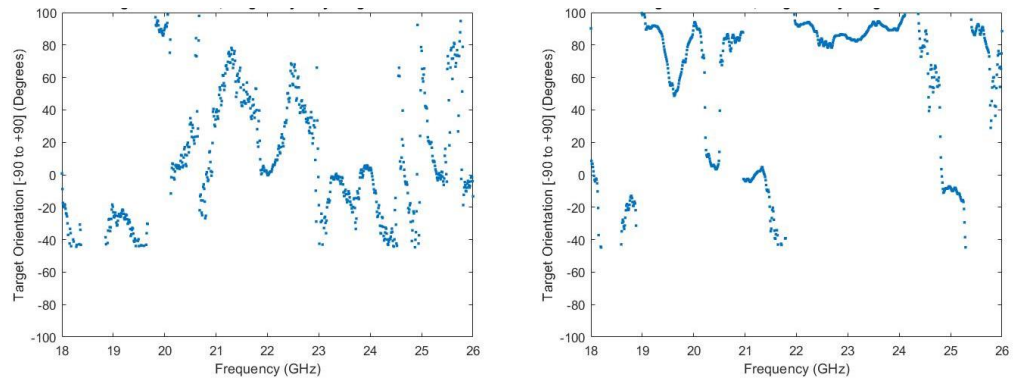


Figure 17-176 Measured orientation angle of the human torso with a vertical gun left, horizontal right

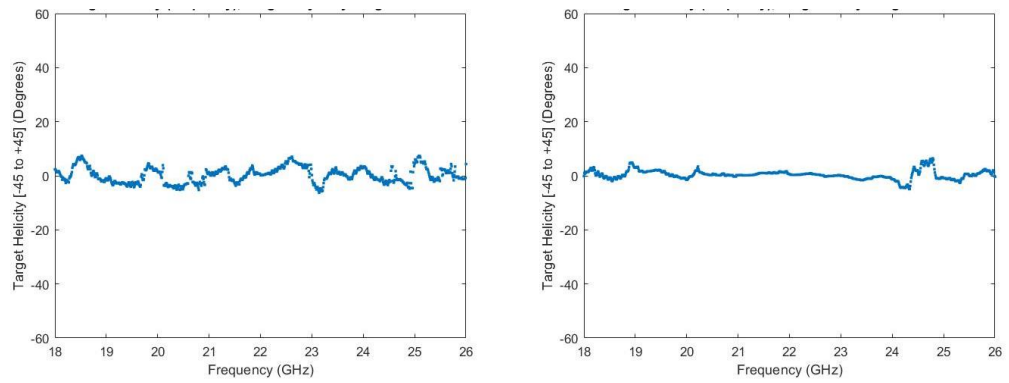


Figure 17-177 Measured helicity angle of the human torso with a vertical gun left, horizontal right

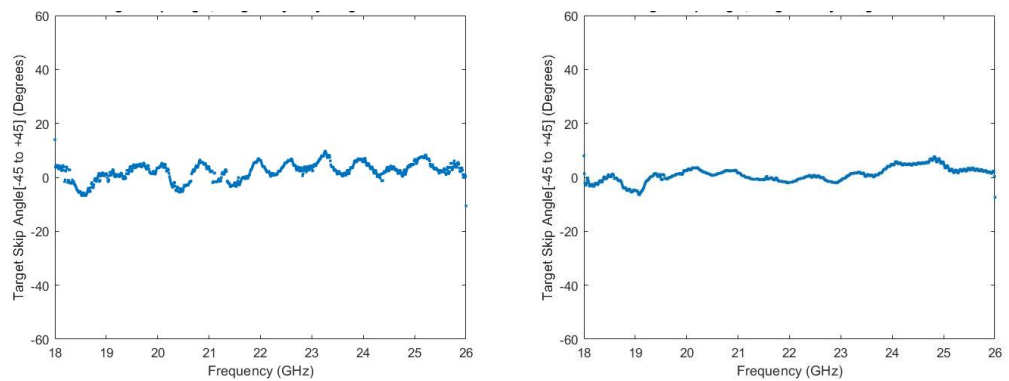


Figure 17-178 Measured skip angle of the human torso with a vertical gun left, horizontal right

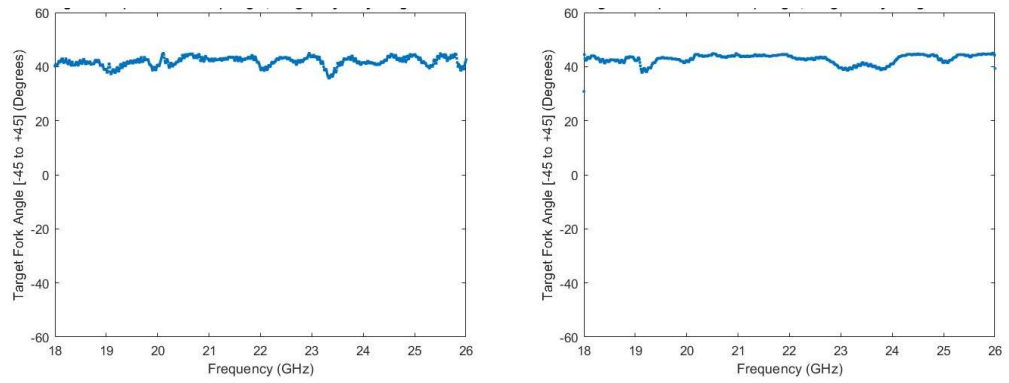


Figure 17-179 Measured fork angle of the human torso with a vertical gun left, horizontal right

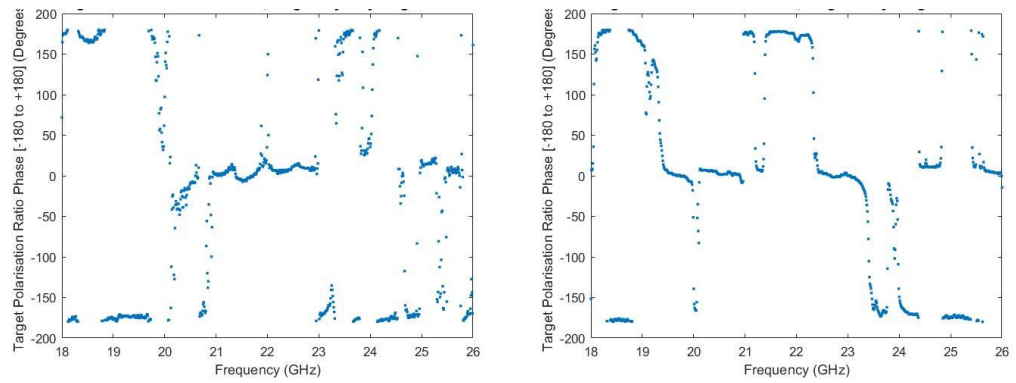


Figure 17-180 Measured polarisation phase ratio of the human torso with a vertical gun left, horizontal right

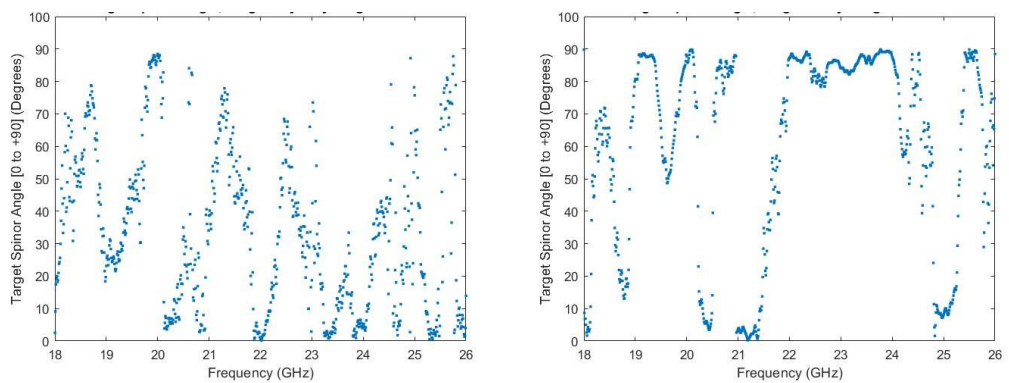


Figure 17-181 Measured spinor angle of the human torso with a vertical gun left, horizontal right

17.23 Shrapnel target on the human torso

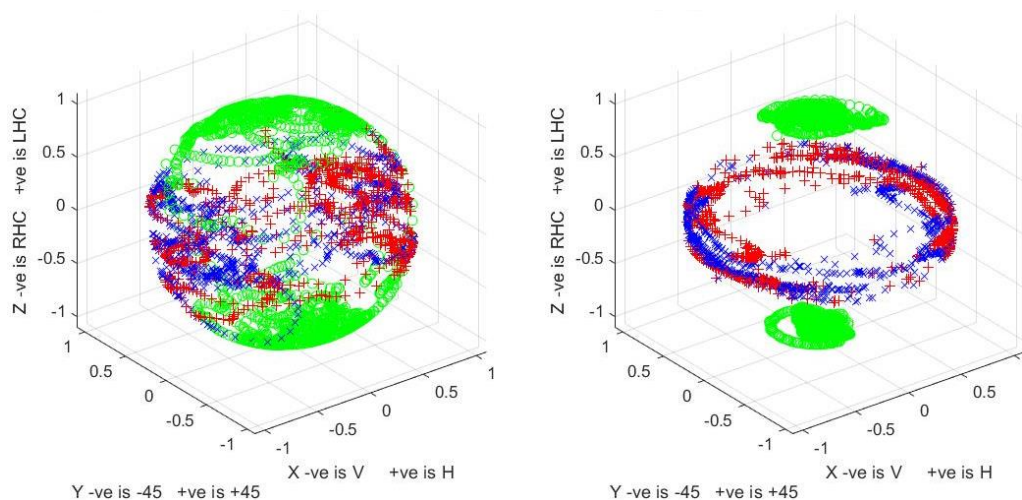


Figure 17-182 Fork plots of shrapnel via measurement on its own left, located on subject 2 torso right

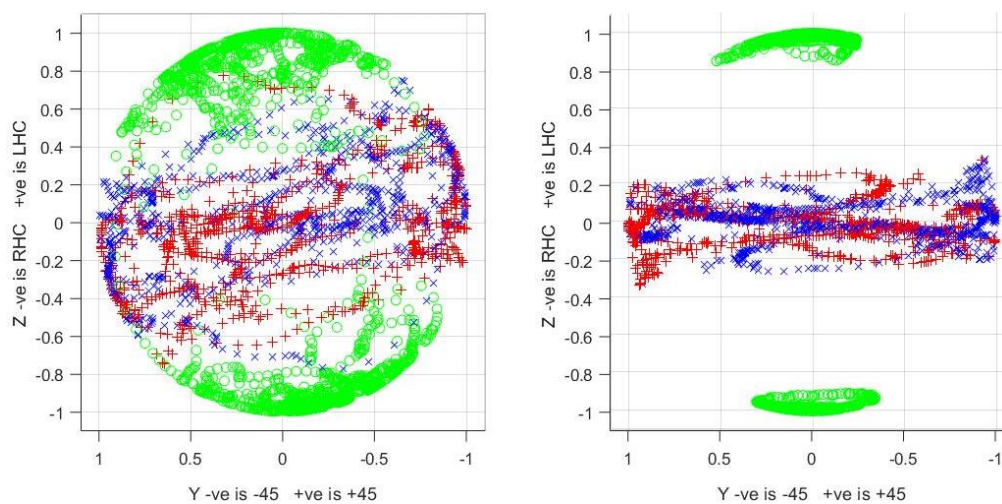


Figure 17-183 Fork plots of shrapnel via measurement on its own left, located on subject 2 torso right (viewed from the vertical polarisation position)

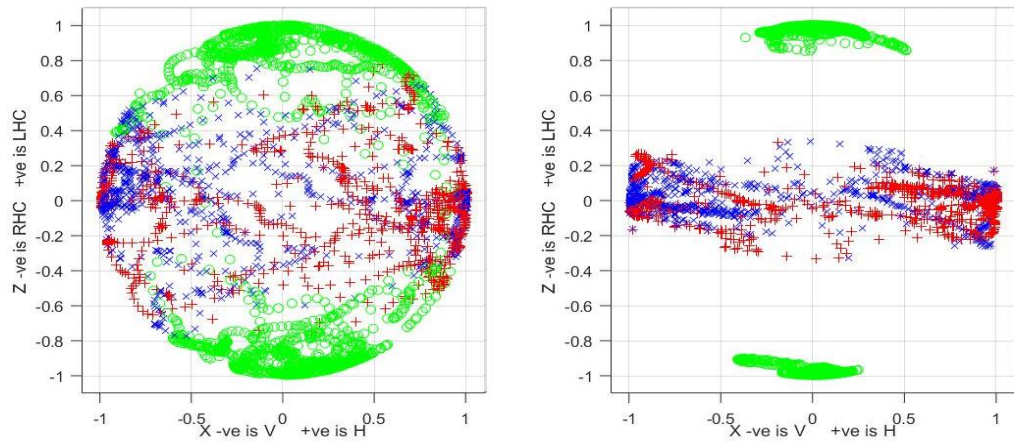


Figure 17-184 Fork plots of shrapnel via measurement on its own left, located on subject 2 torso right (viewed from the -45° polarisation position)

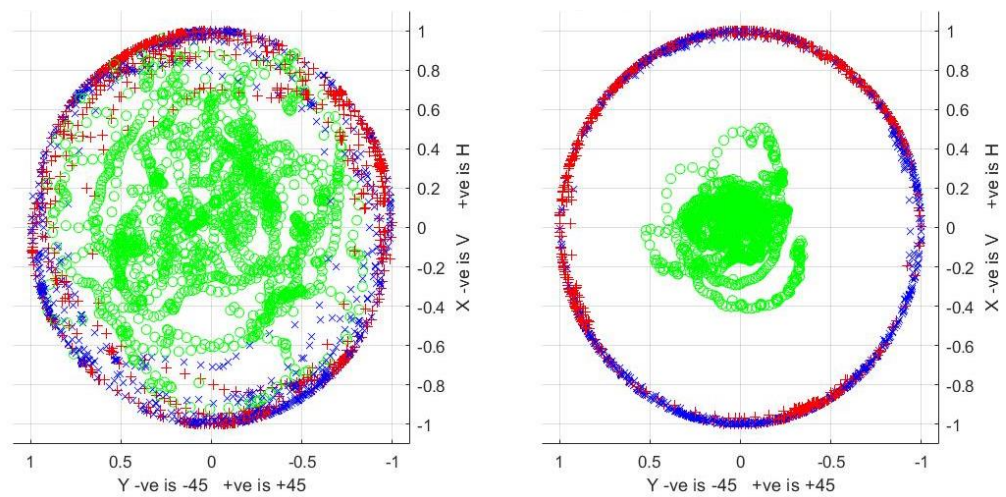


Figure 17-185 Fork plots of shrapnel via measurement on its own left, located on subject 2 torso right (viewed from the zenith)

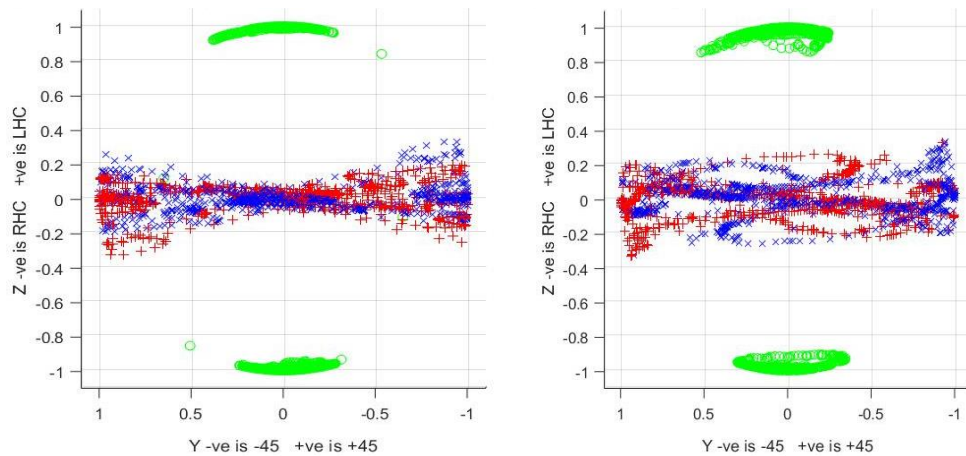


Figure 17-186 Fork plots via measurement of Subject 2 torso with hands at side left, shrapnel on subject 2 right

(viewed from the vertical polarisation position)

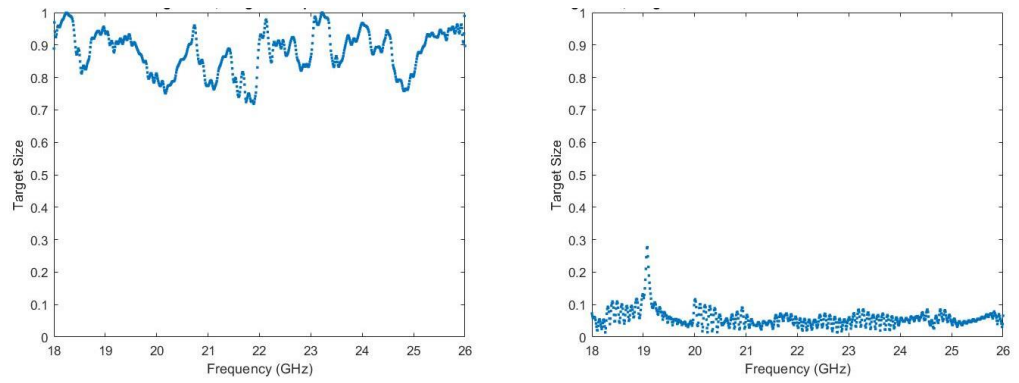


Figure 17-187 Measured target size of shrapnel on its own left, located on subject 2 torso right

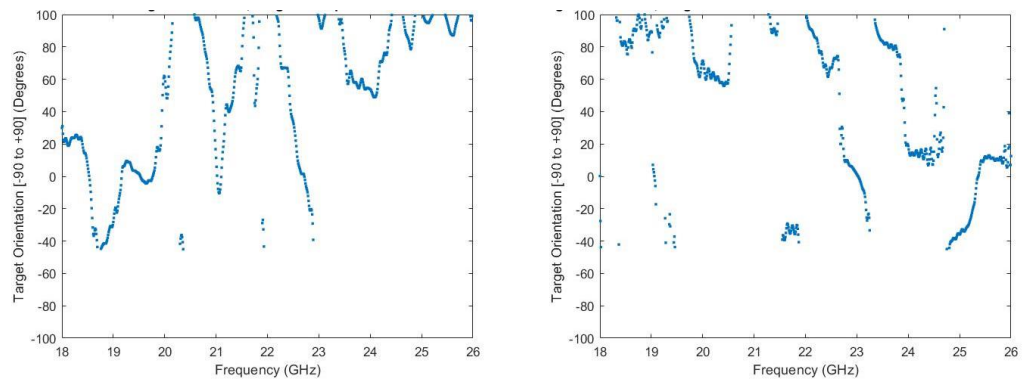


Figure 17-188 Measured orientation angle of shrapnel on its own left, located on subject 2 torso right

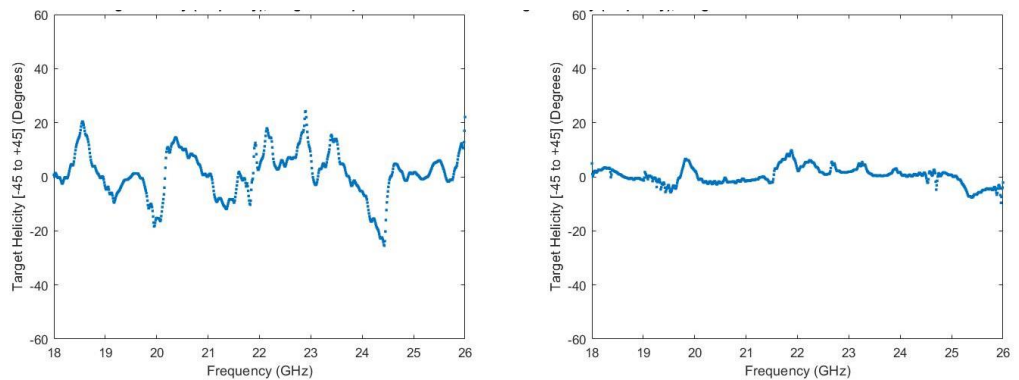


Figure 17-189 Measured helicity angel of shrapnel on its own left, located on subject 2 torso right

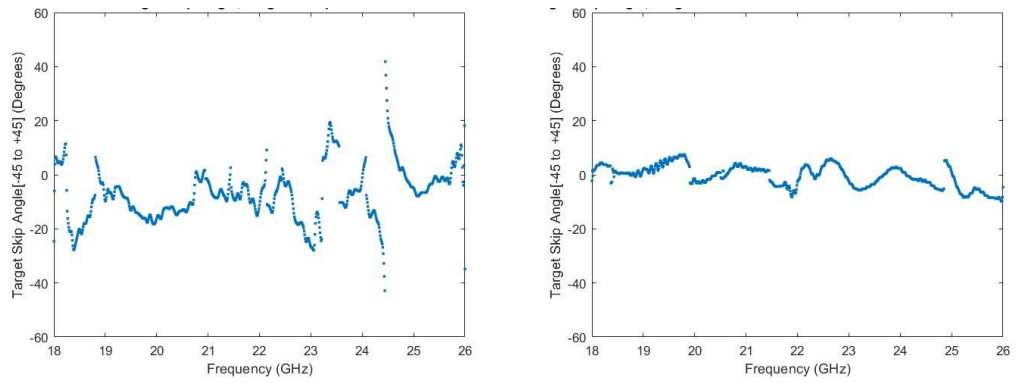


Figure 17-190 Measured skip angle of shrapnel on its own left, located on subject 2 torso right

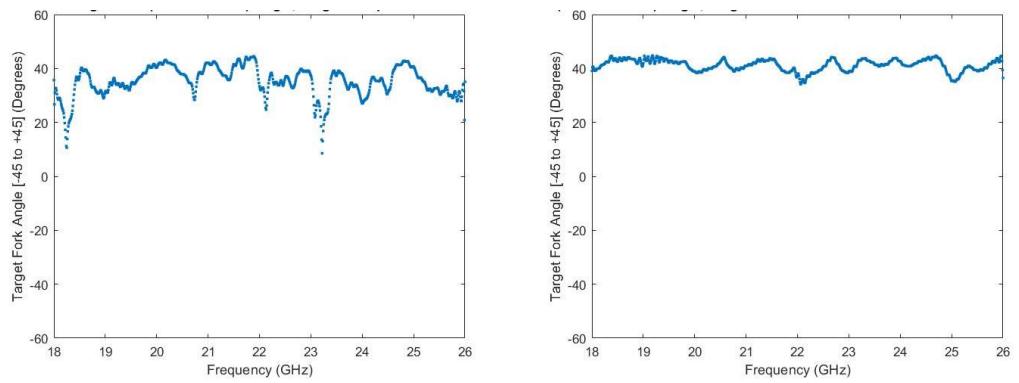


Figure 17-191 Measured fork angle of shrapnel on its own left, located on subject 2 torso right

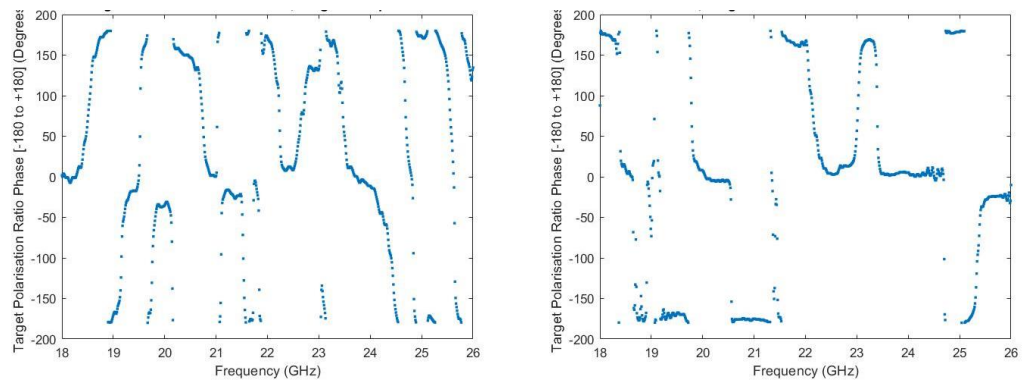


Figure 17-192 Measured polarisation phase ratio of shrapnel on its own left, located on subject 2 torso right

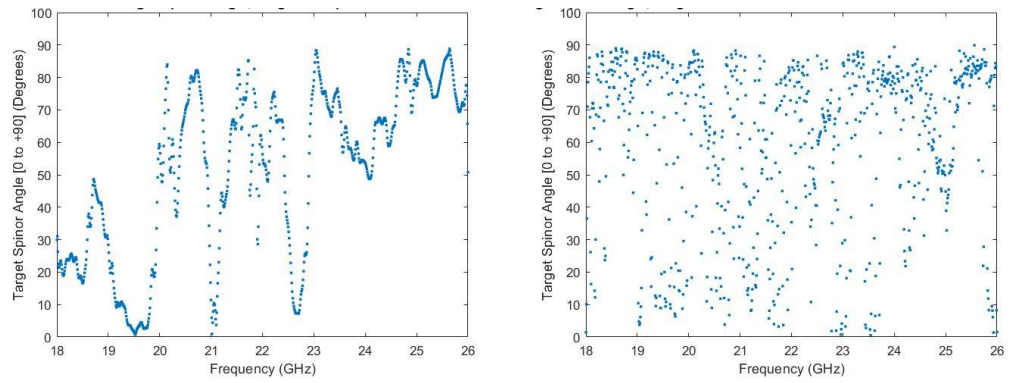


Figure 17-193 Measured spinor angle of shrapnel on its own left, located on subject 2 torso right

17.24 Smartphone



Figure 17-194 Smartphone.

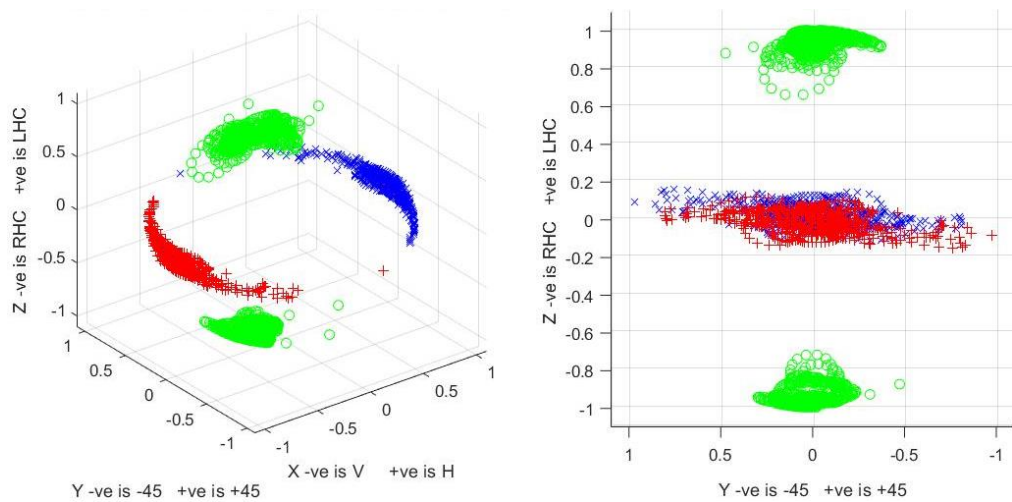


Figure 17-195 Measured Huynen fork plots of a smartphone on its own (left).
Viewed from the vertical polarisation position (right)

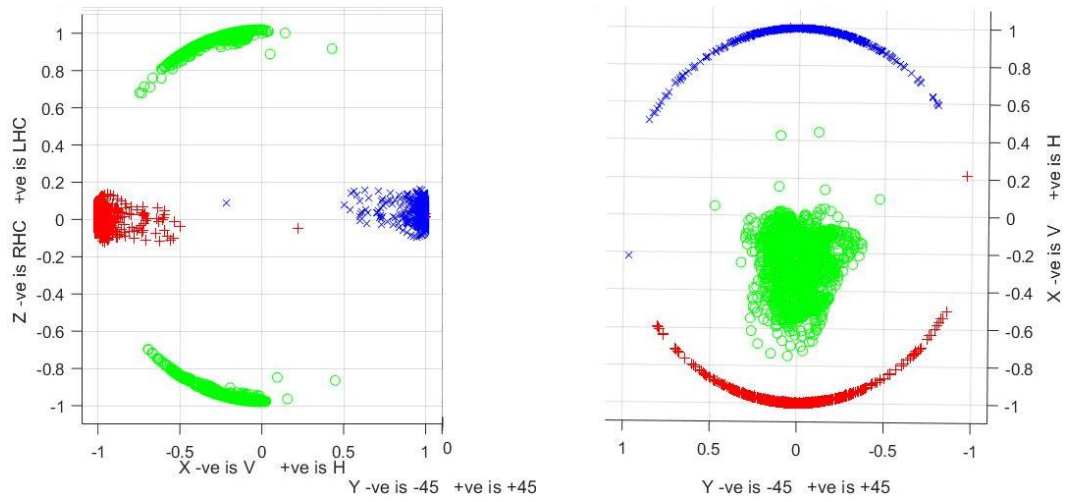


Figure 17-196 Measured Huynen fork plots of a smartphone on its own from the - 45° polarisation position (left), the zenith (right)

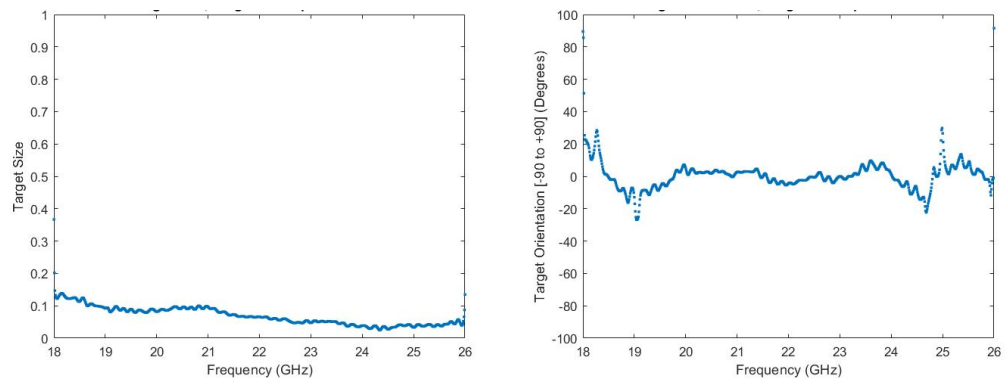


Figure 17-197 Smartphone measured target size left, orientation angle right

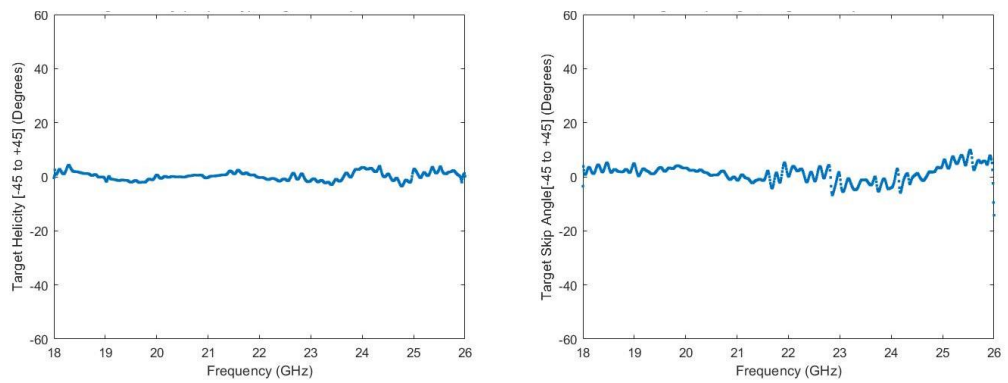


Figure 17-198 Smartphone measured helicity angle left, skip angle right

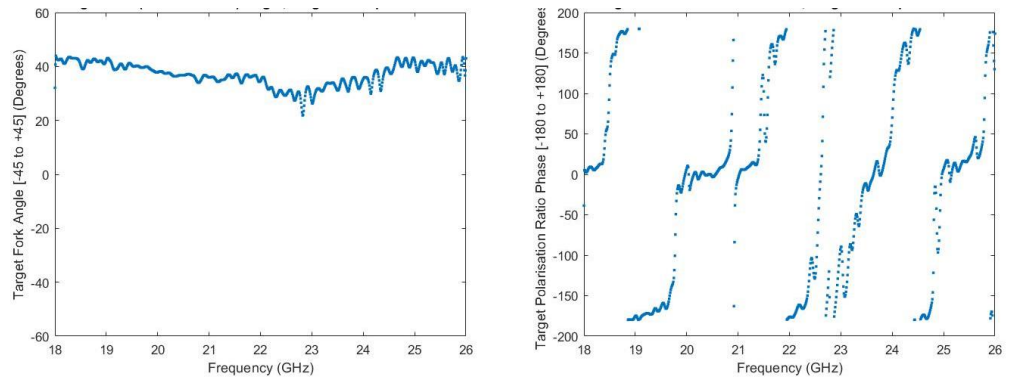


Figure 17-199 Smartphone measured fork angle left, polarisation phase ratio right

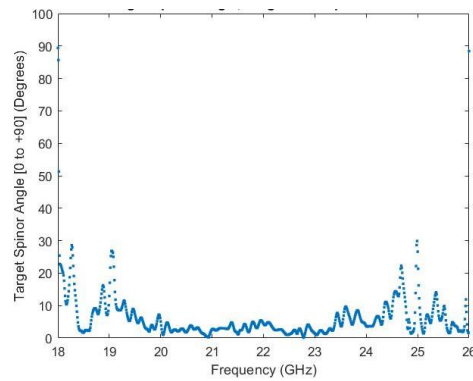


Figure 17-200 Smartphone measured spinor angle

17.25 Set of Keys



Figure 17-201 Set of keys measured on own.

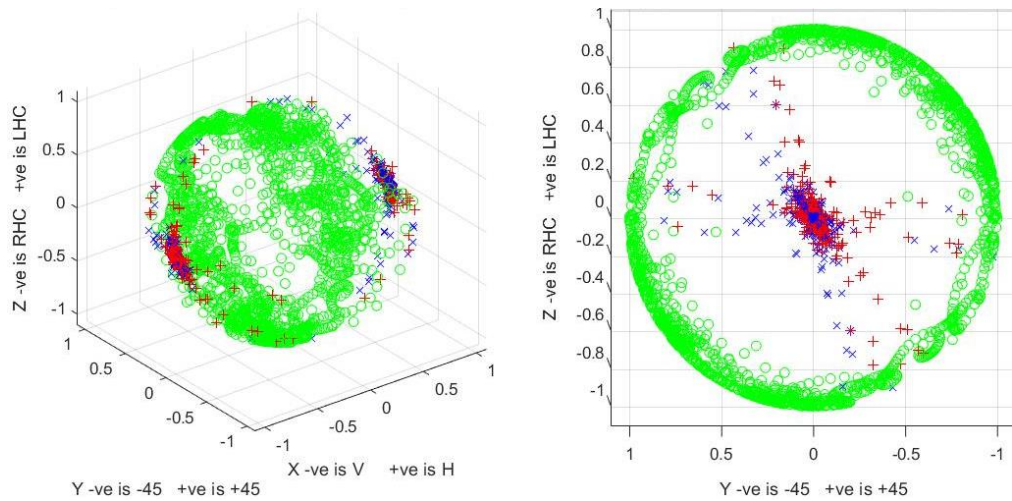


Figure 17-202 Fork plots via measurement for a set of keys

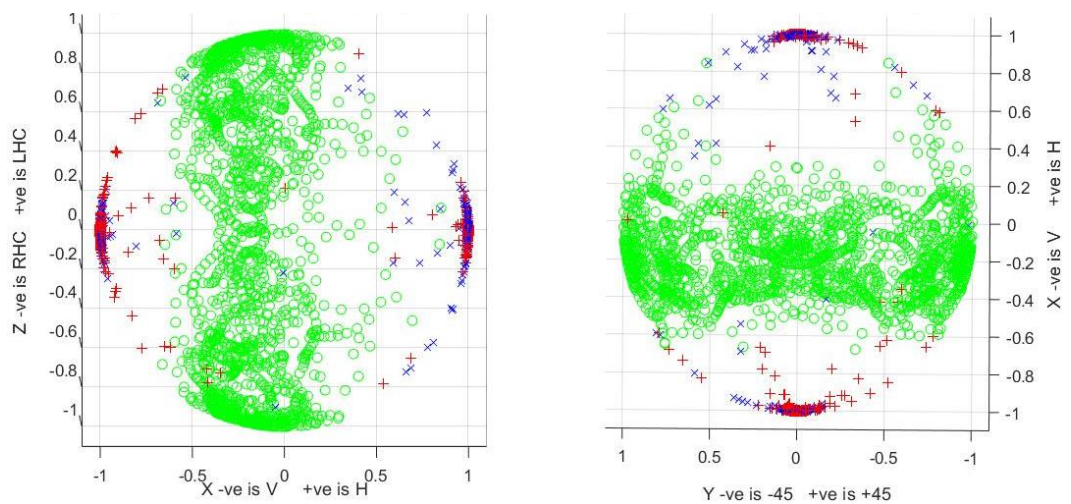


Figure 17-203 Keys fork plots via measurement viewed from the -45° polarisation position (left), from the zenith right

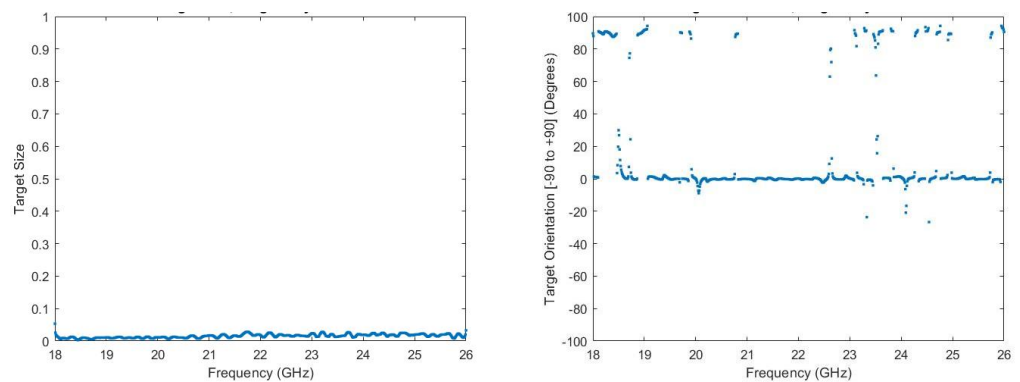


Figure 17-204 Set of keys measured target size left, orientation angle right

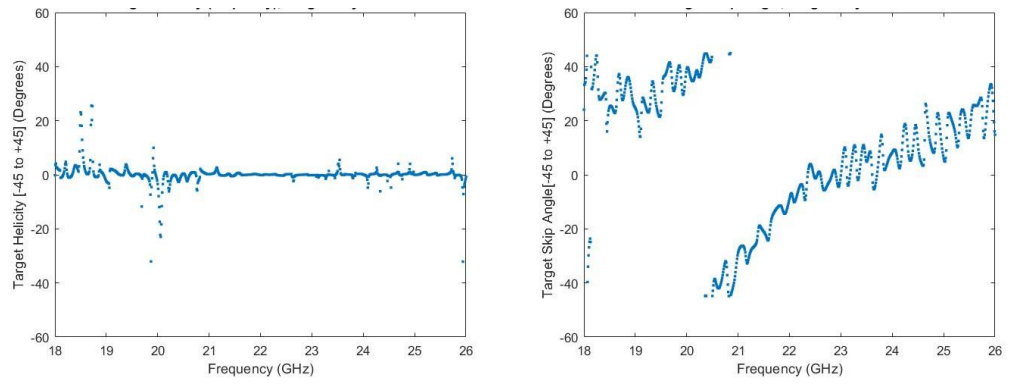


Figure 17-205 Set of keys measured helicity angle left, skip angle right

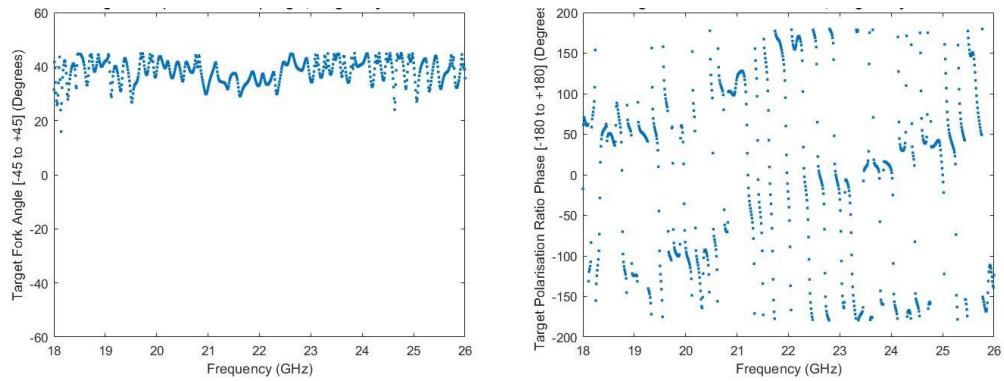


Figure 17-206 Set of keys measured fork angle left, polarisation phase ratio right.

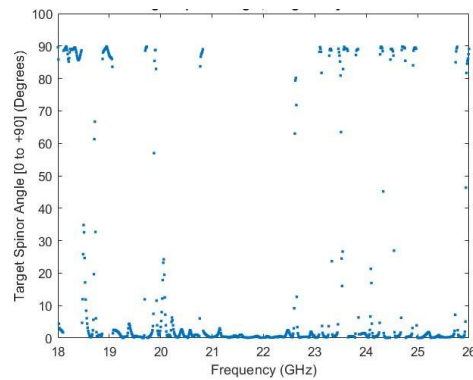


Figure 17-207 Set of keys measured spinor angle